

**Permselective and ion-selective carbon nanopores
and next-generation technologies
for electrochemical water treatment**

Dissertation
zur Erlangung des Grades
des Doktors der Naturwissenschaften
der Naturwissenschaftlich-Technischen Fakultät
der Universität des Saarlandes

von

Yuan Zhang

Saarbrücken
Januar 2022

Tag des Kolloquiums: 19.04.2022

Dekan: Prof. Dr. Jörn Walter

Berichterstatter: Prof. Dr. Volker Presser
Prof. Dr. Markus Gallei
Prof. Dr. Guang Feng

Vorsitz: Prof. Dr. Christian Motz

Akad. Mitarbeiter: Dr. Oliver Janka

Abstract

Owing to an expanding economy and growing population, there is increasing consumer demand for freshwater. However, with global climate change and water pollution issues, there is rising water stress in many countries worldwide. Electrochemical water desalination technologies such as capacitive deionization (CDI) utilize electrical energy to store ions in porous materials and provide energy-efficient water desalination. However, due to the cation and anion exchange process during the charging and discharging processes, CDI is considered suitable for low salinity water desalination (salinity of 1-10 g/L). This dissertation explores novel approaches to next-generation CDI for better desalination performances and water desalination at high ionic strength. In particular, the ability of sub-nanometer carbon pores (ultramicropores) to enable highly efficient CDI even at seawater salinity is demonstrated based on unexpected simulation predictions. This unique ability originates from the energy barrier of ion solvation for pores smaller than the solvation shell. Consequently, uncharged carbon ultramicropores behave ionophobic and overcome the limitation of CDI only to be suitable for remediation of brackish water. Ultramicropores also provide novel perspectives for ion separation via the interplay of intrinsic and kinetic ion selectivity. This work also establishes electrocatalytic fuel cell desalination, whereby conventional fuel cell technology can easily be adapted to generate electricity, heat, and desalinated water concurrently.

Zusammenfassung

Als Resultat der boomenden Wirtschaft und dem weltweiten Bevölkerungswachstum steigt auch der Bedarf an Süßwasser stetig an. Angesichts des globalen Klimawandels und der vorherrschenden Wasserverschmutzung ist die Wasserknappheit längst nicht mehr nur auf einzelne Regionen begrenzt, sondern herrscht bereits in vielen Ländern auf der ganzen Welt vor. Elektrochemische Wasserentsalzungstechnologien wie die kapazitive Deionisation (CDI) nutzen elektrische Energie, um Ionen in porösen Materialien zu speichern und bieten somit die Grundlage für eine energieeffiziente Technologie zur Wasserentsalzung. Aufgrund des Kationen- und Anionenaustausches während des Lade- und Entladevorgangs ist die CDI jedoch nur für die Entsalzung von Brackwasser (Salinität von 1 bis 10 g/L) geeignet. In der vorliegenden Dissertationsschrift werden neue Ansätze für die nächste Generation an CDI zur Verbesserung der Entsalzungsleistung sowie der Wasserentsalzung bei hoher Ionenstärke untersucht. Insbesondere wird auch anhand unerwarteter Simulationsvorhersagen gezeigt, dass Kohlenstoffporen im Subnanometerbereich (Ultramikroporen) eine hocheffiziente CDI selbst beim Salzgehalt von Meerwasser ermöglichen. Diese einzigartige Fähigkeit ergibt sich aus der Energiebarriere der Ionensolvatation für Poren, die kleiner sind als die Solvationsschale. Folglich verhalten sich ungeladene Kohlenstoff-Ultramikroporen ionophob und überwinden die Beschränkung der CDI, so dass sie für die Aufarbeitung von Brackwasser geeignet sind. Ultramikroporen bieten zusätzlich neue Perspektiven für die Ionentrennung durch das Zusammenspiel von intrinsischer und kinetischer Ionenselektivität. Mit dieser Arbeit wird ebenfalls die elektrokatalytische Brennstoffzellenentsalzung eingeführt, wobei die herkömmliche Brennstoffzellentechnologie leicht angepasst werden kann, um gleichzeitig Strom, Wärme und entsalztes Wasser zu erzeugen.

Acknowledgments

First of all, I would like to thank my supervisor, Prof. Volker Presser, who allowed me to work at the Leibniz Institute for New Materials (INM) and has supported me well during my doctoral studies. Thanks to his patience, guidance, and encouragement, I enjoyed my time as a doctoral student and was able to devote myself to the beautiful science world. Having learned a lot from him, I feel lucky to be chosen as one of his students and gained many achievements, including publications and attendance at international conferences.

I would also like to express my appreciation to Prof. Markus Gallei from Saarland University for his supervision and collaboration during my doctoral studies and in being the second reviewer of my doctoral thesis.

Besides, I need to express my deepest gratitude to Prof. Feng Guang for his continuous support, through a lot of fruitful discussions, I have gained a lot of knowledge, and I always feel being inspired and encouraged. Without his help, many excellent works would not have been possible. I feel lucky that I have met him in the journey of science.

In my nearly four years working at INM, I have met many amazing and wonderful people who have supported me and encouraged me to become a stronger person. I would like to thank Dr. Samantha Husmann, Dr. Qingsong Wang, Dr. Juhan Lee, Dr. Hwirim Shim, Dr. Sarah Saleem, Lei Wang, Stefanie Arnold, Tamara Winter, Mohammad Torkamanzadeh, Bowen Dong, Yunjie Li, Panyu Ren for all the thoughtful support both inside and outside INM. Many thanks for the great technical and measurement support to Robert Drumm, Dr. Mesut Aslan, Zeyu Fu, Dr. Kasten Moh, Alexander May, Andrea Jung, Dr. Ingrid Grobelsek, and all members of the INM workshop. The works would have been difficult without the great contribution from the students: Maike Ulbricht, Yang Liu, and Lola Bieber.

Besides, I want to thank my collaborators outside of INM for their kind and strong support for the publications: Dr. John Griffin, Dr. Christian Prehal, Dr. Sheng Bi, and Dr. Luca Cervini. Thanks to their thoughtful discussions and helpful comments, I have broadened my view of the science world. It was an excellent opportunity to network and collaborate with these great scientists worldwide.

Finally, I would like to thank my parents, fiancee, relatives, and friends for their unconditional love during all the difficult periods I went through. I could never be as strong and achieved this far without so much love. I feel blessed to have all of you in my life despite the long distance.

Contents

1. Motivation	1
2. Water treatment: state of the art	2
2.1. Thermal energy-driven desalination technologies	3
2.2. Mechanical energy-driven desalination technologies	4
2.3. Electrical energy-driven desalination technologies	5
2.4. Electrochemical water treatment	5
2.4.1. First Generation: capacitive deionization	5
2.4.2. Carbon materials for water desalination	6
2.5. Cell types	7
2.5.1 Membrane capacitive deionization (MCDI)	8
2.5.2 Asymmetric capacitive deionization	10
2.5.3 Inverted capacitive deionization (i-CDI)	10
2.5.4 Flow electrode capacitive deionization (FCDI)	11
2.5.5 Outlook on capacitive deionization	12
2.6 From capacitive to Faradaic reaction: a nanoconfinement effect	13
2.6.1 Faradaic materials	13
2.6.2 Cell types for Faradaic deionization	15
2.6.3 Second generation: desalination battery	16
2.6.4 Hybrid capacitive deionization (HCDI)	17
2.6.5 Bi-electrolyte	17
2.6.6 Redox electrolyte	18
2.7 Other desalination technologies	19
2.7.1 Microbial desalination	20
2.7.2 Solar energy-driven desalination cells	21
2.7.3 Third generation: chemical energy-driven electrochemical desalination cells	22
2.8 Ion uptake mechanisms	24
2.8.1 Double layer in microporous carbon	24
2.8.2 Classis double layer models: Planner models	24
2.8.3 Donnan model and modified Donnan model	25
2.8.4 Ionic strength influence on permselectivity	27
2.8.5 Pore size effect on ion permselectivity	28
2.8.6 Pore size effect on ion selectivity	32
2.8.8. Ion diffusion influence on the potential window and desalination performance	34
2.9. Electrocatalytic reactions for desalination	37
2.10. Comparison of different electrochemical desalination technologies	38

3. Approach and overview.....	40
4. Peer-reviewed research papers	44
4.1 Effects of pore size on the ion electrosorption and hydrogen/deuterium electrosorption using sodium chloride in H₂O and D₂O.....	45
4.2 Permselective ion electrosorption of subnanometer pores at high molar strength enables capacitive deionization of saline water	60
4.3 Ionophobicity of carbon sub-nanometer pores enables efficient desalination at high salinity.....	84
4.4 Hydration shell energy barrier differences of sub-nanometer carbon pores enable ion sieving and selective ion removal	110
4.5 Polymer ion-exchange membranes for capacitive deionization of aqueous media with low and high salt concentration.....	126
4.6 MXene/activated-carbon hybrid capacitive deionization for permselective ion removal at low and high salinity.....	140
4.7 Particle size distribution influence on capacitive deionization: insights for electrode preparation	162
4.8 Electrocatalytic fuel cell desalination for continuous energy and freshwater generator	175
4.9 From capacitive deionization to desalination batteries and desalination fuel cells.....	190
4.10 Emerging, hydrogen-driven electrochemical water purification	200
5. Conclusions and Outlook.....	207
6. References.....	210

1. Motivation

Although water covers 71% of the earth's surface, only 2.5% of all earthly water is freshwater and primarily exists in glaciers, ice caps, and groundwater.[1] With an ever-growing economy and human population, inadequate access to clean water and sanitation has become one of the most pervasive problems concerning water consumption.[2] Water scarcity continues to grow alongside the progress of climate change.[3, 4] Owing to severe water stress, there exist disaggregations of river basins not only in North Africa and the Near East, but also in North America, Central, and Southern Asia, and on the western coast of Latin America.[5] On average, 10% of the global population lives in countries with high or critical water stress.[5] Water is essential for daily life, industrial needs, agriculture, and food production. An alarmingly increasing quantity of contaminants has entered the global water supply in developing and industrialized nations, ranging from heavy metals to distillates and micropollutants.[2] Prompt action must thus be taken in the coming decades to explore more effective ways of supplying clean water.

There are many different water desalination technologies such as multi-effect distillation (MED), multi-stage flash distillation (MSF), seawater reverse osmosis (SWRO), and electrodialysis (ED).[6-11] These technologies have seen significant improvements over the last decades and dominate today's industrial water desalination sector. However, each technology has certain disadvantages and limitations. More effort is thus required to develop desalination technologies that offer more flexibility, higher energy efficiency, and better performance. Environmental impact and sustainability are also essential requirements to consider. In this work, electrochemical water treatment technologies with mechanism studies and the development of third-generation water desalination technologies are introduced.

2. Water treatment: state of the art

One possible way to address the issue of global water scarcity is to provide clean, potable water via desalination, that is, by removing dissolved salt ions from saline water. Depending on the total dissolved solids (TDS) contained within, saline water can be classified as brackish water (1-5 g/L), seawater and salt lakes (30-40 g/L), or brine water (TDS>100 g/L).[12-14] Most seawater bodies have a TDS value of 30-40 g/L, while freshwater has a TDS value of lower than 1 g/L.[15] Different desalination techniques are applied due to the diversity of water resources. By distinguishing the primary energy input, desalination technologies can be classified as thermal energy-driven, mechanical energy-driven, and electrical energy-driven (**Figure 1**).

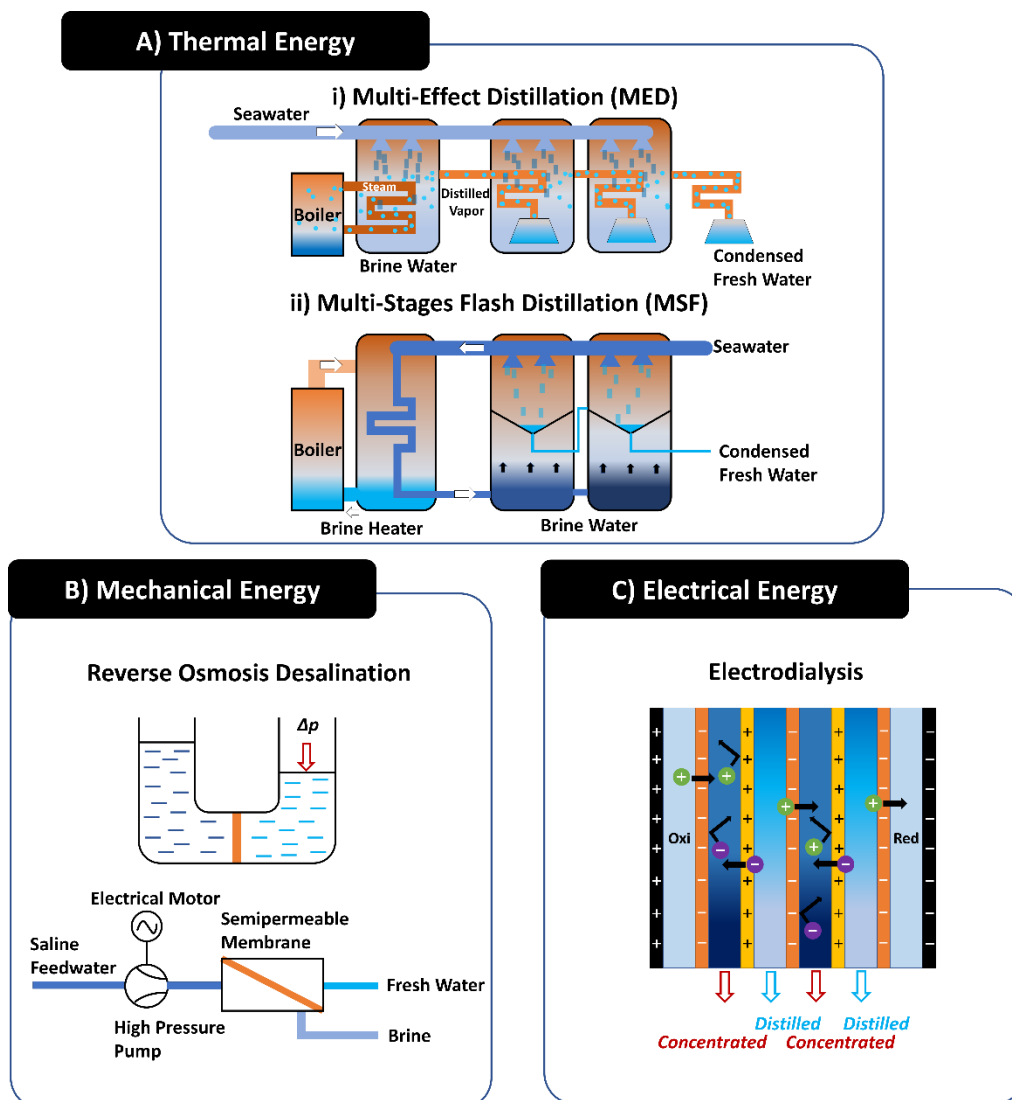


Figure 1: Schematic graphs of the current stage of the art water desalination technologies. They are separated into three categories: A) thermal energy-driven,[16] B) mechanical energy-driven,[11] and C) electrical energy-driven.[17]

2.1. Thermal energy-driven desalination technologies

Water evaporation and condensation are presumably the earliest water desalination methods for producing drinkable water. By applying thermal heat to the saltwater, vapor will form and condense as freshwater. In this case, there are some commonly applied technologies such as multi-effect distillation (MED) and multi-stage flash distillation(MSF).[11]

MED is a technique suitable for seawater desalination. The process is illustrated in **Figure 1Ai**. Seawater is first fed to the effects and heated to form a distilled vapor. The waste heat from the distilled vapor is then used to heat seawater from the next step. This produces more distilled vapor, which then and condenses to become freshwater. Depending on the energy efficiency of the system, the effect level can range from 4 to 21 levels. At the end of the system, room-temperature desalinated water is ultimately produced.[18, 19] MED has a total electricity consumption of 14-21 kWh/m³ with fresh water production of 5000-15000 m³/day.[20]

The working process of the MSF is shown in **Figure 1Aii**. In the MSF process, the feedwater is first heated until it reaches a temperature just below boiling. The hot feedwater is then moved to the next stage via a pressure mechanism where a lower pressure in the first stage draws water from the higher-pressure heating component. In the first stage, the heated feedwater is then converted to vapor due to the decrease in pressure. In this process, the ions in the newly vaporized feed water collect in a brine solution at the bottom of the first stage. The vaporized feedwater in the first stage also works to vaporize fresh feedwater that is fed into the top of the second stage. This further separates the ions from the introduced feedwater, which leads to a collection of more ion-free vapor. The vapor is then made to condense into ion-free water. Via two separate channels, the ion-free water and brine collected in the first stage is input into the second stage via an even lower pressure, and the process repeats until all the condensed freshwater is collected.[18] Due to its economic scale and ability to apply low-temperature steam, MSF is considered an energy-intensive technology with a total electricity consumption of 19-27 kWh/m³. MSF has a fresh water production of 20000-70000 m³/day for each plant and is currently widely applied in the middle east.[18, 20, 21]

2.2. Mechanical energy-driven desalination technologies

The vapor compression (VC) distillation process is often applied with other distillation processes like MED. To evaporate seawater, the heat energy is generated by compressing the vapor. In the next step, the vapor is condensed while the heat from the vapor is used to vaporize the brine water.[18, 20]

Another technology that requires mechanical energy is filtration technology. In this case, freshwater is separated from feedwater using a semipermeable membrane with a certain porosity depending on the size of the species in the water. Depending on the pore size, the membranes can reject different kinds of particles and ions via microfiltration (MF), ultrafiltration (UF), and nanofiltration (NF). Membranes used in reverse osmosis (RO) technology can also reject saltwater ions.[15]

When two solutions with different concentrations are separated by a semipermeable membrane (**Figure 1B**), the water contained within flows spontaneously from the high concentration side to the low concentration side. To balance the energy potential, external pressure must be applied at the high concentrated side. If the pressure is higher than the osmosis pressure, the water flow will be inverted. In this way, water can be extracted from highly concentrated water.[22] For seawater desalination (SWRO), the feedwater pressure ranges from 6000 kPa to 8000 kPa, while for brackish water desalination, the applied pressure ranges from 600 kPa to 3000 kPa. The RO process also has a higher energy efficiency compared to thermal energy-based technologies[23] in that the energy consumption of the former can reach between 4 kWh/m³ to 6 kWh/m³,[20] which is lower than MSF and MED.[20, 23] Thus, RO has become a worldwide leading technology in small and large scale applications.[24] However, membrane fouling and contamination remain challenges to the longevity of RO devices and installations.[15, 25]

2.3. Electrical energy-driven desalination technologies

Electrodialysis (ED) has been employed for over 60 years to treat industrial water and brackish water.[6-9] In an electrodialysis stack, there are two streams of water separated by ion-selective membranes. Under an applied electric potential, the water split into H₂ and O₂ at the two electrodes. To balance the charge, the ions are then transported through ion exchange membranes (IEMs) to the other side of the water channel (**Figure 1C**). As a result, one stream of water becomes desalinated while the other stream increases its concentration of ions. Over the past few decades, the performance of ED has been improved in that it can be scaled up and can desalinate brackish water with concentrations of up to 15 g/L. ED enables water desalination with an energy consumption of 0.7-5.5 kWh/m³.[20]

Apart from ED, other electrochemical desalination processes are being studied to achieve more energy-efficient and effective water treatment in different water conditions. Such examples include first-generation capacitive deionization (CDI), second generation Faradaic deionization (FDI; also known as desalination batteries), hybrid capacitive deionization (HCDI), and other techniques. Moreover, third-generation desalination technologies that utilize chemical energy and renewable energies such as solar power, biomass, and hydrogen, have been studied in recent years. These aspects will be introduced in the following sections.

2.4. Electrochemical water treatment

2.4.1. First Generation: capacitive deionization

Conventional capacitive deionization (CDI) charges one pair (or n pairs) of porous carbon electrodes in contact with flowing feedwater. By applying an electrical voltage between the two electrodes, the cations and anions in the feedwater will be electroadSORBED in carbon (nano)pores to decrease the ion concentration in the effluent stream.[26, 27] Unlike thermal distillation, reverse osmosis, and electrodialysis, CDI allows for straightforward energy and electrode recovery.[28] The immobilized ions will be released during the discharge process by shortcircuiting the electrode pair, lowering the cell voltage, or inverting the cell polarity.[26, 29] Due to the energy and electrode recovery possibility, CDI has emerged as a potentially energy-efficient and cost-effective technology for water desalination.[28] Since the desalination capacity of CDI is strongly related to the specific surface area and pore volume,[30, 31] carbon materials of different desalination capacities have been applied to achieve a higher desalination capacity.

2.4.2. Carbon materials for water desalination

Since Murphy and Caudle applied a symmetric carbon-carbon electrode pair to study the first CDI setup in 1967,[32] a variety of studies on carbon materials have been reported for capacitive deionization applications. It is commonly believed that [26, 29] the carbon materials should have a high specific surface area and pore volume for water desalination. Mesoporous carbons and microporous carbons have been widely explored and studied as a result. According to the IUPAC definition, pores wider than 50 nm are called macropores, pores of intermediate width between 2-50 nm are called mesopores, and pores narrower than 2 nm are called micropores.

Mesoporous carbons have been studied for supercapacitor applications due to their fast inner-pore ion diffusion, which increases cycling stability and improves rate handling ability.[33, 34] The mesopore structure will also enhance the desalination rate in CDI applications. For highly ordered carbon-like carbon nanotubes (CNT), the sp^2 hybridization of carbon will build up a layered structure with van der Waals bonding between the layers.[35, 36] The mesopores of CNT are resulted from the interparticle space due to the small particle size. Apart from CNT, ordered mesoporous carbon can be synthesized by applying hard and soft template-based synthesis and self-assembling block co-polymer surfactant with carbon precursors.[37-41]

Microporous carbons are commonly used in supercapacitors, metal-air batteries, electrocatalysis, and desalination studies due to their high specific surface areas (up to more than $3000\text{ m}^2/\text{g}$) that lead to higher specific capacitance.[31, 42] One strategy for producing microporous carbon is chemical/physical activation under heat treatments of the available carbon sources such as coal, petrol side products, and biomass using acid, base, water steam, or CO_2 as activating agents.[43-45] This method has the advantages of low cost and naturally renewability, however, it involves a lot of impurities in the carbon materials, a wide pore size distribution is often obtained,[46] Another synthesis routine is chlorination of metal carbides under heat treatments, metal atoms are selectively extracted from the carbide, resulting in a porous carbon matrix with a temperature-dependent pore size distribution.[47] Polymer-derived carbon materials are also of great interest due to their flexibility in creating hierarchic pores and controlling pore size.[42, 48, 49] By synthesizing polymers with a controlled particle size as the precursor and followed by pyrolysis and chemical/physical activation, the microporous carbon with controlled particle size can be synthesized. Thus, a

narrow pore size distribution and desirable rate handling abilities and longevities can be achieved.[42] From a capacitance perspective, although having a high specific surface area is very important in increasing the specific capacitance of carbon material, some other aspects (such as pore size distributions, pore volumes, confinement curvature, wettability, and electrical conductivity) also influence the electrochemical performance of the carbon materials.[46] Raymundo-Piñero et al. concluded that there is an optimal subnanometer pore size to achieve a high specific capacitance in different electrolytes (0.7 nm for aqueous and 0.8 nm for organic electrolyte).[50] In the same year, Chmiola et al. applied carbon material at different average pore sizes and shows smaller average pore sizes can contribute to higher ion storage capacitance.[51] For desalination aspects, this optimal average pore size for high charge efficiency and desalination capacity is smaller than 0.6 nm.[52]

2.5. Cell types

Due to the flexibility of adjusting the cell structure, CDI cells can be equipped with different kinds of electrode materials and ion-exchange membranes (IEM). [32] CDI cells have been applied not only for water desalination but also selective ion removal.[31, 53] The cell types for different capacitive deionization techniques are illustrated in **Figure 2**. The most commonly studied type is CDI, which utilizes a pair of porous electrodes on two sides of a feedwater flow. Under an applied cell voltage, the ions in the feedwater are electro-adsorbed into the pores of the electrode materials.[26, 32] A variety of cell structures have been developed to achieve different goals for water treatment (**Figure 2**).

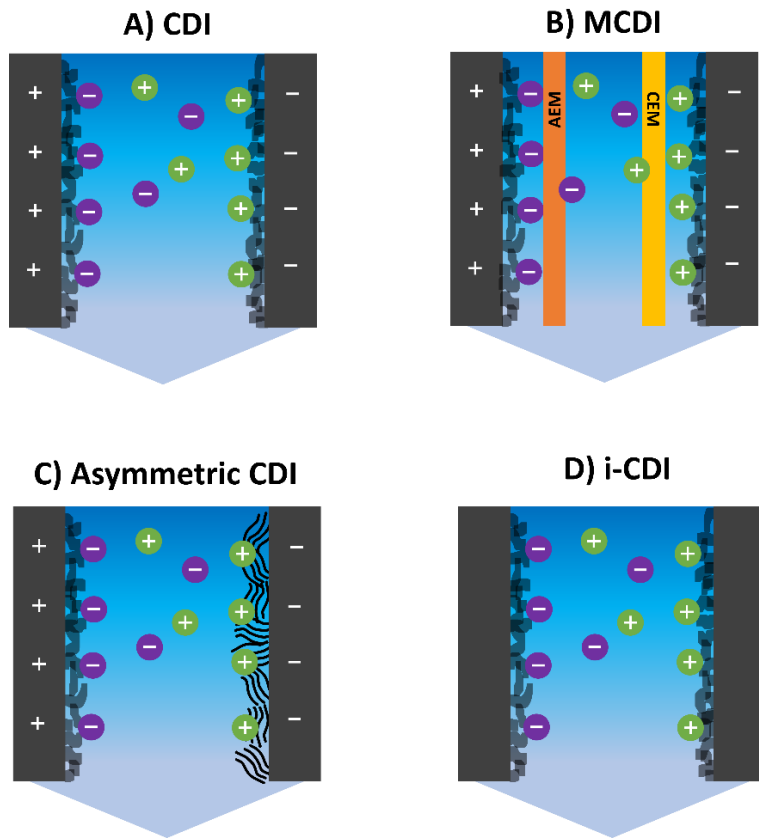


Figure 2: Structures of four different types of CDI. A.) typical CDI cell; B) MCDI; C) an asymmetric CDI cell, and D) i-CDI.

2.5.1 Membrane capacitive deionization (MCDI)

To improve the desalination performance and decrease the influence of co-ion ejection, a pair of ion exchange membranes can be added to the electrodes and separate the feedwater flow. In this case, the cation exchange membranes (CEM) are at the negative electrode and the anion exchange membrane (AEM) at the positive electrode. This technique is called membrane capacitive deionization (MCDI). In this case, a higher charge efficiency and a higher desalination capacity can be obtained. This technique can also be applied in seawater level concentration.[54, 55] MCDI has the potential to be more energy-efficient compared to reverse osmosis and distillation under low salt concentrations.[56]

Polymer-based ion-exchange membranes (IEM) are made from polymers with ionizable functional groups serving as the fixed charges on the polymer backbones.[57, 58] With cation fixed charges, anions can be transported between the backbones (AEM). Cations can then be transported between the backbones (CEM) with anion fixed charges. Thus, ion transportation through the IEM is strongly dependent on the electrostatic interactions between the fixed charge groups and the transported ions.[59-61] Due to different ion distributions between the polymer IEM phase and the solution phase, an electrical potential called Donnan potential is generated at the membrane/solution interface, excluding the co-ions (Donnan exclusion). The Donnan potential can be expressed in **Eq. (1)**:[59, 62]

$$E_{Don} = \Psi^m - \Psi^s = \frac{RT}{F} \ln \left[\frac{a_g^s}{a_g^m} \right] = - \frac{RT}{F} \ln \left[\frac{a_c^s}{a_c^m} \right] \quad \text{Eq. (1)}$$

where Ψ^m and Ψ^s are the electrical potentials of the polymer membrane and the solution, while a_g^s and a_g^m are the thermodynamic activities of the counter-ions in the solution and the membrane. The terms a_c^s and a_c^m represent the activity of co-ions in the solution and membrane. According to this equation, a stronger electrical potential is obtained when there are more fixed charges in the IEMs that lead to a higher difference between a_g^s and a_g^m . A better ion permselectivity can thus be obtained. However, this would require adding more ionogenic groups during the synthesis that makes the IEM more hydrophilic and swollen in the solution.[59] Therefore, facile control of the IEM synthesis to obtain feasible permselective and ion transport properties are of significant importance.

While polymer-based ion-selective membranes are considered to have limited ion permselectivity, ceramic superionic conductors, which have been broadly investigated for batteries and fuel cells,[63, 64] are also of great interest in the field of electrochemical water desalination. Due to the unique crystal structures, the ions hop from one lattice site to another, which results in high ionic conductivity and high ion permselectivity for particular ions such as Na^+ (NASICON) and Li^+ (LISICON).[65]

2.5.2 Asymmetric capacitive deionization

Different electrode materials can also be applied depending on the ability for different ion uptake and the number of capacitive potential windows in aqueous media. This type of cell is called asymmetric capacitive deionization.[66, 67] Different electrode modifications on both electrodes with functional groups can prevent co-ion repulsions and significantly improve the desalination charge efficiency.[67, 68] The addition of metal oxides can enhance the electrochemical stability, and prevent carbon oxidation.[69] Insertion-type Ti_3C_2 MXene has a high cation permselectivity, which enables cation uptake under a high ionic strength. Therefore, pairing Ti_3C_2 MXene with activated carbon with proper mass balancing would greatly improve the desalination performance at the seawater molarity ionic strength.[66]

2.5.3 Inverted capacitive deionization (i-CDI)

For CDI that apply different porous carbon materials, carbon oxidation is an undesirable side reaction that is caused by water splitting when the cell's electrical potential window is inappropriate or the electrode material mass balance is not properly applied. This would result in lower cell cycling stability. In addition, the desalination process always involves electrical input, and the electrodes cannot uptake ions without applying a cell voltage. To address these issues, the inverted-CDI (i-CDI) applies capacitive materials modified with surface positive (negative electrode) and negative (positive electrode) charges. The ion removal process occurs not during the charging of the cell (like in CDI cells) but during the discharging of the cell.[70-72] In the first i-CDI study in 2015, an i-CDI system that included carbon xerogel (CX) with/without surface charges as electrodes were performed for over 600 h. This is approximately a 530% increase in lifetime compared to a regular CDI system operated under similar conditions. The oxidized anodes in the i-CDI system can suppress carbon oxidation in an aqueous solution, which leads to high desalination performance.[72] To improve the desalination performance of the i-CDI cell, the potential of both the cathode and anode must be managed to suitable potential regimes. The zeta potential of the charge-modified electrodes would affect the ion adsorption properties, and is reflected by the shift of the electrode potential zero charges (E_{PZC}) via *Eq. (2)*:

$$\zeta = k_1(pH_{PZC} - pH) = k_2(E - E_{PZC}) \quad \text{Eq. (2)}$$

In **Eq. (2)**, ζ is the zeta potential, pH_{PZC} is the point of zero charge, E_{PZC} is the potential of zero charge, E is the electrode potential, and k_1 and k_2 are positive constants. According to this equation, a decrease in the ζ and pH_{PZC} would lead to an increase of E_{PZC} and vice versa.[73, 74]

2.5.4 Flow electrode capacitive deionization (FCDI)

Although capacitive deionization (CDI) has the advantage of low cost and high energy efficiency under a low or moderate salt concentration,[32, 75] the operation of a CDI cell often involves charging (desalination) and discharging (salination) process. This requires careful consideration of process control and scaling up the CDI process to separate the desalinated and salinated water. To overcome the limitations of CDI, flow electrode capacitive deionization (FCDI) was later developed. Introduced in 1996, the concept of the slurry electrode is a suspension of carbon particles that can transfer charges from an electrochemical cell to a reactor.[76] Jeon et al. applied a process that involved flowing carbon electrode material-suspended saltwater between the ion-exchange membranes and current collectors through a spacer. The resulting continuous ion uptake process shows that the FCDI system can remove 95% of salt from a seawater-like salt concentration of 32.1 g/L.[77] Later, the FCDI system was classified into batch mode and continuous mode by Gendel et al. (**Figure 3**).[78] The continuous mode operation enables desalination, while an electrode slurry under the continuous model further assists in saltwater regeneration. By applying a desalination cell and a concentrating cell simultaneously, the continuous operation mode results in a desalination efficiency of more than 99% for the initial feedwater concentration of 1 g_{NaCl}/L.[78] Porada et al. demonstrated a capacitive mixing technology that utilizes cylindrical ion-exchange membranes as flow channels and continuously extracts energy during the ion removal process.[79] Rommerskirchen et al. also developed an FCDI system using a single flow-electrode and a single model to realize continuous desalination operation with a desalination efficiency of 70% and a water recovery ratio of 0.8.[80] Many factors are essential for the desalination performance of the FCDI system, such as particle dispersion,[81], the feedwater concentration,[82] electrical operation mode,[82, 83] mass loading, and low rate of electrode slurries.[79]

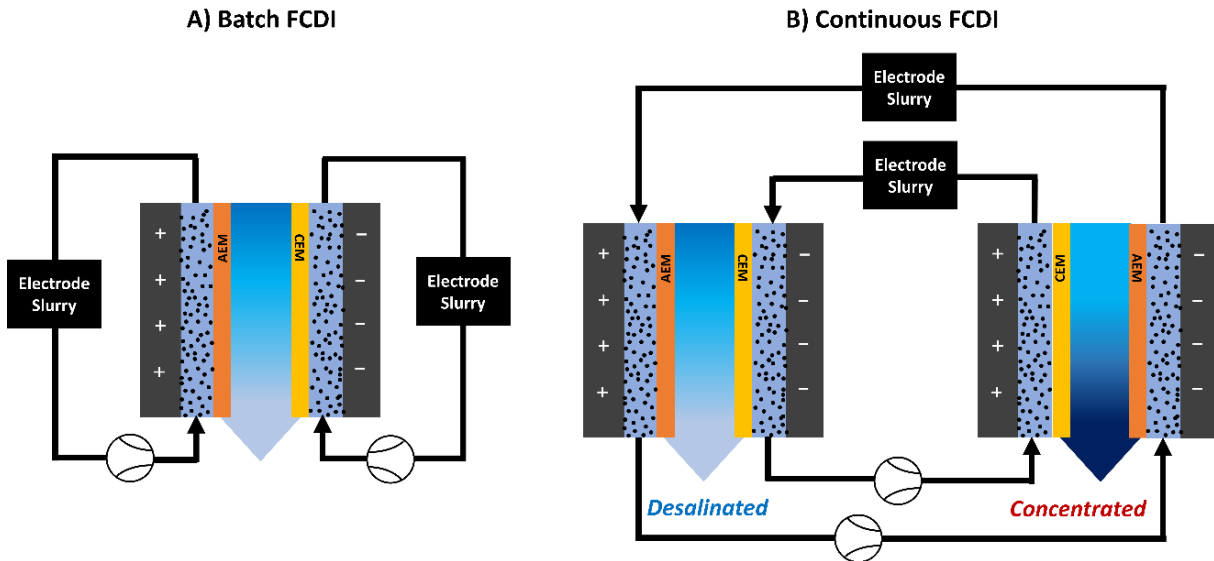


Figure 3: Two FCDI structure types adapted from literature.[78] A) a batch mode CDI B) an FCDI system with continuous operation.

2.5.5 Outlook on capacitive deionization

For electrochemical water desalination applications, CDI is known to be promising for the application in low molarities.[32, 75, 84] Although many studies have shown that specific surface area, specific pore volume, pore size, and pore curvature are important factors in improving the desalination performance, pore size, and carbon particle size are also important parameters to achieve better desalination performance. Recently, CDI was studied for direct seawater desalination and has been proved to be efficient when sub-nanometer porous carbon materials are applied.[52, 85] Although most MCDI studies are focused on the desalination of water at low molarity, MCDI for seawater molar strength is also studied.[55] The desalination performance, especially charge efficiency, is strongly influenced by the salt concentration, voltage operation window, and permselectivity of the ion-exchange membranes. For i-CDI, the E_{PZC} modification of the electrodes can enable a longer lifespan for desalination with lower energy consumption.[86] As for FCDI, the desalination performance is related to the electric conductivity of the electrode suspension, the kinetic effects of ion diffusion, the mass transportation of the electrode, and the saltwater flow rate. Different operation modes (like batch mode and continuous mode)[78] can also influence desalination performance.

The CDI technique enables selective ion removal via carbon material with different subnanometer pore sizes and applying different cell voltages for ion separation applications. This can also be achieved by MCDI, which selectively removes ions by adding selective ion-exchange membranes.[87-89]

2.6 From capacitive to Faradaic reaction: a nanoconfinement effect

2.6.1 Faradaic materials

Due to the cation and anion exchange process during the cycling process of a CDI operation, the desalination performance is decreased when saltwater of higher concentration is applied. This phenomenon would lead to lower desalination capacity, lower charge efficiency, and is not energetically efficient.[52, 90] The limited desalination capacity is related to the intrinsic ion storage capacity of the porous carbon materials,[91] which requires a large number of electrode pairs for CDI application. The parasitic electrochemical reactions such as water splitting and surface oxidation would also deteriorate the electrode material, thereby changing the E_{PZC} and leading to a shorter lifespan and lower desalination performances of the system.[69] To address these issues, Faradaic materials were considered for electrochemical desalination applications due to their high ion storage capacity and intrinsic cation/anion permselectivity. There are three types of electrochemical faradaic reactions: interface redox, insertion type, and conversion type (**Figure 4**).

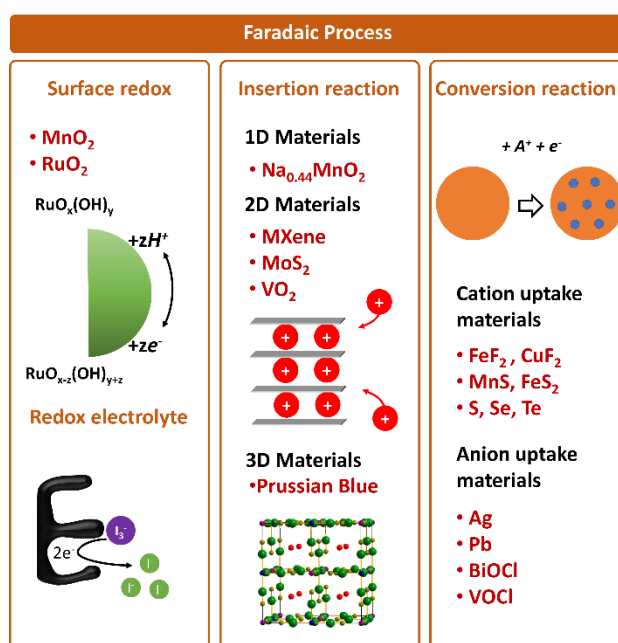


Figure 4: Different types of electrochemical faradaic reactions. Figure adapted from literature.[91, 92]

Interface redox reactions can be separated into two categories: surface redox reactions and electrolyte redox. For surface redox reactions, charged species come to the surface of the electrodes from the bulk solution and transfer/receive electrons from the electrode. This charge transfer process can either have or not have a kinetic limiting effect. For example, RuO₂ and MnO₂ show rectangular cyclic voltammograms (CV) shapes.[92-95] Redox polymers like poly(vinyl ferrocene) show battery-like peaks with reversible redox peaks.[96] For the electrolyte redox reactions,[97] the redox species are in the electrolyte and the charge transfer process is at the electrode/electrolyte interface. Because this system is limited by the kinetics of ion diffusion from the bulk electrolyte to the electrode surface, it thus has a battery-like CV shape.[98-100]

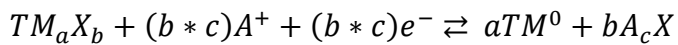
Insertion-type materials have interstitial sites that allow ion insertion and interaction with the host materials. The CV shape for these materials can both be capacitor-like or battery-like.

For insertion type materials, depending on the ion transport type, there are one-dimensional insertion site materials such as LiFePO₄, tunnel structured manganese oxide, two-dimensional materials such as MXenes,[101] transition metal dichalcogenides (TMDs),[102-104] layered transition metal oxides (TMOs),[104] and three-dimensional insertion types materials such as Prussian blues[105] and polyanionic phosphates.[106]

Due to the properties of high theoretical capacity, high energy density, and low toxicity, conversion type materials are regarded as a promising candidate not only for battery research,[107] but also for electrochemical water desalination research.[108, 109] These materials generally have a high theoretical capacity ranging from 500 to 1500 mAh/g.[107]

The conversion-type materials can be transition metal compounds such as transition metal oxides, sulfides, fluorides, phosphides, and nitrides.[107] The reaction can be expressed as in

Eq. (3):



Eq. (3):

Where TM is transition metal, X is anionic species, and A is a cation.

Some chalcogen and halogen compounds can also undergo conversion reactions, which can be expressed in **Eq. (4):**[107] $X + aA^+ + ae^- \rightleftharpoons A_aX$

Eq. (4):

Apart from cations, anions can be stored in conversion-type of materials such as Ag[109], Bi,[110] BiOCl,[111, 112], and VOCl [113].

2.6.2 Cell types for Faradaic deionization

Due to the different Faradaic reaction potential windows and different reaction conditions of the Faradaic materials, Faradaic materials often require particular consideration when being paired with a CDI material. Therefore, careful the desalination cell must be designed to maximize the ion uptake abilities of the system (**Figure 5**).

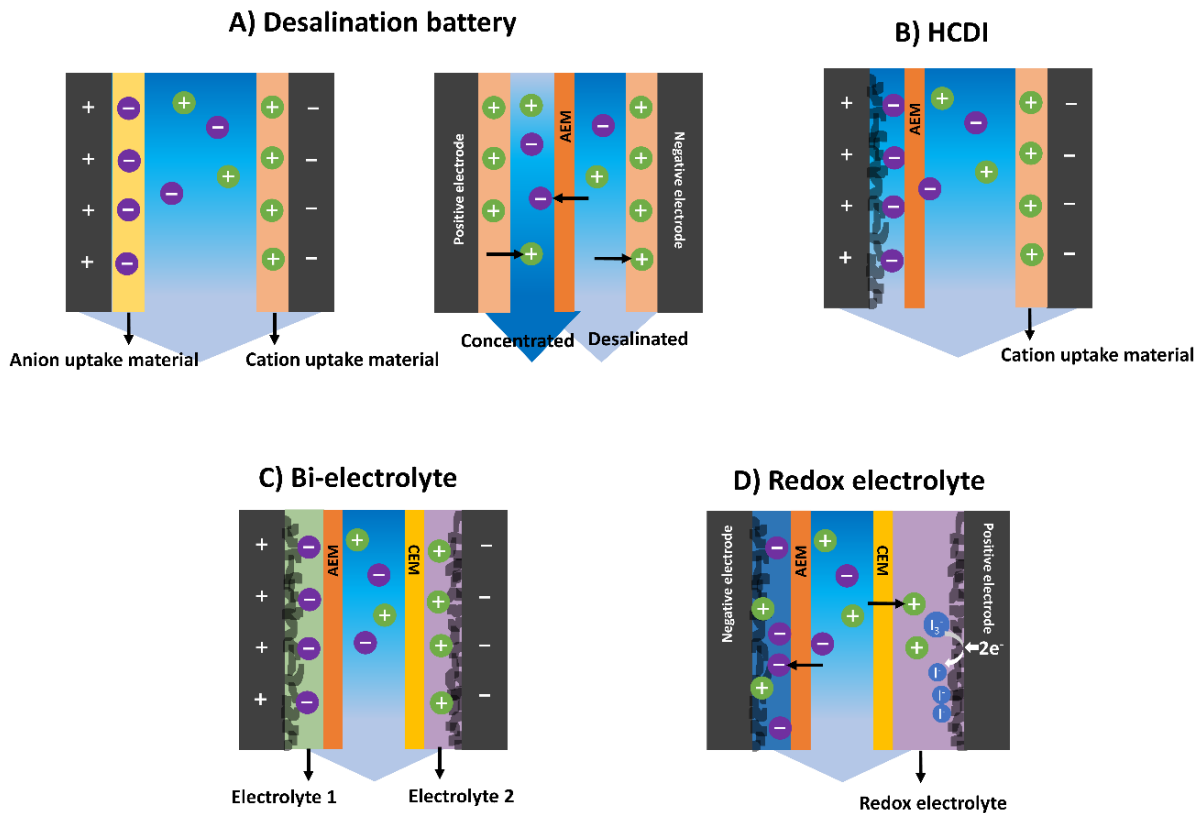


Figure 5: Structures of different types of Faradaic deionization (FDI). A) Desalination battery; B) hybrid capacitive deionization (HCDI); C) bi-electrolyte CDI, and D) redox electrolyte applied for water desalination.

2.6.3 Second generation: desalination battery

In 2012, Pasta et al. demonstrated the concept of “desalination battery”. In this work, they applied $\text{Na}_{2-x}\text{Mn}_5\text{O}_{10}$ nanorods and Ag/AgCl as an electrode pair to uptake Na^+ and Cl^- separately and achieved 20% salt removal with an energy consumption of 0.29 Wh/L [114]. Due to the intrinsic cation/anion permselectivity and high ion storage capacity, desalination batteries have become a very promising desalination technology.[115]

One type of desalination battery consists of a cation storage electrode, a feedwater channel, and an anion storage electrode (**Figure 5A**). When the electrochemical potential for cation storage is lower than for anion storage, the desalination battery can desalinate the feedwater by a charging process. It then recovers the electrode and releases the ions during the discharging of the cell.[116]

Another type of desalination battery is composed of a pair of cation and anion storage electrodes and one ion-exchange membrane to separate two water flow chambers (**Figure 5A**). This type of desalination battery is called a rocking chair desalination battery.[105] By one ion species uptaking/releasing from the same electrode type, the cell can desalinate water in one channel and recover saltwater in the other. This concept was first introduced in 2012, Grygolowicz-Pawlak et al. proposed an electrochemical system for efficient NaCl removal by applying Ag/AgCl electrode to remove chloride ions and a Nafion membrane to transport way sodium ion to balance the charge.[117] In 2016, Smith et al. simulated the Na-ion desalination (NID) battery model and predict the desalination performance (80% recovery efficiency with 700 mM NaCl influent).[118] Different materials for both cation (NID) and anion (CID) storage were later studied.[105, 109, 119]

2.6.4 Hybrid capacitive deionization (HCDI)

The first work of applying capacitive material and faradaic materials in one desalination cell was developed in 1960 by Blair and Murphy, they used carbon and Ag-modified carbon material to remove cation and anion at the two electrodes, separately.[120] In 2014, the concept of asymmetrical hybrid capacitive deionization (HCDI, **Figure 5B**) was introduced by Lee et al. by applying $\text{Na}_4\text{Mn}_9\text{O}_{18}$ as a negative electrode for cation removal and activated carbon (AC) as a positive electrode for anion adsorption instead of an expensive Ag/AgCl electrode.[121, 122] By capturing Na^+ via intercalation into the lattice of $\text{Na}_4\text{Mn}_9\text{O}_{18}$ electrode, this type of technique shows a much higher desalination capacity (31 mg/g) compared to a typical CDI system (14 mg/g) under a 1.2 V cell voltage in a 580 mg/L NaCl solution.[122] More Faradaic materials were later explored in this technology such as Prussian blues,[123] $\text{Na}_{0.71}\text{CoO}_2$ (NCO),[124] $\text{Na}_{0.7}\text{MnO}_2$ (NMO),[125] $\text{NaTi}_2(\text{PO}_4)_3$ (NTP),[126] $\text{Na}_3\text{V}_2(\text{PO}_4)_3$ (NVP),[127] TiS_2 ,[102] and MoS_2 [103].

2.6.5 Bi-electrolyte

For electrochemical water desalination techniques, one limiting parameter is that the water-splitting voltage window and electrochemical water desalination operation beyond the voltage window of 1.2 V would be critical for long-term operations.[128] An organic electrolyte can be applied to increase the ion storage ability and voltage window.[129] For the desalination approach, a side-channel filled with organic propylene carbonate and a

middle channel with brackish water separated by a polymer-based ion-exchange membrane was first applied by Kim et al. (**Figure 5C**). The first electrochemical work on a bi-electrolyte system has achieved a desalination capacity of 64 mg/g at an extended cell voltage of 2.4 V.[130] Based on this technique, the Faradaic desalination process is no longer limited to cathode battery materials that fit the water splitting potential window. Anode materials with much higher charge storage capacity can also be applied for Faradaic applications. Arnold et al. applied alloying reaction type Sb as sodium uptake material soaked in 1 M NaClO₄ in EC/DMC + 5% FEC non-flow organic electrolyte, used a NASICON membrane to separate the water and organic electrolyte phases, and used activated carbon cloth (ACC) as an anion uptake material. This type of HCDI cell achieves an average desodiation capacity of 294 mg_{Na}/g_{Sb} with a charge efficiency of 74% at the voltage range of -2 V to +2 V in 600 mM NaCl solution.[108]

2.6.6 Redox electrolyte

Compared to a capacitive deionization CDI system, one challenge for Faradaic deionization (FDI) is the intrinsically low desalination rate due to the limited ion diffusion kinetics within the solid electrode structures.[115] To enhance the system's desalination rate and have a high desalination capacity, different redox electrolytes have been investigated. By applying dissolved redox-active ions, the ions will be adsorbed on the electrode surface and have charge transfer at the solid-liquid interface of the electrode when applied with an electrical force field. The reaction kinetics for the redox electrolyte system is much faster due to the short ion diffusion length at the surface of the electrodes and faster ion diffusion in the bulk electrolyte compared with ion diffusion in the interstitial crystal structure in the solid phase of the electrode.[131-133] Owing to their high charge storage capacity, high reaction kinetics, and high cycling stabilities, redox electrolytes have attracted great attention in the energy storage research field.[97-100, 134-137] For water treatment, the redox couples must be carefully selected to avoid parasitic reactions and improve the cycling stabilities of different systems.

As is shown in **Figure 5D**, By applying the bi-electrolyte desalination cell structure, redox electrolytes can also be applied for water desalination studies. Lee et al. used activated carbon cloth as electrodes, applied NaI as redox electrolytes, and separated feedwater via a cation-exchange membrane (CEM). With an activated carbon counter electrode and an

anion-exchange membrane, the cell has a desalination capacity of $69 \text{ mg}_{\text{NaCl}}/\text{g}_{\text{electrode}}$, stable performance for over 120 cycles, low energy consumption of 1.63 Wh/L, and a high water production rate of $25 \text{ L/m}^2\text{h}$ for seawater desalination.[131] For a redox electrolyte application in a bi-electrolyte system, the permselectivity of the ion-exchange membranes is very important in preventing water contamination that results in redox ion diffusion into the feed water. In the later work from Lee et al., a NASICON membrane is applied. With activated carbon electrodes and a 600 mM NaI non-flow redox electrolyte, the system has a desalination capacity of $87 \text{ mg}_{\text{NaCl}}/\text{g}_{\text{electrode}}$, a charge efficiency of 81%, and an observed stable performance for more than 400 cycles.[138]

2.7 Other desalination technologies

Electrochemical desalination research has greatly shifted from capacitive materials to Faradaic materials because the latter offer higher capacity, compatibility with high saline concentrations, and the perspective for effective ion separation. Through this line of work, the desalination capacity of these materials has been improved from around 10 mg/g to more than 200 mg/g.[91] Due to the intrinsic limitation of the ion storage capacities of the Capacitive/Faradiac materials, however, a discharge process is always required for electrode recoveries. Furthermore, these ion storage materials for desalination applications require high electrical energy input. To further improve the desalination performance of these electrochemical desalination techniques, new types of desalination methods that apply solar-redox or electrocatalysis reactions to drive desalination have been developed (**Figure 6**).

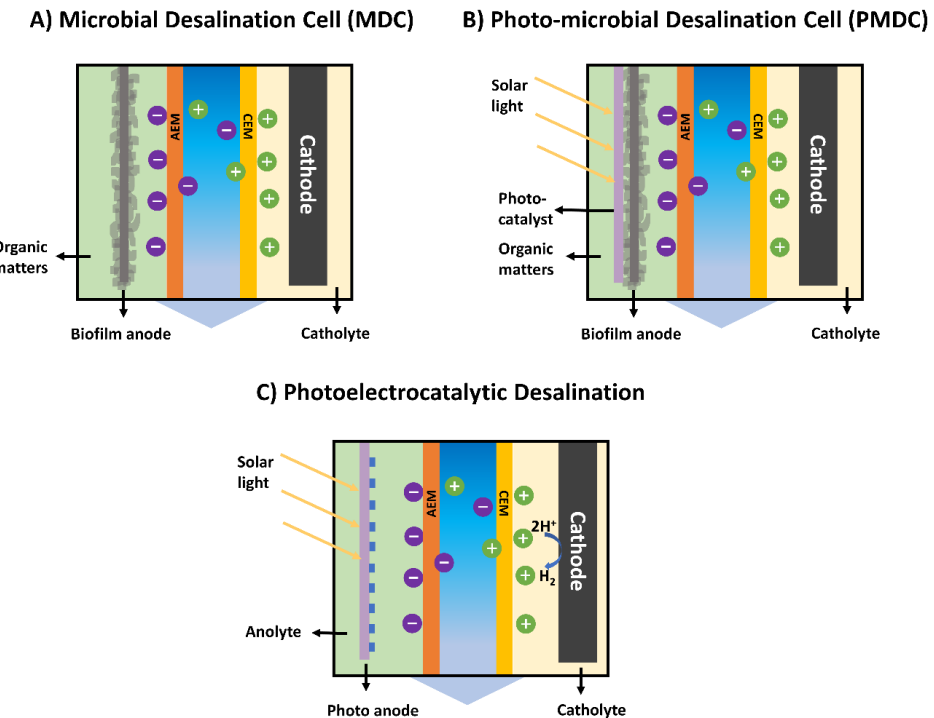


Figure 6: Structural development of desalination cells from bio-materials to photoelectrocatalytic materials. A) Microbial desalination cell (MDC); B) photo-microbial desalination (PMDC); C) photoelectrocatalytic desalination.

2.7.1 Microbial desalination

Since 2009, several studies have been applying bacteria as a current generator for water desalination applications.[139] This type of cell is called a microbial desalination cell (MDC). Inspired by the integration of microbial fuel cells (MFC) and electrodialysis (ED), water desalination can be achieved using bacteria and organic matter instead of electrical energy input or high water pressure energy input (**Figure 6A**). By applying an AEM adjacent to the bacteria biofilm anode and a CEM adjacent to the cathode with K₃Fe(CN)₆ as redox-active catholyte, the ions in the saltwater of the middle channel will be transferred to the two electrode chambers. This process is triggered by the current produced by the bacteria on the anode side and the redox reaction on the cathode side and ultimately results in a full desalination process.[139] In this way, this technique can offer water desalination, wastewater treatment, and electricity generation.[140] MDC reduces energy consumption and greenhouse gases emissions compared to conventional processes since it involves direct chemical energy usage from organic matter.[141] Later studies have reported improvements in the MDC system performance, including improving materials designs,[142-144] cell designs,[145, 146] and operating parameters [147].

There are performance limitations for the MDC system, namely the drastic change in internal resistance during the desalination process, the long starting time, the low pH variation tolerance of the bacteria on the biofilm, and limited potential that can be applied to drive ion migrations that leads to low desalination efficiencies.[141] While most of the works use small volume desalination (<300 mL), only a few works report a volume of over 1 L.[148] For example, there exists a 100 L pilot-scale MDC unit for seawater desalination.[149] The MDC technique is thus regarded as a pretreatment alternative to lower the desalination cost.

2.7.2 Solar energy-driven desalination cells

As a clean and most renewable energy, solar energy is of great interest for water desalination research. In 2016, a bio-photoelectrochemical desalination cell was developed by Liang et al. (**Figure 6B**).[150] Modified from the microbial desalination cell, it applies α -Fe₂O₃ as a photocatalyst at the anode side and achieves a salt removal rate of 96%. [150] This type of cell is called a photo-microbial desalination cell (PMDC). Due to the high electron transfer rate at the electrode/biofilm interface, it achieves a much higher current density compared to the microbial desalination cell.

Later, Kim et al. reported a solar energy-driven photoelectrocatalytic (PEC) desalination setup by placing both tailored TiO₂ nanorods and hydrogen-treated TNR array photoanodes in the anode cell, Pt foils in the cathode cell, and flowing 170 mM NaCl saline water between the cells (**Figure 6C**).[151] Due to the photocatalytic and electrodialysis reaction and at the anode and cathode, Na⁺ and Cl⁻ are transported from the saline water chamber to the two sides of electrodes. Urea at the anode cell was effectively decomposed to N₂ (80%), and H₂ was produced from the water-splitting reaction with a faradaic efficiency of around 80%. Due to the reduced charge transfer resistance, the system achieved a specific energy consumption of 4.4 kWh/m³ for 50% desalination and an energy recovery rate of 0.8 kWh/m³. Chen et al. modified the cell by applying semiconductor-based photoelectric conversion material and TEMPO redox electrolytes based on this cell design. A continuous photo-excited desalination process with energy output is achieved by circulating the redox electrolytes between the anode and cathode.[152] Ramalingam et al. reported integrating a quasi-solid-state dye-synthesized solar cell (q-DSSC) and a redox-flow desalination (RFD) unit. In this cell design, there is one photoelectrode as the anode, an intermediate electrode, and

a counter electrode. One side of the electrode facing the solar cell acts as the positive electrode by applying a bifunctional platinized-graphite-paper electrode. In contrast, the other side, which faces the redox-flow desalination cell, works as a negative electrode. This system achieves a high salt removal rate of around $68 \mu\text{g}/\text{cm}^2\cdot\text{min}$ at an energy consumption of $0.18 \mu\text{mol}/\text{J}$.

2.7.3 Third generation: chemical energy-driven electrochemical desalination cells

Apart from solar energy, chemical energy can also be applied as an energy input for the desalination approach. Compared with CDI and FDI, chemical energy-driven desalination allows for concurrent electricity generation and desalination. By applying redox pairs such as zinc-bromine,[153] zinc-ferricyanide,[154] zinc-oxygen,[155] hydrogen-oxygen,[156] and acid-base[157] at both anode and cathode sides in a multi-channel desalination cell, a very high desalination capacity, and desalination rate can be achieved.[158]

In 2018, a zinc-ferricyanide hybrid flow battery for desalination and electrical energy supply was reported by Desai et al.. This hybrid battery uses Zn as the anode electrode and graphite as the cathode electrode. By applying aqueous $0.3 \text{ M } \text{ZnCl}_2$ and $\text{K}_4\text{Fe}(\text{CN})_6$ (0.3 M) + $\text{K}_3\text{Fe}(\text{CN})_6$ (0.3 M) as anolyte and catholyte solutions, respectively, the ions in the feedwater channel can migrate through a pair of AEM and CEM to the anolyte and catholyte. The system can also operate at a high voltage output ($E_0=1.25 \text{ V}$) and low energy consumption of 2.11 Wh/L for 85% salt removal and a desalination rate of $4.7 \text{ mol/m}^2\text{h}$.

Khalla et al. reported a desalination cell with Zn and Br_2 as anode and cathode reactants, ZnCl_2 and NaBr as anolyte and catholyte materials, and a pair of AEM and CEM ion-exchange membranes to separate the cathode and anode. During the cell operation, Zn is oxidized to Zn^{2+} while Br_2 is converted to Br_3^- and ultimately reduced to Br^- . Meanwhile, Na^+ and Cl^- from the middle water channel are transported to the catholyte and anolyte separately. This cell type can desalinate a feed of around 30 g/L NaCl to near-zero concentration at a 2 mA/cm^2 extracted current. The energy output is 23.5 kWh/m^3 of desalinated water.[153]

In 2020, Srimuk et al. applied exfoliated MoS_2 as a cathode and 0.1 M NaCl as catholyte via electrocatalytic oxygen reduction at the cathode and zinc oxidation in a 1 M ZnCl_2 anolyte (**Figure 7A**). To balance the charge at the anolyte and catholyte, the ions in the feedwater are transferred through the IEMs to the side channels. This type of zinc-air desalination

battery has a desalination capacity of $0.9\text{-}1.0 \text{ mg/cm}^2$, a charge efficiency of 70%, and an energy consumption of 68-92 kJ/mol.[155]

The concept of acid-base neutralization-energy driven desalination was reported by Bhat et al. This type of cell can spontaneously desalinate saline water and concurrently generate electrical energy via a reversible H_2 redox reaction at the anode and cathode and with NaOH and H_2SO_4 as the anolyte and catholyte, respectively. The desalination cell shows a high desalination rate of $18.79 \text{ mmol/h}\cdot\text{cm}^2$ and an energy consumption of 13.6 kJ/mol.[157]

As a clean and suitable renewable energy carrier, hydrogen has attracted great attention for energy applications. In recent years, it has also become an emerging driven energy for electrochemical water purification.[159] In 2019, Suss et al. has brought the concept of the desalination fuel cell, by applying the chemical energy of hydrogen, oxygen, acid, and base electrolyte, such a cell can desalinate water of 500 mM NaCl continuously and produce electricity at the same time.[159, 160] Later, Zhang et al. proved a concept of applying electrocatalytic reactions of H_2 and O_2 in pH-neutral electrolytes to desalinate water at seawater molarity while also generating electrical energy (**Figure 7B**). The fuel cell desalination (FCD) technique has achieved a desalination rate of $16\text{-}18 \text{ g/m}^2\cdot\text{h}$, a charge efficiency of 68%, and an energy generation of $67 \text{ Wh/g}_{\text{NaCl}}$. Acid and base solutions also accumulate at the anolyte and catholyte, which later can be mixed to generate thermal energy.[156]

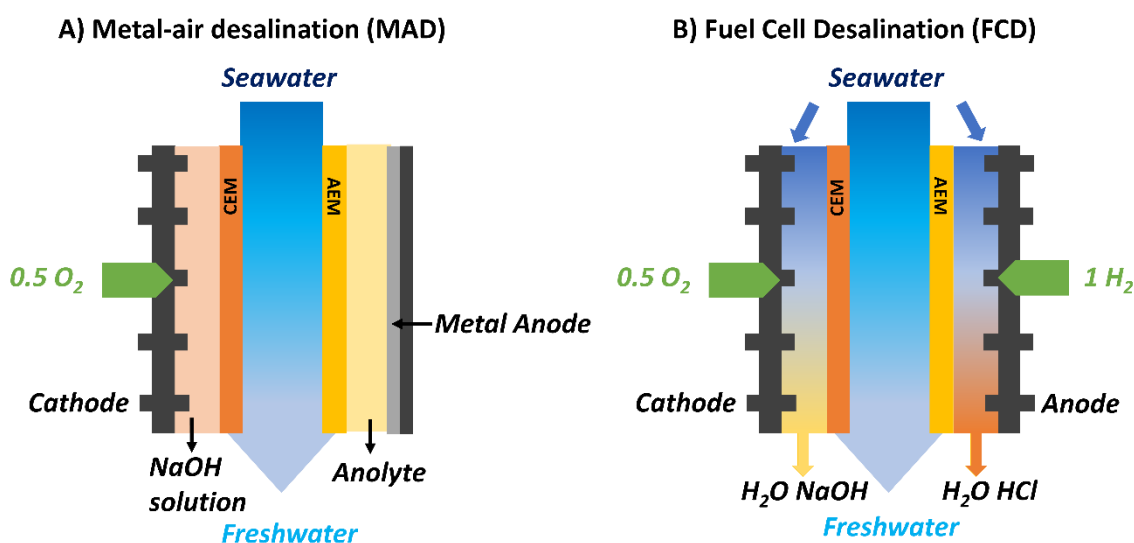


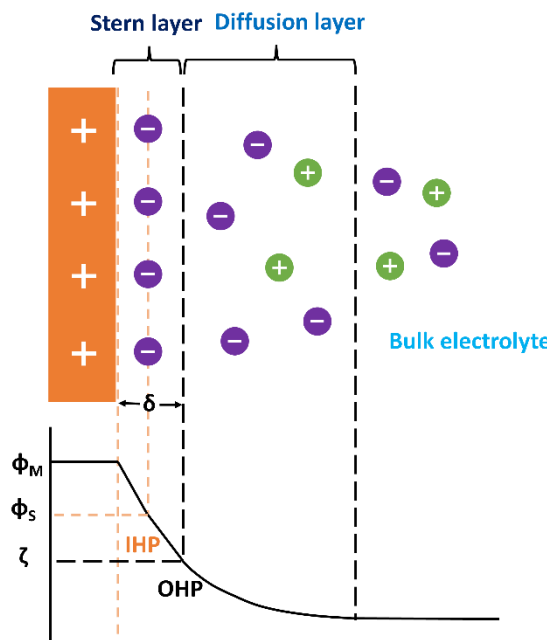
Figure 7: Chemical energy-driven desalination cell structures adapted from literature. [155][156][159] A) Metal-air desalination (MAD); B) fuel cell desalination (FCD).

2.8 Ion uptake mechanisms

2.8.1 Double layer in microporous carbon

Electric double-layer (EDL) forms when two conducting phases contact and meet at an interface.[161] In the context of electrochemical water treatment, the EDL often forms at a solid-solution interface. The double-layer models are often applied to visualize the ion distribution at a charged surface (**Figure 8**).

A) Gouy-Chapman-Stern model



B) Modified Donnan model

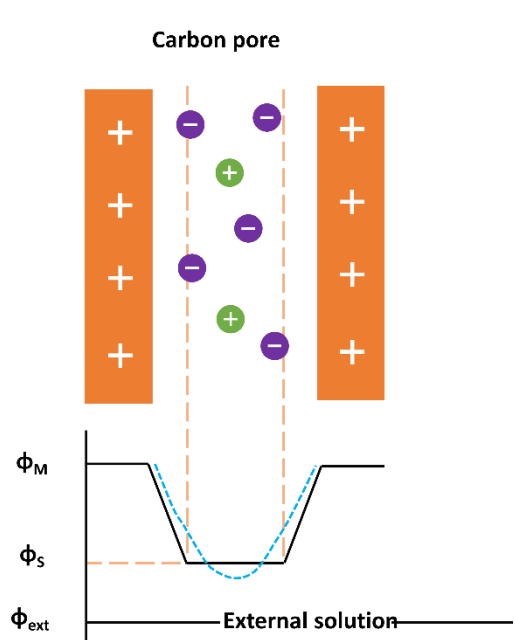


Figure 8: Basic electrical double layer models adapted from literature.[26, 162] A) Classic Gouy-Chapman-Stern model. B) Modified Donnan model.

2.8.2 Classis double layer models: Planner models

The simplest model to approximate the EDL is the Helmholtz model,[162] which describes that the surface charge at the solid phase is compensated by counter ions placed at a distance d . This model hypothesizes a compact layer of opposite charges which do not describe the ion diffusion phenomenon. In the Gouy-Chapman model,[162, 163] the counter ions are not compactly held at the interface but rather diffuse into the liquid. The thickness of the EDL is influenced by the kinetic energy of the ions, while the concentration of the counter ions at the EDL follows the Boltzmann distribution. The Coulombic interaction between the charges is also considered and expressed by the Poisson equation. Although it is a better approximation, the Gouy-Chapman model describes ions as point charges and does not consider physical limits for ions approaching the surface due to their finite sizes. As a solution to this problem, Stern modified the Gouy-Chapman model by declaring that ions

have finite sizes and cannot approach the surface closer than a finite distance δ , which is known as Stern layer (**Figure 8A**).[163] Within the Stern layer, the ions are specifically adsorbed by the surface in the plane δ (Helmholtz layer). The potential drop over the diffuse layer is known as the zeta potential ($\Psi\zeta$).

2.8.3 Donnan model and modified Donnan model

When a porous membrane with a fixed charge is in equilibrium in an electrolyte solution, an electrical potential is established between a membrane and solution. Within a small volume, such as a pore that has a cross-section of a few nm and is lined with charged walls, the ion concentration is different from the value outside of the pore. However, the ion concentration inside the pore is independent of the position. The Donnan model is generally applied to describe the ion concentration of inhomogeneously charged structures like gels and membranes.[164] It is also suitable for the study of ion transportation through membranes.[165]

For microporous carbon materials whose average pore size is smaller than 2 nm, the EDL at the pore walls will strongly overlap due to the small pore size compared to the Debye length.[166] The classical Gouy-Chapman-Stern model is thus no longer suitable to approximate the charge distribution inside the pores and cannot be applied to describe ion transportation.[167, 168]

In response, Biesheuvel et al. modified the classical Donnan model (**Figure 8B**) in two aspects: 1) introducing a Stern layer between the pore solution and carbon matrix, and 2) introducing an additional chemical attraction force μ_{att} for the ions to go from the macropores to the micropores.[166]

In micropores, the concentration of cation and anions can be different from one another. The concentration of ion j can be described by the following equation **Eq. (5)**:[166]

$$C_{j,mi} = C_{mA} \cdot \exp(-Z_j \cdot \Delta\phi_d + \mu_{att}) \quad \text{Eq. (5)}$$

Where C_{mA} is the ion concentration in macropores, Z_j is the charge number of the ions, $Z_j=+1$ for a Na cation, $Z_j=-1$ for a Cl anion, $\Delta\phi_d$ is the Donnan potential difference between the intraparticle and interparticle space, and μ_{att} is the attractive contribution to the ion chemical potential for ion transportation from macropores to the micropores.

In this modified Donnan model, the micropore charges are related to the potential drop within the Stern layer (**Eq. (6)**).

$$c_{charge,mi} \cdot h_{p.mi} = -\frac{V_T}{F} \cdot \Delta\phi_{St} C_{St} \quad \text{Eq. (6)}$$

where $h_{p.mi}$ is the volume/area ratio of the micropores,[164] V_T is the thermal potential, F is the Faraday constant, $\Delta\phi_{St}$ is the potential drop within the Stern layer, and C_{St} is the Stern capacitance.

In CDI studies, the cell potential contributes to Donnan and Stern potentials ($\Delta\phi_d$ and $\Delta\phi_{St}$) when a voltage V_{cell} is applied between the two electrodes, and the process is at an equilibrium state without ion transport. The cell voltage divided by two equals the voltage drop across each EDL in each electrode (**Eq. (7)**).

$$\frac{V_{cell}}{2V_T} = \Delta\phi_d + \Delta\phi_{St} \quad \text{Eq.. (7)}$$

The modified Donnan model describes the ion distribution in the micropores which also represents the interior volume of the carbon particles. By including the Stern layer at the pore walls and considering the attractive force for the ion transport from macropores to micropores, this model is more suitable to describe and analyze the ion distribution and transportation in the microporous carbons.[164]

2.8.4 Ionic strength influence on permselectivity

In the CDI process, when the porous materials such as activated carbon electrodes are placed in an aqueous solution with no applied electrical potential, the pores of the materials are filled with an aqueous electrolyte with both anions and cations. Cations and anions will be transported to the pores of negative and positive electrodes separately under an applied cell voltage if a potential difference is applied between the electrodes during the charge and discharge processes. Meanwhile, the co-ions will be ejected from the electrode pores and returned to the bulk solution. This phenomenon is called the non-permselective ion exchange.[90, 92, 169] Due to the co-ion expulsion from the material pores to the feedwater at both electrode-feedwater interfaces, there will be less salt uptake and a lower charge efficiency for the CDI system under certain energy consumption (**Figure 9A,B,C**).

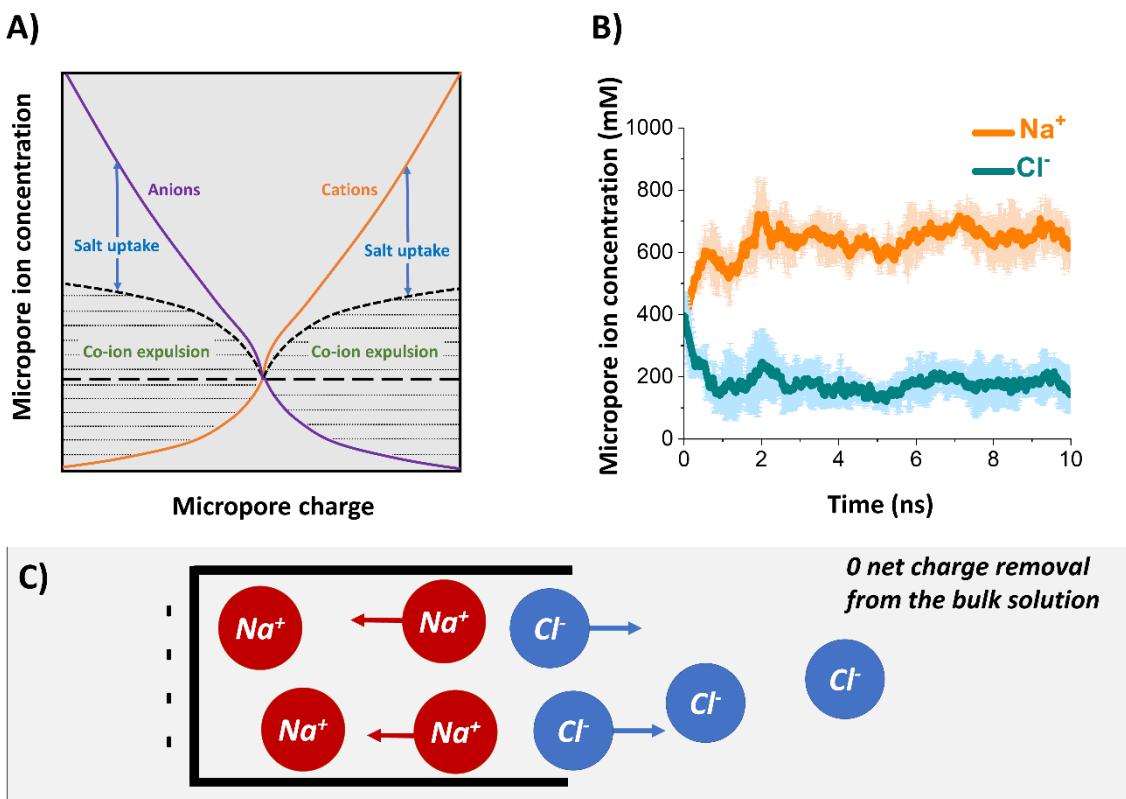


Figure 9: Ion distribution in the micropores adapted from literature. [32][85]. A) Concentration of cations and anions at equilibrium state; B) concentration of cations and anions at 1 V over time; C) scheme of ions in a micropore in a solution at high ionic strength when a negative potential is applied.

The charge efficiency of the CDI process is calculated using **Eq. (8)**.

$$\eta = \frac{F \times DC_{mol}}{M_{salt} \times Q} \times 100\% \quad \text{Eq. (8)}$$

Where F is the Faraday constant, DC_{mol} is the molar desalination capacity, M_{salt} is the molar mass of the salt that is removed, and Q is the total charge normalized to the electrode mass during the charge/discharge processes.

The desalination capacity is calculated by applying **Eq. (9)**.

$$DC = \left(\nu \frac{M_{salt}}{M_{tot}} \right) \int (c_t - c_0) dt, \quad \text{Eq. (9)}$$

Where ν is the flow rate, M_{tot} is the electrode mass, and c_t and c_0 are feedwater concentration at time t and the initial starting point, respectively.

During the ion swapping process, the charge stored in the electrode materials will not fully contribute to the ion removal process due to co-ions ejecting from the pores. This results in a low charge efficiency. In an electrolyte with high ionic strength (higher than seawater level), there will be more ion pairs in the pores when the cell voltage is not applied to the cell. When the cell is undergoing a charging process, there will be more co-ion rejection from the pores, which results in a 1:1 counter-ion and co-ion exchange (**Figure 9C**).[52, 170] In this case, the porous material fails to remove salt from the feed water, and the charge efficiency will be zero. This implies that the CDI technique is only suitable for desalinating water at low concentrations (<100 mM) and will fail when the concentration increases.

2.8.5 Pore size effect on ion permselectivity

In 2006, Raymundo-Piñero et al. showed that from an energy storage point of view, an adequate pore size of carbon is more important than specific surface area.[50] In the same year, Chmiola et al. described a capacitance increase at pore sizes below 1 nm.[51] In their work, this phenomenon is explained by solvation shell distortion or partial desolvation. The screening effect of the in-pore ions allows for an increased number of ions stored in pores smaller than 1 nm. A higher ion storage capacitance is thus obtained. [169, 171, 172] Similarly, an increased desalination performance is also observed in a highly concentrated solution (seawater level) when carbon materials with an average pore size less than 1 nm are applied.[52]

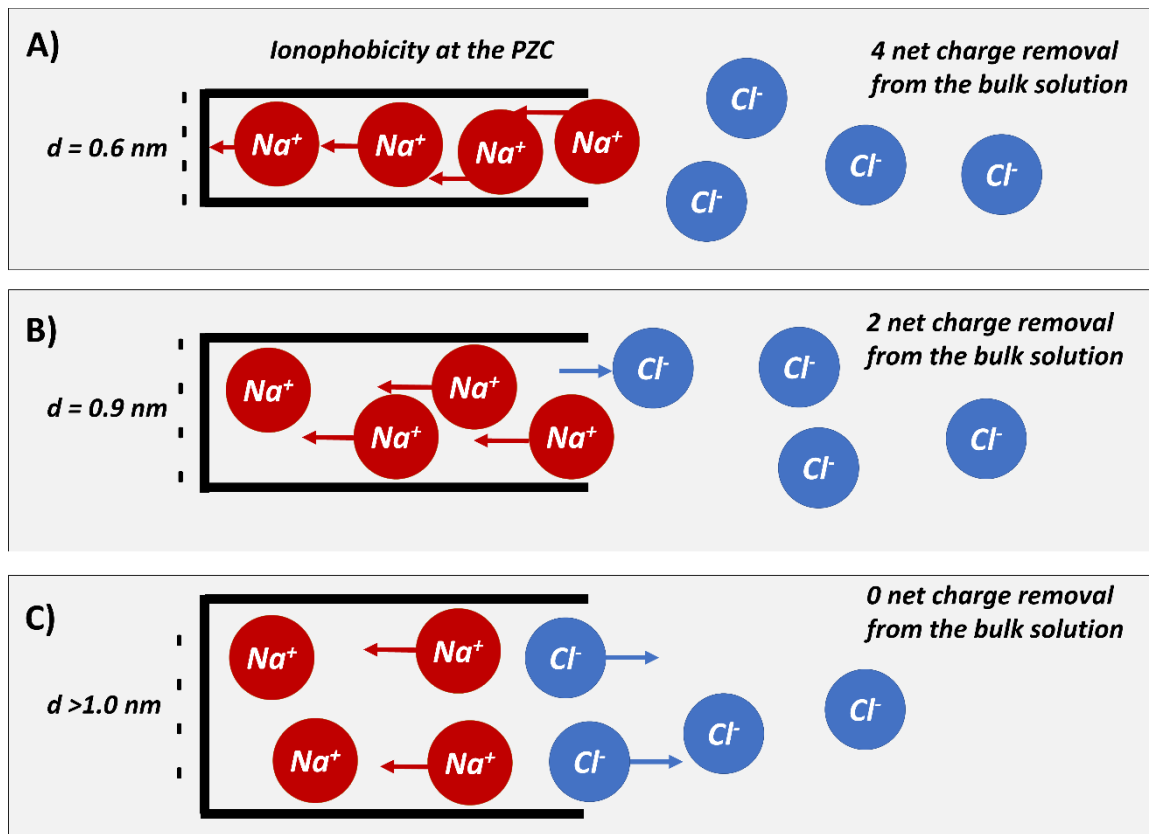


Figure 10: Schematics figure of ion electrosorption mechanisms during the desalination process for carbon pores with different sizes in solutions of high ionic strength. [85] Adapted from literature.[85] A) ion uptake in the pore width of 0.6 nm. B) ion uptake in the pore width of 0.9 nm. C) ion uptake in pore widths larger than 1 nm.[85]

In **Figure 10 A**, the ions cannot enter the pore freely if the carbon pore size is smaller than the hydrated ion size due to the dehydration energy barriers and the larger solvated ions. When a potential difference exceeding the ion desolvation energy barriers is applied, the ions can only be partially desolvated, transferred, and adsorbed in the middle of the pores. The initial state where no ions can enter the pore when no electrical potential is applied (PZC) is an ionophobic one. Due to this phenomenon, there is mostly counter-ion adsorption without co-ion expulsion when the electrical potential is applied. In this case, an increased desalination capacity and charge efficiency can be obtained by using carbon materials with an average pore size smaller than the hydrated ion sizes.[52] This phenomenon shows that carbon has promising potential for the seawater CDI approach as long as the pore size and pore structure of the carbon materials are carefully designed in the sub-nanometer range.

If the pore size increases, but remains below 1 nm (**Figure 10 B**), there may exist a few ions inside of the pores due to their ionophobicity. If the pore is charged, the counter-ions will be electroadsorbed in the pores while the co-ions stored during the PZC state will be expelled from the pore to the feedwater. This process leads to a decreased charge efficiency and limited desalination capacity.

If the pore size exceeds 1 nm (**Figure 10 C**), there will be more ion exchange during the charging process as more and more ions can be initially present in the pores. This will eventually lead to an almost 1:1 cation to anion exchange ratio. If using carbon materials with such a large average pore size, the CDI process would fail to desalinate water at seawater-level ionic strength.[55] At the same time, the ability to store charge remain unimpeded, so that highly concentrated saline media present a suitable electrolyte for supercapacitors.

Figure 11A-B show the pore size dependence of desalination performance and in-pore ion species. From 0.47 nm to 0.77 nm, the desalination capacity rises and reaches the maximum. As the pore size increases further, the desalination capacity suddenly decreases sharply. At pore sizes larger than 1.37 nm, the desalination capacity then decreases to around 3 mg/cm³. The charge efficiency is almost 100% at pore sizes of around 0.47 nm and decreases sharply as the pore size expands. As the pore size nears 3 nm, the charge efficiency stabilizes at around 11%. [85]

When the pore size is smaller than 0.6 nm, there are no ions in the pore at the PZC. In this way, the ion uptake when the cell is charged at 1 V is mostly due to counter-ion adsorption. As the pore size increases, the in-pore salt concentration increases dramatically while the in-pore co-ion concentration keeps increasing. As there is more and more co-ion desorption from the pore when the pore size increases larger than 1 nm, the desalination capacity will drop. Besides, an optimum charge storage capacity is observed at the pore size of 0.77 nm, and it decreases as the pore size increases due to the lower co-ion number at smaller pore sizes. This phenomenon should also be considered when explaining the capacitance increase in smaller pores.

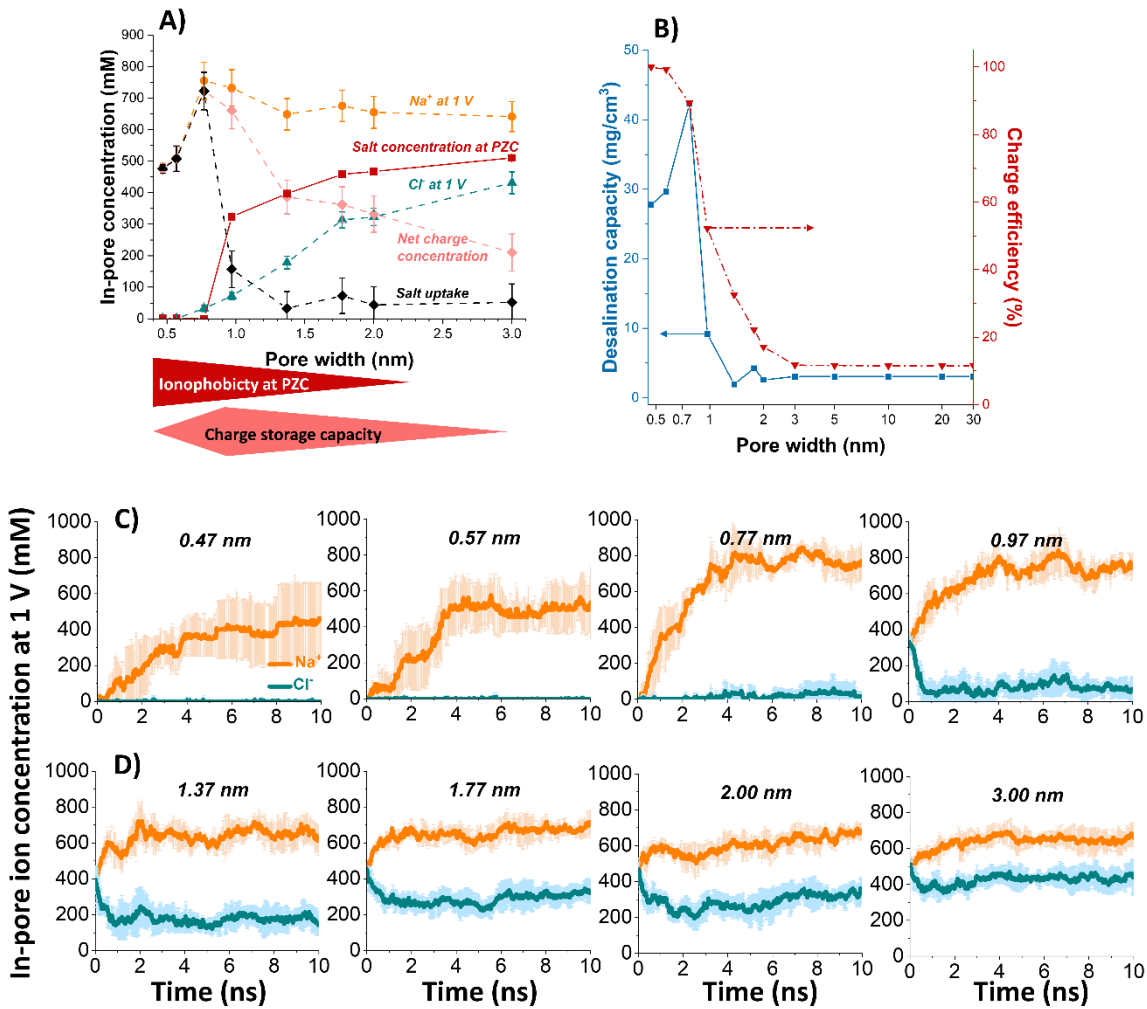


Figure 11: Time-dependent ion concentration evolution of ions with error bars, adapted from literature.[85] A) Calculated (value with error bars) in-pore Na^+ uptake and Cl^- release concentration, the salt concentration at the potential of zero charge, net charge concentration, and salt uptake concentration. B) Calculated desalination capacities and charge efficiencies in pores of different sizes C) Na^+ and anions Cl^- in pores of sub-nanometer sizes. D) Na^+ and Cl^- in pores from 1 nm to 3 nm.

2.8.6 Pore size effect on ion selectivity

The ion selectivity of the CDI system must be studied if the solution contains multiple cations and anions and if some ions species have higher priority for removal. Zhao et al. noticed that during the charging/discharging process of a CDI cell, the initially removed sodium ions are gradually replaced by calcium ions.[173] Dykstra et al. also reported that there is an ion uptake difference between the two kinds of ions due to the kinetic diffusion difference of sodium and potassium ions.[174] Suss et al. applied a theoretical study and concluded that there is an obvious pore size/ion size influence on ion adsorption preference at the equilibrium state.[175] Hou et al. demonstrated that in the mixed-ion electrolyte, there is ion preference depending on ion size and ion charge. While divalent cations are preferred to be adsorbed in the pores due to the high valence, smaller cations are also preferred to be adsorbed first due to the higher mobility in the pores.[176] According to a recent study, an ion dehydration energy barrier influences the ion selectivity in the nanoporous electrodes.[177]

An ion sieving effect is observed when the average size of the carbon pores is 0.6 nm. This ion sieving happens when the pore size is too small for some ions in the electrolyte.[178-180] Thus, while some ions species can be adsorbed in the carbon pores, some larger ions cannot enter the pore due to the larger size and higher dehydration energy barriers. For example, Hawks et al. applied carbon material with a subnanometer pore size (0.68 nm) and achieved nitrate removal from a mixed multi-anion solution.[181] There exist other approaches to enhance the ion selectivity in the multi-ion system, namely the application of IEM or ion-selective coatings,[87, 89, 182-185], and chemical modifications of carbon materials [186-189]. However, in such approaches, the material adaptations will add extra cost and synthesis steps, which is undesirable for CDI application in the ion separation approach.

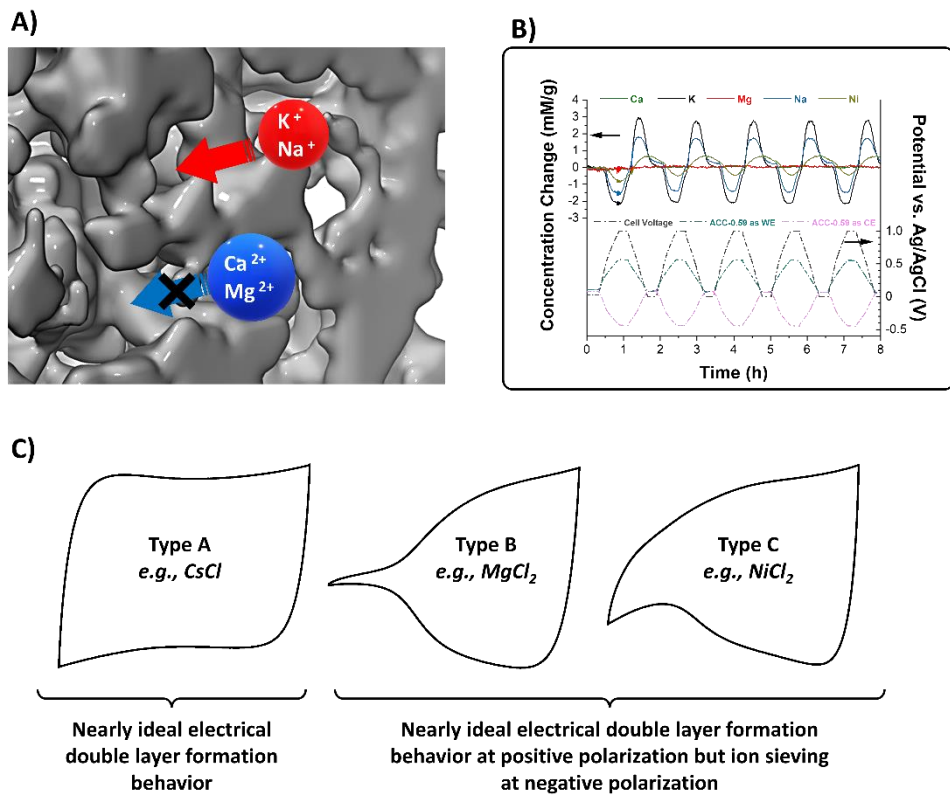


Figure 12: Ion adsorption behavior at different hydrated ion sizes A) Different accessibility of cations at different valent states; B) online monitoring of ion selectivity during the galvanostatic charging/discharging processes; C) different CV shapes for cations at different sizes and valent states. Figures adapted from literature.[190]

The mechanism of selective ion removal under different carbon pore sizes was studied by Zhang et al.[190] **Figure 12A,C** shows the inability of divalent cations to dehydrate and enter the pore if the pore size is smaller than some of the hydrated ions such as Ca²⁺ and Mg²⁺ and if the dehydration energy barrier is higher than the applied potential. This would lead to a much smaller capacitance at the negative potential during the CV measurements compared to that under a positive potential (TYPE B). As the hydrated ions such as Ni²⁺ become smaller, the CV displays an asymmetric profile (TYPE C), which is related to ion dehydration adsorption.[191] As the hydrated ion size becomes smaller, a rectangular CV shape is observed, and the capacitance at both the positive and negative potentials are similar (TYPE A). If the applied electrical potential overcomes the ion dehydration energy barrier, the ions begin to desolvate and enter the pores, which triggers an increased capacitance. In the mixed-ion system, the bigger divalent cations will not be adsorbed in the pores due to this sieving effect. Partially dehydrated Ni²⁺, on the other hand, can absorb in the pores but has

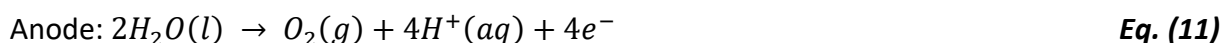
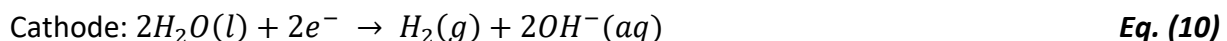
slower kinetics than the monovalent cations. As a result, as shown **Figure 12B**, the monovalent cations with smaller sizes are at the highest selectivity due to their small size and higher mobility inside of the pores.

If the pore size becomes so large that all ions can absorb in the pores and render the sieving effect negligible, divalent cations become preferred over the monovalent cations under the applied potential due to the higher charge number that creates a stronger electric force field compared to the monovalent cations. Among all divalent cations, the ion selectivity follows the size effect. In this case, the ion selectivity is influenced by the size effect and charge effect.

In conclusion, ion selectivity in a mixed-ion system is a combined effect of size, dehydration energy, charge number, and electrical force. Therefore, careful design of both the materials and the experimental parameters is essential for proper ion removal from a multi-ion system.

2.8.8. Ion diffusion influence on the potential window and desalination performance

During the electrochemical process of the CDI operation, redox reactions can also be triggered at the electrode surface in contact with the aqueous electrolyte. If the applied cell voltage exceeds 1.23 V, water-splitting occurs.[192] The positive electrode will consequently experience electrode oxidation and an oxygen evolution reaction (OER), while the negative electrode will experience a hydrogen evolution reaction (HER). Due to these irreversible redox reactions, the Coulombic efficiency and the charge efficiency will diminish. The electrode materials will also suffer from structural change and degradation due to the water-splitting reactions. In a pH-neutral media, the reaction equations of HER and OER are listed in **Eq. (10)** and **Eq. (11)**.



We shall use the HER reaction as an example. The electrochemical overpotential can be determined based on the Nernst equation **Eq. (12)**.

$$E_{HER} = E_{(H_2/H^+)}^0 - \frac{RT}{F} \ln (a_{H^+}/\sqrt{a_{H_2}}) \quad \text{Eq. (12)}$$

while E_{HER} represents the potential in deriving the HER reaction, $E_{(H_2/H^+)}^0$ signifies the standard potential of the H_2/H^+ redox couple, R is the gas constant, F is the Faraday constant, and a_{H^+} and a_{H_2} are the reactivities of the species. E_{HER} should be constant at

standard temperature. To generate current from the HER reaction, a higher potential must be applied (*Eq. (13)*).

$$E_i = E_{HER} + iR + \eta \quad \text{Eq. (13)}$$

where iR is the Ohmic drop in the cell and η is the reaction overpotential.

The current generated from the HER reaction can be expressed in the Butler-Volmer equation, as shown in *Eq. (14)*.

$$j = j_0 \left\{ -\exp \left(-\frac{\alpha nF}{RT} \eta \right) + \exp \left[\frac{(1-\alpha)nF}{RT} \eta \right] \right\} \quad \text{Eq. (14)}$$

Where j_0 is the exchange current density, α is the charge transfer coefficient, and n is the charge number. If η is larger than 50 mV, the overpotential can be expressed as in *Eq. (15)*.

$$\eta = a + b \cdot \log j = \frac{-2.3RT}{\alpha nF} \log j_0 + \frac{2.3RT}{\alpha nF} \log j \quad \text{Eq. (15)}$$

where b is the Tafel slope that can evaluate the reaction rate at a certain overpotential.

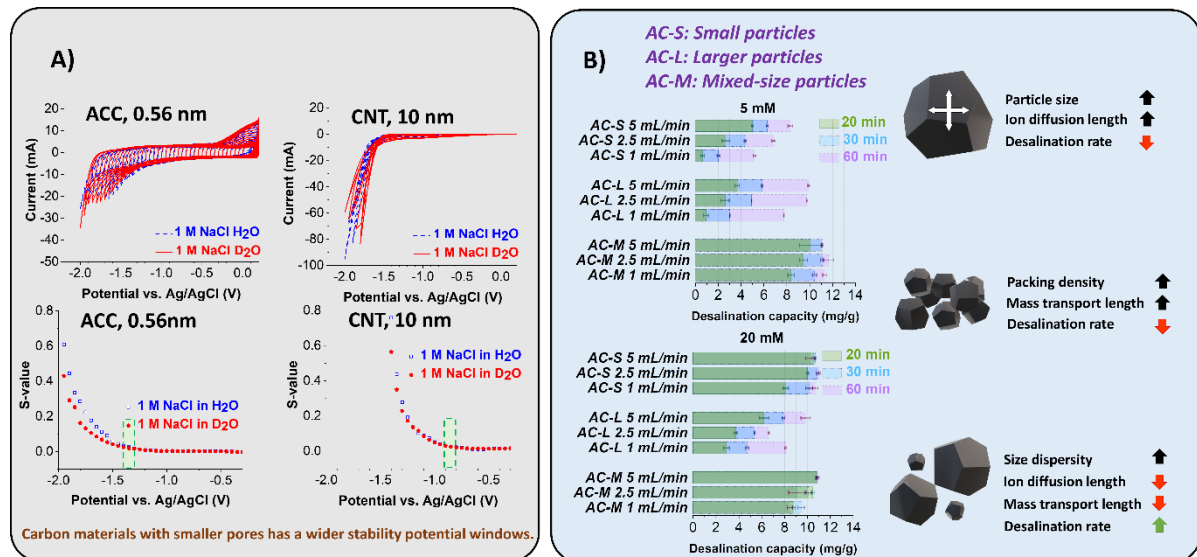


Figure 13: Pore size and particle size influence on the electrochemical stability window and desalination performance A) Pore size influence on the water-splitting overpotential characterized by potential window opening and S-value test; B) Particle size distribution influence on the desalination performance. Figure adapted from literature.[193, 194]

In pores with subnanometer size, there is higher resistance towards ion transport due to the strong ionophobicity and small pore size. Moreover, the mass transport in the subnanometer pores is also slower. A higher overpotential is thus required to observe the HER reaction for carbon materials with an average pore size smaller than 1 nm. In the nanoconfinement, the water molecules are suppressed to form gaseous dihydrogen molecules,[195] and hydrogen electrochemisorption is observed.[193] For carbon materials with subnanometer average pore sizes (**Figure 13A**), the anodic stable potential can reach -1.3 V vs. Ag/AgCl. In comparison, the CNT electrode has a negative potential limit of only up to -0.8 V, which exhibits the high potential for energy storage of sub-nanoconfinement in the aqueous media.[193]

When choosing carbon as an electrode material for CDI, smaller average pore sizes and higher specific surface areas will help to improve the charge efficiency[52] and expand the operation cell voltage.[193] However, the ion diffusion kinetics of the carbon material must also be considered. In the field of energy storage, there have been some studies about the effects of electrode density on battery rate performances.[193, 196] Materials with only subnanometer pores will suppress the ion transport and decrease the desalination rate. In 2013, Porada et al. concluded that there is a strong correlation between electrode packing density and desalination rate.[30] Recently, Shen et al. applied MXene material at different particle sizes and demonstrated that the presence of the smaller particles will help to improve the electrochemical and desalination performance.[197]

As shown by Zhang et al., one microporous carbon with different average particle sizes was applied to study the ion transport in the confinement of an electrode undergoing an electrochemical desalination process by applying different concentrations of NaCl solutions (**Figure 13B**). This work revealed that two factors can influence desalination performances: interparticle ion transportation and intraparticle ion diffusion. The former can be limited by compact packing of the electrodes (e.g., selecting smaller particles for electrode preparation, denser packing). The latter can be limited by factors such as larger particle size and smaller pores sizes.[194]

2.9. Electrocatalytic reactions for desalination

As a clean, light, and carbon-free energy carrier, hydrogen allows the storage of renewable energy from wind, solar, or hydropower via power-to-gas.[198] Hydrogen can be stored and further converted to electrical energy via hydrogen fuel cells, which is an emerging application for fuel-cell electric vehicles (FCEVs).[199] Among all kinds of fuel cells, polymer electrolyte membrane fuel cells (PEMFC) are suitable for portable devices.[200] A PEMFC applies a proton-conducting polymer as the electrolyte (PEM) between the two electrodes (**Figure 14**). The combination of the anode catalyst layer (ACL), membrane, and cathode catalyst layer (CCL) is called a membrane-electrode assembly (MEA). The contact layers between the MEA and the gas flow plates are porous and electrically conductive gas diffusion layers (GDL), which are commonly made of activated carbon.

In commercial PEMFCs, the anodic and cathodic reactions are all catalyzed by Pt metal. The theoretical voltage derived from a hydrogen PEMFC is 1.23 V. The electrode reactions are shown in **Eq. (16-18)**.

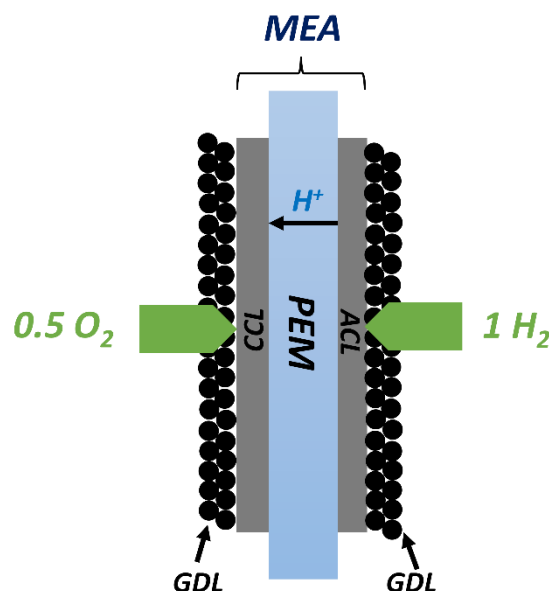
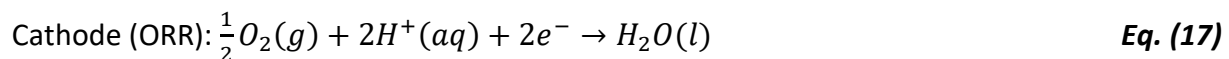


Figure 14: Schematic figure of fuel cell structure including membrane-electrode assembly (MEA) and gas diffusion layer (GDL).

The desalination fuel cell is modified based on the hydrogen PEMFC. Instead of a proton-exchange membrane, a pair of AEMs and CEMs is applied with feedwater flowing in-between. An anolyte and catholyte also flow between the electrodes and the ion exchange membranes to form acid and base solutions separately.

The reaction mechanism of the desalination fuel cell is expressed by *Eq. (19-21)*.[156]



At the anolyte and catholyte sides, H^+ and OH^- are formed. To balance the charge and make the electrolyte electrical neutral, Cl^- and Na^+ are transported through the AEM and CEM. As a result, HCl and NaOH form at the anolyte and catholyte as the feedwater is desalinated.

2.10. Comparison of different electrochemical desalination technologies

Among the different electrochemical desalination techniques in **Figure 15**, the first generation focuses on applying capacitive materials such as microporous carbon materials which have a desalination capacity ranging from 1 mg/g to 64 mg/g depending on the cell structure and operating parameters.[66, 91, 130] In the case of seawater, a desalination capacity of more than 25 mg/g can also be obtained for MCDI.[55] Due to the limited desalination capacity and charge efficiency for activated carbon materials, higher energy consumption can be obtained especially in high concentrations of feedwater compared with the other generations. Nanoporous carbon materials with subnanometer average pore sizes can be applied for seawater desalination.[201, 202] In addition a better material design with higher pore volume and better pore connection must be developed to increase the desalination performances of nanoporous carbon materials.

Second-generation electrochemical desalination (desalination batteries) is based on Faradaic materials to increase the intrinsic ion storage capacity and prevent the non-selective ion processes. Since a variety of Faradaic materials have been applied, a desalination capacity of more than 100 mg/g can be achieved with a moderate energy consumption of less than 20 Wh/mol in seawater molar strength. Compared to CDI, the second-generation techniques are more energy-efficient when the concentration of the solution is higher, which makes them more competitive for seawater desalination compared with first-generation techniques.

Third-generation electrochemical desalination techniques utilize chemical energy to desalinate water without requiring electrical energy during the ion removal process. Rather, they transfer the chemical energy of the reactants into electrical energy and other forms of energy. As the reactants are consumed at the electrodes via electrocatalytic reactions, the desalination process becomes continuous. In this case, an unlimited desalination capacity is achieved. Due to the spontaneous reactions at the catalysts with proper cell parameter design, the desalination rate of the third generation technology is also the highest among all generations. These advantages have shown great potential to develop more economical and environmentally-friendly third-generation desalination technologies for seawater desalination applications.

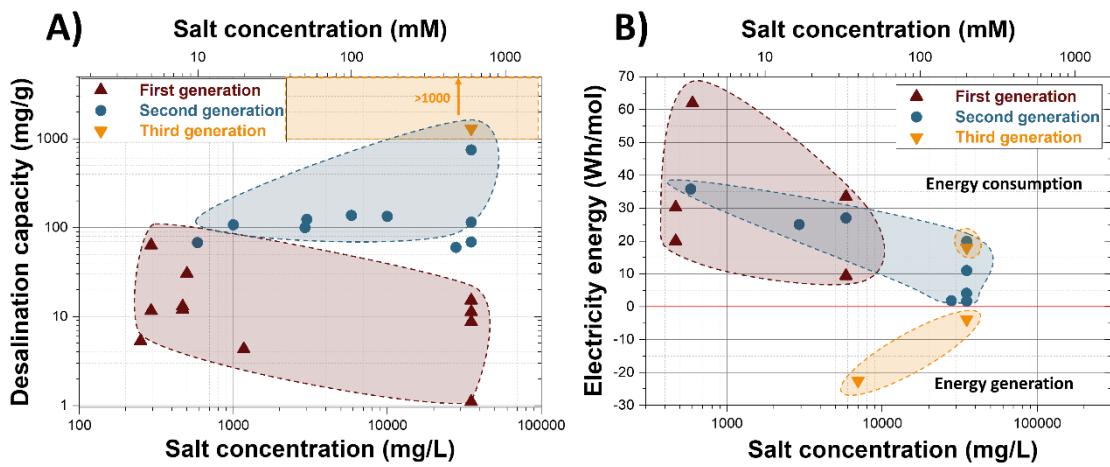


Figure 15: Desalination capacity and electrical energy consumption/generation of three generations of electrochemical water desalination technologies. Figure adapted from literature.[91]

3. Approach and overview

Among all electrochemical desalination technologies, capacitive deionization (CDI) was developed in the 1960s. As more and more theoretical and experimental studies have discovered the mechanisms of this process, many studies have focused on the structural and chemical design of carbon materials to achieve high specific surface area and capacitance. However, carbon materials have developed a stereotype that they are unsuitable for high concentration applications such as seawater desalination due to the co-ion ejection and the 1:1 cation and anion exchange process. Therefore, recent studies focus on Faradaic (battery) material application in desalination research due to the high specific capacity and intrinsic permselectivity in highly concentrated solutions. However, most of the battery materials are less cost-effective than carbon, and many of them suffer from low reversibility and cycling instabilities due to the high potential sensible properties. To address these issues, we must revisit the possibilities of CDI application in seawater ionic strength and further study electrocatalytic desalination technology.

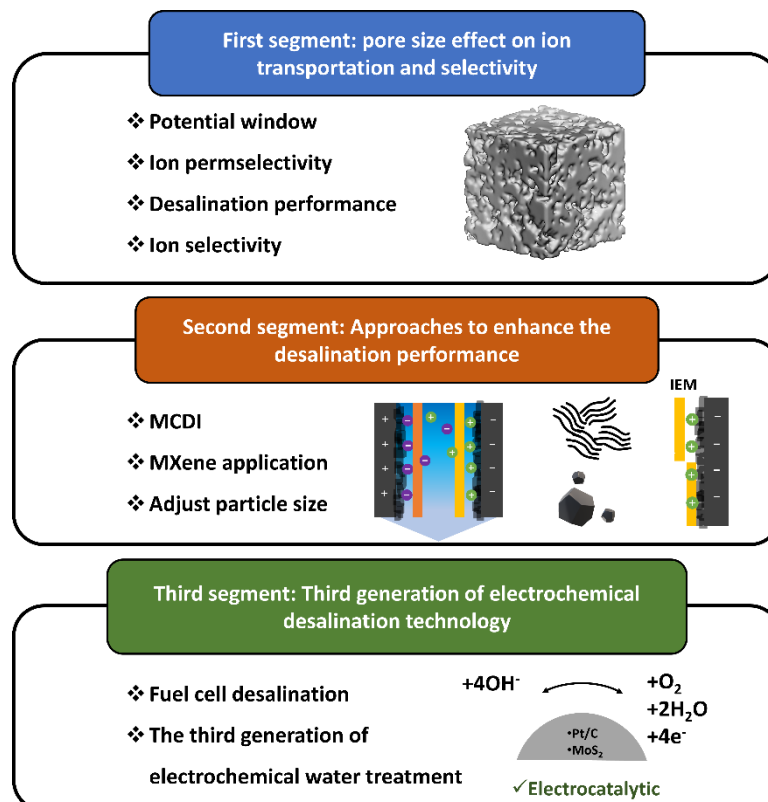


Figure 15: Overview of the three main segments of this dissertation. The carbon model in the first segment is adapted from literature.[190]

My Ph.D. work is separated into three segments (**Figure 15**): pore size effect on ion transportation and selectivity (**first segment**), ways to enhance the desalination performance (**second segment**), and third-generation electrochemical desalination (**third segment**).

In the **first segment**, we study the pore size and solvent influence on voltage window and cycling stability of the electrochemisorption processes of hydrogen and deuterium (**Chapter 4.1**). By applying carbon material with subnanometer pore size, an extended reversible voltage window (-1.3 V to -1.4 V vs. Ag/AgCl) is observed. In comparison, mesoporous carbon nanotubes (CNT) show a voltage window of -0.8 V to +0.9 V vs. Ag/AgCl. Due to the smaller pore sizes, the sub-nanoconfinement of carbon results in a higher ion diffusion resistance and hinders ion transportation in the pores. Higher voltage windows without gas evolution are consequently obtained. When 1 M NaCl dissolved in H₂O and D₂O is used as an electrolyte, the lower ion mobility and reactivity of the D₂O system will increase the kinetic limitations on the deuterium storage in the pores compared to that of hydrogen storage.

In **Chapter 4.2** and **Chapter 4.3**, we revisited the co-ion and counter-ion exchange phenomenon. We discovered a method to prevent this effect and thereby improve the desalination performance of carbon materials by applying ultramicroporous carbon materials with subnanometer average pore size. In **Chapter 4.2**, an increased charge efficiency and desalination capacity are achieved by combining molecular dynamics simulation and desalination experiments. When small carbon pores are not charged, there will be no ions initially contained due to the dehydration energy barriers. However, ions must desolvate before entering the pores during the charging process. This leads to a permselective ion uptake process where charge stored in the carbon material contributes to counter-ion removal rather than co-ion expulsion. In **Chapter 4.3**, by applying carbon materials with an average pore size of around 0.6 nm, a desalination capacity of 12 mg/g, a charge efficiency of 94%, and a 97% charge efficiency retention (200 cycles) are obtained in 600 mM NaCl solution. The molecular dynamic simulation predicts the desalination performances of pores of different sizes. By applying the interpolation method, gas sorption analysis data can be applied to predict the desalination performance of ultramicroporous carbon material in seawater level ionic strength.

In **Chapter 4.4**, the ion selectivity properties of such material types are studied. An ion sieving effect is observed by using ultramicroporous carbon with an average pore size of around 0.6 nm. Due to the small pore size, some divalent cations such as Mg^{2+} and Ca^{2+} with larger hydrated ion sizes cannot enter the pores even under the applied cell voltage (1 V). Other cations can enter the pores, but those with smaller hydrated sizes are preferred. As the pore size become bigger than the hydrated ion sizes, all studied of cations can be adsorbed in the pores. On the contrary, cations with higher valence numbers will be preferred to enter the pores due to stronger electric interactions.

From the **first segment** of my Ph.D. research, I had a glimpse of the ion

In the **second segment**, my research focussed on methods to improve the CDI desalination performance. In **Chapter 4.5**, I have studied the ion transport mechanism in MCDI and possible applications in seawater ionic strength to improve the desalination performance of first-generation electrochemical desalination technologies. When comparing the desalination performance of MCDI cells with free-standing IEM and IEM coatings on the electrodes, a higher desalination performance was achieved by applying free-standing IEMs in 600 mM NaCl. In comparison, IEMs coatings have higher desalination performance in 20 mM NaCl. This behavior can be explained by the difference in ion permselectivity of the IEMs and the water channel behind them. Another way to improve the electrode ion permselectivity is to apply MXene materials. In **Chapter 4.6**, we choose $Ti_3C_2T_x$ -MXene paired with activated carbon through proper mass balancing to adjust the potential windows of the materials. The corresponding desalination cell exhibits permselective ion removal ability in 600 mM NaCl solution. A desalination performance of 8-12 mg/g (desalination capacity) and 85% (charge efficiency) are also achieved.

In **Chapter 4.7**, we studied activated carbon material of different average particle sizes. We reveal two factors that influence desalination performance by separating the material into large and small particle size distributions and testing the desalination performances. One factor is the intraparticle ion diffusion which can be limited by large particle size (longer ion diffusion length) and small pore size. The other factor is interparticle ion diffusion, limited by smaller average particle sizes and higher packing densities. The two limiting factors can be balanced by mixing particles with different sizes, and a higher desalination capacity can be achieved.

The **third segment** was motivated by the fact that all materials geared towards ion storage will be limited by the intrinsic specific capacity and mandate charge/discharge cycling. In **Chapter 4.8**, we studied the electrocatalytic approach of fuel cell desalination (FCD). By utilizing the chemical energy from H₂ and O₂, the desalination fuel cell can continuously remove ions from the feedwater (600 mM NaCl) while also generating electricity, acid solution, and base solution from the cell. Desalination rates of 18 g/m²/h and 16 g/m²/h were observed in 600 mM NaCl and substitute ocean water, respectively. In **Chapter 4.9**, a review article on the development of electrochemical water desalination technologies is provided. Based on the different working principles, the technologies are classified into three generations. In **Chapter 4.10**, a review article on the development of hydrogen energy-driven electrochemical water desalination studies is introduced, as an emerging clean energy source, hydrogen has high potential for sustainable desalination adaptations in the future.

4. Peer-reviewed research papers

- 4.1 Effect of Pore Size on the Ion Electrosorption and Hydrogen/Deuterium Electrosorption Using Sodium Chloride in H₂O and D₂O**
- 4.2 Permselective ion electrosorption of subnanometer pores at high molar strength enables capacitive deionization of saline water**
- 4.3 Ionophobicity of carbon sub-nanometer pores enables efficient desalination at high salinity**
- 4.4 Hydration shell energy barrier differences of sub-nanometer carbon pores enable ion sieving and selective ion removal**
- 4.5 Polymer ion-exchange membranes for capacitive deionization of aqueous media with low and high salt concentration**
- 4.6 MXene/Activated-Carbon Hybrid Capacitive Deionization for Permselective Ion Removal at Low and High Salinity**
- 4.7 Particle size distribution influence on capacitive deionization: insights for electrode preparation**
- 4.8 Electrocatalytic fuel cell desalination for continuous energy and freshwater generation**
- 4.9 From capacitive deionization to desalination batteries and desalination fuel cells**
- 4.10 Emerging, hydrogen-driven electrochemical water purification**

4.1 Effects of pore size on the ion electrosorption and hydrogen/deuterium electrosorption using sodium chloride in H₂O and D₂O

Yuan Zhang,^{1,2} Pattarachai Srimuk,^{1,2} Samantha Husmann,¹
Ming Chen,^{3,4} Guang Feng,^{3,4} and Volker Presser^{1,2,5}

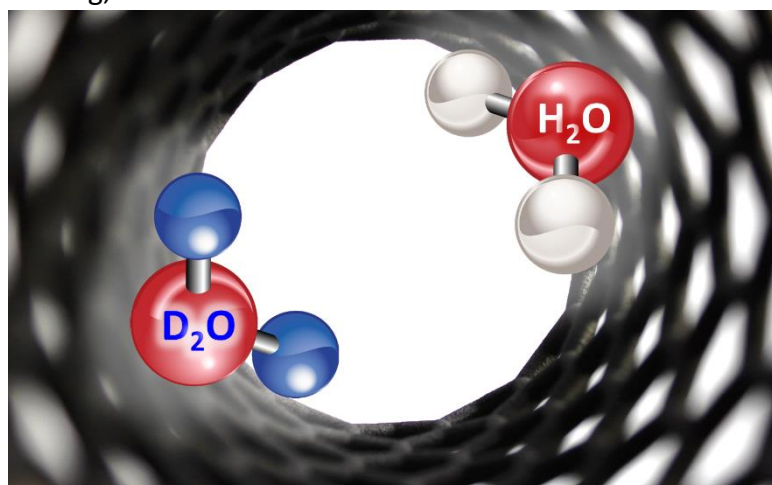
- 1 INM - Leibniz Institute for New Materials, Campus D2 2, 66123 Saarbrücken, Germany
- 2 Saarland University, Campus D2 2, 66123 Saarbrücken, Germany
- 3 State Key Laboratory of Coal Combustion, School of Energy and Power Engineering, Huazhong University of Science and Technology (HUST), Wuhan 430074, China
- 4 Nano Interface Centre for Energy, School of Energy and Power Engineering, HUST, 430074, China
- 5 Saarene - Saarland Center for Energy Materials and Sustainability, Campus C4 2, 66123 Saarbrücken, Germany

Citation:

Y. Zhang, P. Srimuk, S. Husmann, M. Chen, G. Feng and V. Presser, *Effect of Pore Size on the Ion Electrosorption and Hydrogen/Deuterium Electrosorption Using Sodium Chloride in H₂O and D₂O*, Journal of The Electrochemical Society, 2019, **166**(16): A4158-A4167. (DOI: 10.1149/2.0571916jes)

Own contribution:

Methodology, validation, formal analysis, investigation, data curation, writing-original draft, writing-review & editing, visualization.





Effect of Pore Size on the Ion Electrosorption and Hydrogen/Deuterium Electrosorption Using Sodium Chloride in H₂O and D₂O

Yuan Zhang,^{ID 1,2} Pattarachai Srimuk,^{ID 1,2} Samantha Husmann,^{ID 1} Ming Chen,^{ID 3,4} Guang Feng,^{ID 3,4} and Volker Presser^{ID 1,2, z}

¹INM - Leibniz Institute for New Materials, 66123 Saarbrücken, Germany

²Saarland University, 66123 Saarbrücken, Germany

³State Key Laboratory of Coal Combustion, School of Energy and Power Engineering, Huazhong University of Science and Technology (HUST), Wuhan 430074, China

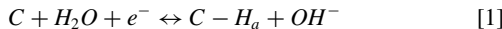
⁴Nano Interface Centre for Energy, School of Energy and Power Engineering, HUST 430074, China

In nanoconfinement, the reversible electrochemisorption of hydrogen extends the voltage window of aqueous electrolytes. This process has been well studied for different aqueous electrolytes but not compared to the performance of heavy water. Herein, we study hydrogen and deuterium electrosorption on a porous carbon electrode under negative polarization using sodium chloride as the salt. As electrodes, we use microporous carbons with an average pore size in the sub-nanometer range and, for comparison, mesoporous carbon nanotube bucky paper. We show that the hydrogen electrochemisorption and gas evolution processes are more pronounced than for deuterium while the same potential is applied. Our data confirm lower ion mobility of D₂O compared to H₂O, and a shift of the reversible charging and discharging process toward more negative potentials.

© 2019 The Electrochemical Society. [DOI: [10.1149/2.0571916jes](https://doi.org/10.1149/2.0571916jes)]

Manuscript submitted September 16, 2019; revised manuscript received November 25, 2019. Published December 16, 2019.

The effective and sustainable use of renewable energy critically requires the further advancement of electrochemical storage systems like batteries, supercapacitors, and hybrid technologies.¹ Batteries employ reversible charge transfer reactions, such as lithium intercalation/deintercalation, to store and recover energy with high capacity.² Compared to batteries, faster charge/discharge rates are enabled when using electrical double-layer capacitors, but at the expense of significantly decreased energy storage capacity.³ Beyond ion electrosorption, the confinement of water molecules in carbon nanopores suppresses the evolution of gaseous di-hydrogen; the reversible electrochemical reduction/oxidation of such weakly chemisorbed hydrogen (H_a, Eq. 1) can significantly enhance the energy storage capacity.⁴



For years, the reversible electrochemisorption of hydrogen on porous carbon electrode materials has been studied for aqueous electrolytes.^{4,5} Initially, reversible hydrogen electrochemisorption was explored for carbon nanotubes electrodes.⁶ Later works showed the promising performance of microporous carbon materials with pores smaller than 1 nm.^{7,8} The electrochemisorption of hydrogen is also influenced by functional groups on carbon surfaces. For example, Gao et al. introduced oxygen functional groups using 35 mass% H₂O₂ to activated carbon in symmetric carbon/carbon capacitor and accomplished a cell voltage of 1.9 V with cycle life over 10,000 cycles and capacitance of 100 F/g in aqueous 2 M Li₂SO₄.⁹ These works also explain the ability of electrical double-layer capacitors based on aqueous electrolytes to operate beyond the theoretical decomposition of water (1.23 V).⁹ At even higher voltages, the evolution of molecular di-hydrogen gas will start, which leads to a measurable increase in pressure inside the cell, performance degradation, and ultimately cell failure.^{4,10} Yet, the larger cell voltage window and the additional charge associated with reversible hydrogen electrochemisorption remain highly attractive for the rational design of electrical double-layer capacitors with enhancing energy storage capacity.^{4,11}

To extend the cell operating voltage and improve hydrogen electrosorption, the type of ions in the electrolyte must also be considered in addition to the pore size of carbon material and the type of functional groups.^{12,13} For example, Ratajczak et al. added sodium molybdate to aqueous 1 M Li₂SO₄ for operation at a cell voltage of 1.5 V.¹⁴ In another work, Fic et al. demonstrated the influence of the pH on the applicable potential window; the cell voltage window was extended to 1.5 V

by introducing 1 M KI neutral electrolyte to the positive electrode and 6 M KOH alkaline electrolyte to the negative electrode.¹⁵ This configuration was evaluated over 16,000 cycles, yielding a specific energy of 17 Wh/g.¹⁵ However, halide ions may also block the active reaction sites needed for the electrochemisorption of hydrogen.^{15–17} By use of aqueous 5 M LiNO₃ for the positive electrode, Fic et al. maintained a stable performance at a cell voltage of 2.1 V by retaining almost 100 F/g after 25,000 cycles at 1 A/g.¹⁵ He et al. reported that aqueous Li₂SO₄ with higher salt concentration can help to enhance the Coulombic efficiency and reduce the amount of volatile side reaction products (e.g., CO, CO₂, and H₂) caused by carbon oxidation and water electrolysis.¹⁰

While the state-of-the-art understanding of hydrogen electrochemisorption has matured, this is not the case for the corresponding processes of deuterium. So far, the use of heavy water (D₂O) was limited only to in situ experiments with conventional electrical double-layer capacitor topics using neutron scattering¹⁷ or electrochemical quartz-crystal microbalance measurements.¹⁸ The former capitalizes on the severely reduced diffuse scattering of D₂O compared to H₂O. The latter benefits from the mass difference of the H₂O and D₂O molecules for gravimetric analysis of the electrosorption processes. These works showed a slightly enhanced specific capacitance, possibly per the closer proximity of ions electrosorbed onto carbon in heavy water.¹⁷ Thermodynamically, heavy water (D₂O) is known to be less reactive than normal water (H₂O), which may enable a larger useable stable (reversible) voltage window for electrochemical applications.^{19,20} The high costs of heavy water prohibit their large scale implementation on a technical level; yet, the study of deuterium electrochemisorption and the comparison with hydrogen is an important task for the basic understanding of interfacial electrochemistry and the effect of nanoconfinement, especially in the context of electrochemisorption of hydrogen vs. deuterium.

To explore deuterium electrochemisorption and compare with hydrogen, we used electrodes of microporous activated carbon cloth with different average pore sizes (0.59 nm, 0.68 nm, and 0.96 nm, namely, ACC-10, ACC-15, and ACC-20) and mesoporous multiwalled carbon nanotubes with an average pore size of about 10 nm. The porosity analysis was accomplished by argon gas sorption. Employing water (H₂O) or heavy water (D₂O) as the solvent, we explored hydrogen or deuterium electrochemisorption in 1 M NaCl. We chose sodium chloride as the salt because of the neutral pH and pD value and its importance in the field of electrochemical water desalination.^{21,22} Our investigation was carried out by electrochemical benchmarking, S-value analysis, galvanostatic measurements, and electrochemical impedance analysis.

^zE-mail: volker.presser@leibniz-inm.de

Experimental

Materials and material characterization.—Commercially available microporous activated carbon cloth Kynol-5092-10, Kynol-5092-15, Kynol-507-20, and carbon nanotubes (CNTs) with thicknesses of 650 μm , 450 μm , 250 μm , and 100 μm , respectively, were cut into discs with a diameter of 12 mm and used as the working electrode for half-cell measurement. The multiwalled CNTs (type NC7000) were purchased from NANOCYL. The three kinds of carbon cloth are labeled ACC-10, ACC-15, and ACC-20, according to the degree of activation. We used an oversized, 650 μm thick activated carbon electrode (YP-80F, Kuraray) mixed with 5 mass% polytetrafluoroethylene as the counter electrode (12 mm in diameter) and a glass fiber mat (GF/A, Whatman) with a diameter of 13 mm as the separator.²³

Argon gas sorption analyses (GSA) were conducted by Quadasorb IQ system at -186°C as controlled by a heated cryostat filled with liquid nitrogen. All carbon samples were degassed under 200°C for 1 h and heated to 300°C for 20 h to remove surface functional groups. The calculated pore size distributions assume slit-shaped pores using quenched solid density functional theory (QSDFT); this model was found to be a good representation of the pore structure of microporous carbons.^{24,25} The average pore size corresponds to the d_{50} value, which is the pore size that cumulatively encompasses half of the maximum pore volume. The BET specific surface area values were calculated within the linear pressure range of 0.05–0.3 to meet the linearity requirements.^{26,27}

CHNS-O measurements were conducted to obtain information about the elemental composition. The H, C, N content was analyzed by using a MICRO Cube (Elementar Analysensysteme GmbH) and applying 1150°C at the combustion tube and 850°C at the reduction tube. The O content was quantified with an OXZ cube elemental analyzer (Elementar Analysensysteme GmbH) with a pyrolysis temperature of 1450°C .

Thermogravimetric analysis (TGA) was carried out with a Netzsch TG-209 system in synthetic air by heating from 25°C to 1000°C at a rate of 5 K/min. Before each measurement, the empty alumina crucible was measured using the same condition to provide a background dataset for the measurements with carbon.

Electrochemical measurements.—To determine the electrochemical stability values (S-value),^{28,29} we used a three-electrode half-cell setup with an Ag/AgCl reference electrode (3 M NaCl) in 1 M NaCl dissolved either in H_2O or D_2O . S-value test was carried out with VSP300 potentiostat/galvanostat from Bio-Logic, and the schematic setup of our electrochemical cells can be found in Ref. 30. In short, our cells have a body made of polyether ether ketone, and two titanium pistons (one of them is spring-loaded) to contact the working and counter electrode. At the plane between the two electrodes, at the height of the separator, there is a cell-opening to accommodate a reference electrode. The electrolyte was vacuum back-filled into the chamber to ensure complete immersion.

According to Xu et al.,²⁹ the S-value for negative potential window opening is calculated by applying the following equation Eq. 2:

$$S = \frac{Q_{\text{neg}}}{Q_{\text{pos}}} - 1 \quad [2]$$

where the charges Q_{neg} and Q_{pos} are calculated by integrating the positive and negative current from one cycle, respectively.

The specific capacity (mAh) is calculated from cyclic voltammetry is calculated via Eq. 3:

$$Q = \frac{\int i \, dt}{3600 \, M} \quad [3]$$

where the current i is integrated over the interval t , and M is the mass of the working electrode.

The electrochemical window opening started from 0.2 V to 0 V vs. Ag/AgCl for 5 cycles; then, the cathodic cutoff potential was increased with 50 mV steps expanding toward -2 V vs. Ag/AgCl, at each potential step, 4 cycles are conducted. For S-value calculation, the data at the

4th cycle is selected so that the electrode is well-conditioned at every vertex potential. A d^2S/dU^2 value of 0.05 was proposed by Weingarth et al.²⁸ for identifying the onset potential of parasitic faradaic reactions in electrochemically inert electrolytes, such as ionic liquids. In our case, however, we do not transition from electrostatic to electrostatic and faradaic charge transfer regimes but explore the reversibility of the faradaic process of electrochemisorption of hydrogen or deuterium. Therefore, we do not use a certain threshold value for the S-value but analyze the voltage-dependency and differences between D_2O and H_2O .

To understand the pore size and solvent influence of the long-term stability at equilibrium state in an electrochemical half-cell, floating tests are conducted. The potential is set from -1.4 V to $+0.2\text{ V}$ (for ACCs) and -1.2 V to $+0.2\text{ V}$ (for CNT) with a specific current of 0.1 A/g for three cycles followed by a potential holding at a low potential process for 10 h. By plotting the capacity values at each cycle after potential holding, we can see the stability change of different materials at different solvent systems.

Electrochemical impedance spectroscopy (EIS) is used to explore the ionic mobility in H_2O and D_2O electrolyte systems. By using the same cell configuration as the same potentiostat as mentioned above, potential (at -1.2 V and 0 V) is applied to the cell with the frequency varying from 100 kHz to 10 mHz. After the first EIS measurement, 10 cyclic voltammograms were recorded from -1.2 V to $+0.2\text{ V}$ with a scan rate of 1 mV/s. Then, the EIS measurement with the same conditions was conducted, followed by galvanostatic charging and discharging from -1.2 V to $+0.2\text{ V}$ at a specific current of 0.01–10 A/g.

Molecular dynamics simulation.—The molecular dynamics (MD) simulations of 1 M NaCl in water (H_2O) and heavy water (D_2O), consisting of 100 pairs of Na^+ and Cl^- ions as well as 5500 H_2O or D_2O molecules, were performed using the MD software package Gromacs 4.6.³¹ The OPLS force field parameters³² were used for Na^+ and Cl^- . The SPC/E model³³ and SPC/HW model³⁴ were adopted for H_2O and D_2O , respectively.

Simulations were implemented in the NPT ensemble at 300 K and 1 atm. Temperature and pressure were controlled through the Nosé-Hoover thermostat^{35,36} and Parrinello-Rahman barostat^{37,38} with coupling constants of 0.5 ps and 1 ps, respectively. Periodic boundary conditions were used in all three dimensions of the simulation system. A cutoff distance of 1.4 nm was employed for van-der-Waals terms and electrostatic interactions, whereas the long-range electrostatic interactions were accounted through the particle mesh Ewald (PME) method.^{39,40} The leapfrog integration algorithm was taken to solve the equations of motion, with a time step of 2 fs. The trajectory was saved every 1 ps. Each simulation was equilibrated within 3 ns. After that, another 10 ns production run was performed for analysis. To certify the accuracy of the simulation results, each case was repeated three times with different initial configurations.

By MD simulation, the self-diffusion coefficients (D) of ions were calculated via the Einstein relation (Eq. 4).⁴¹

$$D = \frac{1}{6} \lim_{t \rightarrow \infty} \frac{d}{dt} \left\langle [\vec{r}(t) - \vec{r}(0)]^2 \right\rangle \quad [4]$$

where the quantity in braces is the ensemble-averaged mean square displacement (MSD) of the species, and \vec{r} is the vector coordinate of the center of mass. Meanwhile, the ionic conductivity can be linked to self-diffusion coefficients given by the Nernst-Einstein (NE) equation (Eq. 5):⁴¹

$$\sigma = \frac{N_{\text{pair}}}{V k_b T} (q_+^2 D_+ + q_-^2 D_-) \quad [5]$$

where σ is the ionic conductivity, N_{pair} is the number of ion pairs in a volume V . The parameters q_+ and q_- are the charges on the cation and anion, respectively, and D_+ and D_- are the self-diffusion coefficients of cation and anion, respectively.

Table I. Chemical analysis of the electrode materials. “n.d.” stands for values below the detection limit of the system (not detected). 9% of ash content (aluminum oxide and metal oxide).

	Carbon (mass%)	Hydrogen (mass%)	Nitrogen (mass%)	Oxygen (mass%)	Ash-content (mass%)
ACC-10	94.2 ± 0.5	1.0 ± 0.1	n.d.	5.1 ± 1.0	<1
ACC-15	95.4 ± 0.6	0.7 ± 0.1	0.1 ± 0.0	2.7 ± 0.1	<1
ACC-20	96.7 ± 0.3	0.8 ± 0.1	0.2 ± 0.0	1.9 ± 0.1	<1
CNT	86.1 ± 0.5	0.7 ± 0.1	n.d.	8.1 ± 2.2	9

Results and Discussion

Porosity analysis and chemical composition of the electrode materials.—All electrode materials consist mainly of carbon (Table I). Within the series of ACC, the carbon content ranges from 94.2 mass% (ACC-10) to 96.7 mass% (ACC-20) from the lowest to the highest degree of activation; correspondingly, the oxygen content varies from 5.1 mass% (ACC-10) to 1.9 mass% (ACC-20). A lower oxygen content found for the more porous ACCs aligns with preferential volatilization of more disordered carbon during the activation process.⁴² For all ACC samples, we found a hydrogen content of about 0.7–1.0 mass% and less than 0.2 mass% of nitrogen. Compared to ACC, the CNTs contain a much higher amount of oxygen (8.1 mass%) but about the same amount of hydrogen (0.7 mass%). The lower total amount of carbon (86.1 mass%) is because of the presence of residual aluminum oxide and metal oxides (*Supporting Information*, Fig. S2) in the CNT material.⁴³ In alignment with the thermal gravimetric analysis (TGA), the residue after complete CNT oxidations in synthetic air is around 9 mass%. Elemental analysis of the CNT powder showed the presence of aluminum oxide and iron (Table I and *Supporting Information*, Fig. S2). The set of ACC carbons shows an ash-content of below 1 mass%, which is in good alignment with the CHNS-O measurements. There is also a small shift of the oxidation onset temperature at 450–500°C (*Supporting Information*, Fig. S1) with the highest oxidation resistance for ACC-20, followed by ACC-15 and ACC-10. The highest degree of carbon oxidation also aligns with the most progressed removal of less-ordered carbon; thereby, the most activated ACC samples have the least amount of remaining less-ordered material (see also Ref. 42) and, therefore, the highest oxidation resistance.

We quantified the pore structure of the different electrode materials by argon gas sorption (Table II). According to the gas sorption isotherms and cumulative pore volume distributions (Figs. 1A–1B), ACCs are predominately microporous while CNTs (in powder and bucky paper form) are dominated by intertubular mesopores. *Supporting Information*, Figure S3 shows the corresponding differential pore size distribution pattern. Within the range of ACC materials, we see a transition from type I(a) for ACC-10 to type I(b) for ACC-20 sorption isotherm (Fig. 1A), which aligns with an increase in the micropore size and pore dispersity.²⁶ CNTs as a powder or as bucky paper show nearly unlimited growth of adsorbate monolayer/multilayers at a high relative pressure (isotherm type II) explained by a continuum of mesopores and macropores in-between the individual nanotubes (Fig. 1A).²⁶ At very low relative pressure, we see a contribution of micropores per the

resemblance of type I(b) isotherm and the H3 hysteresis loop indicates the presence of non-rigid nanotube aggregates.²⁶

As seen in Fig. 1B, ACC-10 has among ACC carbons the smallest cumulative pore volume (0.34 cm³/g) but the narrowest pore size distribution and smallest average pore size (0.56 nm); ACC-20 has the highest cumulative pore volume (0.80 cm³/g) but the widest pore size distribution and largest average pore size (0.98 nm). With the increased extent of activation, we see an increase in pore size, pore-volume, and pore size dispersity when comparing ACC-10, ACC-15, and ACC-20; all ACC materials have average pore sizes below 1 nm and are almost exclusively microporous (98–99% of all pores are ≤2 nm). For CNTs, the distribution of mesopores (i.e., space between nanotubes and their clusters) depends on the degree of compaction, while the amount and dispersity of micropores (i.e., hourglass-like exohedral pores where nanotubes entangle)⁴⁴ remain rather constant. Accordingly, the more consolidated bucky paper (electrode) has a slightly smaller total pore volume (0.42 cm³/g) compared to the loose CNT powder (0.45 cm³/g). In both cases, CNTs yield a very broad, mesopore-dominated pore size distribution pattern with an average pore size of about 10 nm (Table II).

Physicochemical properties of H₂O and D₂O.—H₂O and D₂O have different physicochemical properties as solvents, and some comparative data are compiled in Table III. The different molar mass of D₂O and H₂O may cause different kinetics relevant to ion transport during the electrosorption process. To study the difference of ion transport in H₂O and D₂O, therefore, the coordination of the solvent molecules around the cation and anion is important to consider. As shown by previous work using molecular dynamics modeling, there is a slightly decreased number of solvent molecules for D₂O (6.09) compared to H₂O (6.77) for the chloride ion, but an almost equal number of solvent molecules surrounding the sodium ion (at 1 M: 4.80 for D₂O and 4.71 for H₂O). Besides, the ion self-diffusion coefficient for Na⁺ and Cl⁻ in H₂O compared to D₂O are listed (Table III). Accordingly, the calculated conductivity of 1 M NaCl in D₂O (49.82 ± 3.57 mS/cm) is much smaller compared to H₂O as the solvent (86.57 ± 9.07 mS/cm) according to MD simulation results.

Electrochemical charge storage capacity and power handling ability.—In Fig. 2, we see cyclic voltammetric and galvanostatic charge/discharge data for three different ACC and CNT bucky paper electrodes. In addition to the overall rectangular charge contribution related to ion electrosorption, there is an increased current flow related

Table II. Porosity analysis with argon gas sorption at –186°C using the quenched solid density functional theory (DFT) and the Brunauer-Emmett-Teller theory (BET). SSA: specific surface area. The average pore size refers to the volume-normalized value d₅₀. The pore volume is derived as the maximum cumulative value from the DFT dataset. The DFT micropore contribution is the relative share of the pore volume associated with pores ≤2 nm compared to the DFT total pore volume.

	SSA BET (m ² /g)	SSA DFT (m ² /g)	DFT total pore volume (cm ³ /g)	DFT micropore contribution (%)	Average pore size d ₅₀ (nm)
ACC-10	899	1254	0.34	99.4	0.56
ACC-15	1307	1484	0.59	98.6	0.74
ACC-20	1920	1740	0.80	97.6	0.98
CNT powder	207	202	0.45	11.4	~10
CNT electrode	190	188	0.42	11.5	~10

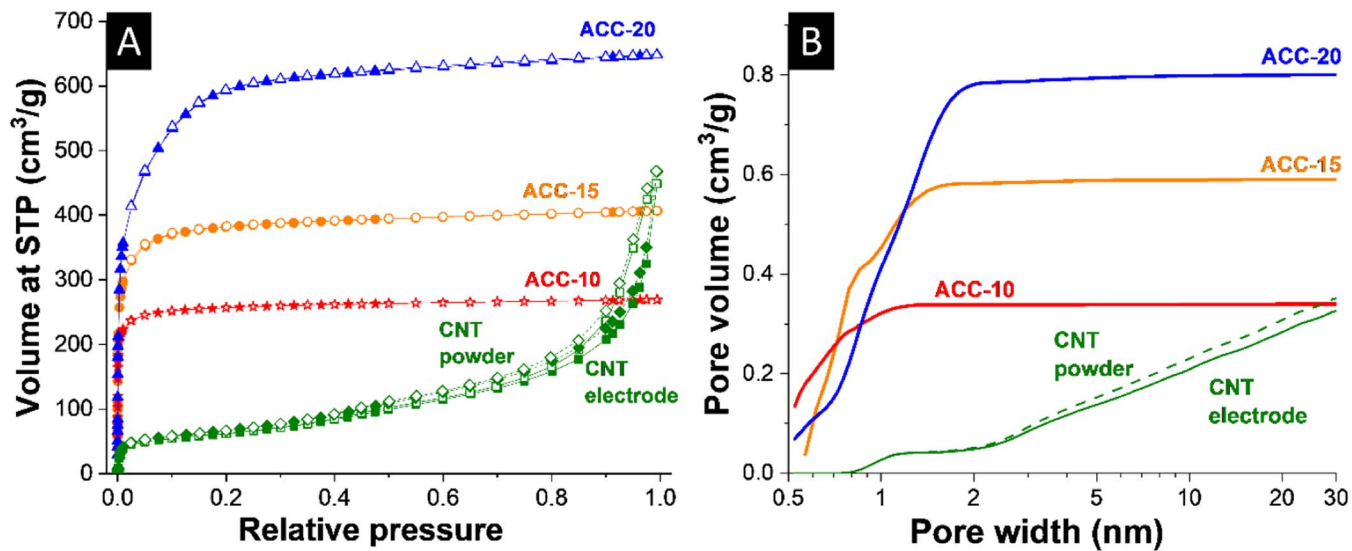


Figure 1. Argon gas sorption isotherms for ACC-10, ACC-15, ACC-20, and CNT powder (A) and calculated pore size distributions using the quenched-solid density functional theory assuming slit-shaped pores (B). STP: standard temperature and pressure.

to reversible hydrogen or deuterium electrochemisorption (Figs. 2A, 2C, 2E, 2G). This redox current is more pronounced for H₂O compared to D₂O, and the corresponding capacitance on the reverse direction after reaching the respective vertex potentials is virtually identical for all ACC materials. Thereby, the difference in capacity is carried by the faradaic process and not by significant differences regarding the ion electrosorption process of the salt ions.

Next, we surveyed the charge storage and recovery performance at different rates (Figs. 2B, 2D, 2F, 2H). Galvanostatic discharge at a low specific current of 10 mA/g yields for ACC-10 a specific capacity of 64 mAh/g (H₂O) and 54 mAh/g (D₂O); these values decreased by 77% (H₂O) and 81% (D₂O) at 10 A/g. For ACC-15, we measured a specific capacity of 77 mAh/g (H₂O) and 65 mAh/g (D₂O) at a rate of 10 mA/g; these values decreased by 60% (H₂O) and 70% (D₂O) at 10 A/g. For ACC-20, the capacity is 91 mAh/g (H₂O) and 72 mAh/g (D₂O) at a rate of 10 mA/g; these values decreased by 62% (H₂O) and 63% (D₂O) at 10 A/g. For comparison, CNT electrodes yield a value of 17 mAh/g (H₂O) and 15 mAh/g (D₂O) at a rate of 100 mA/g; these values decrease by 54% (H₂O) and 61% (D₂O) at 10 A/g. These data reveal two trends: there is an increased capacity of 1 M NaCl dissolved in H₂O that originates from the faster kinetic of hydrogen evolution reaction in nano-confinement, and a lower power handling ability of the D₂O system per the lower diffusion kinetics of the latter.

Electrochemical window opening.—We further studied the electrochemical stability window for 1 M NaCl in either H₂O or D₂O by a successive increase of the voltammetric vertex potential to quantify the Coulombic reversibility of the charge/discharge process (Fig. 3); based on these data, we calculated the stability (S-value) according to Eq. 2. The anodic vertex potential was fixed to +0.2 V vs. Ag/AgCl, and the vertex potential for the cathodic reaction was extended with 50 mV interval. As the cathodic potential is extended to -1.0 V vs. Ag/AgCl, the rectangular-shaped capacitive current response becomes distorted for all tested carbon materials. This distortion is due to the emergence of the redox reaction of hydrogen or deuterium, as evidenced by the increased oxidation and reduction current (Figs. 3A, 3C, 3E, 3G).

The increase of the S-value corresponds with a decreased reversibility of the charge/discharge process, as typical for a transition from a domain of predominant ion electrosorption to a process involving an increased contribution of faradaic reactions. However, the S-value analysis itself cannot identify the actual nature of the irreversibility, including faradaic or non-faradaic processes, as possible sources for the irreversible recovery of the charge. Non-faradaic causes for a reduced S-value may include ion sieving,⁴⁵ ion starvation,⁴⁶ or other kinetically hindered processes.³⁰ For all ACC materials, we see an onset of an increasing S-value at -1.3 V to -1.4 V vs. Ag/AgCl. This onset range is at much more negative potentials compared to the

Table III. Selected physicochemical properties of D₂O and H₂O.

	H ₂ O	D ₂ O	Reference
Molecular mass	18.02 g/mol	20.03 g/mol	58,59
Density at 25°C, 101.325 kPa	997.05 kg/m ³ (liquid)	1104.36 kg/m ³ (liquid)	59,60
Boiling point at 101.325 kPa	100°C	101.42°C	58,61
Gibbs energy of formation	-237.15 kJ/mol (liquid) -228.59 kJ/mol (gas)	-243.44 kJ/mol (liquid) -234.54 kJ/mol (gas)	58,62-64
H-O-H or D-O-D bond angle	105.5° (liquid)	106° (liquid)	65-67
O-H or O-D bond length	0.991 Å (liquid)	0.970 Å (liquid)	65-67
Coordination number for Na ⁺ at 1 M NaCl	4.71	4.80	18
Coordination number for Cl ⁻ at 1 M NaCl	6.77	6.09	18
Water self-diffusion coefficient	2.36 ± 0.01·10 ⁻⁹ m ² /s	1.36 ± 0.01·10 ⁻⁹ m ² /s	This work
Na ⁺ self-diffusion coefficient	1.06 ± 0.10·10 ⁻⁹ m ² /s	0.64 ± 0.08·10 ⁻⁹ m ² /s	This work
Cl ⁻ self-diffusion coefficient	1.33 ± 0.16·10 ⁻⁹ m ² /s	0.72 ± 0.03·10 ⁻⁹ m ² /s	This work
Conductivity	86.57 ± 9.07 mS/cm	49.82 ± 3.57 mS/cm	This work

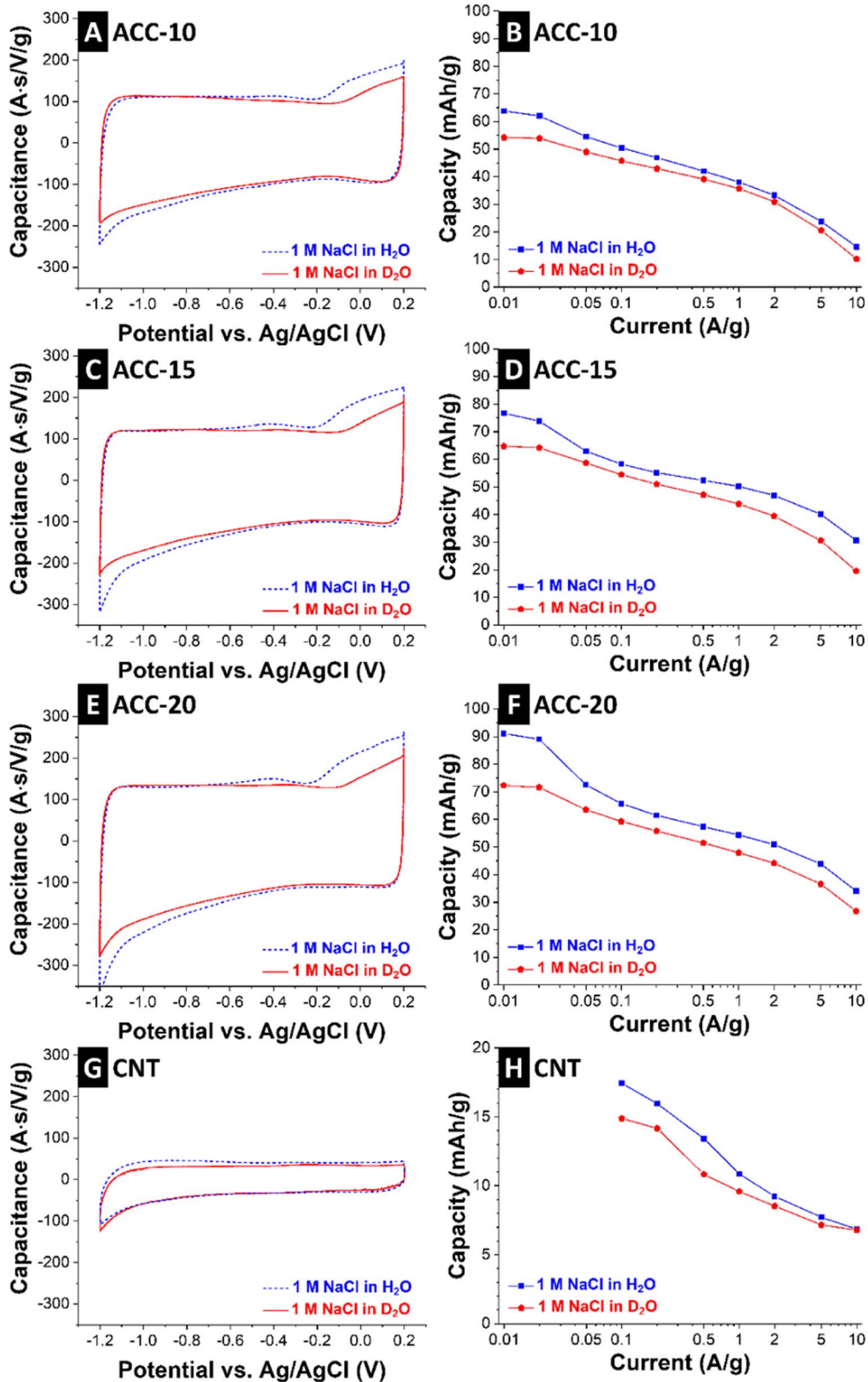


Figure 2. Cyclic voltammograms and electrochemical impedance spectroscopy of ACC-10, ACC-15, ACC-20, and CNT electrode in 1 M NaCl dissolved in either H₂O or D₂O. Applied potential: -1.2 V or 0 V vs. Ag/AgCl.

mostly mesoporous CNT electrode with a value of about -0.8 V to -0.9 V vs. Ag/AgCl (Fig. 2H). As the vertex potential is further extended to the negative values, H₂ and D₂ gas evolution take place, as evidenced by the emergence of a pronounced current (Figs. 3A, 3C, 3E, 3G).⁴⁷ The latter is seen beyond -1.8 V vs. Ag/AgCl for ACC

samples and at about -1.2 V to -1.3 V vs. Ag/AgCl in the case of CNT. For all ACC carbons, the increase of the S-value for D₂O is less steep than that for H₂O when the potential extended to -1.3 V to -1.4 V vs. Ag/AgCl and extended to more negative values. Yet, the larger increase in S-value for D₂O as a solvent than that of H₂O may

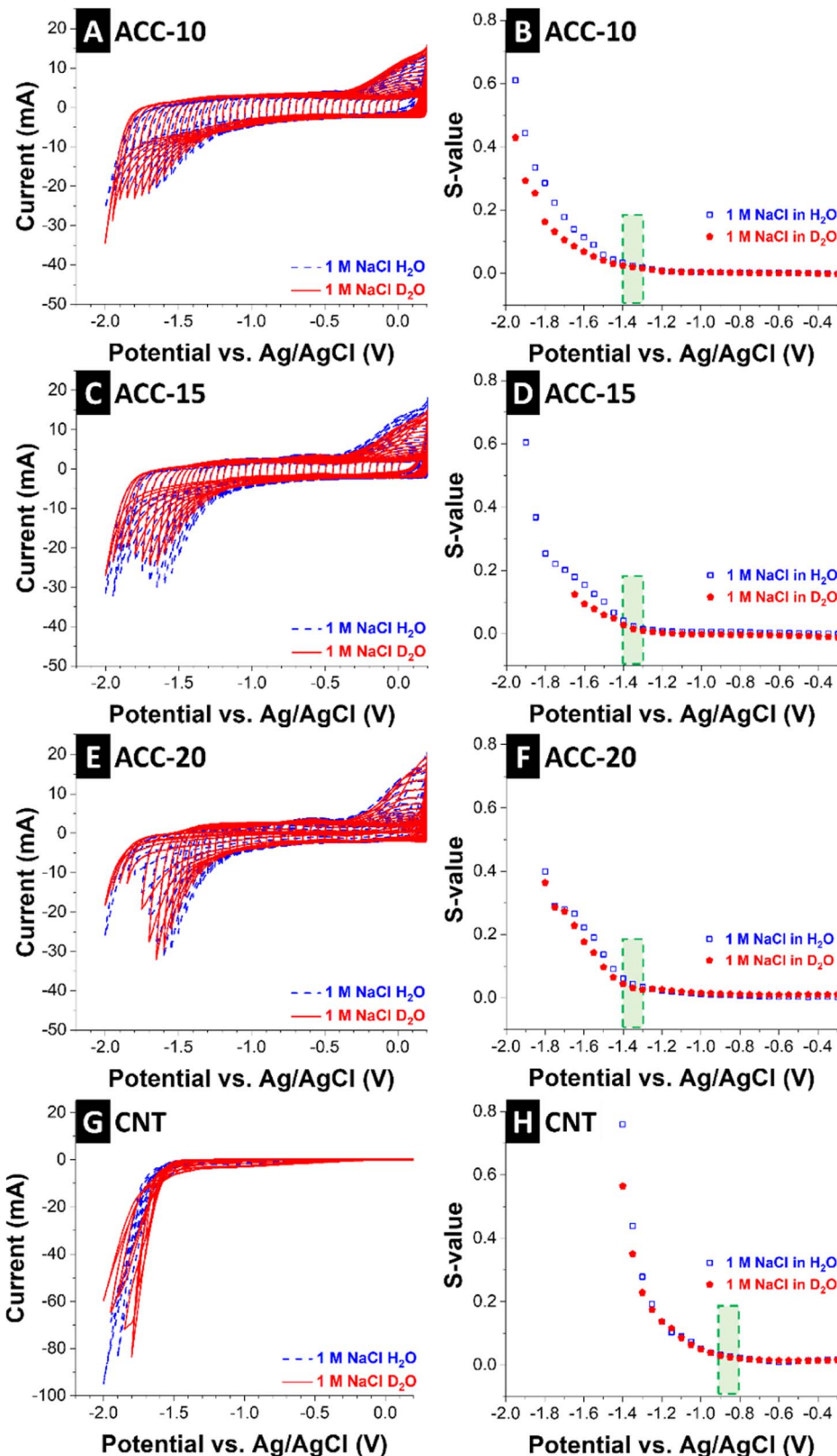


Figure 3. Cyclic voltammetric window opening and derived S-values of ACC-10 (A-B), ACC-15 (C-D), ACC-20 (E-F), and CNT(G-H). All measurements were done with an oversized counter electrode (activated carbon) at a scan rate of 1 mV/s. Each potential step was measured for four cycles, and the window step width was $\Delta 50$ mV.

be related to the degree of nano-confinement that possibly changes the equilibrium of the reaction or the kinetic energy that originated from the diffusivity of solvent.

Correspondingly, the strongest effects occur when comparing micropores (where nanoconfinement occurs) and mesopores (where these effects are mostly absent).

Tafel analysis.—To identify the onset potential for Faradic reactions and to understand the different S-value pattern for H₂O and D₂O solvents, we obtained the Tafel plot (Figs. 4A, 4C, 4E, 4G) from cyclic voltammetry (Fig. 2).⁴⁸ The potential range is selected from -1.2 V to -0.8 V, where redox reaction peaks of hydrogen or deuterium electrochemisorption are observed. To determine the overpotential for

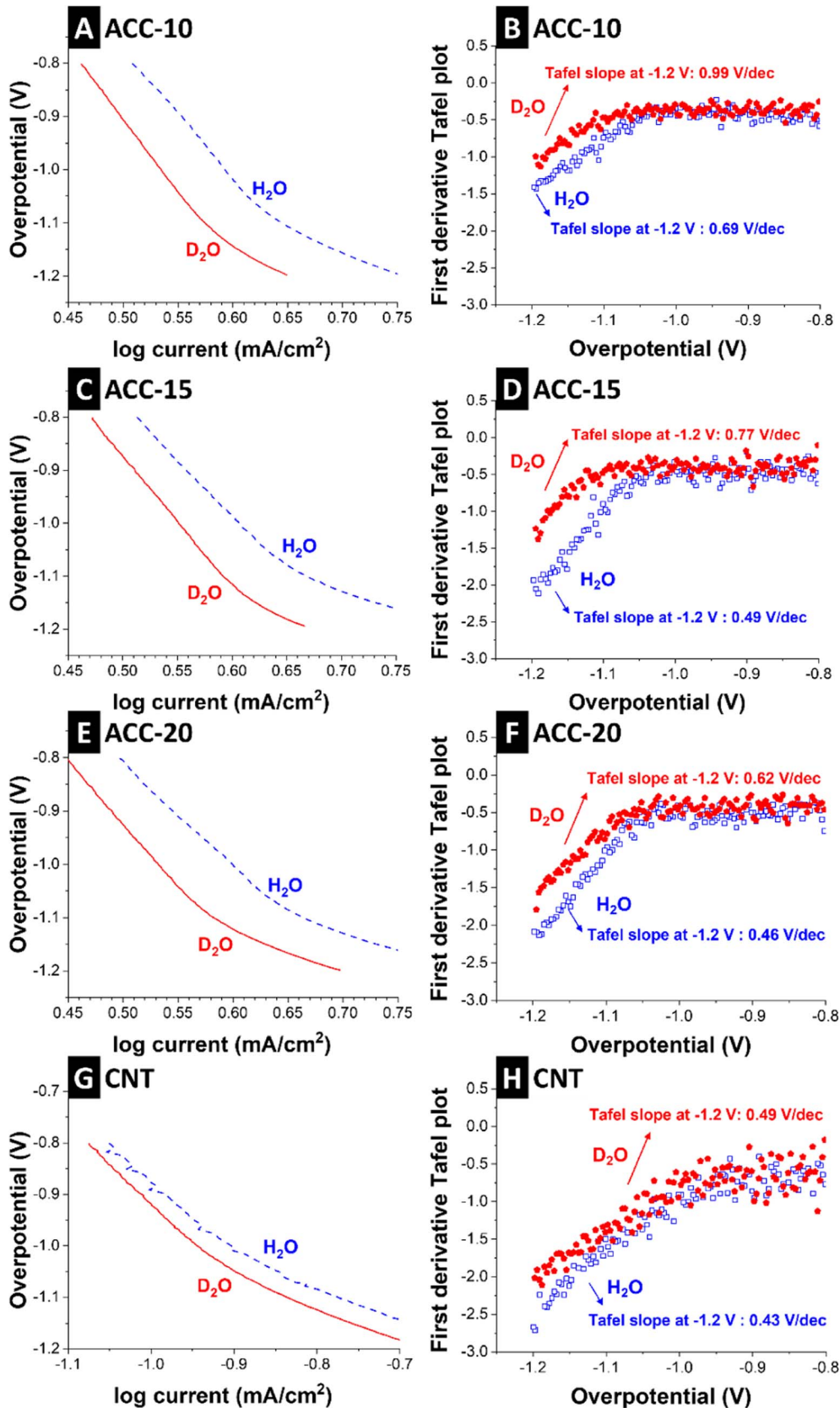


Figure 4. Tafel plot (A,C,E,G) and first derivate (B,D,F,H) of ACC-10, ACC-15, ACC-20, and CNT with either H_2O or D_2O as the solvent for 1 M NaCl. The values for the current density are obtained from cyclic voltammetry (see Fig. 2) in the potential range of -1.2 V to -0.8 V vs. Ag/AgCl.

hydrogen and deuterium electrochemisorption, the first derivative of the Tafel relation (dT/dU) was calculated in Figs. 4B, 4D, 4F, 4H (T: log value of the current density; U: overpotential). Up to about -1 V vs. Ag/AgCl, we see a constant dT/dU value of about 0.5 for all ACC materials. This small value aligns with the fast process of ion electrosorption. As the cathodic potential of the ACC electrodes is below -1 V, the dT/dU values become more negative, indicating slower processes relating to hydrogen and deuterium electrochemisorption.⁴⁹ Within the carbon nanopores, the reactivity of H_2O as the solvent exceeds that of D_2O .

The kinetic isotope effects have been evaluated by zero-point energy (ZPE). Density functional theory calculations were performed to obtain the ZPE of 0.421 eV and 0.579 eV for D_2O and H_2O , respectively (*Supporting Information*, Section 2: *DFT calculations*). The lower ZPE indicates that more energy must be provided to break O–D bond, aligning with a lower rate of the faradaic reactions for D_2O .⁵⁰ The latter also aligns with the lower ion mobility (Table III) for D_2O . Ideally, DFT system including the micropores could take into account the pore confinement, however, the DFT system cannot mimic the realistic pore filled with H_2O and D_2O due to the limitation of computational resource and the complex electrode structure in practice. Herein, we give the values of ZPEs H_2O and D_2O , just to show the qualitative evaluation of their faradaic reactions, and then it is reasonable to think such evaluation would qualitatively hold under the same confinement.

Among the set of ACC carbons, the ion mobility increases from ACC-10 to ACC-15 and to ACC-20. In mesoporous CNT, the onset potential for electrolyte decomposition is already at -0.9 V, and there is no distinct difference of kinetic effect in the H_2O and D_2O system. Since smaller carbon nanopores provide not only more confinement but also longer diffusion pathways, kinetic effects become visible in case of microporous ACC carbons.

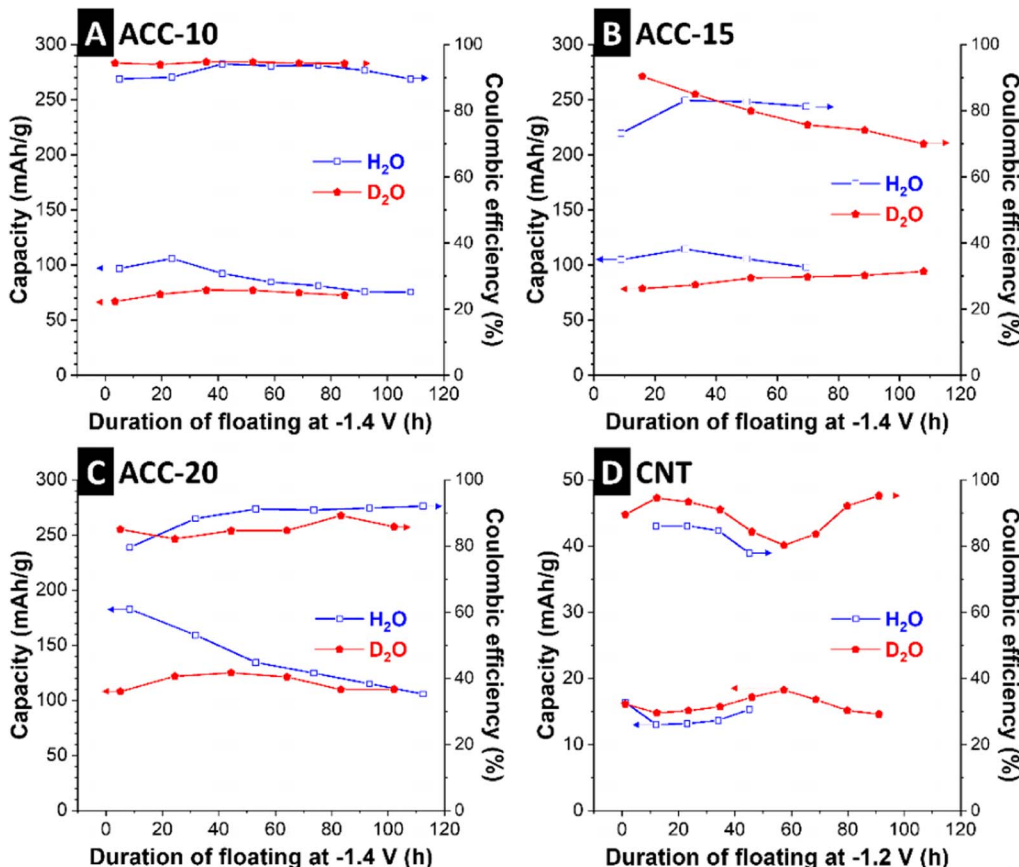


Figure 5. Floating test with 3 cycles of galvanostatic charging and discharging from -1.4 V (ACC carbons)/ -1.2 V (CNT) to 0.2 V in a specific current of 0.1 A/g with potential holding at -1.4 V (ACC carbons)/ -1.2 V (CNT) for 10 h.

Floating test analysis.—Voltage floating is a practical tool to investigate the performance stability related to electrolyte decomposition (or the lack thereof). This is because the system is forced to remain at a certain cell voltage, triggering, and maintaining any irreversible electrolyte process. As seen in Fig. 5, carbon materials in the H_2O system have higher capacity when the same potential range is applied. This agrees with our initial electrochemical testing (Fig. 2). The higher faradaic current related to hydrogen electrochemisorption compared to the kinetically impaired D_2O system explain the small differences in performance stability. Specifically, we see a trend of decreasing capacity but an increase in Coulombic efficiency for H_2O as the solvent in all ACC samples (Figs. 5A–5C). This trend is more pronounced for ACC-20 (Fig. 5C), which has the largest average micropore diameter and the largest total pore volume. In the case of CNT electrodes, there is no distinct capacity difference for H_2O and D_2O electrolytes (Fig. 5D). This observation can be explained by the mesoporous structure that overcomes the difference of ion mobilities in H_2O and D_2O solvents within nanopores and the absence of reversible electrochemisorption of either hydrogen or deuterium.

Electrochemical impedance analysis.—The H_2O and D_2O systems are further characterized by electrochemical impedance spectroscopy. The Nyquist plots in Fig. 6 show four kinds of carbon materials in electrolytes of 1 M NaCl dissolved in H_2O and D_2O at -1.2 V and 0 V vs. Ag/AgCl. For all conditions, the impedance data do not show spectral features characteristic of charge transfer reactions, such as surface redox or ion insertion. At high frequencies, the Nyquist curve shows a 45° angle linear line, which represents reflective finite-length diffusion.^{51,52} The curve gradually becomes more perpendicular as the frequency decreases. For all ACC carbons, the 45° line extends to more resistive values when potentials are applied, and this difference is more pronounced at -1.2 V vs. Ag/AgCl than that at 0 V. Also,

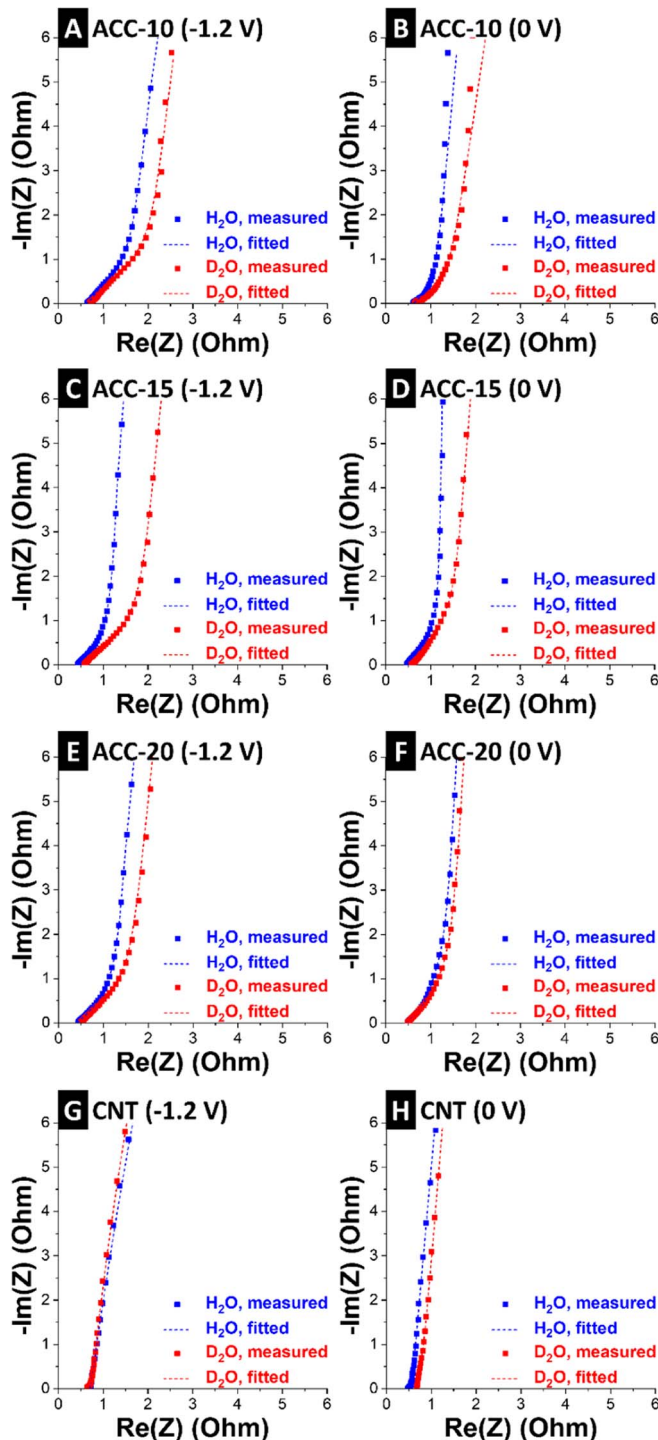


Figure 6. Electrochemical impedance spectroscopy of ACC-10, ACC-15, ACC-20, and CNT electrode in 1 M NaCl dissolved in either H₂O or D₂O. Applied potential: −1.2 V or 0 V vs. Ag/AgCl. See Fig. 7 for the equivalent circuit model used for fitting the impedance data.

this difference is larger for ACC-10 and ACC-15 which have an average pore size smaller than 0.8 nm. For ACC-20 with an average pore size of 0.98 nm, the difference of the EIS curve is smaller, especially when 0 V is applied to the electrode. For the highly mesoporous CNT bucky paper, we see a much smaller difference between the datasets for either of the two different solvents (Figs. 6E–6F). In the absence of diffusion-limiting micropores, there is no 45°-regime either. The longer 45°-regime for ACC carbons at −1.2 V vs. Ag/AgCl compared

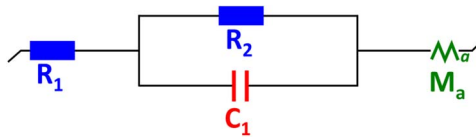


Figure 7. Equivalent circuit model used for fitting of the impedance data.

to 0 V aligns with a different state of charge and the in-pore ion population. At −1.2 V vs. Ag/AgCl, the carbon nanopores are populated by more cations than anions.^{18,53,54} The lower self-diffusion coefficient of Na⁺ compared to Cl[−] (Table III) explains the more extended 45°-regime at negative polarization.

We further analyzed the impedance data (Fig. 6) by the use of a simple equivalent circuit model (Fig. 7) to enable a quantitative comparison between the spectra. The resulting values are provided in Tables IV–V. In the equivalent circuit, R₁ represents the resistance of electrode-electrolyte interphase, R₂ is the charge transfer resistance, and C₁ represents the electrical double-layer capacitance. M_a is modified restricted diffusion with three fitting parameters, namely, R_{ds} (diffusion resistance), t_s (time constant), and a_s (dispersion parameter).^{55–57} When using D₂O as the solvent for 1 M NaCl, the value for R_{ds} is always larger compared to H₂O as a solvent. For CNT bucky paper, R_{ds} is indistinguishable for both solvents per the dominance of mesopores in the system. When comparing the values for R_{ds} and t_s obtained at 0 V and −1.2 V vs. Ag/AgCl, the fitting results indicate that the hydrogen and deuterium evolution/adsorption further extend the diffusion in H₂O and D₂O.

These data align with the findings from the Tafel relation: below −1.1 V vs. Ag/AgCl, the slope values become smaller compared with the corresponding values at a more positive potential. The pore size and electrolyte dependence of R_{ds} also agree with the Tafel slopes shown in Fig. 4, and we confirm kinetically limited faradaic reactions in micropores and when using D₂O rather than H₂O.

Conclusions

We used microporous activated carbon cloth and mesoporous carbon nanotubes as electrodes to study hydrogen and deuterium electrochemisorption in H₂O and D₂O as the solvent for 1 M NaCl. In micropores, hydrogen and deuterium electrosorption occur, but this process is absent in mesopores. The lower ion mobility and reactivity of the D₂O system are seen for all microporous carbons, and the kinetic limitation is more pronounced when decreasing the micropore diameter. This kinetic aspect is important to understand the different rate handling ability of D₂O vs. H₂O systems and the pore size dependence; yet, it does not translate to an overall enhance voltage stability window. The latter pertains more to an equilibrium property, and all our microporous carbons show the onset of irreversible electrochemisorption of deuterium and hydrogen in the range of −1.3 V to −1.4 V vs. Ag/AgCl. Correspondingly, no actual enhancement of the performance stability was found when comparing D₂O and H₂O as a

Table IV. The fitted data from electrochemical impedance spectroscopy of four kinds of carbon materials in both H₂O and D₂O system with an applied potential of −1.2 V vs. Ag/AgCl.

Electrode	Solvent	R ₁ (Ω)	R ₂ (Ω)	C ₁ (F)	R _{ds} (Ω)	t _s (s)	a _s
ACC-10	H ₂ O	0.63	0.44	2.36	1.09	2.52	0.92
	D ₂ O	0.68	0.49	3.87	2.30	6.26	0.93
ACC-15	H ₂ O	0.42	0.27	3.56	1.02	2.27	0.96
	D ₂ O	0.56	0.30	7.52	2.70	6.36	0.94
ACC-20	H ₂ O	0.42	0.29	4.21	1.27	2.83	0.94
	D ₂ O	0.48	0.37	4.88	2.03	4.69	0.94
CNT	H ₂ O	0.58	39.65	0.13	0.02	0.57·10 ^{−3}	0.89
	D ₂ O	0.92	55.88	0.13	0.47	0.02	0.89

Table V. The fitted data from Electrochemical impedance spectroscopy of four kinds of carbon materials in both H₂O and D₂O system with an applied potential of 0 V vs. Ag/AgCl.

Electrode	Solvent	R ₁ (Ω)	R ₂ (Ω)	C ₁ (F)	R _{d5} (Ω)	t ₅ (Ω)	a ₅
ACC-10	H ₂ O	0.61	0.12	8.732	1.02	1.64	0.94
	D ₂ O	0.69	0.10	12.92	1.72	2.47	0.95
ACC-15	H ₂ O	0.45	0.36	2.23	0.97	1.61	0.99
	D ₂ O	0.57	0.52	1.94	1.14	1.62	0.95
ACC-20	H ₂ O	0.46	0.42	3.32	1.19	1.76	0.97
	D ₂ O	0.47	0.44	3.32	1.54	2.46	0.96
CNT	H ₂ O	0.47	0.05	0.07	0.12	5.06·10 ⁻³	0.94
	D ₂ O	0.68	0.09	0.29	4.39·10 ⁻⁶	0.10·10 ⁻⁶	0.95

solvent for 1 M NaCl via voltage floating. The overall enhanced energy storage capacity of the H₂O system over the D₂O system relates to the enhanced contribution of the faradaic process of electrochemisorption of hydrogen. The ion electrosorption capacity in H₂O and D₂O, at least for the probed salt system of sodium chloride, is not distinguishable.

Acknowledgments

The authors thank Eduard Arzt (INM) for his continuing support. We thank Hwirim Shim and Andrea Jung (INM) for their support with thermogravimetric analysis and CHNS-O measurements, respectively. M.C. and G.F. acknowledge funding from the National Natural Science Foundation of China (No. 51836003).

ORCID

Yuan Zhang  <https://orcid.org/0000-0002-4083-0928>
 Pattrachai Srimuk  <https://orcid.org/0000-0002-7303-9876>
 Samantha Husmann  <https://orcid.org/0000-0001-6157-214X>
 Ming Chen  <https://orcid.org/0000-0002-2188-5472>
 Guang Feng  <https://orcid.org/0000-0001-6659-9181>
 Volker Presser  <https://orcid.org/0000-0003-2181-0590>

References

- Z. Yang, J. Zhang, M. C. W. Kintner-Meyer, X. Lu, D. Choi, J. P. Lemmon, and J. Liu, *Chemical Reviews*, **111**, 3577 (2011).
- R. Schöllhorn, *Comments on Inorganic Chemistry*, **2**, 271 (1983).
- M. Salanne, B. Rotenberg, K. Naoi, K. Kaneko, P. L. Taberna, C. P. Grey, B. Dunn, and P. Simon, *Nature Energy*, **1**, 16070 (2016).
- K. Fic, A. Platek, J. Piwek, J. Menzel, A. Slesinski, P. Bujewska, P. Galek, and E. Frackowiak, *Energy Storage Materials*, **22**, 1 (2019).
- F. Béguin, K. Kierzek, M. Friebe, A. Jankowska, J. Machnikowski, K. Jurewicz, and E. Frackowiak, *Electrochimica Acta*, **51**, 2161 (2006).
- E. Frackowiak and F. Béguin, *Carbon*, **40**, 1775 (2002).
- C. Vix-Guterl, E. Frackowiak, K. Jurewicz, M. Friebe, J. Parmentier, and F. Béguin, *Carbon*, **43**, 1293 (2005).
- E. Raymundo-Pinero and F. Béguin, in *Interface Science and Technology*, T. J. Bandosz Editor, p. 293, Elsevier (2006).
- Q. Gao, L. Demarconnay, E. Raymundo-Pinero, and F. Beguin, *Energy & Environmental Science*, **5**, 9611 (2012).
- M. He, K. Fic, E. Frackowiak, P. Novák, and E. J. Berg, *Energy Storage Materials*, **5**, 111 (2016).
- J. Lee, B. Krüner, A. Tolosa, S. Sathyamoorthy, D. Kim, S. Choudhury, K.-H. Seo, and V. Presser, *Energy & Environmental Science*, **9**, 3392 (2016).
- Q. Abbas, B. Gollas, and V. Presser, *Energy Technology*, **7**, 1900430 (2019).
- K. Fic, M. Meller, and E. Frackowiak, *Journal of The Electrochemical Society*, **162**, A5140 (2015).
- P. Ratajczak, K. Jurewicz, and F. Beguin, *Journal of Applied Electrochemistry*, **44**, 475 (2014).
- K. Fic, M. Meller, J. Menzel, and E. Frackowiak, *Electrochimica Acta*, **206**, 496 (2016).
- J. Lee, P. Srimuk, S. Fleischmann, A. Ridder, M. Zeiger, and V. Presser, *Journal of Materials Chemistry A*, **5**, 12520 (2017).
- S. Boukhalfa, L. He, Y. B. Melnichenko, and G. Yushin, *Angewandte Chemie International Edition*, **52**, 4618 (2013).
- P. Srimuk, J. Lee, Ö. Budak, J. Choi, M. Chen, G. Feng, C. Prehal, and V. Presser, *Langmuir*, **34**, 13132 (2018).
- A. Ben-Naim, *Solvation Thermodynamics*, Springer, New York (1987).
- A. A. Sunier and J. Baumbach, *Journal of Chemical & Engineering Data*, **21**, 335 (1976).
- S. Porada, R. Zhao, A. van der Wal, V. Presser, and P. M. Biesheuvel, *Progress in Materials Science*, **58**, 1388 (2013).
- C. Prehal, C. Koczwara, N. Jäckel, A. Schreiber, M. Burian, H. Amenitsch, M. A. Hartmann, V. Presser, and O. Paris, *Nature Energy*, **2**, 16215 (2017).
- J. Lee, N. Jäckel, D. Kim, M. Widmaier, S. Sathyamoorthy, P. Srimuk, C. Kim, S. Fleischmann, M. Zeiger, and V. Presser, *Electrochimica Acta*, **222**, 1800 (2016).
- C. Prehal, S. Grätz, B. Krüner, M. Thommes, L. Borchardt, V. Presser, and O. Paris, *Carbon*, **152**, 416 (2019).
- S. Choudhury, B. Krüner, P. Massuti-Ballester, A. Tolosa, C. Prehal, I. Grobelsek, O. Paris, L. Borchardt, and V. Presser, *Journal of Power Sources*, **357**, 198 (2017).
- M. Thommes, K. Kaneko, A. V. Neimark, J. P. Olivier, F. Rodriguez-Reinoso, J. Rouquerol, and K. S. W. Sing, *Pure and Applied Chemistry*, **87**, 1051 (2015).
- S. Brunauer, P. H. Emmett, and E. Teller, *Journal of the American Chemical Society*, **60**, 309 (1938).
- D. Weingarth, H. Noh, A. Foelske-Schmitz, A. Wokaun, and R. Kötz, *Electrochimica Acta*, **103**, 119 (2013).
- K. Xu, S. P. Ding, and T. R. Jow, *Journal of The Electrochemical Society*, **146**, 4172 (1999).
- D. Weingarth, M. Zeiger, N. Jäckel, M. Aslan, G. Feng, and V. Presser, *Advanced Energy Materials*, **4**, 1400316 (2014).
- B. Hess, C. Kutzner, D. van der Spoel, and E. Lindahl, *Journal of Chemical Theory and Computation*, **4**, 435 (2008).
- W. L. Jorgensen, D. S. Maxwell, and J. Tirado-Rives, *Journal of the American Chemical Society*, **118**, 11225 (1996).
- H. J. C. Berndsen, J. R. Grigera, and T. P. Straatsma, *The Journal of Physical Chemistry*, **91**, 6269 (1987).
- J. R. Grigera, *The Journal of Chemical Physics*, **114**, 8064 (2001).
- S. Nose, *Molecular Physics*, **52**, 255 (1984).
- W. G. Hoover, *Physical Review A*, **31**, 1695 (1985).
- M. Parrinello and A. Rahman, *Journal of Applied Physics*, **52**, 7182 (1981).
- S. Nose and M. L. Klein, *Molecular Physics*, **50**, 1055 (1983).
- T. Darden, D. York, and L. Pedersen, *The Journal of Chemical Physics*, **98**, 10089 (1993).
- U. Essmann, L. Perera, M. L. Berkowitz, T. Darden, H. Lee, and L. G. Pedersen, *The Journal of Chemical Physics*, **103**, 8577 (1995).
- M. P. Allen and D. J. Tildesley, *Computer Simulation of Liquids: Second Edition*, p. 641, Oxford Scholarshi (2017).
- C. Kim, P. Srimuk, J. Lee, S. Fleischmann, M. Aslan, and V. Presser, *Carbon*, **122**, 329 (2017).
- C. M. White, R. Banks, I. Hamerton, and J. F. Watts, *Progress in Organic Coatings*, **90**, 44 (2016).
- M. M. Hantel, V. Presser, J. K. McDonough, G. Feng, P. T. Cummings, Y. Gogotsi, and R. Kötz, *Journal of the Electrochemical Society*, **159**, A1897 (2012).
- R. Lin, P. Huang, J. Ségalini, C. Largeot, P. L. Taberna, J. Chmiola, Y. Gogotsi, and P. Simon, *Electrochimica Acta*, **54**, 7025 (2009).
- M. Aslan, M. Zeiger, N. Jäckel, I. Grobelsek, D. Weingarth, and V. Presser, *Journal of Physics: Condensed Matter*, **28**, 114003 (2016).
- K. Babel, D. Janasiak, and K. Jurewicz, *Carbon*, **50**, 5017 (2012).
- J. Tafel, Über die Polarisation bei kathodischer Wasserstoffentwicklung, in *Zeitschrift für Physikalische Chemie*, p. 641 (1905).
- T. Shinagawa, A. T. Garcia-Esparza, and K. Takanabe, *Scientific Reports*, **5**, 13801 (2015).
- P. Atkins and L. Jones, *Chemical Principles*, p. 1200, W. H. Freeman (2008).
- C. Criado, P. Galán-Montenegro, P. Velásquez, and J. R. Ramos-Barrado, *Journal of Electroanalytical Chemistry*, **488**, 59 (2000).
- T. S. Mathis, N. Kurra, X. Wang, D. Pinto, P. Simon, and Y. Gogotsi, *Advanced Energy Materials*, **9**, 1902007 (2019).
- C. Prehal, C. Koczwara, H. Amenitsch, V. Presser, and O. Paris, *Nature Communications*, **9**, 4145 (2018).
- J. M. Griffin, A. C. Forse, H. Wang, N. M. Trease, P. L. Taberna, P. Simon, and C. P. Grey, *Faraday Discussions*, **176**, 49 (2015).
- B. E. Conway, *Electrochemical Supercapacitors*, p. 736, Springer, Berlin (1999).
- T. Pajkossy, A. P. Borosy, A. Imre, S. A. Martemyanov, G. Nagy, R. Schiller, and L. Nyikos, *Journal of Electroanalytical Chemistry*, **366**, 69 (1994).
- T. Pajkossy and L. Nyikos, *Journal of The Electrochemical Society*, **133**, 2061 (1986).
- D. R. Lide, *Handbook of Chemistry and Physics*, p. 2624, CRC Press, Boca Raton (2004).
- F. J. Millero, R. Feistel, D. G. Wright, and T. J. McDougall, *Deep Sea Research Part I: Oceanographic Research Papers*, **55**, 50 (2008).
- M. Nakamura, K. Tamura, and S. Murakami, *Thermochimica Acta*, **253**, 127 (1995).
- H. Preston-Thomas, *Metrologia*, **27**, 107 (1990).
- G. Job and F. Herrmann, *European Journal of Physics*, **27**, 353 (2006).
- D. D. Wagman, W. H. Evans, V. B. Parker, R. H. Schumm, I. Halow, S. M. Bailey, K. L. Churney, and R. L. Nutall (1982).
- W. A. P. Luck, *Journal of Molecular Structure*, **448**, 131 (1998).
- A. Zeidler, P. S. Salmon, H. E. Fischer, J. C. Neuefeind, J. Mike Simonson, and T. E. Markland, *Journal of Physics: Condensed Matter*, **24**, 284126 (2012).
- K. Ichikawa, Y. Kameda, T. Yamaguchi, H. Wakita, and M. Misawa, *Molecular Physics*, **73**, 79 (1991).
- P. L. Silvestrelli and M. Parrinello, *The Journal of Chemical Physics*, **111**, 3572 (1999).

Supporting Information

Effect of pore size on the ion electrosorption and hydrogen/deuterium electrosorption using sodium chloride in H₂O and D₂O

Yuan Zhang,^{1,2} Pattarachai Srimuk,^{1,2} Samantha Husmann,¹

Ming Chen,^{3,4} Guang Feng,^{3,4} and Volker Presser^{1,2,*}

¹ INM - Leibniz Institute for New Materials, Campus D2 2, 66123 Saarbrücken, Germany

² Saarland University, Campus D2 2, 66123 Saarbrücken, Germany

³ State Key Laboratory of Coal Combustion, School of Energy and Power Engineering, Huazhong University of Science and Technology (HUST), Wuhan 430074, China

⁴ Nano Interface Centre for Energy, School of Energy and Power Engineering, HUST, 430074, China

* Corresponding author's eMail: volker.presser@leibniz-inm.de

Section 1: Supporting Figures

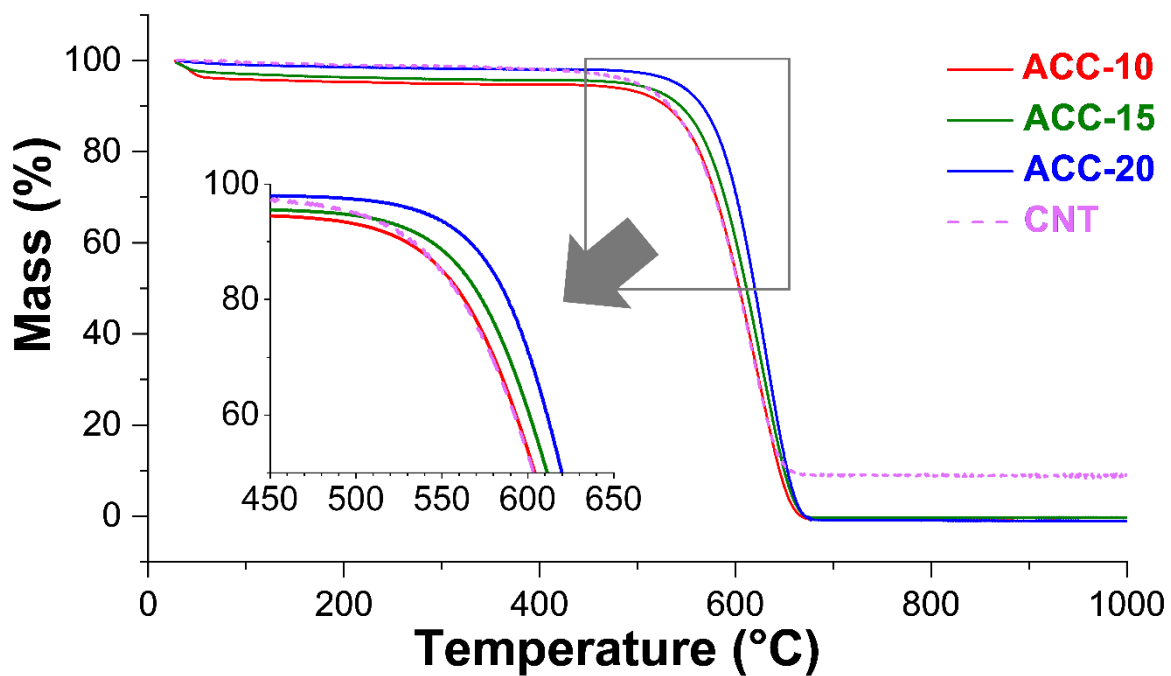


Figure S1: Thermogravimetric analysis of different carbon materials.

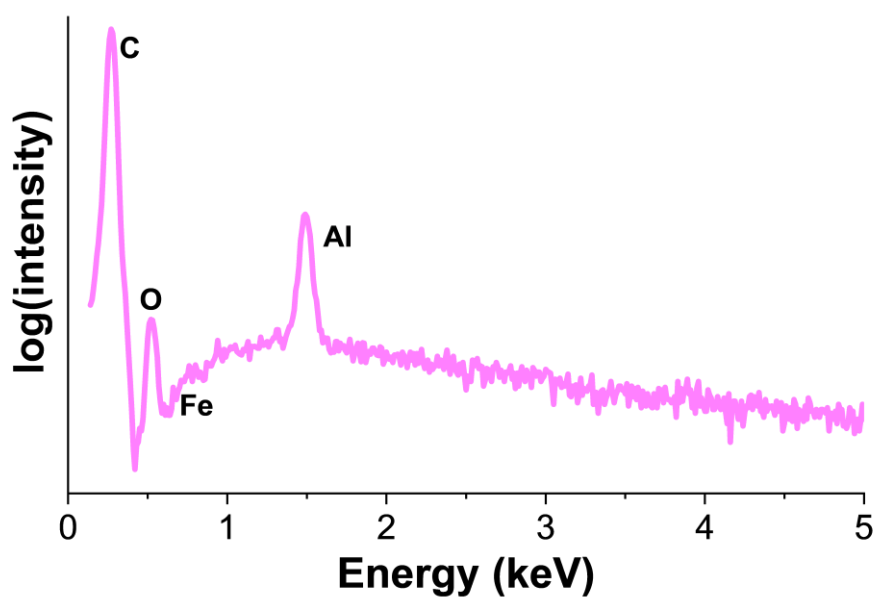


Figure S2: EDX spectrum of the CNT powder.

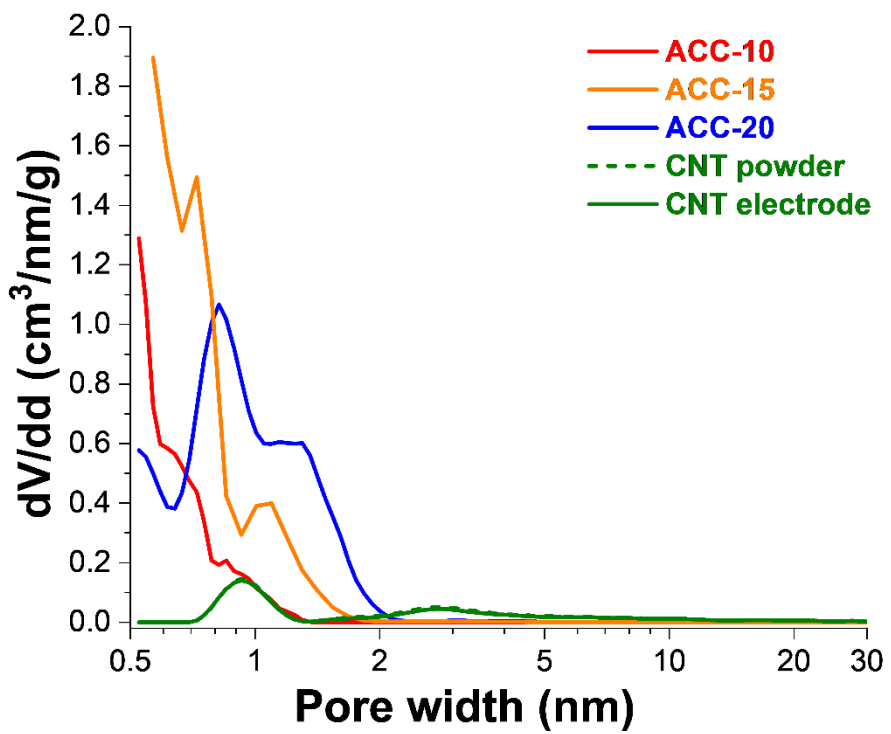


Figure S3: Differential pore size distribution pattern.

Section 2: DFT calculations

Density functional theory (DFT) calculations were carried out using Vienna ab-initio simulation package (VASP)⁽¹⁾ with the Perdew-Burke-Ernzerhof (PBE)⁽²⁾ exchange-correlation functions of generalized gradient approximation (GGA). The projector augmented wave (PAW) method⁽³⁾ with a cutoff energy of 500 eV was adopted to describe the interaction between nuclei and electrons. The H₂O and D₂O systems were established within 20x20x20 Å³ to avoid interaction between periodic images. The convergences of energy and force were employed as 10⁻⁵ eV and 0.01 eV/Å, respectively. The Γ-centered k-point meshes of 1x1x1 were taken. All the models were firstly geometrically optimized, then followed by the zero-point energy (ZPE) calculation. The ZPE is described as:⁽⁴⁾

$$ZPE = \frac{1}{2} \sum_{i=1}^n h\nu_i \quad \text{Equation (S1)}$$

where, h is the Planck constant, and ν_i is the vibration frequency, which is evaluated with the harmonic oscillator approximation.⁽¹⁾ The calculated frequencies of H₂O and D₂O are gathered in **Table S1**.

Table S1. The calculated vibration frequencies of H₂O and D₂O. Unit: THz

	ν_1	ν_2	ν_3	ν_4	ν_5	ν_6
H ₂ O	115.332	111.929	47.616	4.256	1.035	0.061
D ₂ O	84.453	80.612	34.835	3.010	0.745	0.057

References

1. G. Kresse and J. Furthmüller, *Computational Materials Science*, **6**, 15 (1996).
2. J. P. Perdew, K. Burke and M. Ernzerhof, *Phys. Rev. Lett.*, **77**, 3865 (1996).
3. P. E. Blöchl, *Physical Review B*, **50**, 17953 (1994).
4. I. C. Man, H.-Y. Su, F. Calle-Vallejo, H. A. Hansen, J. I. Martínez, N. G. Inoglu, J. Kitchin, T. F. Jaramillo, J. K. Nørskov and J. Rossmeisl, *ChemCatChem*, **3**, 1159 (2011).

4.2 Permselective ion electrosorption of subnanometer pores at high molar strength enables capacitive deionization of saline water

Bi Sheng,^{1,2,+} Yuan Zhang,^{3,4,+} Luca Cervini,⁵ Tangming Mo,^{1,2} John M. Griffin,^{5,6} Volker Presser,^{3,4,7} and Guang Feng^{1,2}

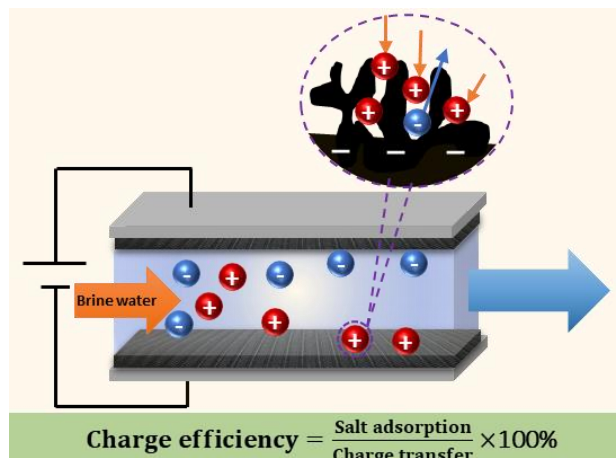
- 1 State Key Laboratory of Coal Combustion, School of Energy and Power Engineering, Huazhong University of Science and Technology (HUST), Wuhan 430074, China.
- 2 Nano Interface Centre for Energy, School of Energy and Power Engineering, HUST, 430074, China.
- 3 INM - Leibniz Institute for New Materials, Campus D2 2, 66123 Saarbrücken, Germany.
- 4 Department of Materials Science and Engineering, Saarland University, Campus D2 2, 66123 Saarbrücken, Germany.
- 5 Department of Chemistry, Lancaster University, Lancaster, LA1 4YB, UK
- 6 Materials Science Institute, Lancaster University, Lancaster, LA1 4YB, UK
- 7 Saarene - Saarland Center for Energy Materials and Sustainability, Campus C4 2, 66123 Saarbrücken, Germany.

Citation:

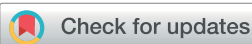
S. Bi, Y. Zhang, L. Cervini, T. Mo, J M. Griffin, V. Presser, *Permselective ion electrosorption of subnanometer pores at high molar strength enables capacitive deionization of saline water*, Sustainable Energy & Fuels, 2020, 4(3): 1285-1295. (DOI: 10.1039/c9se00996e)

Own contribution:

Validation, formal analysis, investigation, data curation, writing-original draft, writing-review & editing, visualization.



PAPER



Cite this: *Sustainable Energy Fuels*,
2020, **4**, 1285

Permselective ion electrosorption of subnanometer pores at high molar strength enables capacitive deionization of saline water†

Sheng Bi, ^{‡ab} Yuan Zhang, ^{‡cd} Luca Cervini,^e Tangming Mo,^{ab} John M. Griffin,^{ef} Volker Presser ^{*cd} and Guang Feng ^{*ab}

Capacitive deionization with porous carbon electrodes is an energy-efficient water treatment technique limited to the remediation of only brackish water due to the severe efficiency drop at high molar strength. Combining experiment and simulation, our work demonstrates the ability of subnanometer pores for permselective ion electrosorption, which enables capacitive deionization for saline media with high concentrations. Molecular dynamics simulations reveal the origin of permselective ion electrosorption in subnanometer pores at high molar strength. Within the subnanometer range, carbon pores with smaller size become more ionophobic and then express a higher ability of permselective ion electrosorption. This can be understood by the effects of the pore size on the microstructure of in-pore water and ions and the nanoconfinement effects on the ion hydration. These findings provide a new avenue for capacitive deionization of saline water (seawater-like ionic strength) to enable the application of highly concentrated saline media by direct use of porous carbons.

Received 24th October 2019
Accepted 14th December 2019

DOI: 10.1039/c9se00996e
rsc.li/sustainable-energy

1. Introduction

Advancing towards a sustainable future requires not only to improve our current ability for water management but also to afford energy-efficient water desalination.¹ With the rising demand for potable water, increased pollution, and global climate change, scientists explore advanced techniques for desalination.² Along these lines, capacitive deionization (CDI) is a still emerging water purification technique that provides energy-efficient desalination of brackish water.^{3–6} The CDI process for water desalination relies on the accumulation of ions in polarized electrodes. By applying an electrical

potential between two electrodes, cations and anions are removed from a water stream passing the electrochemical cell and respectively electro-adsorbed at the negatively and positively charged electrodes.^{6–8} The mechanism of ion electrosorption is well-known in the field of electrical energy storage, which could be exemplified by electrical-double layer capacitors (also called supercapacitors) in many present-day devices, ranging from mobile applications to stationary (grid-scale) systems.^{9–11} With the ability to use charge accumulation to desalinate saline media during the electrode charging process and to recover the electrical energy during electrode regeneration (discharging), CDI units are also uniquely qualified to contribute towards large-scale energy storage and grid management.^{12–14}

The process of ion electrosorption favors porous electrode materials with a high specific surface area. Accordingly, CDI devices commonly employ porous carbons,^{15–17} such as activated carbons,^{18,19} graphene-based materials,^{20–22} carbon nanotubes,^{23,24} or carbon aerogels.²⁵ Like for supercapacitors,²⁶ micropores benefit the performance of CDI electrodes, compared to meso- or macropores.²⁷ However, the detailed understanding of the influence of the pore size on the desalination performance has remained limited. In part, this is caused by the pore size dispersity of carbon electrode materials, which complicates to deconvolute the individual processes occurring in different pores. Modeling ion electrosorption in pores of different sizes is, therefore, an important approach to quantify the behavior and properties of ions in nanoconfinement.^{10,27–30} With the majority of works in the field of

^aState Key Laboratory of Coal Combustion, School of Energy and Power Engineering, Huazhong University of Science and Technology (HUST), Wuhan 430074, China.
E-mail: gfeng@hust.edu.cn

^bNano Interface Centre for Energy, School of Energy and Power Engineering, HUST, 430074, China

^cINM – Leibniz Institute for New Materials, Campus D2 2, 66123 Saarbrücken, Germany. E-mail: volker.presser@leibniz-inm.de

^dDepartment of Materials Science and Engineering, Saarland University, Campus D2 2, 66123 Saarbrücken, Germany

^eDepartment of Chemistry, Lancaster University, Lancaster, LA1 4YB, UK

^fMaterials Science Institute, Lancaster University, Lancaster, LA1 4YB, UK

† Electronic supplementary information (ESI) available: Data for the molecular dynamics simulation setup, characterization of carbons and cell setup, desalination performance measurements with aqueous NaCl solution, basic electrochemical characterization, in-pore ions under different polarizations, water distribution surrounding ions in bulk and inside large pores. See DOI: 10.1039/c9se00996e

‡ These authors contributed equally: Sheng Bi, Yuan Zhang.

supercapacitors using organic electrolytes or ionic liquids,^{10,31–33} quantitative analysis of ion electrosorption in carbon nanopores using aqueous media is still poorly investigated.^{34,35} The specific challenge for CDI modeling is the dependency of the desalination performance on the actual mode of charge storage.³⁶ Specially, we must consider the number of co-ions and counter-ions (that is, ions with same or opposite charge compared to the electrode), and their relative changes as a function of the state of charge.

Different from the charge storage mechanism of supercapacitors, the non-permselective exchange of one cation by one anion during the charging of the positively polarized electrode (and *vice versa* at the negatively polarized electrode) fails to change the concentration of the effluent water stream.³⁰ Instead, desalination is only possible when the change of electro-adsorbed counter-ions exceeds that of electro-desorbed co-ions.³⁷ This fundamental correlation makes the desalination performance of CDI highly dependent on the bulk ion concentration. Carbons may accomplish at low molar strength of about 5–20 mM a desalination capacity of 10–30 mg g⁻¹,^{7,38–41} while many studies have revealed that at high molar strength (>50–100 mM), the charge storage process is dominated by non-permselective ion swapping, and thus effective desalination by CDI becomes impossible.^{30,34,42} Only at molar strength below 50 mM, CDI becomes a promising energy-efficient desalination technology, which limits the technology to remediation of only brackish water.^{16,37,43} Accordingly, the field of electrochemical desalination has moved away from carbon to explore electrode materials capable of ion insertion or conversion reactions.^{44,45} Such faradaic processes could overcome the limitation of electrosorption and allow permselective and energy-efficient ion removal even at high molar strength (*e.g.*, as found for seawater: 600 mM).^{45–47}

Our work was motivated by going in the opposite direction: to turn back to carbon. More precisely, our study shows that as subnanometer-sized pores become more ionophobic, they gain the ability of permselective ion electrosorption at high molar strength. However, such effects have not been found experimentally or correlated with a combined experiment and simulation approach. We demonstrate this unexpected feature by molecular dynamics (MD) simulations, with constant potential method to mimic the applied voltages on the electrode,^{48,49} that allow us to investigate carbon pores individually with charging process and by CDI experiments with activated carbon cloth with equally small pores at high molar strength. The pore-size dependent CDI ability of subnanometer pores and their molecular insights, as well as the origin of the permselective electrode, are clarified and discussed. Thereby, the current paradigm of limiting CDI to just brackish water could be reconsidered as: if appropriate nanopores are being employed, CDI is also capable of desalination of highly saline aqueous media. In this work, we focus mostly on potassium chloride (KCl) solution, considering the smaller size of hydrated potassium ion compared to hydrated sodium ion.⁵⁰ Thereby, we establish the ability to enable permselectivity in sodium chloride (NaCl) and at molar concentrations exceeding that of seawater.

2. Simulation and experimental section

2.1. Molecular dynamics simulations

The electrode pore walls are modeled by fixing three layers of graphene sheets. The pore size, defined as the access width,⁵¹ ranges from 0.47 nm to 1.77 nm. The pore length is set as 5.85 nm, which is long enough to eliminate the entrance effects on the central part of the pore.⁵² The initial configurations of the KCl and NaCl solutions are obtained by randomly distributing ions and water molecules in the accessible space using PACKMOL.⁵³ The detailed numbers of the components (ions and water) in each case are gathered in ESI, Table S1.† For electrodes and aqueous KCl and NaCl electrolytes, we adopted force fields from Cornell *et al.*⁵⁴ and Smith *et al.*,⁵⁵ respectively, and the well-established SPC/E model⁵⁶ was chosen for the water molecules.

2.2. Constant potential implementation

For all simulations, the constant potential method (CPM) was implemented to capture the electrode polarization effects in the presence of an aqueous electrolyte.⁵⁷ This method allows the fluctuation of electrode charge during the simulation so that a constant electrical potential between two electrodes could be maintained.^{58–61} All simulations were performed in the NVT ensemble, using a customized MD package GROMACS⁶² with a time step of 2 fs. The temperature of the electrolyte is maintained at 298 K using the V-rescale thermostat. A fast Fourier transform (FFT) grid spacing of 0.1 nm and cubic interpolation for charge distribution were used to compute the electrostatic interactions in the reciprocal space. We used a cutoff length of 1.2 nm in the calculation of electrostatic and non-electrostatic interactions in the real space. Each simulation started with an annealing process from 350 K to 298 K over a period of 10 ns, followed by another 10 ns to reach equilibrium. After that, a 40 ns production run was performed for analysis. For the sake of the accuracy of modeling, 10 runs were carried out with different initial configurations (*i.e.*, with different locations and velocities of ions and water molecules) to obtain reliable results of charging dynamics.

2.3. Carbon electrodes materials

Four kinds of commercial activated carbon cloth (Kynol ACC-5092-10, Kynol ACC 5092-15, Kynol ACC 507-20, Kynol 507-20+, and Kuraray YP-80F) were applied as electrode materials in this work.⁶³ Among them, Kynol ACC-5092-10, Kynol ACC 5092-15, and Kynol ACC 507-20 and Kynol 507-20+ (labeled as ACC-0.59, ACC-0.67, ACC-0.88, and ACC-1.26) are novolac-derived activated carbon cloth with different degree of the activation process and thickness of 650 µm, 450 µm, and 250 µm, respectively. Thereby, all ACC electrodes were free-standing and binder-free. 95 mass% of YP-80F (labeled AC-1.34) activated carbon material was mixed with 5 mass% polytetrafluoroethylene (PTFE, Sigma-Aldrich) to form a 650 µm thick, free-standing electrode.

2.4. Material characterization

Scanning electron micrographs (ESI, Fig. S1†) were recorded with a JEOL JSM-7500F system at an acceleration voltage of 3 kV. The samples were mounted on sticky tape and analyzed without the aid of an additional, conductive sputter coating.

Nitrogen sorption experiments were performed with an Autosorb iQ system (Quantachrome) at $-196\text{ }^\circ\text{C}$. The samples were degassed at 10^2 Pa at a temperature of $200\text{ }^\circ\text{C}$ for 10 h. The specific surface area (SSA) and pore size distribution (ESI, Table S2 and Fig. S2†) were calculated by applying quenched-solid density functional theory (QSDFT) assuming a slit-shaped pore model.^{64,65}

The chemical composition was quantified with a CHNS analyzer Vario Micro Cube from Elementar. The temperature for the tube was $850\text{ }^\circ\text{C}$ and for the combustion tube $1150\text{ }^\circ\text{C}$. The equipment was calibrated with sulfanilamide. The oxygen content was obtained with a rapid OXY cube from Elementar. The analysis temperature was $1450\text{ }^\circ\text{C}$, and it was calibrated with benzoic acid. See ESI, Table S3.†

2.5. Desalination performance measurements

We used a symmetric full-cell configuration to evaluate the desalination performance. As shown in ESI, Fig. S1,† carbon materials were cut into 30 mm diameter disks. The feed water flows through the middle channel, which is sandwiched by glass fiber separators (Millipore, 4 pieces of $380\text{ }\mu\text{m}$) and activated carbon electrodes. To ensure that the space of the water-flowed middle channel does not collapse during the measurement, 7 pieces of polyethylene terephthalate cloth meshes (28 mm-diameter round pieces) were filled inside of the middle channel. This translates to a spacing of 3 mm between the two electrodes. The flow rate of the feedwater stream was set 5 mL min^{-1} . At the outlet of the cell, pH and conductivity sensors were connected to monitor the pH and concentration fluctuations during the electrochemistry measurements.

We used a Biologic VSP300 system to determine the electrochemical performance, a Metrohm PT1000 conductometric cell to monitor the electrolyte concentration, and the pH values were recorded with a WTW SensoLyte 900P sensor probe. By this way, we determined values for the charge efficiency and desalination capacity. Galvanostatic charge and discharge cycling was carried out at a specific current of 0.1 A g^{-1} using different potential ranges, namely, $0\text{--}0.2\text{ V}$, $0\text{--}0.4\text{ V}$, $0\text{--}0.6\text{ V}$, $0\text{--}0.8\text{ V}$, and $0\text{--}1.0\text{ V}$ with 20 cycles for each potential range. After charging and discharging, 2 min of the potential holding time was applied. The electrode mass was as follows: 145 mg for ACC-0.59, 120 mg for ACC-0.67, 116 mg for ACC-0.88, 64 mg for ACC-1.26, and 172 mg for AC-1.36. The specific current applied was calculated from the total mass of both sides of electrode.

The desalination capacity (DC) was determined by eqn (1):

$$\text{DC} = \left(\nu \frac{M_{\text{salt}}}{m_{\text{tot}}} \right) \int (c_t - c_0) dt \quad (1)$$

where ν is the flow rate of salt solution, M_{salt} is the molecular mass of the salt, m_{tot} is the total mass of both working and

counter electrode, and c_0 and c_t are initial concentration and concentration value at time t .

The charge efficiency (CE) was calculated by eqn (2):

$$\text{CE} (\%) = \frac{F \times \text{DC}_{\text{mol}}}{Q} \times 100\% \quad (2)$$

where F is the Faraday constant (in units of Ah per mol), Q is the invested charge (in units of Ah) including the leakage current, and DC_{mol} is the desalination capacity (in unit of mol).

In our experiments, the error margin for CE and DC was about 5–8%.

2.6. Solid-state nuclear magnetic resonance spectroscopy

We used a 400 MHz Bruker Avance III HD WB spectrometer operating at a magnetic field strength of 9.4 T . Before soaking in 800 mM aqueous NaCl, the samples were dried in an oven at $80\text{ }^\circ\text{C}$ overnight and introduced in 3.2 mm zirconia rotors. The magic angle spinning (MAS) rate was 5 kHz. ^1H NMR spectra were acquired using the DEPTH pulse sequence⁶⁶ with 16 scans phase cycle, 5 s recycle delay, and 90° pulse lengths of 3–3.3 μs at a power of 200 W. ^{23}Na MAS NMR spectra were recorded with a single pulse and 1024–20480 scans depending on the sample, recycle delays of 0.2 s, and 90° pulse lengths of 3.75–4.2 μs at a power of 200 W.

3. Results and discussion

3.1. Capacitive deionization ability of micropores

The key working principle of CDI is demonstrated in Fig. 1a: when saline feed water passes electrically charged electrodes, ions will be electro-adsorbed at the fluid–solid interfaces between the aqueous electrolyte and carbon nanopore surfaces. We first examine the ability of carbon electrodes with different pore sizes to accomplish capacitive deionization at high molar strength even above standard seawater by using 800 mM KCl solution, although nanoporous carbons had shown the inability of activated carbon with pores $>1\text{ nm}$ to accomplish any desalination in 600 mM NaCl solution while it worked well for supercapacitor.⁴² Employing activated carbon cloth (ACC) and activated carbon (AC) as electrodes (ESI, Fig. S1†), we labeled the samples by their average pore size, namely ACC-0.59 (average pore size is 0.59 nm), ACC-0.67 (0.67 nm), ACC-0.88 (0.88 nm), ACC-1.26 (1.26 nm) and AC-1.34 (1.34 nm). From the pore size distribution of these carbon materials (Fig. 1b and ESI, Fig. S2†), we observe the pronouncedly microporous characteristics of all studied ACCs, while the widest pore size distribution is found for AC-1.34 which also contains 13.8% mesopores (diameters within 2–50 nm; ESI, Table S2† provides more data from pore structure analysis). We chose nanoporous carbons with narrow pore size distribution because these specific carbons have a small amount of non-carbon hetero-atoms and surface groups (chemical data can be found in ESI, Table S3†). Fig. 1c shows the desalination capacity for aqueous 800 mM KCl normalized to the specific surface area of the different carbon electrodes at cell voltages up to 1.0 V . Herein, the use of area-normalized desalination capacities is more

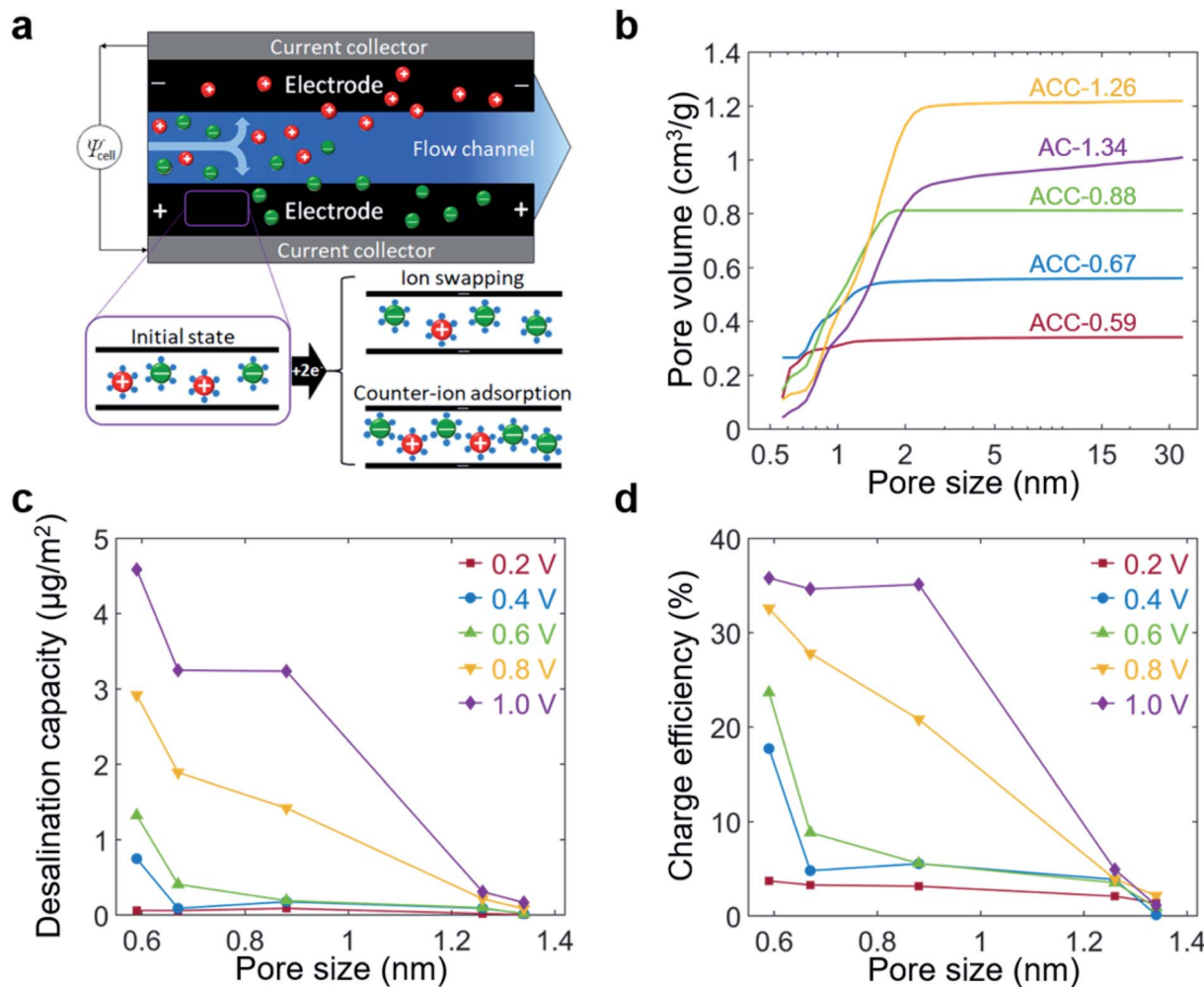


Fig. 1 Capacitive deionization (CDI) of microporous carbons. (a) The schematic figure for a CDI cell using porous carbon electrodes. Charge storage, generally, can be accomplished by permselective counter-ion electrosorption or non-permselective concurrence of co-ion desorption and counter-ion electro-adsorption (ion swapping). (b) Cumulative pore size distribution obtained from nitrogen gas sorption isotherms at -196°C , calculated by applying quenched solid density functional theory (QSDFT) and assuming pores have slit shape. (c and d) Desalination capacity (c) and charge efficiency (d) obtained from CDI experiments on carbon electrodes with different average pore sizes. Experiments were carried out in aqueous 800 mM KCl.

reasonable for a direct comparison of carbons with different surface area compared to mass-normalized values. In alignment with the reported CDI techniques,^{30,34,42} we see the inability of carbon nanopores exceeding 1 nm to desalination even at the highest applied cell voltage. As the average pore size is decreased, there is a significant increase in areal desalination capacity with the highest value found for ACC-0.59 ($4.58 \mu\text{g m}^{-2} = 4.73 \text{ mg g}^{-1}$ at 1.0 V). To the best of our knowledge, these data are the first reports of nanoporous carbons accomplishing actual desalination at high molar strength *via* CDI in the absence of an ion-exchange membrane. The ability for ion removal is also maintained when using 800 mM NaCl solution (ESI, Fig. S3 and S4†).

To scrutinize desalination capacities, the charge efficiency is analyzed in Fig. 1d, correlating the charge corresponding with removed salt ions and the total amount of invested charge. It can be seen that the charge efficiency even at the highest

applied cell voltage of 1.0 V remains close to zero for pores larger than 1.2 nm on average (either ACC-1.26 or AC-1.34), however, when approaching and falling below the 1 nm-range, there is a significant increase in charge efficiency that aligns with the manifestation of desalination. Subnanometer pores at 1.0 V show a charge efficiency of about 36% and this value also contains resistive charge losses of the cell and its graphitic carbon current collectors. This charge efficiency seems small compared to activated carbons commonly used for CDI that provide 60–80% charge efficiency¹⁶ but is very large compared to the performance of micropores exceeding an average of 1.2 nm. Also, considering the pore size dispersity (Fig. 1b), there is an influence of larger pores even for the sample with the smallest average pore size and this may further contribute to a reduced charge efficiency. Theoretically, if all charges would be stored by a one-to-one cation–anion swapping process, no desalination would be observed (like in case of large micropores).⁴² Yet, the

unexpected ability of subnanometer pores to accomplish the actual desalination at high molar strength indicates a significant amount of ion permselectivity, that is, subnanometer pores have a growing preference of counter-ion electro-adsorption instead of co-ion electro-desorption. Such behavior agrees with some previous theoretical work on graphene nanochannels which up-take ions only when electrically charged.⁴⁹ It aligns also with the hindrance of ions such as Na^+ and Cl^- for monolayer water transport across ultrathin graphene channels.⁶⁷

To understand the permselective ion electrosorption of subnanometer pores, we used MD simulations to study the electrochemical operation of aqueous electrolyte at high molar strength. As shown in Fig. 2a, we construct a three-dimensional periodical system with two slit-shaped micropores of adjustable size (d_{slit}) connected by reservoirs of bulk aqueous electrolyte.

The constant potential method is implemented to maintain the potential drop between the two electrodes during the simulations.^{58,59} This computational method allows us to explore the processes of charge storage and dynamically monitor ion electro-sorption/desorption in micropores at the atomic level.^{60,61} As exemplified for all carbon electrode materials in this study by conventional electrochemical operation in a two-electrode cell in 2 M KCl, there is a capacitive response with a rectangular-shape cyclic voltammogram provided by porous carbons (ESI, Fig. S5†), indicating the absence of electrochemically triggered redox reactions. Therefore, MD simulations with aqueous solutions at two high molar strengths (500 mM and 2 M) could be performed to investigate the dynamic process of ion electro-sorption/desorption and its permselectivity by carbon nanopores. As exhibited for the temporal change of ions in the negatively charged electrode in Fig. 2b (results for positive

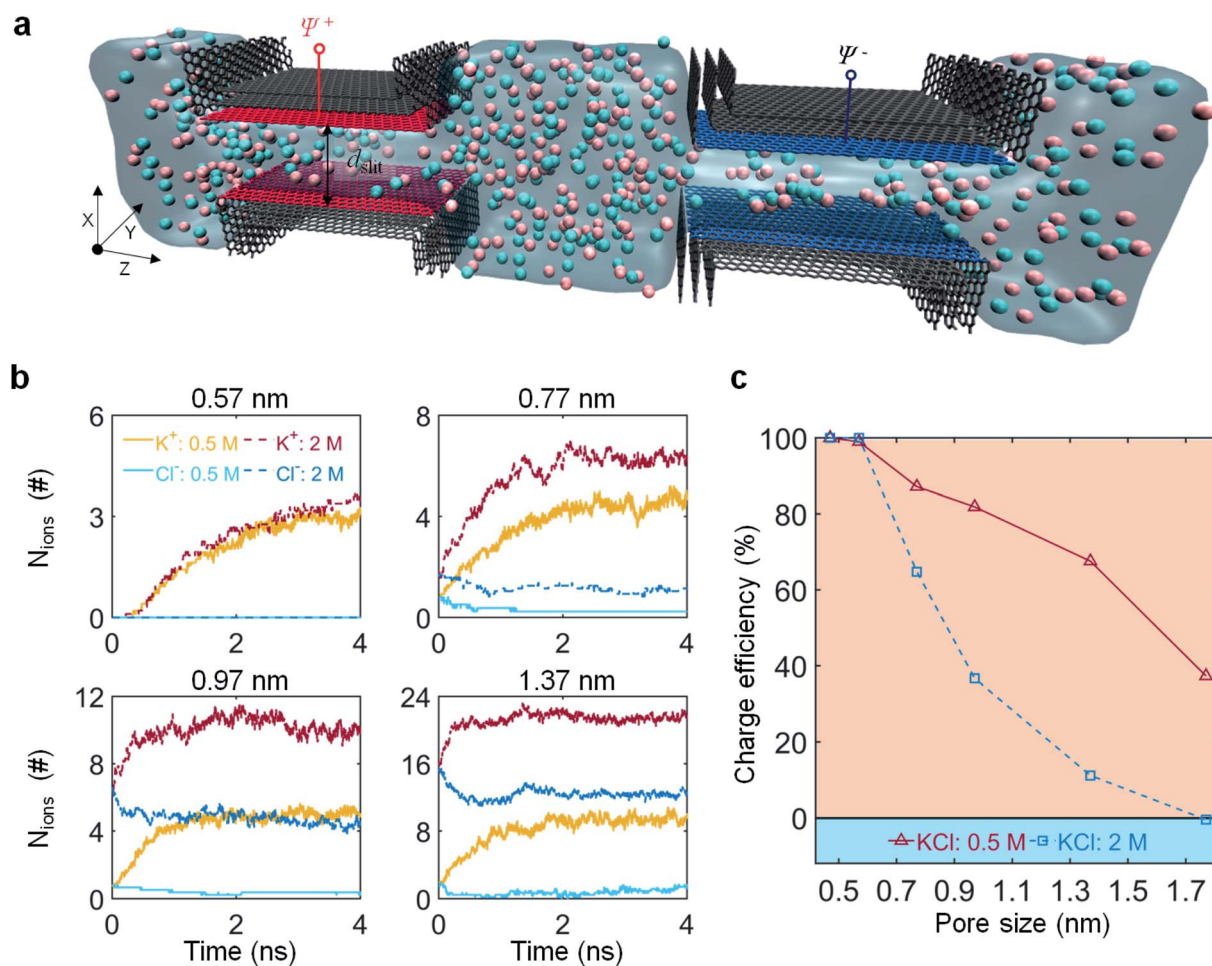


Fig. 2 Molecular understanding of ion permselectivity by micropores. (a) Schematics of the molecular dynamics simulation setup. The pore size, d_{slit} , is defined by the accessible gap between the surfaces of two inner graphene sheets, ranging from 0.47 nm to 1.77 nm, and the slit length is 5.84 nm along the Z-direction. The dimensions of the simulation system are $d_{\text{slit}} + 3.53$ nm, 3.00 nm, and 24 nm. A constant potential drop is applied at the red, and blue labeled carbon atoms, in which red represents positive electrode, and blue represents the negative electrode. The applied voltage between the positive and negative electrode is set at 1.0 V. (b) Time evolution of the number of cation and anion in the negatively charged micropores. Dark red and blue solid lines are, respectively, results for the cation and anion at 2 M molar concentration. Yellow and light blue dashed lines are for cation and anion at 0.5 M molar concentration. These results are evaluated during the charging simulations of each micropore. (c) Charge efficiency, as a function of pore size. Red solid line with triangle markers and blue dashed line with square markers represent results of micropores in aqueous 0.5 M and 2 M KCl solutions, respectively.

electrode in ESI, Fig. S6†), pores of 0.57 nm and 0.77 nm show almost exclusive counter-ion electro-adsorption at 1.0 V and avoidance of co-ions, while pores in larger size (0.97 nm and 1.37 nm) contain a much larger number of co-ions. This trend holds for both 500 mM and 2.0 M aqueous KCl solutions under 1.0 V; however, for 500 mM, we see a much lower number of co-ions populating the pores during the charging process including its initial state. The change of in-pore ion population and charge stored on the pore translates to theoretical charge efficiency, as shown in Fig. 2c. It can be found that the charge efficiency is enhanced with the decrease of either pore size or ion concentration, except its unit value in very small pores (<0.6 nm) due to the absence of ions at the initial state of charging process; the modeling-obtained values of charge efficiency are larger than experiment-measured ones, which may be contributed to the absence of pore size distribution and the simplification of pore surface geometry and chemistry in MD modeling. These findings are validated for different working potential and saline water (*e.g.*, KCl and NaCl solutions under 1.5 V in ESI, Fig. S7†), which qualitatively match with our experimental data (Fig. 1b and c), documenting the ability for subnanometer pores to enable capacitive deionization in saline media with high molar strength (exceeding the ion concentration level of seawater). Our findings are in stark contrast to the current state-of-the-art assessment that membrane-free capacitive carbon electrodes are non-suitable for seawater desalination.^{16,37,43,68}

3.2. Origin of permselective ion electrosorption in subnanometer pores

To better understand the mechanism of permselective ion electrosorption in subnanometer pores, we then explored the equilibrium in-pore distributions for ions and water molecules

by simulations. The intricacies of the electrical double-layer structure at the electrolyte-electrode interface majorly govern the surface charge and the resulting salt adsorption capacity.^{69,70} Fig. 3 depicts the distributions of ions and water molecules inside non-charged and polarized pores of different size. When the electrode is at the potential of zero charge (PZC), shown in Fig. 3b, K^+ or Cl^- ions are unable to enter pores of less than 0.6 nm, although the pore could be wetted, indicating such pores are fully ionophobic.^{51,71} For larger pores, ions are found already inside the pore, seeming larger pores with more ions. These could be further seen in ESI, Fig. S8† that, as the pore size shrinks, the in-pore ion density decreases, suggesting that the pore electrode becomes more ionophobic and ultimately fully ionophobic. When pores get either negatively or positively polarized (Fig. 3a and c), for fully ionophobic pores (<0.6 nm) counter-ions move into the pore and accumulate in its central region; when pores get more ionophilic (>0.6 nm), the electrical double-layer inside the pores becomes rich in counter-ions, and some co-ions are expelled. Moreover, multiple layers of ions, rather than one layer dwelling at the central part of the pores, are formed inside these large pores. Although their size is larger than K^+ cations in bare but similar in full hydration,⁵⁰ Cl^- anions reside closer to the slit wall than cations, suggesting a more fractured hydration shell than that of K^+ ions.

The distribution of in-pore water molecules is strongly influenced by the in-pore ions due to the hydration effect under nanopore confinement. Specifically, in fully ionophobic pores the pure water packing at PZC should be changed by ions electro-adsorbed under polarization; in more ionophilic pores, the adsorbed layer of water distributions in the positive side is higher but thinner than that in the negative side (Fig. 3a and c). To further investigate the microstructures of the water

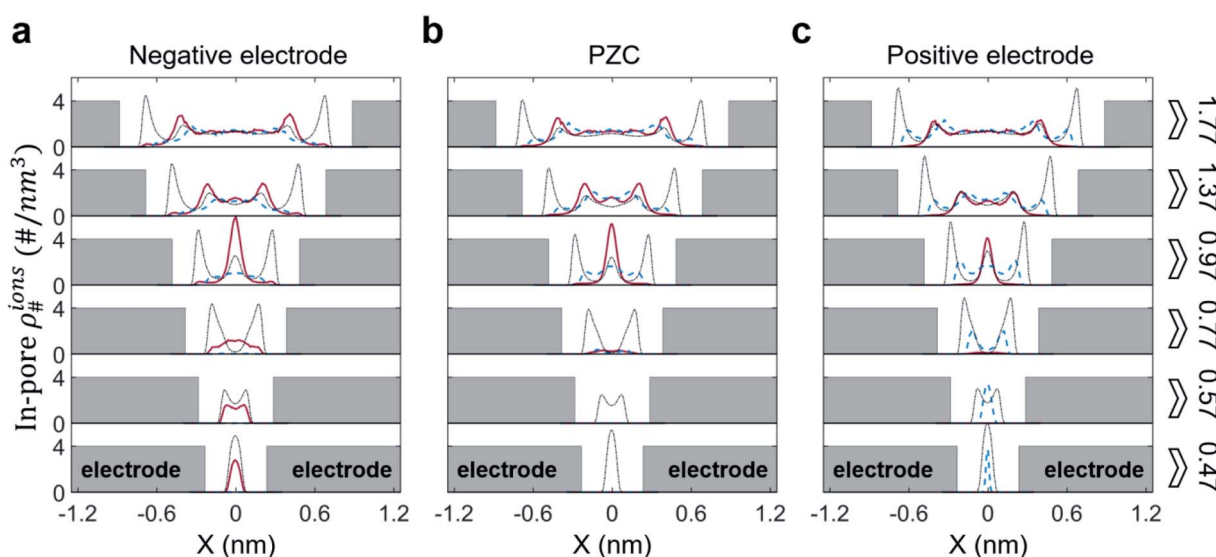


Fig. 3 Ion and water distributions in micropores. (a–c) Data in (a) and (c), respectively, show the number densities of ions and water in the negatively charged micropores and positively charged micropores, for a potential difference of 1.0 V between the two electrodes. Data shown in (b) represent results for the uncharged pore (*i.e.*, at PZC). Red solid, blue dashed, and black dash-dotted curves are results for cations, anions, and water molecules, respectively. The number density of water shown here is scaled by 1/30 for better illustration. $X = 0$ corresponds to the central position of the pore.

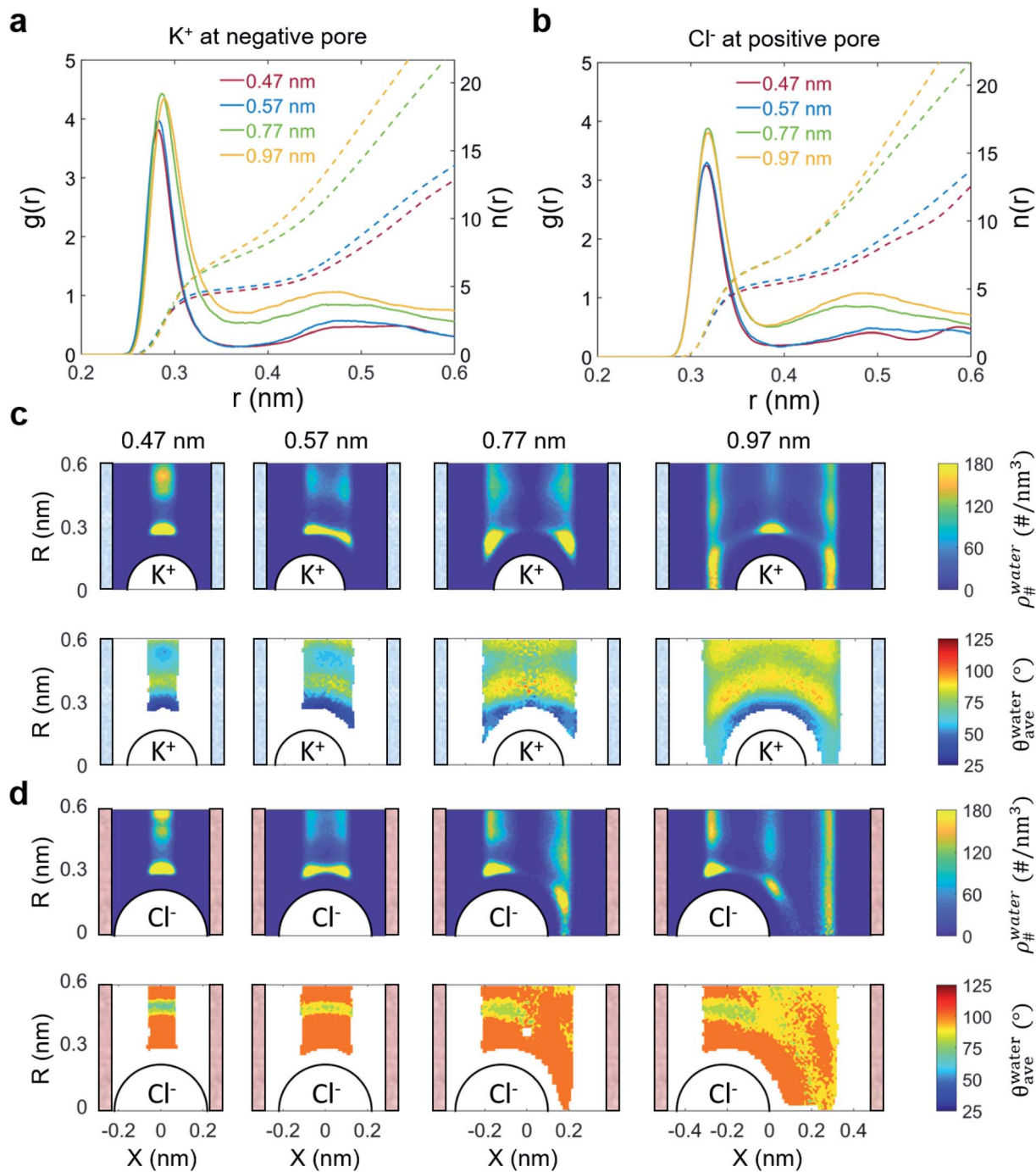


Fig. 4 Structure of hydration shells of ions in polarized micropores. (a and b) Radial distribution function, $g(r)$ (solid lines, left Y-axis), and cumulative distribution function, $n(r)$ (dashed lines, right Y-axis) of hydrated K^+ ions (a) and Cl^- ions (b) in negatively and positively polarized pores, respectively. The applied electrical potential difference between two electrodes is set as 1.0 V. The cumulative distribution function, $n(r)$, is calculated by $n(r) = 4\pi\rho \int g(r)r^2 dr$, where ρ is the water number density in the reservoir. (c and d) Pseudo-2D number density (upper panel) and orientation (lower panel) distributions of water molecules around a K^+ ion (c) and a Cl^- ion (d) in micropores of different pore sizes under negative and positive polarization, respectively.

molecules surrounding an ion inside the micropores, we show in Fig. 4 the radial distribution functions (RDFs) and the cumulative distribution functions (CDFs) between in-pore ions and their surrounding water molecules as well as the corresponding number density and angular distributions of water around an ion at its peak positions (*i.e.*, the closest peak to the

pore wall, Fig. 3). Focusing on the K^+ ion at the negatively charged micropores (Fig. 4a), we see that the coordination number of water molecules decreases as the pore becomes narrow; the value is around 4.8 and 7.6, respectively, for fully ionophobic pores (0.47 nm and 0.57 nm) and the other pores. From the pseudo-two-dimensional water number density near a K^+ (the

upper row of Fig. 4c), we observe that in subnanometer pores water is mainly located along the length of the pore on the top (or below, which is not shown due to the symmetry of data) of the ion, but not between the ion and the pore wall, as observed in Fig. 3 with only one layer of water and ions in such small pores. For a 0.77 nm pore, water in the hydration shell of a K⁺ ion starts to more surround the cation, and for 0.97 nm pore, we see the emergence of more completed hydration shell. Finally, larger micropores (1.37 and 1.77 nm in ESI, Fig. S9†) show an almost full hydration shell of K⁺ ions.

The number of water molecules coordinating a K⁺ ion in bulk simulation of 2 M KCl solution is found to be 6.7 (ESI, Fig. S9†). The comparison between such coordination numbers for ions in bulk and in pore suggests that K⁺ ions in fully ionophobic pores (0.47 nm and 0.57 nm) get partially dehydrated while K⁺ ions in the less ionophobic pores become more hydrated with their hydration shells deformed concomitantly, which makes the water shell become denser and results in a higher coordination number. Such deformations of hydration-shell structures can also be revealed by the pseudo-2D water angular distribution analysis near a K⁺ ion (the lower row of Fig. 4c), in which we compute the averaged angle formed by a water dipole and ion-oxygen vector for the ion with its hydrated water. For pores smaller than 0.97 nm, the orientation of water in the first layer of the hydration shell surrounding K⁺ is majorly less than 45°, indicating that most water molecules are strongly aligned with preference of their dipoles pointing oppositely to its hydrated K⁺ ion; when pore size is no less than 0.97 nm, water located between the K⁺ ion and the pore wall is distorted, with a larger averaged angle (about 60°). Considering the co-ion (Cl⁻) at negative polarization (ESI, Fig. S10†) in pores of 0.97 nm or larger, the structures of the surrounding water molecules are nearly identical to those in bulk region, as well as both have a similar coordination number of 6.6. This aligns with the screening of the charged electrode by counter-ions and water so that most co-ions lay far from the pore surfaces.

We further investigated the state of water around a Cl⁻ ion confined in a positively polarized micropore. It can be observed that regardless of the pore size, Cl⁻ ions prefer to be adsorbed to the electrified pore wall comparing with K⁺ ions (Fig. 3c and the upper row of Fig. 4d) while their hydration shell becomes more

deformed with the pore size decreasing (lower row of Fig. 4d). In terms of RDFs and CDFs, it could be found that the coordination numbers of water are about 5.5 for two small and fully ionophobic nanopores (0.47 nm and 0.57 nm) and approximately 7.0 for the other larger pores. Thereby, except fully ionophobic pores, water molecules in hydration shell get rearranged without ion dehydration, since the coordination number remains close to the bulk value. This phenomenon can be found even in the absence of an applied potential, suggesting that the hydration of the Cl⁻ ion changes little by the nanoconfinement. Moreover, the angular distributions of water in the first hydration shell has an averaged value of around 125°, indicating that one H-O bond of the water rather than the revert of water dipole points to the Cl⁻ ion (lower row of Fig. 4d). These results imply a looser hydration shell of a Cl⁻ compared with that of a K⁺ ion.

As the pore size increases, the pore becomes more ionophilic so that ions are more willing to get into the pore even in the absence of applied electrode potential (ESI, Fig. S8†). In our experiments, the value of ~1 nm seems to be the boundary of pore size of micropores that whether they can be used for desalination or not. Correspondingly in simulations, pores with pore size obviously smaller than 1 nm are less ionophilic (ESI, Fig. S8†) because the entering-ions would experience confinement-caused dehydration in the aqueous solution. On the other hand, the degree of confinement has a significant impact on the dynamics of ions. Indeed, the diffusion coefficients of cation and anion inside a charged pore are much lower than their bulk values ($1.72 \times 10^{-9} \text{ m}^2 \text{ s}^{-1}$ and $1.32 \times 10^{-9} \text{ m}^2 \text{ s}^{-1}$ for Na⁺ and Cl⁻, respectively). Also, as pore size shrinks, the in-pore ions diffuse more slowly (ESI, Fig. S11†), which can be attributed to their more deformed hydration shells under stronger confinement (Fig. 4). However, the structure of water in hydration shells shows a negligible difference when the pore size exceeds 1.0 nm (Fig. 4 and ESI, Fig. S9 and S10†).

3.3. Nuclear magnetic resonance spectroscopy

To correlate the predictions of the MD simulation on the ionophobility, we carried out ¹H and ²³Na solid-state NMR after having soaked the samples in aqueous 800 mM NaCl; we

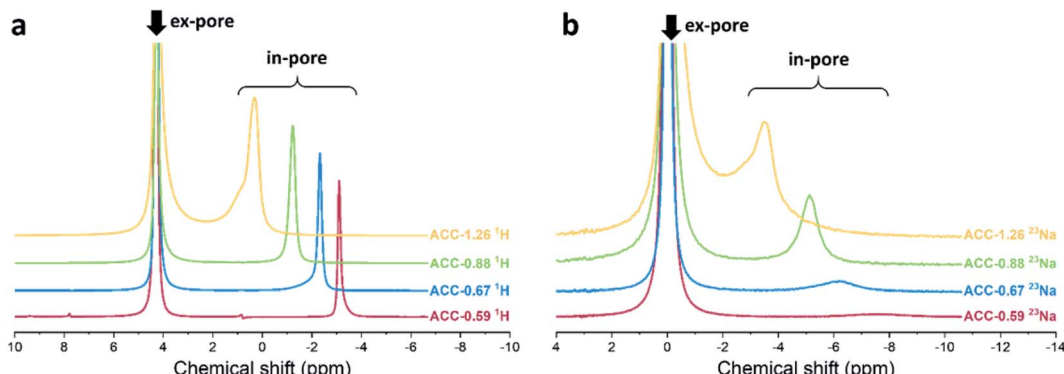


Fig. 5 Solid-state nuclear magnetic resonance spectra after soaking the samples in aqueous 800 mM NaCl. (a) ¹H spectra. (b) ²³Na spectra.

selected ^{23}Na due to the experimental difficulties of observing the low-sensitivity ^{39}K nucleus, which is the only NMR-observable isotope of potassium. For better comparability, considering the influence of the particle size, we investigated the spectra of the ACC samples. As seen from the $^1\text{H-NMR}$ spectra in Fig. 5a, all ACC samples show much narrower ^1H in-pore peaks relative to typical samples activated after crushing pyrolytic carbon sludges. This is due to the fibers having a narrow thickness distribution of modal width less than 100 μm , allowing for very homogeneous activation. The peaks become slightly broader with activation time due to small but inevitable activation inhomogeneities. The ^{23}Na spectra show that the amount of sodium very strongly decreases as the pore size is decreased (Fig. 5b). The overall larger peak width of ^{23}Na compared to ^1H results from faster transverse relaxation, which could suggest slower sodium diffusion. Using the integral peak intensities in Topspin Software, we see that the measured in-pore sodium for ACC-0.59, ACC-0.67, ACC-0.88, and ACC-1.26 corresponds to 1%, 7%, 15%, and 23%, respectively, of the total measured ^{23}Na signal for each sample. Therefore, the proportion of the sodium ions that spontaneously enter the pores is very small for the smallest pore sizes (*i.e.*, they are ionophobic), whereas this increases as the pore size is increased. The strong decrease in sodium in sub-1-nm pores is in alignment with a recent study by Cervini *et al.*³⁵ and agrees with our modeling results.

4. Conclusions

We have investigated the performance of water desalination by micropores (including subnanometer pores) in aqueous media with high molar strength by both modeling and experiment. In contrast to the state-of-the-art CDI techniques, our results demonstrate the ability of subnanometer pores for permselective counter-ion electro-adsorption. This ability enables the use of such carbon electrodes without the need for an ion exchange membrane for CDI of saline media with seawater concentration levels of dissolved ions, as documented for KCl and NaCl in this work. This ability is lost once the pore size approaches and exceeds the 1 nm-range. Molecular dynamics simulations revealed that as the pore size of the electrode decreases, the pore becomes more ionophobic and the ion electrosorption mechanism shifts from non-permselective ion swapping to permselective counter-ion electro-adsorption, increasing the charge efficiency and desalination capacity of the system. In particular, the fully ionophobic pores exhibit complete permselectivity of counter-ions. These phenomena reflect the in-pore electrical double layer, especially the structures of water in the hydration shell of an ion. The increased ionophobicity with small size also aligns with the work that studied polyether-ether-ketone-derived small micropores *via* NMR spectroscopy (ref. 35) and our own NMR results. The findings reported here render a new path for CDI of saline water and briny water and call attention to turn again to porous carbons for CDI, based upon the permselective ion electrosorption of subnanometer pores.

Author contributions

G. F. and V. P. conceptualized the work. S. B. and M. T. M. carried out the simulation and Y. Z. for the experiment. S. B., V. P., and G. F. analyzed the data. L. C. carried out NMR experiments and L. C. and J. G. analyzed NMR data. All authors engaged in discussions and writing of the manuscript.

Conflicts of interest

The authors declare no conflict of interest.

Acknowledgements

G. F., S. B., and M. T. M. acknowledge the funding support from the National Natural Science Foundation of China (51876072, 51836003) and the Fundamental Research Funds for the Central Universities (2019kfyXMBZ040). V. P. and Y. Z. thank Eduard Arzt (INM) for his continuing support. S. B. also acknowledges the financial support from the China Scholarship Council. The computation was accomplished using the Tianhe II supercomputer in the National Supercomputing Center in Guangzhou, China. J. G. and L. C. acknowledge EPSRC and Johnson Matthey plc for the provision of an iCASE studentship. We also thank Lancaster University and the European Regional Development Fund (ERDF) for the provision of characterization facilities under the Collaborative Technology Access Program (cTAP).

References

- 1 M. Elimelech and W. A. Phillip, *Science*, 2011, **333**, 712–717.
- 2 M. A. Shannon, P. W. Bohn, M. Elimelech, J. G. Georgiadis, B. J. Marinas and A. M. Mayes, *Nature*, 2008, **452**, 301–310.
- 3 G. W. Murphy and J. H. Tucker, *Desalination*, 1966, **1**, 247–259.
- 4 Y. Oren, *Desalination*, 2008, **228**, 10–29.
- 5 R. Zhao, S. Porada, P. M. Biesheuvel and A. van der Wal, *Desalination*, 2013, **330**, 35–41.
- 6 A. Subramani and J. G. Jacangelo, *Water Res.*, 2015, **75**, 164–187.
- 7 M. E. Suss, S. Porada, X. Sun, P. M. Biesheuvel, J. Yoon and V. Presser, *Energy Environ. Sci.*, 2015, **8**, 2296–2319.
- 8 G. Amy, N. Ghaffour, Z. Li, L. Francis, R. V. Linares, T. Missimer and S. Lattemann, *Desalination*, 2017, **401**, 16–21.
- 9 J. R. Miller, *Science*, 2012, **335**, 1312–1313.
- 10 M. Salanne, B. Rotenberg, K. Naoi, K. Kaneko, P. L. Taberna, C. P. Grey, B. Dunn and P. Simon, *Nat. Energy*, 2016, **1**, 16070.
- 11 Y. Shao, M. F. El-Kady, J. Sun, Y. Li, Q. Zhang, M. Zhu, H. Wang, B. Dunn and R. B. Kaner, *Chem. Rev.*, 2018, **118**, 9233–9280.
- 12 M. A. Anderson, A. L. Cudero and J. Palma, *Electrochim. Acta*, 2010, **55**, 3845–3856.
- 13 S. I. Jeon, J. G. Yeo, S. Yang, J. Choi and D. K. Kim, *J. Mater. Chem. A*, 2014, **2**, 6378–6383.

- 14 F. Chen, Y. Huang, L. Guo, L. Sun, Y. Wang and H. Y. Yang, *Energy Environ. Sci.*, 2017, **10**, 2081–2089.
- 15 Z.-H. Huang, Z. Yang, F. Kang and M. Inagaki, *J. Mater. Chem. A*, 2017, **5**, 470–496.
- 16 S. Porada, R. Zhao, A. van der Wal, V. Presser and P. M. Biesheuvel, *Prog. Mater. Sci.*, 2013, **58**, 1388–1442.
- 17 F. Perreault, A. Fonseca de Faria and M. Elimelech, *Chem. Soc. Rev.*, 2015, **44**, 5861–5896.
- 18 L. Zou, G. Morris and D. Qi, *Desalination*, 2008, **225**, 329–340.
- 19 S. Porada, F. Schipper, M. Aslan, M. Antonietti, V. Presser and T.-P. Fellinger, *ChemSusChem*, 2015, **8**, 1867–1874.
- 20 P. Y. Liu, T. T. Yan, L. Y. Shi, H. S. Park, X. C. Chen, Z. G. Zhao and D. S. Zhang, *J. Mater. Chem. A*, 2017, **5**, 13907–13943.
- 21 X. Xu, L. Pan, Y. Liu, T. Lu, Z. Sun and D. H. C. Chua, *Sci. Rep.*, 2015, **5**, 8458.
- 22 H. B. Li, L. D. Zou, L. K. Pan and Z. Sun, *Environ. Sci. Technol.*, 2010, **44**, 8692–8697.
- 23 K. Dai, L. Shi, J. Fang, D. Zhang and B. Yu, *Mater. Lett.*, 2005, **59**, 1989–1992.
- 24 Y. Wimalasiri and L. Zou, *Carbon*, 2013, **59**, 464–471.
- 25 J. Biener, M. Stadermann, M. Suss, M. A. Worsley, M. M. Biener, K. A. Rose and T. F. Baumann, *Energy Environ. Sci.*, 2011, **4**, 656–667.
- 26 J. Chmiola, G. Yushin, Y. Gogotsi, C. Portet, P. Simon and P. L. Taberna, *Science*, 2006, **313**, 1760–1763.
- 27 S. Porada, L. Borchardt, M. Oschatz, M. Bryjak, J. S. Atchison, K. J. Keesman, S. Kaskel, P. M. Biesheuvel and V. Presser, *Energy Environ. Sci.*, 2013, **6**, 3700–3712.
- 28 C. Prehal, D. Weingarth, E. Perre, R. T. Lechner, H. Amenitsch, O. Paris and V. Presser, *Energy Environ. Sci.*, 2015, **8**, 1725–1735.
- 29 S. Kondrat, C. R. Perez, V. Presser, Y. Gogotsi and A. A. Kornyshev, *Energy Environ. Sci.*, 2012, **5**, 6474–6479.
- 30 C. Prehal, C. Koczwara, H. Amenitsch, V. Presser and O. Paris, *Nat. Commun.*, 2018, **9**, 4145.
- 31 M. Deschamps, E. Gilbert, P. Azais, E. Raymundo-Piñero, M. R. Ammar, P. Simon, D. Massiot and F. Béguin, *Nat. Mater.*, 2013, **12**, 351–358.
- 32 A. C. Forse, J. M. Griffin, C. Merlet, P. M. Bayley, H. Wang, P. Simon and C. P. Grey, *J. Am. Chem. Soc.*, 2015, **137**, 7231–7242.
- 33 C. Merlet, C. Pean, B. Rotenberg, P. A. Madden, B. Daffos, P. L. Taberna, P. Simon and M. Salanne, *Nat. Commun.*, 2013, **4**, 2701.
- 34 C. Prehal, C. Koczwara, N. Jäckel, A. Schreiber, M. Burian, H. Amenitsch, M. A. Hartmann, V. Presser and O. Paris, *Nat. Energy*, 2017, **2**, 16215.
- 35 L. Cervini, O. D. Lynes, G. R. Akien, A. Kerridge, N. S. Barrow and J. M. Griffin, *Energy Storage Mater.*, 2019, **21**, 335–346.
- 36 J. M. Griffin, A. C. Forse, H. Wang, N. M. Trease, P. L. Taberna, P. Simon and C. P. Grey, *Faraday Discuss.*, 2015, **176**, 49–68.
- 37 P. M. Biesheuvel, S. Porada, M. Levi and M. Z. Bazant, *J. Solid State Electrochem.*, 2014, **18**, 1365–1376.
- 38 M. A. Ahmed and S. Tewari, *J. Electroanal. Chem.*, 2018, **813**, 178–192.
- 39 Y. Cheng, Z. Hao, C. Hao, Y. Deng, X. Li, K. Li and Y. Zhao, *RSC Adv.*, 2019, **9**, 24401–24419.
- 40 T. Kim and J. Yoon, *RSC Adv.*, 2015, **5**, 1456–1461.
- 41 Y. Liu, C. Y. Nie, X. J. Liu, X. T. Xu, Z. Sun and L. K. Pan, *RSC Adv.*, 2015, **5**, 15205–15225.
- 42 P. Srimuk, J. Lee, S. Fleischmann, S. Choudhury, N. Jäckel, M. Zeiger, C. Kim, M. Aslan and V. Presser, *J. Mater. Chem. A*, 2017, **5**, 15640–15649.
- 43 X. Gao, S. Porada, A. Omosebi, K.-L. Liu, P. M. Biesheuvel and J. Landon, *Water Res.*, 2016, **92**, 275–282.
- 44 M. E. Suss and V. Presser, *Joule*, 2018, **2**, 10–15.
- 45 K. Singh, S. Porada, H. D. de Gier, P. M. Biesheuvel and L. C. P. M. de Smet, *Desalination*, 2019, **455**, 115–134.
- 46 M. Pasta, C. D. Wessells, Y. Cui and F. La Mantia, *Nano Lett.*, 2012, **12**, 839–843.
- 47 J. Lee, S. Kim, C. Kim and J. Yoon, *Energy Environ. Sci.*, 2014, **7**, 3683–3689.
- 48 R. K. Kalluri, D. Konatham and A. Striolo, *J. Phys. Chem. C*, 2011, **115**, 13786–13795.
- 49 R. K. Kalluri, M. M. Biener, M. E. Suss, M. D. Merrill, M. Stadermann, J. G. Santiago, T. F. Baumann, J. Biener and A. Striolo, *Phys. Chem. Chem. Phys.*, 2013, **15**, 2309–2320.
- 50 E. R. Nightingale, *J. Phys. Chem.*, 1959, **63**, 1381–1387.
- 51 S. Kondrat and A. Kornyshev, *J. Phys. Chem. C*, 2013, **117**, 12399–12406.
- 52 G. Feng and P. T. Cummings, *J. Phys. Chem. Lett.*, 2011, **2**, 2859–2864.
- 53 L. Martínez, R. Andrade, E. G. Birgin and J. M. Martínez, *J. Comput. Chem.*, 2009, **30**, 2157–2164.
- 54 W. D. Cornell, P. Cieplak, C. I. Bayly, I. R. Gould, K. M. Merz, D. M. Ferguson, D. C. Spellmeyer, T. Fox, J. W. Caldwell and P. A. Kollman, *J. Am. Chem. Soc.*, 1995, **117**, 5179–5197.
- 55 D. E. Smith and L. X. Dang, *J. Chem. Phys.*, 1994, **100**, 3757–3766.
- 56 H. J. C. Berendsen, J. R. Grigera and T. P. Straatsma, *J. Phys. Chem.*, 1987, **91**, 6269–6271.
- 57 S. K. Reed, P. A. Madden and A. Papadopoulos, *J. Chem. Phys.*, 2008, **128**, 124701.
- 58 C. Merlet, B. Rotenberg, P. A. Madden, P. L. Taberna, P. Simon, Y. Gogotsi and M. Salanne, *Nat. Mater.*, 2012, **11**, 306–310.
- 59 J. Vatamanu, O. Borodin and G. D. Smith, *J. Am. Chem. Soc.*, 2010, **132**, 14825–14833.
- 60 S. Bi, R. Wang, S. Liu, J. Yan, B. Mao, A. A. Kornyshev and G. Feng, *Nat. Commun.*, 2018, **9**, 5222.
- 61 C. Péan, C. Merlet, B. Rotenberg, P. A. Madden, P.-L. Taberna, B. Daffos, M. Salanne and P. Simon, *ACS Nano*, 2014, **8**, 1576–1583.
- 62 B. Hess, C. Kutzner, D. van der Spoel and E. Lindahl, *J. Chem. Theory Comput.*, 2008, **4**, 435–447.
- 63 C. Kim, P. Srimuk, J. Lee, S. Fleischmann, M. Aslan and V. Presser, *Carbon*, 2017, **122**, 329–335.
- 64 M. Thommes, K. Kaneko, A. V. Neimark, J. P. Olivier, F. Rodriguez-Reinoso, J. Rouquerol and K. S. W. Sing, *Pure Appl. Chem.*, 2015, **87**, 1051–1069.
- 65 A. V. Neimark, Y. Lin, P. I. Ravikovitch and M. Thommes, *Carbon*, 2009, **47**, 1617–1628.

- 66 M. Robin Bendall and R. E. Gordon, *J. Magn. Reson.*, 1983, **53**, 365–385.
- 67 K. Gopinadhan, S. Hu, A. Esfandiar, M. Lozada-Hidalgo, F. C. Wang, Q. Yang, A. V. Tyurnina, A. Keerthi, B. Radha and A. K. Geim, *Science*, 2019, **363**, 145.
- 68 K. Tang, Y.-h. Kim, J. Chang, R. T. Mayes, J. Gabitto, S. Yiakoumi and C. Tsouris, *Chem. Eng. J.*, 2019, **357**, 103–111.
- 69 J. Chmiola, C. Largeot, P.-L. Taberna, P. Simon and Y. Gogotsi, *Angew. Chem., Int. Ed.*, 2008, **47**, 3392–3395.
- 70 G. Feng, R. Qiao, J. Huang, B. G. Sumpter and V. Meunier, *ACS Nano*, 2010, **4**, 2382–2390.
- 71 S. Kondrat, P. Wu, R. Qiao and A. A. Kornyshev, *Nat. Mater.*, 2014, **13**, 387–393.

Supplementary Information

**Permselective ion electrosorption
of subnanometer pores at high molar strength
enables capacitive deionization of saline water**

Sheng Bi,^{1,2,+} Yuan Zhang,^{3,4,+} Luca Cervini,⁵ Tangming Mo,^{1,2}
John M. Griffin,^{5,6} Volker Presser,^{3,4,*} Guang Feng^{1,2,*}

¹ State Key Laboratory of Coal Combustion, School of Energy and Power Engineering, Huazhong University of Science and Technology (HUST), Wuhan 430074, China.

² Nano Interface Centre for Energy, School of Energy and Power Engineering, HUST, 430074, China.

³ INM - Leibniz Institute for New Materials, Campus D2 2, 66123 Saarbrücken, Germany.

⁴ Department of Materials Science and Engineering, Saarland University, Campus D2 2, 66123 Saarbrücken, Germany.

⁵ Department of Chemistry, Lancaster University, Lancaster, LA1 4YB, United Kingdom.

⁶ Materials Science Institute, Lancaster University, Lancaster, LA1 4YB, United Kingdom.

⁺ These authors contributed equally: Bi Sheng, Yuan Zhang.

^{*} Corresponding authors. Email: volker.presser@leibniz-inm.de (VP); gfeng@hust.edu.cn (GF)

1. Data for the molecular dynamics simulation setup

Table S1. The number of ion pairs ($n_{\text{ion pair}}$) and water molecules (n_{water}) in each molecular dynamics (MD) simulation system.

Pore size (nm)	$n_{\text{ion}}^{\text{pair}}$	n_{water}
0.42	163	4522
0.44	168	4661
0.47	171	4732
0.5	172	4788
0.53	174	4836
0.57	178	4953
0.59	180	4991
0.62	181	5040
0.65	185	5150
0.77	197	5469
0.97	212	5892
1.17	230	6401
1.37	246	6818
1.57	263	7300
1.77	278	7735

2. Characterization of carbons and cell setup

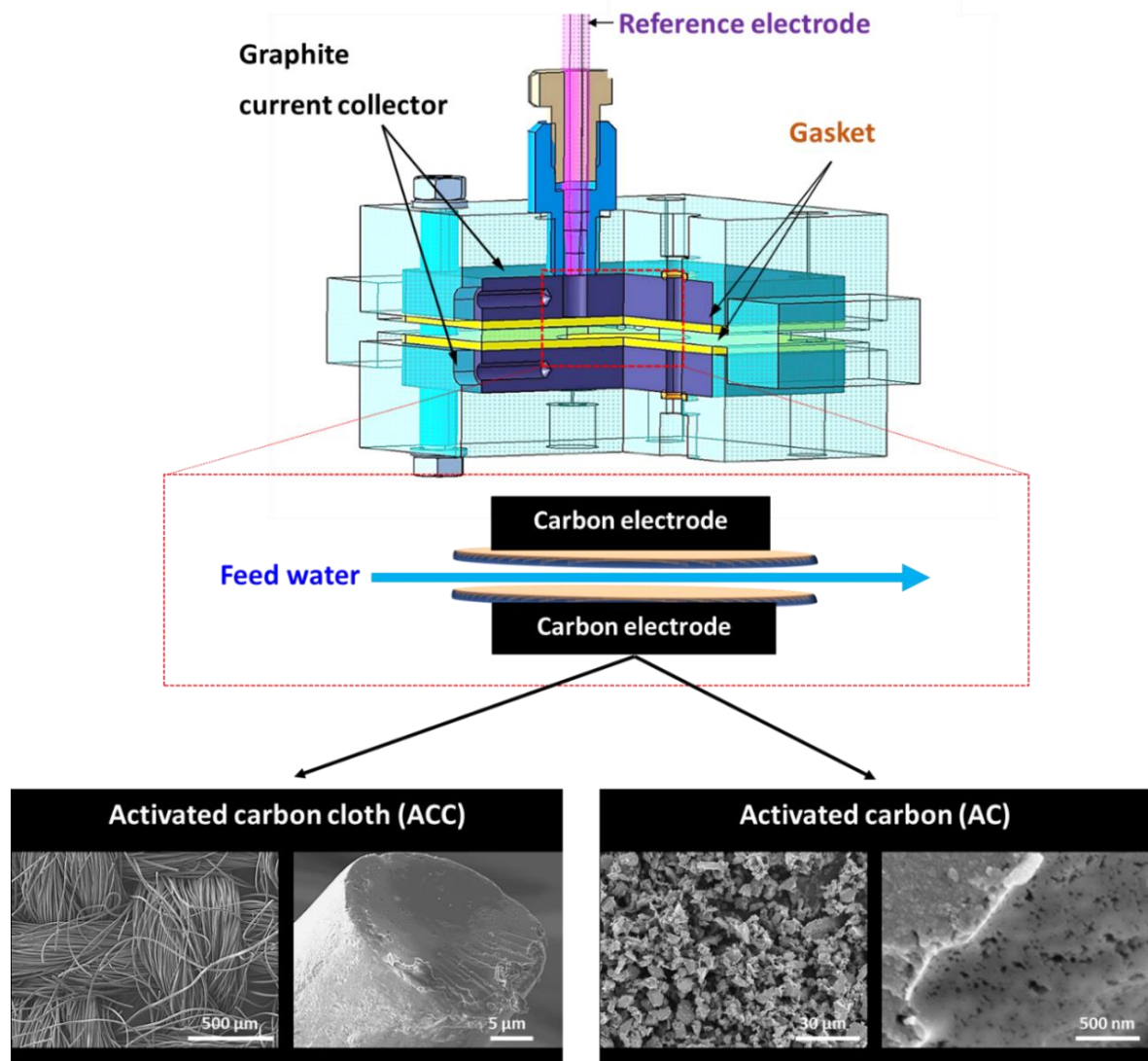


Figure S1. Schematic view of the CDI cell and scanning electron micrographs of carbon electrode materials.

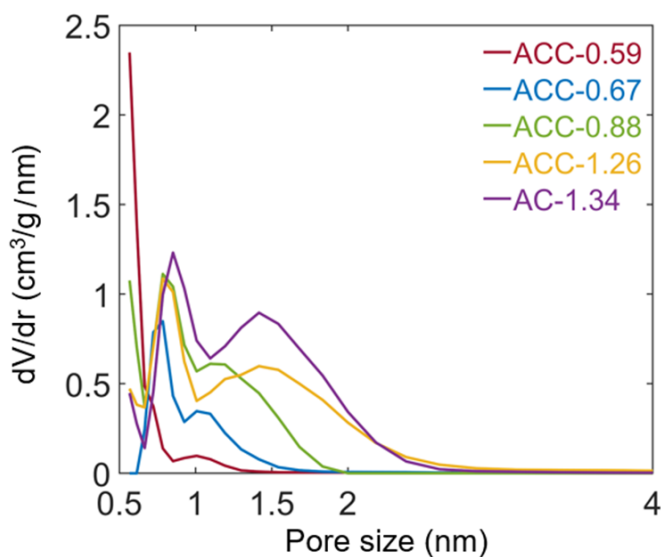


Figure S2. Differential pore size distribution. Data are obtained from nitrogen gas sorption isotherms at -196 °C, calculated by applying quenched solid density functional theory (QSDFT) and assuming pores have slit shape.

Table S2. Specific surface area (BET and DFT), total pore volume, and volume-weighted pore size of ACC-0.59, ACC-0.67, ACC-0.88, ACC-1.26, and AC-1.34.

	SSA BET (m^2/g)	SSA DFT (m^2/g)	Pore volume (cm^3/g)	d_{25} (nm)	d_{50} (nm)	d_{75} (nm)	$d_{75}-d_{25}$ (nm)
ACC-0.59	916	1032	0.34	0.55	0.59	0.68	0.12
ACC-0.67	1478	1550	0.56	0.45	0.67	0.86	0.41
ACC-0.88	2070	1876	0.81	0.64	0.88	1.19	0.55
ACC-1.26	2794	2191	1.22	0.89	1.26	1.61	0.72
AC-1.34	2104	1756	1.00	0.86	1.34	1.80	0.94

Table S3. CHN-O elemental analysis of ACC-0.59, ACC-0.67, ACC-0.88, ACC-1.26, and AC-1.34 (unit: mass%). “n.d.” demarks values below the detection limit of the system (“not detectable”).

	C	H	N	O
ACC-0.59	>94	n.d.	<1	<6
ACC-0.67	>96	<1	<0.1	<2
ACC-0.88	>96	<2	<0.2	<2
ACC-1.26	>96	<1	n.d	<3
AC-1.34	>95	<1	n.d	<4

3. Desalination performance measurements with aqueous NaCl solution

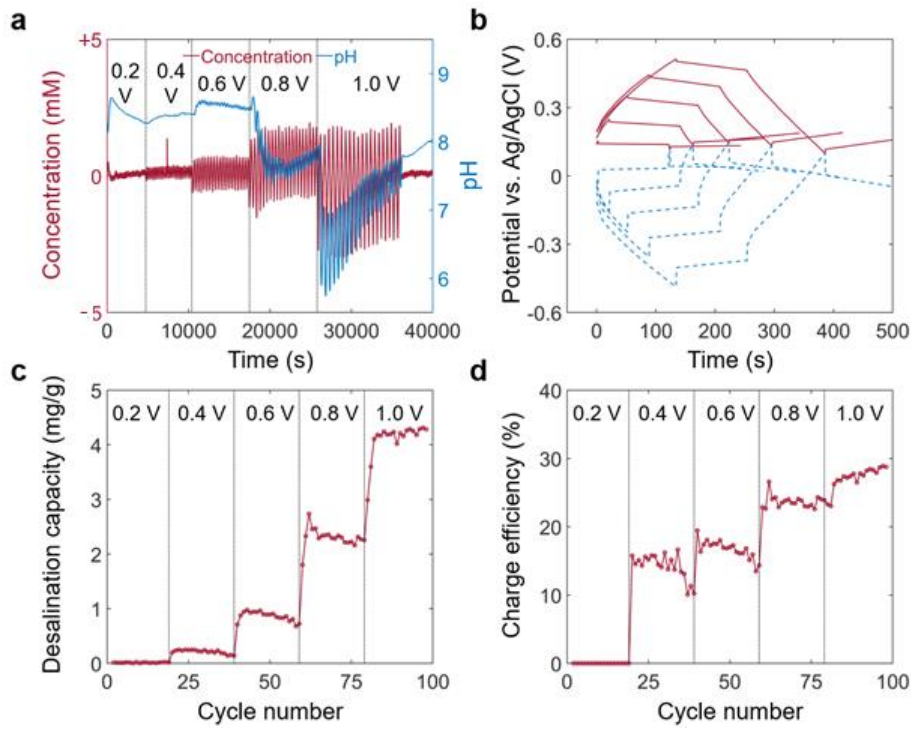


Figure S3. CDI measurement for ACC-0.59 carbon cloth in 800 mM NaCl. **a**, Concentration change (relative to 800 mM) and pH profile. **b**, Galvanostatic charging and discharging for the working electrode (red line) and counter electrode (blue dash line). **c-d**, Desalination capacity (**c**) and charge efficiency (**d**) profile at each cycle.

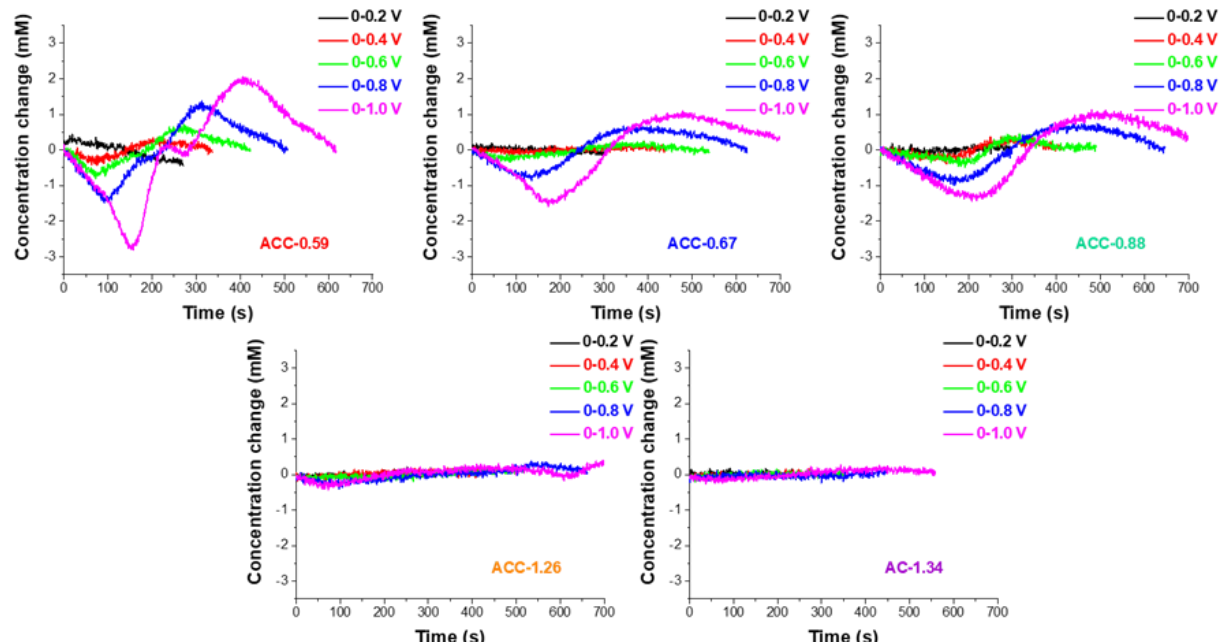


Figure S4. Representative concentration change pattern for different carbon electrode materials in 800 mM NaCl.

4. Basic electrochemical characterization

To determine the basic electrochemical properties of ACC electrodes in 2 M KCl system, half-cell characterization was carried out with a custom-built cell using spring-loaded titanium pistons. To assemble the cell, a 12 mm diameter disk of the ACC electrode material (around 20 mg) was cut and employed as the working electrode. 13 mm diameter of glass fiber mat (GF/A, Whatman) was employed as the separator. As for the counter-electrode, a free-standing YP-80F/PTFE 95:5 electrode (thickness: 650 μm) was used. 12 mm diameter of graphite foil was applied as current collectors. The aqueous 2 M KCl solution was inserted into the cell by vacuum filling with a syringe, and an Ag/AgCl reference electrode (3 M KCl, BASi) was located at the side of the cell body and assembled close to working electrode and counter electrode. The cell was characterized by using VSP300 potentiostat/galvanostat (Bio-Logic). For cyclic voltammetry, the cell was cycled between -0.5 V and +0.5 V vs. Ag/AgCl at the scan rate of 1 mV/s. For galvanostatic charge/discharge, the specific current of 0.1 A/g was applied to the electrode with potential applied from 0 V vs. Ag/AgCl to the cut-off potentials of +0.2 V, +0.4 V, +0.6 V, +0.8 V, and +1.0 V vs. Ag/AgCl (ten cycles for each potential range). The specific capacitance of the electrode is calculated according to **Eq. S1**.

$$C_{\text{specific}} = \frac{1}{U_m} \int_{t_1}^{t_2} I dt \quad (\text{Eq. S1})$$

where U is the voltage difference during the discharge process (excluding the Ohmic drop), m is mass of the working electrode, t_2-t_1 is the discharge time interval, and I is the applied discharge current.

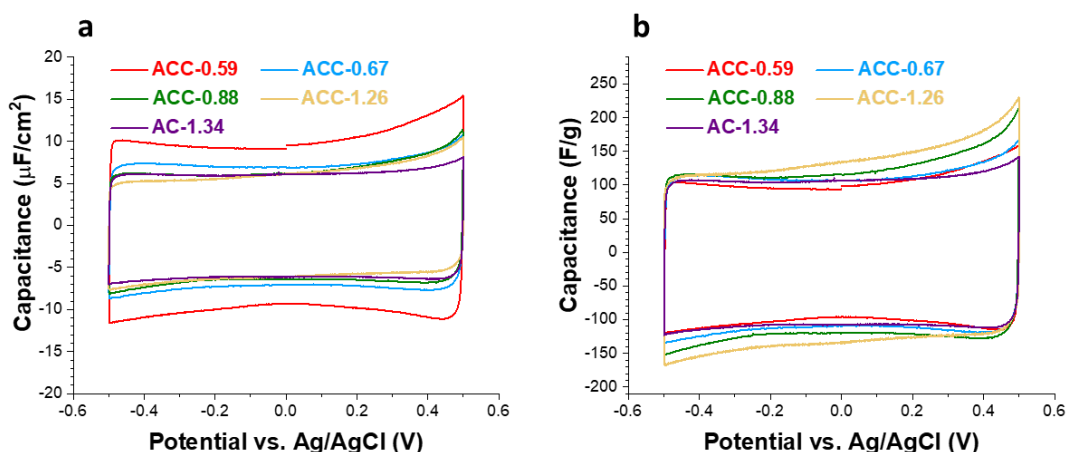


Figure S5. Cyclic voltammogram measurements. Performed at 1 mV/s for five carbon electrodes in 2 M KCl water solution. ACC and AC carbons are applied as working electrodes, and YP-80F+5% PTFE electrodes are applied as counter electrodes. **a**, normalized to specific surface area; **b**, normalized to electrode mass.

5. In-pore ions under different polarizations

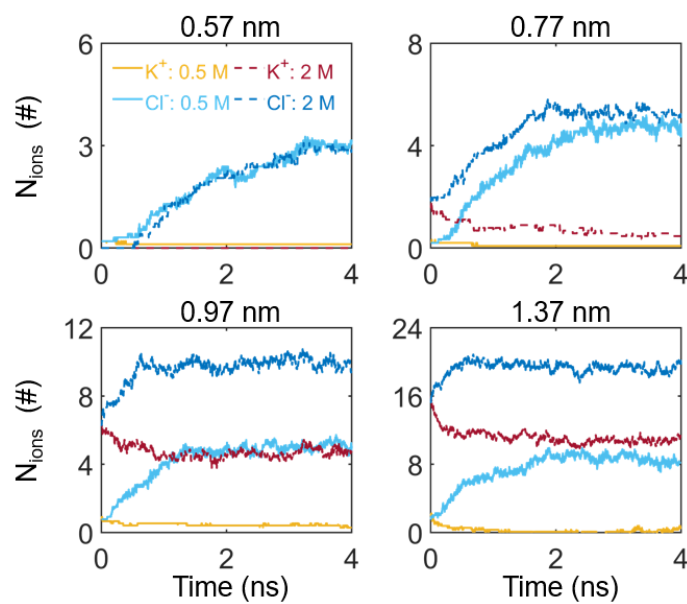


Figure S6. Time evolution of the number of cation and anion in the positively charged micropores. The applied voltage between the positive and negative electrode is set to 1.0 V. Dark red and blue solid lines are, respectively, results for the cation and anion at 2 M concentration. Yellow and light blue dashed lines are for cation and anion at 0.5 M concentration. These results are evaluated on-the-fly during the charging simulations of each micropore.

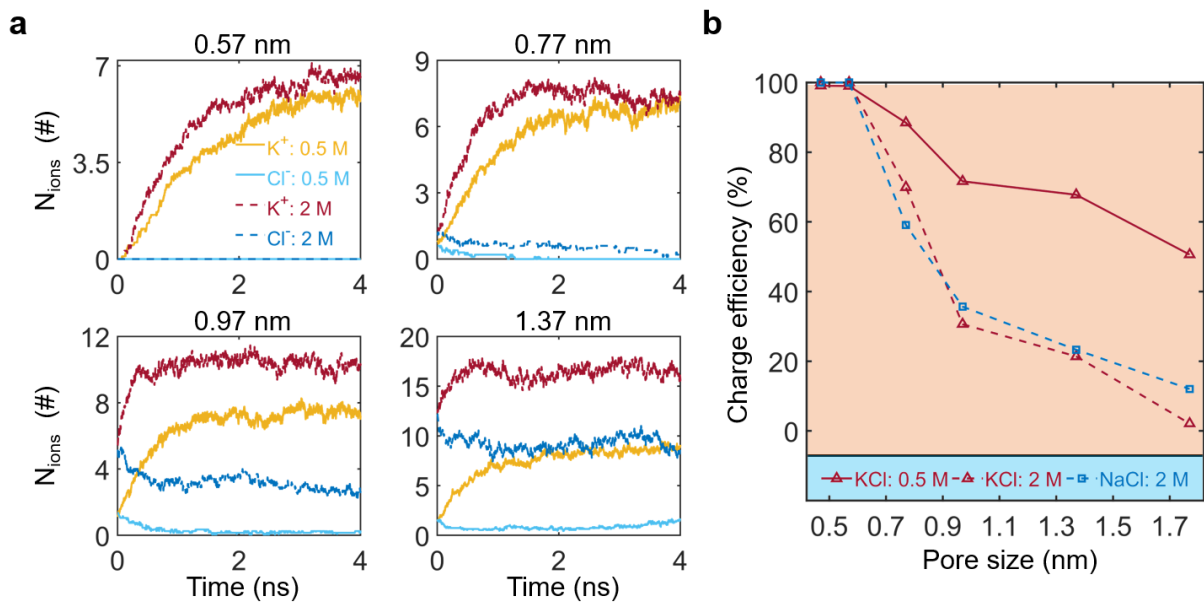


Figure S7. Molecular understanding of ion permselectivity by micropores at 1.5 V. **a**, Time evolution of the number of cation and anion in the negatively charged micropores. Dark red and blue solid lines are, respectively, results for the cation and anion at 2 M. Yellow and light blue dashed lines are for cation and anion at 0.5 M. These results are evaluated during the charging simulations of each micropore. **b**, Charge efficiency, as a function of pore size. Red solid and dashed lines with triangle markers represent results of micropores in aqueous 0.5 M and 2 M KCl solutions, respectively. Blue dashed line with squares: 2 M NaCl solution.

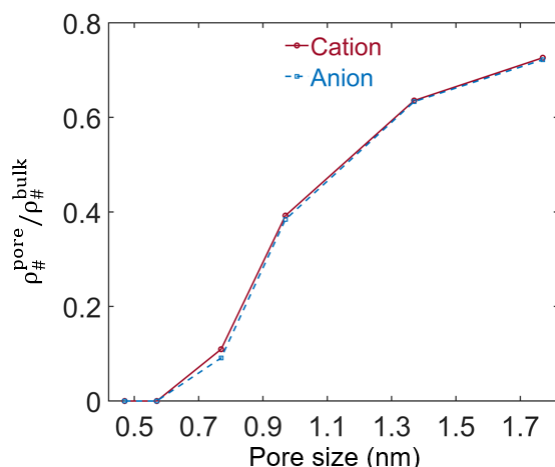


Figure S8. Normalized in-pore ion density at PZC. The in-pore ion density is scaled by bulk ion density. Solid and dash lines are, respectively, for the cation and anion at 2 M.

6. Water distribution surrounding ions in bulk and inside large pores

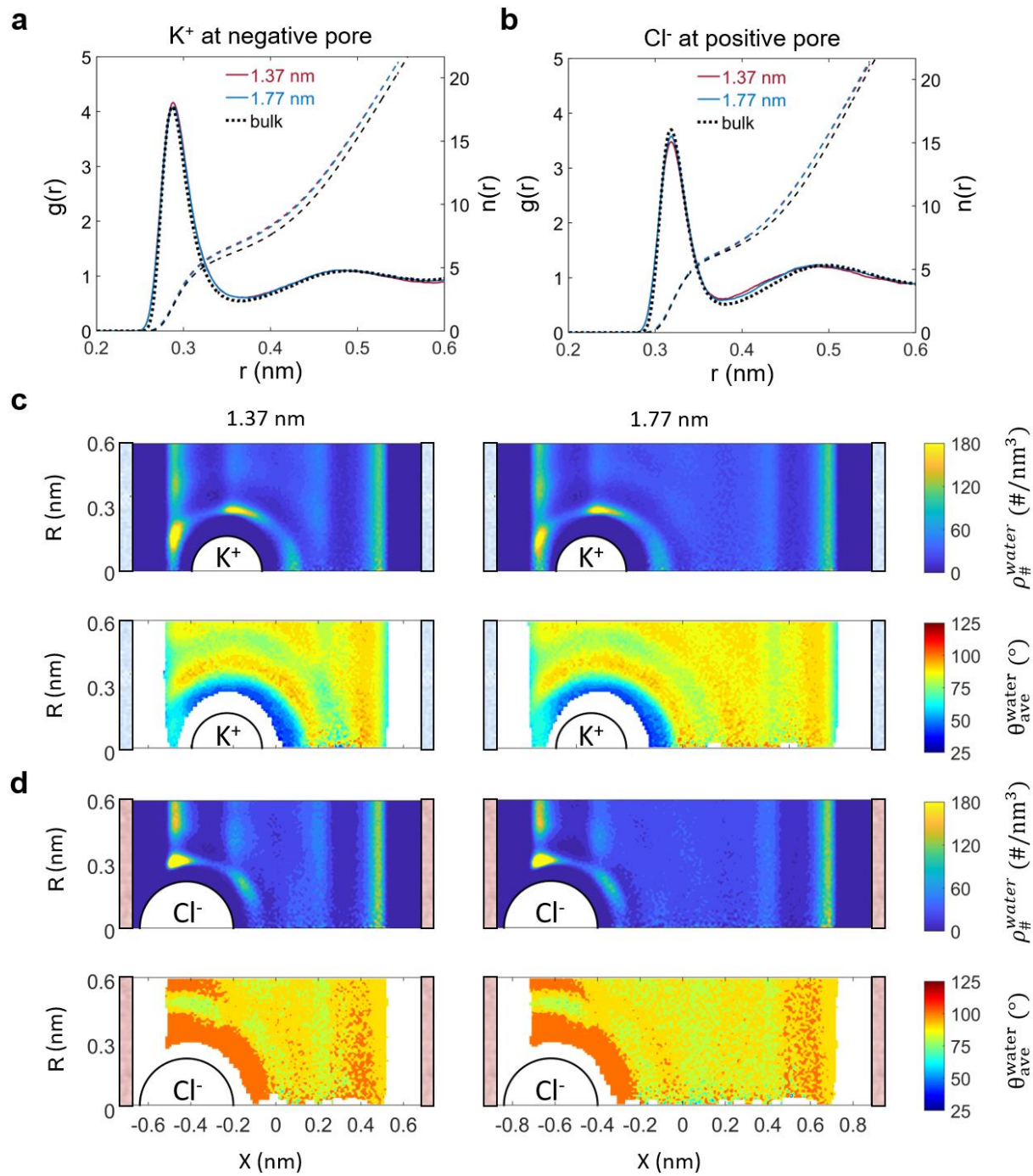


Figure S9. Structure of hydration shells of counter-ions in >1 nm polarized micropores. **a-b**, Radial distribution function, $g(r)$ (solid lines, left Y-axis), and cumulative distribution function, $n(r)$ (dashed, right Y-axis) of hydrated K^+ ions (left panel) and Cl^- ions (right panel) in negatively and positively polarized pores, respectively. Black dot lines are results for ions in bulk simulations. **c-d**, Pseudo-2D number density distributions and orientations of water molecules around an ion in micropores of 1.37 nm and 1.77 nm; the upper two rows and the lower two are results (first number density, then orientation distributions) for water around a K^+ ion under negative polarization and for water around a Cl^- ion under positive polarization, respectively. $X = 0$ corresponds to the central position of the pore.

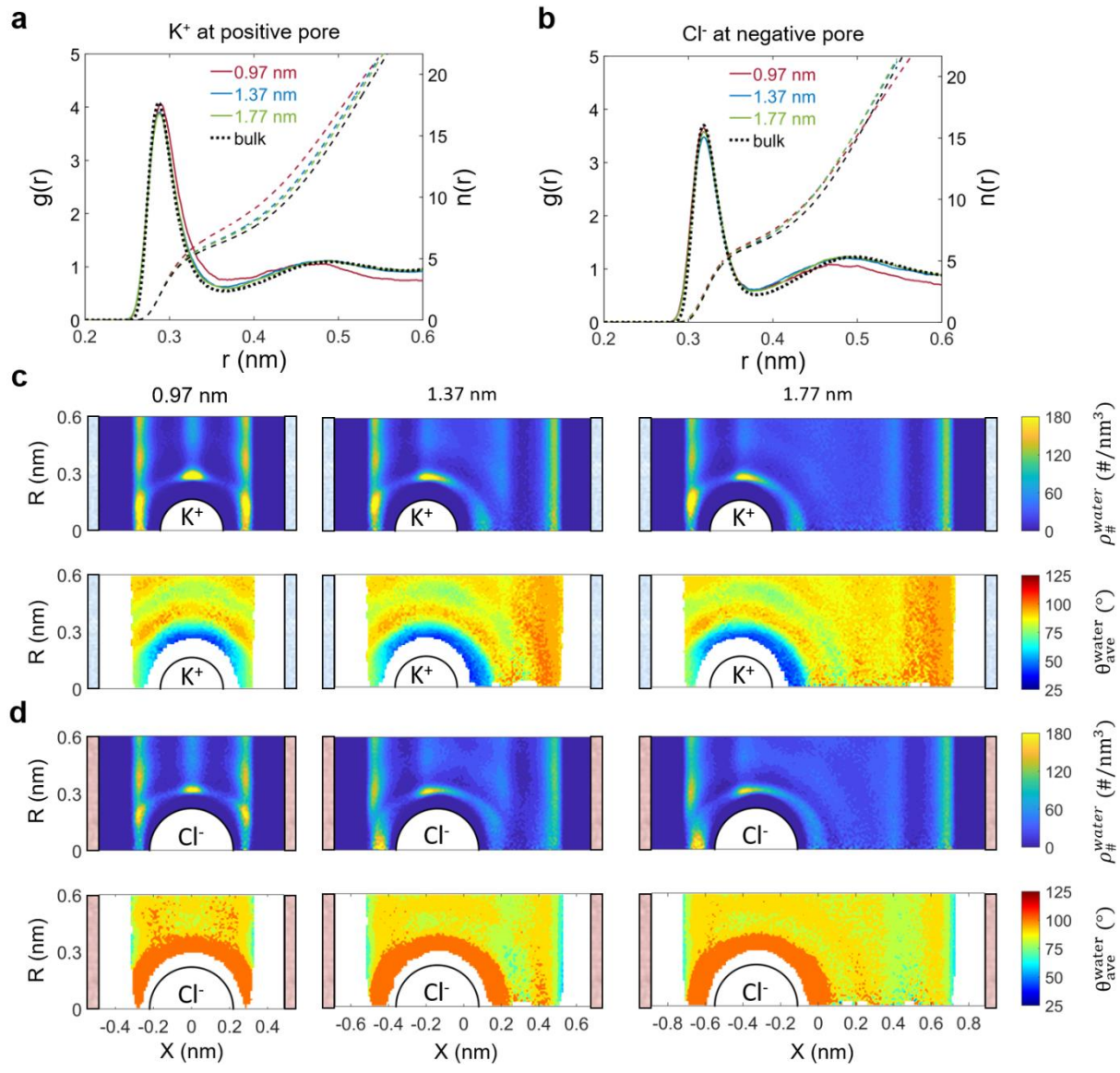


Figure S10. Structure of hydration shells of co-ions in polarized micropores. **a-b**, Radial distribution function, $g(r)$ (solid lines, left Y-axis), and cumulative distribution function, $n(r)$ (dashed, right Y-axis) of hydrated K^+ ions (left panel) and Cl^- ions (right panel) in positively and negatively polarized pores, respectively. Black dot lines are results for ions in bulk simulations. **c-d**, Pseudo-2D number density (upper panel) and orientation (lower panel) distributions of water molecules around a co-ion in micropores of different pore sizes under positive and negative polarizations, respectively. We show K^+ ion (**c**) in positively charged pores and Cl^- ion (**d**) in negatively charged pores. $X = 0$ corresponds to the central position of the pore.

7. Dynamics of ions inside charged pores

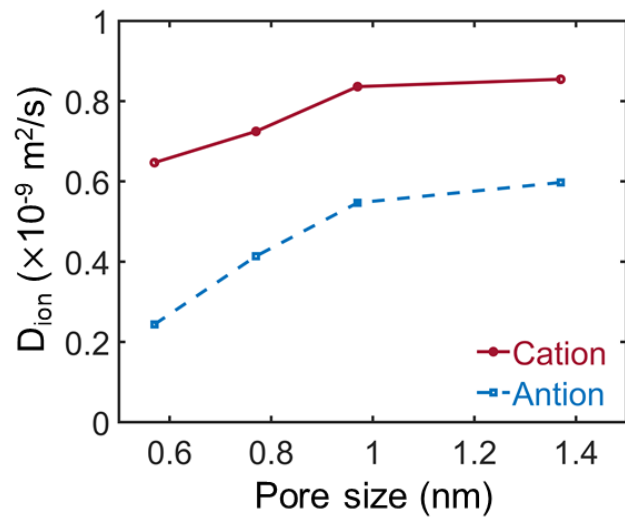


Figure S11. In-pore ion diffusion. Self-diffusion coefficients of cations and anions in negatively and positively charged pores, respectively. The voltage applied between the positive and negative electrode is set at 1.0 V.

4.3 Ionophobicity of carbon sub-nanometer pores enables efficient desalination at high salinity

Yuan Zhang,^{1,2} Christian Prehal,³ Huili Jiang,^{4,5} Yang Liu,^{1,2}
Guang Feng,^{4,5} and Volker Presser^{1,2,6}

1 INM - Leibniz Institute for New Materials, Campus D2 2, 66123 Saarbrücken, Germany

2 Saarland University, Campus D2 2, 66123 Saarbrücken, Germany

3 Department of Information Technology and Electrical Engineering, ETH Zürich, Gloriastrasse 35, 8092 Zürich, Switzerland

4 State Key Laboratory of Coal Combustion, School of Energy and Power Engineering, Huazhong University of Science and Technology (HUST), Wuhan 430074, China

5 Nano Interface Centre for Energy, School of Energy and Power Engineering, HUST, 430074, China

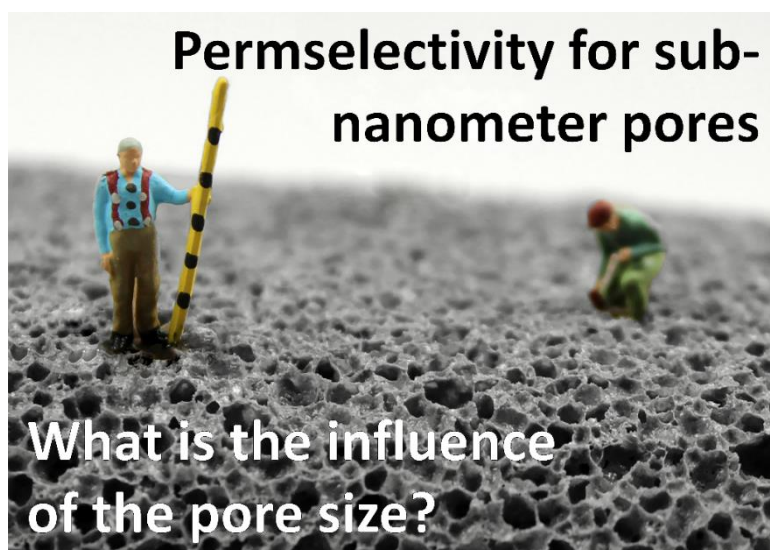
6 Saarene - Saarland Center for Energy Materials and Sustainability, Campus C4.2, 66123 Saarbrücken, Germany

Citation:

Y. Zhang, C. Prehal, H.Jiang, Y. Liu, G.Feng, V. Presser, *Anomalous ionophobicity of carbon sub-nanometer pores enables efficient desalination at high salinity*, Cell reports Physical Science, 2022, 100689. . (DOI: 10.1016/j.xcrp.2021.100689)

Own contribution:

Conceptualization, writing-original draft, investigation, visualization, data curation.



Article

Ionophobicity of carbon sub-nanometer pores enables efficient desalination at high salinity

Ionophobicity of carbon sub-nanometer pores



Yuan Zhang, Christian Prehal,
Huili Jiang, Yang Liu, Guang
Feng, Volker Presser

gfeng@hust.edu.cn (G.F.)
volker.presser@leibniz-inm.de (V.P.)

Highlights

Sub-nanometer carbon pores can
desalinate high-saline water

Predictable desalination
performance at high molar
strength

Pore size of 0.77 nm shows the
highest desalination performance

High charge efficiency and low-
cost seawater desalination

In this work, high capacitive deionization performance is obtained by Zhang et al. using activated carbon with sub-nanometer pore sizes at seawater-level molar strength. Combining experimental results and molecular dynamics simulations shows that desalination performance can be predicted from pore size distribution data.

Zhang et al., Cell Reports Physical Science 3,
100689
January 19, 2022 © 2021 The Author(s).
<https://doi.org/10.1016/j.xcrp.2021.100689>



Article

Ionophobicity of carbon sub-nanometer pores enables efficient desalination at high salinity

Yuan Zhang,^{1,2} Christian Prehal,³ Huili Jiang,^{4,5} Yang Liu,^{1,2} Guang Feng,^{4,5,*} and Volker Presser^{1,2,6,7,*}

SUMMARY

Electrochemical seawater desalination has drawn significant attention as an energy-efficient technique to address the global issue of water remediation. Microporous carbons, that is, carbons with pore sizes smaller than 2 nm, are commonly used for capacitive deionization. However, micropores are ineffective for capacitive deionization at high molar strength because of their inability to permselectively uptake ions. In our work, we combine experimental work with molecular dynamics simulation and reveal the ability of sub-nanometer pores (ultramicropores) to effectively desalinate aqueous media at seawater-like molar strength. This is done without any ion-exchange membrane. The desalination capacity in 600 mM reaches 12 mg/g, with a charge efficiency of 94% and high cycling stability over 200 cycles (97% of charge efficiency retention). Using molecular dynamic simulations and providing experimental data, our work makes it possible both to understand and to calculate desalination capacity and charge efficiency at high molar strength as a function of pore size.

INTRODUCTION

With industrialization and human population growth, the lack of fresh water has become a global issue.¹ About 98% of the water in the world is seawater or brackish water; therefore, efficient water desalination techniques are of great importance.² Many desalination techniques are applied in practice, such as distillation,^{3,4} reverse osmosis,^{5,6} and electrodialysis.⁷ Electrochemical desalination via capacitive deionization and desalination batteries has the potential for energy-efficient water remediation and tailored ion separation.^{8–12} Capacitive deionization (CDI) uses low-cost carbon material electrodes and allows high energy efficiency and a high desalination rate, yet CDI remains restricted to desalination at a low salt concentration, such as found in brackish water.^{3,13} The inability of CDI to accomplish desalination at high molar strength is linked to the permselectivity failure and decrease of charge efficiency, where non-permselective ion exchange processes dominate the charge storage mechanism.¹⁴

CDI cells commonly apply a pair of porous carbon films as the positive and negative electrodes. As salt-containing water flows between the electrode stack, cations and anions are electroadsorbed when the electrodes are being charged; thereby, a stream of desalinated water exits the CDI cell.¹⁵ Ion electrosorption is an interfacial process. Thus, high desalination performance is enabled by electrodes with large pore volume/surface area, such as activated carbons,¹⁶ graphene-based materials,¹⁷ or carbide-derived carbons.¹⁸ Highly microporous carbons provide a large pore volume, but ions in the micropores during the uncharged state present an issue to the application of CDI.¹⁹ During the charging process within the

¹INM – Leibniz Institute for New Materials, Campus D2 2, 66123 Saarbrücken, Germany

²Saarland University, Campus D2 2, 66123 Saarbrücken, Germany

³Department of Information Technology and Electrical Engineering, ETH Zürich, Gloriastrasse 35, 8092 Zürich, Switzerland

⁴State Key Laboratory of Coal Combustion, School of Energy and Power Engineering, Huazhong University of Science and Technology (HUST), Wuhan 430074, China

⁵Nano Interface Centre for Energy, School of Energy and Power Engineering, HUST, Wuhan 430074, China

⁶Saarene – Saarland Center for Energy Materials and Sustainability, Campus C4.2, 66123 Saarbrücken, Germany

⁷Lead contact

*Correspondence: gfeng@hust.edu.cn (G.F.), volker.presser@leibniz-inm.de (V.P.)

<https://doi.org/10.1016/j.xcpr.2021.100689>



electrochemical-potential stability window of water, counter-ions enter the pores to decrease the feed water concentration, and co-ions are ejected from the pore, contributing to a smaller concentration decrease. In solutions with higher salt concentrations, the number of ions initially present inside the pores is higher. During charging, more co-ions are ejected, and fewer counter-ions are adsorbed in the pores, which leads to little concentration change of the feed water.^{18,20}

The CDI process can become more permselective when adding one or multiple ion-exchange membranes (MCDI), thereby trapping co-ions and enhancing the desalination metrics.¹⁵ Although most studies have focused on low concentrations,^{21,22} our past work applied MCDI in 600 mM NaCl to achieve a desalination capacity of 25 mg/g at a potential range of -1 to $+1$ V¹⁷; works such as ours and others show the possibility of applying MCDI for seawater desalination.^{10,23} In desalination batteries,^{23,24} carbon electrodes are replaced by charge-transfer materials, such as metal oxides,²⁰ hexacyanoferrates,²⁵ MXenes,²⁶ redox-electrolytes,²⁷ conversion materials,^{28,29} or alloying materials.³⁰ More recent approaches include electrocatalytic processes.^{31,32} Although implementing CDI with ion-exchange membranes or charge-transfer materials is an effective way to improve desalination performance, it involves additional material costs and complicates electrode fabrication.

Recently, we have shown that carbon electrodes with tailored sub-nanometer pores show an increased ability to accomplish desalination even at higher molar strength.³³ In this way, without requiring expensive ion-exchange membranes or charge-transfer materials, desalination is accomplished by a low ion population inside small carbon pores in the uncharged state; thereby, less ion exchange (undesirable) and more permselective (desirable) ion uptake is enabled. Yet a robust understanding of the pore size dependency of both charge efficiency and predicted desalination capacity is still missing. To eliminate the belief that CDI is unsuitable for seawater desalination, convincing experimental data are also needed to show robust desalination performance.

Our present work shows the ability of ultramicroporous carbons with sub-nanometer pore sizes to afford a stable and high desalination capacity of 12 mg/g in aqueous 600 mM NaCl at a charge efficiency of 94%. Such performance values are highly comparable with what many microporous carbons deliver at low molar strength (e.g., activated carbon cloth at 5–20 mM: up to 16 mg/g with a charge efficiency of up to 80%–90%).^{34,35} As the pore size dispersity of most activated carbons makes it impossible to notice the strong dependency of desalination performance on pore sizes, we have developed a calculation tool that uses pore size distribution data from gas sorption analysis (GSA) and simulation data by applying an interpolation method to predict the desalination performance of a material. With this calculation tool, we vastly advance previous work, such as the “direct prediction of the desalination performance of porous carbon electrodes for capacitive deionization.”³⁶ Our theoretical calculation of desalination performance on the basis of the pore size distribution of carbon materials is extended to 600 mM NaCl and also includes the calculation of charge efficiency in addition to desalination capacity.

Our combined work of experimental desalination and extensive simulation shows that the ability to remove excess salt at high molar strength goes far beyond the “anomalous capacitance increase” in supercapacitors that was explained by the distortion of the solvation shell.³⁵ The improved desalination performance can

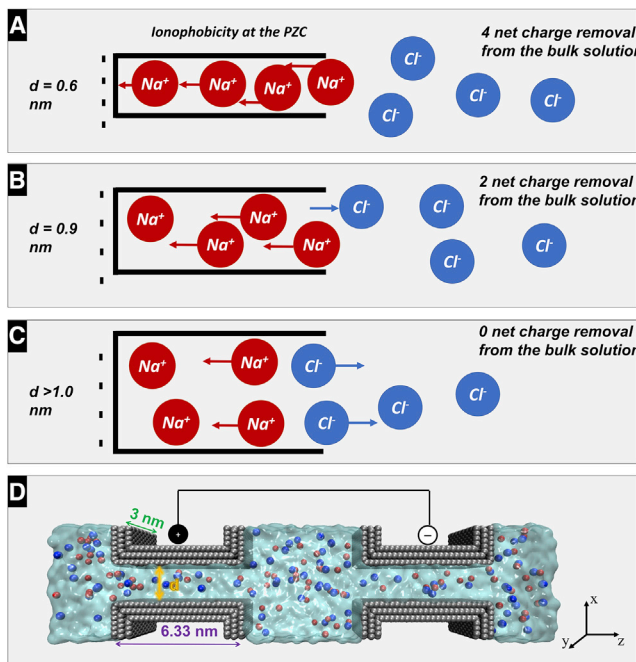


Figure 1. Schematics of possible ion electrosorption mechanisms during the desalination process in high molar salt solutions

- (A) Desalination in pore width of 0.6 nm.
- (B) Desalination in pore width of 0.9 nm.
- (C) Desalination in pore width larger than 1 nm.
- (D) Schematic depiction of the molecular dynamics simulation model for ion electrosorption with a pair of micropores during electric polarization.

be explained by the ionophobicity of sub-nanometer carbon nanopores at the uncharged state, which is caused by the dehydration energy barrier for in-pore ion adsorption rather than functional groups and specific adsorption, with important implications for ion separation and energy storage. Molecular dynamics (MD) simulations demonstrate the enhanced desalination capacity by sub-nanometer pore ionophobicity caused by the significant energetic expense of ion desolvation.

RESULTS

Ion electrosorption mechanisms and characterization

Figures 1A and 1B schematically show possible ion electrosorption mechanisms in sub-nanometer pores. The sub-nanometer pore size is comparable with the size of the solvated ion; this confinement will result in incomplete double-layer structures that cannot be explained by the Gouy-Chapman-Stern model.^{37,38} The smallest category of pores (0.6 nm; Figure 1A) is ionophobic; that is, the ions are required to desolvate so that there are initially no ions inside the pores at the potential of zero charge (PZC).³⁹ Ions would only (partially) desolvate and electroadSORB inside the pores upon negative (or positive) polarizations. As the parasitic co-ion expulsion phenomenon is not possible in initially empty 0.6 nm pores, there is more counterion uptake compared with larger pores. Figure 1B shows the process in slightly larger pores (0.9 nm). Here, some cations and anions are present inside the pores already at the PZC. When the pore is negatively polarized, some Cl^- ions will be rejected while some Na^+ ions enter the pore. Because of this non-permselective ion

Table 1. Chemical analysis of the different carbon electrode materials ACC-0.59, ACC-0.96, and AC-1.39

	Carbon, mass%	Hydrogen, mass%	Nitrogen, mass%	Oxygen, mass%	Ash content, mass%
ACC-0.59	93.4 ± 0.6	1.0 ± 0.0	0.6 ± 0.0	4.0 ± 0.3	<2
ACC-0.96	95.5 ± 1.0	1.1 ± 0.0	0.7 ± 0.1	4.1 ± 1.0	<2
AC-1.39	96.1 ± 0.4	0.6 ± 0.1	0.3 ± 0.1	2.7 ± 0.1	<2

swapping effect, the net charge uptake is less than in the 0.6 nm pore. For pores larger than 1 nm, the in-pore counter-ion and in-pore co-ion concentrations further increase at the PZC. Co-ion repulsion to the bulk electrolyte would further increase, and the total net ion removal would be close to zero for a high molar bulk electrolyte.⁴⁰

The molecular simulation allows the study of correlations among pore size, ionic strength, and the underlying electrosorption mechanism; thereby, it is possible to quantify the achievable desalination performance. Figure 1D shows a three-dimensional model of the MD simulation schematically. The two pairs of 6.33-nm-long graphite pores contact the 600 mM NaCl bulk aqueous electrolyte and represent the positively and negatively polarized slit pores (where the *d*-value corresponds to the slit pore width). With this model, the dynamic process of ion electrosorption, ion exchange, and the permselectivity properties of carbon pores can be simulated. Figure S1 depicts the characterization of two activated carbon cloths (ACC) with different average pore sizes (ACC-0.59 and ACC-0.96). The values 0.56 and 0.98 stand for the average pore sizes (in nanometers) according to gas sorption analysis. The pore size difference is caused by different degrees of the activation process. Figures S1A and S1B shows the scanning electron micrographs of the structures of two materials. As seen from the chemical composition provided in Table 1, there are no significant differences between ACC-0.59 and ACC-0.96. The non-carbon mass content for all materials is between 4 mass% and 7 mass%. For ACC-0.59 and ACC-0.96, the functional groups are dominated by acidic groups such as carbonyl and carboxylic groups.⁴¹

Figures S1C and S1D show the gas sorption isotherm and pore size distribution of the two materials at 87 K (data adapted from Bi et al.¹⁶). The analyzed pore structure data are shown in Table 2. Compared with ACC-0.59, ACC-0.96 is more activated and has more interpore volumes, higher pore volume, and a larger average pore size compared with ACC-0.59.

Experimental desalination performance

Desalination performance was evaluated by applying ACC-0.59 and ACC-0.96 activated carbon cloth electrodes. Using the same desalination parameters (i.e., flow rate, specific current, galvanostatic potential holding time, and electrode thickness), we quantified the desalination performance of the different electrode materials in 5, 20, and 600 mM NaCl aqueous electrolytes. Figures 2A and 2B shows the effluent concentration profile normalized by the surface area of carbon materials during a galvanostatic charging and discharging cycle using ACC-0.59 and ACC-0.96 in NaCl solutions with different concentrations. For ACC-0.59, the CDI cell shows the most significant concentration change in the 600 mM NaCl solution. As the concentration decreases to 20 and 5 mM, the amplitude is significantly smaller. This indicates that the ionic strength of the electrolyte has a significant influence on the ion electrosorption process in ACC-0.59. For ACC-0.96, on the contrary (Figure 2B),

Table 2. Gas sorption analysis with nitrogen gas at -196°C for ACC-0.59,¹⁶ ACC-0.96, YP-80F (AC-1.39) activated carbon and titanium carbide-derived carbon (CDC-0.57) using the quenched solid density functional theory (QSDFT) and the Brunauer-Emmett-Teller theory (BET)

	SSA BET, m^2/g	SSA DFT, m^2/g	DFT total pore volume, cm^3/g	Average pore size d_{50} , nm
ACC-0.59	916	1032	0.34	0.59
ACC-0.96	2209	1940	0.89	0.96
AC-1.39	2598	1631	1.03	1.39
CDC-0.57	1056	1268	0.40	0.57

Average pore size refers to the volume-normalized value d_{50} . SSA, specific surface area.

the amplitude of concentration change decreases as the ionic strength of the electrolyte increases. When comparing the two types of electrodes in 600 mM molarity, ACC-0.59 shows a much higher concentration change amplitude than ACC-0.96. ACC-0.59 and ACC-0.96 in 600 mM NaCl show different desalination abilities, although ACC-0.96 has a larger average pore size that is beneficial for ion transportation, and ACC-0.59 with an average pore size smaller than the solvated ion sizes shows significantly higher ion removal ability. The comparison between ACC-0.59 and ACC-0.96 in different molarities is provided in Figure S2A. It shows that ACC-0.59 with a smaller average pore size has more efficient desalination ability in 600 mM solution under the same processing condition compared with ACC-0.96.

In Figure 2C, the desalination capacities and charge efficiencies are compared. For ACC-0.59, the desalination capacity and charge efficiency are both low at 5 mM molarity. As the electrolyte concentration increases to 20 mM, the desalination capacity and charge efficiencies significantly improve. In 600 mM NaCl electrolytes, the desalination capacity reaches 12 mg/g, and the charge efficiency is 94%, which are the highest value found in this study. To the best of our knowledge, it is also by far the highest performance of carbon materials in 600 mM high molar strength without an ion-exchange membrane because of its high ion permselectivity that results in higher charge efficiency in sub-nanometer pores.

To prove the pore size effect on water desalination for the carbon materials with different morphology and pore curvatures, the desalination performance in 600 mM NaCl of commercially available activated carbon (YP-80F, Kuraray; abbreviated as AC-1.39)^{42–44} and titanium carbide-derived carbon (TiC-CDC; abbreviated as CDC-0.57)^{3,18,45} is provided in Figure S2B. AC-1.39 has more phenolic functional groups, while CDC-0.57 has more Cl^- -containing species.⁴⁶ The gas sorption data for these carbon materials are provided in Table 2. Although the activated carbon has an average pore size of 1.39 nm (pore volume $1.03 \text{ cm}^3/\text{g}$), carbide-derived carbon has a much smaller average pore size of only 0.57 nm (pore volume $0.40 \text{ cm}^3/\text{g}$). Thus, CDC-0.57 and ACC-0.59 are very similar, but the latter has a much sharper pore size distribution. Accordingly, we see CDC-0.57 has a slightly lower desalination capacity (10 mg/g) and charge efficiency (74%) compared with ACC-0.59 (12 mg/g and 94%). These data show that the importance of sub-nanometer pores for the CDI process at high molar strength is not limited to activated carbon cloth. Also, in agreement with the lowered permselectivity of larger micropores, AC-1.39 is not suitable for CDI at 600 mM molar strength.

When the average pore size of the carbon material increases to about 1.0 nm (ACC-0.96), the electrode's permselectivity is less pronounced. Thus, the charge efficiency

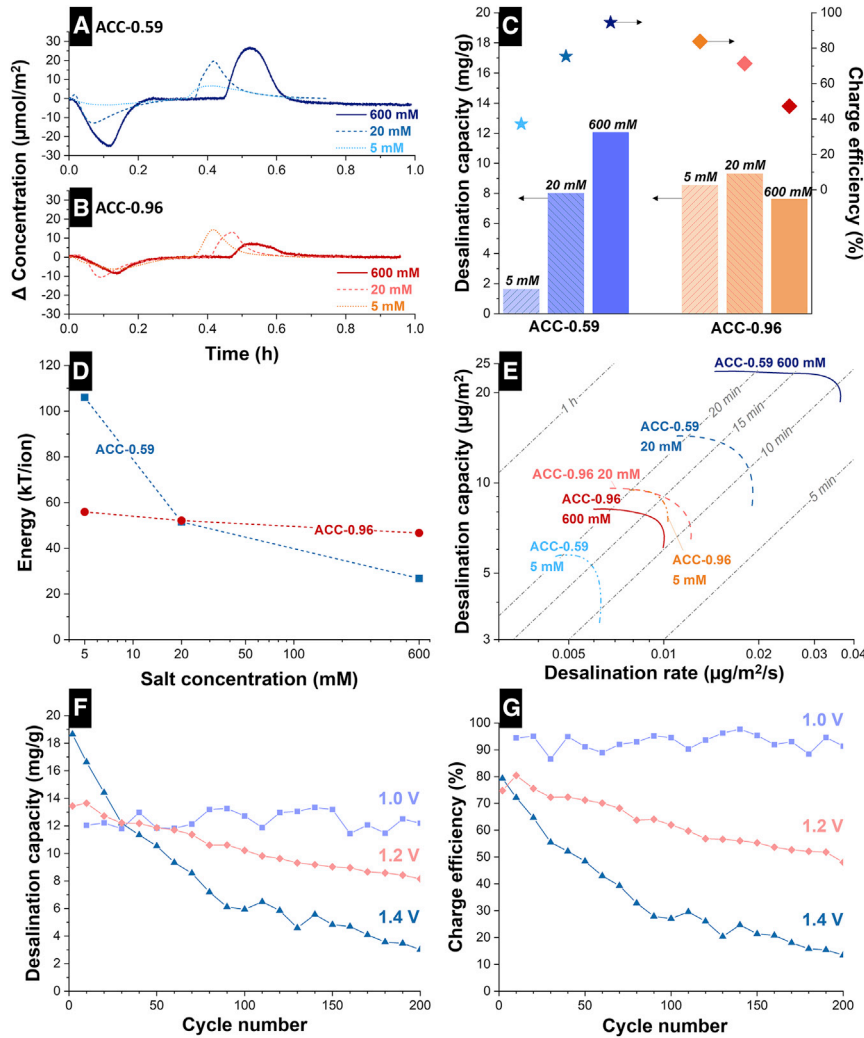


Figure 2. Desalination performance of ACC-0.59 and ACC-0.96 in different concentration of NaCl aqueous solutions

(A) Concentration variation of ACC-0.59 electrode in different molar strength. Galvanosatitic charging/discharging was used with a specific current of 0.1 A/g. A 20 min potential holding period was used.

(B) Concentration variation of ACC-0.96 electrode in different molar strength.

(C) Desalination capacity and charge efficiency of both materials in different molar strength.

(D) Energy consumption of the two materials in different molarities.

(E) Kim-Yoon plot for the two materials in different molarities.

(F and G) Desalination capacity (F) and (G) charge efficiency for ACC-0.59 under 1, 1.2, and 1.4 V throughout 200 cycles.

of the electrode in different electrolytes decreases as the molarity increases. This phenomenon is caused by the increased ion number in the micropores when the cell is not charged, which results in stronger ion swapping under polarization. The desalination capacity of ACC-0.96 in 5 mM NaCl solution is slightly higher than that in ACC-0.59. Under low ionic strength, counter-ion adsorption is generally more dominant than co-ion exclusion, as the in-pore ion concentration at the PZC is low.⁴² Therefore reasonable desalination capacities are possible in all carbons. Contrary to the 600 mM solution, there is no enhanced uptake of counter-ions,

because of the ionophobicity in ACC-059. A further experimental factor is the slow ion diffusion in ACC-0.59 with 5 mM NaCl. Within the 20 min holding time, ACC-0.59 in 5 mM NaCl did not reach the maximum ion uptake capacity. The ion diffusion resistivity for smaller pores is higher than that in larger pores; because of the stronger ion diffusion ability in larger pores, ACC-0.96 shows higher desalination abilities in 5 mM NaCl.⁴³ Compared with ACC-0.59, the desalination capacity of ACC-0.96 is reasonably constant for different salt concentrations, with a maximum value for the 20 mM electrolyte.

The energy consumption of the desalination process per removed ion at different ionic strengths is given in [Figure 2D](#). At the high molarity of 600 mM, ACC-0.96 shows higher energy consumption than ACC-0.59 because of the weakened perm-selectivity that causes ions with opposite charges to be exchanged in the pores. At 5 mM concentration, the energy consumption of ACC-0.96 is lower than ACC-0.59 because of less significant or no desolvation of the ions upon entering the pore of the former.

The desalination Ragone plot (also known as the Kim-Yoon plot) is shown in [Figure 2E](#). Among all studied concentrations, ACC-0.59 in 600 mM offers the highest desalination capacity and desalination rates. As the salt concentration decreases, the performance of ACC-0.59 goes down. ACC-0.96 has the lowest desalination capacity and rate in the 600 mM electrolyte. In the 5 and 20 mM electrolytes, the desalination rate in the 20 mM NaCl electrolyte is slightly higher. For an electrochemical desalination process, the charging/discharging time should be neither so short that the material is not fully charged/discharged nor so long that the desalination process is inefficient. [Figure 2E](#) indicates suitable holding times during a desalination experiment. For example, for ACC-0.59, it is sufficient to have 10 min holding time for desalination at a molarity of 600 mM. However, at a lower concentration, this holding time can be shorter as the feedwater concentration decreases.

Cell voltage strongly influences performance stability in CDI. As shown in [Figures 2F](#) and [2G](#), electrochemical desalination with ACC-0.59 electrodes was conducted at cell voltages of 1.0, 1.2, and 1.4 V. Although increasing cell voltage usually enhances desalination capacity, it may yield accelerated electrode aging and performance degradation.³ Performance degradation during cycling at cell voltages above the water stability window (1.23 V) leads to oxygen/hydrogen evolution, causing surface oxidation and the loss of microporosity.⁴⁷ As shown in [Figures 2F](#) and [2G](#), at 1.0 V polarization, the desalination capacity is 12 mg/g with a charge efficiency of 94%. The desalination performance remains stable, even after 200 cycles (12 mg/g, 91% at the 200th cycle). While increasing potential difference bias to 1.2 V, the initial desalination capacity of ACC-0.59 increased to 13.3 mg/g. Because of water splitting and surface oxidation under such cell voltage, the charge efficiency decreased to about 80% during the first 10 cycles. With further cycling, desalination capacity and charge efficiency decreased to 8 mg/g and 48%, respectively. At a cell voltage of 1.4 V, the initial desalination capacity reached 18.6 mg/g at a charge efficiency of about 80%, because of the stronger electric force. Increased water splitting and surface oxidation reactions reduce desalination performance to 3.1 mg/g and 13% after 200 cycles.

Molecular dynamics simulation of in-pore ion processes

To mechanistically understand capacitive deionization performance as a function of pore size, we performed MD simulations with a 600 mM NaCl aqueous electrolyte

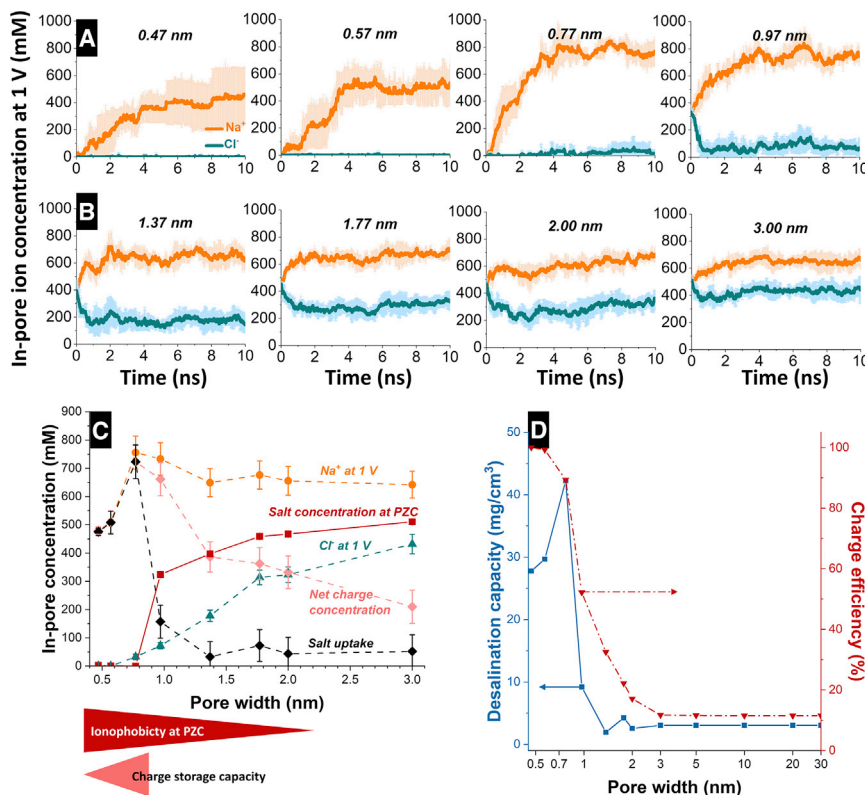


Figure 3. Molecular dynamics simulations of the dynamic change of in-pore ion species under 1 V cell voltage

(A) Numbers of Na⁺ and Cl⁻ in pores of sub-nanometer sizes. Error bars were obtained from four simulations.

(B) Numbers of Na⁺ and Cl⁻ in pores from 1 to 3 nm. Error bars were obtained from four simulations.

(C) Calculated in-pore Na⁺ uptake and Cl⁻ release concentration, salt concentration at the potential of zero charge, net charge concentration, and salt uptake concentration. Values with error bars were obtained from the data of the last 2 ns from (A) and (B).

(D) Calculated desalination capacities and charge efficiencies in pores of different sizes. Time-dependent ion concentration evolution with error bars were obtained from four simulations.

under an electrode potential difference of 1 V. The MD simulation uses the constant potential method,³⁵ as also outlined in more detail in the [Experimental procedures](#).

Time-dependent ion concentration development in negatively charged pores with different sizes are shown in [Figures 3A](#) and [3B](#) (1 V cell voltage in 600 mM NaCl). At t = 0 ns, the Na⁺ and Cl⁻ ion number in pores below 0.77 nm is almost zero. Hence, except for water molecules, pores smaller than the hydrated ion size remain empty in the uncharged state. During negative polarization, the concentration of Na⁺ ions is increased over time, and Cl⁻ exclusion is impossible. Among all sub-nanometer pores, pores with size about 0.77 nm adsorb most additional counterions. As pore size increases to 0.97 nm, a significant number of Na⁺ and Cl⁻ ions are already present at the PZC; during negative polarization, some Cl⁻ exclusion can be observed. As pore size increases from 1.37 to 3.0 nm, the number of ion pairs in the uncharged state increases. During negative polarization, the fraction of Cl⁻ exclusion increases relative to Na⁺ adsorption.

[Figure 3C](#) shows the ion/salt concentration inside the pores at the end of the charging process in [Figures 3A](#) and [3B](#). The Na⁺ uptake and Cl⁻ release

concentrations are the concentration changes between the charged and uncharged states. Salt uptake is calculated by subtracting the Cl^- ion release from Na^+ uptake. The in-pore Na^+ concentration minus the in-pore Cl^- concentration in the charged state corresponds to the net charge concentration (density). Below 0.77 nm, net charge concentration, Na^+ concentration, and salt uptake increase as pore size becomes larger. This aligns with the decreased energy demand for ion desolvation for larger pores. When pore size is larger than 0.77 nm, both cations and anions can enter the pore already at the PZC, and co-ion rejection becomes a limiting factor for salt uptake. As pore size increases further from 0.97 to 1.37 nm, Cl^- ion release during negative polarization becomes more pronounced because of increasing salt concentration at the PZC. Because of the limited capacitance (and hence ionic charge) of a given slit pore, increased Cl^- ion release leads to a decrease in Na^+ uptake. Consequently, total salt uptake decreases dramatically as pore size increases from 0.97 to 3 nm.

From an energy storage point of view, an increased net charge density is observed when pore size decreases from 3 to 0.77 nm, and it decreases when pore size decreases from 0.77 to 0.47 nm. In 2006, Chmiola et al.⁴⁸ described an anomalous capacitance increase at pore size less than 1 nm, which is associated with the distortion or (partial) loss of the solvation shell. The screening of the Coulomb repulsion of in-pore ions by the conductive pore walls allows an increased ion number to populate pores smaller than 1 nm.^{49–51} The enhancement of the CDI capacity in the smallest pores found in this work goes beyond this anomalous capacitance effect and is related to the ionophobicity at the PZC. The counter-ion concentration slightly increases when pore size is decreased from 3 nm to about 0.77 nm. It decreases dramatically when pore size goes down further from 0.77 to 0.47 nm when ion desolvation is required during the charging process. On the other hand, a continuous decrease of in-pore co-ion concentration is observed when pore size is decreased. The capacitance increase (counter-ion concentration minus co-ion concentration) from 3 nm to about 0.77 nm is caused primarily by the changing number of in-pore co-ions rather than counter-ions.

Figure 3D shows the simulated charge efficiency and calculated desalination capacity of pores at different sizes. Smaller sub-nanometer pores have a much higher charge efficiency (close to 100%) due to the more pronounced ionophobicity, which increases as pore size decreases.⁵² However, desalination capacity becomes lower at pore sizes below 0.77 nm, which is due to the higher desolvation energy for solvated ions to enter the smaller pores.⁴⁸ Desalination capacity reaches a maximum of 42 mg/cm³ at 0.77 nm before it decreases significantly to 1.8 mg/cm³ for larger pores. Above 3 nm, the in-pore salt concentration in the charged state and at the PZC remains constant. This implies that desalination capacity and charge efficiency approach constant values at a very low, non-zero level. Figure S3A compares the experimental desalination capacity data from our previous work⁵³ and the charge efficiency data from this work. The calculated desalination performance at different pore sizes for the porosity of ACC-0.59 is plotted in Figure S3B. Although the works show a similar trend, the finding of a pore size effect on desalination performance requires more reliable quantification, especially in seawater molar strength in which ionophobicity plays a vital role.

To better understand the effect of pore size on desalination at a molecular level, we modeled the double-layer structures and calculated the potential distributions in pores of different sizes under 1 V polarization (Figure 4). When pore size is smaller than 3 nm, the extension of the opposed electric double layers (EDLs) at the pore

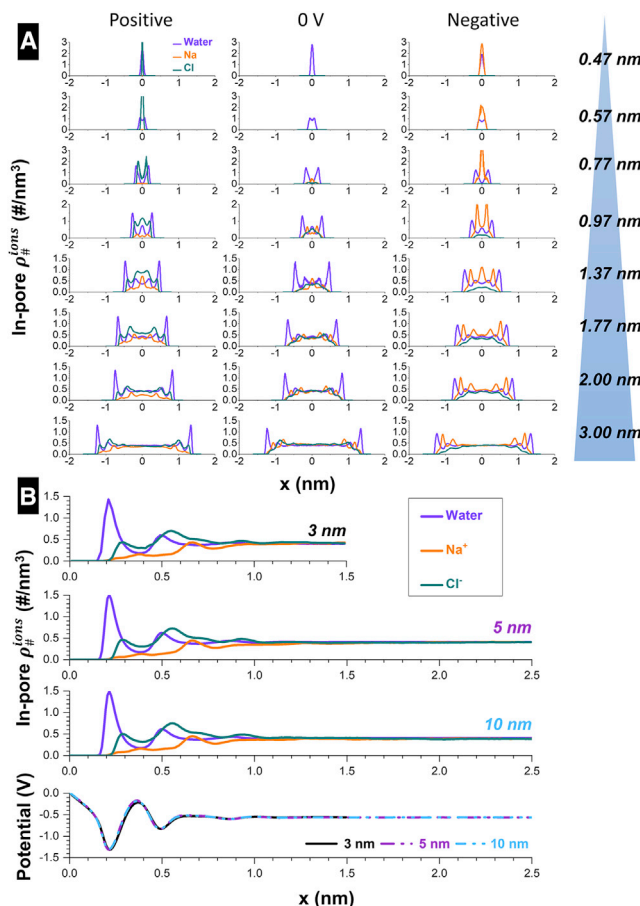


Figure 4. Simulated ion and water distributions in pores under positive polarization, point of zero charge, and negative polarizations

(A) Ion distributions in pores between 0.47 and 3 nm.
 (B) Ion and water density distributions and potential distributions in pores between 3 and 10 nm, under positive polarization. X = 0 corresponds to the wall of the pores. For negative and positive polarization, the potential bias between both electrodes is 1 V. The number density of water is scaled by 1/80.

walls will overlap. This explains the stronger dependency of ion distributions in sub-nanometer pores (Figure 4A). In pores larger than 3 nm (Figure 4B), the EDL structure is well established and stabilized with little overlapping, and in the pore center, the ion concentration is nearly the same as the bulk ion concentration. Accordingly, the ion and potential distributions across EDLs are no longer dependent on the pore size.

The radial distribution functions (RDFs) and cumulative distribution functions (CDFs) between in-pore ions and their surrounding water molecules (Figure S4) indicate that the coordination number of water molecules of ions at 600 mM molar strength changes with pore size. The coordination number of in-pore Na⁺ ions at negative polarization is smaller in ionophobic pores (<0.77 nm; see also Figure S5). This indicates that ion desolvation occurs mainly in ionophobic pores. Upon charging, the negative polarization causes the counter-ions to overcome the desolvation energy penalty so that Na⁺ ions can enter the pore. Hence, the interplay between sub-nanometer pore smaller than the hydrated ion size and the high solvation energies of alkali metal ions in aqueous solution could explain ionophobicity and the high

desalination performance of ACC-0.59. Carbons below the hydrated ion size ([Figure 3D](#)) are ideal for high CDI performance: they are small enough to be ionophobic at the PZC but large enough to accommodate a large number of counter-ions (next to water molecules) upon charge.

On the basis of these findings and MD simulation results in [Figure 3D](#), it is possible to calculate the capacitive seawater desalination performance of porous carbon electrodes ([Data S1](#)). With pore size distribution as input, and desalination performance as output, on the basis of [Figure 3D](#), the pore volume-weighted desalination capacity and pores' charge efficiency at each pore size/volume are calculated by applying the interpolation relation between each simulated point. The total desalination performance of porous carbon electrodes can be predicted by adding up the desalination performance contributions of pores of different sizes. The predicted desalination capacity and charge efficiency value of ACC-0.59 are 10 mg/g and 87%, about 83% of the experimental calculated data (12 mg/g and 94%). The deviation is within the error of the MD simulation (26% at a pore size of 0.57 nm). Snapshots of MD models with different pore sizes are shown in [Figure S6](#).

DISCUSSION

In this combined experimental and modeling work, carbon materials with sub-nanometer average pore sizes are investigated for their desalination application in both low and highly saline media. The pore size dependency of charge efficiency and desalination capacity allows calculation of desalination performance for carbons of specific pore size distributions. ACC-0.59, with an average pore size of about 0.6 nm, shows excellent desalination performance even at seawater-level molar strength. MD simulations explain this unexpectedly high performance to stem from the ionophobia of pores smaller than 0.77 nm. As there are no ions present in the pores at the PZC, the counter-ion uptake upon charge and the desalination performance is large. Only upon charging, counter-ions strip off parts of their hydration shell and enter the sub-nanometer pores.

The desalination capacity of sub-nanometer pores shows a maximum at a pore size of 0.77 nm (42 mg/cm³). Hence, the ideal CDI pore size corresponds to pores small enough to be ionophobic at the PZC yet large enough to take up a large number of counter-ions upon charging. The charge efficiency is shown to be nearly 100% for pores smaller than 0.57 nm, before it decreases significantly as pore size increases from 0.77 to 3 nm. The ability of sub-nanometer carbon pores to accomplish efficient desalination at the seawater concentration level dramatically enhances the practical application portfolio of CDI to overcome a niche application existence.

EXPERIMENTAL PROCEDURES

Resource availability

Lead contact

Further information and requests for resources and materials should be directed to, and will be fulfilled by, the lead contact, Volker Presser (volker.presser@leibniz-inm.de).

Materials availability

This study did not generate new unique materials.

Data and code availability

The datasets generated in this study are available from the lead contact on request.

Materials and reagents

NaCl ($\geq 99\%$) was obtained from Sigma-Aldrich. ACC-0.59 and ACC-0.96 activated carbon cloths were obtained from Kynol. AC-1.39 was obtained from Kuraray. TiC powder was purchased from Sigma-Aldrich.

Carbon materials and characterizations

We used commercially available novolac-derived activated carbon cloth (Kynol ACC 5092-10 and Kynol ACC 507-20) with thicknesses of 600 and 250 μm as electrodes. The carbon cloth was used without adding any binder or conductive additives.

TiC-CDC was synthesized by annealing TiC powder at 400°C in dry chlorine gas for 3 h; then the sample was treated in hydrogen gas at 600°C for 2 h to remove residual chlorine species.³ This sample is labeled CDC-0.57. Commercially available activated carbon YP-80F was used as received and is referred to as AC-1.39 in this paper.⁴⁸

The AC-1.39 and CDC-0.57 electrodes were prepared by mixing the carbon particles with 10 mass% polytetrafluoroethylene (PTFE; Sigma-Aldrich) in ethanol. The obtained homogeneous carbon paste was rolled in an electric hot rolling press (MTI HR01; MTI Corporation) to have electrodes with homogeneous thickness (600 μm for AC-1.39 and 200 μm for CDC-0.57). Afterward, the electrodes were annealed at 120°C for 24 h in a vacuum furnace.

We conducted scanning electron microscopy for ACC-0.59 and ACC-0.96 using a Zeiss Gemini SEM 500 at 1 kV. The samples AC-1.39 and CDC-0.57 were characterized using a JEOL JSM 7500F field emission scanning electron microscope at 3 kV.

Data for the pore structure were adapted from our previous work.^{47,54} In the previous work, argon gas sorption analysis was conducted using an Autosorb iQ system at a temperature of -186°C . The electrode sample was first degassed at 100 Pa and $+200^\circ\text{C}$ for 1 h and then heated to $+300^\circ\text{C}$ for 20 h to remove residual surface functional groups. The pore size distribution is obtained by applying quenched solid density functional theory using a slit-shaped pore kernel.³⁶

The CHNS-O measurement was conducted to obtain element-specific chemical information of the carbon's functional groups. The amounts of H, C, and N were quantified using a Vario MICRO Cube (Elementar Analysensysteme) and heating up to $+1,150^\circ\text{C}$ at the combustion tube and $+850^\circ\text{C}$ at the reduction tube. The O content was quantified with an OXY cube elemental analyzer (Elementar Analysensysteme) at a pyrolysis temperature of $+1450^\circ\text{C}$.

Desalination experiments

A symmetric full-cell configuration in batch mode was applied to test the desalination performance of the activated carbon material. In alignment with previous work,⁴³ the carbon cloth was cut into a pair of round disks 30 mm in diameter. A fixed 3 mm distance is set by the thickness of the middle channel with six glass fiber separators (Millipore) and four pieces of polyethylene terephthalate mesh placed between the two electrodes. The feedwater is pumped at a flow rate of 2.5 mL/min to flow between the electrodes. The feedwater is cycled back to a 10 L reservoir to minimize the concentration fluctuation between charging and discharging processes.

At the CDI cell outlet, the water's ion concentration and pH change were recorded using pH and conductivity sensors (Metrohm 856 conductivity, Metrohm 867 pH Module). A Bio-Logic VSP-300 system was used to determine the electrochemical performance of the CDI cell. Galvanostatic charging and discharging were performed at a specific current of 0.1 A/g between 0 and +1, +1.2, and +1.4 V cell voltages with a holding time of 20 min.

Desalination capacity was determined using [Equation 1](#):

$$DC = \left(v \frac{M_{salt}}{M_{tot}} \right) \int (c_t - c_0) dt , \quad (\text{Equation 1})$$

where M_{salt} is the molar mass of the salt, M_{tot} is the total mass of the two electrodes, v is the flow rate, and c_0 and c_t are the initial outlet salt concentration and concentrate of the feedwater at time t , respectively.

Charge efficiency was calculated according to [Equation 2](#):

$$CE(\%) = \frac{F \times DC_{mol}}{M_{salt} \times Q} \times 100\% , \quad (\text{Equation 2})$$

where F is the Faraday constant (26,801 mAh/mol), DC_{mol} is the desalination capacity from [Equation 1](#), and Q is the average of total charge (normalized to the total electrode mass, mAh/g) stored/released during the desalination/recovering process.

The energy consumption of the CDI process in units of kT/ion (where $T = 298 \text{ K}$ and k_B is the Boltzmann constant) is calculated by dividing the capacitive energy stored by the removed number of ions ([Equation 3](#)).

$$\text{Energy consumption} \left(\frac{kT}{\text{ion}} \right) = \frac{3600}{k_B T} \frac{1}{N_A} \frac{Q_{charge} * U}{n_{removed}} , \quad (\text{Equation 3})$$

where U is the cell voltage (V), Q_{charge} is the charge (Ah) stored during the desalination process, $n_{removed}$ is the amount of salt removed (mol), and N_A is the Avogadro constant.

Molecular dynamics simulations

The molecular dynamics simulation system consists of two slit-shaped pore electrodes immersed in 600 mM NaCl aqueous solution. Three layers of graphene sheets were used to model the walls of the electrode pore, and pore sizes were varied from 0.47 to 10 nm to cover a broad range of pore sizes in practical nanoporous carbon electrodes. The pore length was set to 6.33 nm to ensure that the edge effect of the electrode was not significant.³⁶ Force fields for electrodes and aqueous NaCl electrolytes are from Cornell et al.⁵⁵ and Smith and Dang,⁵⁶ and the SPC/E model⁵⁷ was chosen for the water molecules. The modified MD simulation software on the basis of GROMACS-4.6.7⁵⁸ was used for our simulation. To simulate the capacitive deionization process, a constant potential difference was applied between the two electrodes.⁵⁸ The MD simulation was performed in an isothermal and equal-volume ensemble (NVT) using the V-Resale temperature control method with a time step of 2 fs. The long-range electrostatic interactions are calculated using particle-mesh Ewald (PME) algorithm. The Fourier mesh spacing in reciprocal space is 0.1 nm, and the interpolation method is B-spline interpolation of order four. A cut-off of 1.2 nm was used to calculate the short-range electrostatic interactions and van der Waals interactions. The system was first simulated at 800 K for 2 ns, then cooled to 298 K after a linear annealing process of 5 ns, and then run at 298 K for 20 ns to achieve initial equilibrium. Next, a constant potential difference between the two electrodes was applied to simulate the

desalination process. Each group was simulated four times with different initial configurations to obtain reliable results from the simulation.

SUPPLEMENTAL INFORMATION

Supplemental information can be found online at <https://doi.org/10.1016/j.xcpr.2021.100689>.

ACKNOWLEDGMENTS

We thank Eduard Arzt (INM) for his continuing support. We thank Andrea Jung and Tamara Winter (INM) for support with CHNS-O measurements and SEM characterizations. Y.Z. and V.P. acknowledge support for the MERLIN project from RAG-Stiftung; RAG-Stiftung generates long-term momentum for the transformation of the regions along the Ruhr and Saar rivers and in Ibbenbüren. H.J. and G.F. acknowledge support from the National Natural Science Foundation of China (51836003) and the Program for HUST Academic Frontier Youth Team and also thank Beijing PARATERA Tech Co., Ltd., for providing high-performance computing (HPC) resources to accomplish simulations in this work. This project has received funding from the European Union's Horizon 2020 research and innovation programme under the Marie Skłodowska-Curie grant agreement No. 894042.

AUTHOR CONTRIBUTIONS

Conceptualization, Writing – Original Draft, Investigation, Visualization, and Data Curation, Y.Z.; Writing – Review & Editing, Visualization, Data Curation, and Validation, C.P.; Software, Methodology, Writing – Review & Editing, Visualization, and Data Curation, H.J.; Data Curation, Y.L.; Software, Methodology, Conceptualization, Supervision, Writing – Review & Editing, Project Administration, and Funding Acquisition, G.F.; Conceptualization, Supervision, Writing – Review & Editing, Project Administration, and Funding Acquisition, V.P.

DECLARATION OF INTERESTS

The authors declare no competing interests.

Received: August 25, 2021

Revised: November 3, 2021

Accepted: November 22, 2021

Published: December 13, 2021

REFERENCES

- Shannon, M.A., Bohn, P.W., Elimelech, M., Georgiadis, J.G., Mariñas, B.J., and Mayes, A.M. (2008). Science and technology for water purification in the coming decades. *Nature* 452, 301–310.
- Humplík, T., Lee, J., O’Hern, S.C., Fellman, B.A., Baig, M.A., Hassan, S.F., Atieh, M.A., Rahman, F., Laoui, T., Karnik, R., and Wang, E.N. (2011). Nanostructured materials for water desalination. *Nanotechnology* 22, 292001.
- Porada, S., Borchardt, L., Oschatz, M., Bryjak, M., Atchison, J.S., Keesman, K.J., Kaskel, S., Biesheuvel, P.M., and Presser, V. (2013). Direct prediction of the desalination performance of porous carbon electrodes for capacitive deionization. *Energy Environ. Sci.* 6, 3700–3712.
- Miller, J.E. (2003). Review of water resources and desalination technologies (Albuquerque, NM: Sandia National Laboratories). <https://www.osti.gov/servlets/purl/809106/>.
- Janowska, K., Boffa, V., Jørgensen, M.K., Quist-Jensen, C.A., Hubac, F., Deganello, F., Coelho, F.E.B., and Magnacca, G. (2020). Thermocatalytic membrane distillation for clean water production. *npj Clean Water* 3, 34.
- Ricceri, F., Giagnorio, M., Farinelli, G., Blandini, G., Minella, M., Vione, D., and Tirraferri, A. (2019). Desalination of produced water by membrane distillation: Effect of the feed components and of a pre-treatment by fenton oxidation. *Sci. Rep.* 9, 14964.
- Yao, Y., Zhang, P., Jiang, C., DuChanois, R.M., Zhang, X., and Elimelech, M. (2021). High performance polyester reverse osmosis desalination membrane with chlorine resistance. *Nat. Sustain.* 4, 138–146.
- Inukai, S., Cruz-Silva, R., Ortiz-Medina, J., Morelos-Gomez, A., Takeuchi, K., Hayashi, T., Tanioka, A., Araki, T., Tejima, S., Noguchi, T., et al. (2015). High-performance multi-functional reverse osmosis membranes obtained by carbon nanotube-polyamide nanocomposite. *Sci. Rep.* 5, 13562.
- Uliana, A.A., Bui, N.T., Kamcev, J., Taylor, M.K., Urban, J.J., and Long, J.R. (2021). Ion-capture electrodialysis using multifunctional adsorptive membranes. *Science* 372, 296–299.
- Zhao, R., Porada, S., Biesheuvel, P.M., and van der Wal, A. (2013). Energy consumption in membrane capacitive deionization for different

- water recoveries and flow rates, and comparison with reverse osmosis. *Desalination* 330, 35–41.
11. Pasta, M., Wessells, C.D., Cui, Y., and La Mantia, F. (2012). A desalination battery. *Nano Lett.* 12, 839–843.
 12. Biesheuvel, P.M., Porada, S., Levi, M., and Bazant, M.Z. (2014). Attractive forces in microporous carbon electrodes for capacitive deionization. *J. Solid State Electrochem.* 18, 1365–1376.
 13. Elimelech, M., and Phillip, W.A. (2011). The future of seawater desalination: energy, technology, and the environment. *Science* 333, 712–717.
 14. Anderson, M.A., Cudero, A.L., and Palma, J. (2010). Capacitive deionization as an electrochemical means of saving energy and delivering clean water. Comparison to present desalination practices: will it compete? *Electrochim. Acta* 55, 3845–3856.
 15. Porada, S., Zhao, R., van der Wal, A., Presser, V., and Biesheuvel, P.M. (2013). Review on the science and technology of water desalination by capacitive deionization. *Prog. Mater. Sci.* 58, 1388–1442.
 16. Bi, S., Zhang, Y., Cervini, L., Mo, T., Griffin, J.M., Presser, V., and Feng, G. (2020). Permselective ion electrosorption of subnanometer pores at high molar strength enables capacitive deionization of saline water. *Sustain. Energy Fuels* 4, 1285–1295.
 17. Suss, M.E., Porada, S., Sun, X., Biesheuvel, P.M., Yoon, J., and Presser, V. (2015). Water desalination via capacitive deionization: what is it and what can we expect from it? *Energy Environ. Sci.* 8, 2296–2319.
 18. Porada, S., Weinstein, L., Dash, R., van der Wal, A., Bryjak, M., Gogotsi, Y., and Biesheuvel, P.M. (2012). Water desalination using capacitive deionization with microporous carbon electrodes. *ACS Appl. Mater. Interfaces* 4, 1194–1199.
 19. Shi, W., Li, H., Cao, X., Leong, Z.Y., Zhang, J., Chen, T., Zhang, H., and Yang, H.Y. (2016). Ultrahigh performance of novel capacitive deionization electrodes based on a three-dimensional graphene architecture with nanopores. *Sci. Rep.* 6, 18966.
 20. Srimuk, P., Su, X., Yoon, J., Aurbach, D., and Presser, V. (2020). Charge-transfer materials for electrochemical water desalination, ion separation and the recovery of elements. *Nat. Rev. Mater.* 5, 517–538.
 21. Prehal, C., Weingarth, D., Perre, E., Lechner, R.T., Amenitsch, H., Paris, O., and Presser, V. (2015). Tracking the structural arrangement of ions in carbon supercapacitor nanopores using *in situ* small-angle X-ray scattering. *Energy Environ. Sci.* 8, 1725–1735.
 22. Biesheuvel, P.M., and van der Wal, A. (2010). Membrane capacitive deionization. *J. Membr. Sci.* 346, 256–262.
 23. Zhang, Y., Srimuk, P., Aslan, M., Gallei, M., and Presser, V. (2020). Polymer ion-exchange membranes for capacitive deionization of aqueous media with low and high salt concentration. *Desalination* 479, 114331.
 24. Tang, K., Kim, Y.-h., Chang, J., Mayes, R.T., Gabitto, J., Yiacoumi, S., and Tsouris, C. (2019). Seawater desalination by over-potential membrane capacitive deionization: opportunities and hurdles. *Chem. Eng. J.* 357, 103–111.
 25. Chen, F., Huang, Y., Guo, L., Sun, L., Wang, Y., and Yang, H.Y. (2017). Dual-ions electrochemical deionization: a desalination generator. *Energy Environ. Sci.* 10, 2081–2089.
 26. Smith, K.C., and Dmello, R. (2016). Na-ion desalination (NID) enabled by Na-blocking membranes and symmetric Na-intercalation: porous-electrode modeling. *J. Electrochem. Soc.* 163, A530–A539.
 27. Porada, S., Shrivastava, A., Bukowska, P., Biesheuvel, P.M., and Smith, K.C. (2017). Nickel hexacyanoferrate electrodes for continuous cation intercalation desalination of brackish water. *Electrochim. Acta* 255, 369–378.
 28. Srimuk, P., Kaasik, F., Krüner, B., Tolosa, A., Fleischmann, S., Jäckel, N., Tekeli, M.C., Aslan, M., Suss, M.E., and Presser, V. (2016). MXene as a novel intercalation-type pseudocapacitive cathode and anode for capacitive deionization. *J. Mater. Chem. A Mater. Energy Sustain.* 4, 18265–18271.
 29. Zhang, Q., Aung, S.H., Oo, T.Z., and Chen, F. (2020). Continuous electrochemical deionization by utilizing the catalytic redox effect of environmentally friendly riboflavin-5'-phosphate sodium. *Mater. Today Commun.* 23, 100921.
 30. Cai, P.F., Su, C.J., Chang, W.T., Chang, F.C., Peng, C.Y., Sun, I.W., Wei, Y.L., Jou, C.J., and Wang, H.P. (2014). Capacitive deionization of seawater effected by nano Ag and Ag@C on graphene. *Mar. Pollut. Bull.* 85, 733–737.
 31. Nam, D.-H., and Choi, K.-S. (2017). Bismuth as a new chloride-storage electrode enabling the construction of a practical high capacity desalination battery. *J. Am. Chem. Soc.* 139, 11055–11063.
 32. Arnold, S., Wang, L., Budak, Ö., Aslan, M., Srimuk, P., and Presser, V. (2021). Antimony alloying electrode for high-performance sodium removal: how to use a battery material not stable in aqueous media for saline water remediation. *J. Mater. Chem. A Mater. Energy Sustain.* 9, 585–596.
 33. Zhang, Y., Wang, L., and Presser, V. (2021). Electrocatalytic fuel cell desalination for continuous energy and freshwater generation. *Cell Reports Physical Science* 2, 100416.
 34. Atlas, I., Khalla, S.A., and Suss, M.E. (2020). Thermodynamic energy efficiency of electrochemical systems performing simultaneous water desalination and electricity generation. *J. Electrochem. Soc.* 167, 134517.
 35. Uwayid, R., Seraphim, N.M., Guyes, E.N., Eisenberg, D., and Suss, M.E. (2021). Characterizing and mitigating the degradation of oxidized cathodes during capacitive deionization cycling. *Carbon* 173, 1105–1114.
 36. Kim, C., Srimuk, P., Lee, J., Fleischmann, S., Aslan, M., and Presser, V. (2017). Influence of pore structure and cell voltage of activated carbon cloth as a versatile electrode material for capacitive deionization. *Carbon* 122, 329–335.
 37. Partheniades, E. (2009). Forces between clay particles and the process of flocculation. In *Cohesive Sediments in Open Channels*, E. Partheniades, ed. (Boston: Butterworth-Heinemann), pp. 47–88.
 38. Levy, A., de Souza, J.P., and Bazant, M.Z. (2020). Breakdown of electroneutrality in nanopores. *J. Colloid Interface Sci.* 579, 162–176.
 39. Hess, B., Kutzner, C., van der Spoel, D., and Lindahl, E. (2008). GROMACS 4: algorithms for highly efficient, load-balanced, and scalable molecular simulation. *J. Chem. Theory Comput.* 4, 435–447.
 40. Reed, S.K., Madden, P.A., and Papadopoulos, A. (2008). Electrochemical charge transfer at a metallic electrode: a simulation study. *J. Chem. Phys.* 128, 124701.
 41. Feng, X., Dementev, N., Feng, W., Vidic, R., and Borguet, E. (2006). Detection of low concentration oxygen containing functional groups on activated carbon fiber surfaces through fluorescent labeling. *Carbon* 44, 1203–1209.
 42. Prehal, C., Koczwara, C., Amenitsch, H., Presser, V., and Paris, O. (2018). Salt concentration and charging velocity determine ion charge storage mechanism in nanoporous supercapacitors. *Nat. Commun.* 9, 4145.
 43. Zhang, Y., Srimuk, P., Husmann, S., Chen, M., Feng, G., and Presser, V. (2019). Effect of pore size on the ion electrosorption and hydrogen/deuterium electrosorption using sodium chloride in H_2O and D_2O . *J. Electrochem. Soc.* 166, A4158–A4167.
 44. Jäckel, N., Weingarth, D., Schreiber, A., Krüner, B., Zeiger, M., Tolosa, A., Aslan, M., and Presser, V. (2016). Performance evaluation of conductive additives for activated carbon supercapacitors in organic electrolyte. *Electrochim. Acta* 191, 284–298.
 45. Dash, R., Chmiola, J., Yushin, G., Gogotsi, Y., Laudisio, G., Singer, J., Fischer, J., and Kucheyev, S. (2006). Titanium carbide derived nanoporous carbon for energy-related applications. *Carbon* 44, 2489–2497.
 46. Karamanova, B., Stoyanova, A., Shipochka, M., Girginov, C., and Stoyanova, R. (2019). On the cycling stability of biomass-derived carbons as electrodes in supercapacitors. *J. Alloys Compd.* 803, 882–890.
 47. Presser, V., Heon, M., and Gogotsi, Y. (2011). Carbide-derived carbons—from porous networks to nanotubes and graphene. *Adv. Funct. Mater.* 21, 810–833.
 48. Chmiola, J., Yushin, G., Gogotsi, Y., Portet, C., Simon, P., and Taberna, P.L. (2006). Anomalous increase in carbon capacitance at pore sizes less than 1 nanometer. *Science* 313, 1760–1763.
 49. Merlet, C., Péan, C., Rotenberg, B., Madden, P.A., Daffos, B., Taberna, P.L., Simon, P., and Salanne, M. (2013). Highly confined ions store charge more efficiently in supercapacitors. *Nat. Commun.* 4, 2701.
 50. Kondrat, S., and Kornyshev, A. (2011). Superionic state in double-layer capacitors with nanoporous electrodes. *J. Phys. Condens. Matter* 23, 022201.

51. Prehal, C., Koczwara, C., Jäckel, N., Schreiber, A., Burian, M., Amenitsch, H., Hartmann, M.A., Presser, V., and Paris, O. (2017). Quantification of ion confinement and desolvation in nanoporous carbon supercapacitors with modelling and *in situ* X-ray scattering. *Nat. Energy* 2, 16215.
52. Merlet, C., Rotenberg, B., Madden, P.A., Taberna, P.-L., Simon, P., Gogotsi, Y., and Salanne, M. (2012). On the molecular origin of supercapacitance in nanoporous carbon electrodes. *Nat. Mater.* 11, 306–310.
53. Porada, S., Schipper, F., Aslan, M., Antonietti, M., Presser, V., and Fellinger, T.-P. (2015). Capacitive deionization using biomass-based microporous salt-templated heteroatom-doped carbons. *ChemSusChem* 8, 1867–1874.
54. Aslan, M., Zeiger, M., Jäckel, N., Grobelsek, I., Weingarth, D., and Presser, V. (2016). Improved capacitive deionization performance of mixed hydrophobic/hydrophilic activated carbon electrodes. *J. Phys. Condens. Matter* 28, 114003.
55. Cornell, W.D., Cieplak, P., Bayly, C.I., Gould, I.R., Merz, K.M., Ferguson, D.M., Spellmeyer, D.C., Fox, T., Caldwell, J.W., and Kollman, P.A. (1995). A second generation force field for the simulation of proteins, nucleic acids, and organic molecules. *J. Am. Chem. Soc.* 117, 5179–5197.
56. Smith, D.E., and Dang, L.X. (1994). Computer simulations of NaCl association in polarizable water. *J. Chem. Phys.* 100, 3757–3766.
57. Feng, G., and Cummings, P.T. (2011). Supercapacitor capacitance exhibits oscillatory behavior as a function of nanopore size. *J. Phys. Chem. Lett.* 2, 2859–2864.
58. Berendsen, H.J.C., Grigera, J.R., and Straatsma, T.P. (1987). The missing term in effective pair potentials. *J. Phys. Chem.* 91, 6269–6271.

Supplemental information

**Ionophobicity of carbon sub-nanometer pores
enables efficient desalination at high salinity**

Yuan Zhang, Christian Prehal, Huili Jiang, Yang Liu, Guang Feng, and Volker Presser

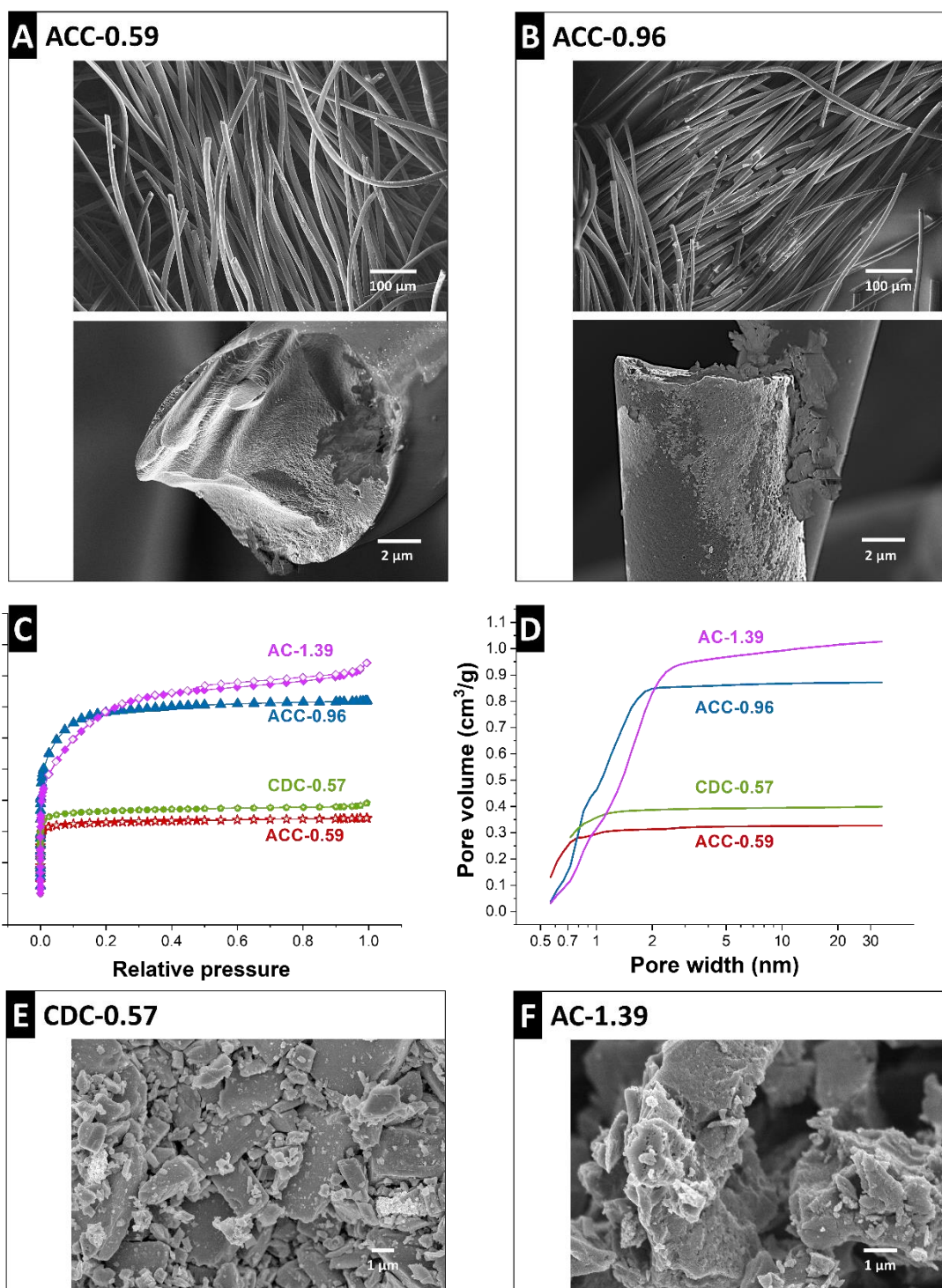


Figure S1: Material characterizations A) Scanning electron micrographs of ACC-0.59; B) Scanning electron micrographs of ACC-0.96. C) Nitrogen gas sorption isotherms, recorded at -196°C for ACC-0.59, ACC-0.96, CDC-0.57, and AC-1.39. STP = standard temperature and pressure. D) Cumulative pore size distribution obtained from QSDFT analysis of the gas sorption isotherm data. E) Scanning electron micrographs of CDC-0.57; F) Scanning electron micrographs of AC-1.39.

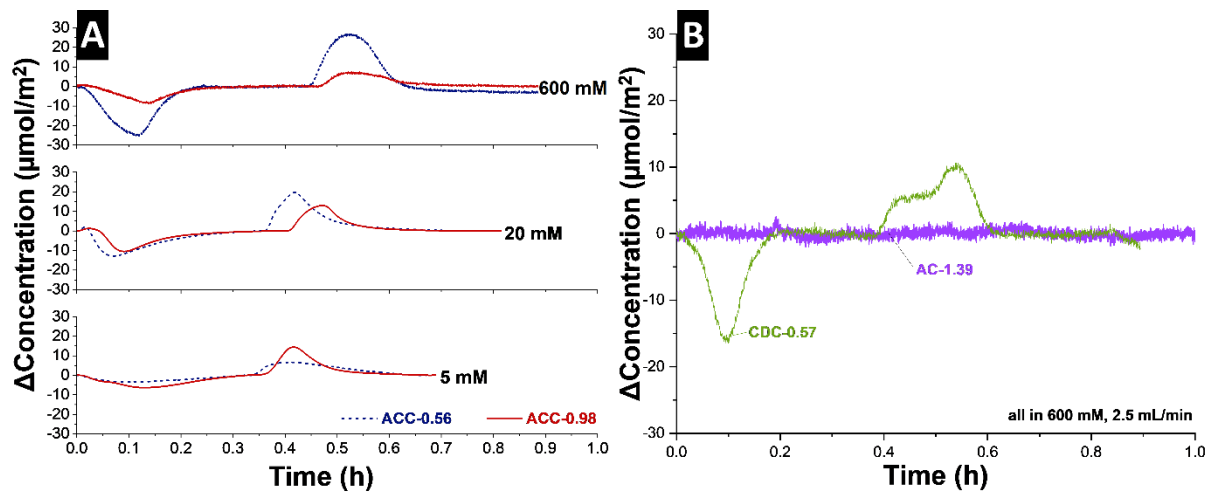


Figure S2: Concentration variations A) ACC-0.59 and ACC-0.96 electrodes in 5 mM, 50 mM, and 600 mM aqueous NaCl solution. B) Comparison with the concentration variation of commercially available activated carbon AC-1.39 and carbide-derived carbon CDC-0.57 in 600 mM NaCl solution. Considering the different surface areas of each carbon, the concentration variation is normalized to the specific surface area (**Table 2**).

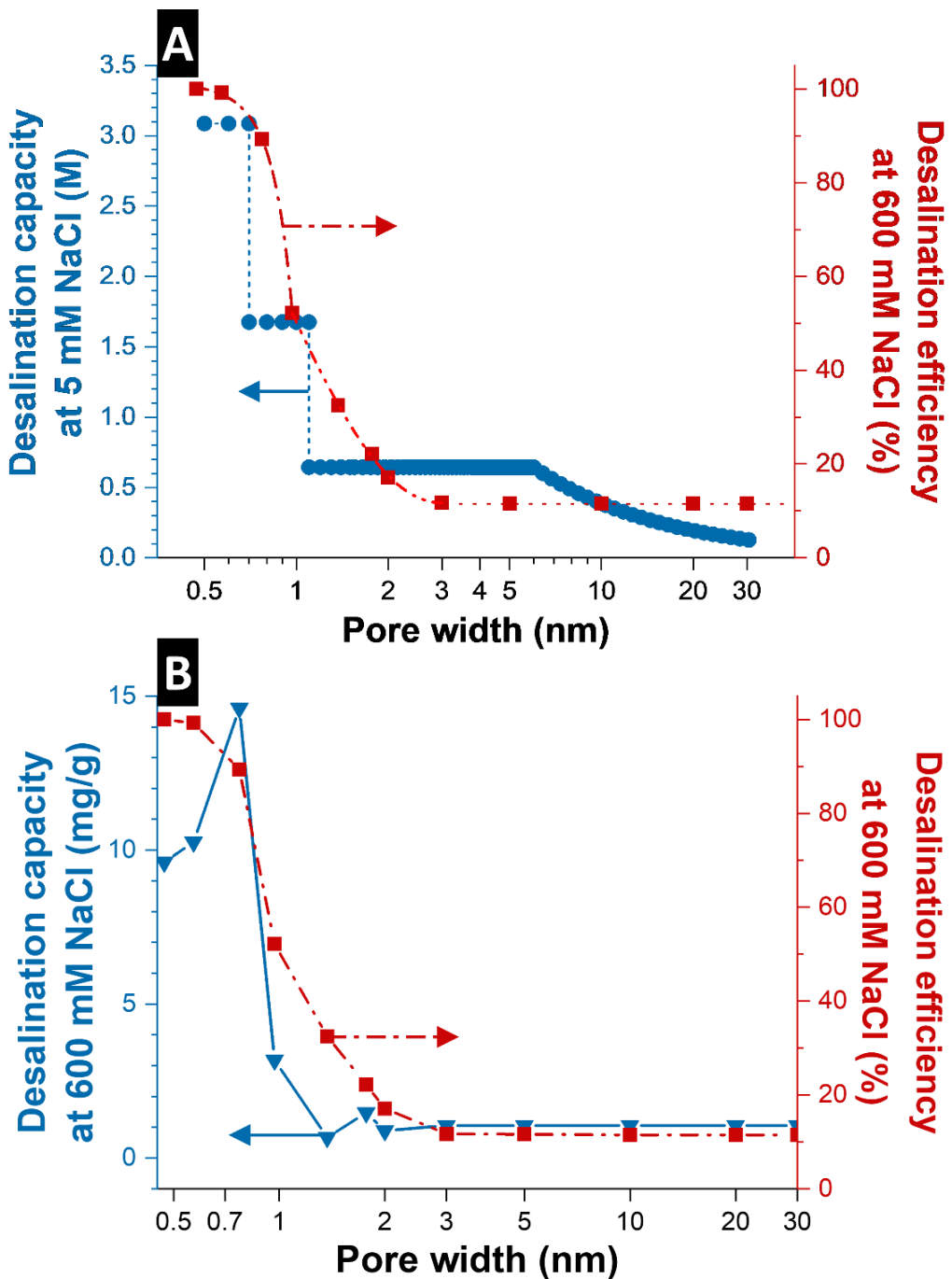


Figure S3: Pore size dependency of desalination capacity and charge efficiency A) Comparison of the simulated charge efficiency at 600 mM NaCl from this work and the pore size differentiated experimental desalination capacity from Porada et al. (Ref. [1]). B) Comparison of the simulated desalination capacity and charge efficiency at 600 mM NaCl from this work.

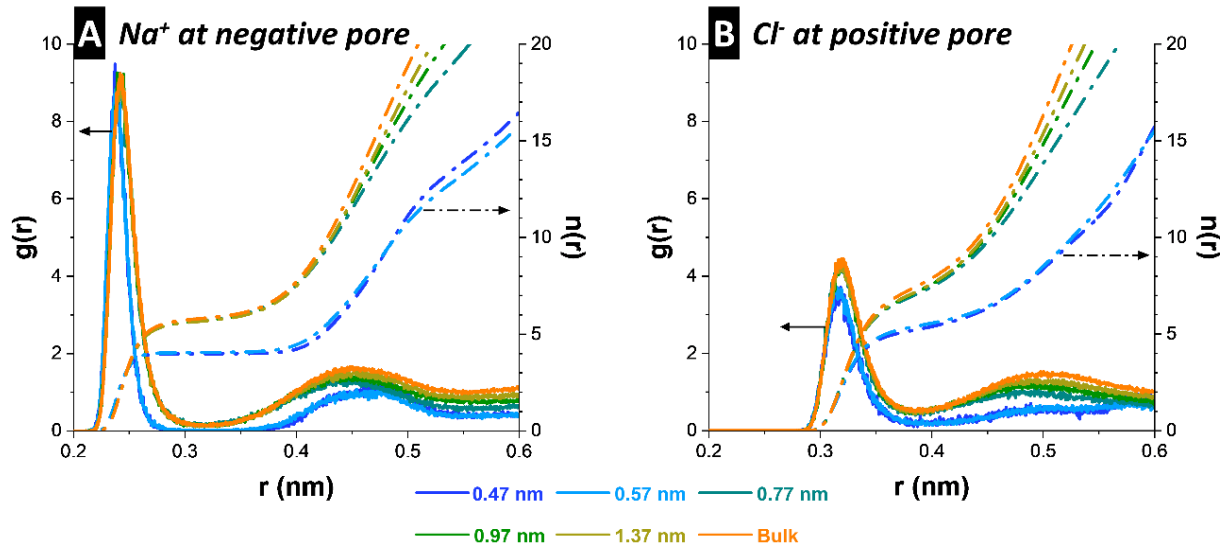


Figure S4: Structure of the ion hydration shell in polarized micropores at 1 V cell voltage A) Hydrated Na^+ ions. Radial distribution function, $g(r)$ (solid lines, left Y-axis), and cumulative distribution function, $n(r)$ ($n(r) = 4\pi\rho \int g(r)r^2 dr$) in negatively and positively polarized pores, respectively.; B) Hydrated Cl^- ions.

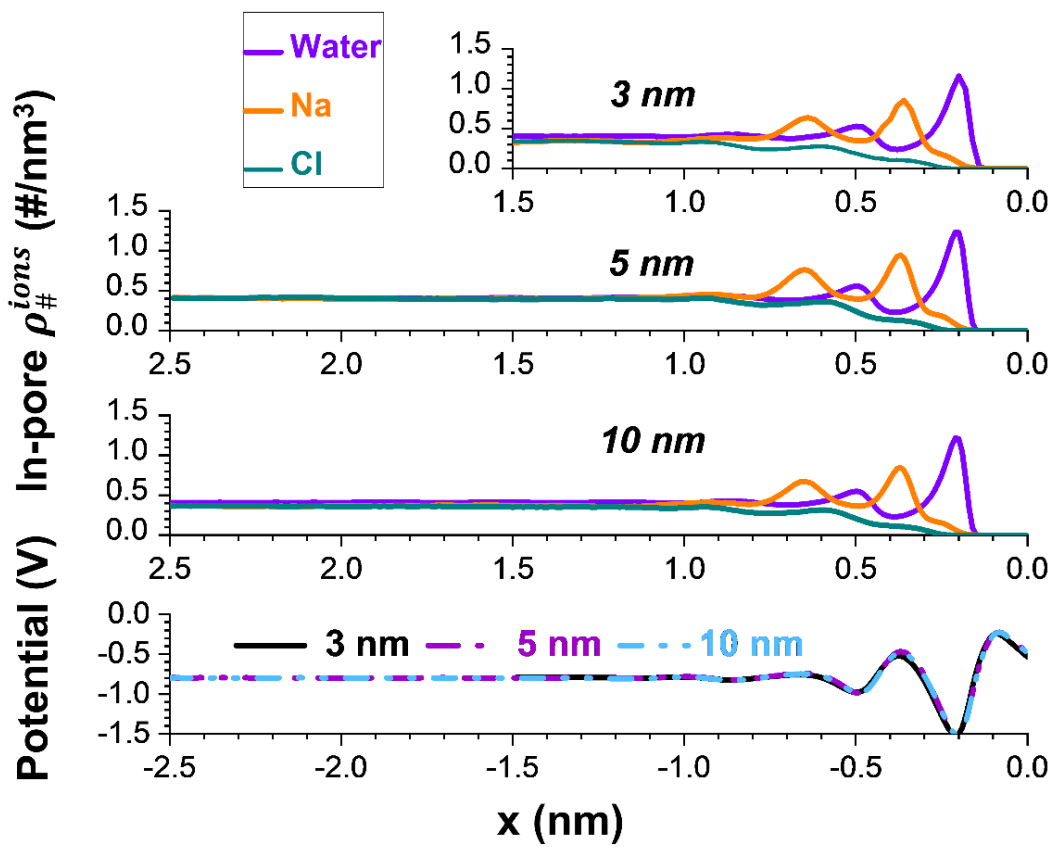


Figure S5: Simulated ion and water distributions and potential distributions in pores under positive polarizations between 3 nm to 10 nm. The value of $x=0$ corresponds to the wall of the electrode.

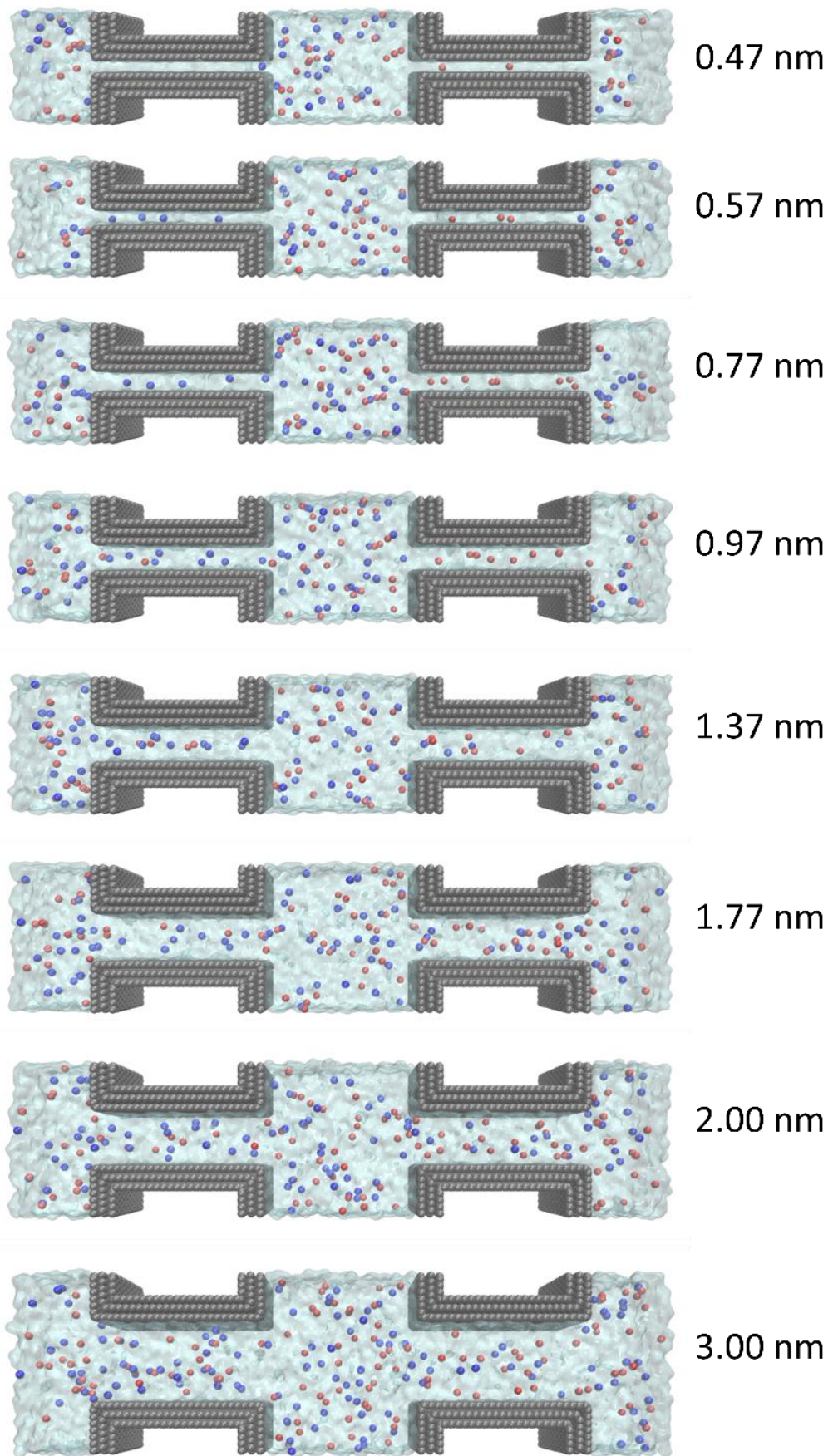


Figure S6: MD simulation snapshots of pores with different pore sizes at the charged state

Supplemental Information

[1] S. Porada, L. Borchardt, M. Oschatz, M. Bryjak, J.S. Atchison, K.J. Keesman, S. Kaskel, P.M. Biesheuvel, V. Presser, Direct prediction of the desalination performance of porous carbon electrodes for capacitive deionization, *Energy & Environmental Science*, 6 (2013) 3700-3712.

4.4 Hydration shell energy barrier differences of sub-nanometer carbon pores enable ion sieving and selective ion removal

Yuan Zhang,^{1,2} Jiaxing Peng,^{3,4} Guang Feng,^{3,4} and Volker Presser^{1,2,5}

1 INM - Leibniz Institute for New Materials, Campus D2 2, 66123 Saarbrücken, Germany

2 Saarland University, Campus D2 2, 66123 Saarbrücken, Germany

3 State Key Laboratory of Coal Combustion, School of Energy and Power Engineering, Huazhong University of Science and Technology (HUST), Wuhan 430074, China

4 Nano Interface Centre for Energy, School of Energy and Power Engineering, HUST, 430074, China

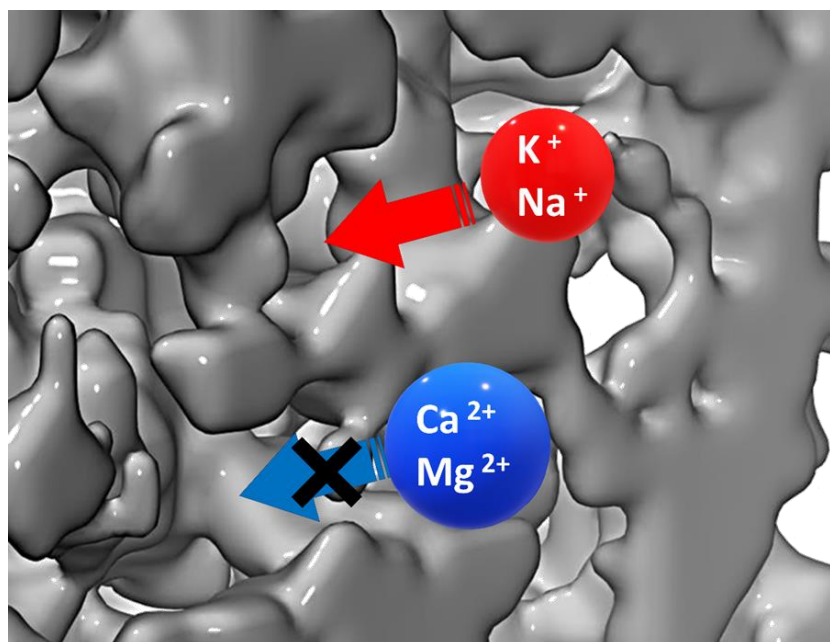
5 Saarene - Saarland Center for Energy Materials and Sustainability, Campus C4 2, 66123 Saarbrücken, Germany

Citation:

Y. Zhang, J. Peng, G. Feng, V. Presser, *Hydration shell energy barrier differences of sub-nanometer carbon pores enable ion sieving and selective ion removal*, Chemical Engineering Journal, 2021, 419: 129438. (DOI: 10.1016/j.cej.2021.129438)

Own contribution:

Methodology, validation, formal analysis, investigation, data curation, writing-original draft, writing-review & editing, visualization.





Hydration shell energy barrier differences of sub-nanometer carbon pores enable ion sieving and selective ion removal

Yuan Zhang ^{a,b}, Jiaxing Peng ^{c,d}, Guang Feng ^{c,d}, Volker Presser ^{a,b,*}

^a INM - Leibniz Institute for New Materials, Campus D2 2, 66123 Saarbrücken, Germany

^b Saarland University, Campus D2 2, 66123 Saarbrücken, Germany

^c State Key Laboratory of Coal Combustion, School of Energy and Power Engineering, Huazhong University of Science and Technology (HUST), Wuhan 430074, PR China

^d Nano Interface Centre for Energy, School of Energy and Power Engineering, HUST, 430074, PR China



ARTICLE INFO

Keywords:

Ultramicropores
Microporous carbon
Capacitive deionization
Ion selectivity
Sieving effect
Hydration energy

ABSTRACT

Subnanometer pores of carbon discriminate against ions based on their size. Capitalizing on such nuanced differences enables ion separation via charge/discharge cycling during ion electrosorption. Different ion uptake capacities in aqueous media with multiple, competing ions are also of high importance to understand capacitive deionization of surface water or industrial process water. In our experiments, we observed divalent cations sieving in pores smaller than 0.6 nm. By applying this phenomenon, a desalination cell with online concentration monitoring was used to study the ion-selectivity. We concluded that in pores below 0.6 nm, divalent Mg^{2+} and Ca^{2+} are entirely blocked, and the K^+ over Na^+ selectivity corresponds with their size ratio. Larger micropores show a preference for divalent cations with higher charge numbers. In both materials, a dynamic monovalent cation and divalent cation replacement dependent on the potential variation is observed.

1. Introduction

The increasing demand for freshwater and energy-efficient water remediation technologies has intensified research on distillation, reverse osmosis, electrodialysis, and capacitive deionization (CDI) [1]. CDI is very attractive for ion removal due to its simple operation, low cost (facile electrode regeneration), and fast response ion electrosorption process [2-4]. While ion electrosorption itself applies to all sorts of electrically charged species, special consideration needs to be applied for aqueous systems that contain multiple anions or cations. On the one hand, there are time-dependent effects. For example, Zhao et al. [5] demonstrated the initial preference for removing sodium from saline media via online monitoring of the effluent stream; however, throughout the charging/ion removal process, all initially removed sodium is replaced by, for example, calcium within carbon nanopores. As shown by Dykstra et al., there is also a kinetic difference in the removal (and release) rate when comparing Na^+ and K^+ ion electrosorption [6]. On the other hand, the equilibrium preference of anions and cations compared to other ions also depends on the ratio between pore size and ion size [7]. This aspect aligns with the pore size dependency of the charge storage capacity known for aqueous (and non-aqueous) systems

but is more complex per the presence of competing ions [8-10].

A convenient way to selectively remove small ions is via sieving, that is, applying a pore size large enough for the target ions to pass through but too small for other ions [11]. For example, this ion sieving was described by Segalini et al. [12] for carbide-derived carbons with a narrow distribution of the pores (average pore size of 0.68 nm) [13]. Hawks et al. recently applied carbon with subnanometer pore size to achieve nitrate removal from an anion mixture and obtained a high selectivity of nitrate over sulfate and chloride [14]. While ion sieving is useful for blocking the pathway of larger ions, such as Ca^{2+} , Mg^{2+} , or SO_4^{2-} , it is less useful for small ions separation, such as Li^+ , Na^+ , or K^+ [7]. Hou et al. demonstrated that ion charge and ion size determine the pore accessibility in mixed-ion electrolytes [15]. Therefore, divalent cations preferentially screen the surface charge due to their high valence, and small monovalent cations approach closer to the charged surface [15]. Zhan et al. combined density functional theory to investigate the adsorption processes of alkali metal ions in carbon nanopores, and found that cations with larger ionic radius are more favorable to enter the nanopores due to a lower energy barrier of ion desolvation [16].

Chemical modification of carbon also allows for achieving ion

* Corresponding author at: INM - Leibniz Institute for New Materials, Campus D2 2, 66123 Saarbrücken, Germany.

E-mail address: volker.presser@leibniz-inm.de (V. Presser).

selectivity. For example, applying oxidized carbon cloth enhances the selectivity of K^+ over Li^+ from ~1.0 to 1.8 [17]. Other approaches combine oxidized and aminated carbon for selectivity towards divalent cations [18], functionalizing carbon with quaternary amines to selectively and passively trap nitrate ions [19], or apply ethylenediamine triacetic acid to functionalize graphene to remove Pb^{2+} ions selectively [20].

The use of ion-exchange membranes also allows for ion selectivity [21–24]. For example, Luo et al. studied ion selectivity of three types of cation exchange membranes for both mono/monovalent and bi-/monovalent cations and shows the cation selectivity of ion exchange membranes is related to membrane conductivity and swelling degree. Zuo et al. applied a coating based on quaternary amine functionalized polyvinyl alcohol applied onto a carbon electrode and exhibited strong selectivity of SO_4^{2-} over Cl^- at $Cl^-:SO_4^{2-}$ concentration ratios up to 20:1 [25]. Similarly, Kim et al. developed a Ca^{2+} selective nanocomposite coating to be applied onto the carbon electrode; thereby, they accomplished a Ca^{2+} over Na^+ selectivity of 3.5–5.4 at $Na^+: Ca^{2+}$ equivalent concentration ratio from 10:1 to 1:1 [26].

While both the chemical modification and the adaptation of an ion-exchange material are promising routes, they add extra synthesis steps and additional costs. Therefore, a better understanding of the ion preference of carbon electrodes with sub-nanometer pore size is needed. Herein, we applied a carbon cloth with sub-nanometer pore size to study the ion sieving of monovalent and divalent cations and, for the first time, the effect of long-term cycling [27] on the selectivity. We use on-line concentration monitoring to observe the dynamic ion selectivity of carbon materials with different average pore sizes and provide a better understanding of ion-selective electrosorption.

2. Experimental description

2.1. Materials

The electrochemical measurements were carried out by using a three-electrode cell for all electrochemical measurements [28]. As working electrodes, we used as-received microporous activated carbon cloth Kynol ACC-5092-10 and ACC-507-20 with thicknesses of 600 μm and 250 μm , respectively. For electrochemical measurements and desalination, two layers of the 250 μm electrode were used to compensate for the two carbons' different thicknesses. These materials are referred to as "ACC-0.59" and "ACC-0.88" to reflect the intrinsic average pore size of 0.59 nm and 0.88 nm. From the cloth, we cut the disc with a 12 mm diameter and soaked it in the measured solution for 15 min under vacuum condition to remove the bubbles in the electrodes before cell assembly.

The choice of ACC as the working electrode is motivated by the narrow pore size distribution of novolac-derived activated carbon. Further, ACC allows using binder-free, free-standing electrodes, whereby any pore blockage caused by the binder's presence is avoided [9,29].

The counter electrode was made by mixing 5 mass% of polytetrafluoroethylene with activated carbon powder YP-80F (Kuraray) for a free-standing film with a thickness of 650 μm and a diameter of 12 mm [30]. The counter electrodes have a mass three times higher compared to the working electrode. We used a glass fiber mat (GF/A, Whatman) with a 13 mm diameter as the separator.

2.2. Material characterization

Nitrogen gas sorption analysis (GSA) was conducted by a Quadasorb IQ system at –196 °C and is controlled by a heated cryostat filled with liquid nitrogen. The samples were first degassed at +200 °C for 1 h and then heated to +300 °C for up to 20 h to remove the material's functional groups and humidity. The pore size distribution was obtained by assuming a slit-shaped pore configuration and using quenched solid

density functional theory (QSDFT), a good representation of the microporous structure of carbon materials [31,32]. The average pore size d_{50} was calculated by selecting half of the maximum cumulative pore volume. The BET specific surface area (after Brunauer Emmett Teller) was calculated within the linear pressure range of 0.05–0.3 [33,34].

To obtain the chemical information of the materials. CHNS-O measurements were conducted. The chemical composition of H, C, and N was analyzed by applying a MICRO Cube (Elementar Analysensysteme GmbH) and heating up to +1150 °C at the combustion tube and +850 °C at the reduction tube. The oxygen content was quantified with an OXY cube elemental analyzer (Elementar Analysensysteme GmbH) with a pyrolysis temperature of +1450 °C.

Small-angle X-ray scattering (SAXS) was used to characterize the pore structure of ACC-0.59 and ACC-0.88 (*Supporting Information, Fig. S3B*) [35].

The nanoporous structure models shown in *Fig. 1B* were obtained from the SAXS data using the Gaussian random field (GRF) method. GRF uses a set of random fields to describe the structure of a two-phase system in 3D coordinates consisting of randomly attributed fields [36]. The random fields in GRF are randomly generated following four parameters obtained by fitting SAXS data, where ξ is related to the mean pore size of the sample, d is accounting for the local correlation among pores, α and β are for the specific pore volume [31]. In our case, we employed the following parameters: $\xi = 0.250$, $d = 3.317$, $\alpha = -1.043$, $\beta = 1.460$ for ACC-0.59; $\xi = 0.297$, $d = 11.487$, $\alpha = -4.3477$, $\beta = 0.3255$ for ACC-0.88.

Scanning electron microscope (SEM) characterization was conducted to observe the microstructure of the carbon electrode materials. A field emission electron microscope (JEOL JSM-7500F) was applied at the operating voltage of 3 kV.

2.3. Electrochemical measurements

The schematic setup of the custom-made cell used in this work is provided in Ref. [28]. Three-electrode cells, two half-cells with an Ag/AgCl reference electrode, were used for the electrochemical characterization. The cells have a body made of polyether ether ketone, and there are two titanium pistons (one of them is spring-loaded). Before cells were assembled, the reference electrode was kept in a 3 M NaCl solution. In this work, we used 1 M aqueous electrolyte with either LiCl, NaCl, KCl, MgCl₂, CaCl₂, or NiCl₂. This concentration was chosen to avoid the ion starvation phenomenon. Cyclic voltammetry, impedance spectroscopy, and galvanostatic charging/discharging experiments were conducted using VSP-300 potentiostat/galvanostat from Bio-Logic.

The cyclic voltammetry was conducted at a scan rate of 10 mV/s between –0.5 V and +0.5 V vs. Ag/AgCl. We carried out 300 cycles to investigate the different single cation cycling stability contained electrolytes. After the cyclic voltammetry sequence, the cells were turned to the open circuit potential for the electrochemical impedance spectroscopy. The specific capacitance was calculated by applying Eq. (1):

$$C = \frac{I}{\nu \cdot m} \quad (1)$$

I is the measured current, ν is the cyclic voltammetric measurement scan rate, and m is the working electrode's mass loading.

Electrochemical impedance spectroscopy (EIS) measurements were recorded before cyclic voltammetry and were measured at the potential of –0.4 V and +0.4 V to avoid Faradaic reactions. The frequency range was set to vary from 1 MHz to 10 mHz with an amplitude of 10 mV. Between the EIS measurements' changing potential, we applied an open circuit potential (OCV).

2.4. Inductively coupled plasma-optical emission spectroscopy (ICP-OES)

To test the materials' ion selectivity in a mixed cation system,

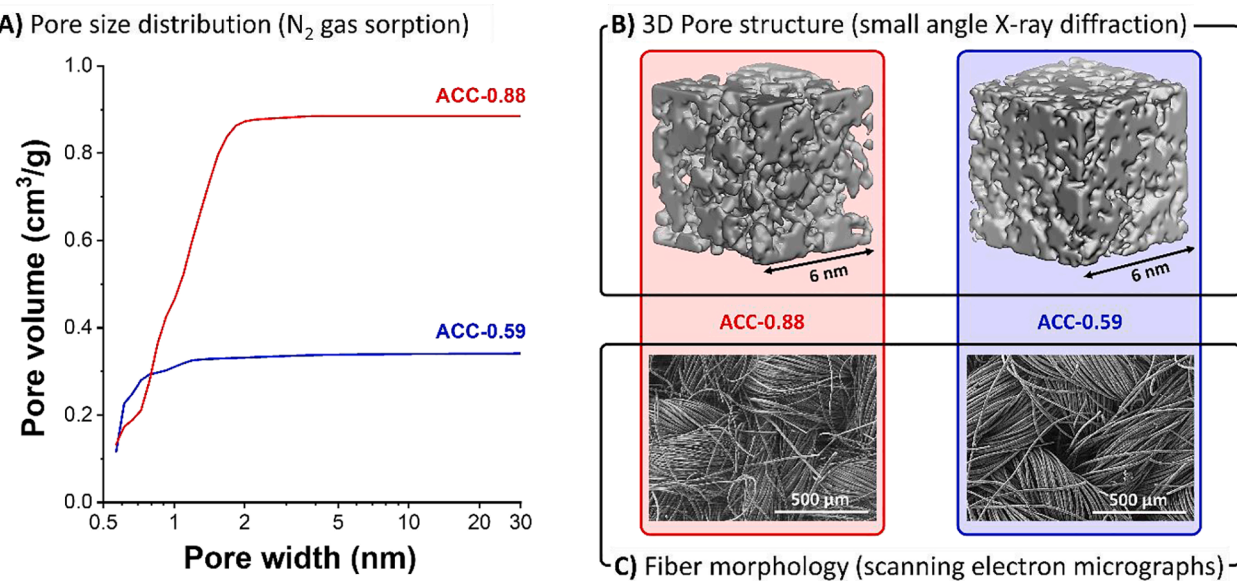


Fig. 1. Material characterization of ACC-0.59 and ACC-0.88. A) Cumulative pore size distribution obtained from nitrogen gas sorption (assuming slit-shaped pores and applying the quenched solid density functional theory). B) Three-dimensional pore structure obtained from small-angle X-ray diffraction (applying the Gaussian random field method). C) Fiber morphology characterized by scanning electron microscopy.

inductively coupled plasma-optical emission spectroscopy (ICP-OES) is conducted. The schematic drawing of online monitoring is shown in *Supporting Information, Fig. S1*. The aqueous electrolyte contains a mix of 10 mM of NaCl, KCl, CaCl₂, MgCl₂, and NiCl₂. The cells for ICP-OES consisted of two electrode pairs stacked on each other separated by nonconductive porous spacers made of glass fibers (glass fiber pre-filter, Millipore, with a thickness of 380 μm).

Two different cells were assembled, and we used a flow-by-cell configuration for both (Ref. [30,37]). In one cell, only ACC-0.59 was applied for both the cathode and anode sides. In another cell, ACC-0.88 was applied as cathode for cation removal, and ACC-0.59 was applied as anode for Cl⁻ removal due to its high permselectivity in smaller pores that only allow one charge species to transport [38]. In the latter case, ion swapping during cation removal is significantly suppressed [38]. The electrolyte with different cation systems was pumped through the cells at a flow rate of 2 mL/min continuously during charging and discharging. During the ion adsorption and desorption process, the cell was galvanostatically charged to 1 V at a specific current of 0.01 A/g and then hold the potential for 15 min. Afterward, the cells were discharged to 0 V at 0.01 A/g with the following holding time of 15 min. The electrolyte that flowed out of the cell was then pumped out to the ICP-OES system (ARCO FHX22, SPECTRO Analytical Instruments) at a flow rate of 2 mL/min. The electrolyte was stored and cycled in a 10 L tank reservoir, which is de-aerated with N₂ gas bubbles. The electrolyte from the cells was pumped through the nebulizer into a spray chamber, and the aerosol was introduced into the argon plasma, which has high energy to excite ions to emit specific wavelengths. The intensity measured for an ion-specific wavelength is converted to the ions' concentration in the effluent stream coming from the cell. The specific ion uptake capacities were calculated by applying Eq. (2):

$$\text{Ion uptake capacity} = \frac{\nu \cdot M_{\text{cation}}}{m_{\text{electrode}}} \int c \cdot dt \quad (2)$$

where ν is the flow rate of the electrolyte, M_{cation} is the molar mass of the cations, $m_{\text{electrode}}$ is the mass of one side of the electrode, c is the concentration of the cation in the outlet stream, and t is the duration time of the operation.

3. Results and discussion

3.1. Porosity analysis and chemical composition of the electrode materials

For the two carbon materials investigated in our study, the cumulative pore size distribution patterns obtained from nitrogen gas sorption are displayed in Fig. 1A, and characteristic pore structure data are provided in Table 1. ACC-0.59 has a smaller average pore size (0.59 nm), smaller pore volume (0.34 cm³/g), and a smaller specific surface area (1032 m²/g) compared to ACC-0.88 (0.88 nm, 0.81 cm³/g, and 1876 m²/g). Also, ACC-0.59 has a narrower pore size distribution compared to ACC-0.88. This can be quantified by the difference between d_{75} and d_{25} ($\Delta d_{75}-d_{25}$), that is, the diameter corresponding with 75% and 25% of the total cumulative pore volume. Thereby, ($\Delta d_{75}-d_{25}$) quantifies the width of pore size dispersion for 50% of the total pore volume centered around the volume-weighted average pore diameter d_{50} . For ACC-0.59, we see a value for ($\Delta d_{75}-d_{25}$) of 0.12 nm, and ACC-0.88 yields a value of 0.56 nm. Fig. 1B shows the three-dimensional pore structures of ACC-0.59 and ACC-0.88 obtained by Gaussian random fields data analysis of small-angle X-ray diffraction data [31]. Among two carbon fibers, ACC-0.88 has more interpore volume, and the pore volume is larger than that of the ACC-0.59 material. The scanning electron micrographs presented in Fig. 1C show an identical fiber morphology for ACC-0.59 and ACC-0.88. Both carbon textiles are composed of individual fibers with an average diameter of about 12 μm.

Table 1

Porosity analysis with nitrogen gas sorption at -196 °C using the quenched solid density functional theory (DFT; assuming slit-shaped pores) and the Brunauer-Emmett-Teller theory (BET). SSA: specific surface area. The average pore size refers to the volume-normalized value d_{50} .

	SSA BET (m ² /g)	SSA DFT (m ² /g)	DFT total pore volume(cm ³ / g)	Average pore size d_{50} (nm)
ACC-0.59	916	1032	0.34	0.59
ACC-0.59 in 1 M CaCl ₂	954	1063	0.36	0.62
ACC-0.59 after 300 cycles in mixed ion electrolyte	894	1079	0.33	0.56
ACC-0.88	2070	1876	0.81	0.88

The chemical composition of the carbon materials (**Table 2**) was obtained from CHNS-O measurement. ACC-0.59 has an oxygen content of 5.1 mass%, while ACC-0.88 has 1.9 mass%. Both materials have about 1 mass% of combined hydrogen and nitrogen. Besides, ACC-0.59 material after electrochemical measurements in 1 M NaCl, 1 M CaCl₂, and 1 M NiCl₂ are also washed, dried, and collected for CHNS-O measurements.

For analyzing the ion selectivity behavior of the carbon materials, the ionic diameter of different ion species is listed in **Table 3** [39]. Among all ions, divalent cations have a bigger hydrated ion size compared to monovalent cations. The hydrated ion size is in order of Mg²⁺>Ca²⁺>Ni²⁺>Na⁺>K⁺ (i.e., 0.856 nm > 0.824 nm > 0.808 nm > 0.716 nm > 0.662 nm), and the dehydrated ion size follows K⁺>Ca²⁺>Na⁺>Ni²⁺>Mg²⁺, that is, the following sequence: 0.266 nm > 0.198 nm > 0.190 nm > 0.140 nm > 0.124 nm.

3.2. Cyclic voltammetry and electrochemical cycling stability

We first characterized the electrochemical response of the carbon materials by cyclic voltammetry. **Fig. 2A** shows the tenth cycles of the ACC-0.59, and ACC-0.88 in aqueous 1 M LiCl, 1 M NaCl, 1 M KCl, 1 M CsCl, 1 M MgCl₂, 1 M CaCl₂, and 1 M NiCl₂. All cyclic voltammograms using electrolytes with monovalent cations (Li⁺, Na⁺, K⁺, Cs⁺) show for ACC-0.59 a rectangular shape (TYPE A; see **Fig. 2C** for a type characterization of different shapes of cyclic voltammograms). The capacitance is almost identical during both positive polarization (from 0 to + 0.4 V)

Table 2

Chemical analysis of the electrode materials. “n.d.” stands for “not detected”, that is, values below the detection limit of the system.

	Carbon (mass %)	Hydrogen (mass%)	Nitrogen (mass%)	Oxygen (mass %)	Ash- content (mass%)
ACC-0.88	96.7 ± 0.3	0.8 ± 0.1	0.2 ± 0.0	1.9 ± 0.1	<1
ACC-0.59	94.2 ± 0.5	1.0 ± 0.0	n.d.	5.1 ± 1.0	<1
ACC-0.59 aftercycling in 1 M NaCl	93.6 ± 0.1	0.9 ± 0.0	0.2 ± 0.0	4.3 ± 0.1	<1
ACC-0.59 aftercycling in 1 M NiCl ₂	92.0 ± 0.9	1.0 ± 0.0	0.2 ± 0.0	5.2 ± 0.6	<2
ACC-0.59 aftercycling in 1 M CaCl ₂	91.5 ± 0.2	1.0 ± 0.0	0.1 ± 0.0	5.9 ± 0.2	<2
ACC-0.59 after300 cycles in mixed ion electrolyte	92.2 ± 0.7	1.0 ± 0.1	0.5 ± 0.2	4.4 ± 0.1	<2
ACC-0.88 aftercycling in 1 M LiCl	95.1 ± 0.8	0.8 ± 0.1	0.5 ± 0.0	3.1 ± 0.3	<1
ACC-0.88 aftercycling in 1 M NaCl	94.1 ± 0.7	0.8 ± 0.1	0.5 ± 0.1	3.1 ± 0.1	<2
ACC-0.88 aftercycling in 1 M KCl	94.8 ± 0.3	0.7 ± 0.0	0.4 ± 0.0	3.1 ± 0.2	<1
ACC-0.88 aftercycling in 1 M CsCl	93.4 ± 2.0	0.7 ± 0.0	0.5 ± 0.2	2.8 ± 0.2	<3
ACC-0.88 aftercycling in 1 M MgCl ₂	93.9 ± 1.0	0.7 ± 0.0	0.4 ± 0.1	3.1 ± 0.1	<2
ACC-0.88 aftercycling in 1 M CaCl ₂	96.1 ± 2.3	0.7 ± 0.0	0.4 ± 0.1	3.0 ± 0.4	<1
ACC-0.88 aftercycling in 1 M NiCl ₂	93.1 ± 2.0	0.7 ± 0.0	0.5 ± 0.1	3.6 ± 0.5	<3

and negative polarization (from 0 to – 0.4 V). In 1 M CsCl, the negative potential region’s capacitance value is slightly higher than that in the positive potential region. When applying divalent cations like Mg²⁺, Ca²⁺, and Ni²⁺, we see a narrowing of the current signal of the measured cyclic voltammograms (TYPE B and TYPE C). The narrowed cyclic voltammograms below – 0.1 V vs. Ag/AgCl indicate that the ions are obstructed from entering the carbon nanopores (sieving) [12]. Ca²⁺ and Mg²⁺ ions show a very low capacitance during negative polarization compared to the capacitance value during positive polarization (where the charge compensation is carried by ion electrosorption of the anion, chlorine). In contrast to the TYPE B shape of MgCl₂ or CaCl₂, the cyclic voltammogram for the NiCl₂ electrolyte displays an asymmetric TYPE C shape with a characteristic minimum during the negative scanning at around – 0.2 V vs. Ag/AgCl. This potential-dependent electrochemical phenomenon is related to ion desolvation adsorption. As the potential goes to a lower region that overcomes the desolvation energy barrier, the ions start to desolvate and enter the pores, thus the capacitance increases as the potential goes to a more negative region [40]. For ACC-0.88 electrodes, we see that all electrolytes, containing monovalent cations and containing divalent cations, exhibit the cyclic voltammograms TYPE A expected from a nearly perfect electrical double-layer capacitor (**Fig. 2B**).

To further study the stability of this size effect, cyclic voltammetry is carried out for 600 cycles. For ACC-0.59, all electrolytes with monovalent cations show the same shape during the cyclic voltammetric measurement (**Fig. 3A-B**); however, as for Mg²⁺, Ca²⁺, and Ni²⁺, the amplitude of the sieving effect gradually fades over time as the capacitance of the cyclic voltammogram at the negative potential region expands. From the 10th cycle to the 300th cycle and the 600th cycle, this difference decreases over time, although the capacitance difference between positive and negative polarization is still apparent. As for ACC-0.88, all cyclic voltammograms show a nearly rectangular shape in each electrolyte system, and there is no significant change when comparing initial and progressed (300th/600th) cycles, as seen in **Fig. 2B** and **Fig. 3C-D**.

To explore the possible change in surface functionality or general carbon oxidation by the electrochemical operation, we conducted an elemental analysis of ACC-0.59 and ACC-0.88 electrodes after cyclic voltammetric measurements. As seen from **Table 2**, there is no statistically significant change in the chemical composition; especially, there is no significant change in the amount of oxygen. A small change in pore structure (5% of average pore size change) is found after the electrochemical operation; as seen from **Table 1**, ACC-0.59 operated in 1 M CaCl₂ after 600 cycles show a small increase in the pore volume from 0.34 cm³/g to 0.36 cm³/g) and an associated small increase in the average pore size from 0.59 nm to 0.62 nm. *Supporting Information*, **Fig. S2A-B** shows the gas sorption isotherms and cumulative pore size distribution pattern of the original ACC-0.59 and ACC-0.59 after cycling in 1 M CaCl₂ electrolyte. This result shows that the pore size is slightly expanded during charging and discharging.

3.3. Impedance measurement

To further compare the ion accessibility of different ion species, electrochemical impedance spectroscopy (EIS) was conducted. Firstly, we investigated electrolytes with monovalent cations. **Fig. 4** provides EIS data for 1 M LiCl, 1 M KCl, 1 M NaCl, and 1 M CsCl. According to the Nyquist plot result, no significant Faradaic reaction features occur in all electrolyte systems. The 45° angle linear curve represents reflective finite-length diffusion at high frequency, indicating ion diffusion and EDL formation inside the carbon materials’ pores [41-43]. At lower frequency values, the Nyquist curve tends to be more perpendicular. During the negative polarization (-0.4 V), the high frequency and low-frequency region’s impedance values show the same trend during the positive polarization (+0.4 V) process. This feature does not change when comparing the initial impedance value before cyclic voltammetry

Table 3

Ionic diameter of hydrated and dehydrated ions of Na^+ , K^+ , Mg^{2+} , Ca^{2+} , and Ni^{2+} [39,49]. “n.d.” stands for “not detected”, that is, values below the detection limit of the system. Hydration energy is synonymous with desolvation energy.

	Solvated(nm)	Desolvated(nm)	Hydrationenergy(kJ/mol)	Selectivityin ACC-0.59vs. Na	Reference
Na^+	0.716	0.190	-365	1	[49,50]
K^+	0.662	0.266	-295	1.5	[49,50]
Mg^{2+}	0.856	0.124	-1830	n.d.	[49]
Ca^{2+}	0.824	0.198	-1505	n.d.	[49]
Ni^{2+}	0.808	0.140	-1980	0.43	[49]

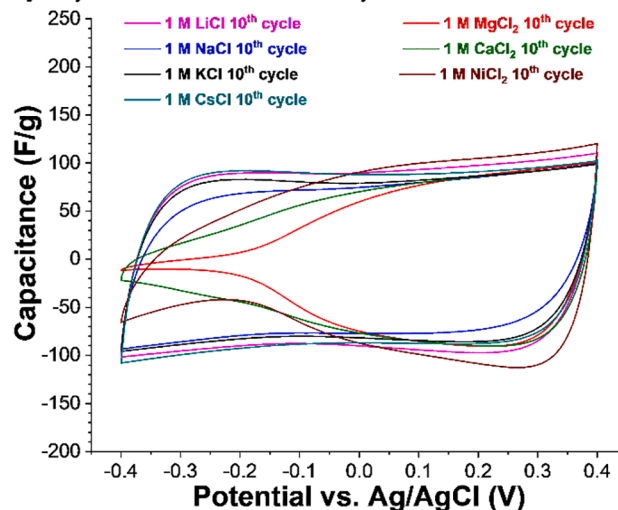
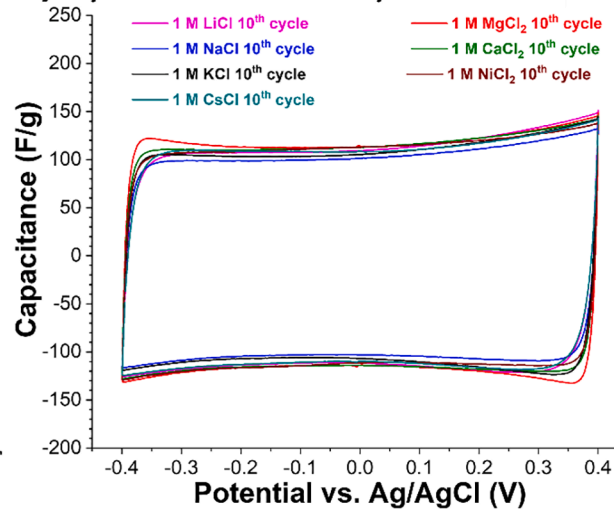
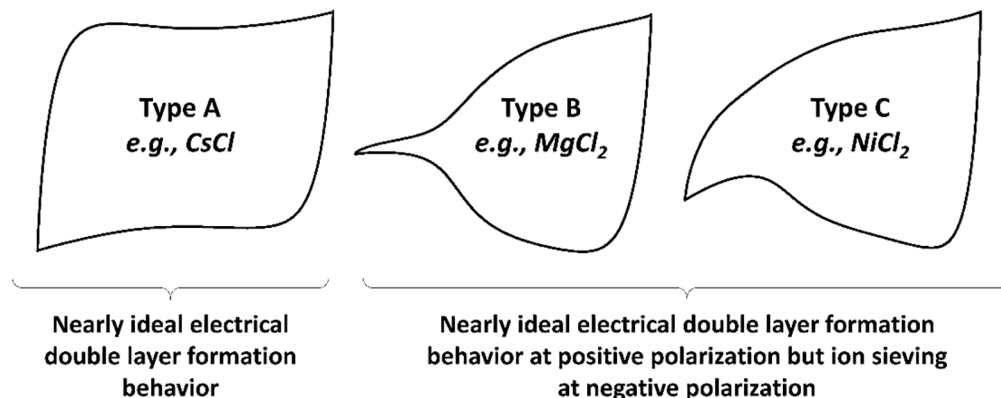
A) Cyclic voltammetry ACC-0.59**B) Cyclic voltammetry ACC-0.88****C) Types of shapes of cyclic voltammograms**

Fig. 2. Cyclic voltammograms of ACC-0.59 and ACC-0.88 in 1 M LiCl, 1 M NaCl, 1 M KCl, 1 M CsCl, 1 M MgCl_2 , 1 M CaCl_2 , and 1 M NiCl_2 recorded at a scan rate of 10 mV/s.

with the impedance curve after cyclic voltammetry. This phenomenon shows for monovalent cations, the ion mobilities in the micropores of carbon are almost the same as anions mobility inside the micropores of carbon, which does not change after cyclic voltammetry.

In Fig. 5, the electrochemical impedance spectra of three different divalent cations contained electrolyte (1 M MgCl_2 , 1 M CaCl_2 , and 1 M NiCl_2) are compared. Fig. 5A-C shows that before cyclic voltammetry, the Nyquist plots of ACC-0.59 in 1 M MgCl_2 , 1 M CaCl_2 , and 1 M NiCl_2 during the negative polarization is shifted to higher resistance compared to positive polarization. When comparing the data at negative polarization with positive polarization, the length of the 45° angle linear curve, which shows the ion diffusivity under specific potentials, extends to a more resistive region under negative polarization compared to the

Nyquist curve under positive polarization. This length difference shows the different accessibility of the ions. The anion adsorption is much easier than the cation adsorption, which is in good alignment with the sieving effect from cyclic voltammetry. After the cyclic voltammetric operation, this length difference became smaller, showing the cation access is becoming easier after cycling. A decreased amplitude of ion sieving aligns with the increased pore size after electrochemical cycling. This can be caused by the oxidation of carbon in the aqueous electrolyte [27].

3.4. ICP-OES measurements and selectivity of cations

Actual ion selectivity cannot be directly concluded from only

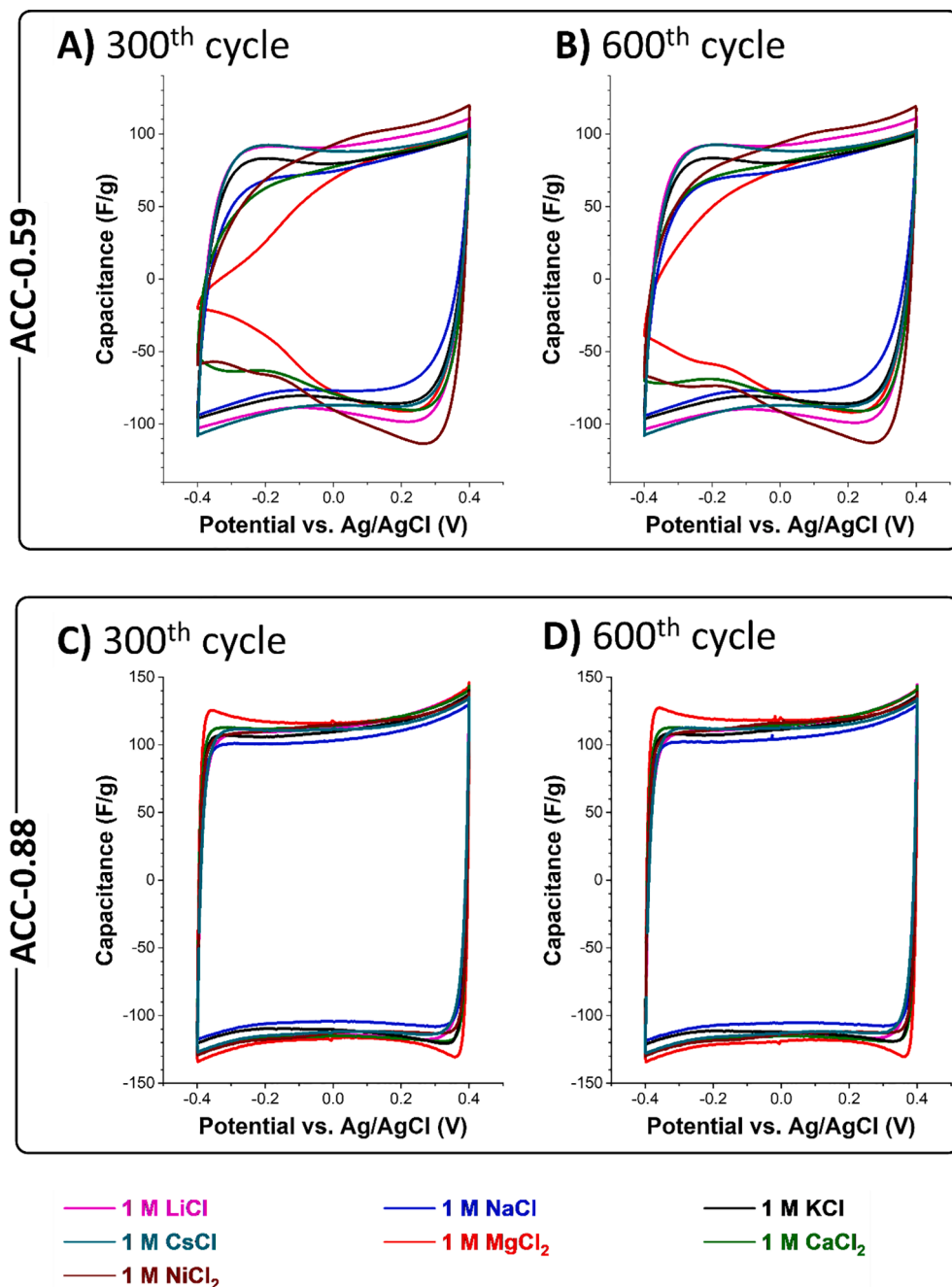


Fig. 3. Cyclic Voltammetry of ACC-0.59 and ACC-0.88 in 1 M LiCl, 1 M NaCl, 1 M KCl, 1 M CsCl, 1 M MgCl₂, 1 M CaCl₂, and 1 M NiCl₂ recorded at a scan rate of 10 mV/s.

carrying out electrochemical measurements. Therefore, we analyzed the ion composition of the effluent stream via online monitoring using an ICP-OES system (*Supporting Information, Fig. S1*). **Fig. 6** shows the result from a mixture of 10 mM of each NaCl, KCl, CaCl₂, MgCl₂, and NiCl₂ electrolyte. The symmetric cell with ACC-0.59 carbon electrodes is cycled between 0 to +1 V to conduct the ion adsorption and desorption. We did not polarize up to +1.2 V to avoid possible electrochemical degradation. At the beginning of the measurement, the cell is operated from OCV, resting for 20 min, and then charged to +1 V cell voltage. A small aliquot of the flow-by cell's outlet is extracted and pumped into the ICP-OES to online-monitor the different cation species' concentration change in the electrolyte. According to the ICP-OES measurement, among all cations, all the divalent cations show much less concentration change, and among all ions, Mg²⁺ and Ca²⁺ do not show any

pronounced concentration variations. However, all the monovalent cations show pronounced concentration change, and the concentration variation of K⁺ (from -2.10 mM/g to +2.92 mM/g) is higher than that of Na⁺ (from -1.48 mM/g to +1.79 mM/g). Although Ni²⁺ is a divalent cation, it has a smaller hydrated ion size than Mg²⁺ and Ca²⁺. Accordingly, the concentration of Ni²⁺ is more pronounced compared to Mg²⁺ and Ca²⁺, but less than K⁺ and Na⁺ (**Fig. 6**). The concentration peak positions of Ni²⁺ for both adsorption and desorption are seen later compared to the peak positions of K⁺ and Na⁺. This observation indicates slower kinetics of Ni²⁺ adsorption and desorption compared to K⁺ and Na⁺ ions.

Although Ni²⁺ ions carry twice the charge compared to K⁺ and Na⁺, it has a much larger hydrated ion size and experiences a more pronounced sieving effect in ACC-0.59 (**Table 3**); accordingly, hydrated

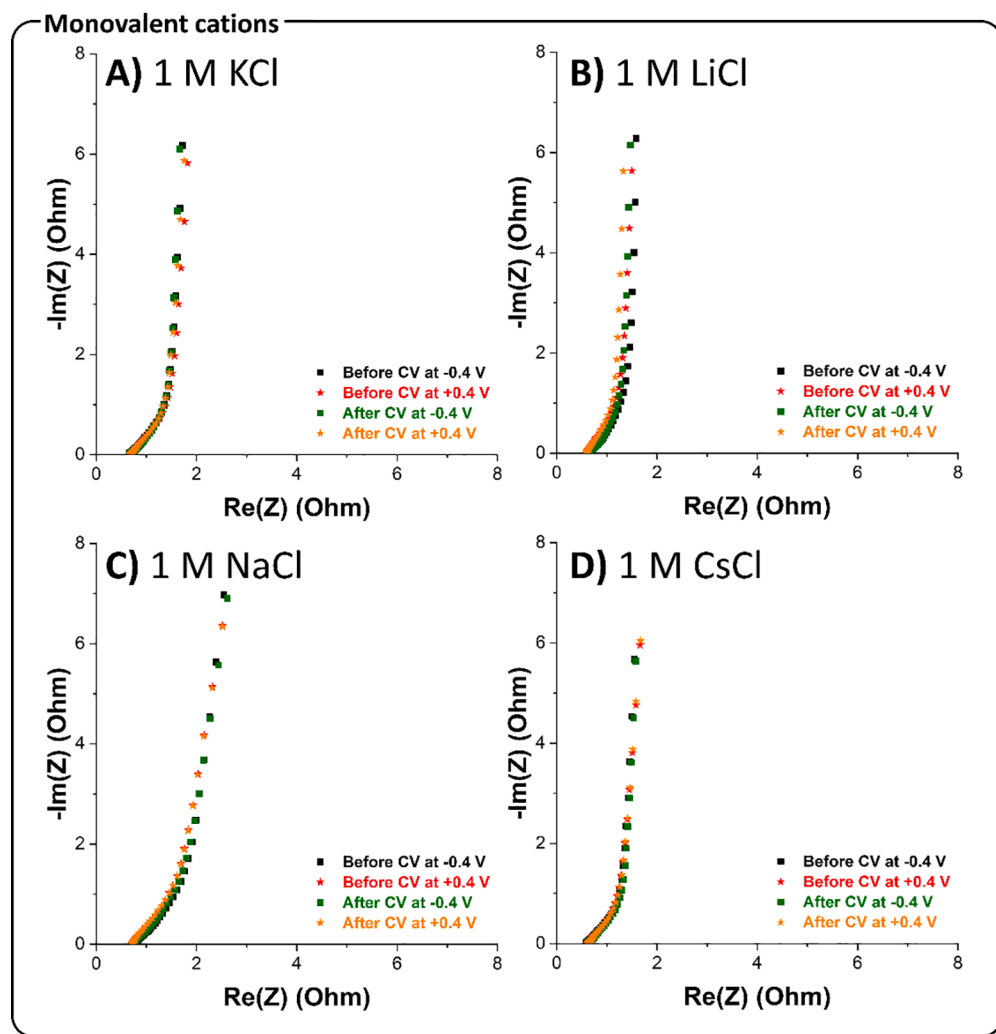


Fig. 4. Nyquist plots from electrochemical impedance measurement of ACC-0.59 in 1 M KCl, 1 M LiCl, 1 M NaCl, and 1 M CsCl at different applied potentials before and after having carried out cyclic voltammetry (CV).

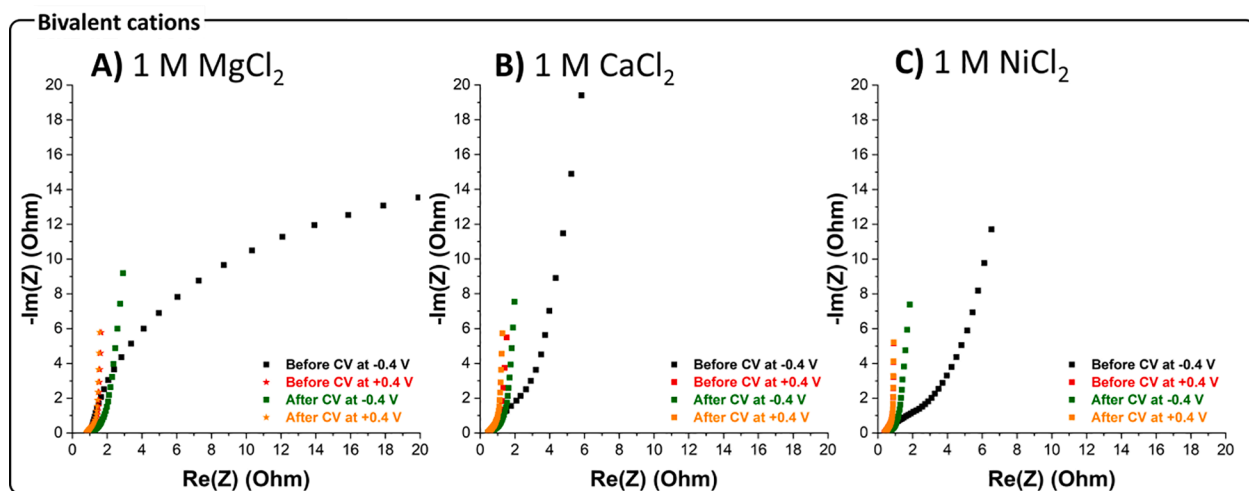


Fig. 5. Nyquist plots from electrochemical impedance measurement of ACC-0.59 in 1 M MgCl_2 , 1 M NiCl_2 , and 1 M CaCl_2 at the polarization of -0.4 V and $+0.4\text{ V}$ before and after cyclic voltammetry (CV).

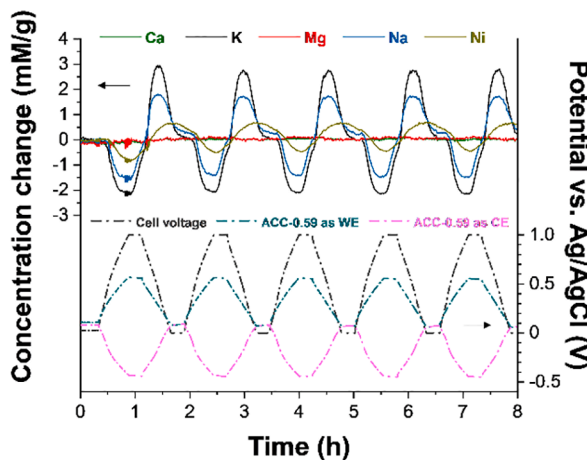
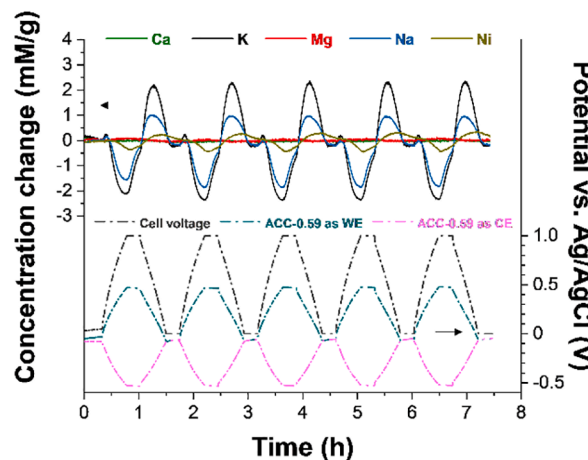
A) Before 300 cycles**B) After 300 cycles**

Fig. 6. ICP-OES measurement of the symmetric CDI cell A) before and B) after 300 cycles test. The concentration of K^+ , Na^+ , Ni^{2+} , Mg^{2+} , Ca^{2+} is shown. WE = working electrode; CE = counter electrode. Cell voltage is the potential bias between the working electrode and the counter electrode (not the potential vs. $Ag/AgCl$).

ions with smaller size and higher ion mobilities are preferred to enter/leave the pores during the charging/discharging process. According to the previous work [38] and the desolvation energy listed in Table 3, the desolvation energy for K^+ and Na^+ is lower, and the ions will desolvate partially in the micropores of ACC-0.59. In contrast, the higher desolvation energy of cations like Ni^{2+} , Mg^{2+} , and Ca^{2+} serves as an energy barrier for the desolvation process. For ACC-0.59, these data indicate a high K^+ and Na^+ selectivity over Ni^{2+} , and very high K^+ and Na^+ selectivity over Mg^{2+} and Ca^{2+} . The reason behind this relates to the size difference of hydrated ions and the difference in desolvation energy.

The ICP-OES measurement after 300 galvanostatic charge/discharge cycles (Fig. 6B) do not show any noticeable concentration change for divalent cations Mg^{2+} and Ca^{2+} . Also, Ni^{2+} has a less obvious concentration decrease trend during all the charging process (minimum value changed from -0.5 mM/g to $+0.4$ mM/g), and the desorption peak value is still shifted to a similar place compared to K^+ and Na^+ , which will be seen later. For K^+ and Na^+ , the concentration changes remain the highest among all the other ion species. K^+ shows a higher concentration change (with a minimum value up to $+2.3$ mM/g) than Na^+ (with a minimum value up to $+1.8$ mM/g). After 300 cycles, a decay of concentration change is observed, which relates to the ion uptake capacity decrease of K^+ and Na^+ after 300 cycles.

For K^+ and Na^+ , we observe a concentration inversion at the beginning of the charging process. The concentration for K^+ and Na^+ first increases before decreasing during the charging process; Ni^{2+} does not follow this trend. The concentration of Mg^{2+} and Ca^{2+} changes slightly in the opposite way: Mg^{2+} goes up to 0.07 mM/g from 0 mM/g, and Ca^{2+} rises from 0 to 0.01 mM/g. According to Hou et al. [15], divalent cations have a higher valence number and an energetic preference for screening the charge of the electrode surface. In contrast, monovalent cations are smaller and exhibit higher ion transport mobility in porous carbon electrodes. These two factors are related to the carbon electrodes' pore size and the magnitude of surface charge. In the case of ACC-0.59, the size effect is dominant compared to the degree of charge effect, and after 300 cycles, monovalent cations still have much higher preferences over divalent cations. Although all the other cations have concentration amplitude decay, this carbon material still has high K^+ and Na^+ selectivity over all the other cations.

Fig. 7 shows the ion uptake capacity of all cation species. In Fig. 7A, before 300 cycles, K^+ , Na^+ and Ni^{2+} uptake capacity for the first 10 cycles is around 0.09 mM/g, 0.06 mM/g, and 0.025 mM/g. The uptake capacities of Mg^{2+} and Ca^{2+} cations cannot be determined within the instrument's detection limit, as is inferred from the lack of noticeable concentration changes in the online-monitored profiles. This shows the

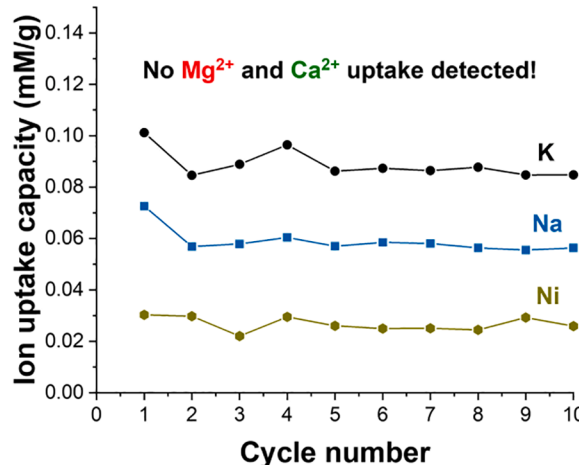
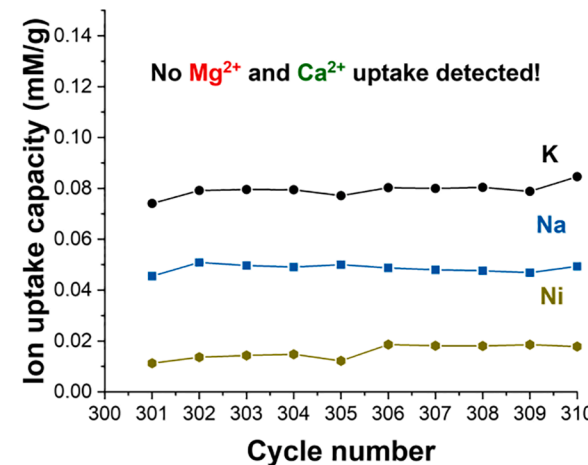
A) Before 300 cycles**B) After 300 cycles**

Fig. 7. ICP-OES measurement of the symmetric CDI cell A) before and B) after 300 cycles. The concentration of K^+ , Na^+ , Ni^{2+} , Mg^{2+} , and Ca^{2+} is calculated.

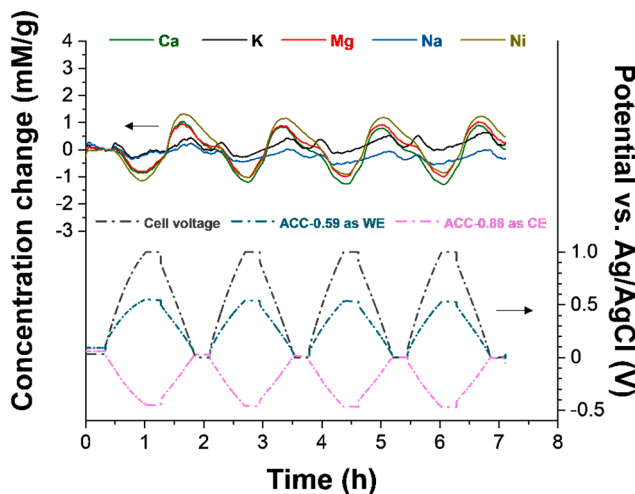
high K^+ and Na^+ selectivity compared to Mg^{2+} and Ca^{2+} . After 300 cycles, the K^+ , Na^+ , and Ni^{2+} uptake capacities are decreased to 0.08 mM/g, 0.05 mM/g, and 0.02 mM/g (Fig. 7B). As for Mg^{2+} and Ca^{2+} , from the beginning to > 300 cycles, the concentration change is always below 0.1 mM/g, and due to the inverted concentration change compared to the other cations, there is no net uptake capacity. These results show the strong K^+ and Na^+ selectivity over Mg^{2+} and Ca^{2+} divalent cations. In Table 1, and Supporting Information, Fig. S2, gas sorption analysis data of ACC-0.59 after 300 cycles are shown. There is no obvious accumulative volume or increase of the average pore size after 300 cycles. The CHNS-O analysis after 300 cycles also shows no significant change in the oxygen content (Table 2).

In the experiments so far, we used symmetric cell of ACC-0.59 paired with ACC-0.59. We now paired ACC-0.59 as the working electrode and ACC-0.88 as the counter electrode to test the cation selectivity's pore size influence. With an average pore size of 0.88 nm, the ion storage of ACC-0.88 is accomplished by adsorption of the counter-ions and ejecting of the co-ions [37,38]. To minimize the permselectivity influence of the Cl^- adsorption electrode, ACC-0.59 is applied as a working electrode with high ion permselectivity to remove Cl^- . Among all investigated cations, K^+ and Na^+ have a concentration increase at the beginning of

the charging process and then decrease as the cell voltage goes up (Fig. 8A). For Ca^{2+} , Mg^{2+} , and Ni^{2+} , the concentrations decrease immediately as the cell voltage rises, and as cell voltage decreases, the concentrations increase dramatically. K^+ and Na^+ only show a small concentration variation, and the unusual increase of concentration change is always observed at the beginning of every charging process. According to the Schulze-Hardy rule, the coagulating power increases very strongly with the charge number of the counterions. Thus, the ions with higher charge numbers will have stronger interactions with the pores [44–48]. Throughout four cycles, the concentration variation of K^+ and Na^+ gradually separated, the K^+ curve tends to shift up, which indicates that ions tend to leave the pores more than adsorb, and the Na^+ curve tends to go down, which suggests that ions are gradually stored in the carbon material.

The ICP-OES results shown in Fig. 8A exclude a poor permselectivity of the larger pores: Although divalent cations have larger solvated ion size and lower ion mobility, they have higher selectivity in larger pores. Besides, a 'charge inversion' phenomenon is observed [15], resulting in K^+ and Na^+ 's ejection to fulfill the maximum charge/volume ratio. As for ACC-0.59 in Fig. 8B, when most Ca^{2+} , Mg^{2+} , and some Ni^{2+} ions are blocked outside of the pores because of the sieving effect, Na^+ and K^+

A) ACC-0.88 as counter electrode, ACC-0.59 as working electrode



B) ACC-0.59 as both counter and working electrode

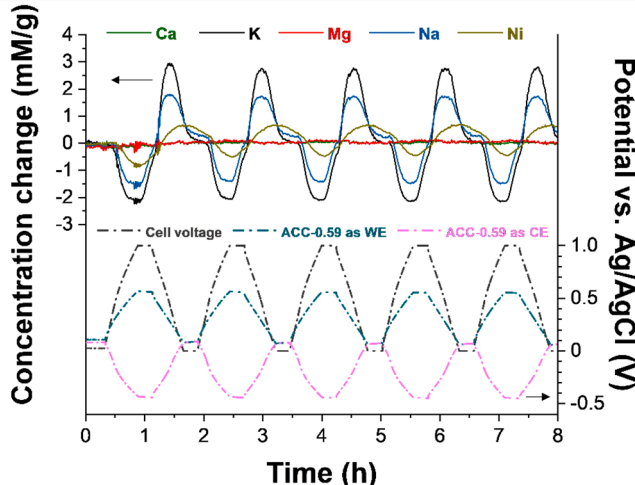


Fig. 8. Concentration profiles and corresponding applied potential. ICP-OES measurements. (A) Asymmetric CDI cell before the 300 cycles test. ACC-0.59 is applied as WE, Ag/AgCl electrode (stored in 3 M NaCl water solution) is applied as the reference electrode, ACC-0.88 is applied as CE. For comparison, (B) the ACC-0.59 symmetric cell is also plotted. For the cell voltage, we refer to the potential bias between the working electrode and counter electrode (not the potential vs. Ag/AgCl).

could be all adsorbed in the pores. Further, ACC-0.59 shows K^+ selectivity over Na^+ in alignment with the smaller hydrated ion size of K^+ .

The time-dependent (dynamic) change in concentration change of K^+/Na^+ , K^+/Ni^{2+} , and K^+/Mg^{2+} is exemplified in *Supporting Information, Fig. S4*. In addition to the different intrinsic uptake capacity for certain ions (Fig. 7), the dynamic changes in concentration profiles and ion-replacement effects allow to modify the ion selectivity.

4. Conclusions

In this work, two kinds of microporous carbon materials, with narrowly distributed sub-nanometer sized pore sizes of 0.59 nm and 0.88 nm, are applied. By applying electrochemical measurements like cyclic voltammetry and EIS measurements, the ion sieving effect in ACC-0.59 activated carbon cloth is observed, and the large hydrated ion diffusion resistance causes this phenomenon in the pores of the carbon. By applying these two material electrodes in CDI applications and combine them with the ICP-OES online monitoring method, the dynamic change of ion concentration during charging and discharging is observed. ACC-0.59 shows sieving of divalent cations. Therefore, Ca^{2+} and Mg^{2+} cannot enter the pores, and Ni^{2+} has a much smaller concentration change. In contrast, monovalent cations like Na^+ and K^+ partially desolvate to be electrosorbed in small pores; consequently, we see a significant concentration change during charging and discharging for such ions. The ion uptake capacity of Na^+ is smaller than K^+ due to the larger hydrated ion size. ACC-0.88 has an average pore size larger than all kinds of cations; accordingly, divalent cations are preferred due to the higher charge numbers. Although Na^+ and K^+ have higher ion mobilities due to the smaller hydrated ion size, they have less ion uptake capacities during the charging and discharging process.

Ion selectivity in larger pores is influenced by the combination of size effect, dehydration effect, and charge effect. In carbon materials with an average pore size smaller than the divalent cations, the size effect plays a dominant role in blocking divalent cations with bigger hydrated ion size and higher desolvation energy. In this work, it is possible to reach pure monovalent cation selectivity over divalent cations in the long term by controlling the narrow pore size distribution of small pores in carbon materials.

Our data show the cation replacement during electrochemical measurements, revealing the dynamic ion-selective mechanism. Thereby, one can design conditions for the optimized removal of specific ions by selection a certain pore size and charge/discharge rate; future work will have to more precisely dissection optimized conditions for an array of specific aqueous systems and ion species.

Declaration of Competing Interest

The authors declare that they have no known competing financial interests or personal relationships that could have appeared to influence the work reported in this paper.

Acknowledgments

We acknowledge support for the MERLIN project from the RAG-Stiftung; the RAG-Stiftung generates long-term momentum for the transformation of the regions along the Ruhr and Saar Rivers and in Ibbenbüren. Y.Z. and V.P. thank Eduard Arzt (INM) for his continuing support. We thank Dr. Pattarachai Srimuk (INM) for past discussions, and Andrea Jung (INM) for her support with CHNS-O measurements. J. X.P. and G.F. acknowledge funding from the National Natural Science Foundation of China (No. 51836003) and also thank Beijing PARATERA Tech CO., Ltd. for providing HPC resources to accomplish modeling in this work.

Appendix A. Supplementary data

Supplementary data to this article can be found online at <https://doi.org/10.1016/j.cej.2021.129438>.

References

- [1] M.A. Anderson, A.L. Cudero, J. Palma, Capacitive deionization as an electrochemical means of saving energy and delivering clean water. Comparison to present desalination practices: Will it compete? *Electrochim. Acta* 55 (12) (2010) 3845–3856.
- [2] S. Porada, R. Zhao, A. van der Wal, V. Presser, P.M. Biesheuvel, Review on the science and technology of water desalination by capacitive deionization, *Prog. Mater. Sci.* 58 (8) (2013) 1388–1442.
- [3] M.E. Suss, S. Porada, X. Sun, P.M. Biesheuvel, J. Yoon, V. Presser, Water desalination via capacitive deionization: what is it and what can we expect from it? *Energy Environ. Sci.* 8 (2015) 2296–2319.
- [4] E. García-Quismondo, C. Santos, J. Soria, J. Palma, M.A. Anderson, New operational modes to increase energy efficiency in capacitive deionization systems, *Environ. Sci. Technol.* 50 (11) (2016) 6053–6060.
- [5] R. Zhao, M. van Soestbergen, H.H.M. Rijnaarts, A. van der Wal, M.Z. Bazant, P. M. Biesheuvel, Time-dependent ion selectivity in capacitive charging of porous electrodes, *J. Colloid Interface Sci.* 384 (1) (2012) 38–44.
- [6] J.E. Dykstra, J. Dijkstra, A. van der Wal, H.V.M. Hamelers, S. Porada, On-line method to study dynamics of ion adsorption from mixtures of salts in capacitive deionization, *Desalination* 390 (2016) 47–52.
- [7] M.E. Suss, Size-based ion selectivity of micro-pore electric double layers in capacitive deionization electrodes, *J. Electrochim. Soc.* 164 (9) (2017) E270–E275.
- [8] G. Feng, P.T. Cummings, Supercapacitor capacitance exhibits oscillatory behavior as a function of nanopore size, *The Journal of Physical Chemistry Letters* 2 (22) (2011) 2859–2864.
- [9] N. Jäckel, M. Rodner, A. Schreiber, J. Jeongwook, M. Zeiger, M. Aslan, D. Weingarth, V. Presser, Anomalous or regular capacitance? The influence of pore size disparity on double-layer formation, *J. Power Sources* 326 (2016) 660–671.
- [10] E. Raymundo-Pinero, K. Kierzek, J. Machnikowski, F. Béguin, Relationship between the nanoporous texture of activated carbons and their capacitance properties in different electrolytes, *Carbon* 44 (12) (2006) 2498–2507.
- [11] B. Corry, Mechanisms of selective ion transport and salt rejection in carbon nanostructures, *MRS Bull.* 42 (04) (2017) 306–310.
- [12] L. Eliad, G. Salitra, A. Soffer, D. Aurbach, Ion sieving effects in the electrical double layer of porous carbon electrodes: Estimating effective ion size in electrolytic solutions, *J. Phys. Chem. B* 105 (2001) 6880–6887.
- [13] J. Segalini, E. Iwama, P.-L. Taberna, Y. Gogotsi, P. Simon, Steric effects in adsorption of ions from mixed electrolytes into microporous carbon, *Electrochim. Commun.* 15 (1) (2012) 63–65.
- [14] S.A. Hawks, M.R. Cerón, D.I. Oyarzun, T.A. Pham, C. Zhan, C.K. Loeb, D. Mew, A. Deinhart, B.C. Wood, J.G. Santiago, M. Stadermann, P.G. Campbell, Using ultramicroporous carbon for the selective removal of nitrate with capacitive deionization, *Environ. Sci. Technol.* 53 (18) (2019) 10863–10870.
- [15] C.H. Hou, P. Taboada-Serrano, S. Yiakoumi, C. Tsouris, Electrosorption selectivity of ions from mixtures of electrolytes inside nanopores, *J. Chem. Phys.* 129 (2008), 224703.
- [16] C. Zhan, F. Aydin, E. Schwegler, A. Noy, T.A. Pham, Understanding cation selectivity in carbon nanopores with hybrid first-principles/continuum simulations: Implications for water desalination and separation technologies, *ACS Applied Nano Materials* 3 (10) (2020) 9740–9748.
- [17] E.N. Guyes, T. Malka, M.E. Suss, Enhancing the ion-size-based selectivity of capacitive deionization electrodes, *Environ. Sci. Technol.* 53 (14) (2019) 8447–8454.
- [18] Z.Y. Leong, H.Y. Yang, Capacitive deionization of divalent cations for water softening using functionalized carbon electrodes, *ACS Omega* 5 (5) (2020) 2097–2106.
- [19] D.I. Oyarzun, A. Hemmatifar, J.W. Palko, M. Stadermann, J.G. Santiago, Ion selectivity in capacitive deionization with functionalized electrode: Theory and experimental validation, *Water Research X* 1 (2018) 100008, <https://doi.org/10.1016/j.wro.2018.100008>.
- [20] P. Liu, T. Yan, J. Zhang, L. Shi, D. Zhang, Separation and recovery of heavy metal ions and salt ions from wastewater by 3D graphene-based asymmetric electrodes via capacitive deionization, *J. Mater. Chem. A* 5 (28) (2017) 14748–14757.
- [21] X. Zhang, K. Zuo, X. Zhang, C. Zhang, P. Liang, Selective ion separation by capacitive deionization (CDI) based technologies: a state-of-the-art review, *Environ. Sci. Water Res. Technol.* 6 (2020) 243–257.
- [22] T. Luo, F. Roghman, M. Wessling, Ion mobility and partition determine the counter-ion selectivity of ion exchange membranes, *J. Membr. Sci.* 597 (2020), 117645.
- [23] T. Luo, S. Abdu, M. Wessling, Selectivity of ion exchange membranes: A review, *J. Membr. Sci.* 555 (2018) 429–454.
- [24] J.M. Dickhout, J. Moreno, P.M. Biesheuvel, L. Boels, W.M. de Vos, R.G. H. Lammertink, Produced water treatment by membranes: A review from a colloidal perspective, *J. Colloid Interface Sci.* 487 (2017) 523–534.
- [25] K. Zuo, J. Kim, A. Jain, T. Wang, R. Verduzco, M. Long, Q. Li, Novel composite electrodes for selective removal of sulfate by the capacitive deionization process, *Environ. Sci. Technol.* 52 (16) (2018) 9486–9494.

- [26] J. Kim, A. Jain, K. Zuo, R. Verduzco, S. Walker, M. Elimelech, Z. Zhang, X. Zhang, Q. Li, Removal of calcium ions from water by selective electrosorption using target-ion specific nanocomposite electrode, *Water Res.* 160 (2019) 445–453.
- [27] R. Uwayid, N.M. Seraphim, E.N. Guyes, D. Eisenberg, M.E. Suss, Characterizing and mitigating the degradation of oxidized cathodes during capacitive deionization cycling, *Carbon* 173 (2021) 1105–1114.
- [28] D. Weingarth, M. Zeiger, N. Jäckel, M. Aslan, G. Feng, V. Presser, Graphitization as a universal tool to tailor the potential-dependent capacitance of carbon supercapacitors, *Adv. Energy Mater.* 4 (2014) 1400316.
- [29] M. Aslan, D. Weingarth, N. Jäckel, J.S. Atchison, I. Grobelsek, V. Presser, Polyvinylpyrrolidone as binder for castable supercapacitor electrodes with high electrochemical performance in organic electrolytes, *J. Power Sources* 266 (2014) 374–383.
- [30] M. Aslan, M. Zeiger, N. Jäckel, I. Grobelsek, D. Weingarth, V. Presser, Improved capacitive deionization performance of mixed hydrophobic/hydrophilic activated carbon electrodes, *J. Phys.: Condens. Matter* 28 (11) (2016) 114003, <https://doi.org/10.1088/0953-8984/28/11/114003>.
- [31] C. Prehal, S. Grätz, B. Krüner, M. Thommes, L. Borchardt, V. Presser, O. Paris, Comparing pore structure models of nanoporous carbons obtained from small angle X-ray scattering and gas adsorption, *Carbon* 152 (2019) 416–423.
- [32] S. Choudhury, B. Krüner, P. Massuti-Ballester, A. Tolosa, C. Prehal, I. Grobelsek, O. Paris, L. Borchardt, V. Presser, Microporous novolac-derived carbon beads / sulfur hybrid cathode for lithium-sulfur batteries, *J. Power Sources* 357 (2017) 198–208.
- [33] M. Thommes, K. Kaneko, A.V. Neimark, J.P. Olivier, F. Rodriguez-Reinoso, J. Rouquerol, K.S.W. Sing, Physisorption of gases, with special reference to the evaluation of surface area and pore size distribution, *Pure Appl. Chem.* 87 (2015) 1051–1069.
- [34] S. Brunauer, P.H. Emmett, E. Teller, Adsorption of gases in multimolecular layers, *J. Am. Chem. Soc.* 60 (2) (1938) 309–319.
- [35] C. Prehal, D. Weingarth, E. Perre, R.T. Lechner, H. Amenitsch, O. Paris, V. Presser, Tracking the structural arrangement of ions in carbon supercapacitor nanopores using in situ small-angle X-ray scattering, *Energy Environ. Sci.* 8 (6) (2015) 1725–1735.
- [36] C. Prehal, C. Koczwara, N. Jäckel, A. Schreiber, M. Burian, H. Amenitsch, M. A. Hartmann, V. Presser, O. Paris, Quantification of ion confinement and desolvation in nanoporous carbon supercapacitors with modelling and in situ X-ray scattering, *Nat. Energy* 2 (2017) 16215.
- [37] Y. Zhang, P. Srimuk, M. Aslan, M. Gallei, V. Presser, Polymer ion-exchange membranes for capacitive deionization of aqueous media with low and high salt concentration, *Desalination* 479 (2020), 114331.
- [38] S. Bi, Y. Zhang, L. Cervini, T. Mo, J.M. Griffin, V. Presser, G. Feng, Permselective ion electrosorption of subnanometer pores at high molar strength enables capacitive deionization of saline water, *Sustainable Energy Fuels* 4 (3) (2020) 1285–1295.
- [39] E.R. Nightingale, Phenomenological theory of ion solvation, Effective radii of hydrated ions, *The Journal of Physical Chemistry* 63 (9) (1959) 1381–1387.
- [40] R.K. Kalluri, M.M. Biener, M.E. Suss, M.D. Merrill, M. Stadermann, J.G. Santiago, T. F. Baumann, J. Biener, A. Striolo, Unraveling the potential and pore-size dependent capacitance of slit-shaped graphitic carbon pores in aqueous electrolytes, *PCCP* 15 (7) (2013) 2309, <https://doi.org/10.1039/c2cp43361c>.
- [41] Y. Zhang, P. Srimuk, S. Husmann, M. Chen, G. Feng, V. Presser, Effect of pore size on the ion electrosorption and hydrogen/deuterium electrosorption using sodium chloride in H_2O and D_2O , *J. Electrochem. Soc.* 166 (16) (2019) A4158–A4167.
- [42] C. Criado, P. Galán-Montenegro, P. Velásquez, J.R. Ramos-Barrado, Diffusion with general boundary conditions in electrochemical systems, *J. Electroanal. Chem.* 488 (1) (2000) 59–63.
- [43] T.S. Mathis, N. Kurra, X. Wang, D. Pinto, P. Simon, Y. Gogotsi, Energy storage data reporting in perspective - guidelines for interpreting the performance of electrochemical energy storage systems, *Adv. Energy Mater.* 9 (2019) 1902007.
- [44] M. Mirkik, Schulze-Hardy rule and mass action law, *Nature* 190 (4777) (1961) 689–690.
- [45] J.T.G. Overbeek, The rule of Schulze and Hardy, *Pure Appl. Chem.* 52 (1980) 1151–1161.
- [46] Y. Chu, J. Chen, F. Haso, Y. Gao, J.E.S. Szymanowski, P.C. Burns, T. Liu, Expanding the Schulze-Hardy Rule and the Hofmeister Series to Nanometer-Scaled Hydrophilic Macroions, *Chemistry – A, European Journal* 24 (21) (2018) 5479–5483.
- [47] W. Nowicki, G. Nowicka, Verification of the Schulze-Hardy rule: A colloid chemistry experiment, *J. Chem. Educ.* 71 (1994) 624.
- [48] G. Trefalt, I. Szilagyi, G. Téllez, M. Borkovec, Colloidal stability in asymmetric electrolytes: Modifications of the Schulze-Hardy rule, *Langmuir* 33 (2017) 1695–1704.
- [49] Y. Marcus, Thermodynamics of solvation of ions. Part 5. —Gibbs free energy of hydration at 298.15 K, *J. Chem. Soc., Faraday Trans.* 87 (18) (1991) 2995–2999.
- [50] S. KUBOTA, S. OZAKI, J. ONISHI, K. KANO, O. SHIRAI, Selectivity on ion transport across bilayer lipid membranes in the presence of gramicidin A, *Anal. Sci.* 25 (2) (2009) 189–193.

Supporting Information

Hydration Shell Energy Barrier Differences of Sub-Nanometer Carbon Pores Enable Ion Sieving and Selective Ion Removal

Yuan Zhang,^{1,2} Jiaxing Peng,^{3,4} Guang Feng,^{3,4} and Volker Presser^{1,2,*}

¹ INM - Leibniz Institute for New Materials, Campus D2 2, 66123 Saarbrücken, Germany

² Saarland University, Campus D2 2, 66123 Saarbrücken, Germany

³ State Key Laboratory of Coal Combustion, School of Energy and Power Engineering, Huazhong University of Science and Technology (HUST), Wuhan 430074, China

⁴ Nano Interface Centre for Energy, School of Energy and Power Engineering, HUST, 430074, China

* Corresponding author's eMail: volker.presser@leibniz-inm.de

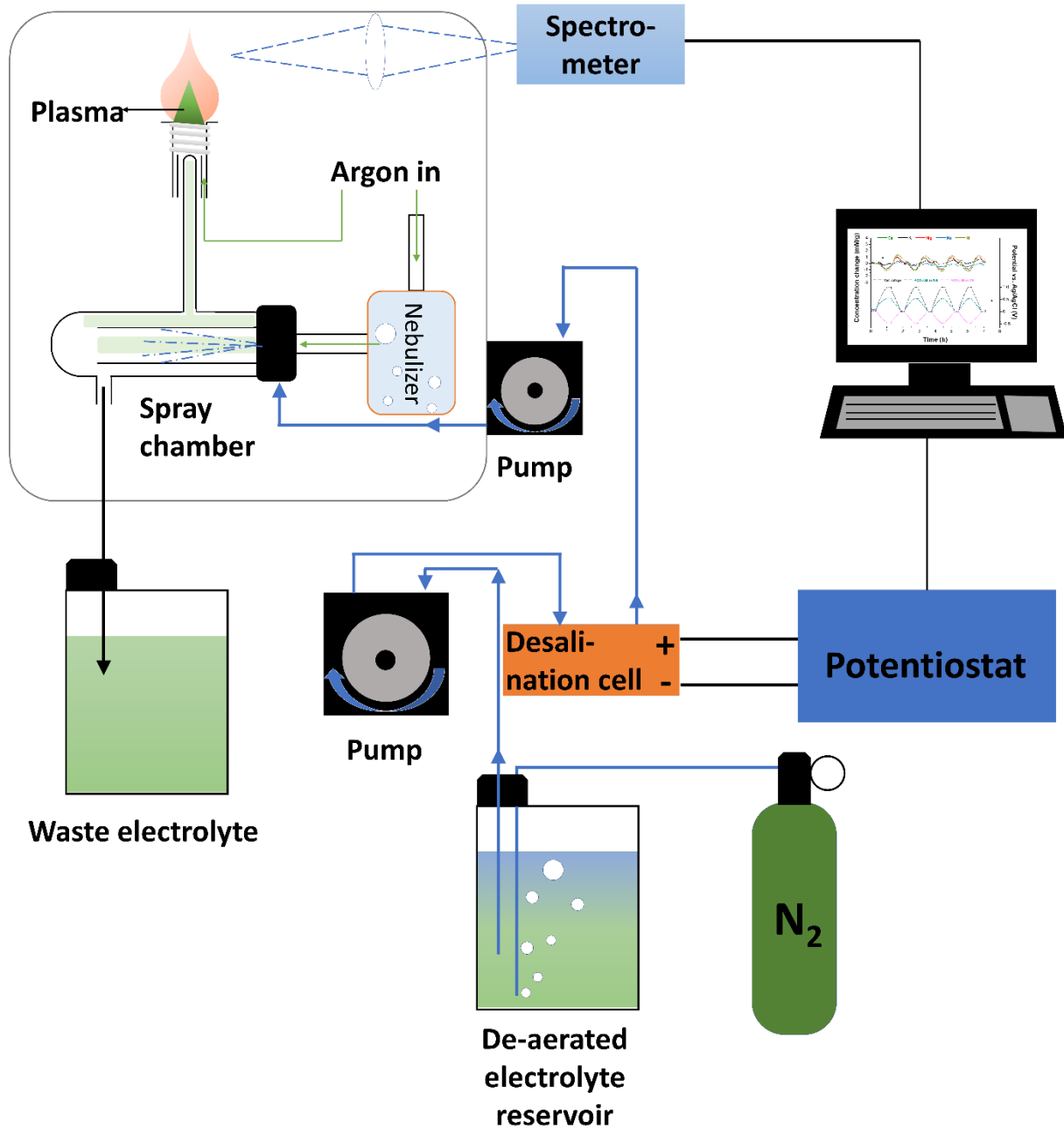


Figure S1: Schematic illustration of chemical online monitoring of the effluent stream's composition via inductively coupled plasma optical emission spectroscopy.

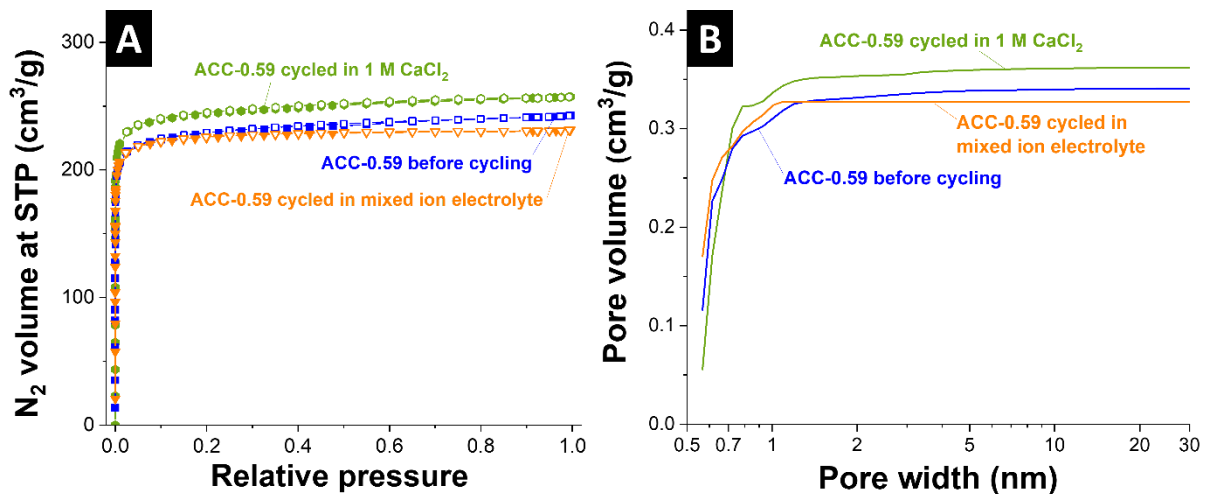


Figure S2: Nitrogen gas sorption isotherms for ACC-0.59, ACC-0.59 after CV cycling in 1 M NaCl electrolyte, and ACC-0.59 after 300 cycles in 10 mM KCl + NaCl + MgCl₂ + CaCl₂ + NiCl₂ mixture. (A) and calculated pore size distribution applying the quenched-solid density functional theory assuming slit-shaped pores (B). STP: standard temperature and pressure.

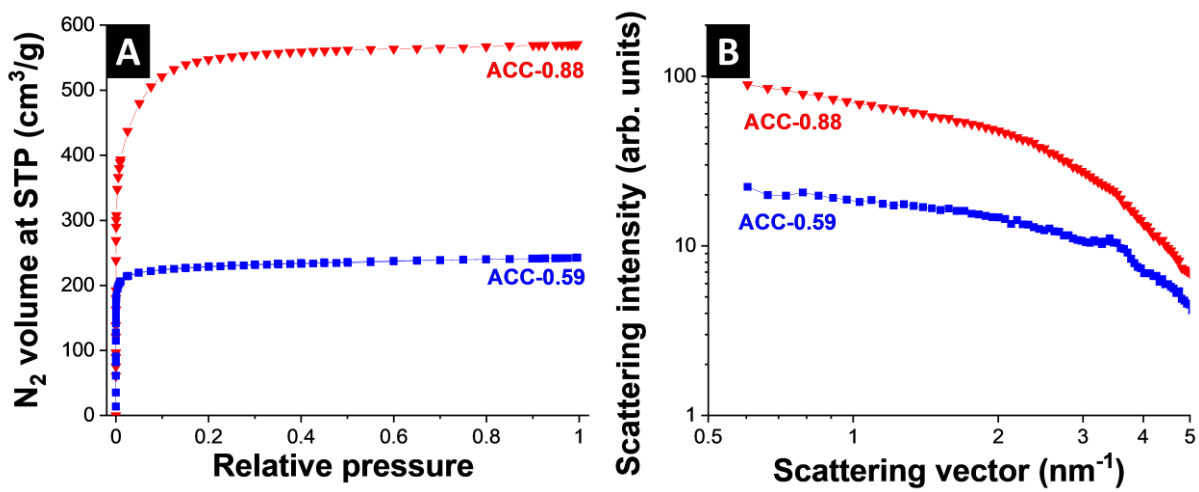


Figure S3: (A) Nitrogen gas sorption isotherms for ACC-0.59 and ACC-0.88. (B) Small-angle X-ray scattering curves of ACC-0.59 and ACC-0.88.

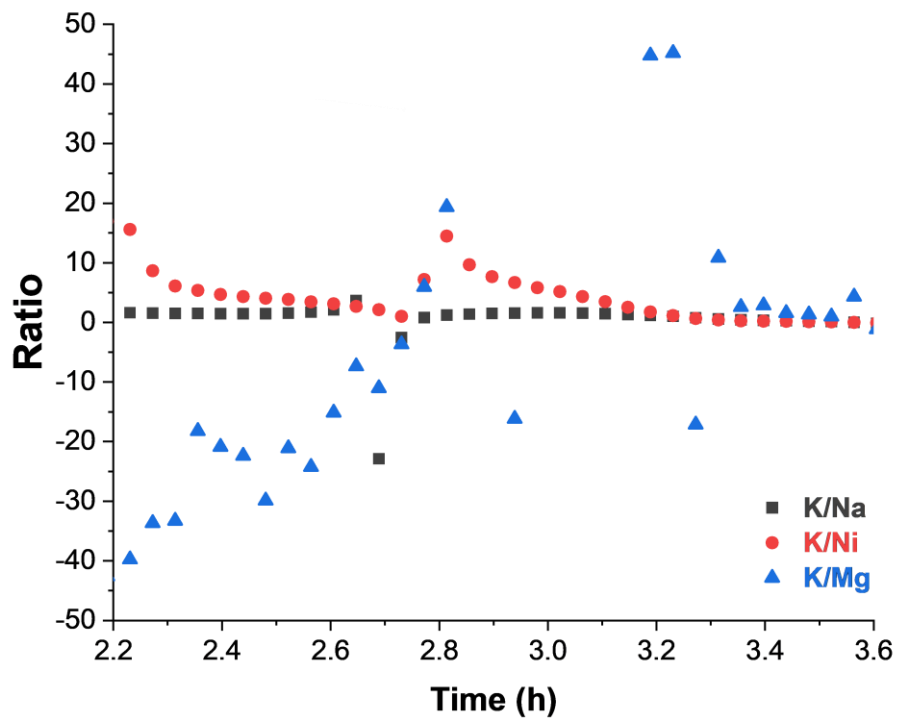


Figure S4: Concentration change ratio for K/Na, K/Ni, and K/Mg taken from Figure 8B.

4.5 Polymer ion-exchange membranes for capacitive deionization of aqueous media with low and high salt concentration

Yuan Zhang,^{1,2} Pattarachai Srimuk,^{1,2} Mesut Aslan,² Markus Gallei,³ and Volker Presser^{1,2,4}

1 INM - Leibniz Institute for New Materials, Campus D2 2, 66123, Saarbrücken, Germany

2 Department of Materials Science and Engineering, Saarland University, Campus D2 2, 66123, Saarbrücken, Germany

3 Polymer Chemistry, Saarland University, Campus D2 2, 66123, Saarbrücken, Germany

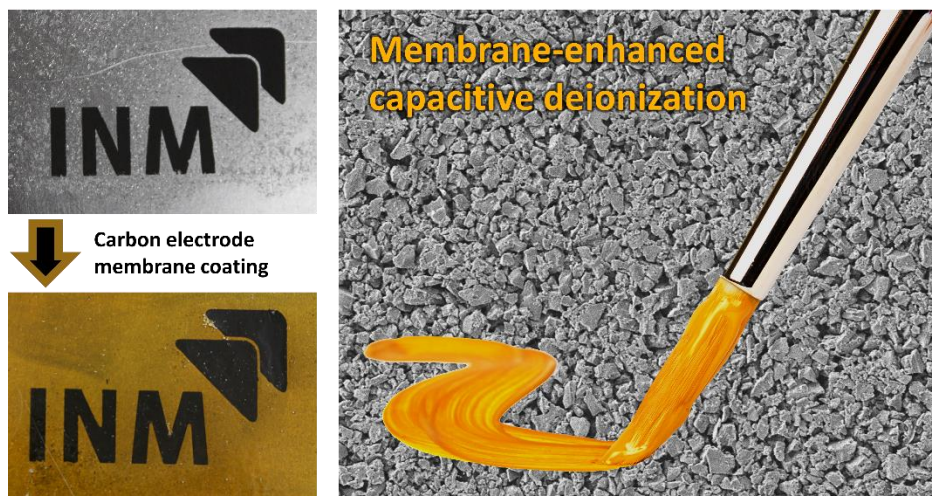
4 Saarene - Saarland Center for Energy Materials and Sustainability, Campus C4 2, 66123 Saarbrücken, Germany

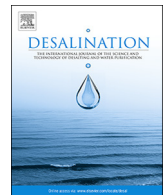
Citation:

Y. Zhang, P. Srimuk, M. Aslan, M.Gallei, V. Presser, *Polymer ion-exchange membranes for capacitive deionization of aqueous media with low and high salt concentration*, Desalination, 2020, 479: 114331. (DOI: 10.1016/j.desal.2020.114331)

Own contribution:

Methodology, validation, formal analysis, investigation, data curation, writing-original draft, writing-review & editing, visualization.





Polymer ion-exchange membranes for capacitive deionization of aqueous media with low and high salt concentration

Yuan Zhang^{a,b}, Pattarachai Srimuk^{a,b}, Mesut Aslan^b, Markus Gallei^c, Volker Presser^{a,b,*}

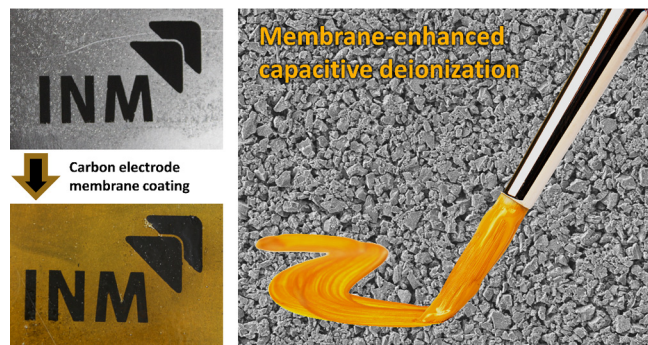
^a INM - Leibniz Institute for New Materials, Campus D2 2, 66123 Saarbrücken, Germany

^b Department of Materials Science and Engineering, Saarland University, Campus D2 2, 66123, Saarbrücken, Germany

^c Polymer Chemistry, Saarland University, Campus C4 2, 66123, Saarbrücken, Germany



GRAPHICAL ABSTRACT



ARTICLE INFO

Keywords:
Capacitive deionization
Water remediation
Desalination
Ion-exchange membrane

ABSTRACT

In this work, carbon electrode modified polymer membrane and free-standing polymer membranes are applied for desalination via capacitive deionization with microporous activated carbon. The desalination performance under different concentrations (20 mM and 600 mM) of feed water and different voltage operation mode (zero-volt and voltage-reversal operation). For the ion exchange membrane coating under 20 mM NaCl solution at a cell voltage of 0/+1 V, the desalination capacity reached 22.7 mg/g at the charge efficiency of 142.1%. In the case of the free-standing membrane, under 600 mM NaCl solution at a voltage range of -1/+1 V, the desalination capacity reached 26.0 mg/g with a charge efficiency of 61.5%. These results not only show the possibility of membrane capacitive deionization (MCDI) application in seawater desalination but also reveals different ion transport mechanisms of the coated membrane and free-standing membranes under different molar strength of feed water.

1. Introduction

Due to the rapid population growth, industrialization, contamination of available freshwater resources, and climate change, water scarcity has become one of the most challenging worldwide issues

[1,2]. Over the years, different desalination methods are studied and developed, such as distillation, reverse osmosis, electrodialysis, and capacitive deionization (CDI) [3]. As an electrochemical water treatment process, capacitive deionization has emerged as a robust, energy-efficient, and cost-effective technology suitable for the remediation of

* Corresponding author at: INM-Leibniz Institute for New Materials, Campus D2 2, 66123 Saarbrücken, Germany.
E-mail address: volker.presser@leibniz-inm.de (V. Presser).

water with low salt concentration [3–5]. By applying an electrical potential difference between two porous carbon electrodes, cations and anions flowing between these electrodes will be electro-adsorbed at the fluid/solid interface; thereby, the effluent stream shows a decreased ionic strength compared to the feedwater [6,7]. Electro-adsorbed (immobilized) ions and the corresponding electrical charges are released once the electrodes are discharged, either by shorting the electrode pair, lowering the cell bias, or by inverting the cell polarity [6,8]. Intrinsically, the process of ion electrosorption is not necessarily permselective [9,10]. At high molar strength, a 1:1 exchange of co-ions (ions with the same charge as the electrode) and counter-ions dominates the charge/discharge domain in pores larger than about 1 nm [11]. At low molar strength, once the population of co-ions has become depleted within nanopores, permselective counter-ion electrosorption dominates and enables not only charge storage but actual desalination [12].

To overcome the limitation of CDI to only be suitable for remediation of molar media below 50–100 mM, it is possible to implement an ion-exchange membrane [13]. The latter can be polymer-based or ceramic [14–16]. Depending on their permselectivity, ion-exchange membranes suppress the non-permselective ion exchange, and co-ions trapped behind the membrane may further enhance the desalination metrics. CDI with ion-exchange membranes (MCDI) has, therefore, been intensively studied as an advanced desalination technology, but most works have only explored the low-molar strength regime (i.e., below 20–50 mM NaCl). Zhao et al. proposed different operational modes (at constant voltage and constant current) and presented an extensive dataset for the energy requirement of membrane capacitive desalination [17]. In another work, Dykstra et al. showed that without energy recovery, the values of energy consumption of constant voltage and constant current operation are almost the same [18]. Meanwhile, membrane materials, fabrication methods, and commercial applications have been explored. Kim et al. coated porous carbon electrodes with cation-exchange membranes and improved the salt-removal efficiencies of MCDI cells by 27–56% compared to the CDI cell in low salt concentration (200 mg/L) at a cell voltage of 1.5 V [19]. Lee et al. applied carbon cloth coated with bromomethylated poly(2,6-dimethyl-1,4-phenylene)oxide (BPPO) and reduced interfacial resistance between the membrane and the carbon electrode; therefore, MCDI has better performance at a salt concentration of 100 mg/L from the perspective of energy consumption and charge efficiency compared to CDI [20]. Ahualli et al. used a combination of polyelectrolyte coatings on carbon electrode with ion exchange membrane and reach partially water desalination in 100 mM of NaCl solution (desalination capacity of 6 mg/g and charge efficiency of about 70%) [21]. These performance values are explained by the combination of a soft electrolyte layer, and the membrane layer enhances the accumulation of co-ions in the macropores while favoring the entrance of counter-ions [21]. Many of these studies applied cell voltages far beyond the electrochemical stability window of water of up to 1.8–2.4 V [15]. While MCDI is known to suppress carbon oxidation per peroxide formation [22], such high voltages are prone to yield reduced long-term performance and energy efficiency metrics.

While previous experimental and theoretical studies are focused on MCDI at low salt concentration [2,13,19,20,23,24], only a few works have explored MCDI for desalination of water with high molar strength, including seawater-like salinity. For example, Cho et al. explored ion-exchange membranes implemented into honeycomb-like ceramic (pore size of 10–30 µm) flow-channels for the desalination of 600 mM NaCl via suspension electrodes; while the latter did not provide values for the desalination capacity, and an overall charge efficiency of 81% was reported [25]. More recently, Tang et al. studied the MCDI system for seawater desalination by applying a vast over-potential (2.4 V) and obtained a salt removal capacity of 64.7 mg/g for 500 mM NaCl solution [15]. Accordingly, the comparative performance of MCDI at high and low molar strength and the comparison of zero-volt discharge vs. voltage-inversion remain incompletely analyzed. This includes the

comparison of free-standing membranes placed in front of the electrodes and such membranes that are coated onto the electrodes directly. In our study, we compare the performance of MCDI with free-standing ion-exchange membranes and carbon electrodes coated with an ion-exchange layer for galvanostatic operation at 0/+1 V and -1/+1 V in low (20 mM) and high (600 mM) molar strength of NaCl in aqueous media.

2. Experimental description

2.1. Materials preparation and characterization

2.1.1. Electrodes: materials and preparation

Activated carbon (AC) powder type YP-80F from Kuraray Chemicals was used as the active material for the preparation of electrodes. 1-Methyl-2-pyrrolidone, NMP (Sigma-Aldrich) was used as the solvent for the casting of the electrodes with poly(vinylidene) fluoride, PVDF (Alfa Aesar) as the polymer binder. Graphite sheets of 250 µm thickness were used as current collectors (Sigraflex, SGL Carbon). The AC film electrodes were prepared by casting NMP-based AC slurries on graphite current collector applying doctor blade method. The slurry of AC/PVDF, which has a mass ratio of 9:1 and with a solid particle content of 15 mass%, was homogenized in a speed mixer for 6 min (Hauschild Engineering).

The wet film electrodes from these slurries were applied on graphite with a doctor blade of 200 µm gap and 13 cm width. Then the wet films were kept for 15 h in the fume hood for pre-drying and afterward placed into a drying oven and dried at 115 °C for 15 h. The resulting dry thickness of the carbon coating was 140 µm with a specific resistivity of about 7 Ω·cm.

From the graphite sheets with the coated AC layer, the electrodes of the desired size were cut, and the coating area was 33.75 cm².

2.1.2. Ion-exchange membranes: materials and preparation

We used free-standing, polyester-reinforced ion exchange membranes purchased from Fumatech, namely, a cation exchange membrane type FKS-PET-130, and an anion exchange membrane type FAS-PET-130. These membranes are labeled in our manuscript as FS-CEM and FS-AEM (FS = free-standing; CEM: cation exchange membrane; AEM: anion exchange membrane). In general, we refer to such free-standing ion-exchange membranes as FS-IEM.

The solutions for the preparation of anion exchange membranes and cation exchange membranes (solutions of functionalized polyphenylene oxide in NMP) were purchased from Siontech. The electrodes with coated membranes are labeled C-AEM and C-CEM (C: coating). The membrane coating of electrodes was performed by the dip-coating method: the electrodes were dipped into the membrane solution, kept for 1 min and slowly moved out at a speed of 0.5 mm/min. Later, the membrane-coated electrodes were vertically mounted with the help of clips and pre-dried in a fume hood at room temperature until the membrane layer was no longer sticky. Then, the membrane-coated electrodes were placed between polytetrafluoroethylene plates with a 0.5 mm thick graphite distance holder and dried at room temperature for 24 h. Further drying was carried out in a vacuum oven (5 kPa), first at 40 °C for 15 h, and then at 80 °C for 5 h. As seen from Supporting information, Fig. S1A–B, the membrane coating in the dry state was about 10–15 µm. We refer to the coated ion-exchange membranes as C-IEM.

For testing of bulk membrane properties (permselectivity and thermogravimetric), we need to exclude the influence of carbon electrode; therefore, we could not directly use carbon-modified membrane electrodes. Instead, we fabricated free-standing ion exchange membranes from PPO solutions by infiltrating a polyester mesh on a polytetrafluoroethylene plate (Sefar PET 1500, thickness 210 µm, mesh opening 294 µm). These special samples are labeled C_{PET}-AEM and C_{PET}-CEM. The removal of excess solution and drying of the infiltrated

mesh in analogy to the coated electrodes were conducted as described before for FKS-PET-130 and FAS-PET-130. Thereby, our setup is different from other permselectivity test setups, such as provided in Ref. [26].

After drying the membrane-coated electrodes, as well as the free-standing polyester-supported membrane films, the membrane-coated electrodes and membranes were stored in deionized water. Before assembling the cell, the ion exchange membranes were taken out of deionized water and were soaked in the measured saltwater (either 20 mM or 600 mM NaCl water solution) for 24 h.

2.1.3. Membrane characterization

For the estimation of membranes permselectivity, a membrane testing unit (Phywe Systeme) consisting of two cylindrical compartments (each 50 mL volume connectable with screw clips) was used. The setup is shown in Supporting information, Fig. S2A, B. One chamber was filled with 1 M NaCl, and the other chamber, separated by the membrane, was filled with deionized water. The liquids in the chambers were stirred magnetically to equalize local concentration gradients. The setup was placed in a climate chamber with a constant temperature of 25 ± 1 °C. The electrical conductivity of the measured solution in the chamber initialized by deionized water was measured to estimate the permselectivity of the ion-exchange membrane (Metrohm 856). Later, the conductivity was converted in concentration by using calibration data.

Scanning electron microscopy (SEM) was performed to examine the morphologies of IEMs with a field emission scanning electron microscope (JEOL JSM-7500F) at an operating voltage of 3 kV.

For the characterization of water uptake, the dry membranes were stored in deionized water, and their time-dependent weight gain was determined with a high precision balance (Sartorius, Q-Stat).

Thermogravimetric analysis (TGA) was carried out with a Netzsch TG-209 system in synthetic air (with N₂:O₂ ratio of 8:2) by heating from 25 °C to 800 °C at a heating rate of 5 °C/min. Before measuring each sample, the empty alumina crucible was measured using the same condition to provide a reliable background. Then, the membrane samples were loaded on the same crucible that measured before to have more accurate datasets. Before the TGA measurements, the membrane samples were soaked in different salt molar strength of water solutions (deionized water, 20 mM NaCl, and 600 mM NaCl). After 24 h of soaking, the surface solution of the membranes was carefully wiped; then, the membranes were dried at 80 °C in vacuum for 12 h.

2.2. Desalination performance measurements

In this work, two different MCDI cell configurations (membrane coating and free-standing membrane assembling) are applied, as illustrated in Supporting information, Fig. S2C. Desalination measurements were carried out with a flow-by conventional CDI system by using one pair electrodes [27], which were separated by a nonconductive porous spacer (glass fiber pre-filter, Millipore, compressed thickness of a single layer: 380 µm). The electrolyte of different NaCl concentrations (20 mM, 600 mM) was pumped through the cell at a flow rate of 5 mL/min.

We used a Bio-logic VSP-300 system to determine the electrochemical performance, a Metrohm PT1000 conductometric cell to monitor the electrolyte concentration, and the pH values were recorded with a WTW SensoLyt 900P sensor probe. Following the procedure outlined in previous work [14,28], we determined values for the charge efficiency and desalination capacity. Galvanostatic charge and discharge cycling were carried out at a specific current of 0.25 A/g using different potential ranges, namely, 0/+1 V and -1/+1 V, for 200 cycles for each potential range. After both the charging and discharging process, 10 min of the potential holding (voltage floating) was applied.

The desalination capacity (DC) was determined by Eq. (1):

$$DC = \frac{v \cdot M_{salt}}{m_{tot}} \int [c(t) - c_0] dt \quad (1)$$

where M_{salt} is the molecular mass of the salt, m_{tot} is the total mass of both positive and negative electrode, c_0 and $c(t)$ are initial concentration and concentration value at time t , and v is the flow rate of feed-water stream.

The charge efficiency (CE) was calculated by Eq. (2):

$$CE (\%) = \frac{F \cdot DC}{3600 \cdot Q \cdot M_{salt}} \cdot 100\% \quad (2)$$

where F is the Faraday constant, Q is the invested charge, and DC is the desalination capacity. The invested charge in our calculation also contains the leakage current. The reproducibility of the desalination performance data was found to be in the range of 5–10% based on repeated experiments.

3. Results and discussion

3.1. Water uptake, permselectivity, and thermogravimetric analysis of the membranes

As a first characterization, we monitored the water uptake. Over the course of about one week of being immersed in water, the membranes increased their mass by 7–14 mass% (Fig. 1A). The water uptake remains below 10 mass% for FS-CEM, FS-AEM, and C_{PET}-AEM, while the values found for C_{PET}-CEM exceed that threshold slightly. An increased water uptake may indicate a lower degree of cross-linking and lower permselectivity. It is important to measure the permselectivity independently from the water uptake because the latter is a less precise diagnostic tool for ion transport metrics. Therefore, we carried out conductivity measurements in a concentration-gradient cell. A perfectly permselective membrane would negate transport of co-ions (from the point of view of the membrane). Because charge neutrality must be preserved, this would translate to a constant electrolyte conductivity of the distilled water reservoir. As can be seen in Fig. 1B, the free-standing membranes type FS-CEM and FS-AEM show the lowest increase in electrolyte conductivity of 76 µM/h and 264 µM/h, respectively. C_{PET}-AEM and C_{PET}-CEM show a significantly higher rate of concentration increase of 569 µM/h and 994 µM/h, respectively. The latter aligns well with the higher water-uptake of C_{PET}-CEM as well. The generally lower permselectivity of C_{PET}-AEM and C_{PET}-CEM may be explained by an overall lower degree of cross-linking in these self-manufactured membranes [29,30]. From the results obtained on C_{PET}-AEM and C_{PET}-CEM, we could expect similar permselectivity behavior of C-IEMs.

We carried out a thermogravimetric analysis (TGA) to assess the ion-uptake of the ion exchange membranes after soaking in aqueous media with different salt concentrations. We would expect pickup of some ions which would be electrostatically immobilized at the intrinsic charge center within the IEM structure. As seen in Fig. 2, all IEMs soaked in distilled water, and all AEMs show no significant residual mass after heating to 800 °C. This is in line with the absence of ion and the ability of chloride to be completely volatilized at elevated temperatures [31,32]. More information about the ion-uptake is accessible for CEMs. After soaking in 20 mM NaCl, we see for C-CEM and FS-CEM a virtually identical mass loss of 95% after TGA measurements (Fig. 2B). After soaking in 600 mM, the resulting mass-loss of FS-CEM is 92% and 86% for C-CEM (Fig. 2C). The higher residual mass for C-CEM after soaking in 600 mM aqueous NaCl solution agrees with the higher water uptake and lower permselectivity, indicating the presence of more salt solution stored in the membrane. This difference is likely invisible in 20 mM because of the low molar strength and the limitations of the TGA method.

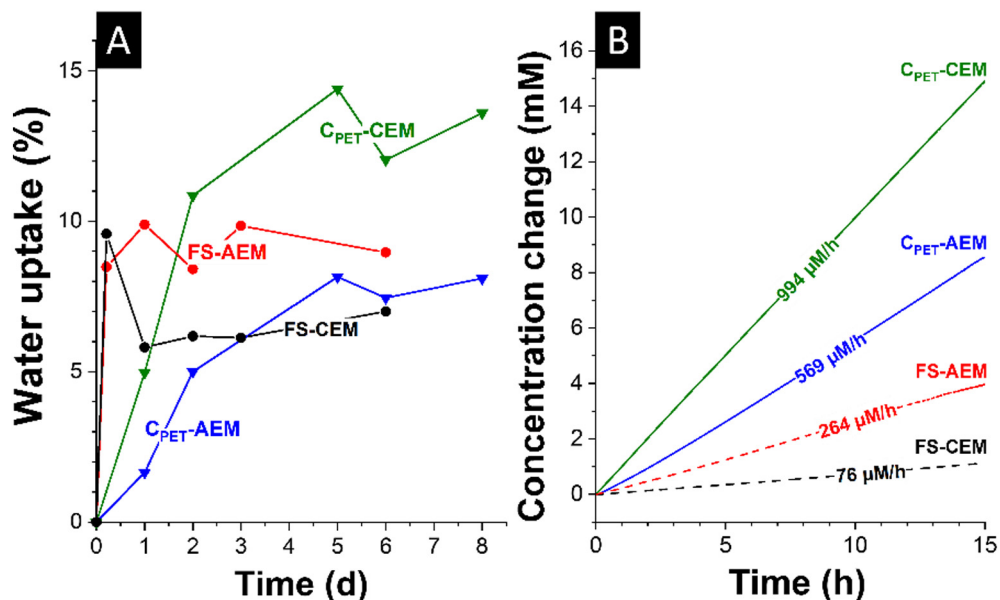


Fig. 1. (A) Water uptake of the the ion exchange membranes using distilled water over time. (B) The concentration changes between a reservoir with distilled water and aqueous 1 M NaCl. The data are provided for free-standing membranes FS-CEM, FS-AEM, C_{PET}-CEM, and C_{PET}-AEM.

3.2. Water desalination measurement

To observe the ion adsorption and desorption kinetics, concentration changes of the saltwater under different molar strength and different potential ranges during the charging and discharging process were analyzed. Our data compare free-standing membranes (130 μm thick; FS-AEM and FS-CEM) with coated membranes (10 μm dry thickness; C-AEM and C-CEM) and CDI cells without membranes. For all experiments, the mass of the carbon electrodes is the same (160 mg), for the CDI experiments without membranes, the mass of the carbon electrodes are all 150 mg. Table 1 lists the performance metrics for all experiments.

As common for MCDI, the concentration decreases during the charging process for all membranes at high salt concentration, when the potential range of 0/+1 V is applied (Fig. 3A). The reverse is observed during discharging. When using the free-standing membranes (FS-AEM, FS-CEM), there is a faster change in the concentration compared to the coated membranes. This result indicates faster ion transport kinetics in FS-AEM and FS-CEM membranes. In the low-molar regime (20 mM), the peak concentration change is reached faster compared to operation in 600 mM NaCl. The latter regime also shows a broader (flattened) concentration profile at an overall lower amplitude (Fig. 3A–B).

The general feature of desalination during charging and ion-release during discharging is maintained for 20 mM and 600 mM NaCl, also when reversing the potential (-1/+1 V; Fig. 3C–D); however, the conductivity change profiles are broader and overall at a lower amplitude. Inverting the potential allows for transferring more charge to the electrodes, namely, charge that corresponds to a total potential difference of $\Delta 2$ V compared to a value of $\Delta 1$ V when just cycling between +1 V and 0 V. It also presents the unique situation that ion transport across the ion exchange membrane sees, for example, cations rushing toward the negative electrode and then being actively ejected during inversion of the potential. While discharging to 0 V only ejects counter-ions at a level that re-establishes the initial uncharged state condition (1,1 of anions and cations ideally), voltage inversion (-1 V) will lead to an active depletion of counter-ions relative to the co-ions since the latter cannot move to the vicinity of the electrode under the electric field across the counter-ion-selective ion-exchange membrane. The lower permselectivity of the coated membranes allow co-ions transport across the membrane and yield, because of this effect, a double-peak during desalination and electrode regeneration (Fig. 3C). This phenomenon relates to the permselectivity of the membranes [4]. Our C-IEMs greatly improved counter-ion adsorption under low concentration of the feedwater (Fig. 3B, D), but the reduced

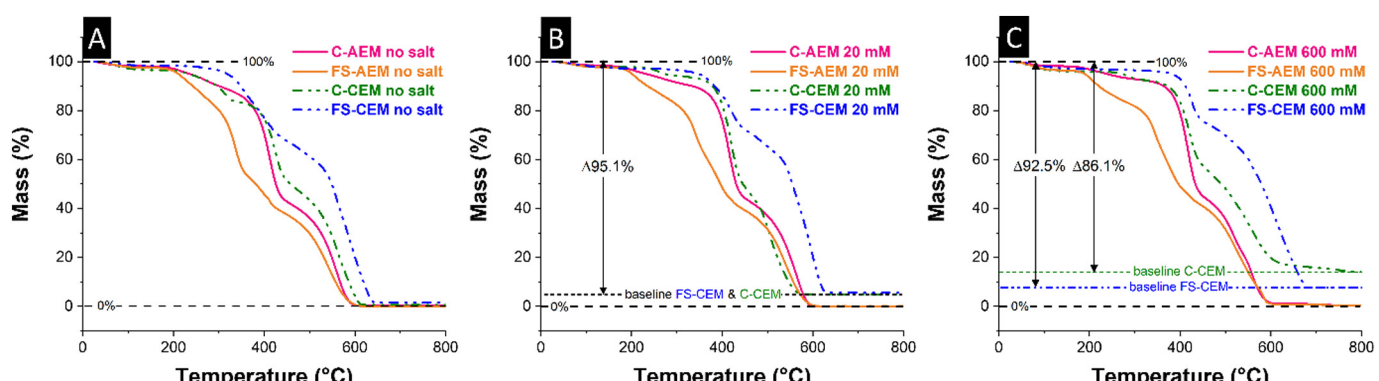


Fig. 2. TGA results of the different ion-exchange membranes soaked in different aqueous solutions (no salt = no salt was added to deionized water). (A) C-IEMs and FS-IEMs soaked in deionized water; (B) C-IEMs and FS-IEMs soaked in 20 mM NaCl aqueous solution; (C) C-IEMs and FS-IEMs soaked in 600 mM NaCl aqueous solution.

Table 1

Comparison of desalination performance and longevity of two types of MCDI cells and CDI cells without membranes at different charge/discharge potential regimes and different salt concentrations.

	NaCl concentration (mM)	Voltage operation	Desalination capacity (mg/g)				Charge efficiency (%)			
			1st cycle	10th cycle	180th cycle	Ø	1st cycle	10th cycle	180th cycle	Ø
C-IEM	20	0/+1 V	22.6	19.3	18.0	18.6	142	134	132	135
		-1/+1 V	22.8	24.5	21.7	22.8	83	87	66	75
C-IEM	600	0/+1 V	8.3	7.6	9.0	8.7	45	33	40	39
		-1/+1 V	10.5	17.4	14.6	15.2	38	62	52	54
FS-IEM	20	0/+1 V	9.4	9.8	10.1	9.8	83	86	89	88
		-1/+1 V	12.0	13.5	16.7	15.5	76	81	85	83
FS-IEM	600	0/+1 V	11.8	11.6	11.5	11.3	54	61	63	62
		-1/+1 V	26.0	25.8	25.4	25.6	62	62	59	60

	NaCl concentration (mM)	Voltage operation	Desalination capacity (mg/g)				Charge efficiency (%)			
			1st cycle	10th cycle	100th cycle	Ø	1st cycle	10th cycle	100th cycle	Ø
Without IEM	20	0/+1 V	4.3	3.7	2.8	3.2	57	49	39	43
		-1/+1 V	2.3	1.9	1.4	1.6	12	10	7	9
	600	0/+1 V	1.7	0.9	0.9	0.8	8	4	5	4
		-1/+1 V	1.0	1.1	2.3	2.5	2	2	5	5

permselectivity, as seen from Fig. 3A, C is related to co-ion ejection. The double-peak (Fig. 3C) is more pronounced when ejecting the ionic species compared to the desalination phase. Also, the C-IEMs do not show the double-peak profile at low molar strength (20 mM). According

to Donnan's theory, as the electrolyte concentration increases, the number of co-ions in the membrane phase also increases, which gives rise to the double-peak feature in the case of C-IEM [33].

Fig. 4 plots the desalination capacity and charge efficiency profile

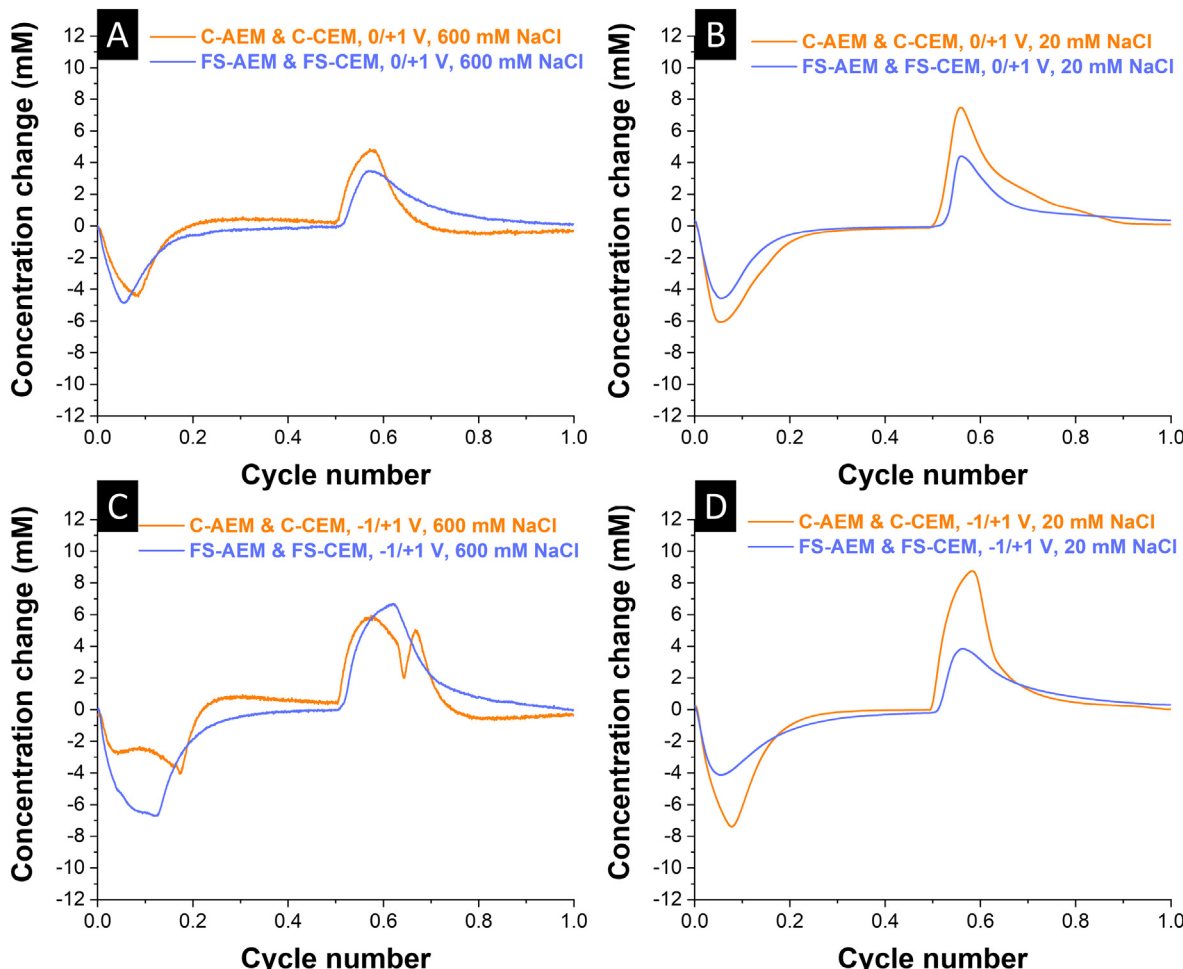


Fig. 3. MCDI concentration change profiles for C- and FS-membranes at different salt concentration regimes (A,C: 600 mM; B,D: 20 mM) and charge/discharge protocols (A,B: 0/+1 V; C,D: -1/+1 V).

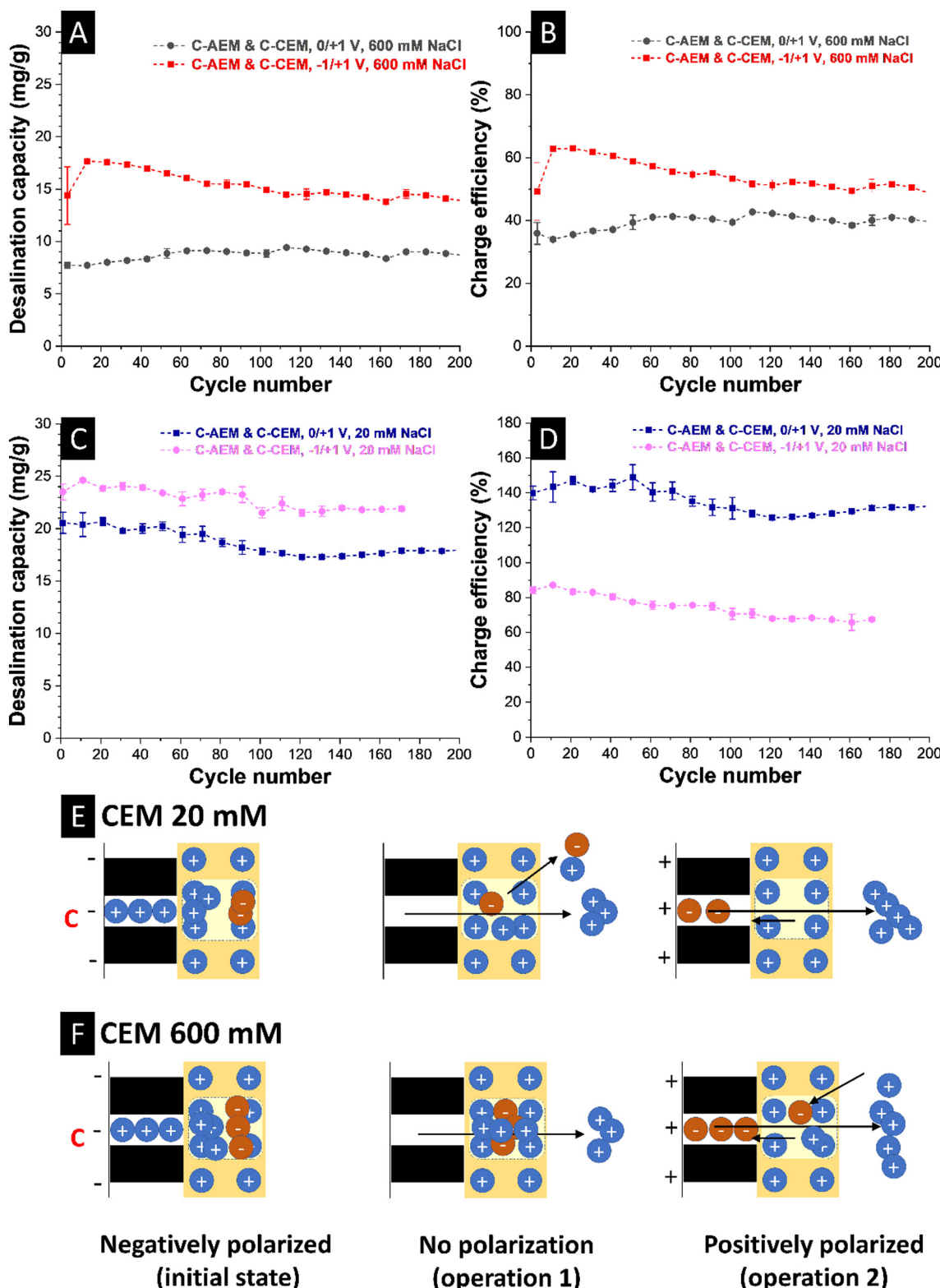


Fig. 4. Water desalination performance of membrane-coated electrodes C-AEM and C-CEM. (A–B) Desalination capacity and charge efficiency profile of 200 cycles in 600 mM NaCl water solution and (C–D) 20 mM NaCl water solution. Data were obtained from galvanostatic measurements with the potential range of 0/+1 V and -1/+1 V using a specific current of 0.25 A/g. (E–F) Schematic graph of the mechanism of the ion transport in C-CEM and the carbon electrode.

for C-IEM cells at different operational modes (i.e., zero-volt discharge and voltage-reversal). The average numbers of each 10 cycles and the standard errors in this work are all calculated and plotted. In the case of a high concentration of feed water (Fig. 4A–B), the MCDI cell under reversed potential range (-1/+1 V) shows a higher desalination

capacity (14 mg/g) compared to the MCDI cell under the potential range of 0/+1 V (9 mg/g). The charge efficiency of reversed potential operation is similar (44%) to the one obtained at 0/+1 V operation (40%) after 200 cycles. These low values align with the limited permselectivity of our C-IEMs.

From Fig. 4C–D, we see that the desalination capacity for deionization of 20 mM aqueous NaCl is increased compared to that at high molarity (600 mM). For the potential range of 0/+1 V, the desalination capacity is slightly lower (16 mg/g) compared to that in the potential range of -1/+1 V (21 mg/g). The charge efficiency for the potential range of 0/+1 V exceeds 100% to reach a value of 140%; after 200 cycles, the charge efficiency remains beyond 130%, while in the case reversed potential operation, the charge efficiency is 80%. At first, exceeding the theoretical limit of 100%, and doing so for 200 cycles, seems implausible. However, this effect can be explained because ion immobilization is not only just accomplished by the carbon electrode via ion electrosorption but also by the low permselectivity of ion exchange membranes makes them act as an additional soft electrode [34–36]. Similarly, Tang et al. reported (in their Supporting information Fig. S7) a charge efficiency in excess of 100% for MCDI [15].

In Fig. 4E–F, the desalination mechanisms are illustrated, according to the estimation of Zabolosky et al., while the void radius exceeds 1.5 nm, the electro-neutral solution will fill the space, and therefore extra ions will be stored in the void [34,37]. When the applied potential is 0/+1 V in low molarity feed water condition, during the charging and discharging process, counter ions will be stored in the pores of the carbon electrodes and also within the pores of ion-exchange membranes. To contribute toward the actual desalination, the maximum storage capacity of ions within the IEM must be higher than the ion concentration within the saline medium. This seems to be the case in 20 mM NaCl, and accordingly, we see a boost of charge efficiency beyond 100%. During charging and discharging at the potential range of 0/+1 V, more counter-ions are attracted in the pores of the membrane, and these ions diffuse toward the electrode side under the electric field. During the discharging process, due to the higher charge density (concentration) in the pores of the membranes, extra ions (both counter and co-ions) stored in the pores will diffuse to the bulk of electrolyte under the concentration gradient. In the case of 600 mM, the IEMs do not provide extra ion storage capacity, and their chemical charge cannot enable added-value for the desalination process. In the case of reversed potential (Fig. 4C–D), instead of co-ion ejection, co-ions will diffuse under the electrostatic force toward carbon electrode and adsorbed on the surface of the pores when the potential further changed from 0 to -1 V. In this case, a portion of the charge storage is compensated by co-ion adsorption which causes a lower charge capacity (Fig. 4D).

As seen in Fig. 5A–B, FS-IEMs operated in 600 mM NaCl provide a desalination capacity of 12 mg/g for 0/+1 V and of 25 mg/g for -1/+1 V. This performance is much higher compared to C-IEMs, which aligns with the much better ion permselectivity of the former. The corresponding charge efficiency is around 60% for both operation modes of 0/+1 V and -1/+1 V. Still, a performance of 25 mg/g for seawater-like NaCl concentrations is as good as most carbon-based CDI works at concentrations below 20 mM with a value range of 10–30 mg/g [38]. As the concentration of feed water decreased to 20 mM (Fig. 5C–D), the desalination capacity is 10 mg/g for 0/+1 V and 17 mg/g for -1/+1 V after 200 cycles. Although the reversed potential operation shows slightly lower charge efficiency compared to that with 0/+1 V potential range, the values are very similar (ca. 84%). This might be related to the less water uptake in FS-IEMs and the amount of ion diffusion from the void of membranes to the electrolyte when the potential change from 1 V to 0 V under the concentration gradient (from the membrane to low concentration electrolyte) is comparably small.

Fig. 5E–F schematically depicts the influence of permselectivity (or reduction thereof) on the desalination process via capacitive deionization. For FS-IEM cells, the number of the co-ions store behind the membrane is essential to enable an enhanced counter-ion uptake and higher desalination performance (Fig. 5E, F). In 600 mM NaCl solution, there is a larger number of co-ions stored behind the membrane compared to 20 mM NaCl solution, thus enabling a higher desalination

performance. The reduced permselectivity and larger water-uptake of C-IEMs will lead to an increased number of counter-ions within the IEM layer. This effect allows the C-IEM to serve as a soft-electrode and increases the charge efficiency; however, this is accomplished only at low molar strength. In general (Table 1), the higher permselectivity of FS-IEMs allows at all regimes for a higher desalination capacity when normalized to the electrode mass (Fig. 6A) or membrane area (Fig. 6B).

For comparison, the CDI performance of the carbon electrodes in absence of an ion-exchange membrane are shown in Supporting information, Fig. S3, Fig. 6, and Table 1. Using 20 mM NaCl solution at the potential range of 0/+1 V, we see a desalination performance of 3 mg/g at a charge efficiency of 43%. For the reversed potential operation (-1/+1 V), the number of co-ions in the carbon pores drastically increased, which resulted in the decreased desalination capacity (2 mg/g) and charge efficiency (9%). As for the CDI cell in the 600 mM NaCl solution, the desalination performance is extremely low both at the potential range of 0/+1 V (1 mg/g, 4%) and -1/+1 V (3 mg/g, 5%) due to low permselective charge storage [11].

Fig. 7 shows the Kim Yoon plot of the different MCDI cells under different molar strength and different operation modes. Under low concentration at the voltage operation of both 0/+1 V and -1/+1 V, C-IEMs shows higher desalination capacity and desalination rate. At the high concentration condition at two different voltage operation modes, FS-IEMs shows higher desalination performance. C-IEM in 600 mM NaCl solution at -1/+1 V shows the lowest desalination rate, which indicates the slowest ion transport during the desalination process. This could result from the ion exchange process inside of the C-IEM membrane, which has a reduced permselectivity compared to FS IEMs and voltage range of 0/+1 V data sets. For FS-IEMs, in different potential windows at low molarity, there is no significant difference in desalination rate in the case of FS-IEMs at different potential ranges. Instead, at high molarity, FS-IEM cell shows a higher desalination rate at the potential range of -1/+1 V. This phenomenon indicates two different ion transport (desalination) mechanisms of C-IEM cells and FS-IEM cells. The C-IEM cell at low molar strength shows no water channel between the membrane and electrode, and high charge efficiency and desalination capacity are dominated by the added number of counter-ions (ion diffusion under the electric field) inside of the membranes. For FS-IEM cells with the presence of a water channel between membrane and electrode, and better permselectivity of the membranes, co-ions in the water channel between the membrane and electrodes makes the essential contribution of high desalination performance of an MCDI cell.

4. Conclusions

In this work, we compared the desalination performance for two different types of ion-exchange membranes (carbon electrode modified and free-standing) and comparing zero-volt and voltage-reversal operation for 20 mM and 600 mM NaCl aqueous solutions. Coated membranes enable per reduced permselectivity the higher ion uptake capacity, and enhanced desalination performance at low molar strength. This benefit disappears at high molar concentration. The best performance at the high molar strength of seawater-like 600 mM NaCl was found to be 25 mg/g for FS-IEMs. The charge efficiency at that concentration regime is low, with only about 60%, but these data still show the ability to use carbon electrodes for sweater desalination as long as membranes are implemented. This work reveals the different working mechanisms of two different MCDI systems under different concentrations and different voltage operations and provides a possibility of seawater desalination application. Besides, our results also show that membranes with worse permselectivity can also benefit the desalination performance in the case of membrane coating.

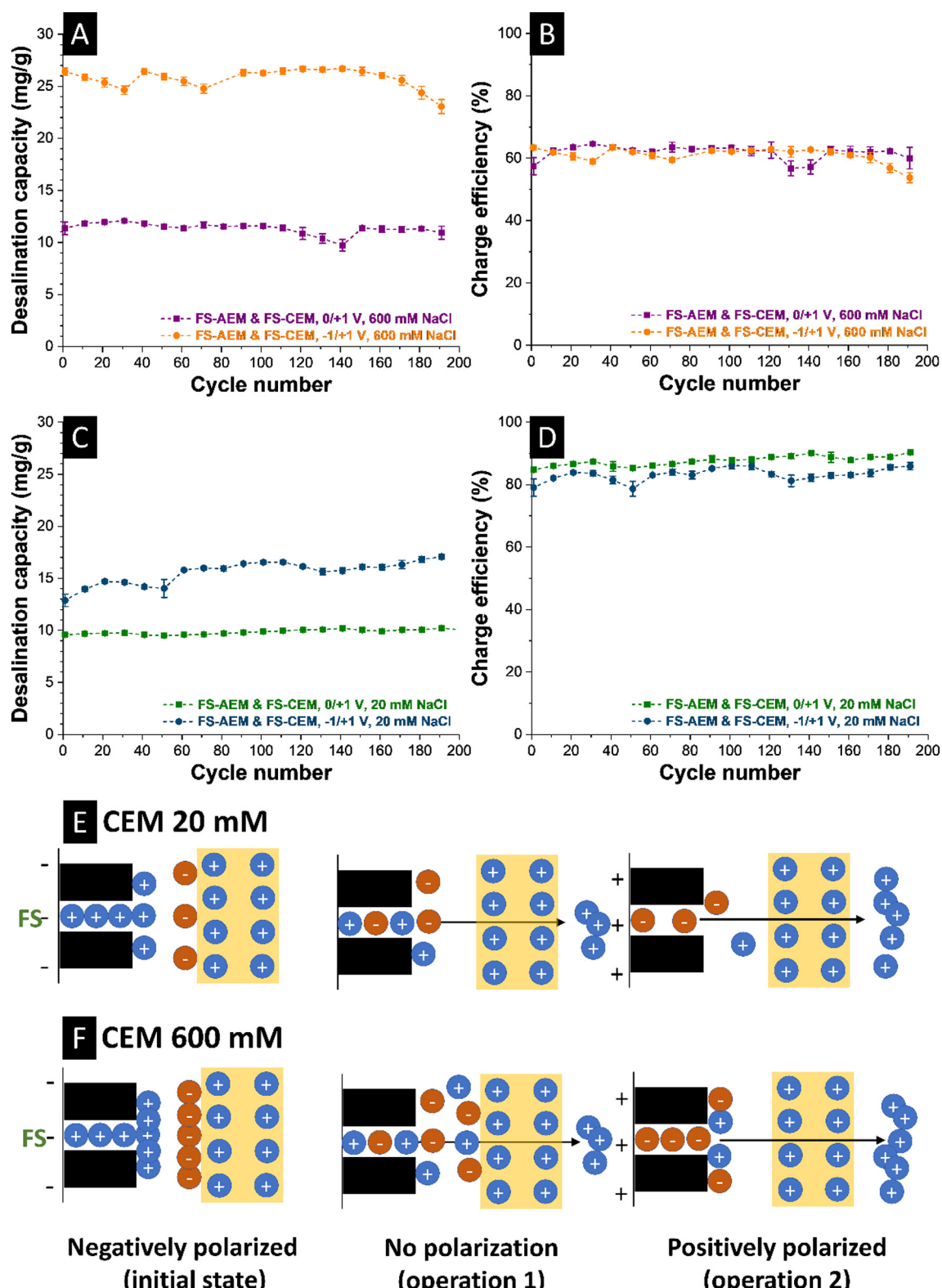


Fig. 5. Water desalination performance of free-standing ion-exchange membranes FS-AEM and FS-CEM. (A–B) Desalination capacity and charge efficiency profile of 200 cycles in 600 mM NaCl water solution and (C–D) in 20 mM NaCl water solution. Data were obtained from galvanostatic measurements with the potential range of 0/+1 V and -1/+1 V using a specific current of 0.25 A/g. (E–F) Schematic graph of the mechanism of the ion transport in FS-CEM and the carbon electrode.

CRediT authorship contribution statement

Yuan Zhang: Investigation, Data curation, Writing - original draft, Writing - review & editing. **Pattarachai Srimuk:** Conceptualization, Data curation, Writing - original draft, Writing -

review & editing. **Mesut Aslan:** Supervision, Writing - original draft, Writing - review & editing. **Markus Gallei:** Writing - original draft, Writing - review & editing. **Volker Presser:** Conceptualization, Supervision, Writing - original draft, Writing - review & editing.

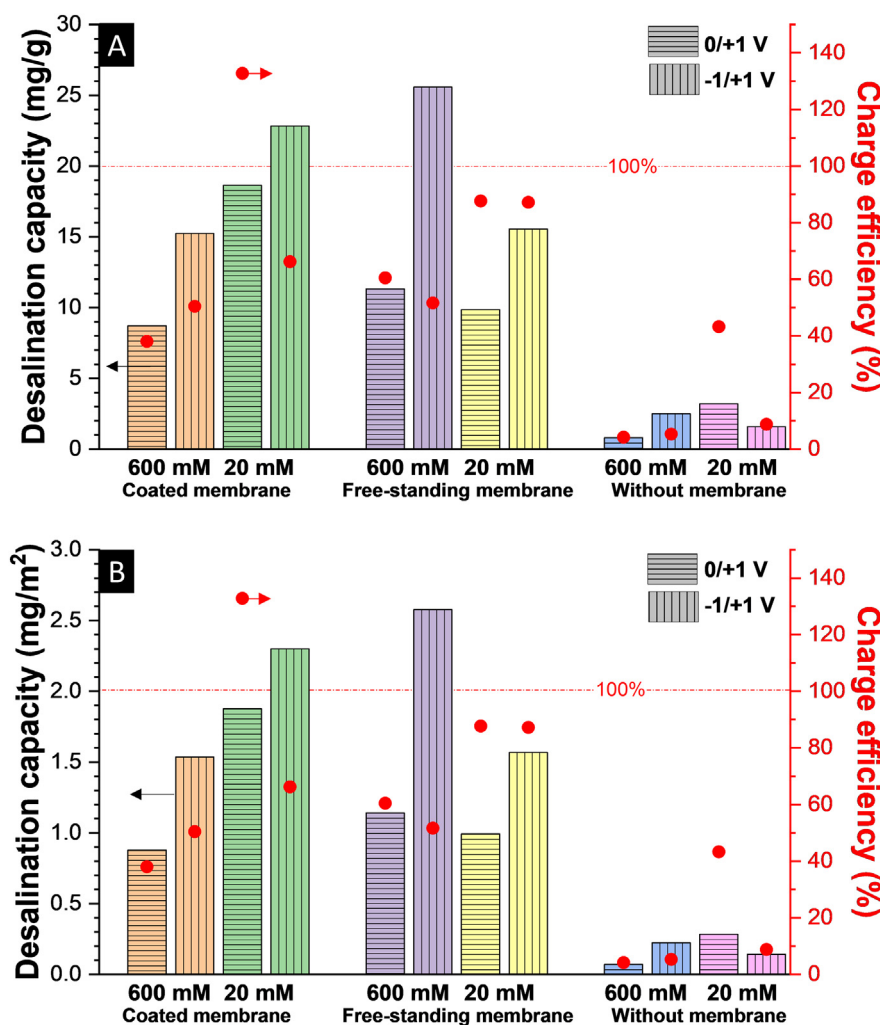


Fig. 6. MCDI/CDI performance comparison at different charge/discharge potential regimes and different salt concentrations. (A) Normalized to electrode mass, (B) normalized to membrane area.

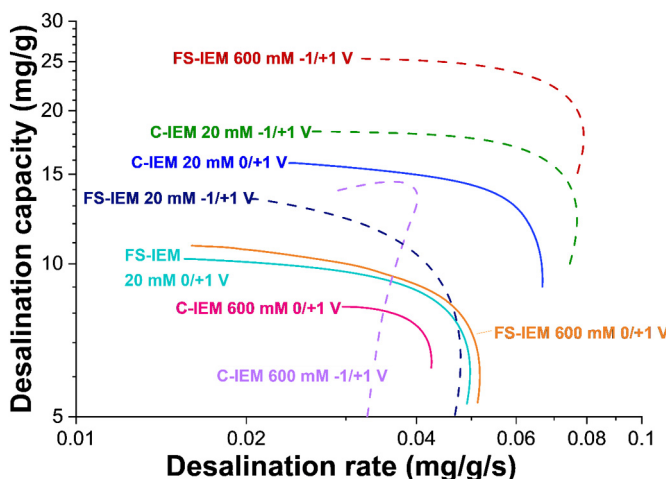


Fig. 7. Kim-Yoon plot of the different MCDI cells at different charge/discharge potential regimes and different salt concentrations.

Declaration of competing interest

The authors declare that they have no known competing financial interests or personal relationships that could have appeared to influence the work reported in this paper.

Acknowledgments

The authors thank Eduard Arzt (INM) for his continuing support. We thank Ingrid Grobelsek (INM) for her support with scanning electron microscopy.

Appendix A. Supplementary data

Supplementary data to this article can be found online at <https://doi.org/10.1016/j.desal.2020.114331>.

References

- [1] R.F. Service, Desalination freshens up, *Science* 313 (2006) 1088–1090.
- [2] M. Elimelech, W.A. Phillip, The future of seawater desalination: energy, technology, and the environment, *Science* 333 (2011) 712–717.
- [3] M.A. Anderson, A.L. Cudero, J. Palma, Capacitive deionization as an electrochemical means of saving energy and delivering clean water. Comparison to present desalination practices: will it compete? *Electrochim. Acta* 55 (2010) 3845–3856.
- [4] S. Porada, R. Zhao, A. van der Wal, V. Presser, P.M. Biesheuvel, Review on the science and technology of water desalination by capacitive deionization, *Prog. Mater. Sci.* 58 (2013) 1388–1442.
- [5] Q. Dong, G. Wang, T. Wu, S. Peng, J. Qiu, Enhancing capacitive deionization performance of electrospun activated carbon nanofibers by coupling with carbon nanotubes, *J. Colloid Interface Sci.* 446 (2015) 373–378.
- [6] M.E. Suss, S. Porada, X. Sun, P.M. Biesheuvel, J. Yoon, V. Presser, Water desalination via capacitive deionization: what is it and what can we expect from it? *Energy Environ. Sci.* 8 (2015) 2296–2319.
- [7] G. Amy, N. Ghaffour, Z. Li, L. Francis, R.V. Linares, T. Missimer, S. Lattemann,

- Membrane-based seawater desalination: present and future prospects, *Desalination* 401 (2017) 16–21.
- [8] T. Kim, J.E. Dykstra, S. Porada, A. van der Wal, J. Yoon, P.M. Biesheuvel, Enhanced charge efficiency and reduced energy use in capacitive deionization by increasing the discharge voltage, *J. Colloid Interface Sci.* 446 (2015) 317–326.
- [9] P.M. Biesheuvel, S. Porada, M. Levi, M.Z. Bazant, Attractive forces in microporous carbon electrodes for capacitive deionization, *J. Solid State Electrochem.* 18 (2014) 1365–1376.
- [10] C. Prehal, C. Koczwarra, H. Amenitsch, V. Presser, O. Paris, Salt concentration and charging velocity determine ion charge storage mechanism in nanoporous supercapacitors, *Nat. Commun.* 9 (2018) 4145.
- [11] S. Bi, Y. Zhang, L. Cervini, T. Mo, J.M. Griffin, V. Presser, G. Feng, Permselective ion electrosorption of subnanometer pores at high molar strength enables capacitive deionization of saline water, *Sustainable Energy & Fuels* (2020), <https://doi.org/10.1039/c9se00996e>.
- [12] N. Shpigel, M.D. Levi, S. Sigalov, D. Aurbach, L. Daikhin, V. Presser, Novel in situ multiharmonic EQCM-D approach to characterize complex carbon pore architectures for capacitive deionization of brackish water, *J. Phys. Condens. Matter* 28 (2016) 114001.
- [13] P.M. Biesheuvel, A. van der Wal, Membrane capacitive deionization, *J. Membr. Sci.* 346 (2010) 256–262.
- [14] J. Lee, P. Srimuk, R.L. Zornitta, M. Aslan, B.L. Mehdi, V. Presser, High electrochemical seawater desalination performance enabled by an iodide redox electrolyte paired with a sodium superionic conductor, *ACS Sustain. Chem. Eng.* 7 (2019) 10132–10142.
- [15] K. Tang, Y. Kim, J. Chang, R.T. Mayes, J. Gabitto, S. Yiacoumi, C. Tsouris, Seawater desalination over-potential membrane capacitive deionization: opportunities and hurdles, *Chem. Eng. J.* 357 (2019) 103–111.
- [16] J.H. Choi, D.J. Yoon, The maximum allowable charge for operating membrane capacitive deionization without electrode reactions, *Sep. Purif. Technol.* 215 (2019) 125–133.
- [17] R. Zhao, P.M. Biesheuvel, A. van der Wal, Energy consumption and constant current operation in membrane capacitive deionization, *Energy Environ. Sci.* 5 (2012) 9520–9527.
- [18] J.E. Dykstra, S. Porada, A. van der Wal, P.M. Biesheuvel, Energy consumption in capacitive deionization - constant current versus constant voltage operation, *Water Res.* 143 (2018) 367–375.
- [19] Y.J. Kim, J.H. Choi, Improvement of desalination efficiency in capacitive deionization using a carbon electrode coated with an ion-exchange polymer, *Water Res.* 44 (2010) 990–996.
- [20] J.Y. Lee, S.J. Seo, S.H. Yun, S.H. Moon, Preparation of ion exchanger layered electrodes for advanced membrane capacitive deionization (MCDI), *Water Res.* 45 (2011) 5375–5380.
- [21] S. Ahualli, S. Orozco-Barrera, M.D.M. Fernandez, A.V. Delgado, G.R. Iglesias, Assembly of soft electrodes and ion exchange membranes for capacitive deionization, *Polymers* 11 (2019) 1556.
- [22] D. He, C.E. Wong, W. Tang, P. Kovalsky, T.D. Waite, Faradaic reactions in water desalination by batch-mode capacitive deionization, *Environmental Science & Technology Letters* 3 (2016) 222–226.
- [23] J.-B. Lee, K.-K. Park, H.-M. Eum, C.-W. Lee, Desalination of a thermal power plant wastewater by membrane capacitive deionization, *Desalination* 196 (2006) 125–134.
- [24] L. Wang, S. Lin, Membrane capacitive deionization with constant current vs. constant voltage charging: which is better? *Environ. Sci. Technol.* 52 (7) (2018) 4051–4060.
- [25] Y. Cho, K.S. Lee, S. Yang, J. Choi, H.R. Park, D.K. Kim, A novel three-dimensional desalination system utilizing honeycomb-shaped lattice structures for flow-electrode capacitive deionization, *Energy Environ. Sci.* 10 (2017) 1746–1750.
- [26] L. Cseri, J. Baugh, A. Alabi, A. Altafaj, L. Zou, R.A.W. Dryfe, P.M. Budd, G. Szekely, Graphene oxide–polybenzimidazolium nanocomposite anion exchange membranes for electrodialysis, *J. Mater. Chem. A* 6 (2018) 24728–24739.
- [27] M. Aslan, M. Zeiger, N. Jäckel, I. Grobelsek, D. Weingarth, V. Presser, Improved capacitive deionization performances of mixed hydrophobic/hydrophilic activated carbon electrodes, *J. Phys. Condens. Matter* 28 (2016) 114003.
- [28] J. Lee, P. Srimuk, R. Zwingelstein, R.L. Zornitta, J. Choi, C. Kim, V. Presser, Sodium ion removal by hydrated vanadyl phosphate for electrochemical water desalination, *J. Mater. Chem. A* 7 (2019) 4175–4184.
- [29] A. Hassanvand, K. Wei, S. Talebi, G.Q. Chen, S.E. Kentish, The role of ion exchange membranes in membrane capacitive deionisation, *Membranes* 7 (2017) 54.
- [30] S. He, L. Liu, X. Wang, S. Zhang, M.D. Guiver, N. Li, Azide-assisted self-crosslinking of highly ion conductive anion exchange membranes, *J. Membr. Sci.* 509 (2016) 48–56.
- [31] J. Kamcev, D.R. Paul, B.D. Freeman, Effect of fixed charge group concentration on equilibrium ion sorption in ion exchange membranes, *J. Mater. Chem. A* 5 (2017) 4638–4650.
- [32] G.M. Geise, L.P. Falcon, B.D. Freeman, D.R. Paul, Sodium chloride sorption in sulfonated polymers for membrane applications, *J. Membr. Sci.* 423–424 (2012) 195–208.
- [33] F.G. Donnan, The theory of membrane equilibria, *Chem. Rev.* 1 (1924) 73–90.
- [34] V.I. Zabolotsky, V.V. Nikonenko, Effect of structural membrane inhomogeneity on transport properties, *J. Membr. Sci.* 79 (1993) 181–198.
- [35] T. Luo, S. Abdu, M. Wessling, Selectivity of ion exchange membranes: a review, *J. Membr. Sci.* 555 (2018) 429–454.
- [36] K.-D. Kreuer, S.J. Paddison, E. Spohr, M. Schuster, Transport in proton conductors for fuel-cell applications: simulations, elementary reactions, and phenomenology, *Chem. Rev.* 104 (2004) 4637–4678.
- [37] K.-D. Kreuer, Ion conducting membranes for fuel cells and other electrochemical devices, *Chem. Mater.* 26 (2014) 361–380.
- [38] Y. Cheng, Z. Hao, C. Hao, Y. Deng, X. Li, K. Li, Y. Zhao, A review of modification of carbon electrode material in capacitive deionization, *RSC Adv.* 9 (2019) 24401–24419.

Supporting Information

**Polymer ion-exchange membranes for capacitive deionization
of aqueous media with low and high salt concentration**

Yuan Zhang,^{1,2} Pattarachai Srimuk,^{1,2}

Mesut Aslan,² Markus Gallei,³ and Volker Presser^{1,2*}

¹ INM - Leibniz Institute for New Materials, Campus D2 2, 66123, Saarbrücken, Germany

² Department of Materials Science and Engineering, Saarland University, Campus D2 2, 66123, Saarbrücken, Germany

³ Polymer Chemistry, Saarland University, Campus C4 2, 66123, Saarbrücken, Germany

* Corresponding author's e-mail: volker.presser@leibniz-inm.de

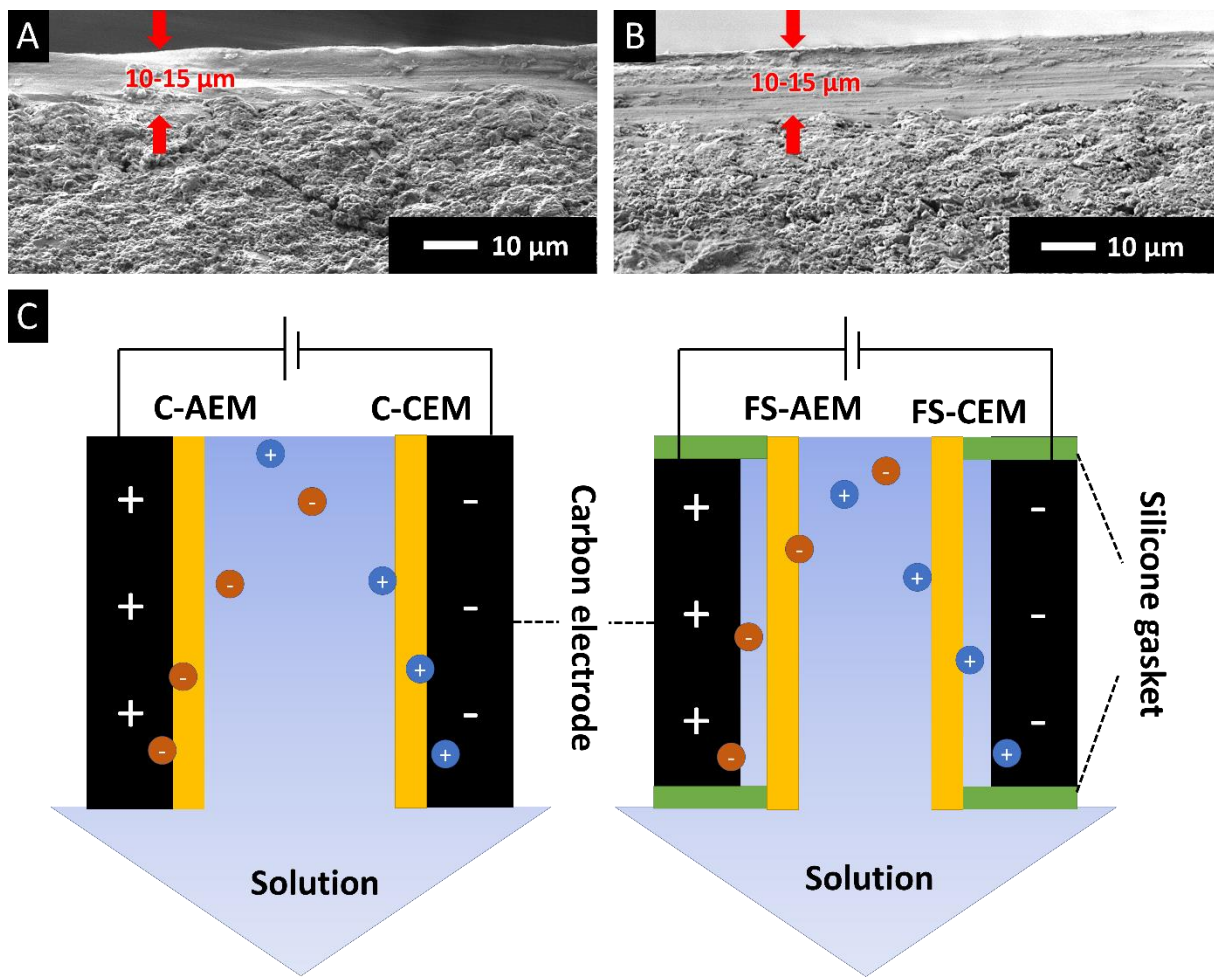


Figure S1: Scanning electron micrographs of **(A)** C-AEM, **(B)** C-CEM coatings. The thickness relates to the dry membrane. **(C)** Schematic drawing of the membrane coating (labeled as C) MCDI cell and free-standing membrane (labeled as FS) MCDI cell.

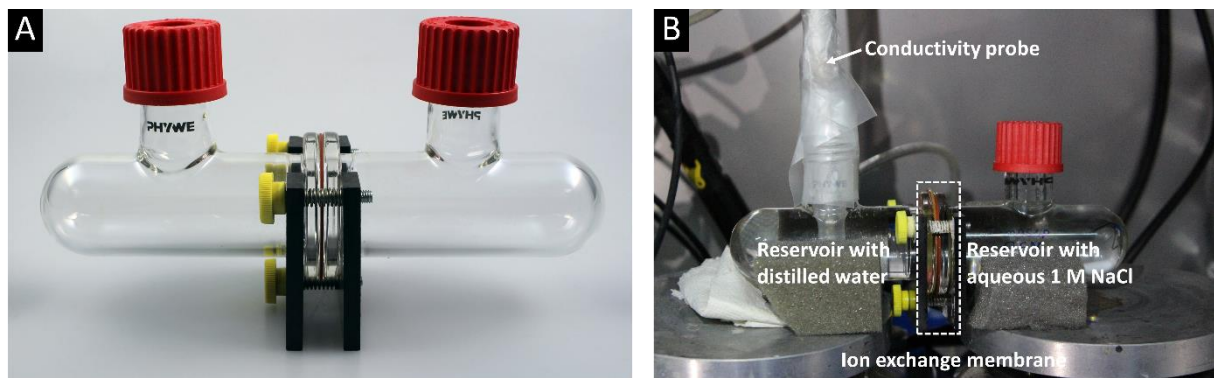


Figure S2: Membrane permselectivity test setup design.

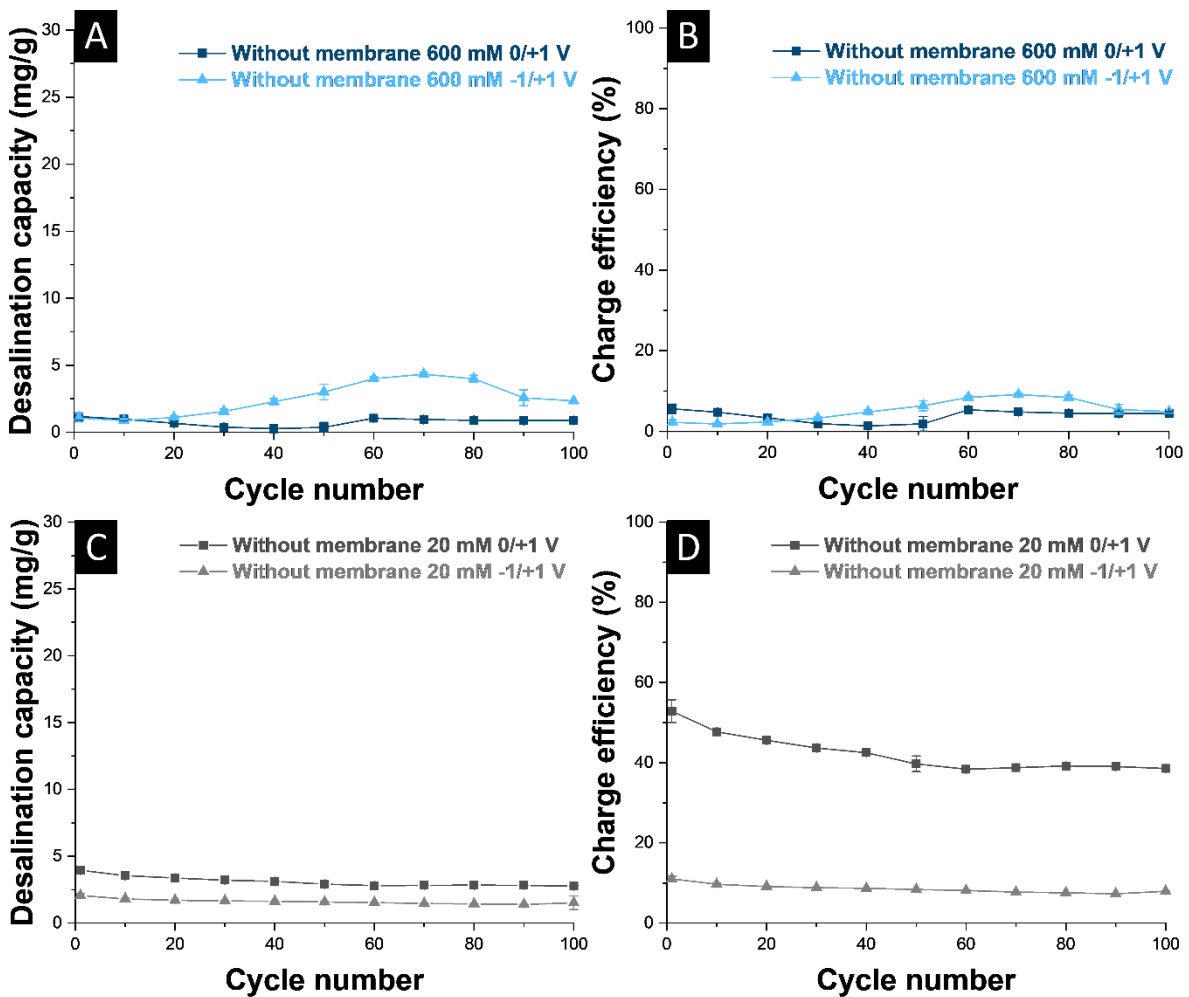


Figure S3: Water desalination performance of carbon-coated electrodes without membranes. **(A-B)** Desalination capacity and charge efficiency profile of 100 cycles in 600 mM NaCl water solution and **(C-D)** 20 mM NaCl water solution. Data were obtained from galvanostatic measurements with the potential range of 0/+1 V and -1/+1 V using a specific current of 0.25 A/g.

4.6 MXene/activated-carbon hybrid capacitive deionization for permselective ion removal at low and high salinity

Mohammad Torkamanzadeh,^{1,2} Lei Wang,^{1,2} Yuan Zhang,^{1,2}
 Öznil Budak,^{1,2} Pattarachai Srimuk,¹ Volker Presser,^{1,2,3}

1 INM - Leibniz Institute for New Materials, D2 2, 66123, Saarbrücken, Germany

2 Department of Materials Science & Engineering, Saarland University, Campus D2 2, 66123, Saarbrücken, Germany

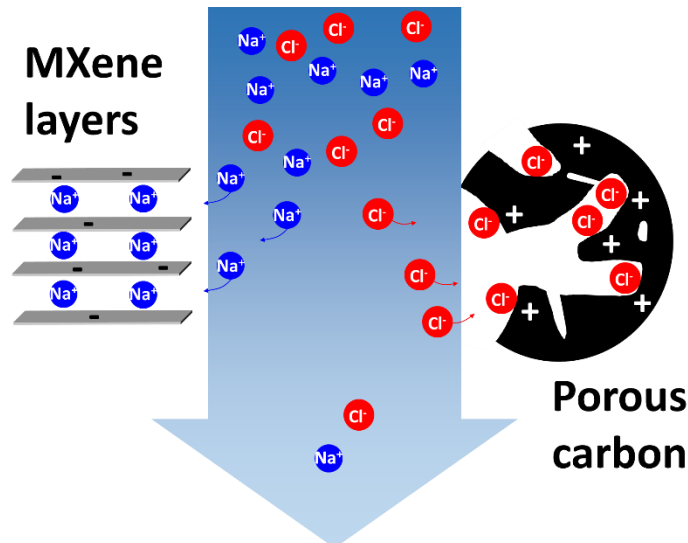
3 Saarene - Saarland Center for Energy Materials and Sustainability, Campus C4 2, 66123 Saarbrücken, Germany

Citation:

M. Torkamanzadeh, L. Wang, Y. Zhang, Ö. Budak, P. Srimuk, V. Presser, *MXene/activated-carbon hybrid capacitive deionization for permselective ion removal at low and high salinity*, ACS Applied Materials & Interfaces, 2020, 12(23): 26013-26025. (DOI: 10.1021/acsami.0c05975)

Own contribution:

Formal analysis, investigation, data curation, writing-review & editing.



MXene/Activated-Carbon Hybrid Capacitive Deionization for Permselective Ion Removal at Low and High Salinity

Mohammad Torkamanzadeh, Lei Wang, Yuan Zhang, Öznil Budak, Pattarachai Srimuk, and Volker Presser*



Cite This: *ACS Appl. Mater. Interfaces* 2020, 12, 26013–26025



Read Online

ACCESS |

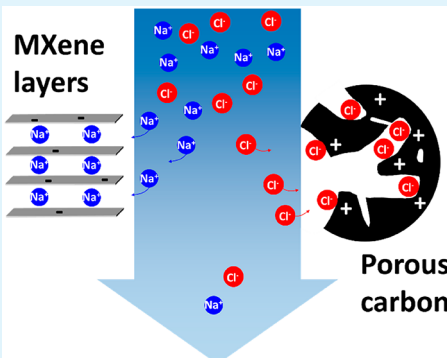
Metrics & More

Article Recommendations

Supporting Information

ABSTRACT: Two-dimensional, layered transition metal carbides (MXenes) are an intriguing class of intercalation-type electrodes for electrochemical applications. The ability for preferred counterion uptake qualifies MXenes as an attractive material for electrochemical desalination. Our work explores $Ti_3C_2T_x$ -MXene paired with activated carbon in such a way that both electrodes operate in an optimized potential range. This is accomplished by electrode mass balancing and control over the cell voltage. Thereby, we enable effective remediation of saline media with low (brackish) and high (seawater-like) ionic strength by using 20 and 600 mM aqueous NaCl solutions. It is shown that MXene/activated-carbon asymmetric cell design capitalizes on the permselective behavior of MXene in sodium removal, which in turn forces carbon to mirror the same behavior in the removal of chloride ions. This has minimized the notorious co-ion desorption of carbon in highly saline media (600 mM NaCl) and boosted the charge efficiency from 4% in a symmetric activated-carbon/activated-carbon cell to 85% in a membrane-less asymmetric MXene/activated-carbon cell. Stable electrochemical performance for up to 100 cycles is demonstrated, yielding average desalination capacities of 8 and 12 mg/g, respectively, for membrane-less MXene/activated-carbon cells in NaCl solutions of 600 mM (seawater-level) and 20 mM (brackish-water-level). In the case of the 20 mM NaCl solutions, surprising charge efficiency values of over 100% have been obtained, which is attributed to the role of MXene interlayer surface charges.

KEYWORDS: MXene, intercalation, capacitive deionization, desalination, seawater, asymmetric



1. INTRODUCTION

The development of sustainable water desalination technologies is crucial as clean water shortage has become a global concern.¹ This challenge pertains to enhanced energy efficiency and performance durability at low operational costs. Capacitive deionization (CDI) is a promising water desalination technology that offers certain advantages over other widely employed alternatives such as reverse osmosis, and thermal desalination.² CDI devices operate at low pressure and have reduced energy consumption, especially at ultralow to low salinity levels.³ A CDI cell is conceptually a flow-through electrochemical capacitor.⁴ Upon charging the CDI cell, water-dissolved ions are removed from the saline water feed stream via electrosorption: Sodium ions are attracted to the negatively charged electrode, and chloride ions are attracted to the positively charged electrode. Upon discharging, the ions are released back to the stream, and, as a result, the regenerated electrodes can be used in the subsequent cycle. At the same time, the invested electrical charge is (mostly) recovered by which feature added energy efficiency of the CDI technology is afforded. In this context, there are two important, among other performance metrics: the desalination capacity (DC) measures the effective amount of salt removed per mass

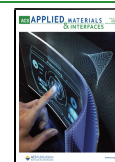
of the electrode and the charge efficiency (CE) gives the ratio of invested total charge versus the charge corresponding to the removed ionic species.⁵

Until recently, CDI research had focused on carbon-based materials as electrodes.⁶ The large surface area of nanoporous carbon provides microporous channels for effective electrostatic immobilization of ions at the carbon/electrolyte interface.⁷ In the absence of intrinsic permselectivity, co-ion desorption of microporous carbon prevents bulk ion removal via ion electrosorption at high molar strength, such as that found in saline water or brine.⁷ This issue can, partially, be remedied by implementing ion-exchange membranes, giving rise to membrane CDI (MCDI).⁸ However, while the implementation of ion-exchange membranes also allows the design of multichannel desalination cells,⁹ it adds additional costs and cannot overcome the intrinsic charge-limitation of

Received: March 31, 2020

Accepted: May 13, 2020

Published: May 13, 2020



carbon material. Alternatively, permselective counterion adsorption via suppressed co-ion presence can be enhanced even at high molar strength when lowering the carbon pore size below 1 nm.¹⁰

In recent years, electrochemical desalination employing Faradaic (charge-transfer) materials has overcome the limitation to low molar regimes (<100–200 mM) and limited desalination capacity (ca. 20–30 mg_{NaCl}/g_{electrode}) of carbon-based CDI.¹¹ In 2012, Pasta et al. introduced a desalination battery by employing layered sodium manganese oxide to remove sodium ions from seawater without a need for ion-exchange membranes.¹² Lee et al. introduced the combination of a Faradaic and an electrosorption (carbon) electrode to enhance the CDI performance, but without accessing high molar strength regimes.¹³ Until now, a large and rapidly growing number of charge-transfer materials have already been explored, including intercalation compounds,¹⁴ conversion materials,¹⁵ electroactive polymers,¹⁶ redox-active electrolytes,¹⁷ and combinations of such materials. Even more advanced approaches utilize high-capacity processes, such as oxidant generation¹⁸ or metal–air processes.¹⁹

Of interest for any application involving the intercalation of cations and anions are two-dimensional (2D) materials. For example, Ti₃C₂T_x is a member of a large family of 2D materials called MXene.²⁰ MXene is derived via selective etching of A-site atoms from a M_{n+1}AX_n phase, where M stands for an early transition metal, A stands for group 13 or 14 elements (typically Al), X stands for carbon and/or nitrogen, and n = 1, 2, or 3.²¹ To carry the meaning of surface functional groups, T_x is added to the chemical formula of MXene, to describe fluorine-, chlorine-, and oxygen-containing functionalities.²² For instance, Ti₃C₂T_x is commonly obtained by removing Al from Ti₃AlC₂ through aqueous HF etching (but nonaqueous processing is also possible).²³ Upon etching, Al is replaced by a mixture of surface terminations (O, OH, and F), rendering a typical MXene hydrophilic with a negative surface charge.²⁰ The layered structure of MXene allows for ions to be inserted into the material (ion intercalation), a property that in addition to a high conductivity²⁴ and facile processability²⁵ makes MXene attractive for electrochemical energy storage and water remediation. MXenes have shown promise in numerous energy storage applications as lithium-ion battery²⁶ or supercapacitor²⁷ electrodes, as well as in environmental remediation applications such as ion-sieving membranes²⁸ or heavy metal ion removal.²⁹

Electrochemical desalination is a less widely explored domain of MXene research.³⁰ As the first, Srimuk et al. introduced Ti₃C₂T_x-MXene in a symmetric cell for desalination of low molar (5 mM NaCl) water.¹⁴ Using MXene as an intercalation type material for both electrodes, a desalination capacity of 13 mg_{NaCl}/g_{electrode} was obtained with stable performance for 30 cycles. Subsequent works on MXene electrochemical desalination have focused on postprocessing and modification of Ti₃C₂T_x MXene to enhance its salt removal capacity. The latter works include vacuum freeze-drying and (45 mg_{NaCl}/g_{electrode}),³¹ substituting HF-etching with LiF/HCl treatment (68 mg_{NaCl}/g_{electrode}),³² and nitrogen-doping (44 mg_{NaCl}/g_{electrode})³³ to prevent restacking of MXene layers and form electrochemically active porous structures. These promising works underline MXene as an aspiring material for water treatment applications.³⁴

However, Ti-based MXenes operated in aqueous environments are notoriously affected by aging via hydrolysis-aided

oxidation.³⁵ This issue particularly affects the usefulness of Ti₃C₂T_x as the positively polarized electrode for electrochemical desalination of water. To fully capitalize on the electrochemical performance of Ti-MXene in aqueous media, it is convenient to limit its application to the negatively polarized electrode where no oxidation will occur. Unlike operation as asymmetric supercapacitors,³⁶ asymmetric desalination cells with MXene as only one of the electrode pair has remained incompletely explored.³⁴ This includes the important aspect of mass balancing to optimize the operational cell voltage of each of the two electrodes, as recently shown by Dryfe's group for carbon-based CDI.³⁷ Mechanistically, the interesting aspect of addressing is the degree of permselectivity of the nanoporous carbon electrode when paired with a permselective intercalation-type electrode, such as MXene. We explore if the permselective behavior of the intercalation electrode will "force" the carbon electrode to prefer counterions rather than 1:1 exchange a co-ion with a counterion. This is of high importance for saline media with high salt concentration because using only one intercalation-type electrode paired with activated carbon as the other electrode would lower system cost because of the high abundance of carbon and eliminate the need for expensive ion-exchange membranes.

Our study investigates the desalination of seawater-level saline solutions (600 mM NaCl) and brackish water (20 mM NaCl). We paired Ti₃C₂T_x-MXene with activated carbon in an asymmetric cell so that we can capitalize on sodium-ion intercalation on the MXene side and chloride ion electrosorption within carbon nanopores. Our focus is not the optimization toward the highest possible desalination metrics; instead, our work focuses on the mechanistic aspect of the desalination process. Specifically, our work explores the ion permselectivity of the carbon electrode paired with that of MXene by comparing cell performance with and without adding a polymeric ion-exchange membrane in front of the activated carbon. Thereby, we can compare the electrochemical desalination performance of the cell when the carbon electrode is shielded (with an ion-exchange membrane) or directly exposed to the saline medium. Characterization of the MXene-CNT electrodes before and after use for over 100 cycles provides insights into performance stability and degradation mechanisms.

2. MATERIALS AND METHODS

2.1. Electrode Preparation and Electrochemical Measurements.

The following materials were used as-received: activated carbon (type YP-80F, Kuraray), multiwalled carbon nanotubes (CNT, Graphene Supermarket), and Ti₃C₂T_x-MXene (Laizhou Kai Kai Ceramic Materials Co.). As seen from Figure S1, activated carbon has a large surface area of 1644 m²/g and is composed of internal porosity within the activated carbon particles. In contrast, carbon nanotubes have a very small surface area of just 71 m²/g (Figure S1) which relates to external porosity.³⁸

To prepare carbon electrodes, activated carbon and polytetrafluoroethylene binder (PTFE, 60 mass% solution in water from Sigma-Aldrich) in a 95:5 carbon/binder mass-ratio were mixed in ethanol to give a homogeneous carbon paste.³⁹ Afterward, the carbon paste was rolled (MTI HR01, MIT Corp.) to 600 μm thick freestanding electrode films, which was then dried in a vacuum oven at +120 °C overnight.

To prepare MXene-CNT electrodes, Ti₃C₂T_x-MXene and CNT in a 10:1 MXene/CNT mass ratio were tip-sonicated in ethanol for 30 min.⁴⁰ The solution was subsequently vacuum filtered through polyvinylidene fluoride (PVDF) membranes (0.22 μm, Durapore)

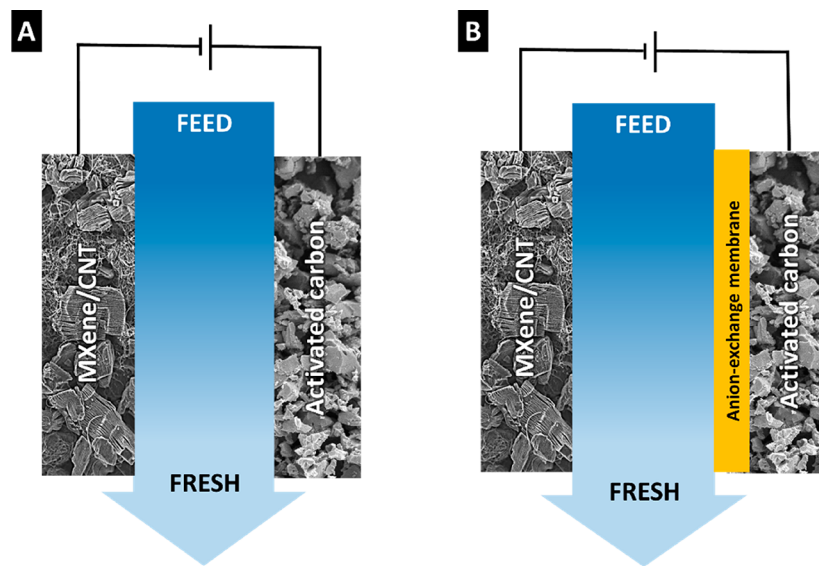


Figure 1. Schematic of an asymmetric electrochemical water desalination cell (A) without an ion-exchange membrane and (B) with an anion-exchange membrane.

and dried in an oven at +80 °C overnight. This electrode is labeled MXene-CNT in our work.

In a typical half-cell experiment, circular-shaped 12 mm diameter pieces were punched out of the MXene-CNT electrode and used as the working electrode. An oversized activated carbon electrode was used as counter electrode and glass fiber (GF/A, Whatman) was used as a separator. All components were placed in a custom-built cell between spring-loaded titanium pistons.⁴¹ A reference electrode (Ag/AgCl, 3 M NaCl) was mounted onto the side of the cell in a way that its porous frit was near the working and counter electrodes. The cell was filled with 600 mM NaCl aqueous electrolyte by vacuum backfilling using a syringe. Cyclic voltammetry (CV; scan rate: 1 mV/s) and galvanostatic charge/discharge tests were performed with a VSP300 potentiostat/galvanostat (Bio-Logic).

For full-cell electrochemical water desalination, a 30 mm diameter MXene-CNT electrode was punched out and used as the working electrode. On the basis of the mass of MXene-CNT, an activated carbon electrode with a suitable mass ratio (section 2.2) was cut and used as the counter electrode. The working and counter electrodes were stacked together and separated by glass fiber membranes. Thereby, the middle channel was formed and provided a pathway for 600 mM NaCl electrolyte to flow in between the electrodes (flow-by mode, Figure 1).⁴² A nonreinforced 31 ± 2 µm thick anion-exchange membrane (Fumatech, FAS-30) was used on the side of the carbon electrode in certain cells. An Ag/AgCl spectator reference electrode was used to allow recording the electrode potentials of the activated carbon and MXene-CNT electrodes individually.

2.2. Electrode Mass Balancing. To determine the suitable mass ratio between MXene-CNT and activated carbon electrodes in a full desalination cell, cyclic voltammetric window-opening experiments⁴³ were performed at both negative and positive potentials. The results of this method reveal the ideal stable potential window for each of the electrode materials, as well as quantifying the amount of charge storable in each electrode at a certain potential. Using eq 1, one can balance the mass ratio of the electrodes based on cyclic voltammetric window-opening experiments:

$$\frac{m_{\text{MXene-CNT}}}{m_{\text{Activated_carbon}}} = \frac{Q_{\text{Activated_carbon}}}{Q_{\text{MXene-CNT}}} \quad (1)$$

where $Q_{\text{MXene-CNT}}$ (C/g) and $Q_{\text{Activated_carbon}}$ (C/g) are, respectively, the specific electric charge stored in MXene-CNT and activated carbon electrodes at a certain potential. The value of $m_{\text{MXene-CNT}}/m_{\text{Activated_carbon}}$ then gives the mass ratio between the two electrodes,

based on which a full cell with maximum desalination performance can be fabricated.

2.3. Desalination Experiments. All desalination experiments were performed using galvanostatic cycling with potential limitation (GCPL) technique via VSP300 potentiostat/galvanostat (Bio-Logic) electrochemical workstation at +25 °C. Each cycle duration was 2 h and consisted of two half-cycles. In the first half-cycle, the cell was charged to 1.2 V and held at that voltage for 1 h. In the second half-cycle, the cell was discharged to 0.3 V and at that voltage for another 1 h. Both charging and discharging steps were accomplished at 0.1 A/g current density (normalized to the combined mass of both activated carbon and MXene-CNT electrodes). A stream of saline was pumped into the cell at a 2 mL/min rate from a reservoir tank, which contained 10 L of electrolyte and was constantly bubbled with nitrogen prior to and during the experiments to deaerate the fluid. The effluent stream flowed out of the cell into a conductivity meter (Metrohm PT1000) and pH meter (WTW SensoLyte 900P) and flowed back into the tank to complete the loop. The pH and conductivity data were recorded every second online by computer. Calculations regarding the correlation of pH and conductivity data to concentration may be found in our previous work.⁴⁴ The desalination capacity ($\text{mg}_{\text{NaCl}}/\text{g}_{\text{electrode}}$) was calculated according to eq 2:

$$\text{desalination capacity (DC)} = \frac{\nu M_{\text{NaCl}}}{m_{\text{total}}} \int \Delta C \, dt \quad (2)$$

where ν is the flow rate (mL/min), M_{NaCl} is the molecular weight of NaCl (58.44 g/mol), m_{total} is the total mass of electrodes (g), t is the time over the adsorption or desorption step (min), and ΔC is the concentration change of NaCl (mM) in the effluent stream of the cell. The charge efficiency (%) was calculated following

$$\text{charge efficiency (CE)} = \frac{\frac{\text{DC}}{M_{\text{NaCl}}}}{\frac{Q}{F}} \times 100\% \quad (3)$$

where F is the Faraday constant (26 801 mAh/mol) and Q is the average of total charge stored in the two electrodes normalized to the total electrode mass (mAh/g).

2.4. Material Characterization. X-ray diffraction (XRD) analysis was conducted using a D8 Advance diffractometer (Bruker AXS) with a Ni-filtered copper X-ray source (Cu K α , 40 kV, 40 mA) and a 2D detector (VANTEC-500). A JEOL JSM 7500F field-emission scanning electron microscope (JEOL) was used to record scanning electron microscopy (SEM) images. Energy-dispersive X-ray spec-

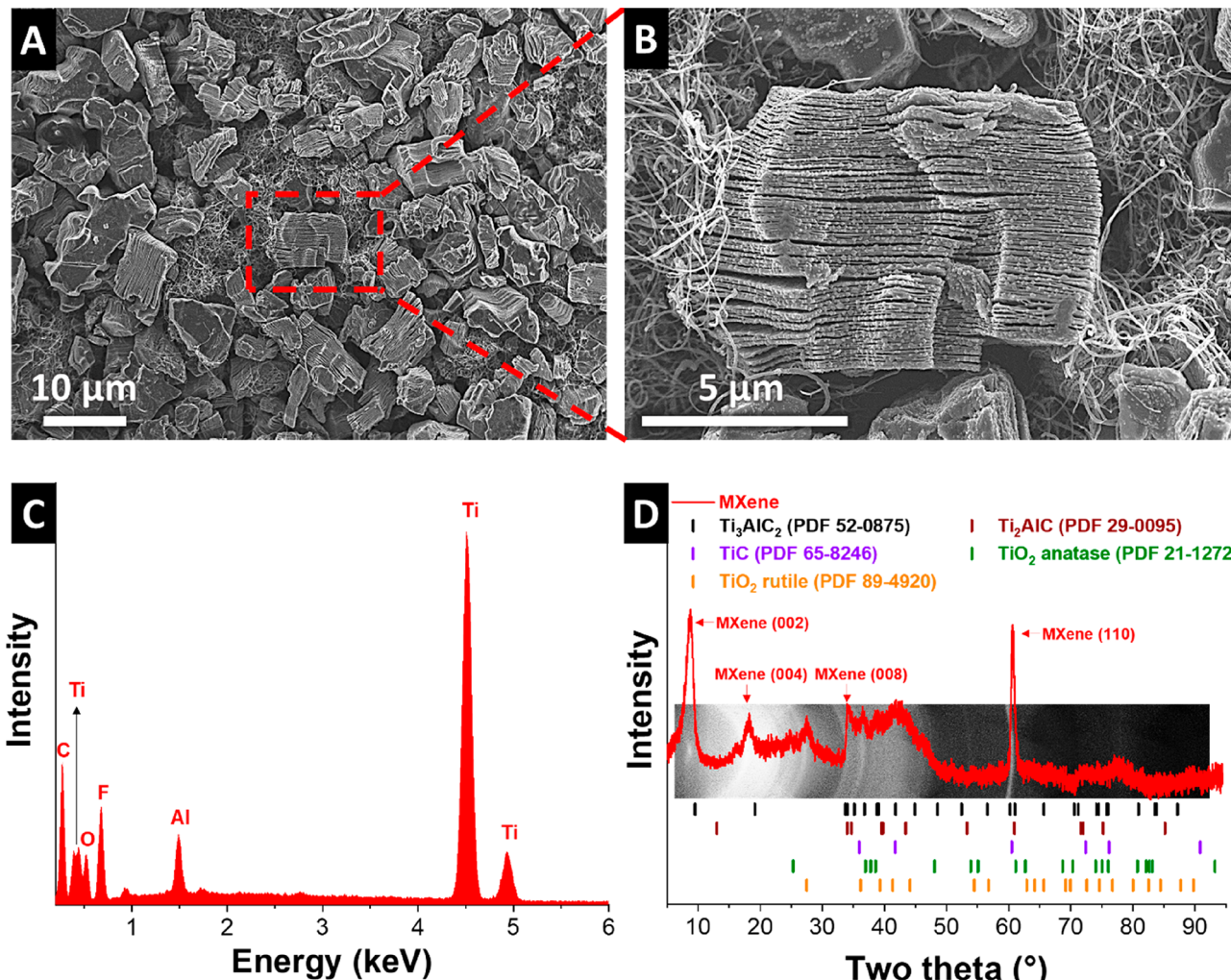


Figure 2. Characterization of the MXene-CNT electrode. (A, B) Scanning electron micrographs, (C) energy-dispersive X-ray spectrum (EDX), and (D) X-ray diffractogram and overlaid 2D diffraction pattern of $\text{Ti}_3\text{C}_2\text{T}_x$ -MXene alongside ideal pattern of different phases [Powder Diffraction File (PDF) nos. 21-1272, 29-0095, 52-0875, 65-8246, and 89-4920 are Joint Committee on Powder Diffraction Standards, 2004].

troscopy (EDX) was carried out at 12 kV with an X-Max Silicon Detector from Oxford Instruments using the AZtec software. Transmission electron microscopy (TEM) was conducted using a JEOL JEM-2100F system at an operating voltage of 200 kV. The samples were dispersed in ethanol and tip-sonicated briefly. The dispersion was then drop casted on a TEM copper grid with a lacy carbon film.

We used an Autosorb iQ system (Quantachrome) for nitrogen sorption at -196°C . The samples were degassed at 100 Pa and 200°C for 1 h and then at 300°C for 20 h. Alongside the isotherm of activated carbon, carbon nanotubes, MXene powder, and MXene-CNT electrodes, the specific surface area (SSA) was obtained via Brunauer–Emmett–Teller (BET) theory and by applying the quenched-solid density functional theory (QSDFT), assuming a slit-shaped pore model as provided in Figure S1.

The streaming potential was measured using a Mütek PCD-T3 instrument with the particle charge detection method. In a typical experiment, 50 mg of MXene or YP-80F carbon was dispersed in 30 mL of water. The mixture was then poured into a cylindrical PTFE container of the instrument with a PTFE piston inside. The automatic titration was conducted by gradual injection of HCl or NH_3 solutions into the mixture while the potential recorded online.

3. RESULTS AND DISCUSSION

3.1. Material Characterization. The SEM images depicted in Figure 2A show the morphology of pristine MXene-CNT electrodes. $\text{Ti}_3\text{C}_2\text{T}_x$ -MXene structures are observed with their typical layered accordion-like morphologies, entangled by CNTs. TEM images of the CNTs are provided in Figure S2. The incorporation of CNTs improves the mechanical stability of the electrode, as well as enhancing the electrical conductivity.⁴⁰ CNTs themselves have a specific surface area of $71 \text{ m}^2/\text{g}$, which is predominately on the outer surface. $\text{Ti}_3\text{C}_2\text{T}_x$ -MXene exhibits an external surface area of $3 \text{ m}^2/\text{g}$, and the mechanical mixture of 10 mass % CNTs and 90 mass % of MXene yields a surface area of $12 \text{ m}^2/\text{g}$. The latter value is very close to the theoretical value of such a mixture (i.e., $10 \text{ m}^2/\text{g}$), and the same goes for the corresponding pore volume ($0.04 \text{ cm}^3/\text{g}$ measured for the composite electrode; Figure S1). The low values of surface area and pore volume originate from the porous space between the MXene bundles (Figure 2A) and not from within the interlayers of MXenes. There is no detriment to such a low level of porosity since electrochemical desalination via MXene is not based on ion electrosorption but on the ion intercalation between the layers of the electrode material. In addition to providing electronic

Table 1. EDX Elemental Analysis of the Pristine MXene-CNT and Post-Mortem Electrodes of Different Cells after Long-Term Cycling^a

	C	Ti	O	Al	F	Na	Cl
pristine	13 ± 9	57 ± 13	9 ± 3	3 ± 3	17 ± 6		
post-mortem (600 mM + AEM)	12 ± 2	53 ± 5	22 ± 3	1 ± 0	6 ± 1	3 ± 0	3 ± 1
post-mortem (600 mM)	15 ± 3	58 ± 8	16 ± 4	0 ± 0	8 ± 2	2 ± 1	1 ± 0
post-mortem (20 mM + AEM)	10 ± 2	67 ± 8	15 ± 4	0 ± 0	5 ± 2	2 ± 0	1 ± 0
post-mortem (20 mM)	10 ± 2	61 ± 7	22 ± 4	1 ± 0	6 ± 2	1 ± 0	0 ± 0

^aAll values in mass %.

pathways and entangling MXene flakes, the CNTs also likely provide facile ion-transport pathways by preventing too tight packing of MXene particles.

At a higher resolution, we also see from the SEM image in Figure 2B, the presence of cuboid particles spread over the MXene surface. The latter particles are consistent with titanium oxide, and the presence of oxygen is confirmed by the EDX spectrum displayed in Figure 2C (EDX results are listed in Table 1). Ti-based MXene is known to oxidize in air, especially in the presence of humidity.³⁵ The EDX results also show a low amount (around 3 mass%) of residual aluminum, which stems from nonetched MAX phases or traces of aluminum fluoride from the etching products of the MAX phases.

XRD analysis confirms the presence of $\text{Ti}_3\text{C}_2\text{T}_x$ -MXene. The XRD pattern in Figure 2D shows a strong (002) peak at $8.59^\circ 2\theta$ of $\text{Ti}_3\text{C}_2\text{T}_x$, compared to the initial value of (002)- Ti_3AlC_2 of the parent MAX phase at $9.52^\circ 2\theta$. This corresponds with an 11% increase in the *d*-spacing along the *c*-axis. In addition to higher-order (00*l*)-type MXene reflections, we also see the characteristic MXene-peak related to (110)- $\text{Ti}_3\text{C}_2\text{T}_x$ at about $61^\circ 2\theta$.⁴⁵ No significant amounts of either Ti_2AlC or TiC are found from the diffraction pattern analysis. We also see the presence of minor amounts of titanium oxide (possibly rutile) from the diffraction signal generate at about $27^\circ 2\theta$. Figure S3 provides the XRD pattern of the corresponding phases with their relative intensities.

3.2. Electrochemical Behavior. In the first step to determining the stable electrochemical potential window of the MXene-CNT and activated carbon electrodes, half-cell cyclic voltammetric window-opening measurements at a scan rate of 1 mV/s were carried out with 100 mV increments (Figure 3A,B). These experiments were carried out in aqueous 600 mM NaCl to avoid issues of ion starvation and to provide a baseline for later desalination experiments at seawater-like ionic strength.⁴⁶

The cyclic voltammograms of activated carbon are rectangular-shaped, showing a near-ideal capacitive behavior (Figure 3A). As the potential difference is increased, there is a notable increase in the capacitance during positive and negative polarization when comparing identical potential window widths. This effect is linked to the quantum capacitance effect induced by the increased number of charge carriers in carbon, as the latter is not a perfect metallic conductor.^{41,47} At very high positive potentials, starting at around +0.6 V vs Ag/AgCl, we also see an irreversible increase in transferred charge linked to water splitting.³⁸ We note a similar capacitance during positive and negative polarization, which would indicate a similar ability to serve as an electrode for sodium and chloride removal (under the condition of permselectivity).^{48,49} These features make activated carbon

electrodes suitable for positive and negative polarization regimes in the context of capacitive deionization.

For MXene-CNT electrodes, an onset of the oxygen evolution peak is seen at positive potentials as early as +0.3 V vs Ag/AgCl (Figure 3B). This makes the chosen MXene-CNT electrodes unsuitable to serve as the positive electrode in our setup. During negative polarization, there is a continued increase in the corresponding capacitance when increasing the voltage bias. This process aligns with the conditioning of the MXene interlayer space and is irreversible. The latter is obvious when comparing the low capacitance found during the initial cycles at low potential bias, seeing the increased area under the cyclic voltammogram as the lower scan limit transitions toward more negative polarization, and the significantly increased capacitance for small voltage windows during repeat measurements (solid line graphs in Figure 3C). Electrochemical dilatometry also shows the increased strain of the MXene-CNT electrode when the polarization bias is increased (Figure 3D). The electrode shrinking follows the same pattern observed during negative polarization in Na_2SO_4 reported before and is aligned with the stronger MXene layer attraction in the sodiated state.⁵⁰ This process is likely to be accompanied by a change in the number of solvent molecules within the interlayer space.⁵¹ We also note the prominent current-peak at -0.5 V (cathodic scan) and -0.3 V (anodic scan), which may be related to interlayer proton-redox processes and ion arrangement effects.⁵² In past works, this peak was mostly reported and analyzed in aqueous H_2SO_4 electrolytes.⁵²

Half-cell cyclic voltammograms of CNTs are provided in Figure S4. Cyclic voltammograms show a rectangular-shaped profile typical for ion electrosorption. The low surface area of CNTs explains the low capacitance of about 20–30 F/g (depending on the potential range). Given that CNTs account for only 10 mass % of the MXene-CNT electrodes, the electrochemical contribution arising from CNTs to the total capacitance of about 120 F/g of the electrode is negligible. Specifically, at a polarization potential of -0.8 V vs Ag/AgCl, for instance, the charge stored in CNT electrodes is only 6% that of MXene-CNT (Figure 3B).

Galvanostatic charge/discharge cycling was employed to quantify the specific capacitance (Figure 3E) and specific capacity (Figure 3F) of the electrodes. Galvanostatic charge/discharge cycling at 0.1 A/g gave a capacitance of 123 F/g for MXene-CNT at the potential window between -1 and 0 V vs Ag/AgCl and 95 F/g for activated at the potential window from 0 to +0.4 V vs Ag/AgCl. For the two materials, the capacitance originates from different electrochemical processes. While the large surface area of activated carbon ($1644 \text{ m}^2/\text{g}$; Figure S1A) enables ion electrosorption, we see pseudocapacitive ion intercalation of sodium for MXene-CNT considering the low surface area ($3 \text{ m}^2/\text{g}$ for MXene and $12 \text{ m}^2/\text{g}$ for

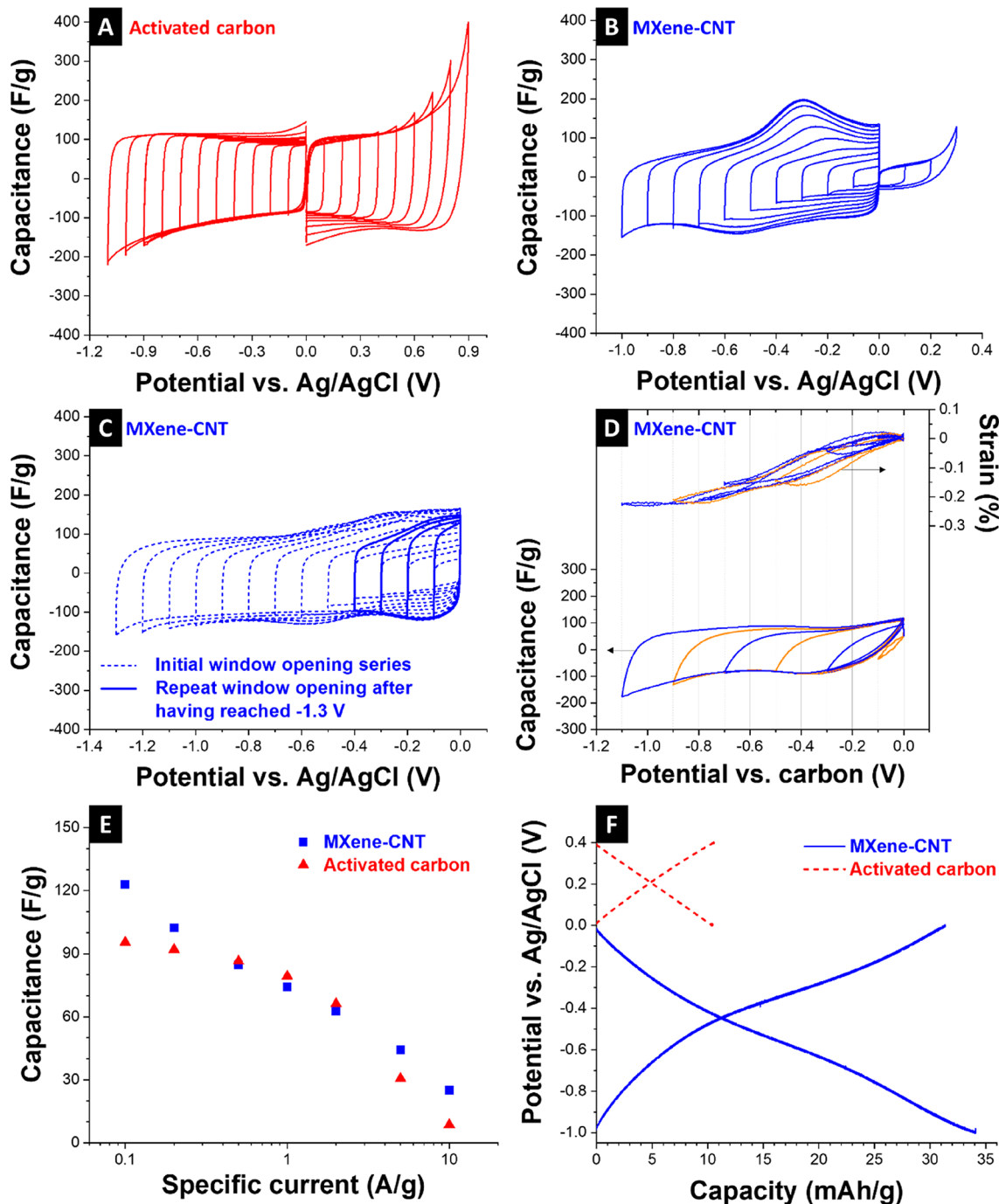


Figure 3. Half-cell electrochemical characterizations: window-opening cyclic voltammograms of (A) activated carbon and (B) MXene-CNT; (C) initial and repeated cyclic voltammetric window opening. (D) Cyclic voltammograms and corresponding dilatograms (electrode height change/initial height = strain; the different colors help to differentiate between individual scans). (E) Gravimetric capacitance of MXene-CNT (−1 to 0 V vs Ag/AgCl) and activated carbon (0 to +0.4 V vs Ag/AgCl), and (F) corresponding capacities. All measurements were carried out in aqueous 600 mM NaCl.

MXene-CNT; Figure S1C,D). At a rate of 2 A/g, both electrodes yield a comparable capacitance of 63–66 F/g, and we see a lower rate handling ability of the activated carbon electrode compared to MXene-CNT. Characteristic galvanostatic charge/discharge profiles are displayed in Figure 3F, and we chose capacity as the displayed unit to correctly quantify the charge and to compensate for any deviation from a perfectly rectangular cyclic voltammogram found for MXene-CNT. The capacity of about 10 mAh/g for activated carbon

and 34 mAh/g for MXene-CNT informed the mass balancing, which will be used in section 3.3.

3.3. Desalination Performance. On the basis of the electrochemical results obtained by half-cell measurements, asymmetric full-cells comprising of MXene-CNT and activated carbon electrodes were fabricated. For the desalination cell, we chose the mass ratio between the two electrodes that was optimized according to the method explained in section 2.2. We also carefully adjusted the potential window to cycle between cell voltages 1.2 and 0.3 V instead of discharging to 0

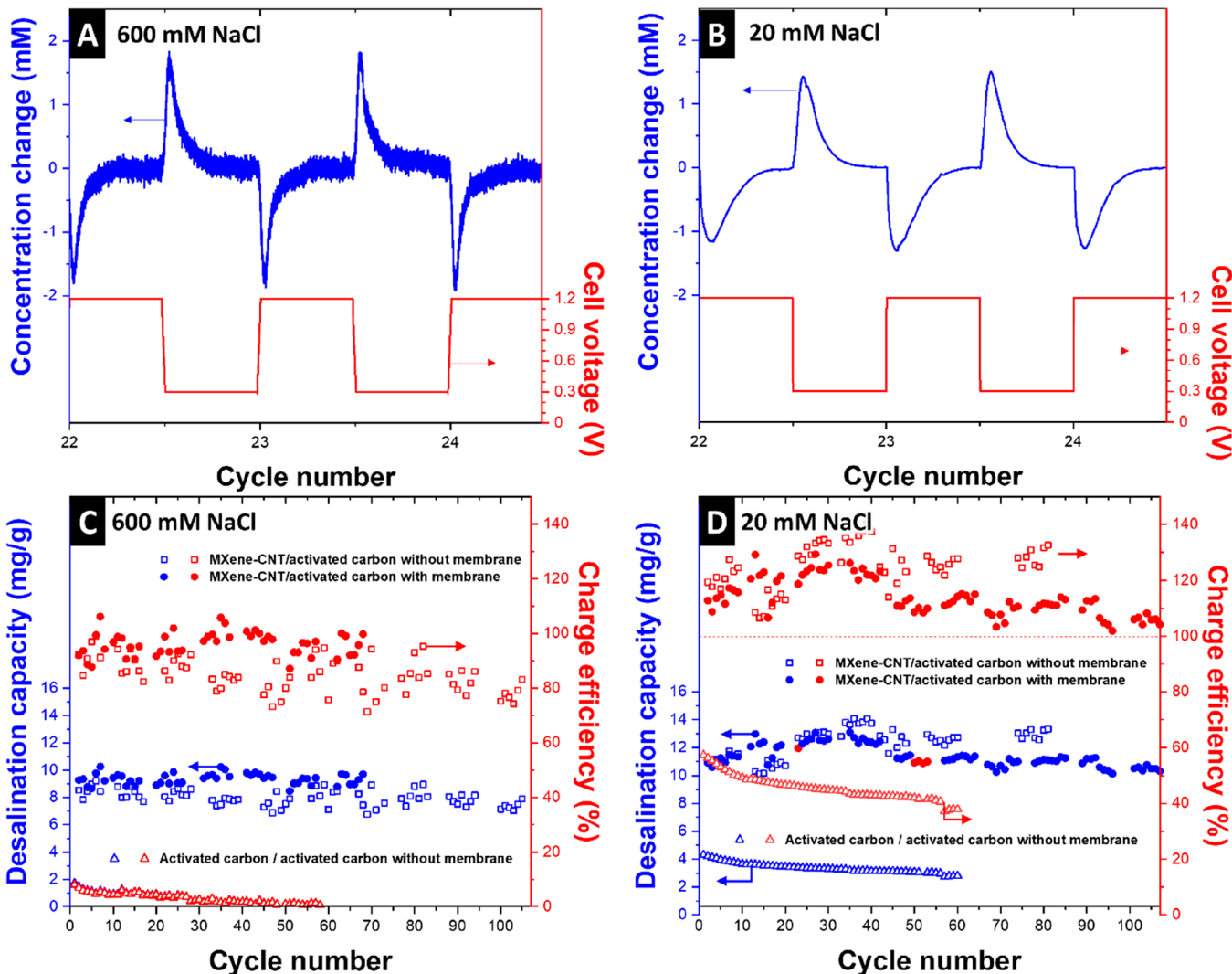


Figure 4. Effluent concentration change and cell voltage profiles of MXene/activated-carbon cell for two full cycles in (A) 600 mM NaCl and (B) 20 mM NaCl, both without membrane. Salt removal capacity stability and charge efficiency for cells with and without membrane in (C) 600 mM NaCl and (D) 20 mM NaCl, alongside membrane-less symmetric activated-carbon cells (the latter includes 60 cycles).

V to ensure activated carbon remains within the positive polarization regime (and, in return, MXene-CNT remains negatively polarized). The potential profiles of the individual MXene-CNT and activated carbon electrodes are provided in Figure S5. To ensure stable performance and to avoid first-cycle effects, all cells were initially cycled for around 30 cycles before the desalination experiments. As was seen from the electrochemical characterization data, the low amount of low-surface area carbon nanotubes aligns with a small contribution to the charge capacity of the MXene-CNT electrode, and as a consequence, the contribution of desalination via ion electrosorption by the CNTs is negligible (based on 2–3 F/g via 10 mass% of pure CNTs, the corresponding desalination capacity is expected to be below 1 mg_{NaCl}/g_{electrode}).⁵³

Figure 4A,B shows the effluent salt concentrations (alternating peaks and troughs) alongside the voltage profile applied (without the use of an anion-exchange membrane). Upon charging the cell to 1.2 V, ions are attracted to the electrodes, causing a sudden drop in the concentration of the effluent stream. The concentration then levels off to the previous level before discharging, indicating that the system is approaching equilibrium and that the electrodes are saturating

with salt ions. Likewise, a similar process occurs upon discharging the cell to 0.3 V, where electrodes are depleted from ions and are regenerated for the next cycle.

The potential distribution between MXene-CNT and activated-carbon electrodes in different cells are shown in Figure S5. At 600 mM NaCl in the absence of an ion-exchange membrane (Figure S5A), we see the highly linear slope of charge/discharge profiles of each monitored electrode potential. The potential range of activated carbon remains fully in the positive polarization regime and has a lower amplitude compared to the MXene-CNT electrode. This is because of the different charge storage capacities of the two electrode materials and the chosen mass ratio. At low molar strength (20 mM NaCl), we note the presence of short-lived spikes in the potential curves of MXene-CNT at vertex potentials (Figure S5C). This is because of the lowered ion mobility at low molar strength; since we only control the cell voltage and just monitor the individual electrode potentials, we see a quicker charging behavior of the activated carbon electrode because the latter capitalizes on interfacial charge storage via ion electrosorption. In contrast, charge transfer is slightly slower in the case of ion intercalation in MXene-CNT,

whereby, upon charging and discharging, the slower electrode is briefly forced to higher potentials. Each small spike in the profile of MXene-CNT is accompanied by a small notch in the profile of the activated carbon electrode.

Figure 4C,D shows the desalination capacity and charge efficiency of up to 100 cycles in aqueous 600 mM NaCl and 20 mM NaCl. In the absence of an ion-exchange membrane, we see at 600 mM a desalination capacity of $8 \pm 1 \text{ mg}_{\text{NaCl}}/\text{g}_{\text{electrode}}$ at a charge efficiency of $85 \pm 6\%$; at 20 mM, we find a desalination capacity of $12 \pm 1 \text{ mg}_{\text{NaCl}}/\text{g}_{\text{electrode}}$ at a charge efficiency of $125 \pm 8\%$ (we comment on exceeding 100% charge efficiency and its importance later in this section).

For comparison: In a membrane-free configuration, activated carbon only affords at 600 mM a desalination capacity of $0.8 \pm 0.3 \text{ mg}_{\text{NaCl}}/\text{g}_{\text{electrode}}$ at a charge efficiency of $4 \pm 2\%$; at 20 mM, we find a desalination capacity of $3 \pm 1 \text{ mg}_{\text{NaCl}}/\text{g}_{\text{electrode}}$ at a charge efficiency of $41 \pm 9\%$. The data for using only activated carbon for both electrodes is from a previous study where a cell voltage of 1.0 V and discharging to 0 V was employed.⁵⁴ Higher desalination capacities for this type of activated carbon are found for membrane-free desalination only at lower molar strength; for example, we found at 5 mM a desalination capacity of about $10 \text{ mg}_{\text{NaCl}}/\text{g}_{\text{electrode}}$ at a corresponding charge efficiency of 75–79%.⁴⁶

Figure 4C,D displays the desalination capacity and charge efficiency for the cell modified by placing an anion-exchange membrane in front of the activated-carbon electrode. This means that the positively polarized carbon electrode allows (almost exclusively) only the uptake of counterions because of the permselective feature of the ion-exchange membrane.^{8,54} For this case, we find at 600 mM a desalination capacity of $9 \pm 0 \text{ mg}_{\text{NaCl}}/\text{g}_{\text{electrode}}$ at a charge efficiency of $96 \pm 4\%$; at 20 mM, we find barely statistically differentiable values, namely, a desalination capacity of $11 \pm 1 \text{ mg}_{\text{NaCl}}/\text{g}_{\text{electrode}}$ at a charge efficiency of $114 \pm 7\%$. The corresponding electrode potentials are found in Figure S5B,D. While the potential profiles with or without the anion-exchange membrane are highly comparable at aqueous 600 mM NaCl (Figure S5A–B), there is a notable difference at 20 mM. As seen from Figure 4C,D, the spikes in the potential profiles of MXene-CNT in the configuration without the ion-exchange membrane are absent after adapting the anion-exchange membrane in front of the activated-carbon electrode. This caused in return a more sluggish ion transport toward the nanoporous carbon electrode through the ion-exchange membrane, which kinetically resulted in a slower process compared to ion intercalation within the MXene interlayers. Accordingly, there are visible spikes in the potential distribution of the activated-carbon electrode and corresponding notches in the MXene-CNT profiles.

3.4. Why Is the Asymmetric Cell Accomplishing Desalination Even at High Molar Strength? As seen from our data (and previous works), it is well-known that activated carbon with pores larger than 1 nm fails to provide any significant permselectivity in the context of counterion electrodosorption during capacitive deionization.^{10,55} The activated carbon used in this study has a rather wide pore size of 1.3 nm (Figure S1A), which is much larger than the hydrated sodium or chloride ions ($\sim 4 \text{ \AA}$).^{56,57} Since the pristine activated carbon used in this study is neither oxidized nor reduced, few surface groups must exist on the carbon surface, rendering it nonstereoselective and nonmolecular sieving without discrimination toward cations or anions. In other words, in an uncharged state, both sodium and chloride

ions coexist within carbon micropores, as previously shown in our work, by use of *in situ* small-angle X-ray scattering⁵⁸ and via modeling.¹⁰ Therefore, when two activated-carbon electrodes are paired in a symmetrical desalination cell, carbon micropores will both desorb co-ions (undesired) and attract counterions (desired). At a high molar strength, the co-ion expulsion dominates to such a great extent that effectively no desalination is accomplished (Figure 4C).

When MXene is paired with activated carbon, a charge efficiency of above 80% is maintained in the case of 600 mM without any ion-exchange membrane. This high charge efficiency implies that minimal co-ion expulsion takes place at both MXene and activated-carbon electrodes in an asymmetric configuration. On the side of the MXene-CNT electrode, the negative surface charges repel chloride ions that approach the surface, and as a result, no electric charge is wasted repelling the chloride ions but rather is exclusively invested to intercalating of sodium ions in between the MXene sheets. Given that the bulk solution must be electroneutral, chloride ions are then forced to be electrosorbed onto the otherwise nonpermselective activated carbon. MXene itself has the intrinsic ability to intercalate cations and anions; however, it does so in a nearly perfectly permselective manner, that is, the screened environment within the MXene interlayers allows for counterion intercalation at low and high molar strength of the bulk electrolyte.^{14,40}

The permselectivity forced upon the activated carbon by the MXene-CNT electrode can also be aided by the asymmetric electrode potential distribution. In regular CDI with symmetric cells and two electrodes composed of activated carbon, the cell is usually discharged to 0 V. The potential range around 0 V, however, is the regime in which the electroneutrality within the carbon nanopores is re-established by replenishing the initial population of co- and counterions (ideally in the same ratio as that found in bulk).^{48,49,59} Keeping the carbon electrode at all times outside that potential regime aids in avoiding the regime of permselectivity failure.⁶⁰ For example, Kim et al. demonstrated for a symmetric CDI system based on a similar activated carbon (Kuraray YP-50F) cycled between 0.3 and 1.2 V cell voltage a maximum desalination capacity of about $9 \text{ mg}_{\text{NaCl}}/\text{g}_{\text{electrode}}$ at a corresponding charge efficiency of 60–90% (depending on the half-cycle time) at a molar strength of 20 mM NaCl.⁶¹ However, it is not realistic to assume that the permselective regime can be accessed by activated carbon within the range of +0.2 V to +0.5 V vs Ag/AgCl at high molar strength, such as studied by us when using 600 mM NaCl. At such a high ion concentration, the entire potential range is dominated by nonpermselective ion-exchange.⁵⁸

When we now compare the performance at low and high molar strength with or without the added ion-exchange membrane to screen ions moving toward the carbon electrode, we see only small effective differences in the desalination performance. At 20 mM NaCl, the desalination capacity is virtually indistinguishable, while at 600 mM, there is a small increase when using the anion-exchange membrane. For the system at 20 mM, it is reasonable to assume that the potential range control of activated carbon and the intrinsic uptake of counterions of MXene-CNT alone allow for permselective ion removal. Adding an ion-exchange membrane has little effect in that case. However, for 600 mM, the carbon electrode is forced by the permselectivity of MXene-CNT to also behave permselectively: This is not a perfect state, and we see an improvement in desalination performance in case of enhancing

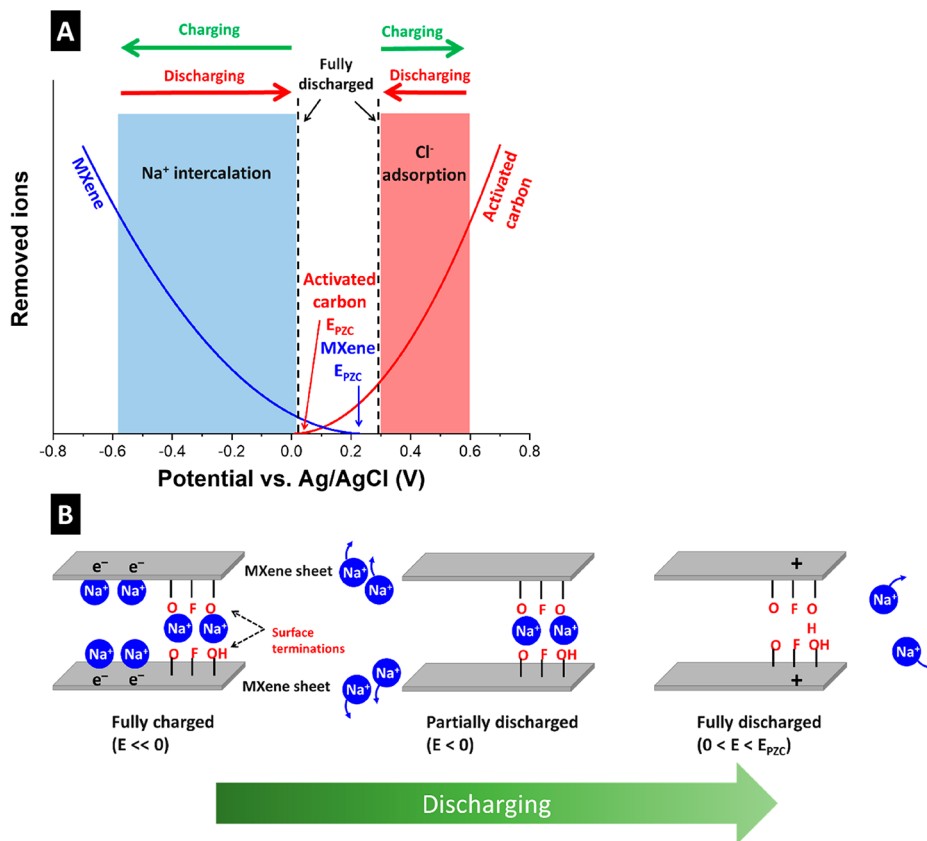


Figure 5. (A) Illustration of (approximate) location of potential at zero charge and the population of adsorbed ions upon charge/discharge. The E_{PZC} values of MXene and carbon electrodes are meant to schematically show the relative positions of these values with respect to each other. (B) Schematic representation of sodium ions interaction with MXene surface terminations during discharge half-cycle.

the carbon electrode's permselectivity further with an added ion-exchange membrane allowing only the removal of anions.

The enhanced permselectivity of the asymmetric MXene-CNT/activated-carbon system over that of the symmetric activated-carbon/activated-carbon system is seen from the corresponding energy consumptions (Figure S6). In all MXene/activated-carbon cells, the energy consumed per removed salt ion is around 40 kT, and it barely changes across the two concentrations tested. However, activated-carbon/activated-carbon cells show an energy consumption of 82 kT at 20 mM and 670 kT at 600 mM, showing ineffective desalination in case of the latter salt concentration. The energy consumed to accomplish desalination could be an important metric to take into consideration when comparing various CDI systems with each other, as well as comparisons across available desalination technologies.

3.5. Why Is the Asymmetric System Exceeding a Charge Efficiency of 100% at 20 mM? In the 20 mM system, the charge efficiency repeatedly exceeds 100% and stays there persistently for the whole duration of measurements. This effect, at low molar strength, is not limited to the presence of an ion-exchange membrane, so we cannot explain the charge efficiency in terms of an addition ion-removal capacity of the (mass-wise not accounted) anion-exchange membrane (as shown, for example, by Zhang et al.⁵⁴ and Tang et al.).⁶² This effect also enhanced the average desalination capacity at 20 mM system (12 mg/g for the cell without membrane) compared to that in the 600 mM system (8 mg/g for the cell without membrane). In the system operated at aqueous 20 mM NaCl, we do not see much of a statistically

significant difference between operation with or without the anion-exchange membrane regarding the charge efficiency. A charge efficiency above 100% means that per 1 mole of electric charge invested upon charging, more than 1 mole of salt ions is removed (or released upon discharging). This surprising effect might be explained in the context of MXene surface charges and the concept of potential at zero charge (E_{PZC}), which follows herein.

$Ti_3C_2T_x$ -MXene has negatively charged surface functionalities such as $-O^-$, $-OH$, or $-F^-$,⁶³ and as a result has a strong affinity toward positive ionic species such as metal cations^{64,65} in aqueous media even under no applied potential (MXene as an adsorbent powder, not as an electrode). These negative surface charges shift the E_{PZC} toward positive potentials. This is evidenced by the streaming potential measurements (Figure S7) on MXene that show a point of zero charge at a pH of 1.5. This means that MXene is negatively charged all the way down to this highly acidic pH, at which point it exhibits a neutral net electric charge, possibly due to protonation of the hydroxyl terminal groups of MXene.⁶⁵ Zeta potential measurements on $Ti_3C_2T_x$ -MXene in other studies has also shown a point of zero charge at pH values between 2 and 3.^{64,65} For comparison, the activated carbon reaches charge neutrality at a pH value of about 3.5 but with a much steeper streaming potential profile as a function of the pH value (in agreement with previous work).⁴⁶

The applied potential range has an important effect on the charge efficiency of a desalination cell.^{42,66,67} Systematic studies on symmetric activated-carbon CDI cells^{48,49} have shown that highest charge efficiencies (i.e., low co-ion

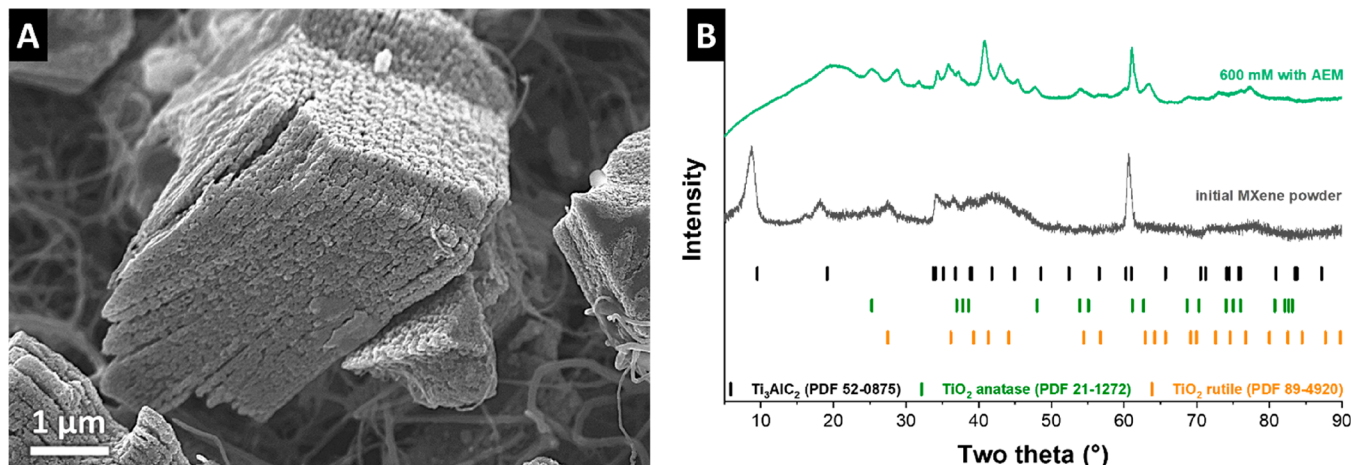


Figure 6. (A) SEM image of post mortem MXene-CNT electrode after long-term cycling and (B) its corresponding X-ray diffractograms, compared to those of pristine MXene-CNT and a number of different titanium oxide species [Powder Diffraction File (PDF) nos. 21-1272, 52-0875, and 89-4920, Joint Committee on Powder Diffraction Standards, 2004].

expulsion/high counterion uptake) are obtained when the cell is not fully discharged to E_{PZC} , but rather to a potential far enough thereof.⁶¹ This condition has apparently been met in our work by cycling within 0.3–1.2 V, as shown schematically in Figure 5A. Discharging to a lower potential limit of 0.3 V prevents MXene and activated carbon to cross their respective E_{PZC} and minimizes parasitic co-ion expulsion phenomenon, resulting in a high charge efficiency. This effect, however, does not explain why the system at low molar strength would be able to exceed charge efficiency values of 100%.

The additional gain in charge efficiency above 100% should then be attributed to the negative surface charges of MXene, which serve as an additional chemical charge.⁶⁹ When MXene is negatively polarized, sodium ions intercalate between MXene sheets due to the attraction they feel from both negative applied electric charge and negative surface dipole of functional groups, as schematically illustrated in Figure 5B. Upon discharging the MXene-CNT electrode to 0 V vs Ag/AgCl (Figure S5), all the said applied negative electric charge are retracted, resulting in the release of the corresponding sodium ions adsorbed, while the surface charges still cling to their corresponding sodium ions. Upon further discharging to potentials slightly higher than zero (but still away from E_{PZC}), a positive charge is induced in MXene sheets, which helps to overcome the negative charge of surface charges and thereby releasing the remaining sodium ions and regenerating the surface groups. At this point, sodium ions are again in part spontaneously adsorbed to the surface charges in addition to the attraction arising from electric charges. The former is similar to the inverted CDI system at a lower voltage limit, that is, ion adsorption upon discharge due to electrode surface charges.⁶⁸ The spontaneous chemisorption of sodium ions onto the negative surface functionalities of MXene could explain the additional gain in charge efficiency. That is, no electric charge is invested for those fractions of ions desalinated via interaction with MXene surface terminations. Consequently, the system capitalizes on MXene surface charges and can remove more than one ion per one electron charge invested; hence, a charge efficiency of above 100% is obtained.

3.6. Post-Mortem Analysis of MXene-CNT Electrodes after Desalination Operation.

Post-mortem data of the

MXene-CNT electrodes after long-term cycling, including electron microscopy, EDX analysis, and X-ray diffraction, are shown in Figure 6 and Table 1. The data shown in Figure 6 originate from the cell with an anion-exchange membrane at a discharged state cycled in 600 mM solution; SEM images and X-ray diffraction data for post-mortem samples after the operation at 20 mM (with and without ion-exchange membrane) and at 600 mM without the anion-exchange membrane are found in Figures S8 and S9.

As seen in Figure 2, the pristine MXene surface is already slightly oxidized, covered with cuboid-like titanate particles. A comparison of SEM images of pristine MXene-CNT (Figure 2A) and post-mortem electrodes (Figure 6A) reveals a much larger degree of coverage of MXene layers with titanium oxide particles. The increase in oxygen (found for all samples) is mostly accomplished by a decrease in the content of fluorine (Table 1).

The X-ray diffraction pattern of the post-mortem electrode is consistent with previous works on oxidized $\text{Ti}_3\text{C}_2\text{T}_{x,\text{f}}$;⁶⁹ specifically, we note the absence of the characteristic (002)-MXene peak due to oxidation-related disruption in the stacking periodicity and the development of a broad peak at around 20° 2θ . The disappearance of the (002) peak can also relate to the insertion/deinsertion of sodium ions between the MXene layers during the electrochemical process and the formation of TiO_2 crystals; both effects disrupt the initial MXene-layer stacking order. The low temperature of the oxidation process and the small length-scale of the formed titanium oxide domains are mostly consistent with the formation of nanorutile, but further TiO_2 phases (such as anatase) cannot be excluded.

4. CONCLUSIONS

Our work explores the electrochemical desalination of asymmetric hybrid CDI using MXene-CNT paired with activated carbon for electrochemical desalination of brackish- and seawater-level NaCl concentrations in aqueous media. Using $\text{Ti}_3\text{C}_2\text{T}_{x,\text{f}}$ -MXene as the negative electrode and nanoporous activated carbon as the positive electrode, stable desalination performance for up to 100 cycles has been accomplished with desalination capacities up to 12 mg/g and charge efficiencies over 80%. It was shown that in the case of

asymmetric configuration permselective behavior is observed without the use of an ion-exchange membrane. While at 20 mM NaCl, the attained permselectivity of the system's response can be rationalized by the selected potential range (avoiding 0 V), it cannot explain the near-100% charge efficiency when using 600 mM NaCl. In addition, we see an excess of the charge efficiency beyond 100% at low molar strength, which can only be explained by the active role played by interlayer surface termination of MXene during the electrochemical desalination cycling. Our data show that at slightly reduced charge efficiency and desalination capacity MXene-CNT paired with activated carbon does not require an ion-exchange membrane for remediation of aqueous 600 mM NaCl. The omission of the ion-exchange membrane from the cell components can thus significantly reduce the overall costs in light of industrial applications.

■ ASSOCIATED CONTENT

Supporting Information

The Supporting Information is available free of charge at <https://pubs.acs.org/doi/10.1021/acsami.0c05975>.

Nitrogen gas sorption isotherms, transmission electron micrograph images of CNT, cyclic voltammetry of CNT, potential distribution profiles of MXene-CNT/AC cells, energy consumption, streaming potential response of MXene and AC, SEM and XRD of post-mortem MXene-CNT electrodes([PDF](#))

■ AUTHOR INFORMATION

Corresponding Author

Volker Presser — INM - Leibniz Institute for New Materials, 66123 Saarbrücken, Germany; Department of Materials Science & Engineering, Saarland University, 66123 Saarbrücken, Germany;  [0000-0003-2181-0590](https://orcid.org/0000-0003-2181-0590); Email: presser@presser-group.com

Authors

Mohammad Torkamanzadeh — INM - Leibniz Institute for New Materials, 66123 Saarbrücken, Germany; Department of Materials Science & Engineering, Saarland University, 66123 Saarbrücken, Germany

Lei Wang — INM - Leibniz Institute for New Materials, 66123 Saarbrücken, Germany; Department of Materials Science & Engineering, Saarland University, 66123 Saarbrücken, Germany

Yuan Zhang — INM - Leibniz Institute for New Materials, 66123 Saarbrücken, Germany; Department of Materials Science & Engineering, Saarland University, 66123 Saarbrücken, Germany

Öznur Budak — INM - Leibniz Institute for New Materials, 66123 Saarbrücken, Germany; Department of Materials Science & Engineering, Saarland University, 66123 Saarbrücken, Germany

Pattarakai Srimuk — INM - Leibniz Institute for New Materials, 66123 Saarbrücken, Germany

Complete contact information is available at:

<https://pubs.acs.org/doi/10.1021/acsami.0c05975>

Notes

The authors declare no competing financial interest.

■ ACKNOWLEDGMENTS

We acknowledge funding of the MXene-CDI project (PR-1173/11) by the German Research Foundation (DFG, Deutsche Forschungsgemeinschaft). L.W. acknowledges funding from the Chinese Scholarship Council (CSC) via award number 201906260277. We thank Eduard Arzt (INM) for his continuing support.

■ REFERENCES

- (1) Elimelech, M.; Phillip, W. A. The Future Of Seawater Desalination: Energy, Technology, And The Environment. *Science* **2011**, *333* (6043), 712–717.
- (2) Suss, M. E.; Porada, S.; Sun, X.; Biesheuvel, P. M.; Yoon, J.; Presser, V. Water Desalination Via Capacitive Deionization: What Is It And What Can We Expect From It? *Energy Environ. Sci.* **2015**, *8* (8), 2296–2319.
- (3) Porada, S.; Zhao, R.; Van Der Wal, A.; Presser, V.; Biesheuvel, P. Review On The Science And Technology Of Water Desalination By Capacitive Deionization. *Prog. Mater. Sci.* **2013**, *58* (8), 1388–1442.
- (4) Andelman, M. D. The Flow Through Capacitor: A New Tool In Wastewater Purification. *Filtr. Sep.* **1998**, *May*, 345–347.
- (5) Porada, S.; Weinstein, L.; Dash, R.; Van Der Wal, A.; Bryjak, M.; Gogotsi, Y.; Biesheuvel, P. Water Desalination Using Capacitive Deionization With Microporous Carbon Electrodes. *ACS Appl. Mater. Interfaces* **2012**, *4* (3), 1194–1199.
- (6) Srimuk, P.; Su, X.; Yoon, J.; Aurbach, D.; Presser, V. Charge-Transfer Materials For Electrochemical Water Desalination, Ion Separation And The Recovery Of Elements. *Nat. Rev. Mater.* **2020**, DOI: [10.1038/s41578-020-0193-1](https://doi.org/10.1038/s41578-020-0193-1).
- (7) Zhao, R.; Biesheuvel, P.; Van der Wal, A. Energy Consumption And Constant Current Operation In Membrane Capacitive Deionization. *Energy Environ. Sci.* **2012**, *5* (11), 9520–9527.
- (8) Biesheuvel, P. M.; van der Wal, A. Membrane Capacitive Deionization. *J. Membr. Sci.* **2010**, *346* (2), 256–262.
- (9) Kim, N.; Lee, J.; Kim, S.; Hong, P. S.; Lee, C.; Yoon, J.; Kim, C. Short Review Of Multichannel Membrane Capacitive Deionization: Principle, Current Status, And Future Prospect. *Appl. Sci.* **2020**, *10* (2), 683.
- (10) Bi, S.; Zhang, Y.; Cervini, L.; Mo, T.; Griffin, J. M.; Presser, V.; Feng, G. Permselective Ion Electrosorption Of Subnanometer Pores At High Molar Strength Enables Capacitive Deionization Of Saline Water. *Sustainable Energy Fuels* **2020**, *4* (3), 1285–1295.
- (11) Singh, K.; Porada, S.; de Gier, H. D.; Biesheuvel, P. M.; de Smet, L. C. P. M. Timeline On The Application Of Intercalation Materials In Capacitive Deionization. *Desalination* **2019**, *455*, 115–134.
- (12) Pasta, M.; Wessells, C. D.; Cui, Y.; La Mantia, F. A Desalination Battery. *Nano Lett.* **2012**, *12* (2), 839–843.
- (13) Lee, J.; Kim, S.; Kim, C.; Yoon, J. Hybrid Capacitive Deionization To Enhance The Desalination Performance Of Capacitive Techniques. *Energy Environ. Sci.* **2014**, *7* (11), 3683–3689.
- (14) Srimuk, P.; Kaasik, F.; Krüner, B.; Tolosa, A.; Fleischmann, S.; Jäckel, N.; Tekeli, M. C.; Aslan, M.; Suss, M. E.; Presser, V. MXene As A Novel Intercalation-Type Pseudocapacitive Cathode And Anode For Capacitive Deionization. *J. Mater. Chem. A* **2016**, *4* (47), 18265–18271.
- (15) Srimuk, P.; Husmann, S.; Presser, V. Low Voltage Operation Of A Silver/Silver Chloride Battery With High Desalination Capacity In Seawater. *RSC Adv.* **2019**, *9* (26), 14849–14858.
- (16) Su, X.; Hatton, T. A. Redox-Electrodes For Selective Electrochemical Separations. *Adv. Colloid Interface Sci.* **2017**, *244*, 6–20.
- (17) Lee, J.; Srimuk, P.; Zornetta, R. L.; Aslan, M.; Mehdi, B. L.; Presser, V. High Electrochemical Seawater Desalination Performance Enabled By An Iodide Redox Electrolyte Paired With A Sodium Superionic Conductor. *ACS Sustainable Chem. Eng.* **2019**, *7* (11), 10132–10142.

- (18) Kim, S.; Kim, C.; Lee, J.; Kim, S.; Lee, J.; Kim, J.; Yoon, J. Hybrid Electrochemical Desalination System Combined With An Oxidation Process. *ACS Sustainable Chem. Eng.* **2018**, *6* (2), 1620–1626.
- (19) Srimuk, P.; Wang, L.; Budak, Ö.; Presser, V. High-Performance Ion Removal Via Zinc-Air Desalination. *Electrochim. Commun.* **2020**, *115*, 106713.
- (20) Naguib, M.; Mashtalir, O.; Carle, J.; Presser, V.; Lu, J.; Hultman, L.; Gogotsi, Y.; Barsoum, M. W. Two-Dimensional Transition Metal Carbides. *ACS Nano* **2012**, *6* (2), 1322–1331.
- (21) Gogotsi, Y.; Anasori, B. The Rise of MXenes. *ACS Nano* **2019**, *13* (8), 8491–8494.
- (22) Anasori, B.; Lukatskaya, M. R.; Gogotsi, Y. 2D Metal Carbides And Nitrides (MXenes) For Energy Storage. *Nat. Rev. Mater.* **2017**, *2*, 16098.
- (23) Natu, V.; Pai, R.; Sokol, M.; Carey, M.; Kalra, V.; Barsoum, M. W. 2D $Ti_3C_2T_x$ Mxene Synthesized By Water-Free Etching Of Ti_3AlC_2 In Polar Organic Solvents. *Chem.* **2020**, *6* (3), 616–630.
- (24) Shahzad, F.; Alhabeb, M.; Hatter, C. B.; Anasori, B.; Man Hong, S.; Koo, C. M.; Gogotsi, Y. Electromagnetic Interference Shielding With 2D Transition Metal Carbides (MXenes). *Science* **2016**, *353* (6304), 1137–1140.
- (25) Orangi, J.; Hamade, F.; Davis, V. A.; Beidaghi, M. 3D Printing Of Additive-Free 2D $Ti_3C_2T_x$ (MXene) Ink For Fabrication Of Micro-Supercapacitors With Ultra-High Energy Densities. *ACS Nano* **2020**, *14* (1), 640–650.
- (26) Sun, D.; Wang, M.; Li, Z.; Fan, G.; Fan, L.-Z.; Zhou, A. Two-Dimensional Ti_3C_2 As Anode Material For Li-Ion Batteries. *Electrochim. Commun.* **2014**, *47*, 80–83.
- (27) Lukatskaya, M. R.; Mashtalir, O.; Ren, C. E.; Dall'Agnese, Y.; Rozier, P.; Taberna, P. L.; Naguib, M.; Simon, P.; Barsoum, M. W.; Gogotsi, Y. Cation Intercalation And High Volumetric Capacitance Of Two-Dimensional Titanium Carbide. *Science* **2013**, *341* (6153), 1502–1505.
- (28) Ren, C. E.; Hatzell, K. B.; Alhabeb, M.; Ling, Z.; Mahmoud, K. A.; Gogotsi, Y. Charge-And Size-Selective Ion Sieving Through $Ti_3C_2T_x$ MXene Membranes. *J. Phys. Chem. Lett.* **2015**, *6* (20), 4026–4031.
- (29) Peng, Q.; Guo, J.; Zhang, Q.; Xiang, J.; Liu, B.; Zhou, A.; Liu, R.; Tian, Y. Unique Lead Adsorption Behavior Of Activated Hydroxyl Group In Two-Dimensional Titanium Carbide. *J. Am. Chem. Soc.* **2014**, *136* (11), 4113–4116.
- (30) Rasool, K.; Pandey, R. P.; Rasheed, P. A.; Buczek, S.; Gogotsi, Y.; Mahmoud, K. A. Water Treatment And Environmental Remediation Applications Of Two-Dimensional Metal Carbides (MXenes). *Mater. Today* **2019**, *30*, 80–102.
- (31) Bao, W.; Tang, X.; Guo, X.; Choi, S.; Wang, C.; Gogotsi, Y.; Wang, G. Porous Cryo-Dried MXene For Efficient Capacitive Deionization. *Joule* **2018**, *2* (4), 778–787.
- (32) Ma, J.; Cheng, Y.; Wang, L.; Dai, X.; Yu, F. Free-Standing $Ti_3C_2T_x$ MXene Film As Binder-Free Electrode In Capacitive Deionization With An Ultrahigh Desalination Capacity. *Chem. Eng. J.* **2020**, *384*, 123329.
- (33) Amiri, A.; Chen, Y.; Bee Teng, C.; Naraghi, M. Porous Nitrogen-Doped MXene-Based Electrodes For Capacitive Deionization. *Energy Storage Materials* **2020**, *25*, 731–739.
- (34) Chen, B.; Feng, A.; Deng, R.; Liu, K.; Yu, Y.; Song, L. MXene as a Cation-Selective Cathode Material for Asymmetric Capacitive Deionization. *ACS Appl. Mater. Interfaces* **2020**, *12* (12), 13750–13758.
- (35) Huang, S.; Mochalin, V. N. Hydrolysis Of 2D Transition-Metal Carbides (MXenes) In Colloidal Solutions. *Inorg. Chem.* **2019**, *58* (3), 1958–1966.
- (36) Tian, Y.; Yang, C.; Tang, Y.; Luo, Y.; Lou, X.; Que, W. $Ti_3C_2T_x//AC$ Dual-Ions Hybrid Aqueous Supercapacitors With High Volumetric Energy Density. *Chem. Eng. J.* **2020**, *393*, 124790.
- (37) Carmona-Orbezo, A.; Le Fevre, L. W.; Dryfe, R. A. W. Performance Optimization Of Carbon Electrodes For Capacitive Deionization By Potentiostatic Analysis. *Electrochim. Acta* **2019**, *325*, 134898.
- (38) Zhang, Y.; Srimuk, P.; Husmann, S.; Chen, M.; Feng, G.; Presser, V. Effect Of Pore Size On The Ion Electrosorption And Hydrogen/Deuterium Electrosorption Using Sodium Chloride In H_2O And D_2O . *J. Electrochem. Soc.* **2019**, *166* (16), A4158–A4167.
- (39) Jäckel, N.; Weingarth, D.; Zeiger, M.; Aslan, M.; Grobelsek, I.; Presser, V. Comparison Of Carbon Onions And Carbon Blacks As Conductive Additives For Carbon Supercapacitors In Organic Electrolytes. *J. Power Sources* **2014**, *272* (1), 1122–1133.
- (40) Srimuk, P.; Halim, J.; Lee, J.; Tao, Q.; Rosen, J.; Presser, V. Two-Dimensional Molybdenum Carbide (MXene) With Divacancy Ordering For Brackish And Seawater Desalination Via Cation And Anion Intercalation. *ACS Sustainable Chem. Eng.* **2018**, *6* (3), 3739–3747.
- (41) Weingarth, D.; Zeiger, M.; Jäckel, N.; Aslan, M.; Feng, G.; Presser, V. Graphitization As A Universal Tool To Tailor The Potential-Dependent Capacitance Of Carbon Supercapacitors. *Adv. Energy Mater.* **2014**, *4* (13), 1400316.
- (42) Zornitta, R. L.; Srimuk, P.; Lee, J.; Krüner, B.; Aslan, M.; Ruotolo, L. A. M.; Presser, V. Charge And Potential Balancing For Optimized Capacitive Deionization Using Lignin-Derived, Low-Cost Activated Carbon Electrodes. *ChemSusChem* **2018**, *11* (13), 2101–2113.
- (43) Weingarth, D.; Noh, H.; Foelske-Schmitz, A.; Wokaun, A.; Kötz, R. A Reliable Determination Method Of Stability Limits For Electrochemical Double Layer Capacitors. *Electrochim. Acta* **2013**, *103*, 119–124.
- (44) Srimuk, P.; Lee, J.; Fleischmann, S.; Choudhury, S.; Jäckel, N.; Zeiger, M.; Kim, C.; Aslan, M.; Presser, V. Faradaic Deionization Of Brackish And Sea Water Via Pseudocapacitive Cation And Anion Intercalation Into Few-Layered Molybdenum Disulfide. *J. Mater. Chem. A* **2017**, *5* (30), 15640–15649.
- (45) Ghidiu, M.; Barsoum, M. W. The {110} Reflection In X-Ray Diffraction Of Mxene Films: Misinterpretation And Measurement Via Non-Standard Orientation. *J. Am. Ceram. Soc.* **2017**, *100* (12), 5395–5399.
- (46) Aslan, M.; Zeiger, M.; Jäckel, N.; Grobelsek, I.; Weingarth, D.; Presser, V. Improved Capacitive Deionization Performance Of Mixed Hydrophobic/Hydrophilic Activated Carbon Electrodes. *J. Phys.: Condens. Matter* **2016**, *28* (11), 114003.
- (47) Gerischer, H.; McIntyre, R.; Scherson, D.; Storck, W. Density Of The Electronic States Of Graphite: Derivation From Differential Capacitance Measurements. *J. Phys. Chem.* **1987**, *91* (7), 1930–1935.
- (48) Avraham, E.; Noked, M.; Bouhadana, Y.; Soffer, A.; Aurbach, D. Limitations Of Charge Efficiency In Capacitive Deionization II. On The Behavior Of CDI Cells Comprising Two Activated Carbon Electrodes. *J. Electrochim. Soc.* **2009**, *156* (10), P157–P162.
- (49) Avraham, E.; Noked, M.; Bouhadana, Y.; Soffer, A.; Aurbach, D. Limitations Of Charge Efficiency In Capacitive Deionization Processes III: The Behavior Of Surface Oxidized Activated Carbon Electrodes. *Electrochim. Acta* **2010**, *56* (1), 441–447.
- (50) Come, J.; Black, J. M.; Lukatskaya, M. R.; Naguib, M.; Beidaghi, M.; Rondinone, A. J.; Kalinin, S. V.; Wesolowski, D. J.; Gogotsi, Y.; Balke, N. Controlling The Actuation Properties Of MXene Paper Electrodes Upon Cation Intercalation. *Nano Energy* **2015**, *17*, 27–35.
- (51) Srimuk, P.; Lee, J.; Budak, Ö.; Choi, J.; Chen, M.; Feng, G.; Prehal, C.; Presser, V. In Situ Tracking Of Partial Sodium Desolvation Of Materials With Capacitive, Pseudocapacitive, And Battery-Like Charge/Discharge Behavior In Aqueous Electrolytes. *Langmuir* **2018**, *34* (44), 13132–13143.
- (52) Sun, Y.; Zhan, C.; Kent, P. R. C.; Naguib, M.; Gogotsi, Y.; Jiang, D. E. Proton Redox And Transport In Mxene-Confined Water. *ACS Appl. Mater. Interfaces* **2020**, *12* (1), 763–770.
- (53) Porada, S.; Borchardt, L.; Oschatz, M.; Bryjak, M.; Atchison, J. S.; Keesman, K. J.; Kaskel, S.; Biesheuvel, P. M.; Presser, V. Direct Prediction Of The Desalination Performance Of Porous Carbon Electrodes For Capacitive Deionization. *Energy Environ. Sci.* **2013**, *6* (12), 3700–3712.

- (54) Zhang, Y.; Srimuk, P.; Aslan, M.; Gallei, M.; Presser, V. Polymer Ion-Exchange Membranes For Capacitive Deionization Of Aqueous Media With Low And High Salt Concentration. *Desalination* **2020**, *479*, 114331.
- (55) Biesheuvel, P. M.; Porada, S.; Levi, M.; Bazant, M. Z. Attractive Forces In Microporous Carbon Electrodes For Capacitive Deionization. *J. Solid State Electrochem.* **2014**, *18* (5), 1365–1376.
- (56) Salitra, G.; Soffer, A.; Eliad, L.; Cohen, Y.; Aurbach, D. Carbon Electrodes For Double-Layer Capacitors I. Relations Between Ion And Pore Dimensions. *J. Electrochem. Soc.* **2000**, *147* (7), 2486.
- (57) Avraham, E.; Yaniv, B.; Soffer, A.; Aurbach, D. Developing Ion Electrodosorption Stereoselectivity, By Pore Size Adjustment With Chemical Vapor Deposition Onto Active Carbon Fiber Electrodes. Case of $\text{Ca}^{2+}/\text{Na}^+$ Separation In Water Capacitive Desalination. *J. Phys. Chem. C* **2008**, *112* (19), 7385–7389.
- (58) Prehal, C.; Koczwara, C.; Amenitsch, H.; Presser, V.; Paris, O. Salt Concentration And Charging Velocity Determine Ion Charge Storage Mechanism In Nanoporous Supercapacitors. *Nat. Commun.* **2018**, *9* (1), 4145.
- (59) Gao, X.; Omosebi, A.; Ma, Z.; Zhu, F.; Landon, J.; Ghorbanian, M.; Kern, N.; Liu, K. Capacitive Deionization Using Symmetric Carbon Electrode Pairs. *Environ. Sci.: Water Res. Technol.* **2019**, *5* (4), 660–671.
- (60) Shpigel, N.; Levi, M. D.; Sigalov, S.; Aurbach, D.; Daikhin, L.; Presser, V. Novel In Situ Multiharmonic EQCM-D Approach To Characterize Complex Carbon Pore Architectures For Capacitive Deionization Of Brackish Water. *J. Phys.: Condens. Matter* **2016**, *28* (11), 114001.
- (61) Kim, T.; Dykstra, J. E.; Porada, S.; van der Wal, A.; Yoon, J.; Biesheuvel, P. M. Enhanced Charge Efficiency And Reduced Energy Use In Capacitive Deionization By Increasing The Discharge Voltage. *J. Colloid Interface Sci.* **2015**, *446*, 317–326.
- (62) Tang, K.; Kim, Y.-h.; Chang, J.; Mayes, R. T.; Gabitto, J.; Yiakoumi, S.; Tsouris, C. Seawater Desalination By Over-Potential Membrane Capacitive Deionization: Opportunities And Hurdles. *Chem. Eng. J.* **2019**, *357* (1), 103–111.
- (63) Alhabeb, M.; Maleski, K.; Anasori, B.; Lelyukh, P.; Clark, L.; Sin, S.; Gogotsi, Y. Guidelines For Synthesis And Processing Of Two-Dimensional Titanium Carbide ($\text{Ti}_3\text{C}_2\text{T}_x$ MXene). *Chem. Mater.* **2017**, *29* (18), 7633–7644.
- (64) Fard, A. K.; Mckay, G.; Chamoun, R.; Rhadfi, T.; Preud'Homme, H.; Atieh, M. A. Barium Removal From Synthetic Natural And Produced Water Using MXene As Two Dimensional (2-D) Nanosheet Adsorbent. *Chem. Eng. J.* **2017**, *317*, 331–342.
- (65) Shahzad, A.; Rasool, K.; Miran, W.; Nawaz, M.; Jang, J.; Mahmoud, K. A.; Lee, D. S. Two-Dimensional $\text{Ti}_3\text{C}_2\text{T}_x$ MXene Nanosheets For Efficient Copper Removal From Water. *ACS Sustainable Chem. Eng.* **2017**, *5* (12), 11481–11488.
- (66) Abu Khalla, S.; Suss, M. E. Desalination Via Chemical Energy: An Electrodialysis Cell Driven By Spontaneous Electrode Reactions. *Desalination* **2019**, *467*, 257–262.
- (67) Porada, S.; Schipper, F.; Aslan, M.; Antonietti, M.; Presser, V.; Fellinger, T.-P. Capacitive Deionization Using Biomass-Based Microporous Salt-Templated Heteroatom-Doped Carbons. *ChemSusChem* **2015**, *8* (11), 1867–1874.
- (68) Gao, X.; Omosebi, A.; Landon, J.; Liu, K. Surface Charge Enhanced Carbon Electrodes For Stable And Efficient Capacitive Deionization Using Inverted Adsorption–Desorption Behavior. *Energy Environ. Sci.* **2015**, *8* (3), 897–909.
- (69) Zhang, M.; Chen, X.; Sui, J.; Abraha, B. S.; Li, Y.; Peng, W.; Zhang, G.; Zhang, F.; Fan, X. Improving the Performance of Titanium Carbide MXene in Supercapacitor by Partial Oxidation Treatment. *Inorg. Chem. Front.* **2020**, *7* (5), 1205–1211.

Supporting Information

MXene/activated carbon hybrid capacitive deionization for permselective ion removal at low and high salinity

Mohammad Torkamanzadeh,^{1,2} Lei Wang,^{1,2} Yuan Zhang,^{1,2}
Öznil Budak,^{1,2} Pattarachai Srimuk,¹ Volker Presser,^{1,2,*}

¹ INM - Leibniz Institute for New Materials, D2 2, 66123, Saarbrücken, Germany

² Department of Materials Science & Engineering, Saarland University, Campus D2 2, 66123, Saarbrücken, Germany

* Corresponding author's email: presser@presser-group.com

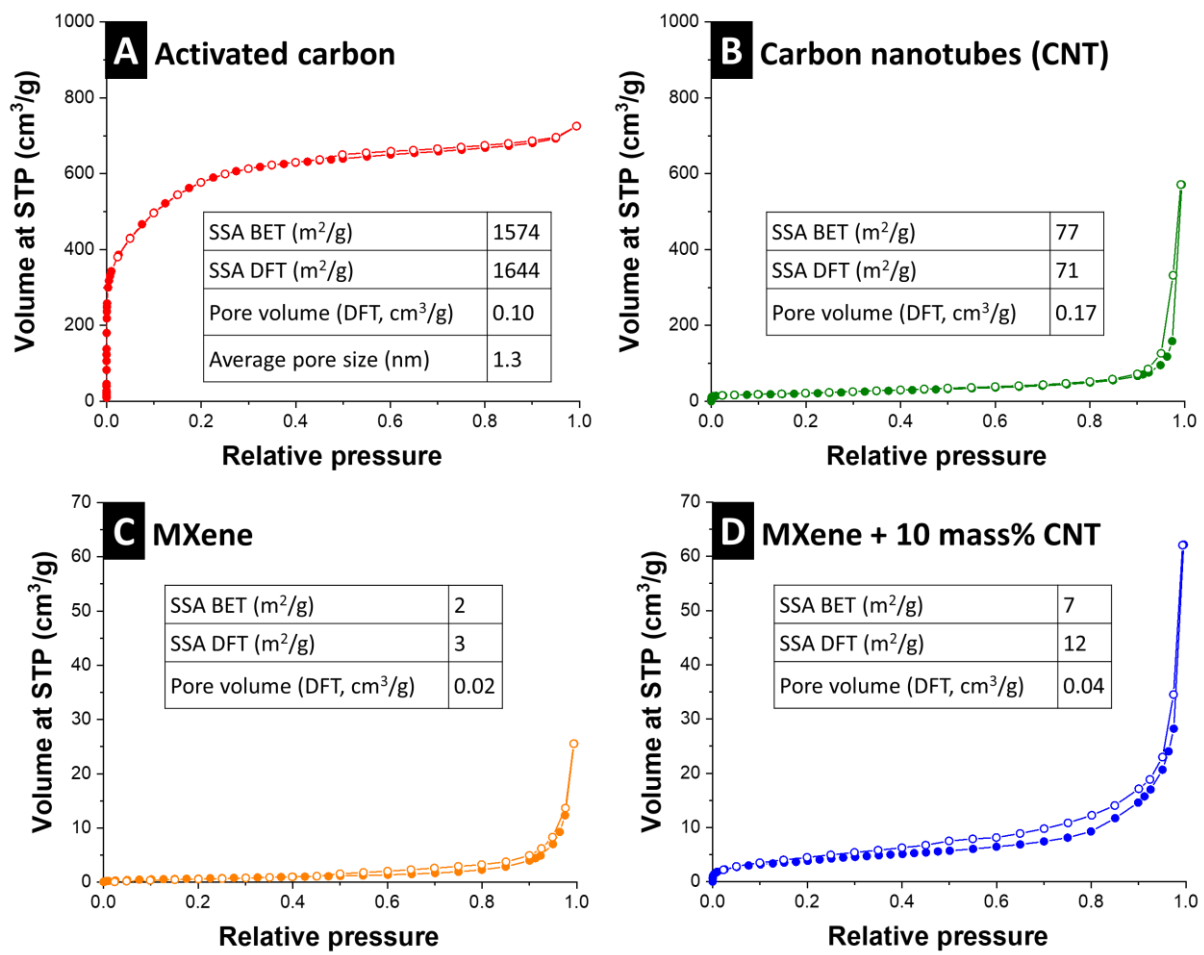


Figure S1: Nitrogen gas sorption isotherm of (A) activated carbon, (B) carbon nanotubes, (C) MXene powder, and (D) MXene/carbon nanotube electrodes recorded at a temperature of -196 °C. STP: standard temperature and pressure.

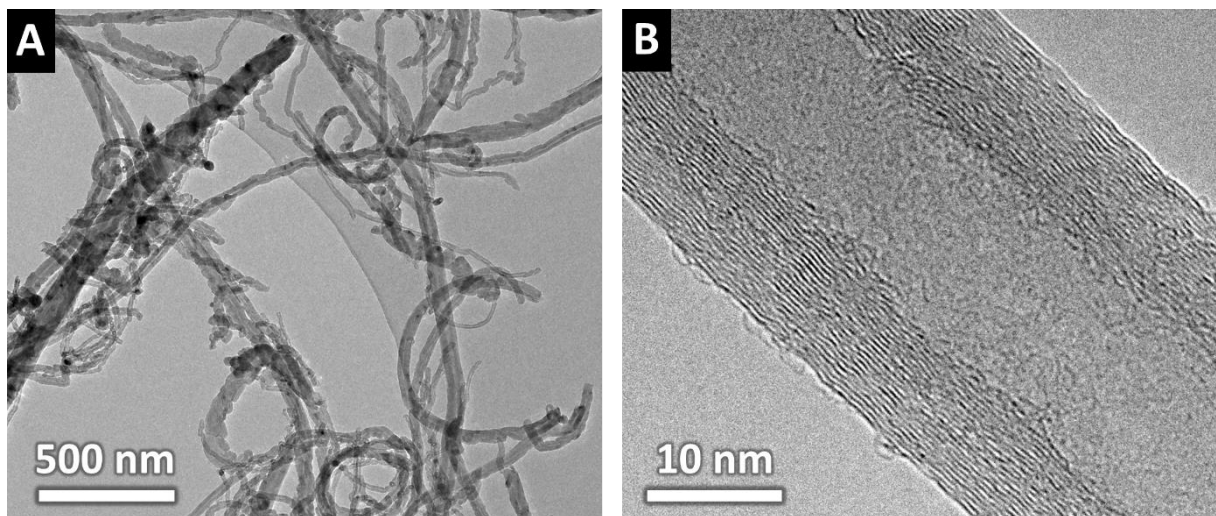


Figure S2: Transmission electron micrographs of the carbon nanotubes.

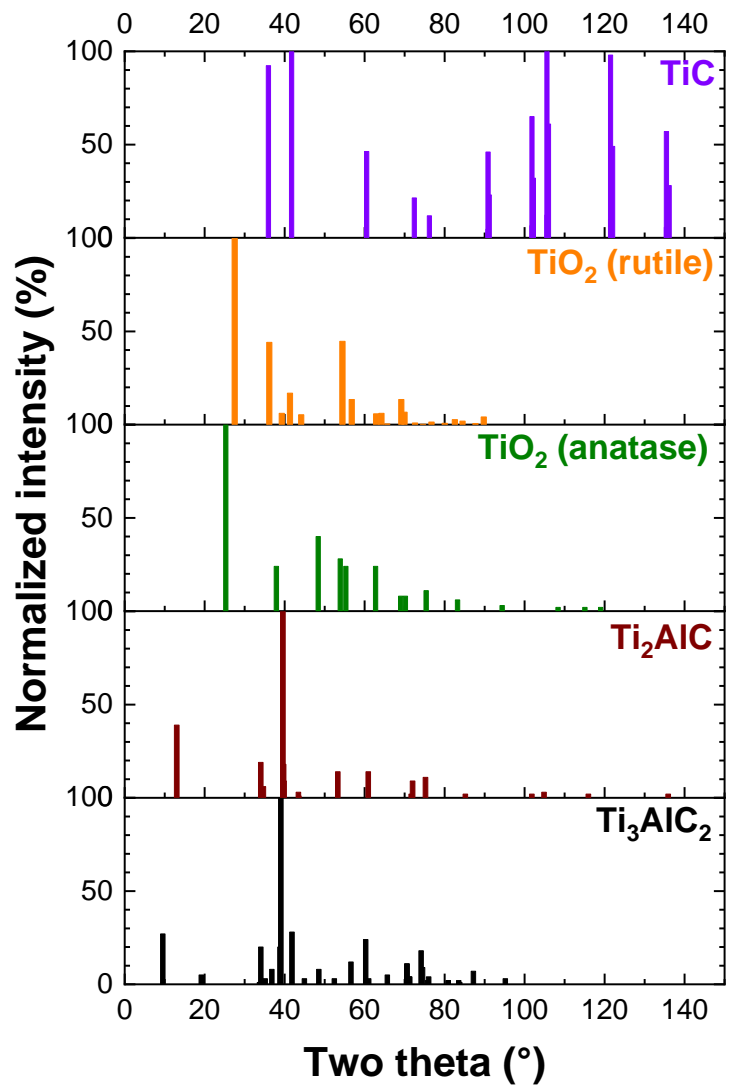


Figure S3: Relative intensities of the reference phases provided in Figure 2D.

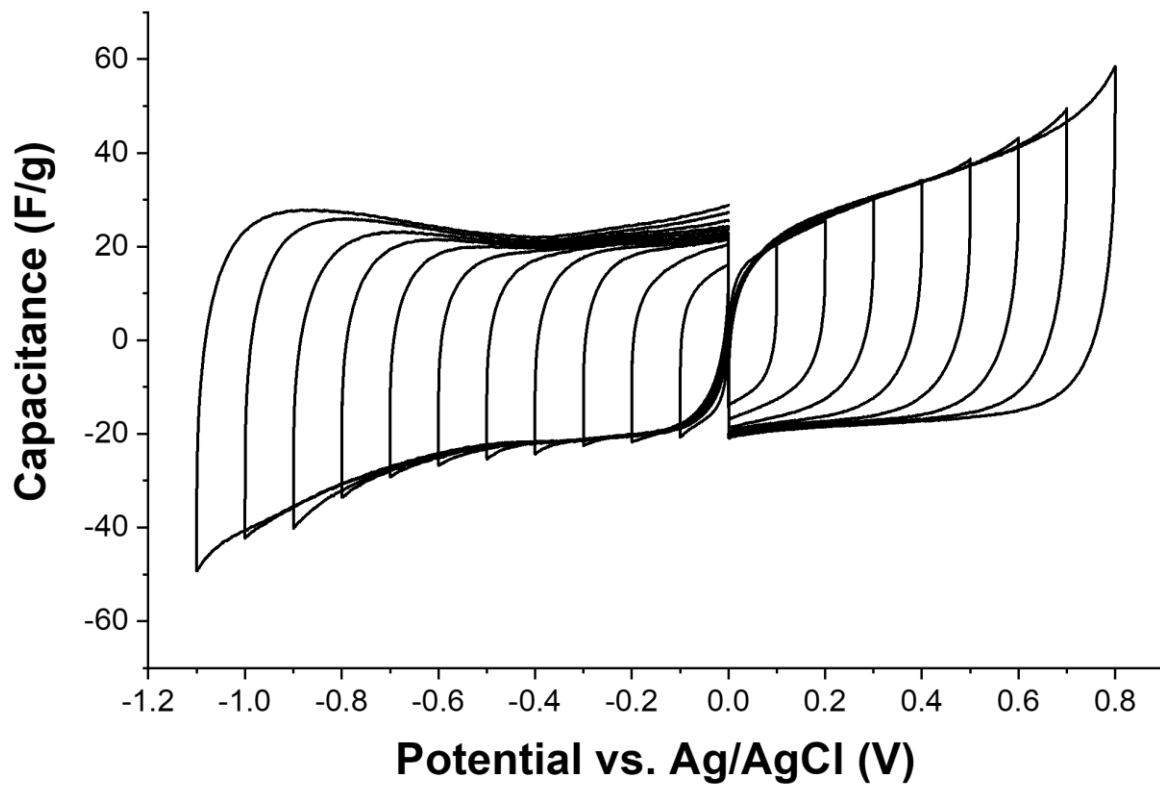


Figure S4: Half-cell window opening cyclic voltammograms of electrodes just composed of CNTs in aqueous 1 M NaCl electrolyte.

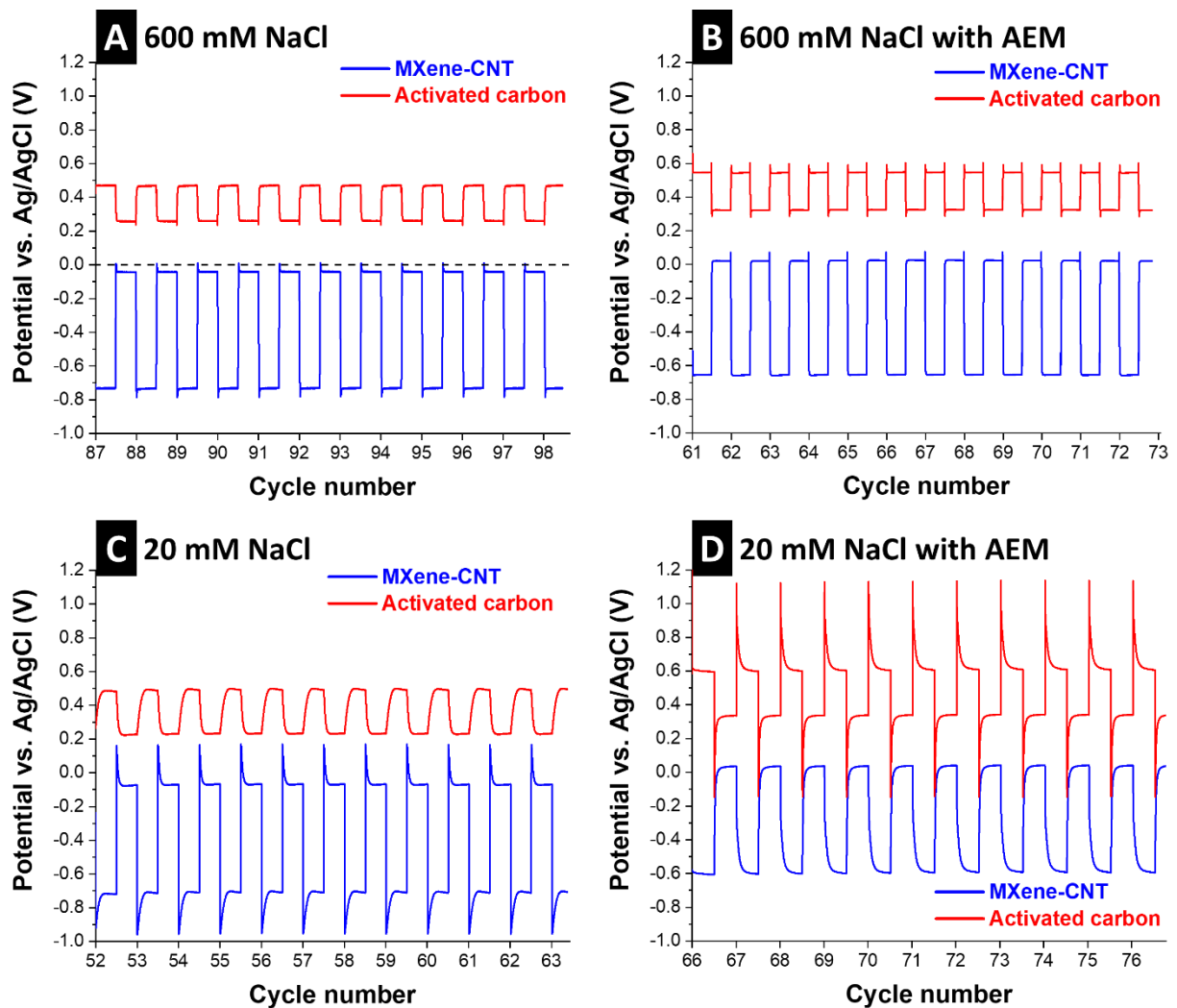


Figure S5: Potential development of individual electrodes upon charging the MXene/AC cell to a cell voltage of 1.2 V and discharging to a cell voltage of 0.3 V. (A-B) aqueous 600 mM NaCl; (C-D) aqueous 20 mM NaCl; (A,C) without an anion-exchange membrane (AEM) placed in front of the activated carbon electrode; (B,D) experiments with an AEM at the activated carbon electrode.

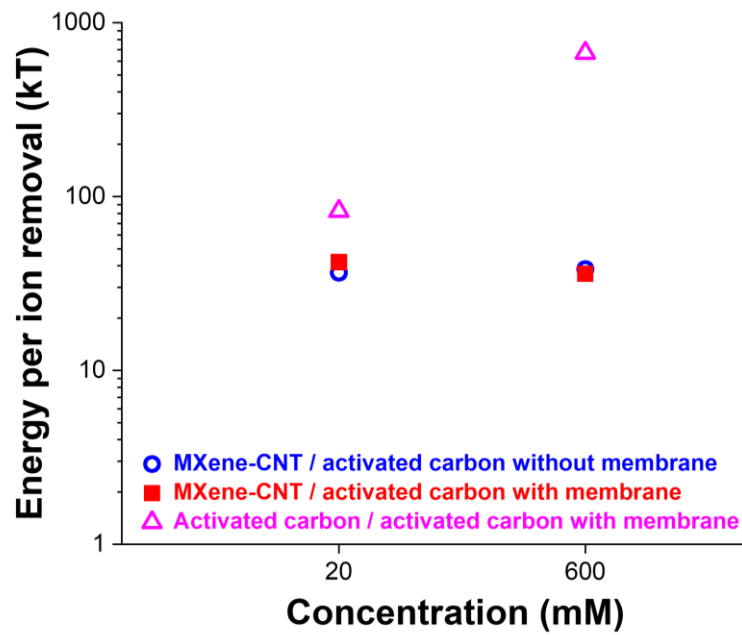


Figure S6: Energy consumption per ion removal.

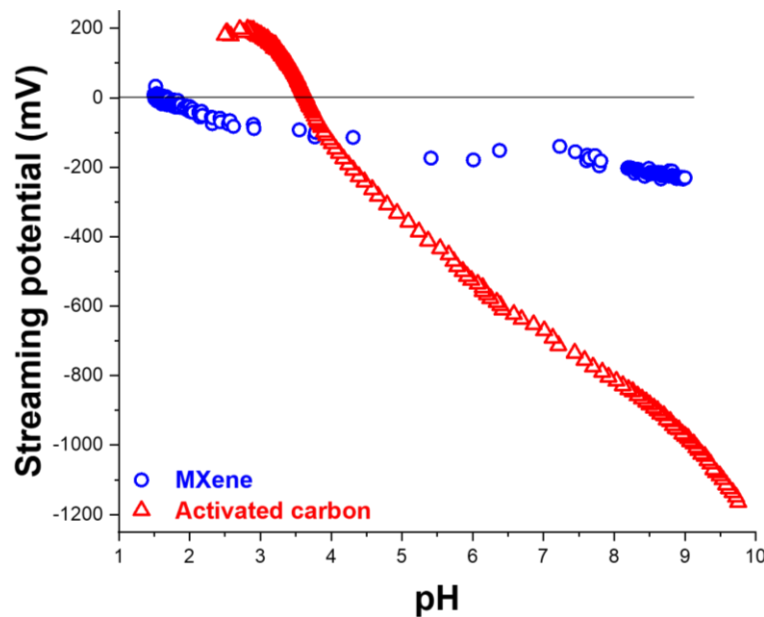


Figure S7: Streaming potential response of MXene and activated carbon in water.

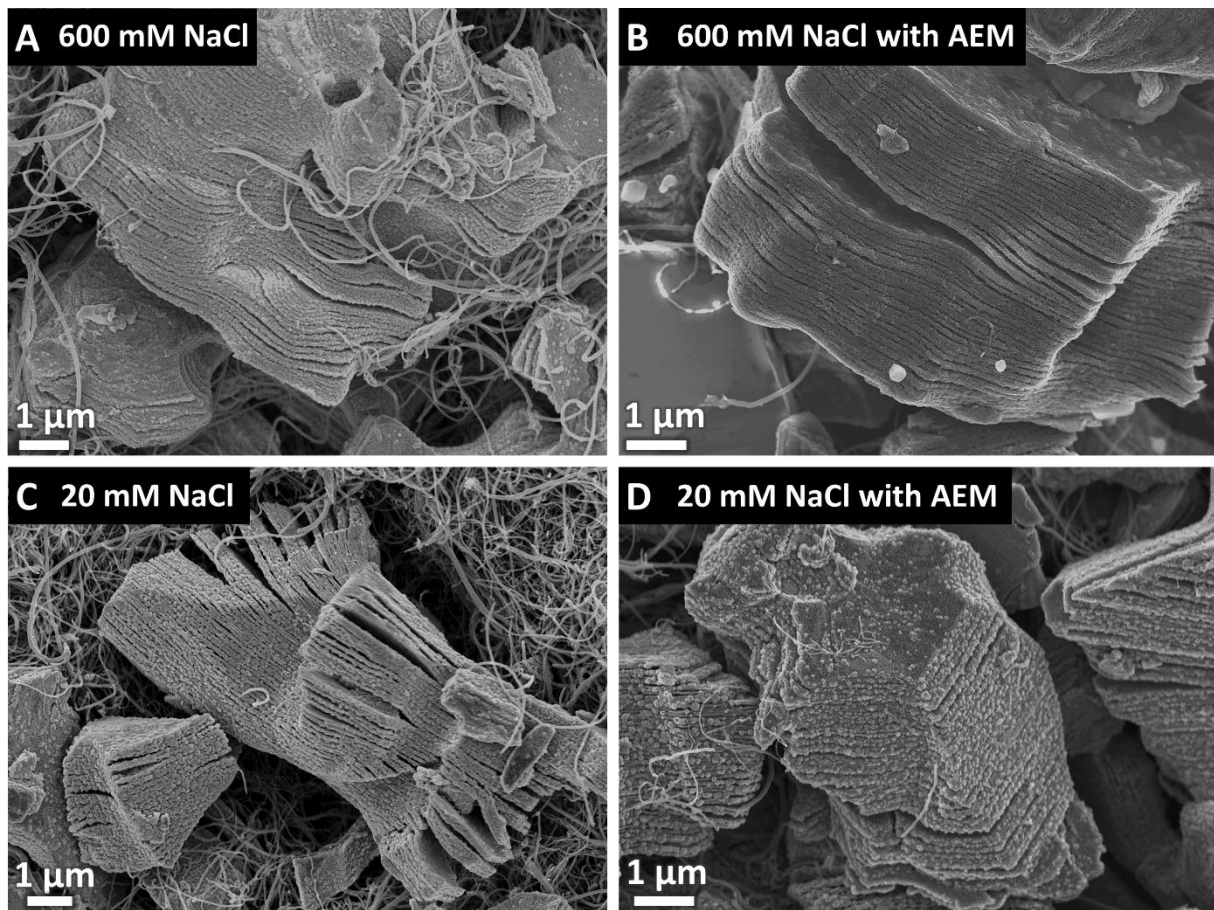


Figure S8: Post mortem scanning electron micrographs of MXene-CNT electrodes.

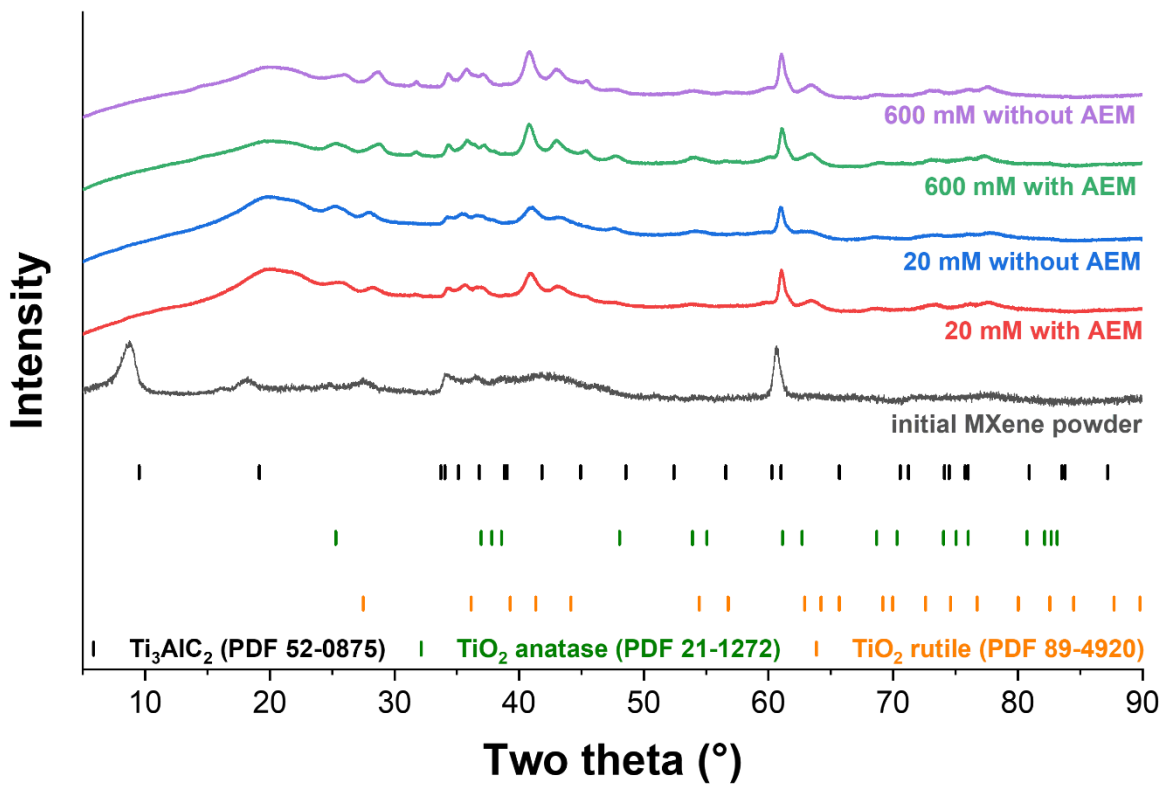


Figure S9: X-ray powder diffraction pattern of the initial MXene powder and after electrochemical operation for desalination (post mortem).

4.7 Particle size distribution influence on capacitive deionization: insights for electrode preparation

Yuan Zhang,^{1,2} Panyu Ren,^{1,2} Yang Liu,^{1,2} and Volker Presser^{1,2,3}

1 INM - Leibniz Institute for New Materials, Campus D2 2, 66123 Saarbrücken, Germany

2 Saarland University, Campus D2 2, 66123 Saarbrücken, Germany

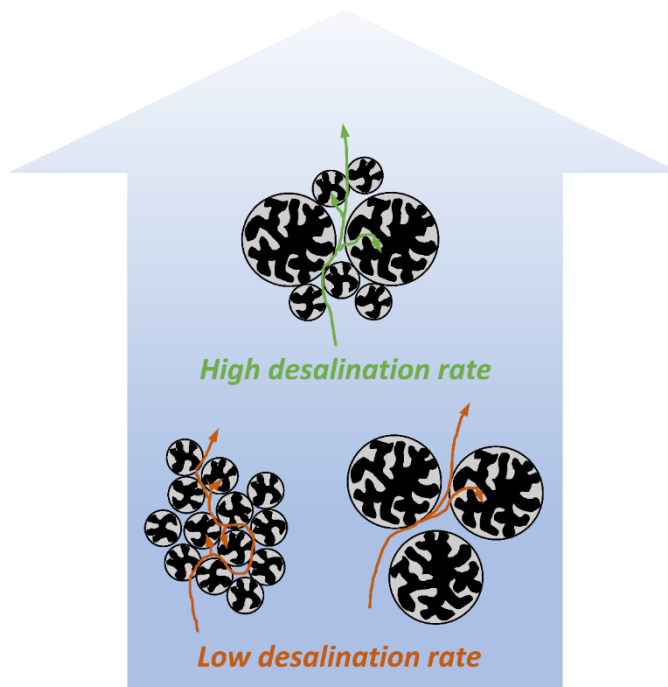
3 Saarene - Saarland Center for Energy Materials and Sustainability, Campus C4 2, 66123 Saarbrücken, Germany

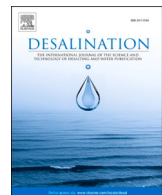
Citation:

Y. Zhang, P. Ren, Y. Liu, V. Presser, *Particle size distribution influence on capacitive deionization: insights for electrode preparation*, Desalination, 2021,

Own contribution:

Data curation, writing-original draft, supervision, visualization, investigation.





Particle size distribution influence on capacitive deionization: Insights for electrode preparation

Yuan Zhang ^{a,b}, Panyu Ren ^{a,b}, Yang Liu ^{a,b}, Volker Presser ^{a,b,c,*}

^a INM - Leibniz Institute for New Materials, Campus D2 2, 66123 Saarbrücken, Germany

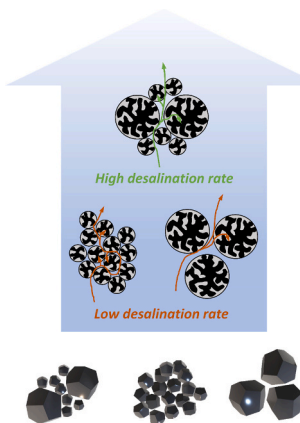
^b Saarland University, Campus D2 2, 66123 Saarbrücken, Germany

^c Saarene - Saarland Center for Energy Materials and Sustainability, Campus C4 2, 66123 Saarbrücken, Germany

HIGHLIGHTS

- Activated carbon powders consist of particles of different size which can be separated via physical methods.
- Different particle sizes of activated carbon electrodes will provide different performance for capacitive deionization.
- A mixture of larger and smaller particles was found to be most beneficial for electrochemical desalination.

GRAPHICAL ABSTRACT



ARTICLE INFO

Keywords:

Microporous carbon
Particle size
Ion transport
Water desalination

ABSTRACT

As freshwater shortage has become a global issue, water desalination technique is of great importance to meet the increasing demand for freshwater resources of human beings. Capacitive deionization (CDI) has attracted significant attention in the current desalination technology portfolio. This is because of the use of low-cost electrode materials and the promise of high energy efficiency when including the energy recovery process. CDI, which has its advantage for applying low ionic strength by using various materials, has been explored to improve the system's performance. However, very few have addressed the importance of proper parameter designs, especially the electrodes. In our work, the same activated carbon of different average particle sizes has been studied by applying different desalination parameters (flow rate, holding time, salt concentrations). Our data show that larger particles limit intraparticle ion transportation because of the increased diffusion path length. We also see that a higher packing density, often favored by smaller particles or distribution of particle sizes, is detrimental to interparticle ion transportation. Our work addressed the importance of proper electrode and desalination parameter design for higher desalination performances.

* Corresponding author at: Saarland University, Campus D2 2, 66123 Saarbrücken, Germany.

E-mail address: volker.presser@leibniz-inm.de (V. Presser).

1. Introduction

Freshwater scarcity has been increasingly perceived as a global issue [1]. With the large water consumption compared with freshwater availability, the river flows have decreased, with the lake water and groundwater levels declining. Around two-thirds of the global population live under severe water scarcity at least one month of the year [2]. With almost 98% of the water in the world being seawater or brackish water, the increasing demand for freshwater had aroused great attention in the water desalination area [3]. Conventional desalination technologies, including thermal distillation [4–6], electrodialysis [7,8], and reverse osmosis [9–11], are effective, but more energy-efficient technologies are in high demand to reach the goal of sustainable water remediation [12]. Electrochemical water desalination technologies are attracting increasing attention in the water treatment field. Due to the higher reversibility of the capacitive electrode materials, this technology can recover most of the energy consumed for desalination by releasing the charge to a saline medium [13]. Capacitive deionization (CDI), which applies capacitive materials with highly porous pore structures and high surface areas as electrodes, is beneficial from energy efficiency and long-term stability point of view [14–16]. The use of ion-exchange membranes (membrane capacitive deionization) and/or chemically functionalized carbon electrodes (inverted capacitive deionization) allows to increase the desalination performance [17,18].

In 1960, Blair and Murphy first introduced an electrochemical desalination setup that applies carbon and Ag/AgCl to store/release Na^+ and Cl^- separately [19]. Later in 1967, Murphy and Caudle applied a symmetric carbon-carbon electrode pair to study the first CDI setup [20]. Later on, the first theoretical study of the CDI has addressed the importance of the surface area of the carbon materials in 1971 [21]. Thus, in recent decades, more CDI works are applying carbon materials with high specific surface areas such as carbon xerogels [22], carbon nanotubes [23], graphene [24], activated carbon [25], carbide-derived carbons [26,27], and salt-templated carbon materials [3]. Microporous carbons, which have an average pore size smaller than 2 nm, are of greater interest due to higher specific surface area compared to mesoporous carbons (2–50 nm) and carbon macropores (>50 nm) [28]. For pores smaller than 2 nm, due to the strong overlapping of the electrical double layer, the classical Gouy-Chapman-Stern model is no longer suitable to describe the ion distribution within a charged pore [29,30]. Instead, a Donnan model is developed by Basser et al. to describe ion distributions in micropores where electrostatic repulsion should be considered at low ionic strength [27]. Later, Biesheuvel et al. considered the charge transfer processes, extended the theory, and modified the Donnan theory significantly [31].

While past works attributed a dominant role for water desalination performance with CDI to the specific surface area and pore volume of carbon materials, in recent years, the ionic strength and pore size distribution are important factors. The former strongly influences the ion number repelled from a charged electrode during the desalination process, and the latter influences the number of ion pairs initially existed at the uncharged state [32]. When a potential is applied to the carbon electrodes, the counter-ions (ions with opposite charge) will be electro-adsorbed in the pore of the electrodes, and meantime, the co-ions (ions with the same charge as the electrode) will be repelled and released from the pores. In high ionic strength, this co-ion and counter-ion exchange would reach a 1:1 ratio [33]. When the pore size decreases to below 1 nm, where the ion solvation shell being distorted, there is not only anomalous capacitance increase [34] but also increased ion permselectivity in the carbon pores, which is caused by ionophobicity at the uncharged state and thus much less co-ion release during the cycling process [34].

From a carbon material point of view, choosing carbon materials with small pore size distribution and high surface area can improve the desalination performance. For subnanometer size pores, the ion transport kinetics will also be limited [35]. Thus, it is not practical to have

large carbon materials with single pore size distribution because ion transportation from the bulk electrolyte to the pores (interparticle ion transportation in carbon materials) [36] is also an essential factor in the desalination process which has not been well explored yet. Porada et al. showed that there is a strong correlation between electrode packing density and desalination rate [3]. By varying the particle size distributions, a clear change of desalination performance can be obtained. Recently, Shen et al. applied MXene of different sizes and showed that smaller particles improve the electrochemical and desalination performance [34]. In their work, the mixture of small and large particles exhibited the best performance (169 F/g and 72 mg_{NaCl}/gelectrode) [34]. Yet, a more systematic study based on ion transportation mechanisms under different particle size distributions is needed to find out the limiting factor to change the desalination performance.

Therefore, when designing a CDI electrode, texture (interparticle space) and ion transport pathlength (intraparticle pore volume) must be considered. Yet, any activated carbon powder always contains particles of different sizes – so what is the best particle size for capacitive deionization? In our work, the activated carbon material is separated by different particle size distributions by applying different desalination parameters (ion concentration, potential holding time, feedwater flow rate), a deeper understanding of particle size influence on ion transport and desalination performance are explored. To that end, we choose commercially available activated carbon as a model material to show that the right electrode design must critically consider particle size aspects to enable an optimized desalination performance.

2. Experimental description

2.1. Materials preparation

Commercially available activated carbon YP-80F from Kuraray was used in this study. The particles with different size distributions were separated by the centrifugation method. 20 g of YP-80F was added to 750 g of ethanol and was mixed by magnetic stirring for 1 h to form a uniform dispersion solution at the first step. Then the mixture is centrifuged at different speeds and periods to separate the particles depending on their sizes. To obtain large particles, the mixture was centrifuged at a rate of 500 rpm for 1 min, and the obtained sediment material is labeled as AC-L; for the smaller particles, the mixture was centrifuged at a speed of 1000 rpm for 1 min, and the obtained supernatant material is labeled as AC-S. The original material without particle separation is labeled as AC-M. Later on, the obtained sediment and supernatant material was collected and dried in the oven at 80 °C under a vacuum condition to obtain dry carbon powders for electrode preparations.

For electrode preparation, the carbon powder samples were first mixed with ethanol to form a uniform slurry in a mortar, then a water dispersion with polytetrafluoroethylene (PTFE; 60 mass%) from Sigma Aldrich was added and mixed with the carbon slurry with a carbon:binder mass ratio of 9:1. The mixing process is accomplished by stirring in the mortar to prevent destroying the carbon particles. Then the obtained carbon paste was rolled and pressed by an electric hot rolling press (MTI HR01, MTI Corporation) to have electrodes with a homogeneous thickness of 600 µm. Afterward, the electrodes were placed in the oven and heated at 120 °C for 24 h under a vacuum condition. The electrode densities of different materials are listed in Table 1. Two different electrode compactations were studied for the initial material AC-M: densified AC-M-d with a heavier mass loading and AC-M with lower packing density (Table 1). Both AC-M and AC-M-d electrodes have the same electrode area and thickness.

2.2. Materials characterization

2.2.1. Laser diffraction

The particle size distribution of the carbon samples was

Table 1
Electrode packing densities.

Material	Electrode density (g/cm ³)
AC-M	0.11
AC-L	0.25
AC-S	0.14
AC-M-d	0.34

characterized by laser diffraction technology. The carbon samples were flushed with deionized water and fed to the Mastersizer 2000. Once the obscuration degree of the particle suspension reaches a suitable range (8–14%), each sample was measured three times, and an average particle size distribution result was obtained at a size range of 0.02–2000 μm.

2.2.2. Nitrogen gas sorption analysis

Nitrogen gas sorption analysis (GSA) was conducted to analyze the pore size distribution of the materials. An Autosorb IQ system was applied with a liquid nitrogen-controlled temperature of −196 °C for the analysis process. At first, the samples were degassed at +200 °C for 1 h and then heated to 300 °C for up to 20 h to remove the humidity and solvent residue. Then, the samples were analyzed via nitrogen gas sorption at −196 °C. A slit-shaped pore configuration was assumed, and a quenched solid density functional theory was applied to analyze the pore size distribution of the microporous carbon materials [37,38]. The average pore size d_{50} was calculated by using the pore size of half of the maximum cumulative pore volume. The BET surface area (named after Brunauer Emmett Teller) was determined within the linear pressure range [39,40].

2.2.3. Scanning electron microscope

A Zeiss Gemini SEM 500 is applied at 1 kV with a working distance of 2–4 mm to observe the particle morphology and compare the particle size of the obtained carbon materials. The samples were sticked on copper tape without any sputtering coating on top.

2.2.4. CHNS-O elemental analysis

To compare the chemical information and possible functional groups of the samples, the CHNS-O measurement was conducted. The amount of H, C, and N was quantified using a Vario MICRO Cube (Elementar Analysensysteme GmbH) and heating up to +1150 °C at the combustion tube and +850 °C at the reduction tube. The O content was quantified with an OXY cube elemental analyzer (Elementar Analysensysteme GmbH) at a pyrolysis temperature of +1450 °C.

2.3. Desalination experiments

In this work, a symmetric cell type was chosen to test the desalination materials at different conditions. In alignment with previous work [41], the free-standing carbon electrodes were cut into a 30 mm diameter round disk with a thickness of 600 μm. Between the two electrodes, a fixed 3 mm distance is separated by the middle feedwater channel. There is a 3 mm thick, 30 mm diameter flow chamber filled with six glass fiber separators (Millipore) and four pieces of polyethylene terephthalate in the feedwater channel. The feedwater is pumped at a flow rate of 1 mL/min, 2.5 mL/min, or 5 mL/min to flow between the electrodes. The feedwater is cycled back to a 10 L reservoir to minimize the concentration fluctuation between the desalination cycles. In this work, to study the ionic strength influence on desalination performance, NaCl (Sigma Aldrich) was dissolved in MiliQ water to prepare 5 mM and 20 mM of NaCl solution.

At the outlet of the CDI cell, the feedwater conductivity and pH change were recorded by pH (Metrohm 867 pH Module) and conductivity (Metrohm 856 conductivity) sensors. A Bio-Logic VSP-300 system was used to observe the electrochemical performance of the system. For

each galvanostatic charging and discharging step, a specific current of 0.1 A/g was set between 0 and +1.0 V cell voltages, after reaching the set voltage, a potential holding time of 20 min, 30 min, and 60 min was applied. The cycling number for 20 min, 30 min, and 60 min holding times are 6, 5, and 4, separately. To avoid the effect of first-cycle conditioning, the calculation of the performance metrics is carried out only starting with the second cycle for each condition.

The desalination capacity was determined by Eq. (1):

$$DC = \left(v \frac{M_{salt}}{M_{tot}} \right) \int (c_t - c_0) dt \quad (1)$$

where M_{salt} is the molar mass of the salt, M_{tot} is the total mass of the two electrodes, v is the flow rate, c_0 and c_t are the initial outlet salt concentration and concentrate of the feedwater at time t , respectively.

The charge efficiency was calculated according to the following Eq. (2):

$$CE(\%) = \frac{F \times DC_{mol}}{M_{salt} \times Q} \times 100\% \quad (2)$$

where F is the Faraday constant (26,801 mAh/mol), DC_{mol} is the desalination capacity obtained from Eq. (1), and Q is the total charge (normalized to the total electrode mass, mAh/g) stored/released during the cycling process.

3. Results and discussion

3.1. Materials

The morphologies, particle size distributions, and pore size distributions are shown in Fig. 1. In Fig. 1A-C, the scanning electron micrographs show AC-M, AC-L, and AC-S are composed of particles of different sizes. Among them, AC-M is a mixture of particles with different sizes, AC-L and AC-S are the larger and smaller particles obtained from the sediment and supernatant of the centrifuging process, separately. In Fig. 1D, the laser scattering data shows the different particle size distribution of the three samples. AC-S shows the smallest particle size with an average particle size of 1.8 μm (d_{50}). Since AC-M is a mixture of particle sizes without particle separation treatment, it shows a broader particle size distribution compare to AC-L, and the average particle size (d_{50}) of AC-L (6.2 μm) is slightly larger compared to AC-M (5.4 μm).

Fig. 1E shows the pore size distribution of the materials. Comparing the three materials, AC-L and AC-S show similar pore size distributions, while AC-M shows slightly higher cumulative pore volume, especially at the pore size below 2 nm. The gas sorption data are given in Table 2. Despite that the centrifuging treatment of the carbon samples seemingly slightly reduces the micropore volume to around 10–13%, the difference of particle size distributions has little influence on the pore size distributions of the materials, in this case, the pore size influence of the desalination performances can be excluded.

Table 3 shows the CHNO-S chemical analysis results. The carbon content of all samples is above 93%, with some oxygen content of less than 8%, the nitrogen and hydrogen contents are all below 2%. According to the chemical analysis data, there is no significant chemical composition difference among the three samples.

3.2. Concentration profiles

The concentration profiles of activated carbons with different particle size distributions are plotted in Fig. 2. We show the concentration profiles at different flow rates during galvanostatic cycling (3 cycles). Three materials of different particle size distributions were compared at different salt concentrations and feedwater flow rates. In each cycle, one negative and one positive peak of concentration change can be observed. As the flow rate increases, the concentration change amplitudes will

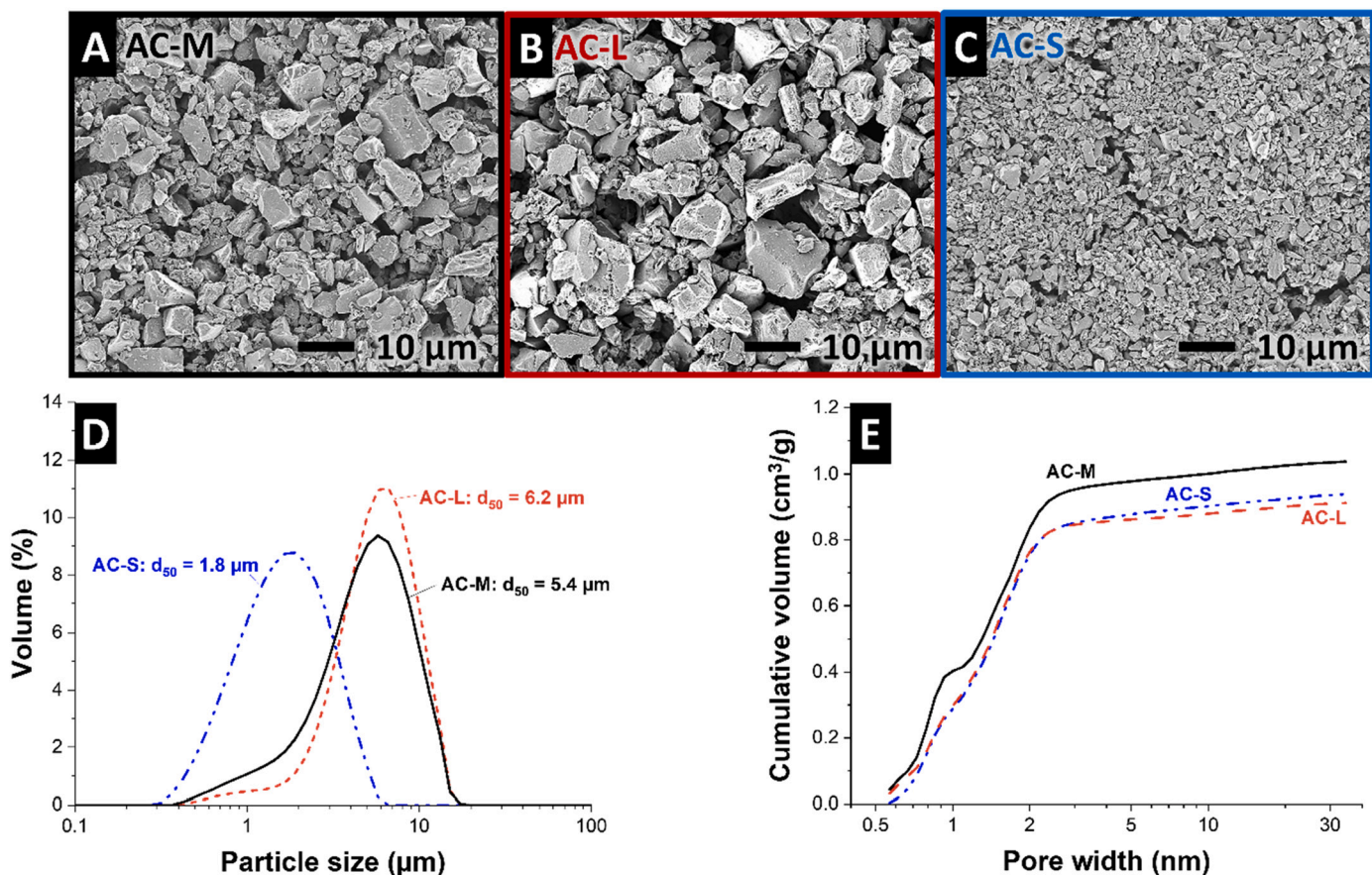


Fig. 1. Material characterization of AC-M, AC-L, and AC-S. A, B, C) SEM images of the three samples at the same scale; D) laser diffraction result of three samples showing the different particle size distributions. d_{50} is the average particle size of the material; E) Cumulative pore size distribution of the three samples, obtained from QSDFT analysis of nitrogen gas sorption data.

Table 2

Gas sorption analysis with nitrogen at -196°C for the electrode materials using the quenched solid density functional theory (QSDFT) and the Brunauer-Emmett-Teller theory (BET). The average pore size refers to the volume-normalized value d_{50} . The micropore volume percentage pertains to the volume fraction of micropores regarding the total pore volume.

Material	d_{50} (nm)	Specific surface area (m^2/g)	Micropore volume (cm^3/g)	Total pore volume (cm^3/g)
AC-M	1.34	1741	0.84 (80.0%)	1.04
AC-L	1.34	1489	0.76 (83.5%)	0.91
AC-S	1.39	1449	0.76 (80.8%)	0.94

Table 3

CHNO elemental chemical analysis of the electrode materials.

Material	Carbon (mass %)	Hydrogen (mass %)	Nitrogen (mass %)	Oxygen (mass %)
AC-M	94.58	0.564	0.57	2.488
AC-L	94.95	0.718	0.48	3.105
AC-S	93.22	0.609	1.13	7.321

decrease accordingly for all carbon materials.

Compared to the material with a larger average particle size (AC-L), the amplitude of the measured concentration changes of AC-M are consistently higher at different flow rates and different concentrations (Fig. 2A, D, G). The adsorption and desorption peaks are also more narrow, and the concentration profile reaches an equilibrium value faster than AC-L. As the flow rate increases from 1 mL/min to 2.5 mL/

min for AC-M, both adsorption and desorption peaks get narrower. As the flow rate increases to 5 mL/min, the adsorption peaks in 5 mM NaCl get wider, and the concentration stabilization time for AC-M becomes longer. For AC-M, when the flow rate of feedwater exceeds 2.5 mL/min, the interparticle ions were easily transported away before they were able to be adsorbed inside of the carbon pores. Thus, the intraparticle ion diffusion will become a more dominating limiting factor, the increase of the flow rate will lead to a non-effective ion uptake process. This phenomenon is more evident in the electrolyte with low ionic strength (5 mM) since, in lower electrolyte concentrations, the interparticle ion number is lower. This seemingly limits the ion transport from the bulk electrolyte to the particles.

As shown in Fig. 2B, E, H, the material with a larger average particle size (AC-L) shows an intense diffusion-limited effect in 5 mM and 20 mM NaCl solutions. In 5 mM NaCl solution, although by increasing the flow rate, the desorption peaks became narrower, in all different flow rates, the concentration profiles for adsorption processes require longer time to stabilize. Due to the larger average particle size, the intraparticle ion diffusion has a longer pathway than smaller particles. Thus, it becomes the limiting factor of ion uptake rate.

For AC-S (Fig. 2C, F, I), the average particle size of the activated carbon is smaller compared to AC-M and AC-L. In direct comparison with AC-L, we see AC-S providing much more narrow concentration change profiles. AC-S and AC-M, however, show a comparable pattern at all concentrations and all flow rates (Fig. 2). However, AC-S requires more time until an equilibrium concentration is reached; this makes the width of the adsorption/desorption peaks at the base broader in the case of AC-S in comparison with AC-M (and AC-L). This phenomenon is due to the smaller particles being closely packed. Thus, there is a more

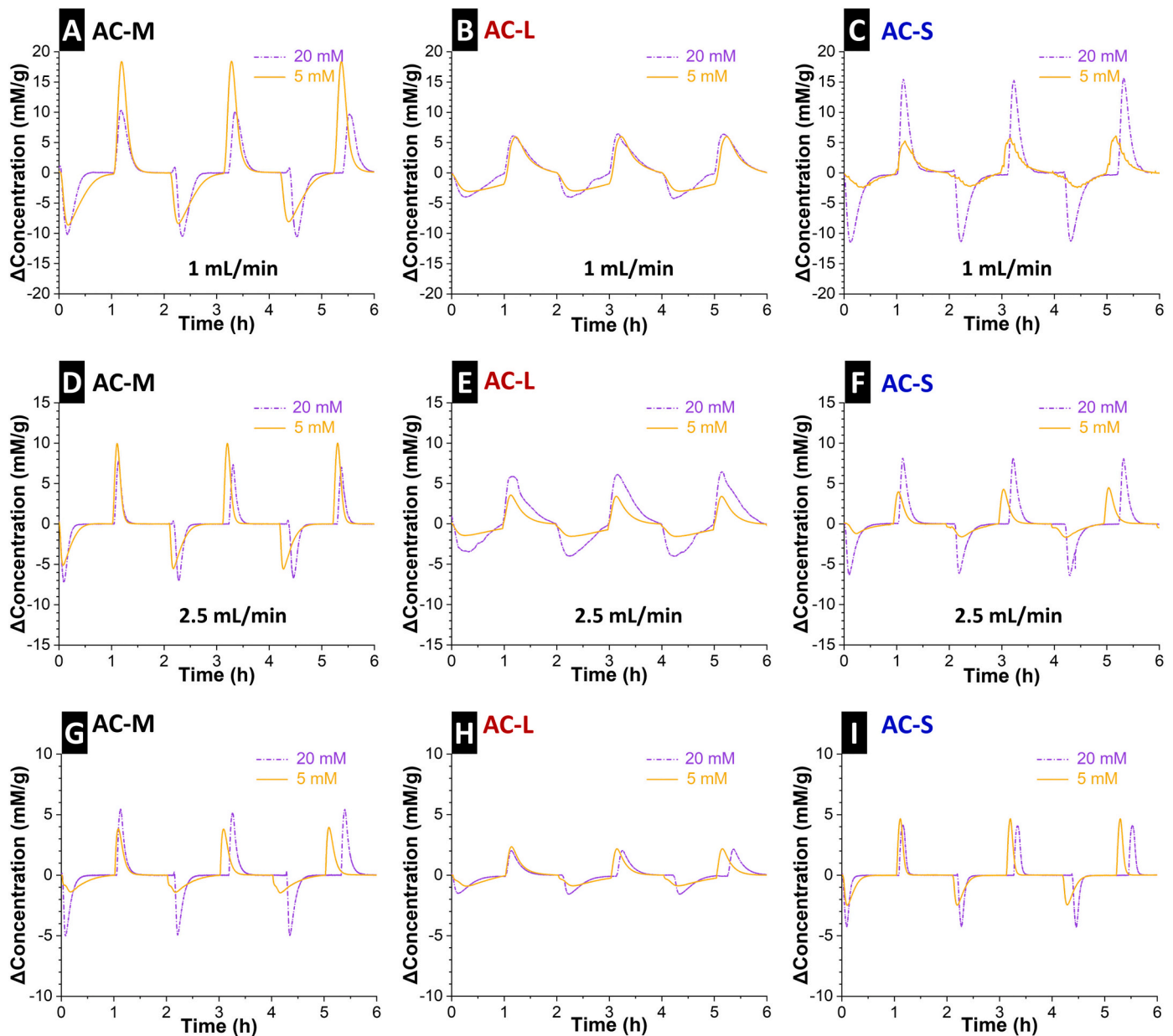


Fig. 2. Concentration profiles of different samples in 5 mM and 20 mM NaCl NaCl solutions under different flow rates. A-C) 1 L/min; D-F) 2.5 mL/min; G-I) 5 mL/min. Under all working conditions, the holding time is 60 min.

tortuous interparticle electrolyte pathway than that of AC-M, which slows down ion transport. As the flow rate increases from 1 mL/min to 5 mL/min, the adsorption and desorption peaks are sharper, indicating faster interparticle ion transport. When 20 mM NaCl is applied as the electrolyte, the concentration is reaching maximum adsorption more quickly (baseline). Sharp adsorption and desorption peaks are also observed due to the increased ionic strength that improves the interparticle ion transport.

3.3. Desalination capacity comparison

The desalination performance for AC-M, AC-L, AC-S in different salt concentrations, with varying times of holding and flow rates, are summarized and compared in Fig. 3. The individual desalination performance for each configuration is summarized in *Supporting Information*, Fig. S1. Among the materials studied by us, AC-M shows the highest desalination performance, and the extension of holding time and the

electrolyte flow rate has only slightly increased the desalination performance (Fig. 3A-B). In addition, in 5 mM salt concentration, the use of AC-S and AC-L increases the desalination capacity and charge efficiency as the holding time increases. This behavior indicates that the desalination processes did not reach an equilibrium during shorter holding times due to slower ion transport kinetics. As the flow rate increases, the desalination performance for both AC-S and AC-L increases, showing that the accelerated electrolyte flow can improve the rate-limiting desalination performances of the two materials.

As seen in Fig. 3C-D, similarly, AC-M shows a slight reduction in desalination performance in 20 mM NaCl, yet it shows a much higher desalination performance compared to AC-L. The desalination performance for AC-S has vastly improved when using 20 mM NaCl solution instead of 5 mM. Its desalination capacity has increased from 5 to 8 mg/g to nearly 11 mg/g at the holding time of 60 min, and the charge efficiency has increased from 54–70% to 79–86%. The same trend is observed when 20 min and 30 min holding time were applied. This

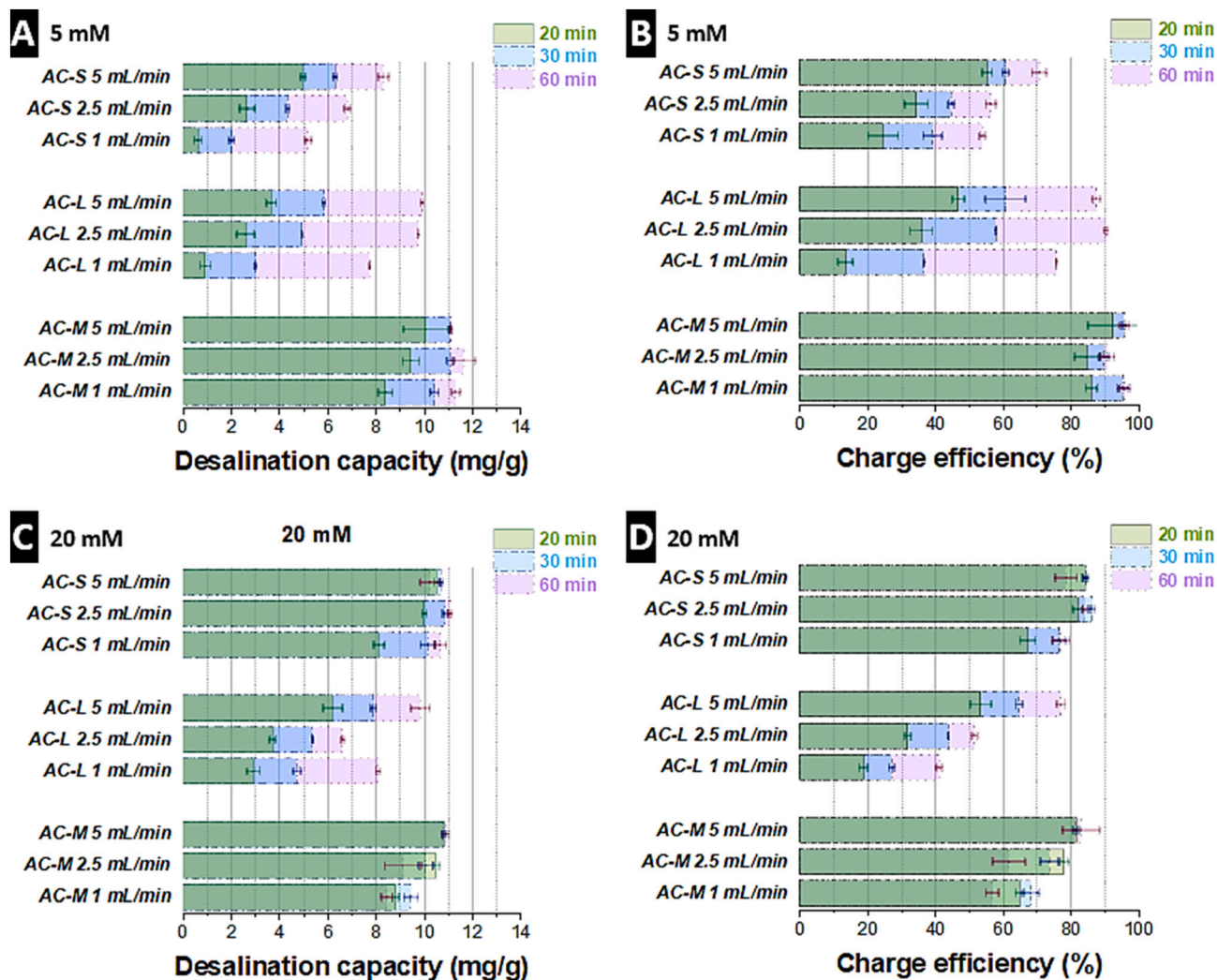


Fig. 3. Summary of desalination capacity and charge efficiency of activated carbon of different average particle sizes AC-M, AC-L, and AC-S in different concentrations. A-B) 5 mM; C-D) 20 mM. The effect of different holding times and flow rates has been compared.

observation agrees with improved interparticle ion transport. For AC-L in 20 mM NaCl, although by increasing the feedwater flow rate, a higher desalination performance is obtained, the desalination performance is lower than that in 5 mM, even a longer holding time was applied. Due to the larger average particle size, the ion diffusion in the particles is slower so that increasing the ionic strength or the flow rate of the feedwater is not effective to improve the desalination performance. Moreover, the increase of the ionic strength would lead to more co-ion and counter-ion exchange during the cycling process and cause a decrease in charge efficiency [42].

Apart from the particle size of the materials, the packing density of the electrode should also be considered. Merrill et al. applied graphene macro-assembly electrodes in supercapacitors and showed that high electrode density leads to a slower charging/discharging process [43]. Jelle et al. have investigated the electrode density influence on Li-ion battery performance [37]. They show that for electrodes with lower packing density, a higher performance is observed at high rates [37]. In our study, the desalination performance of AC-M-d with a much higher packing density is shown in *Supporting Information*, Fig. S2, a higher electrode density provides less space for the electrolyte and more tortuous for ion transport in electrolytes [34]. Thus, the slower ion transport kinetics result in a lower desalination capacity and a lower desalination rate.

3.4. Kim-Yoon plot and kinetic discussions

Fig. 4A, B, C shows the Kim-Yoon plot of the three materials in different concentrations and flow rates. For a better comparison of the desalination rate, the desalination capacity is normalized by the highest desalination capacity. The Kim Yoon plot of desalination capacity vs. desalination rate is shown in *Supporting Information*, Fig. S3. By increasing the flow rate of the feedwater, the desalination rate for all materials increases at different molarities. Among all materials, AC-L (**Fig. 4B**) shows the slowest desalination rates at all flow rates, the absence of plateau shows the desalination process was not reaching equilibrium. For AC-M (**Fig. 4A**), the desalination rate is much higher, the increase of flow rate and ionic strength improve the desalination rates. As seen from the data plotted in **Fig. 4C**, AC-S shows a much higher desalination rate in 20 mM NaCl solution (0.007, 0.010, 0.014 mg/g/s) than in 5 mM NaCl solution (0.001, 0.003, 0.005 mg/g/s) at the flow rates of 1, 2.5, and 5 mL/min.

These results show that two kinetic limitations can decrease the desalination rate, as illustrated in **Fig. 5**, one of them is intraparticle ion diffusion, another limitation is interparticle ion transportation. When the particle size is bigger, the ion diffusion length inside of the particle is longer, when the particle size is smaller, the interparticle ion transport length will become longer, which can also lead to higher electrode packing density. For the former case, it can be improved by decreasing

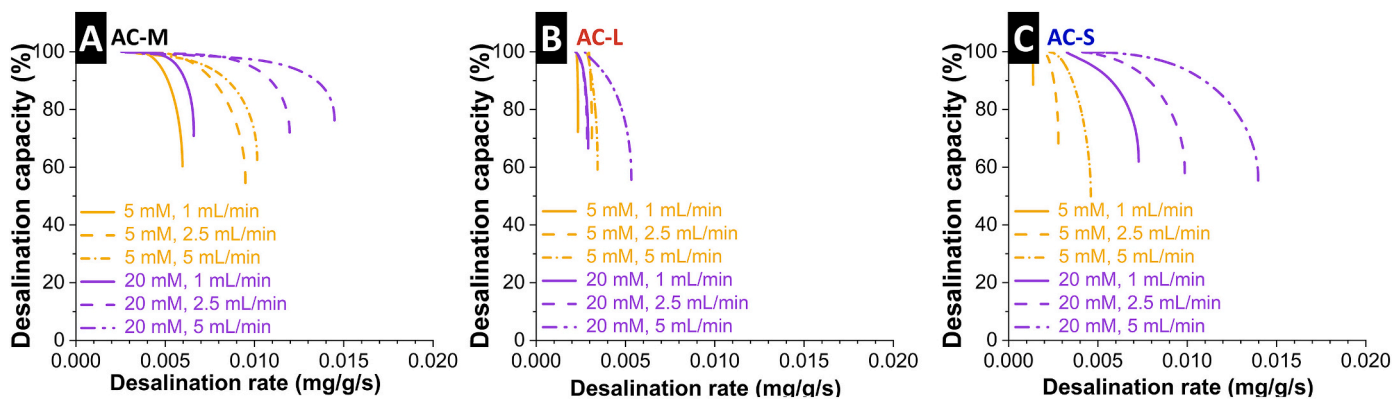


Fig. 4. Normalized Kim-Yoon plot of different average particle sizes under different ionic strengths and flow rates. A) AC-M; B) AC-L; C) AC-S. The desalination capacity is normalized to each maximum value for better comparison.

the average particle size. For the latter case, it can be improved by improving the mass transport (increasing the flow rate or the concentration) of the feed water. When mixing the larger particle with the smaller particles, the two limiting factors can be weakened at the same

time. The involvement of the smaller particles can help to improve the intraparticle ion diffusion, and the existence of the larger particles can help to shorten the interparticle ion transport pathway.

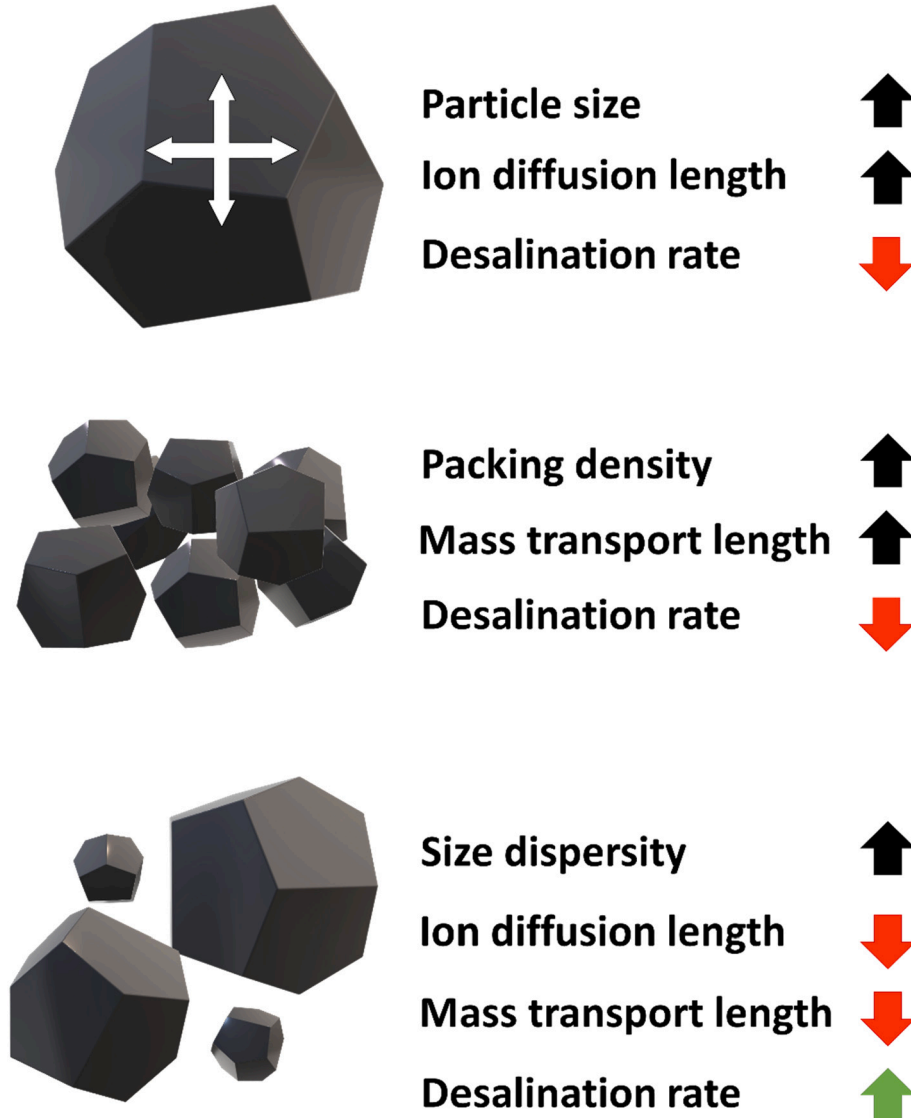


Fig. 5. Schematic illustration of particle influence on desalination rate.

4. Conclusions

In this work, the microporous activated carbon of different particle size distributions has been studied. Two factors that influence desalination performance have been studied by applying different desalination parameters, like different ionic strengths (5 mM and 20 mM NaCl solution) and different feedwater flow rates and holding times. One of them is the intraparticle ion diffusion length that is caused by different particle sizes. Another factor is the diffusion length of the ion transport pathway that relates to smaller average particles with higher packing densities. Specifically, in lower feedwater concentrations and electrodes with larger particle sizes, intraparticle and interparticle ion diffusion can limit the desalination capacity.

In comparison, intraparticle ion diffusion is the main limiting factor in higher feedwater concentrations. By mixing larger and smaller particles to form a broad particle size distribution (d_{50} of 5.4 μm), increasing the feedwater flow rate (5 mL/min) and meanwhile using electrodes with a lower packing density (0.11 g/cm³), the two limiting factors can be balanced. Thus higher desalination performances can be obtained. Our results show the importance of average particle size and packing density for making the electrodes and have optimized electrode preparation for capacitive deionization applications.

Declaration of competing interest

The authors declare the following financial interests/personal relationships which may be considered as potential competing interests: Volker Presser reports financial support was provided by RAG-Stiftung.

Acknowledgments

The authors thank Eduard Arzt (INM) for his continuing support. The authors thank Andrea Jung, Maike Ulbricht, and Aron Schorr (all at INM) for their support with CHNS-O measurements, scanning electron microscopy, and laser diffraction characterizations. Y.Z. and V.P. acknowledge support for the MERLIN project from the RAG-Stiftung; the RAG-Stiftung generates long-term momentum for the transformation of the regions along the Ruhr and Saar Rivers and in Ibbenbüren.

CRediT author statement

Y.Z.: Data Curation, Writing - Original Draft, Supervision, Visualization, Investigation.

P.R.: Validation, Review & Editing, Investigation.

Y.L.: Data Curation, Review & Editing, Investigation.

V.P.: Conceptualization, Data Curation, Writing - Review & Editing, Visualization, Funding acquisition, Project administration, Supervision

Appendix A. Supplementary data

Supplementary data to this article can be found online at <https://doi.org/10.1016/j.desal.2021.115503>.

References

- [1] M.A. Shannon, P.W. Bohn, M. Elimelech, J.G. Georgiadis, B.J. Mariñas, A.M. Mayes, Science and technology for water purification in the coming decades, *Nature* 452 (2008) 301–310.
- [2] T. Humplík, J. Lee, S.C. O’Hern, B.A. Fellman, M.A. Baig, S.F. Hassan, M.A. Atieh, F. Rahman, T. Laoui, R. Karmik, E.N. Wang, Nanostructured materials for water desalination, *Nanotechnology* 22 (2011), 292001.
- [3] S. Porada, L. Borchardt, M. Oschatz, M. Bryjak, J.S. Atchison, K.J. Keesman, S. Kaskel, P.M. Biesheuvel, V. Presser, Direct prediction of the desalination performance of porous carbon electrodes for capacitive deionization, *Energy Environ. Sci.* 6 (2013) 3700–3712.
- [4] M.M. Mekonnen, A.Y. Hoekstra, Four billion people facing severe water scarcity, *Sci. Adv.* 2 (2016), e1500323.
- [5] J.E. Miller, Review of Water Resources and Desalination Technologies, in, United States, 2003.
- [6] Z. Wang, T. Horseman, A.P. Straub, N.Y. Yip, D. Li, M. Elimelech, S. Lin, Pathways and challenges for efficient solar-thermal desalination, *Science Advances* 5 (2019), eaax0763.
- [7] A.D. Khawaji, J.K. Kutubkhana, J.-M. Wie, Advances in seawater desalination technologies, *Desalination* 221 (2008) 47–69.
- [8] A.M. El-Nashar, Cogeneration for power and desalination - state of the art review, *Desalination* 134 (2001) 7–28.
- [9] S. Al-Amshawee, M.Y.B.M. Yunus, A.A.M. Azoddein, D.G. Hassell, I.H. Dakhil, H. A. Hasan, Electrodialysis desalination for water and wastewater: a review, *Chem. Eng. J.* 380 (2020), 122231.
- [10] L.F. Greenlee, D.F. Lawler, B.D. Freeman, B. Marrot, P. Moulin, Reverse osmosis desalination: water sources, technology, and today’s challenges, *Water Res.* 43 (2009) 2317–2348.
- [11] Y. Ayyash, H. Imai, T. Yamada, T. Fukuda, Y. Yanaga, T. Taniyama, Performance of reverse osmosis membrane in Jeddah Phase I plant, *Desalination* 96 (1994) 215–224.
- [12] B. Durham, A. Walton, Membrane pretreatment of reverse osmosis: long-term experience on difficult waters, *Desalination* 122 (1999) 157–170.
- [13] S.H. Ebrahim, M.M. Abdel-Jawad, M. Safar, Conventional pretreatment system for the Doha reverse osmosis plant: technical and economic assessment, *Desalination* 102 (1995) 179–187.
- [14] S. Lin, Energy efficiency of desalination: fundamental insights from intuitive interpretation, *Environ. Sci. Technol.* 54 (2020) 76–84.
- [15] F. Chen, Y. Huang, L. Guo, L. Sun, Y. Wang, H.Y. Yang, Dual-ions electrochemical deionization: a desalination generator, *Energy Environ. Sci.* 10 (2017) 2081–2089.
- [16] L. Wang, Y. Zhang, K. Moh, V. Presser, From capacitive deionization to desalination batteries and desalination fuel cells, *Curr. Opin. Electrochem.* 29 (2021), 100758.
- [17] J. Landon, X. Gao, A. Omosebi, K. Liu, Progress and outlook for capacitive deionization technology, *Curr. Opin. Chem. Eng.* 25 (2019) 1–8.
- [18] P.M. Biesheuvel, A. van der Wal, Membrane capacitive deionization, *J. Membr. Sci.* 346 (2010) 256–262.
- [19] M.A. Anderson, A.L. Cudero, J. Palma, Capacitive deionization as an electrochemical means of saving energy and delivering clean water. Comparison to present desalination practices: will it compete? *Electrochim. Acta* 55 (2010) 3845–3856.
- [20] S. Porada, R. Zhao, A. van der Wal, V. Presser, P.M. Biesheuvel, Review on the science and technology of water desalination by capacitive deionization, *Prog. Mater. Sci.* 58 (2013) 1388–1442.
- [21] J.W. Blair, G.W. Murphy, Electrochemical demineralization of water with porous electrodes of large surface area, in: *Saline water conversion*, American Chemical Society, 1960, pp. 206–223.
- [22] J. Landon, X. Gao, B. Kulengowski, J.K. Neathery, K. Liu, Impact of pore size characteristics on the electrosorption capacity of carbon xerogel electrodes for capacitive deionization, *J. Electrochim. Soc.* 159 (2012) A1861–A1866.
- [23] G.W. Murphy, D.D. Caudle, Mathematical theory of electrochemical demineralization in flowing systems, *Electrochim. Acta* 12 (1967) 1655–1664.
- [24] A.M. Johnson, J. Newman, Desalting by means of porous carbon electrodes, *J. Electrochim. Soc.* 118 (1971) 510.
- [25] L. Wang, M. Wang, Z.-H. Huang, T. Cui, X. Gui, F. Kang, K. Wang, D. Wu, Capacitive deionization of NaCl solutions using carbon nanotube sponge electrodes, *J. Mater. Chem.* 21 (2011) 18295.
- [26] W. Shi, H. Li, X. Cao, Z.Y. Leong, J. Zhang, T. Chen, H. Zhang, H.Y. Yang, Ultrahigh performance of novel capacitive deionization electrodes based on a three-dimensional graphene architecture with nanopores, *Sci. Rep.* 6 (2016) 18966.
- [27] S. Porada, L. Weinstein, R. Dash, A. van der Wal, M. Bryjak, Y. Gogotsi, P. M. Biesheuvel, Water desalination using capacitive deionization with microporous carbon electrodes, *ACS Appl. Mater. Interfaces* 4 (2012) 1194–1199.
- [28] P. Ratajczak, M.E. Suss, F. Kaasik, F. Béguin, Carbon electrodes for capacitive technologies, *Energy Storage Mater.* 16 (2019) 126–145.
- [29] A. Levy, J.P. de Souza, M.Z. Bazant, Breakdown of electroneutrality in nanopores, *J. Colloid Interface Sci.* 579 (2020) 162–176.
- [30] E. Partheniades, Forces between clay particles and the process of flocculation, in: E. Partheniades (Ed.), *Cohesive Sediments in Open Channels*, Butterworth-Heinemann, Boston, 2009, pp. 47–88.
- [31] S. Porada, F. Schipper, M. Aslan, M. Antonietti, V. Presser, T.-P. Fellinger, Capacitive deionization using biomass-based microporous salt-templated heteroatom-doped carbons, *ChemSusChem* 8 (2015) 1867–1874.
- [32] P.J. Basser, A.J. Grodzinsky, The donnan model derived from microstructure, *Biophys. Chem.* 46 (1993) 57–68.
- [33] P.M. Biesheuvel, Y. Fu, M.Z. Bazant, Diffuse charge and Faradaic reactions in porous electrodes, *Phys. Rev. E* 83 (2011), 061507.
- [34] S. Bi, Y. Zhang, L. Cervini, T. Mo, J.M. Griffin, V. Presser, G. Feng, Permselective ion electrosorption of subnanometer pores at high molar strength enables capacitive deionization of saline water, *Sustain. Energy Fuel* 4 (2020) 1285–1295.
- [35] J. Chmiola, G. Yushin, Y. Gogotsi, C. Portet, P. Simon, P.L. Taberna, Anomalous increase in carbon capacitance at pore sizes less than 1 nanometer, *Science* 313 (2006) 1760–1763.
- [36] K. Breitsprecher, M. Janssen, P. Srimuk, B.L. Mehdi, V. Presser, C. Holm, S. Konrat, How to speed up ion transport in nanopores, *Nat. Commun.* 11 (2020) 6085.
- [37] Y. Zhang, P. Srimuk, S. Husmann, M. Chen, G. Feng, V. Presser, Effect of pore size on the ion electrosorption and hydrogen/deuterium electrosorption using sodium chloride in H₂O and D₂O, *J. Electrochim. Soc.* 166 (2019) A4158–A4167.

- [38] X. Shen, Y. Xiong, R. Hai, F. Yu, J. Ma, All-MXene-based integrated membrane electrode constructed using Ti₃C₂Tx as an intercalating agent for high-performance desalination, *Environ. Sci. Technol.* 54 (2020) 4554–4563.
- [39] C. Prehal, S. Grätz, B. Krüner, M. Thommes, L. Borchardt, V. Presser, O. Paris, Comparing pore structure models of nanoporous carbons obtained from small angle X-ray scattering and gas adsorption, *Carbon* 152 (2019) 416–423.
- [40] S. Choudhury, B. Krüner, P. Massuti-Ballester, A. Tolosa, C. Prehal, I. Grobelsek, O. Paris, L. Borchardt, V. Presser, Microporous novolac-derived carbon beads/sulfur hybrid cathode for lithium-sulfur batteries, *J. Power Sources* 357 (2017) 198–208.
- [41] M. Thommes, K. Kaneko, A.V. Neimark, J.P. Olivier, F. Rodriguez-Reinoso, J. Rouquerol, K.S.W. Sing, Physisorption of gases, with special reference to the evaluation of surface area and pore size distribution, *Pure Appl. Chem.* 87 (2015) 1051–1069.
- [42] S. Brunauer, P.H. Emmett, E. Teller, Adsorption of gases in multimolecular layers, *J. Am. Chem. Soc.* 60 (1938) 309–319.
- [43] M.D. Merrill, E. Montalvo, P.G. Campbell, Y.M. Wang, M. Stadermann, T. F. Baumann, J. Biener, M.A. Worsley, Optimizing supercapacitor electrode density: achieving the energy of organic electrolytes with the power of aqueous electrolytes, *RSC Adv.* 4 (2014) 42942–42946.

Supporting Information

Particle size distribution influence on capacitive deionization: insights for electrode preparation

Yuan Zhang,^{1,2} Panyu Ren,^{1,2} Yang Liu,^{1,2} and Volker Presser^{1,2,3*}

INM - Leibniz Institute for New Materials, Campus D2 2, 66123 Saarbrücken, Germany

Saarland University, Campus D2 2, 66123 Saarbrücken, Germany

Saarene - Saarland Center for Energy Materials and Sustainability, Campus C4 2, 66123 Saarbrücken, Germany

* Corresponding author's eMail: volker.presser@leibniz-inm.de

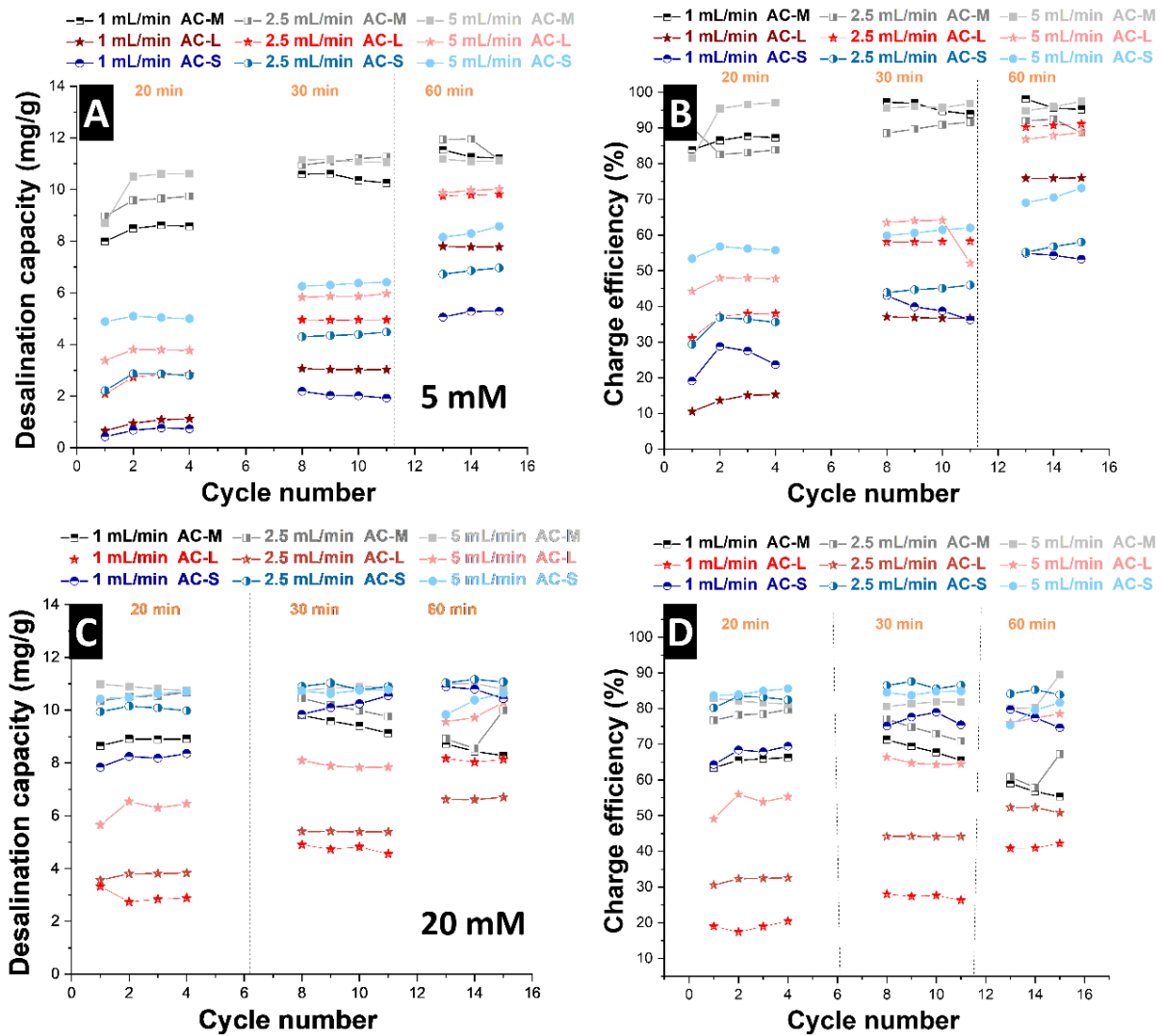


Figure S1: Desalination capacity and charge efficiency of activated carbon of different average particle sizes AC-M, AC-L, and AC-S in different concentrations. A-B) 5 mM; C-D) 20 mM. The performance under different holding times and flow rates have been compared.

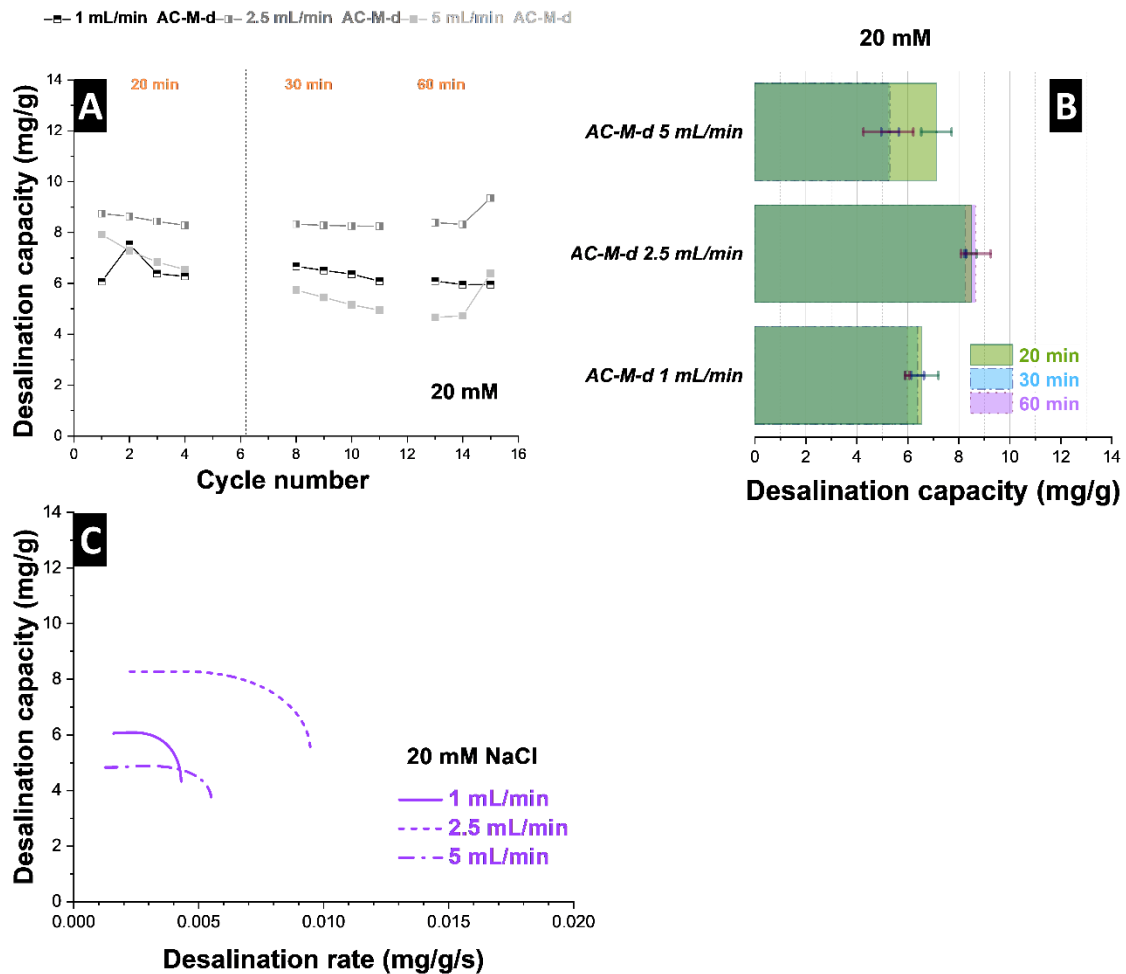


Figure S2: The desalination capacity of AC-M-d material with higher electrode packing density under 20 mM NaCl molar strength. Different holding times and flow rates have been applied for comparison. A) Desalination performance over the 15 cycles; B) Desalination capacity at different holding times; C) Kim-Yoon plot at different flow rates.

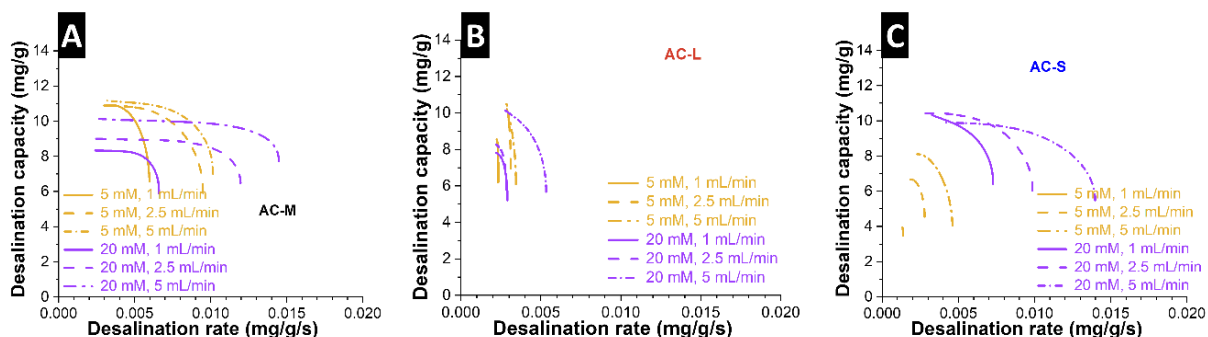


Figure S3: Conventional Kim-Yoon plot of materials of different average particle sizes under different ionic strengths and flow rates. A) AC-M; B) AC-L; C) AC-S.

4.8 Electrocatalytic fuel cell desalination for continuous energy and freshwater generator

Yuan Zhang,^{1,2} Lei Wang,^{1,2} and Volker Presser^{1,2,3}

1 INM - Leibniz Institute for New Materials, Campus D2 2, 66123 Saarbrücken, Germany

2 Saarland University, Campus D2 2, 66123 Saarbrücken, Germany

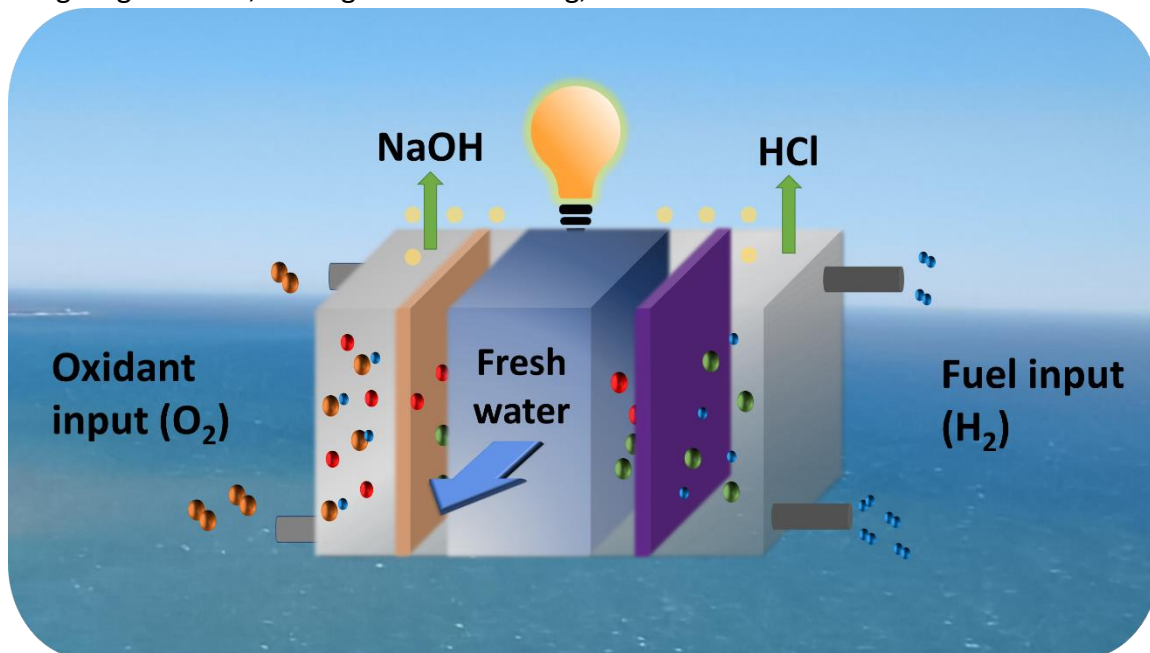
3 Saarene - Saarland Center for Energy Materials and Sustainability, Campus C4 2, 66123 Saarbrücken, Germany

Citation:

Y. Zhang, L. Wang, V. Presser, *Electrocatalytic fuel cell desalination for continuous energy and freshwater generator*, Cell reports Physical Science, 2021, 2(5): 100416. (DOI: 10.1016/j.xcrp.2021.100416)

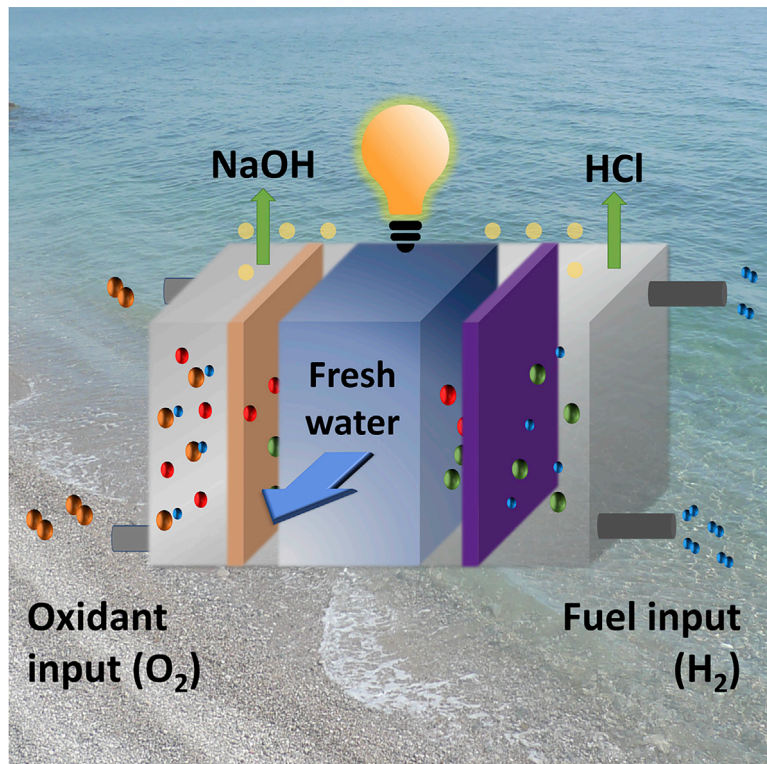
Own contribution:

Conceptualization, methodology, validation, formal analysis, investigation, data curation, writing-original draft, writing-review & editing, visualization.



Report

Electrocatalytic fuel cell desalination for continuous energy and freshwater generation



Yuan Zhang, Lei Wang, Volker

Presser

volker.presser@leibniz-inm.de

Highlights

Continuous seawater desalination system based on H_2 fuel cell

Desalination cell produces acid and base at the same time

Generates 67 mWh of electricity by removing 1 g NaCl

No water contamination or carbon emission involved

In this proof-of-concept work, Zhang et al. used hydrogen as an energy carrier in multi-channel fuel-cell desalination (FCD) with ion-exchange membranes designed for direct seawater desalination. The cell simultaneously produces electricity, acid, and base as byproducts for other possible industry applications.

Report

Electrocatalytic fuel cell desalination for continuous energy and freshwater generation

Yuan Zhang,^{1,2} Lei Wang,^{1,2} and Volker Presser^{1,2,3,*}

SUMMARY

Advanced hydrogen technologies contribute essentially to the de-carbonization of our industrialized world. Large-scale hydrogen production would benefit from using the abundantly available water reservoir of our planet's oceans. Current seawater-desalination technologies suffer from high energy consumption, high cost, or low performance. Here, we report technology for water desalination at seawater molarity, based on a polymer ion-exchange membrane fuel cell. By continuously supplying hydrogen and oxygen to the cell, a 160-mM concentration decrease from an initial value of 600 mM is accomplished within 40 h for a 55-mL reservoir. This device's desalination rate in 600 mM NaCl and substitute ocean water are 18 g/m²/h and 16 g/m²/h, respectively. In addition, by removing 1 g of NaCl, 67 mWh of electric energy is generated. This proof-of-concept work shows the high application potential for sustainable fuel-cell desalination (FCD) using hydrogen as an energy carrier.

INTRODUCTION

The lack of clean freshwater is associated with severe global ramifications.^{1,2} With almost 98% of the water being seawater or brackish water, the increasing demand for freshwater has intensified worldwide research efforts dedicated to efficient and effective desalination technologies.³ Today, there exists an array of desalination concepts, including distillation,^{4,5} reverse osmosis (RO),^{6–8} and electrodialysis (ED).⁹ Reverse osmosis is a widely used, reliable method, but the energy consumption must be lessened to qualify as a sustainable technology.¹⁰ In recent decades, capacitive deionization,^{11–13} and battery desalination³ have been explored as potentially energy-efficient alternatives (or additions) to existing desalination technologies. However, capacitive deionization, based on carbon electrodes, cannot desalinate seawater because carbon nanopores fail to provide permselectivity at high molar strength.¹⁴ This can be, in part, overcome by implementing ion-exchange membranes shielding the carbon electrodes.¹⁵ Desalination batteries apply charge-transfer materials, such as the ones found in sodium-ion batteries or other aqueous batteries, and can be used directly for seawater desalination, without the need for an ion-exchange membrane.^{16,17} However, the ion-storage mechanism related to ion intercalation or similar Faradaic processes still leaves room for improvement in the search for electrochemical processes with even greater charge-transfer capacity. This also pertains to the non-continuous operation mode, with a sequence of charge and discharge half-cycles, of conventional desalination batteries.

Sustainable seawater desalination using renewable energy, such as wind, solar, and hydropower, has attracted increasing attention. These types of renewable energy

¹INM - Leibniz Institute for New Materials, Campus D2 2, 66123 Saarbrücken, Germany

²Saarland University, Department of Materials Science and Engineering, Campus D2 2, 66123 Saarbrücken, Germany

³Lead contact

*Correspondence:
volker.presser@leibniz-inm.de

<https://doi.org/10.1016/j.xcnp.2021.100416>



can be stored in different forms, and hydrogen is considered to have a critical and enabling role in a low-carbon future.^{14,18} As a clean and light energy carrier with abundant elemental storage on the earth, hydrogen can be stored and further converted electrochemically in hydrogen fuel cells to produce electricity. Thus, it is an emerging application for fuel-cell electric vehicles (FCEVs).¹⁹ For H₂ generation, especially for proton-exchange membrane (PEM) electrolysis, one bottleneck is the availability of highly pure feed water. If seawater could be directly used for hydrogen production, and freshwater is produced, this system would be of great commercial potential.

In 2004, Al-Hallaj et al.²⁰ proposed integrating fuel cells with a desalination system using the exhaust heat from fuel cells. Such thermal-energy applications show significant heat loss and lead to low energy efficiency. Recently, Atlas et al.²¹ proposed a framework of using electrochemical systems and redox-active chemicals to desalinate water and simultaneously generate electricity and predicted a maximum energy output up to around 25.7 kWh/m³ using H₂/O₂ redox neutralization processes in HCl and NaOH electrolytes.

In contrast to reverse ED, which uses the chemical potential of the concentration difference between the salt and freshwater channels to generate energy²¹ and, meanwhile, forms acid and bases, we apply hydrogen as an energy carrier by using multi-channel fuel-cell desalination (FCD) with ion-exchange membranes to desalinate seawater. While deionized water and electricity are generated, in separate reservoirs, an acid (HCl) and a base (NaOH) are formed. The remixing of the acid and base generated from the seawater can also generate thermal energy. Our work demonstrates that FCD can be used for continuous water desalination with applications either for drinking-water generation or deionized water for hydrogen generation.

RESULTS

Electrode characterization

Two pieces of Vulcan carbon cloth supported by a 40% Pt-C gas-diffusion electrode (0.3 mg/cm² loading; Fuel Cell Store), which consists of a gas-diffusion layer (GDL) and microporous carbon with a platinum-coated layer, was applied and cut into 34-mm-diameter, round disks as both the cathode and anode materials. As shown in Figure S1A, the gas-diffusion layer side of the electrode consists of Vulcan carbon cloth with a fiber diameter of around 10 µm. Figure S1B shows the electrode structure from a microporous carbon-crack point, with a platinum-coated layer after the desalination experiment in 600 mM NaCl solution. In addition, the material consists of a high degree of graphitized carbon (Figure S1C), which provides in-plane electrical conductivity.

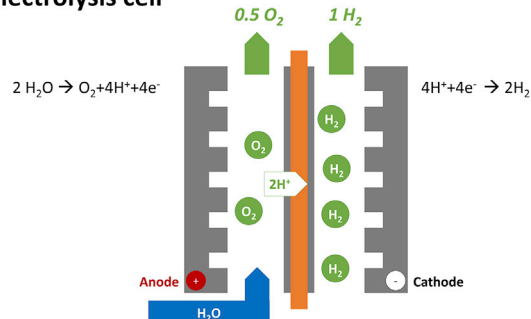
Working principle of the FCD

The hydrogen gas is generated by applying a PEM electrolysis cell (a schematic diagram is shown in Figure 1A). By supplying electricity to the electrolysis cell, water molecules are split into H₂ at the cathode and O₂ and H⁺ at the anode. The multi-channel cell configuration is shown in Figure 1B. The desalination fuel-cell-device operation relies on the electrocatalytic reaction of the hydrogen oxidation reaction (HOR) and the oxygen reduction reaction (ORR) of the platinum catalyst. The reaction at the anode is shown in Equation 1:



The reaction at the cathode is shown in Equation 2:

A PEM electrolysis cell



B Desalination fuel cell

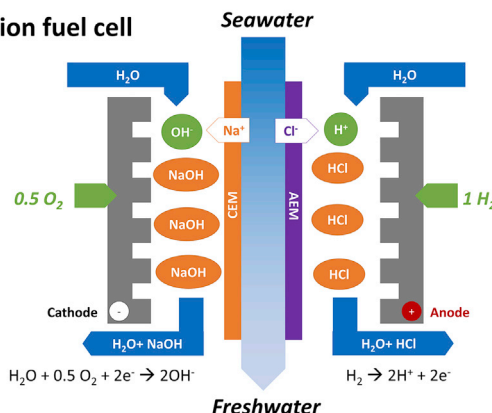
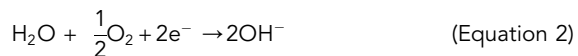


Figure 1. Schematic showing of the working principle of fuel cell desalination

(A) PEM electrolyzer.
(B) Desalination fuel cell.



In this water-desalination technique, the chemical energy of the hydrogen gas is converted to output electric energy, the potential energy to drive ion migration through the ion-exchange membranes, and chemical energy is stored in the form of HCl and NaOH (which can be described as neutralization heat energy that can be used). Part of the heat loss during the cell operation carried by the water flow also belongs to the heat-energy generation.

Electrical performance of the FCD

Figure 2A shows the desalination fuel cell's polarization curve and displays the voltage output at a particular current density. The figure is separated into three regions. Region A shows that the cell voltage at zero current density is around 0.7 V, which is lower than PEM fuel cells, and in this work, a much smaller slope at the low-current region is observed.²² When the electrodes are flooded, and the water cannot flow out of the cell, the cell voltage decreases, which causes a fluctuation in the cell voltage during the desalination processes (Figures 2C and 2D). Thus, the limited fuel crossover most probably causes this potential loss at the fuel/flowing liquid/flooded electrode interface, leading to slow reactions. At region B (Figure 2A), there is a rapid linear potential drop of around 0.25 V. This region is related to the catalyst-activation loss. There is an ohmic loss in region C (Figure 2A) because of the electrical resistance and interconnections of all cell components. Because of

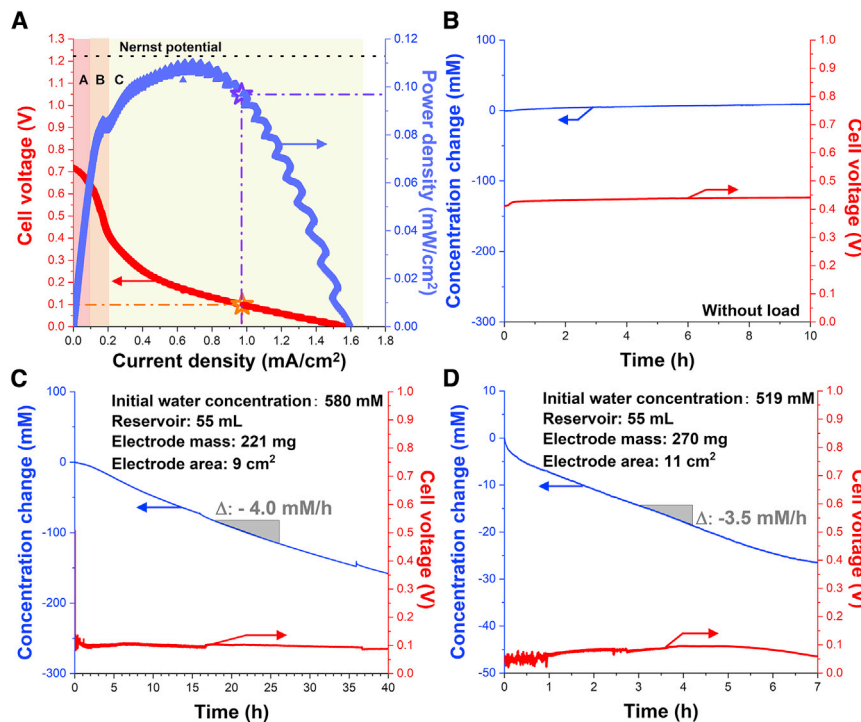


Figure 2. Electric and desalination performance of the FCD

- (A) Polarization and power density curve of the FCD with a continuous flow of anolyte, catholyte, and feed water.
- (B) Fuel cell desalination performance in 600 mM NaCl water solution without a load.
- (C) Fuel cell desalination performance in 600 mM NaCl water solution with a connected load (10 mW).
- (D) Fuel cell desalination with a connected load in substitute ocean water.

the flowing electrolytes, there is no mass transport loss, so there is no steep voltage decrease after region C (Figure 2A); however, pumping causes the undulating curve shape exhibited within region C. The power density is calculated by multiplying the voltage and the current density. The optimal power density is found at 0.15 V to be 0.11 mW/cm² with a current density of 0.7 mA/cm². When the load is connected to the FCD, the cell voltage is decreased to 0.1 V because of the potential drop in regions A, B, and C shown in Figure 2A, which relates to a power density of 0.097 mW/cm² and a current density of 0.97 mA/cm².

Desalination performance

To test the desalination performance of the FCD, a 600-mM NaCl aqueous solution is applied. In the feed-water channel, the saltwater to be desalinated is kept cycling in a 55-mL reservoir at a 20-mL/min flow rate. The anolyte and catholyte are kept cycling at a 7-mL/min flow rate and are separated into two 200-mL volumes. When no load is applied, the cell voltage is about 0.40–0.45 V without any current output (Figure 2B). Without the flow of an external electrical current, there is no charge imbalance, and the permselectivity of the ion-exchange membranes prohibits the transport of charged species. There is no significant change in the effluent concentration (most notably, there is no decrease in ionic strength).

Once the load is connected, a current starts to flow in the outside of the circuit. According to the polarization curve in Figure 2A, because of the ohmic loss of the cell, the cell voltage is decreased to around 0.1 V, and the concentration of the feed water

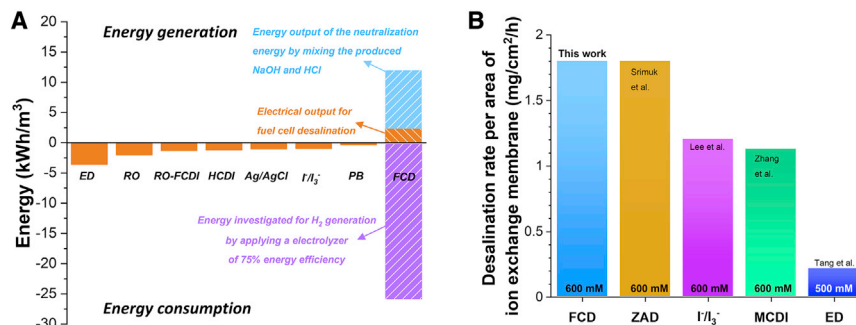


Figure 3. A comparison of different electricity energy of seawater desalination techniques

(A) Desalination rate per area by different water desalination techniques normalized by 1 m³ of produced freshwater.

(B) Data adapted from various references.^{25–32,34,35}

ED, electrodialysis; RO, reverse osmosis; RO-FCDI, reverse osmosis combined with flow electrode capacitive deionization; PB, Prussian blue; FCD, fuel cell desalination; MCDI, membrane capacitive deionization.

starts to decline gradually (Figure 2C). The device was then continuously operated for 40 h. After 40 h, the feed-water concentration decreased continuously to 420 mM from 580 mM. That reduction was accomplished at a rate of 4 mM/h, which correlates to 18 g/m²/h normalized by unit area of the ion-exchange membrane contacted to the feed water (7 cm²). After the desalination experiment, the pH values of the catholyte and anolyte are 12.9 and 2.1, respectively. This demonstrates that the NaCl from the feed water is extracted to the two electrodes to form NaOH and HCl.

To further verify the practicality of this setup concept in seawater applications, substitute ocean-water was prepared according to the ASTM D1141 standard.²⁴ The substitute ocean-water was applied to simulate seawater desalination.²³ The composition of simulated seawater is shown in Table S1. In Figure 2D, after connecting the load, the open-circuit cell voltage was around 0.06 V and fluctuated between 0.05 V and 0.09 V. This was possibly caused by a slight electrode flooding. Within a duration of 6 h, the feed-water concentration decreased from 519 mM to 495 mM. When conducting the middle region's linear fitting, the desalination rate was around 3.5 mM/h, which correlates to a desalination rate of 16 g/m²/h, normalized by unit area of the ion-exchange membrane that contacted the feed water. The electrode composition after the electrochemical desalination operation is shown in Figure S3.

According to the data on the FCD in 600 mM NaCl (Figure 2C), by removing 1 g of NaCl from the feed water, 67 mWh of electrical energy is generated. Because of the limited permselectivity of the ion-exchange membranes and the ohmic loss of the cell, the charge efficiency was 68%. In future studies, thinner ion-exchange membranes with higher permselectivity should be employed to further optimize and enhance the performance. Theoretically, while consuming 1 mole of H₂, after mixing the acid and base produced by this technique, the heat released by the neutralization reaction can heat 1 L of pure water from 25°C to 94.6°C. Because of the continuous operation, there is no capacity limitation on this cell design, as long as the chemical energy via H₂ and O₂ is provided.

In Figure 3A, with the development of water-desalination techniques, greater energy-efficient systems have been developed. Unlike the other current seawater-desalination

technologies, FCD continuously deionizes seawater without any recovery operation and continually produces electricity. Desalination of 1 m³ of seawater to freshwater consumes 26.4 kWh with a 75% energy efficiency (for the H₂ production). In addition, 2.3 kWh of electricity and 9.6 kWh of heat energy are obtained by mixing the produced acid and base. Although creating such an amount of hydrogen gas consumes energy, the power-to-gas processes employ renewable energy, which allows for sustainable hydrogen generation.

Based on the data from the International Energy Agency (IEA) policy (2016), global average aggregate carbon emissions should be reduced from 515 g/kWh to 355 g/kWh.²⁴ Assuming a certain technological portfolio for energy generation, electrical energy can be converted to carbon emission. Seawater desalination techniques, such as ED,²⁵ RO,²⁶ hybrid capacitive deionization (HCDI),²⁷ chloride ion desalination batteries,²⁸ redox electrolyte desalination using I⁻/I₃⁻,²⁹ RO combined with flow electrode capacitive deionization (RO-FCDI),³⁰ and desalination batteries using Prussian blue electrodes,³¹ consume energy, which is most often and commonly generated by conventional electricity production; unless renewable energy sources are used, that energy consumption contributes toward carbon emissions. As long as H₂ and O₂ are generated by renewable energy, electrocatalytic FCDs will produce electrical energy and provide desalination without carbon emissions. For example, by replacing RO with an FCD supplied with hydrogen provided by renewable processes, 1.6 kg of carbon emissions in India, 1.0 kg of carbon emissions in the United States, and 0.7 kg of carbon emissions in Europe would be reduced and produce 1 m³ of freshwater.

The desalination rate is also an important performance metric. Figure 3B compares the desalination rates measured in our experiments with those from other electrochemical water-desalination techniques. The FCD has a much better performance compared with I⁻/I₃⁻redox electrolyte desalination,³² membrane capacitive deionization (MCDI),³⁰ and ED,¹⁶ and is comparable to the desalination rate of zinc-air desalination (ZAD).³³

DISCUSSION

This work demonstrated the use of a fuel cell for direct seawater desalination with experimental data. We developed a multi-channel cell with a pair of ion-exchange membranes by adopting a PEM fuel cell. This shows that, in principle, any PEM fuel cell can be converted into a desalination fuel cell; therefore, existing fuel cells could be used for concurrent power generation and water remediation. However, the durability in long-term operations and the optimum operational parameters of the FCD presented remain to be explored.

By continually feeding hydrogen and oxygen from a PEM electrolyzer, the desalination fuel cell continuously removes salts from the feed water at seawater molarity. At the same time, the cell produces acid and base at the catholyte and anolyte, respectively, and acts as a power supplier for the output power of the load. The byproducts of acid and base can, later, be remixed to produce heat under proper thermal-energy design to release the heat in a better-controlled way to reduce the thermal-energy heat loss. Thus, an FCD power plant would provide freshwater, thermal energy, and electricity and consume seawater and hydrogen via renewable energy, like solar or wind power. High-performance seawater desalination via an FCD would also be a facile way to generate deionized water for use in an electrolyzer because the present-day technology remains limited in seawater's direct use for hydrogen

generation. However, because of the high cost and the challenged chemical stability of platinum-based catalysts in seawater, platinum-free and seawater-resistive catalyst materials are important to develop in future work.

EXPERIMENTAL PROCEDURES

Resource availability

Lead contact

Further information and requests for resources and materials should be directed to and fulfilled by the lead contact, Volker Presser (volker.presser@leibniz-inm.de).

Materials availability

This study does not generate new unique materials.

Data and code availability

The datasets generated in this study are available from the lead contact on request.

Materials and reagents

NaCl (≥99%), MgCl₂·6H₂O (≥99%), CaCl₂(≥96%), KCl (≥96%), NaHCO₃ (99.5%), KBr (≥99%), H₃BO₃ (≥99.9999%), NaF (≥99%), and NaOH (≥98%) were obtained from Sigma-Aldrich. SrCl₂·6H₂O (≥99%) was obtained from Carl Roth International. Na₂SO₄ (≥99%) was obtained from Honeywell Fluka. Pt/C with 40% Pt loading was obtained from the Fuel Cell Store. Ion-exchange membranes FAS-PET-130 and FKS-PET-130 were obtained from Fumatech.

Materials characterization

A scanning electron microscope (SEM) image was taken to observe the electrode structure. A Zeiss Gemini 500 SEM was used with an accelerating voltage of 3 kV and a working distance of 4 mm applied. X-ray diffraction (XRD) measurement of the electrode was conducted with a D8 Discover diffractometer (Bruker AXS). A Cu-K_α source ($\lambda = 1.5406 \text{ \AA}$) was used in combination with a VANTEC-500 two-dimensional X-ray detector positioned at 20° 2θ, 40° 2θ, 60° 2θ, and 80° 2θ with 1,000 s/step to record five frames. Raman spectroscopy was measured with a Renishaw inVia microscope with a neodymium-doped yttrium garnet laser (532 nm) at a power of 0.5 mW. Ten different locations were selected with five accumulations, and the exposure time was 30 s.

Cell components

This cell has one pair of gas channels to feed hydrogen and oxygen, one pair of anolytes and catholytes, and a central water channel. An anion-exchange membrane (AEM; Fumasep, FAS-PET-130) is placed between the anolyte and water channel, and a cation exchange membrane (CEM; Fumasep, FKS-PET-130) is placed between the catholyte and the water channel. Together, the space of the anolyte, catholyte, and the feed water has a 30-mm-diameter round shape and a 2 mm thickness and is filled with glass-fiber separators (Millipore, four pieces of 380 μm). The diameter of the ion-exchange membranes that are exposed to the feed water is 30 mm. The anolyte, catholyte, and feed water are all continuously pumped.

Desalination experiment

An electrolyzer from H-TEC supplies the hydrogen and oxygen. After feeding Milli-Q water to the cell and applying 1.2 V, 1 A to the electrolyzer using an ALC 8500 Expert power supply, hydrogen, and oxygen will be produced and separated into two cylinders fed to the anode and cathode separately. When the FCD is fed with hydrogen

and oxygen and the electrolytes are flowing in the cell, the cell is connected to a 10-mW load. Then, the FCD starts under room temperature of ~20°C. The setup is shown in [Figure S2](#).

We used a Squid potentiostat (Admiral) to characterize the electrochemical behavior of the cell. When the fuel cell is fed with hydrogen and oxygen and continuously pumped with catholyte, anolyte, and feed water, the cell is disconnected from the load. The hydrogen-side electrode is connected to the counter and reference electrode, and the oxygen-side electrode is connected to the working electrode, a linear potential sweep is scanned from 1 V to 0 V at a scan rate of 10 mV/s, and the current resonance is recorded for the polarization curve.

After starting up the FCD, the saltwater of the same ion content as that of the feed water (600 mM NaCl or substitute ocean water) is pumped to both the anolyte and catholyte. The volume of both catholyte and anolyte are all 200 mL. The feed saltwater (600 mM NaCl or substitute ocean water) reservoir had a volume of 55 mL, and the flow rate of the feed-water stream was set at 20 mL/min. At the cell's outlet, a conductivity sensor was connected to monitor the concentration fluctuations during fuel-cell operation. We used a Squid potentiostat (Admiral) to determine the electrochemical performance and a Metrohm PT1000 conductometric cell to monitor the electrolyte concentration. In that way, we determined values for the desalination capacity and rate. The open-circuit potential was monitored and recorded with a connected load. Before the desalination measurement, a standardization measurement of the conductivity value at different molarities was used to calculate the concentration.

SUPPLEMENTAL INFORMATION

Supplemental information can be found online at <https://doi.org/10.1016/j.xcpr.2021.100416>.

ACKNOWLEDGMENTS

The authors thank Eduard Arzt (INM) for his continuing support. Lei Wang acknowledges funding from the Chinese Scholarship Council (CSC) via award number 201906260277. We thank Karsten Moh and Alexander May (INM) for discussions and kind support on the facilities.

AUTHOR CONTRIBUTIONS

Y.Z. conceptualized and performed the experiments, the electrochemical characterizations, and the data analysis and prepared the manuscript. L.W. contributed Raman and XRD measurements and reviewed and edited the manuscript. V.P. contributed to the conceptualization and the data curation and reviewed and edited the manuscript.

DECLARATION OF INTEREST

The authors declare no competing interests.

Received: January 26, 2021

Revised: March 15, 2021

Accepted: April 6, 2021

Published: April 26, 2021

REFERENCES

1. Shannon, M.A., Bohn, P.W., Elimelech, M., Georgiadis, J.G., Mariñas, B.J., and Mayes, A.M. (2008). Science and technology for water purification in the coming decades. *Nature* 452, 301–310.
2. Humplík, T., Lee, J., O'Hern, S.C., Fellman, B.A., Baig, M.A., Hassan, S.F., Atieh, M.A., Rahman, F., Laoui, T., Karnik, R., and Wang, E.N. (2011). Nanostructured materials for water desalination. *Nanotechnology* 22, 292001.
3. Porada, S., Borchardt, L., Oschatz, M., Bryjak, M., Atchison, J.S., Keesman, K.J., Kaskel, S., Biesheuvel, P.M., and Presser, V. (2013). Direct prediction of the desalination performance of porous carbon electrodes for capacitive deionization. *Energy Environ. Sci.* 6, 3700–3712.
4. Miller, J.E. (2003). Review of Water Resources and Desalination Technologies (Sandia National Laboratories).
5. Khawaji, A.D., Kutubkhana, I.K., and Wie, J.-M. (2008). Advances in seawater desalination technologies. *Desalination* 221, 47–69.
6. El-Nashar, A.M. (2001). Cogeneration for power and desalination—state of the art review. *Desalination* 134, 7–28.
7. Ayyash, Y., Imai, H., Yamada, T., Fukuda, T., Yanaga, Y., and Taniyama, T. (1994). Performance of reverse osmosis membrane in Jeddah phase I plant. *Desalination* 96, 215–224.
8. Durham, B., and Walton, A. (1999). Membrane pretreatment of reverse osmosis: long-term experience on difficult waters. *Desalination* 122, 157–170.
9. Ebrahim, S.H., Abdel-Jawad, M.M., and Safar, M. (1995). Conventional pretreatment system for the doha reverse osmosis plant: Technical and economic assessment. *Desalination* 102, 179–187.
10. Al-Amshawee, S., Yunus, M.Y.B.M., Azoddein, A.A.M., Hassell, D.G., Dakhlil, I.H., and Hasan, H.A. (2020). Electrodialysis desalination for water and wastewater: A review. *Chem. Eng. J.* 380, 122231.
11. Park, K., Kim, J., Yang, D.R., and Hong, S. (2020). Towards a low-energy seawater reverse osmosis desalination plant: A review and theoretical analysis for future directions. *J. Membr. Sci.* 595, 117607.
12. Biesheuvel, P.M., Porada, S., Levi, M., and Bazant, M.Z. (2014). Attractive forces in microporous carbon electrodes for capacitive deionization. *J. Solid State Electrochem.* 18, 1365–1376.
13. Elimelech, M., and Phillip, W.A. (2011). The future of seawater desalination: energy, technology, and the environment. *Science* 333, 712–717.
14. Pasta, M., Wessells, C.D., Cui, Y., and La Mantia, F. (2012). A desalination battery. *Nano Lett.* 12, 839–843.
15. Bi, S., Zhang, Y., Cervini, L., Mo, T.M., Griffin, J.M., Presser, V., and Feng, G. (2020). Permeselective ion electrosorption of subnanometer pores at high molar strength enables capacitive deionization of saline water. *Sustain. Energy Fuels* 4, 1285–1295.
16. Zhang, Y., Srimuk, P., Aslan, M., Gallei, M., and Presser, V. (2020). Polymer ion-exchange membranes for capacitive deionization of aqueous media with low and high salt concentration. *Desalination* 479, 114331.
17. Yu, F., Wang, L., Wang, Y., Shen, X., Cheng, Y., and Ma, J. (2019). Faradaic reactions in capacitive deionization for desalination and ion separation. *J. Mater. Chem. A Mater. Energy Sustain.* 7, 15999–16027.
18. Staffell, I., Scamman, D., Velazquez Abad, A., Balcombe, P., Dodds, P.E., Ekins, P., Shah, N., and Ward, K.R. (2019). The role of hydrogen and fuel cells in the global energy system. *Energy Environ. Sci.* 12, 463–491.
19. Brandon, N.P., and Kurban, Z. (2017). Clean energy and the hydrogen economy. *Philos. Trans. A Math Phys. Eng. Sci.* 375, 20160400.
20. Al-Hallaj, S., Alasfour, F., Parekh, S., Amiruddin, S., Selman, J.R., and Ghezel-Ayagh, H. (2004). Conceptual design of a novel hybrid fuel cell/desalination system. *Desalination* 164, 19–31.
21. Atlas, I., Abu Khalla, S., and Suss, M.E. (2020). Thermodynamic energy efficiency of electrochemical systems performing simultaneous water desalination and electricity generation. *J. Electrochem. Soc.* 167, 134517.
22. Lacey, R.E. (1980). Energy by reverse electrodialysis. *Ocean Eng.* 7, 1–47.
23. Wu, J., Galli, S., Lagana, I., Pozio, A., Monteleone, G., Yuan, X.Z., Martin, J., and Wang, H. (2009). An air-cooled proton exchange membrane fuel cell with combined oxidant and coolant flow. *J. Power Sources* 188, 199–204.
24. Quality Systems, Specification, and Statistics Subcommittee (2013). D1141-98: Standard Practice for the Preparation of Substitute Ocean Water (ASTM International).
25. Zhang, X., Zhang, H., Zhao, C., and Yuan, J. (2019). Carbon emission intensity of electricity generation in Belt and Road Initiative countries: a benchmarking analysis. *Environ. Sci. Pollut. Res. Int.* 26, 15057–15068.
26. Doornbusch, G.J., Tedesco, M., Post, J.W., Borneman, Z., and Nijmeijer, K. (2019). Experimental investigation of multistage electrodialysis for seawater desalination. *Desalination* 464, 105–114.
27. Gude, V.G. (2012). Energy consumption and recovery in reverse osmosis. *Desalination Water Treat.* 36, 239–260.
28. Srimuk, P., Lee, J., Tolosa, A., Kim, C., Aslan, M., and Presser, V. (2017). Titanium disulfide: a promising low-dimensional electrode material for sodium ion intercalation for seawater desalination. *Chem. Mater.* 29, 9964–9973.
29. Srimuk, P., Husmann, S., and Presser, V. (2019). Low voltage operation of a silver/silver chloride battery with high desalination capacity in seawater. *RSC Advances* 9, 14849–14858.
30. Lee, J., Srimuk, P., Carpier, S., Choi, J., Zornitta, R.L., Kim, C., Aslan, M., and Presser, V. (2018). Confined redox reactions of iodide in carbon nanopores for fast and energy-efficient desalination of brackish water and seawater. *ChemSusChem* 11, 3460–3472.
31. Chung, H.J., Kim, J., Kim, D.I., Gwak, G., and Hong, S. (2020). Feasibility study of reverse osmosis-flow capacitive deionization (RO-FCDI) for energy-efficient desalination using seawater as the flow-electrode aqueous electrolyte. *Desalination* 479, 114326.
32. Lee, J., Kim, S., and Yoon, J. (2017). Rocking chair desalination battery based on prussian blue electrodes. *ACS Omega* 2, 1653–1659.
33. Patel, S.K., Qin, M., Walker, W.S., and Elimelech, M. (2020). Energy efficiency of electro-driven brackish water desalination: Electrodialysis significantly outperforms membrane capacitive deionization. *Environ. Sci. Technol.* 54, 3663–3677.
34. Srimuk, P., Wang, L., Budak, Ö., and Presser, V. (2020). High-performance ion removal via zinc-air desalination. *Electrochim. Commun.* 115, 106713.
35. Tang, K., Yiakoumi, S., Li, Y., Gabitto, J., and Tsouris, C. (2020). Optimal conditions for efficient flow-electrode capacitive deionization. *Sep. Purif. Technol.* 240, 116626.

Supplemental information

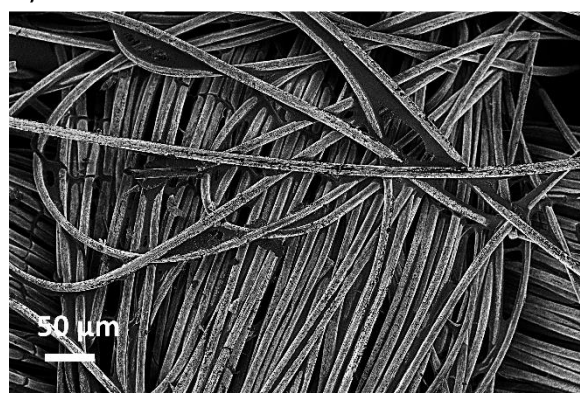
**Electrocatalytic fuel cell desalination
for continuous energy and freshwater generation**

Yuan Zhang, Lei Wang, and Volker Presser

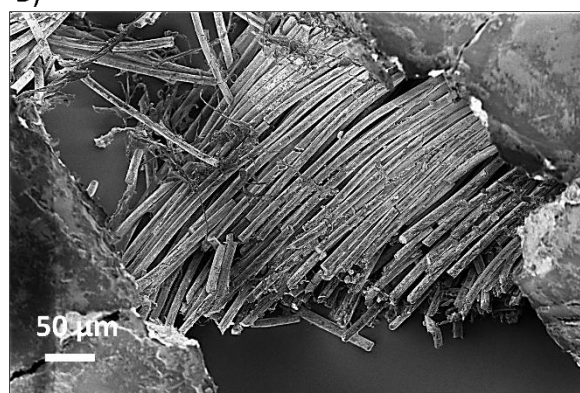
1. Supplemental Experimental Procedures

Scanning electron microscopy and Raman spectroscopy

A)



B)



C)

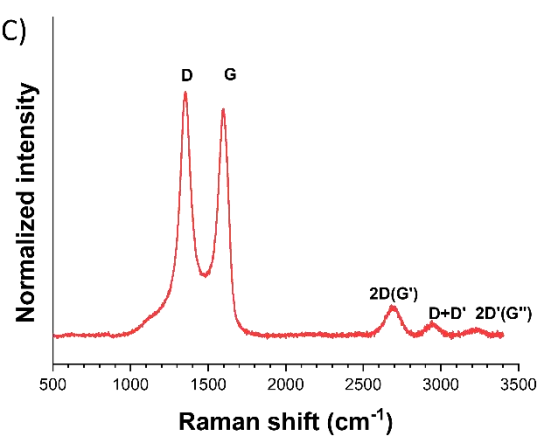


Figure S1: Electrode characterizations. A) Scanning electron micrograph of the gas diffusion layer (GDL). B) the crack point of the microporous carbon with platinum-coated layer after the desalination experiment in 600 mM NaCl solution. C) Raman spectrum of the Pt-C electrode before desalination experiments.

Experimental setup

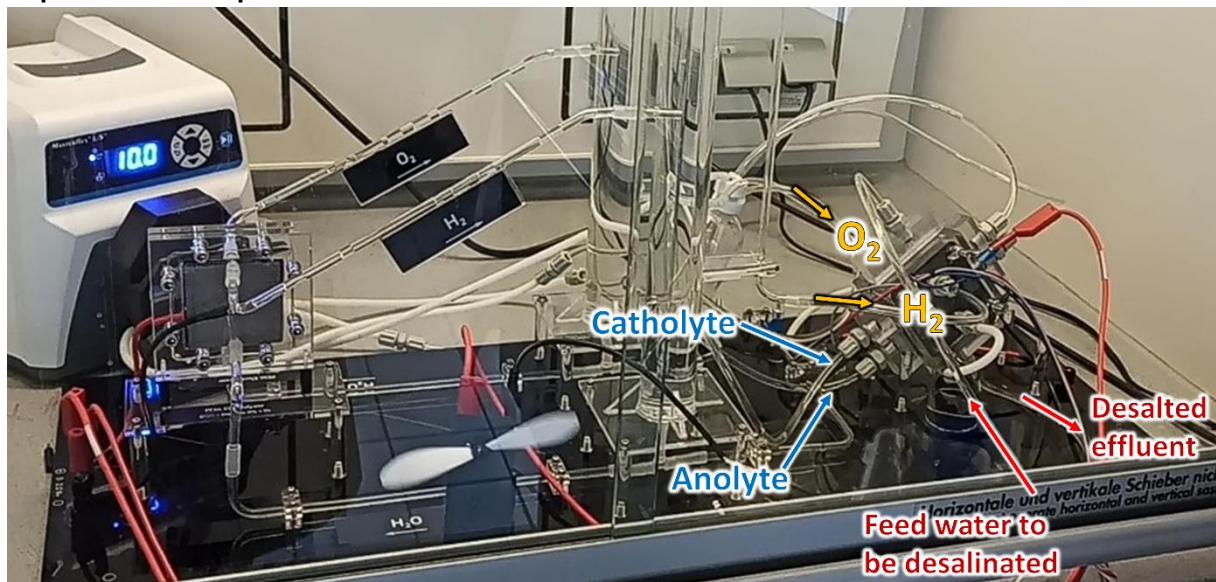


Figure S2: Photograph of the setup during continuous desalination operation. The desalination fuel cell has 5 channels, one for the feedwater, one pair for anolyte and catholyte, and one pair for H₂ and O₂.

X-ray diffraction

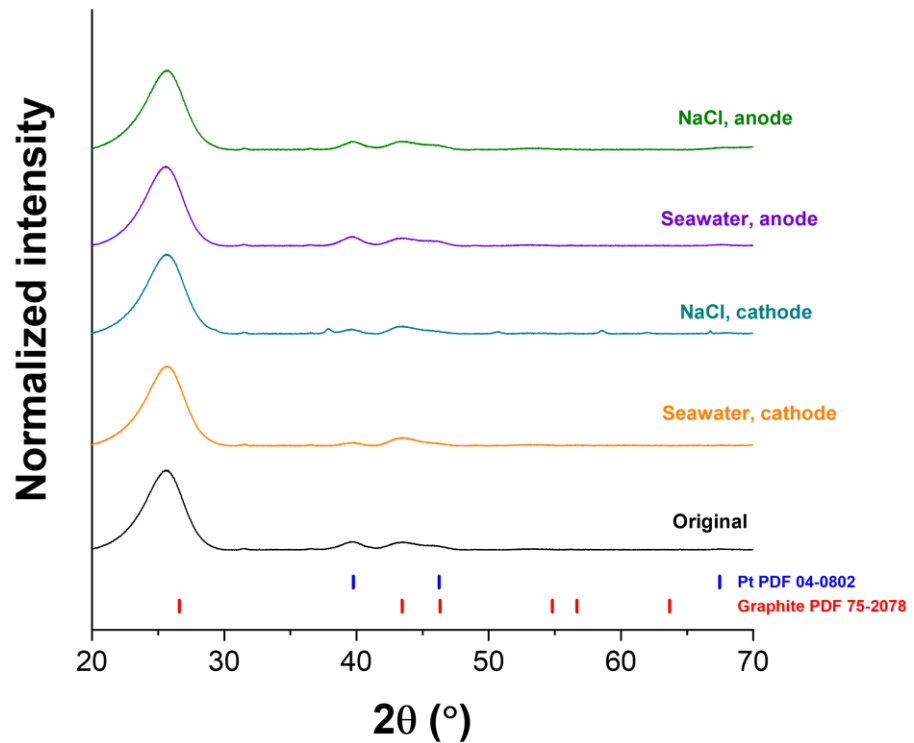


Figure S3: X-ray diffractograms of the PtC electrodes

XRD characterizations are conducted before and after desalination experiments in 600 mM NaCl and substitute ocean water.

Chemical composition

Table S1: The components of artificial sea water used in this study.

Ion	Concentration (mmol/L)
Na ⁺	477.5
K ⁺	9.322
Mg ²⁺	54.6
Ca ²⁺	10.45
Sr ²⁺	0.16
Cl ⁻	139.74
Br ⁻	0.85
F ⁻	0.071
SO ₄ ²⁻	28.79
BO ₃ ²⁻	0.44
HCO ₃ ⁻	2.39
pH	~8

4.9 From capacitive deionization to desalination batteries and desalination fuel cells

Lei Wang,^{1,2} Yuan Zhang,^{1,2} Karsten Moh,¹ Volker Presser,^{1,2,*}

1 INM - Leibniz Institute for New Materials, Campus D2 2, 66123 Saarbrücken, Germany

2 Saarland University, Campus D2 2, 66123 Saarbrücken, Germany

3 Saarene - Saarland Center for Energy Materials and Sustainability, Campus C4 2, 66123 Saarbrücken, Germany

Citation:

L. Wang, Y. Zhang, V. Presser, *From capacitive deionization to desalination batteries and desalination fuel cells*, Current Opinion in Electrochemistry, 2021, 29: 100758. (DOI: 10.1016/j.coelec.2021.100758)

Own contribution:

Validation, data curation, writing-review & editing, visualization.

Review Article

From capacitive deionization to desalination batteries and desalination fuel cells



Lei Wang^{1,2}, Yuan Zhang^{1,2}, Karsten Moh¹ and Volker Presser^{1,2}

Abstract

The considerable growth of the world population, concomitant with an increase in environmental pollution, aggravates the antinomy between supply and demand for drinking water. Various desalination technologies have been developed to address this issue, allowing for abundant saltwater as a source for drinking water. Electrochemical desalination attracts more and more attention due to its high energy efficiency, facile operation, and low cost. Especially within the last decade, tremendous scientific progress on electrochemical desalination technologies has been made. This article reviews the development of electrochemical desalination technologies and introduces a facile classification into three generations based on the different working principles. The cell architecture, metrics, advantages, and disadvantages of other electrochemical desalination technologies are introduced and compared.

Addresses

¹INM - Leibniz Institute for New Materials, D2 2, 66123, Saarbrücken, Germany

²Department of Materials Science & Engineering, Saarland University, Campus D2 2, 66123, Saarbrücken, Germany

Corresponding author: Presser, Volker (volker.presser@leibniz-inm.de)

Current Opinion in Electrochemistry 2021, **29**:100758

This review comes from a themed issue on **Electrochemical Materials and Engineering**

Edited by Fabio La Mantia

For a complete overview see the [Issue](#) and the [Editorial](#)

Available online 30 April 2021

<https://doi.org/10.1016/j.colec.2021.100758>

2451-9103/© 2021 Elsevier B.V. All rights reserved.

Keywords

Electrochemical desalination, Desalination batteries, Capacitive deionization, Metal air desalination.

Introduction

Water scarcity is one of the grand challenges of the 21st century. In 2018, about 3 billion people did not have access to clean, potable water [1], and by 2025, approximately two-thirds of the world's population may have to live under water-stressed conditions [2]. Water

technology is not just crucial to generate drinking water but is equally essential for agriculture, mining, and industrial production. Various water purification technologies have been developed to address this issue, such as multistage flash [3], reverse osmosis [4], forward osmosis [5], and electrodialysis [6]. Among them, reverse osmosis has been widely used for water desalination of brackish water and seawater on an industrial scale [7]. Although the cost has been reduced significantly from 20 kWh/m³ to 2–4 kWh/m³ [8], reverse osmosis remains energy-intensive to meet the enormous demand for remediated water [4].

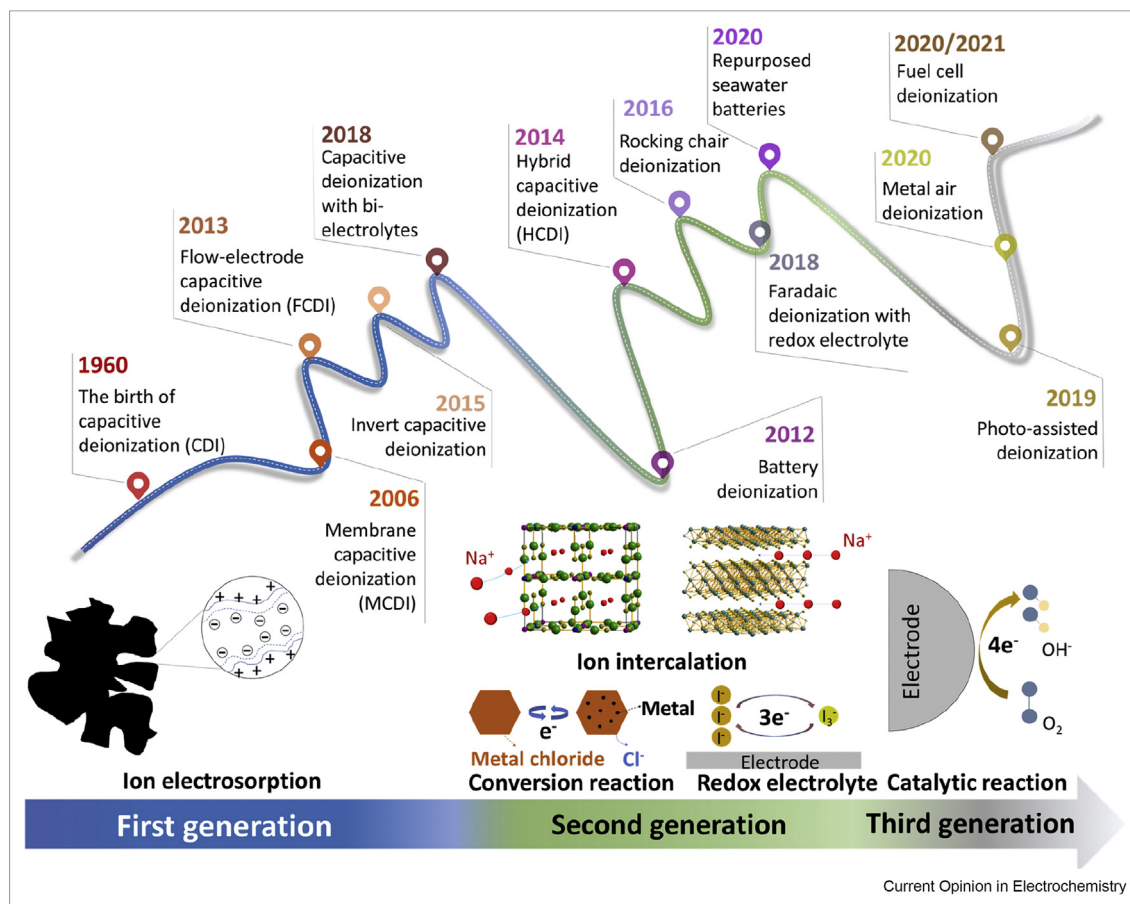
To decrease the energy consumption and improve the desalination performance, some of the desalination technology, based on other electrochemical principles, such as electrosorption [9], reversible electro-redox reaction [10], and electrocatalysis [11–13], have rapidly emerged as promising alternatives to the traditional desalination technologies for their high industrial application potential. In this paper, these emerging technologies are systematically divided into three generations according to their ion-removal mechanism (collectively referred to as electrochemical desalination technologies). The principle, merits, and limitations of the three generations are introduced and future perspectives on the emerging trends in electrochemical desalination technologies are discussed.

First-generation: carbon electrodes and ion electrosorption

In 1960, Blair and Murphy [14] opened the carbon ages of electrochemical desalination by using porous carbon electrodes. This technology can be classified as first-generation (Figure 1). A first-generation cell is known as capacitive deionization (CDI) because of the mechanism of ion electrosorption [15]. The cell contains one carbon electrode pair and a single middle channel for the feed water (Figure 2A). When the cell is charged, the ions are removed from the water and immobilized via electrosorption in the electrical double layer at the fluid/solid interface in the electrodes' pores (Figure 1), introduced by Johnson and Newman [16].

CDI electrodes usually use nanoporous carbon with facile ion access to a large pore volume and specific

Figure 1



The timeline and working principle of the first-, second-, and third-generation of electrochemical desalination methods. The terms deionization and desalination is used interchangeably in the literature.

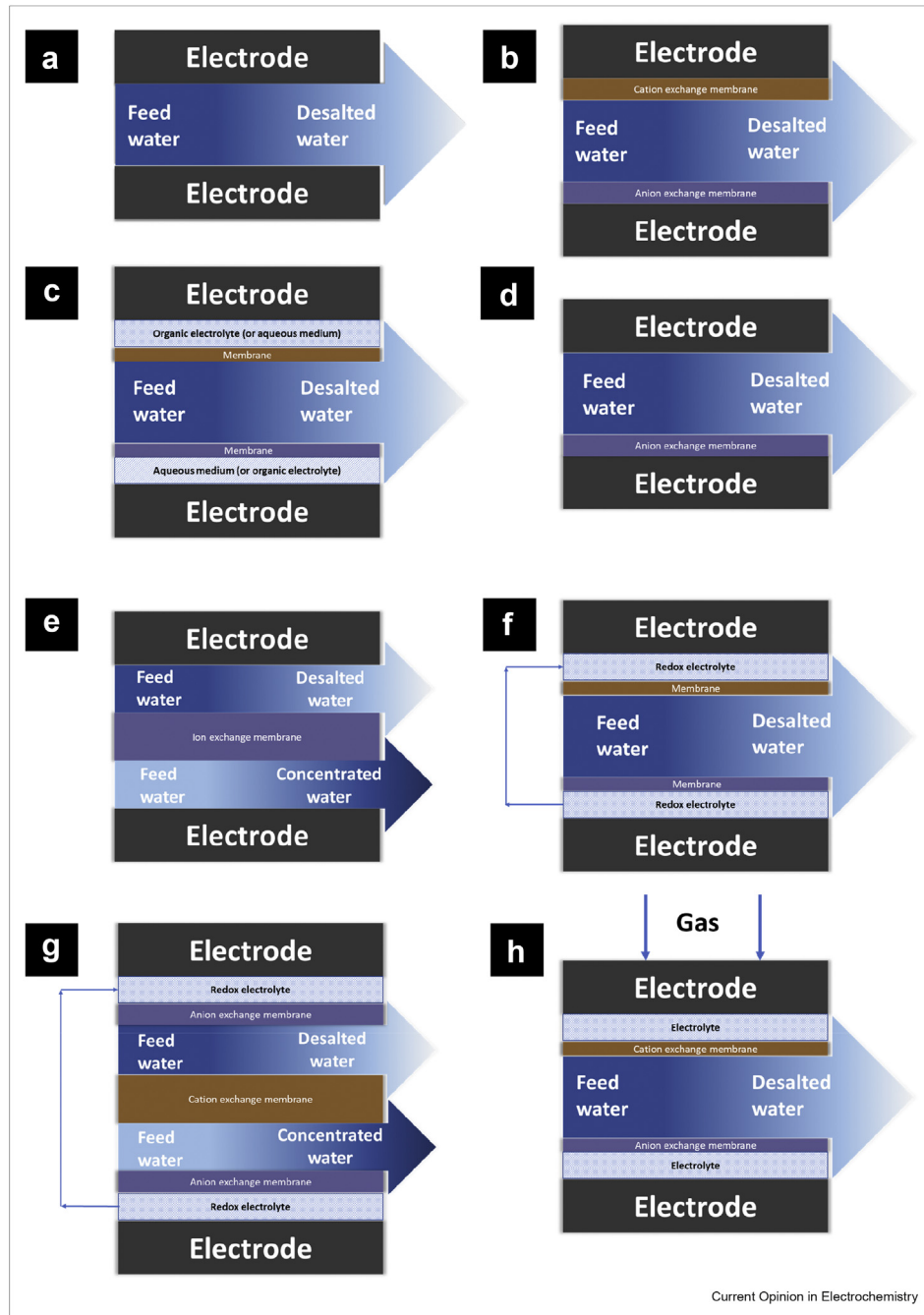
surface area. Even in the uncharged state, the pores are already populated by some ions. Expelling ions with the same charge as the electrode (co-ions) while attracting ions with the opposite charge (counter-ions) achieve facile charge storage. Still, it fails to accomplish any desalination as long as the ratio between counter ions and co-ions 1:1 [17]. This issue prevails for feed water with high salinity. In seawater, for instance, the desalination capacity of activated carbon (with an average pore size of more than 1 nm) is only around 1 mg/g with a charge efficiency (ratio of salt removal over charge) of about 10% [18]. However, micropores smaller than 1 nm become increasingly permselective and enable CDI to operate even in saline media with high molarity [19].

The desalination capacity is limited by the specific capacitance of carbon, around 0.1 F/m² [20]. Thus optimizing the cell voltage [21] is also important. When applying higher cell voltage, there may be water splitting and carbon oxidation [22], which reduces the charge

efficiency and causes significant performance degradation. Besides, inverting the CDI process by modifying the carbon surface with chemical charge can mitigate the oxidation of the anode and consequently improve stability [23]. Ions are immobilized via the chemical charge of surface groups and released when an electric potential is applied [24].

The first-generation electrochemical desalination is a promising technology, with a desalination capacity of (5–30 mgNaCl/g_{electrodes}) and low energy consumption (10–40 Wh/molNaCl) for low to medium brackish water (0.1–1 g/L) but does not work sufficiently well in seawater (Figure 3). Commonly, it has a desalination rate of 0.03–0.6 mgNaCl/gelectrode/s (Table 1), which greatly depends on the operation parameters such as the feedwater salinity, charge/discharge rate, flow rate, and so on, apart from the pore size effect [9,25]. The first-generation also exhibits stable desalination performance (80–97% desalination capacity retention after several hundred cycles) analogous to the long life

Figure 2



Cell architectures: conventional capacitive deionization (a), membrane capacitive deionization (b), bielectrolyte deionization (c), hybrid capacitive deionization (d), sodium ion desalination (e), desalination based on redox-electrolyte (f), photo-redox desalination (g), metal-air batteries desalination (h).

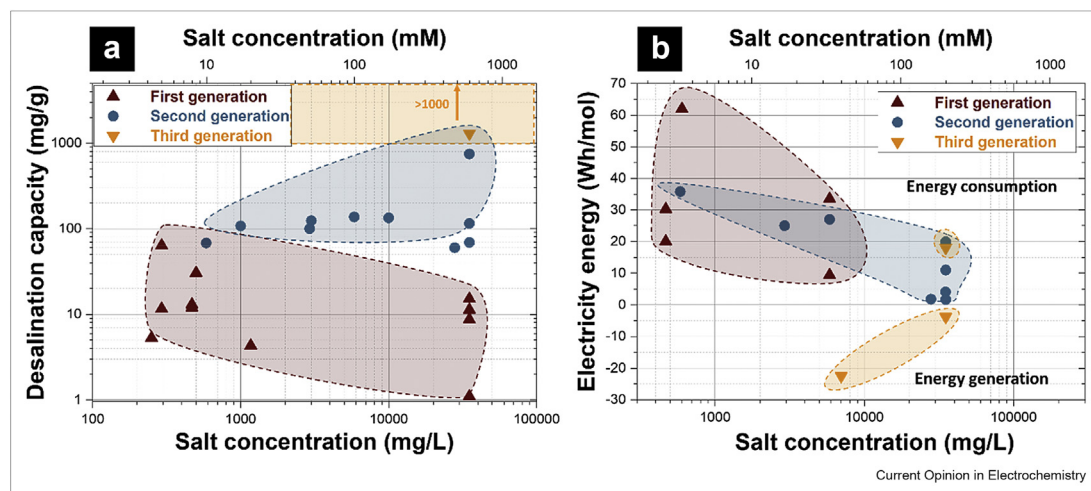
span of electrical double layer capacitors (Table 1) [26].

First-generation 1.1: ion-exchange membranes

To enhance the performance of CDI, in 2006, Lee et al. [27] proposed a membrane capacitive deionization (MCDI) technology. In this case, ion-exchange

membranes (IEMs) are added between the electrode pair and the water channel (Figure 2B). Implementing a pair of IEMs provides permselectivity to the nonperm-selective carbon electrodes and suppresses the detrimental Faradaic side reactions, such as oxygen reduction at the cathode [28]. Compared with conventional CDI, the desalination capacity of MCDI for remediation of

Figure 3



The desalination capacity (a) and electricity energy consumed (positive value) and energy generated (negative value) (b) of different generations at various concentrations. Data adapted from [9,10,18,33,41,44,46,48,53,54,58–69].

water with low ionic molarity are improved [29] to 15–30 mg_{NaCl}/g_{electrodes}, with charge efficiency higher than 80% [18,30,31]. Besides, MCDI allows for seawater desalination [32]. The high cost of IEMs raises the desalination costs.

MCDI with multichannel structures allows for more diversity in cell designs. In 2018, a CDI cell containing two different electrolytes was introduced (Figure 2C) [33]. By immersing one electrode in the organic electrolyte, the cell voltage could reach 2.4 V, significantly improving the desalination capacity to 64 mg_{NaCl}/g_{electrodes}.

First-generation 1.2: suspension electrodes

Owing to the limited system capacities of immobile solid electrodes (M)CDI systems require electrode regeneration (discharging) once the electrode pores are saturated for ion adsorption, which leads to inefficiency of (M)CDI technology. To overcome this, flow electrode capacitive deionization was introduced by Jeoh et al. in 2013 (Figure 1) [34]. The basic concept of suspension electrodes dates back to Bertel Kastening and Faul [35]. With a separated regeneration process of the electrodes, the electrode suspension's mobility enables electrode regeneration during desalination and allows continuous operation [36].

Second-generation: desalination batteries

To overcome the intrinsic capacitance limitations of carbon, one needs to move beyond. In 2012, Pasta et al. [37] used a pair of Faradaic electrodes, namely, Na_xMn₅O₁₀ and Ag, to desalinate seawater. Unlike the first-generation, the second-generation (desalination

batteries) applies Faradic materials to store ions in the crystallographic sites, between the electrode material's atomic planes, or immobilized through a conversion reaction (Figure 1). This ion-storage mechanism of Faradic materials enables higher desalination capacity (Figure 3A) as they have higher charge storage capacities than carbon electrodes. Besides, desalination batteries allow for higher charge efficiency due to intrinsic permselectivity, which enables effective and efficient desalination at the seawater salinity and beyond [38].

Different kinds of Faradaic materials have been used as electrodes. Most of them are intercalation-type materials, such as sodium manganese oxides [39], NaTi₂(PO₄)₃ [40], Na₃V₂(PO₄)₃ [10], Prussian blue [41], and MXenes, [42]. Commonly they are used as cathodes, providing a desalination capacity of around 50–150 mg_{NaCl}/g_{electrodes} in the feed water with the salinity of 1–35 g/L (Figure 3A). Similar to MXenes or different transition metal dichalcogenides, some materials also enable intercalation of anions [43]. Often, conversion materials such as Ag [44], Bi [45], or BiOCl [46] are chosen as the anode to store chloride. Attributed to the conversion reaction, these materials generally have a higher capacity (100–150 mg_{NaCl}/g_{electrode}) but reduced performance stability, compared with intercalation-type materials. Recently, the water-sensitive electrode (such as metallic sodium [47]), and alloying material (e.g. antimony [48]) are also applied in the desalination, using sodium super ion conductor. Compared with the first-generation, the Faradaic materials suffer commonly from lower desalination rates (because of the slow ions diffusion rates in bulk material) [41] and lower stability (due to irreversible

Table 1

The desalination rates, stability, technology-readiness level, and key-aspects of the three generations of electrochemical desalination technologies.

Generation of electrochemical desalination technology	Materials and technologies	Feed water salinity (mg/L)	Operation mode ^a	Desalination rates (mg _{NaCl} /gelectrode/s; or other)	Desalination capacity retention (%)	Cycle number	Reference	Technology-readiness level TRL ^b	Key aspects
First-generation	Block copolymer-based porous carbon fibers//block copolymer-based porous carbon fibers, CDI	500	C.V., 1.0 V	0.63	No obvious decrease	30	[9]	6–8	For CDI, scale-up; For MCDI, the cost control of the ion exchange membrane and scale-up
	H ₂ activated carbon//H ₂ activated carbon, CDI	292.5	C.V., 1.2 V	0.1	90%	100	[68]		
	Activated carbon//Activated carbon, MCDI	35100	C.C., 250 mA/g + C.V., 1.0 V	~0.05	97	180	[18]		
	Activated carbon cloth//Activated carbon cloth, bi-electrolyte	292.5	C.C., 30 mA/g	0.015	62	25	[33]		
Second-generation	Na ₃ V ₂ (PO ₄) ₃ -graphene aerogel//AgCl-graphene aerogel, DEDI	1000	C.C., 100 mA/g	0.035	86	50	[10]	3–5	The synthesis of the electrode material with low cost, high capacity, and high selectivity
	Na ₃ V ₂ (PO ₄) ₃ //AgCl, DEDI	1000	C.C., 100 mA/g	–	73	50	[10]		
	Prussian blue/PANI//C, hybrid cell	500	C.C., 100 mA/g	0.03	No obvious decrease	250	[41]		
	Ag//AgCl, CID	35100	C.C., 100 mA/g	0.38	61	15	[44]		
Third-generation	BiOCl-CNF//Bi-CNF	3000	C.C., 500 mA/g	0.52	90	30	[46]		
	Sb/C//C, bi-electrolyte	35100	C.C., 200 mA/g	–	51	40	[48]		
	Zn//K ₃ Fe(CN) ₆	35000	C.C., 1.3 mA/cm ²	2.0 mg _{NaCl} /cm ² /h	–	–	[62]		
	Na _{0.44} MnO ₂ //BiOCl, EDI	760	C.C., 100 mA/g	0.021	~61%	50	[64]		
	Na ₃ V ₂ (PO ₄) ₃ /AC	5850	C.V., 1.0 V	0.07 mg _{NaCl} /g _{NVP} /s	–	–	[65]		
	Zinc air desalination	35100	C.C., 1 mA/cm ²	1.8 mg _{NaCl} /cm ² /h	93	20	[58]	3–5	The design of catalytic electrodes.
	Fuel cell desalination	35100	no power supply	1.8 mg _{NaCl} /cm ² /h	–	–	[12]		

MCDI, membrane capacitive deionization.

^a C.C. and C.V. are the abbreviation of constant current and constant voltage, respectively.

^b It is estimated according to the criteria announced by the European Union [70].

processes) [25]. These challenges can be addressed by optimization of the crystal structure, reducing the particle size to the nanometer range, and hybridizing with conductive materials [25].

Hybrid CDI (Figure 2D) was introduced by Lee et al., in 2014 (Figure 1) [49]. In HCDI, a Faradaic electrode is coupled with a capacitive electrode, and a rapid ion removal rate is achieved. Technically, this was already explored by Blair and Murphy (where activated carbon and a silver electrode were used) [14]. Asymmetric systems require careful adjustment of mass ratio and operating potential widows of the two electrodes to optimize the desalination performance [50].

Standard desalination batteries use dual-ion architectures, with each electrode takes up one charge species. It is also possible to have a pair of the same electrodes with different oxidation and reduction states, which uptake or release the same ion kind at the same time. This cell concept requires an IEM to separate two flow channels. Charge compensation of the electrolyte is accomplished via ion transport across the IEM, yielding an increase of ionic strength in one channel and the mirror-image decrease in ion concentration in the other (Figure 2E). This concept was demonstrated for chloride-ion desalination [44,51], and sodium-ion desalination [52].

Second-generation 2.1: redox electrolytes

Besides solid electrodes, redox electrolytes have also been applied (Figure 2F) [53]. Redox electrolytes benefit from high redox kinetics and better stability compared with solid Faradaic electrodes [54]. Typical values for the desalination capacities are about 70–90 mg_{NaCl}/g_{electrodes} [53–55]. Such systems also allow a continuous operation to desalinate water [56]. Taking the redox couple of ferricyanide/ferrocyanide as the example, during the charging process, the ferrocyanide is oxidized into ferricyanide on the anode's surface and then anions are attracted to balance the charge. On the cathode side, ferricyanide is reduced to ferrocyanide, and sodium immigrates from the feed water to the electrolyte. By cycling the redox electrolyte from the anode side to the cathode side (or by using a second cell), continuous operation can be achieved.

Third-generation: catalytic interface reactions

Recently, the third-generation of electrochemical desalination is budding, introducing catalytic material and redox couples into the multichannel system. In 2019, Chen et al. [57] developed a photo-redox desalination generator using LEG4 dye-modified TiO₂ as the photoanode and a mixture of 2,2,6,6-tetramethyl piperidinyl-oxide (TEMPO) and NaCl as the electrolyte. The system contains two AEMs placed at the anode and cathode and one CEM in the middle of two

water channels (Figure 2G). Under irradiation with visible light, the TEMPO is oxidized into TEMPO⁺, attracting the chloride in the feed water to pass the membrane to the electrolyte. This generator is driven by light energy, which enables water desalination and energy release simultaneously.

Apart from the photocatalytic materials, the electrocatalytic reaction for the redox couple is also applied in water desalination. Srimuk et al. [58] introduced a zinc air desalination cell consisting of a MoS₂ cathode for the oxygen reduction reaction (ORR) and Zn/Zn²⁺ redox couple at the anode, with a feedwater channel in the middle separated by a pair of IEMs (Figure 2H). When the cell is discharged, Na⁺ and Cl⁻ immigrate from the feed water into the anolyte and catholyte with a desalination rate of 0.9–1.0 mg_{NaCl}/cm²_{IEM} (Figure 3). Bhat et al. [11] used Pt/C electrodes to utilize the H₂/H⁺ redox couple as an energy carrier and the neutralization energy of NaOH and HCl as fuels; thereby, the cell removes NaCl to balance the charge of the electrocatalytic H₂/H⁺ reaction under the acidic and alkali environment. The NaCl concentration decreased from 4 M to about 1 M with a low energy consumption of 13.6 kJ/mol_{NaCl} in 22 h. Zhang et al. used a pair of Pt/C electrodes, by applying the electrocatalytic reaction of H₂/H⁺ and O₂/OH⁻, by removing 1 g of NaCl at a desalination rate of 18 g_{NaCl}/m²_{IEM}/h; 67 mWh of electric energy is generated. Meanwhile, NaOH and HCl are produced at the anolyte and catholyte [12].

Perspective

Over three generations of technological development, electrochemical desalination technologies have diversified both in device types and target applications. Apart from commonly required improvement, such as the establishment of more reasonable performance metrics, synthesis of novel IEMs, and so on, the future study of three generations could focus on different aspects, according to different technologies-readiness levels.

Owing to its relatively low ion storage capacity, the first-generation seems not suitable for desalinating the seawater alone. But it is greatly beneficial when combined with other technologies, such as nanofiltration. How to extend it from lab scale to the full scale could be studied. Accompanying issues, such as the setup of commercial benchmarks or the blockage of the electrode by fouling, need to be addressed.

The second-generation benefits from higher capacity and efficiency but suffers from limited redox potential window and stability. A material-characterization-performance database should be established for better exploration of stable, low-cost materials. The study of selective electrodes toward specific ions could also be an

attractive research branch. The third-generation has high-performance desalination potential, but designing robust catalytic interfaces, reducing energy consumption, and improving the desalination rate may be challenging in more demanding water environments.

Declaration of competing interest

The authors declare that they have no known competing financial interests or personal relationships that could have appeared to influence the work reported in this article.

Acknowledgements

The authors acknowledge support from the RAG-Stiftung for the MERLIN project and thank Eduard Arzt (INM) for his continued support. L.W. acknowledges funding from the China Scholarship Council (CSC) via award number 201906260277.

References

Papers of particular interest, published within the period of review, have been highlighted as:

- * of special interest
- ** of outstanding interest

- Water U: *Sustainable Development Goal 6 synthesis report on water and sanitation*. 2018.
 - Cosgrove CE, Cosgrove WJ: *The dynamics of global water futures: driving forces 2011–2050, report on the findings of phase one of the UNESCO-WWAP water scenarios project to 2050*. UNESCO; 2012. 9230010359.
 - Lv H, Wang Y, Wu L, Hu Y: *Numerical simulation and optimization of the flash chamber for multi-stage flash seawater desalination*. *Desalination* 2019, **465**:69–78.
 - Park K, Kim J, Yang DR, Hong S: *Towards a low-energy seawater reverse osmosis desalination plant: a review and theoretical analysis for future directions*. *J Membr Sci* 2020, **595**:117607.
 - Firouzjaei MD, Seyedpour SF, Aktij SA, Giagnorio M, Bazrafshan N, Mollahosseini A, Samadi F, Ahmadalipour S, Firouzjaei FD, Esfahani MR, Tiraferri A, Elliott M, Sangermano M, Abdelrasoul A, McCutcheon JR, Sadrizadeh M, Esfahani AR, Rahimpour A: *Recent advances in functionalized polymer membranes for biofouling control and mitigation in forward osmosis*. *J Membr Sci* 2020, **596**:117604.
 - Al-Amshawee S, Yunus MYBM, Azoddein AAM, Hassell DG, Dakhil IH, Hasan HA: *Electrodialysis desalination for water and wastewater: a review*. *Chem Eng J* 2020, **380**:122231.
 - Qasim M, Badrelzaman M, Darwish NN, Darwish NA, Hilal N: *Reverse osmosis desalination: a state-of-the-art review*. *Desalination* 2019, **459**:59–104.
 - Meerganz von Medeazza GL: *“Direct” and socially-induced environmental impacts of desalination*. *Desalination* 2005, **185**:57–70.
 - Liu T, Serrano J, Elliott J, Yang X, Cathcart W, Wang Z, He Z, Liu G: *Exceptional capacitive deionization rate and capacity by block copolymer-based porous carbon fibers*. *Sci Adv* 2020, **6**: eaaz0906.
 - Zhao W, Ding M, Guo L, Yang HY: *Dual-ion electrochemical deionization system with binder-free aerogel electrodes*. *Small* 2019, **15**:1805505.
 - Bhat ZM, Pandit D, Ardo S, Thimmappa R, Kottaichamy AR, Christudas Dargily N, Devendrachari MC, Ottakam Thotiyil M: *An electrochemical neutralization cell for spontaneous water desalination*. *Joule* 2020, **4**:1730–1742.
- This paper introduced a novel concept of electrochemical desalination based on hydrogen reduction and evolution. In 22 h, NaCl concentration decreases from 4 M to 1 M with a low energy consumption of 13.6 kJ/mol. And as time increases, the concentration of NaCl will continuously go down. This conception opens up an unprecedented pathway for the obtain of drinking water
- Zhang Y, Wang L, Presser V: *Electrocatalytic fuel cell desalination for continuous energy and freshwater generation*. *Cell Rep Phys Sci* 2021.
 - Atlas I, Khalla SA, Suss ME: *Thermodynamic energy efficiency of electrochemical systems performing simultaneous water desalination and electricity generation*. *J Electroch Soc* 2020, **167**:134517.
 - Blair JW, Murphy GW: *Electrochemical demineralization of water with porous electrodes of large surface area*. In *ACS publications*; 1960.
 - Farmer J, Fix D, Mack G: *Capacitive deionization of water: an innovative new process*. CA (United States): Lawrence Livermore National Lab.; 1995.
 - Johnson A, Newman J: *Desalting by means of porous carbon electrodes*. *J Electroch Soc* 1971, **118**:510.
 - Suss ME, Presser V: *Water desalination with energy storage electrode materials*. *Joule* 2018, **2**:10–15.
 - Zhang Y, Srimuk P, Aslan M, Gallei M, Presser V: *Polymer ion-exchange membranes for capacitive deionization of aqueous media with low and high salt concentration*. *Desalination* 2020, **479**:114331.
 - Bi S, Zhang Y, Cervini L, Mo T, Griffin JM, Presser V, Feng G: *Permselective ion electrosorption of subnanometer pores at high molar strength enables capacitive deionization of saline water*. *Sust Ener Fuels* 2020, **4**:1285–1295.
 - This paper demonstrates the carbon electrode, without any modification, could also work in high salinity water when the pores are less than 1 nm. This provides a new avenue about how to use the carbon electrode in high salinity water.
 - Jäckel N, Simon P, Gogotsi Y, Presser V: *The increase in capacitance by subnanometer pores in carbon*. *ACS Energy Lett* 2016, **1**:1262–1265.
 - Lu D, Cai W, Wang Y: *Optimization of the voltage window for long-term capacitive deionization stability*. *Desalination* 2017, **424**:53–61.
 - Zhang C, He D, Ma J, Tang W, Waite TD: *Faradaic reactions in capacitive deionization (CDI) - problems and possibilities: a review*. *Water Res* 2018, **128**:314–330.
 - Gao X, Omosebi A, Landon J, Liu K: *Surface charge enhanced carbon electrodes for stable and efficient capacitive deionization using inverted adsorption–desorption behavior*. *Energy Environ Sci* 2015, **8**:897–909.
 - Tu Y-H, Liu C-F, Wang J-A, Hu C-C: *Construction of an inverted-capacitive deionization system utilizing pseudocapacitive materials*. *Electrochim Commun* 2019, **104**:106486.
 - Srimuk P, Su X, Yoon J, Aurbach D, Presser V: *Charge-transfer materials for electrochemical water desalination, ion separation and the recovery of elements*. *Nat Rev Mat* 2020, **5**:517–538.
 - Liu J, Wang J, Xu C, Jiang H, Li C, Zhang L, Lin J, Shen ZX: *Advanced energy storage devices: basic principles, analytical methods, and rational materials design*. *Adv Sci* 2018, **5**:1700322.
 - Lee J-B, Park K-K, Eum H-M, Lee C-W: *Desalination of a thermal power plant wastewater by membrane capacitive deionization*. *Desalination* 2006, **196**:125–134.
 - Kim N, Lee J, Kim S, Hong SP, Lee C, Yoon J, Kim C: *Short review of multichannel membrane capacitive deionization: principle, current status, and future prospect*. *Appl Sci* 2020, **10**:683.
 - Hassanvand A, Chen GQ, Webley PA, Kentish SE: *A comparison of multicomponent electrosorption in capacitive deionization and membrane capacitive deionization*. *Water Res* 2018, **131**:100–109.

30. Liu D, Ning X-a, Hong Y, Li Y, Bian Q, Zhang J: **Covalent triazine-based frameworks as electrodes for high-performance membrane capacitive deionization.** *Electrochim Acta* 2019, **296**:327–334.
31. Shi P, Wang C, Sun J, Lin P, Xu X, Yang T: **Thermal conversion of polypyrrole nanotubes to nitrogen-doped carbon nanotubes for efficient water desalination using membrane capacitive deionization.** *Separ Purif Technol* 2020, **235**: 116196.
This paper synthesized the hybrid of polyaniline and Prussian blue. This material exhibits excellent stability (with no fading during 250 cycles) and a high salt removal rate. Density functional theory (DFT) calculations were further conducted to investigate the interaction between polyaniline and Prussian blue, contributing to this material's good rate performance.
32. Tang K, Kim Y-h, Chang J, Mayes RT, Gabbitto J, Yiakoumi S, Tsouris C: **Seawater desalination by over-potential membrane capacitive deionization: opportunities and hurdles.** *Chem Eng J* 2019, **357**:103–111.
33. Kim C, Srimuk P, Lee J, Presser V: **Enhanced desalination via cell voltage extension of membrane capacitive deionization using an aqueous/organic bi-electrolyte.** *Desalination* 2018, **443**:56–61.
34. Jeon S-i, Park H-r, Yeo J-g, Yang S, Cho CH, Han MH, Kim DK: **Desalination via a new membrane capacitive deionization process utilizing flow-electrodes.** *Energy Environ Sci* 2013, **6**: 1471–1475.
35. Kastening B, Faul W: **Herstellung von Wasserstoffperoxid durch kathodische Reduktion von Sauerstoff.** *Chem Ing Tech* 1977, **49**. 911–911.
36. Rommerskirchen A, Linnartz CJ, Egidi F, Kendir S, Wessling M: **Flow-electrode capacitive deionization enables continuous and energy-efficient brine concentration.** *Desalination* 2020, **490**:114453.
37. Pasta M, Wessells CD, Cui Y, La Mantia F: **A desalination battery.** *Nano Lett* 2012, **12**:839–843.
38. Metzger M, Besli MM, Kuppan S, Hellstrom S, Kim S, Sebiti E, Subban CV, Christensen J: **Techno-economic analysis of capacitive and intercalative water deionization.** *Energy Environ Sci* 2020, **13**:1544–1560.
This work conducted a techno-economic analysis of electrochemical desalination technology. It compares the cost, volume, and energy consumption of membrane capacitive deionization, hybrid capacitive deionization, and sodium intercalation desalination by establishing the module. The results show that sodium intercalation desalination technology only needs 27% costs and 20% device volume of membrane capacitive with a similar desalination performance. This work points out the potential direction in the industrial application of electrochemical desalination technology.
39. Zhao Y, Liang B, Zong M, Duan M, Li K, Lv C: **Different crystallographic sodium manganese oxides for capacitive deionization: performance comparison and the associated mechanism.** *Environ Sci: Nano* 2019, **6**:3091–3101.
This work reveals the relation between the crystal structure of sodium manganese oxides (NMO) and its electrochemical capacity and desalination performance. It shows the layered NMO has a better behavior than the tunnel NMO and the P2-group layered NMO is better than O3-group layered NMO. According to the postmortem XPS measurement, the different performance between these three materials is due to the different levels of Mn⁴⁺/Mn³⁺ species.
40. Han C, Meng Q, Cao B, Tian G: **Enhanced hybrid capacitive deionization performance by sodium titanium phosphate/reduced porous graphene oxide composites.** *ACS Omega* 2019, **4**:11455–11463.
41. Shi W, Liu X, Deng T, Huang S, Ding M, Miao X, Zhu C, Zhu Y, Liu W, Wu F, Gao C, Yang S-W, Yang HY, Shen J, Cao X: **Enabling superior sodium capture for efficient water desalination by a tubular polyaniline decorated with prussian blue nanocrystals.** *Adv Mater* 2020, **32**:1907404.
42. Chen B, Feng A, Deng R, Liu K, Yu Y, Song L: **MXene as a cation-selective cathode material for asymmetric capacitive deionization.** *ACS Appl Mater Interfaces* 2020, **12**: 13750–13758.
43. Karthikeyan P, Elanchezhiyan SS, Preethi J, Talukdar K, Meenakshi S, Park CM: **Two-dimensional (2D) Ti3C2Tx MXene nanosheets with superior adsorption behavior for phosphate and nitrate ions from the aqueous environment.** *Ceram Int* 2021, **47**:732–739.
44. Srimuk P, Husmann S, Presser V: **Low voltage operation of a silver/silver chloride battery with high desalination capacity in seawater.** *RSC Adv* 2019, **9**:14849–14858.
45. Chang J, Duan F, Su C, Li Y, Cao H: **Removal of chloride ions using a bismuth electrode in capacitive deionization (CDI).** *Environ Sci: Water Research & Technology* 2020, **6**: 373–382.
46. Liu Y, Gao X, Wang Z, Wang K, Dou X, Zhu H, Yuan X, Pan L: **Controlled synthesis of bismuth oxychloride-carbon nano-fiber hybrid materials as highly efficient electrodes for rocking-chair capacitive deionization.** *Chem Eng J* 2021, **403**: 126326.
47. Kim N, Park J-S, Harzandi AM, Kishor K, Ligaray M, Cho KH, Kim Y: **Compartmentalized desalination and salination by high energy density desalination seawater battery.** *Desalination* 2020, **495**:114666.
48. Arnold S, Wang L, Budak Ö, Aslan M, Srimuk P, Presser V: *** Antimony alloying electrode for high-performance sodium removal: how to use a battery material not stable in aqueous media for saline water remediation.** *J Mater Chem* 2021, **9**: 585–596.
This paper introduced an alloying material, previously considered not suitable for aqueous electrolyte, for desalination batteries. Attributed to the high capacity of antimony, the hybrid desalination cell provides a high desalination capacity of 294 mg_{Na} g_{SB}⁻¹ (748 mg_{NaCl} g_{SB}⁻¹). The convergence of battery desalination and seawater batteries is a synergistic and dynamic research domain.
49. Lee J, Kim S, Kim C, Yoon J: **Hybrid capacitive deionization to enhance the desalination performance of capacitive techniques.** *Energy Environ Sci* 2014, **7**:3683–3689.
50. Torkamanzadeh M, Wang L, Zhang Y, Budak Ö, Srimuk P, Presser V: **MXene/activated carbon hybrid capacitive deionization for permselective ion removal at low and high salinity.** *ACS Appl Mater Interfaces* 2020, **12**: 26013–26025.
51. Grygolowicz-Pawlak E, Sohail M, Pawlak M, Neel B, Shvarev A, de Marco R, Bakker E: **Coulometric sodium chloride removal system with nafion membrane for seawater sample treatment.** *Anal Chem* 2012, **84**:6158–6165.
52. Smith KC, Dmello R: **Na-ion desalination (NID) enabled by Na-blocking membranes and symmetric Na-intercalation: porous-electrode modeling.** *J Electrochem Soc* 2016, **163**: A530.
53. Kim N, Hong SP, Lee J, Kim C, Yoon J: **High-desalination performance via redox couple reaction in the multichannel capacitive deionization system.** *ACS Sustainable Chem Eng* 2019, **7**:16182–16189.
54. Lee J, Srimuk P, Carpier S, Choi J, Zornitta RL, Kim C, Aslan M, Presser V: **Confined redox reactions of iodide in carbon nanopores for fast and energy-efficient desalination of brackish water and seawater.** *ChemSusChem* 2018, **11**: 3460–3472.
55. Lee J, Srimuk P, Zornitta RL, Aslan M, Mehdi BL, Presser V: **High electrochemical seawater desalination performance enabled by an iodide redox electrolyte paired with a sodium superionic conductor.** *ACS Sustainable Chem Eng* 2019, **7**: 10132–10142.
56. Ramalingam K, Liang M, Pyae NLW, Aung SH, Oo TZ, Srimuk P, Ma J, Presser V, Chen F, Waite TD: **Self-sustained visible-light-driven electrochemical redox desalination.** *ACS Appl Mater Interfaces* 2020, **12**:32788–32796.
57. Chen F, Karthick R, Zhang Q, Wang J, Liang M, Dai J, Jiang X, Jiang Y: *** Exploration of a photo-redox desalination generator.** *J Mater Chem* 2019, **7**:20169–20175.
This work introduced a new architecture of electrochemical desalination, a photo-redox catalysis desalination generator. This cell utilizes the electrolyte's redox reaction driven by the photo-excited

semiconductor and removes the salt by electrostatic force. The utilization of solar energy effectively reduced the energy consumption and cost of electrochemical desalination.

58. Srimuk P, Wang L, Budak Ö, Presser V: **High-performance ion removal via zinc-air desalination.** *Electrochim Commun* 2020, **115**:106713.
59. Qu Y, Campbell PG, Gu L, Knipe JM, Dzenitis E, Santiago JG, Stadermann M: **Energy consumption analysis of constant voltage and constant current operations in capacitive deionization.** *Desalination* 2016, **400**:18–24.
60. Chen Y-J, Liu C-F, Hsu C-C, Hu C-C: **An integrated strategy for improving the desalination performances of activated carbon-based capacitive deionization systems.** *Electrochim Acta* 2019, **302**:277–285.
61. Gao X, Omosebi A, Landon J, Liu K: **Enhanced salt removal in an inverted capacitive deionization cell using amine modified microporous carbon cathodes.** *Environ Sci Technol* 2015, **49**: 10920–10926.
62. Desai D, Beh ES, Sahu S, Vedharathinam V, van Overmeere Q, de Lannoy CF, Jose AP, Völkel AR, Rivest JB: **Electrochemical desalination of seawater and hypersaline brines with coupled electricity storage.** *ACS Energy Lett* 2018, **3**: 375–379.
63. Lee J, Kim S, Yoon J: **Rocking chair desalination battery based on prussian blue electrodes.** *ACS Omega* 2017, **2**:1653–1659.
64. Chen F, Huang Y, Guo L, Sun L, Wang Y, Yang HY: **Dual-ions electrochemical deionization: a desalination generator.** *Energy Environ Sci* 2017, **10**:2081–2089.
65. Cao J, Wang Y, Wang L, Yu F, Ma J: **$\text{Na}_3\text{V}_2(\text{PO}_4)_3 @ \text{C}$ as faradaic electrodes in capacitive deionization for high-performance desalination.** *Nano Lett* 2019, **19**:823–828.
66. Wei X, Zhao Y, Liang B, Mo X, Li K: **Core-shell nanoparticles of Prussian blue analogues as efficient capacitive deionization electrodes for brackish water desalination.** *Separ Purif Technol* 2020;117899.
67. Srimuk P, Lee J, Tolosa A, Kim C, Aslan M, Presser V: **Titanium disulfide: a promising low-dimensional electrode material for sodium ion intercalation for seawater desalination.** *Chem Mater* 2017, **29**:9964–9973.
68. Krüner B, Srimuk P, Fleischmann S, Zeiger M, Schreiber A, Aslan M, Quade A, Presser V: **Hydrogen-treated, sub-micrometer carbon beads for fast capacitive deionization with high performance stability.** *Carbon* 2017, **117**:46–54.
69. Dai J, Win Pyae NL, Chen F, Liang M, Wang S, Ramalingam K, Zhai S, Su CY, Shi Y, Tan SC, Zhang L, Chen Y: **Zinc-air battery-based desalination device.** *ACS Appl Mater Interfaces* 2020, **12**: 25728–25735.
70. **Technology readiness levels (TRL); extract from Part 19 - commission decision C. 4995..** In *European commission*, 2014; 2014.

4.10 Emerging, hydrogen-driven electrochemical water purification

Matthew E Suss^{1,2,3,*}, Yuan Zhang^{4,5}, Imri Atlas⁶, Youri Gendel^{7,*}, Erez B. Ruck⁷, Volker Presser^{4,5,8,*}

- 1 Faculty of Mechanical Engineering, Technion – Israel Institute of Technology, Haifa, Israel.
- 2 Wolfson Department of Chemical Engineering, Technion – Israel Institute of Technology, Haifa, Israel.
- 3 Grand Technion Energy Program, Technion – Israel Institute of Technology, Haifa, Israel.
- 4 INM – Leibniz Institute for New Materials, Campus D22, 66123 Saarbrücken, Germany.
- 5 Department of Materials Science and Engineering, Saarland University, Campus D22, 66123 Saarbrücken, Germany.
- 6 Russell Berrie Nanotechnology Institute, Technion – Israel Institute of Technology, Haifa, Israel.
- 7 Faculty of Civil and Environmental Engineering, Technion – Israel Institute of Technology, Haifa, Israel.
- 8 Saarene, Saarland Center for Energy Materials and Sustainability, Campus D42, 66123 Saarbrücken, Germany.

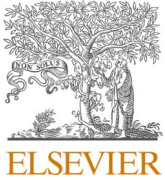
Citation:

Suss, M. Zhang, Y. Atlas, I. Gendel, Y. Ruck, E. B. Presser, V, "Emerging, hydrogen-driven electrochemical water purification." Electrochemistry Communications, 2022, 107211. (DOI: 10.1016/j.elecom.2022.107211)

Own contribution:

Validation, data curation, writing-review & editing, visualization.





Emerging, hydrogen-driven electrochemical water purification

M.E. Suss^{a,b,c,*}, Y. Zhang^{d,e}, I. Atlas^f, Y. Gendel^{g,*}, E.B. Ruck^g, V. Presser^{d,e,h,*}

^a Faculty of Mechanical Engineering, Technion – Israel Institute of Technology, Haifa, Israel

^b Wolfson Department of Chemical Engineering, Technion – Israel Institute of Technology, Haifa, Israel

^c Grand Technion Energy Program, Technion – Israel Institute of Technology, Haifa, Israel

^d INM – Leibniz Institute for New Materials, Campus D22, 66123 Saarbrücken, Germany

^e Department of Materials Science and Engineering, Saarland University, Campus D22, 66123 Saarbrücken, Germany

^f Russell Berrie Nanotechnology Institute, Technion – Israel Institute of Technology, Haifa, Israel

^g Faculty of Civil and Environmental Engineering, Technion – Israel Institute of Technology, Haifa, Israel

^h Saarene, Saarland Center for Energy Materials and Sustainability, Campus D42, 66123 Saarbrücken, Germany

ARTICLE INFO

Keywords:

Desalination
Electrochemistry
Water remediation
Hydrogen
Fuel cell

ABSTRACT

Energy-efficient technologies for the remediation of water and generation of drinking water is a key towards sustainable technologies. Electrochemical desalination technologies are promising alternatives towards established methods, such as reverse osmosis or nanofiltration. In the last few years, hydrogen-driven electrochemical water purification has emerged. This review article explores the concept of desalination fuel cells and capacitive-Faradaic fuel cells for ion separation.

1. Introduction

1.1. State-of-the-art in water purification

While 71% of the earth is covered by water, freshwater occupies only 2.5% of the total water and is mostly stored as glaciers, ice caps, and groundwater [1]. With the rapid economic growth and urbanization, access to clean water for all human beings has become inadequate [2]. On average, 10% of the global population lives in countries with high or critical water stress [3]. Under this circumstance, an array of measures must be taken to mitigate clean water scarcity. One active method of securing clean water supplies is seawater and brackish water desalination. Conventional desalination technologies can be classified into thermal energy-driven, mechanical energy-driven, and electrical energy-driven [4].

As the earliest water desalination method, water evaporation and condensation are applied in thermal energy-driven technologies such as multi-stage flash distillation (MSF) and multi-effect distillation (MED) [5]. By using multiple steps, water from brines is evaporated and condensed to freshwater. Mechanical energy-driven desalination technologies, such as reverse osmosis (RO), are based on semipermeable membranes, which enable water molecules to be transported through

while rejecting salt ions. By applying pressure to the feedwater above its osmotic pressure, freshwater can be extracted from seawater [6]. Typically, the energy efficiency of RO is higher than the thermal-energy-driven technologies for seawater desalination [7]. As for electrical energy-driven desalination technologies, the major types include electrodialysis (ED) [8,9], a mature technology explored for the past six decades, and the emerging technology of capacitive deionization (CDI) [10] and desalination batteries [11,12]. The latter two immobilize salt ions into capacitive or Faradaic electrode materials [11]. Such systems are highly promising towards ion selective separations and brackish water desalination, but require a cyclic, two-stage charge-discharge process, during which energy is alternately stored and released by electrodes [13].

In recent years, a chemical-driven class of desalination technologies has emerged. Such cells are often distinct because of the form of the input energy and because they can co-generate electricity and clean water [14]. Hydrogen can be used as one of the necessary chemical reactants to drive such processes. Particularly attractive is green hydrogen, which leverages renewable energies such as solar, wind, and hydropower energies. Hydrogen gas is a well-known reducing agent in water treatment processes, for example, in dehalogenation of organic compounds [15], phenol reduction into less toxic cyclohexane [16],

* Corresponding authors at: Faculty of Mechanical Engineering, Technion – Israel Institute of Technology, Haifa, Israel (M.E. Suss). INM – Leibniz Institute for New Materials, Campus D22, 66123 Saarbrücken, Germany (V. Presser).

E-mail addresses: mesuss@me.technion.ac.il (M.E. Suss), ygndel@technion.ac.il (Y. Gendel), volker.presser@leibniz-inm.de (V. Presser).

catalytic hydrogenation to convert nitrite and nitrate into N_2 and ammonia [17,18], and catalytic reduction of ClO_4^- and BrO_3^- by H_2 gas into Cl^- and Br^- , respectively [19,20]. Hydrogen may also be used indirectly for ion separations. For example, Al-Hallaj et al. proposed a fuel cell desalination system that uses the electricity and exhaust heat from the fuel cells to power RO or MSF units [21].

While hydrogen has had a role in water treatment as a reducing agent or indirectly driving separations, it was only recently that hydrogen had been explored towards directly driving separations using a single electrochemical cell. Two types of such cells have emerged in the past three years, including desalination fuel cells (DFCs) and capacitive-Faradaic fuel cells (CFFCs; Fig. 1). This very recent technological advancement

has resulted in a fast-growing number of publications. We here will review and discuss the emerging field of direct hydrogen-driven electrochemical water purification.

1.2. Desalination fuel cells for simultaneous production of clean water and electricity

The DFC has its roots in ED, where a typical ED cell contains a pair of membranes, one anion exchange, and the other cation, and is driven by a voltage or current applied to a pair of electrodes sandwiching the cell [8,30]. Several classical ED cells and stacks have been explored in recent years, including shock ED [31], bipolar ED [32], and multi-stage ED

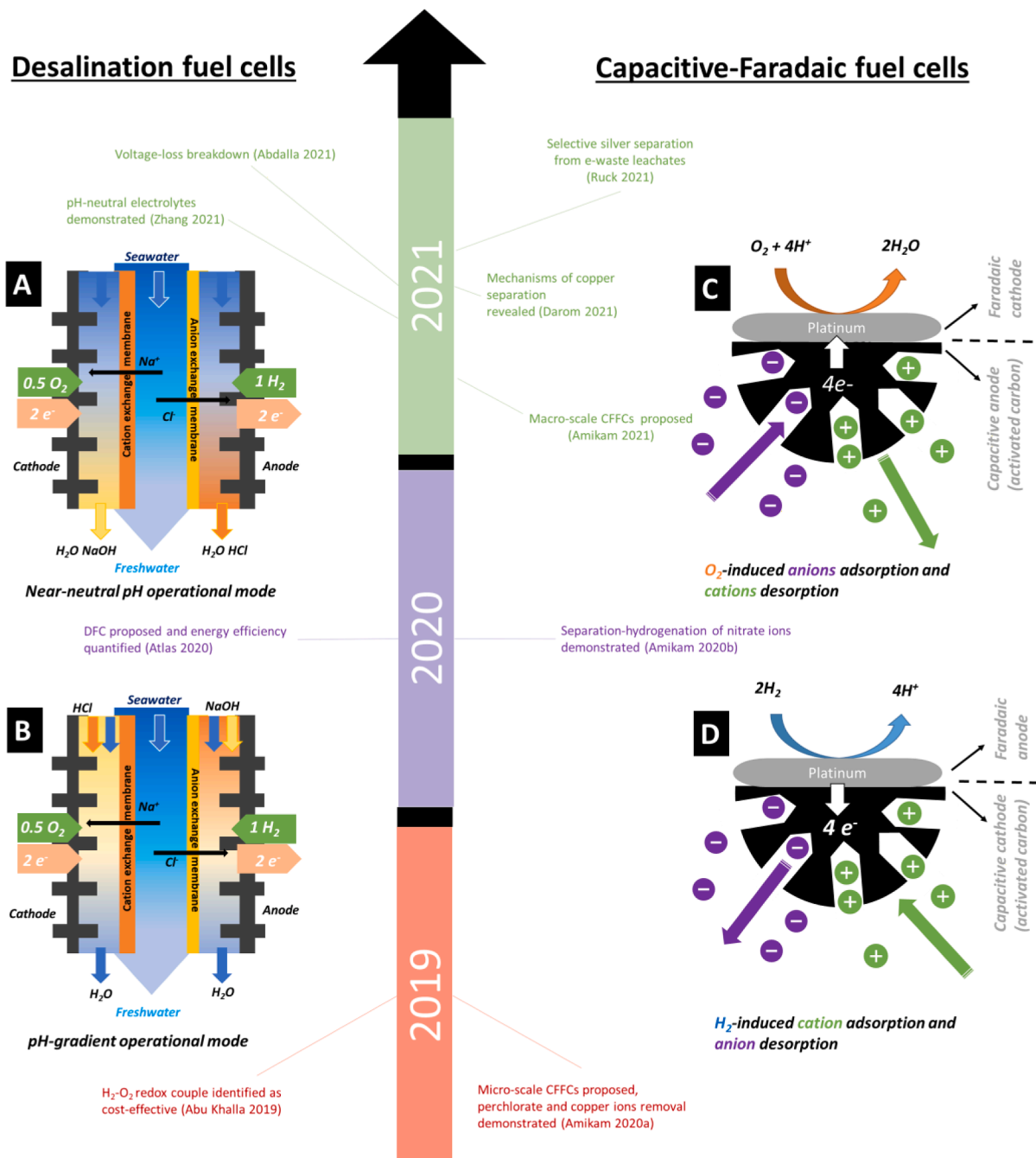


Fig. 1. Timeline on the development of hydrogen-driven water purification technologies, including the desalination fuel cell (DFC) [14,22–24] and capacitive-Faradaic fuel cells (CFFC) [25–29]. Also provided are schematics showing the operational modes of a-b) the DFC, and c-d) the CFFC. List of references: Abdalla 2021: [23]; Abu Khalla 2019: [24]; Amikam 2020a: [25]; Amikam 2020b: [28]; Amikam 2021: [26]; Atlas 2020: [14]; Darom 2021: [27]; Ruck 2021: [29]; Zhang 2021: [22].

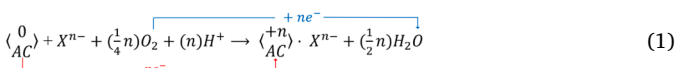
[33]. Another variation is the use of chemical energy rather than electrical energy to drive the separation [24,34]. This technique is unique because it allows the cell to drive separation and generate net electricity simultaneously [35]. In contrast to microbial desalination cells [36], these ED systems are driven by inorganic redox couples but do not employ microbes as microorganisms can limit electricity production and salt removal rates. ED cells driven by chemical energy perform a combined reaction-separation process that is thermodynamically spontaneous [14]. Atlas et al. calculated the maximum available energy from this combined process and quantified the thermodynamic efficiency of cells driven by chemical energy, finding that for specific chemistries, up to 25 kWh of net electricity per m³ of treated seawater can be produced [14]. This technology can thus generate significant excess electricity, well above what is needed for pre-treatment and post-treatment of the feed, which is approximately 1 kWh/m³ [6].

One feature of chemical energy-driven ED is many possible redox couples which can be used to drive the process, each with potential benefits and drawbacks. Thus far, this concept has been tested with a small subset of possible chemistries, including zinc-bromine [24], zinc-air [37,38], aluminum-air [35], hydrogen-oxygen [14,22], and acid-base couples [39]. Among these, the hydrogen-oxygen couple is particularly promising, as it relies on relatively inexpensive gas-phase reactants, and the likely product of the chemical reaction is simply water. Cells that use the hydrogen-oxygen chemistry are termed “desalination fuel cells”, depicted in Fig. 1A-B [14]. Other cell chemistries that rely on liquid-solvated reactants or that produce a waste product can complicate brine disposal. The use of hydrogen can also lead to an important and growing role for water treatment in the hydrogen economy. The main drawback of using the hydrogen-oxygen redox couple is the need to often-expensive metal-based catalysts for the oxygen reduction and hydrogen oxidation reactions.

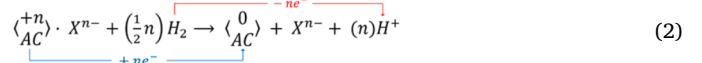
1.3. Capacitive-Faradaic fuel cells for ion separation

The electrolytic water treatment reactors such as electrocoagulation, electrodialysis, and electrooxidation can be classified as Faradaic cells because they contain anodes and cathodes where oxidation and reduction (i.e., Faradaic processes) take place. The galvanic desalinating Faradaic cells are powered by oxidants (i.e., oxygen) and fuels (e.g., hydrogen) which are reacted on cathode and anode, respectively [22,34]. In capacitive cells, the electrical current is mostly non-Faradaic; that is, both the anode and cathode act as capacitors charged within an application of an external voltage source, which results in electrosorption of ions and capacitive deionization (CDI) of water [40,41]. The capacitive-Faradaic cells contain both the Faradaic and the capacitive electrodes; that is, during the operation, the oxidation or the reduction processes proceed on one electrode, and the electrosorption takes place on the counter electrode. Capacitive-Faradaic cells that separate ionic pollutants or valuable ions from water and wastewater can be electrolytic or galvanic [42,43]. Amikam et al. have recently proposed capacitive-Faradaic cells powered by hydrogen and oxygen gases [25].

Micro-scale capacitive-Faradaic fuel cells (CFFCs) comprise activated carbon (AC) particles loaded with nanoscale platinum catalyst crystals. Upon immersion of CFFCs into an aerated aqueous solution, the oxygen reduction reaction (ORR) on the platinum catalyst (the Faradaic electrode) consumes the electrons from the AC (the capacitive electrode) that results in adsorption of anions into the electrical double-layer of electron-deficient AC to maintain its electroneutrality, as described by Eq. (1) ($\langle \overset{0}{AC} \rangle$ – uncharged activated carbon; $\langle \overset{+n}{AC} \rangle \cdot X^{n-}$ – activated carbon that lost n electrons within the electrosorption of X^{n-} anion) [25].



The electrosorption of anions proceeds until the complete saturation of the electrical double-layer in the CFFC. The saturated cells must be regenerated, and the anions released into the concentrate solution. The regeneration of the CFFCs is accomplished via the hydrogen oxidation reaction (HOR) on Pt that results in the accumulation of electrons in the activated carbon and a release of anions into a brine solution (Eq. (2)).



Overall, the anions in the treated solution are “replaced” with electrogenerated hydroxyl ions (OH⁻). The principle of ions separation by capacitive-Faradaic cells is shown in Fig. 1C-D.

The separation of cations can be achieved if ORR follows HOR. In this case, the removed cations are compensated in solution by the anodically produced hydronium ions (H₃O⁺) [25]. The undivided electrodes of the CFFCs establish different potentials in hydrogenated or aerated aqueous solutions, and this cell potential drives electrosorption, HOR, and ORR. Thus, at pH=7, the CFFC's open-cell potentials in aerated and hydrogenated NaCl solution approaches 200 mV and 760 mV, respectively [26]. The separation of ions by CFFCs is powered by the chemical energy of hydrogen and oxygen gases. However, the micro-scale CFFCs originally proposed by Amikam et al. [25] do not generate an electrical current that can be used for powering an external load. In this respect, the micro-scale CFFCs are different from the classical fuel cells and the macro-scale divided CFFCs which can produce electricity [26].

2. Thermodynamics underpinning desalination fuel cells

The DFC is distinct from other desalination technologies, as it does not perform solely a separation process, but a combined chemical reaction and separation process. To evaluate the thermodynamics energy efficiency (TEE) of a desalination fuel cell (DFC), we cannot use the same methods used for MSF, RO, ED, and CDI, where TEE is defined as the energy required in practice divided by the minimum energy of the reversible separation process. For a DFC, TEE is the ratio of experimentally extracted electricity per desalinated water volume, w_e , to maximum available energy per desalinated water volume, w , giving TEE $\equiv w_e/w$ [14]. The parameter w can be decomposed to $w = w_{chem} + w_s$, where w_{chem} and w_s are chemical and the separation work per desalinated water volume. We define w_{chem} as the change in Gibbs free energy per desalinated water volume of H⁺ and OH⁻ between the initial and complete reactant consumption states (Eq. (3)) [14]:

$$w_{chem} = \Delta c \left[F(E_c^0 - E_a^0) + 2RT \ln \left(\frac{c_{B|A}}{c^0} \right) \right] \quad (3)$$

E_c^0 is the standard potential of the cathode half-reaction, E_a^0 of the anode half-reaction, F Faraday's constant, Δc is the change in concentration of the feedwater over the process, R the ideal gas constant, T the absolute temperature, and c^0 is the concentration at standard state, which is 1 M. Further, $c_{B|A}$ is the initial concentration of acid/base in the catholyte/anolyte, respectively. We invoke assumptions such as neglecting the crossover of reactants or products and assuming ideally selective membranes. Complete reactant consumption is attained at the maximal water recovery $\phi_{max} = (2\Delta c/c_{B|A} + 1)^{-1}$, here the complete utilization of H⁺ and OH⁻ in catholyte and anolyte, respectively.

Similarly, we define w_s as the change in Gibbs free energy per volume of desalinated water of both Na⁺ and Cl⁻ between the initial and final states. For complete consumption of the reactants, we obtain w_s via Eq. (4):

$$w_s = 2RT \left[c_{NaCl}^F \ln \left(\frac{c_{NaCl}^F}{c^0} \right) - (c_{NaCl}^F - \Delta c) \ln \left(\frac{c_{NaCl}^F - \Delta c}{c^0} \right) \right] + \frac{2\Delta c RT}{c_{B|A}} \left[(c_{NaCl}^F + c_{B|A}) \ln \left(\frac{c_{NaCl}^F + c_{B|A}}{c^0} \right) - (c_{NaCl}^F + 2c_{B|A}) \ln \left(\frac{c_{NaCl}^F + 2c_{B|A}}{c^0} \right) \right] \quad (4)$$

Here, c_{NaCl}^F is the initial salt concentration of the feedwater.

In Fig. 2, we show calculations of w , for a DFC, as a function of the acidity (basicity) of the catholyte (anolyte). As can be seen, more energy is available per m^3 of treated water for increasing pH gradient between the anode and cathode (Fig. 1B), as expected since this increases the available neutralization energy. For example, for a cell operating with neutral pH anolyte and catholyte (Fig. 1A), the available energy remains below 20 kWh/ m^3 . In contrast, for a cell with an anolyte of pH 0 and a catholyte of pH 14, the available energy is well over 30 kWh/ m^3 . As shown by Abdalla et al., [23] the voltage losses in near-neutral pH operating mode are much more severe, especially at low currents, making it more difficult to extract near-to-the maximum available energy level for that operating mode. The pH gradient mode, by contrast, limits voltage losses and allows for extracting electrical energy closer to the maximum available energy.

3. Electrode materials and performance

3.1. Desalination fuel cell performance

The DFC concept is in its infancy, with only a handful of experimental reports thus far. In 2019, Khalla et al. performed a preliminary techno-economic analysis of chemical-driven ED cells, finding that hydrogen-oxygen redox couple was highly promising due to its reliance on low-cost reactants [24]. In 2020, Atlas et al. built and characterized a DFC with a cell containing three flows, an anolyte pumped between the anode and anion exchange membrane, a catholyte between a cathode and cation exchange membrane, and a feedwater channel between the two membranes [14]. Their cell utilized an acidic catholyte and alkaline anolyte to boost open-circuit voltage (and so electricity production), termed pH gradient operational mode [14]. They found that the cell had an open circuit voltage of about 1.7 V, and desalinated a 0.5 M NaCl stream at a current efficiency of circa 80% [14]. The electrical production was quantified via TEE, where TEE of the DFC reached up to 68% at

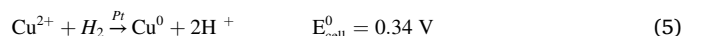
low current densities of about 1 mA/cm², and efficiency dropped as extracted current density was increased [14]. This efficiency was lower than that achieved for other chemistries, such as zinc-bromine chemistry. In 2021, Zhang et al. demonstrated a DFC which operated without acid and base in the anolyte and catholyte, respectively, which is termed the “near-neutral pH” operational mode [22]. They reported relatively low cell voltages of < 0.7 V, which limited electricity production to 67 mWh per 1 g NaCl removed while desalinating a 0.6 M NaCl feed [22].

Possible reasons for the low energy efficiencies and energy production of the cells of Atlas et al. [14] and Zhang et al. [22] was determined by Abdalla et al., [23] who performed a voltage loss breakdown in a DFC operating both in near-neutral and pH gradient operational modes. They incorporated quasi-reference Ag/AgCl electrodes into each of the three channels of a DFC prototype, allowing independent measurement of electrode voltages and voltage drops across membranes [23]. Major Nernstian losses occurred at the cathode in both operational models [23]. The reason proposed for these losses was the poisoning of the platinum cathode catalyst by chloride ions, which shifted the oxygen reduction reaction to the less-energetic two-electron pathway, which produces hydrogen peroxide. As shown in a recent work by Abu Khalla et al., when adjusting the TEE calculation to account for solely two-electron oxygen reduction, and operating in pH gradient mode, TEE was reported to be up to 95.6% [44]. Significant activation losses were seen in the near-neutral pH operational mode, both at the anode and cathode, which at the cathode was determined to be largely due to low H⁺ concentration rather than Pt poisoning [44]. The latter work served to highlight the importance of catholyte composition and cathode catalyst material in DFC performance, and provides several pathways for improvement for future DFC designs.

3.2. Capacitive-Faradaic fuel cell performance

First, the H₂-powered capacitive-Faradaic separation of ions was proven for ClO₄⁻ removal [25]. Aeration of 480 mL NaClO₄ solution ([ClO₄⁻]₀ = 212 mg/L) on 12 g of 5 mass%-loaded Pt CFFCs (further termed 5.0%Pt-CFFCs) resulted in circa 80% of ClO₄⁻ ions removal. The salt adsorption capacity (SAC) of the microscale CFFCs was 0.06 meq/g (equivalent to 3.5 mg_{NaCl}/g), which is significantly lower than the SAC values reported for regular CDI (3.7–13.0 mg_{NaCl}/g) [25]. Fig. 3A shows the results of ClO₄⁻ ions removal from pure NaClO₄ solutions using the CFFC that comprised 5.0% and 0.1% of Pt catalyst on a granular activated carbon. As it appears in Fig. 3A, a 50-fold decrease in the platinum loading did not result in any significant performance decrease of the CFFCs for ClO₄⁻ removal. This finding shows that effective CFFCs with a low Pt load and a competitive cost can be developed for environmental applications.

In the original study of Amikam et al., [25]. The separation of copper by the CFFCs was demonstrated, and Cu²⁺ ions separation was initially attributed to the capacitive-Faradaic mechanism explained above [25]. Darom et al. showed that separation of copper ions by the Pt-loaded carbon is governed not by the electrosorption but rather by the Pt-catalyzed reduction of Cu²⁺ (Eq. (5)) and oxidation of elemental Cu particles into Cu²⁺ (Eq. (6)) in H₂-induced and O₂-induced steps of the process, respectively [27]. Fig. 3B shows the Cu crystals formed within the hydrogenation of pure CuCl₂ solution on the CFFCs.



Recently Ruck et al. [29] reported on the selective recovery of silver ions using the Pt-catalyzed hydrogenation-oxygenation process proposed by Darom et al. [27].

The CFFCs were also shown effective for the separation of nitrate ions [28]. Moreover, the CFFCs with bimetallic 5%Pt-1%Cu catalyst resulted in a complete reduction of nitrate ions into the N₂ (selectivity of

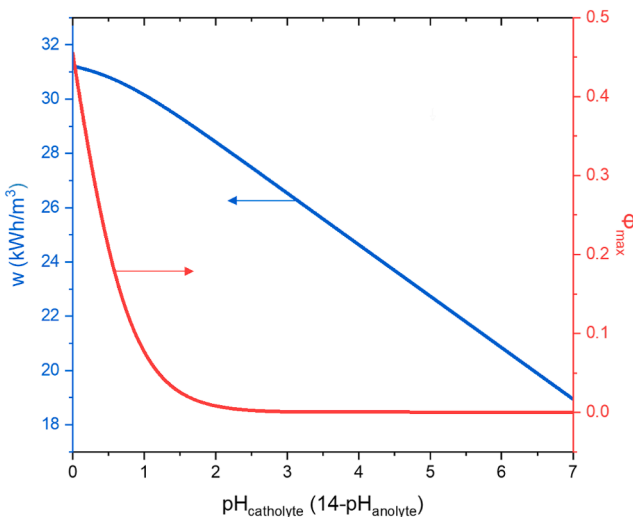


Fig. 2. Calculated maximum available energy from a desalination fuel cell, w , versus the pH of the anolyte and catholyte streams. Also plotted is the maximum water recovery, ϕ_{max} .

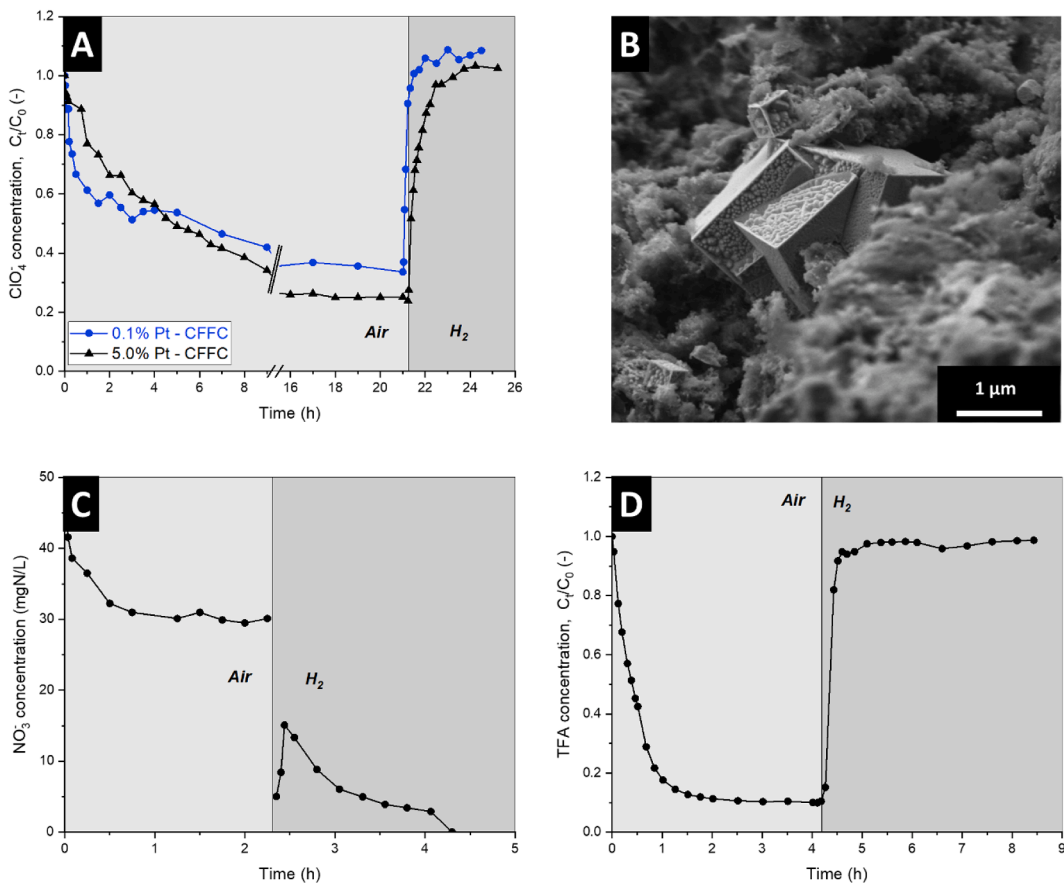


Fig. 3. Results of oxygenation-hydrogenation of perchlorate, copper, nitrate and trifluoracetic acid (TFA) solutions in a batch mode system operated with 7.5 g of CFFCs of granular activated carbon (CH104, mesh size 12–20, Spectrum) [28]. (A) Separation of perchlorate ions ($[\text{ClO}_4^-]_0 = 200 \text{ mg/L}$, 300 mL); (B) Scanning electron micrograph of the crystals of elemental Cu formed on the 0.1%Pt-CFFC within the hydrogenation of CuCl_2 solution ($[\text{Cu}^{2+}]_0 = 500 \text{ mg/L}$, pH = 0, 1 L); (C) Separation-hydrogenation of nitrates in NaNO_3 solution ($[\text{NO}_3^-]_0 = 300 \text{ mg/L}$, 300 mL) using 1.0%Pt-0.2%In-CFFCs. After the air-induced separation the NaNO_3 solution was replaced with 300 mL of deionized water for the hydrogenation step. (D) Separation of TFA using 0.5%Pt-CFFCs ($[\text{TFA}]_0 = 5 \text{ mg/L}$, 1 L).

ca. 55%) gas and ammonia within the hydrogenation step of the process (Eq. (7) and (8)) [28]:



Besides Pt-Cu other catalysts can be applied for nitrite and nitrate hydrogenation by the CFFCs [45]. Fig. 3C shows the results of nitrate separation and hydrogenation conducted using the 1.0%Pt-0.2%In-CFFCs that comprised 1.0% platinum and 0.2 % indium (In) metals in granular activated charcoal. The selectivity of the process towards the N_2 gas was as high as about 90%.

CFFCs have many other potential applications for removal of hazardous anionic compounds, for instance, the highly toxic trifluoroacetic acid exists in water mostly as a trifluoroacetate anion that can be separated by electrosorption and by the CFFCs. Fig. 3D shows the results of the oxygenation-hydrogenation cycle of TFA solution in a batch mode system with 0.5%Pt-CFFCs.

Experiments aimed at separating Na^+ and NH_4^+ by the micro-scale or undivided macro-scale CFFCs revealed that electrosorption of these cations is very poor [26]. This phenomenon was attributed to an influence of H^+ cations (produced within the HOR) that occupy the activated carbon surface or/and create the low local pH in the CFFCs, resulting in the positively charged surface of the CFFCs and repulsion of cations [26].

The main potential advantage of the micro-scale CFFCs is that no wiring, spacers, or gaskets are required for the process that can be

performed in simple packed-bed or fluidized-bed reactors. The second advantage is that regeneration of the (electro)adsorbent does not involve the application of acids, salts, or bases. Cons include utilization of expensive Pt catalyst, low salt adsorption capacity, and co-production of H^+ and OH^- ions that occupy SAC of the CFFCs and even prevent separation of cations. Further studies are required to reveal the mechanisms of ions separation, develop mechanistic models describing the kinetics, decrease Pt-loading or use of non-noble metal catalysts, increase selectivity towards the specific pollutants, and to develop a process with an efficient H_2 gas utilization.

4. Outlook, and next steps

With its almost 100-year history, fuel-cells have not stopped bringing forth novel technologies [46]. There is no indication that hydrogen-driven technologies will tire in the future of being an engine to innovation and provide opportunities towards sustainability. Hydrogen as the fuel for water remediation requires careful consideration of the eco-balance. Today, 95% of the hydrogen production relates to non-renewable sources, such as coal and gas [47]. The global efforts towards a more sustainable, industrialized world will require transformative changes and monumental investments so that renewable energy combined with electrolysis and other green hydrogen generation pathways will make an impact. Yet, even today, already 5% of the global hydrogen production relates to hydrogen being a by-product of other chemical processes, foremost chlorine production [47]. Thereby, the future adaptation of hydrogen-driven water purification may also

extend to other by-product gases, such as methane.

As for the material- and system-related challenges, it will be essential to establish both robust long-term performance metrics and to strive towards the use of lower-cost electrode materials. Finding a good balance between high performance, stability, use of abundant materials, use of low-cost materials, and competition with other desalination technologies will be a critical challenge.

CRediT authorship contribution statement

M.E. Suss: Conceptualization, Writing – original draft, Writing – review & editing, Visualization. **Y. Zhang:** Writing – review & editing, Visualization. **I. Atlas:** Writing – review & editing, Visualization. **Y. Gendel:** Conceptualization, Writing – original draft, Writing – review & editing, Visualization. **E.B. Ruck:** Writing – review & editing, Visualization. **V. Presser:** Conceptualization, Writing – original draft, Writing – review & editing, Visualization.

Declaration of Competing Interest

The authors declare that they have no known competing financial interests or personal relationships that could have appeared to influence the work reported in this paper.

References

- [1] A. Alkaisi, R. Mossad, A. Sharifian-Barforoush, A Review of the Water Desalination Systems Integrated with Renewable Energy, *Energy Proc.* 110 (2017) 268–274.
- [2] A.Y. Hoekstra, M.M. Mekonnen, A.K. Chapagain, R.E. Mathews, B.D. Richter, Global Monthly Water Scarcity: Blue Water Footprints versus Blue Water Availability, *PLoS ONE* 7 (2012), e32688.
- [3] Progress on the level of water stress. Global status and acceleration needs for SDG indicator 6.4.2, FAO and UN Water, 2021.
- [4] R. Epsztain, R.M. DuChanois, C.L. Ritt, A. Noy, M. Elimelech, Towards single-species selectivity of membranes with subnanometre pores, *Nat. Nanotechnol.* 15 (2020) 426–436.
- [5] D. Curto, V. Franzitta, A. Guercio, A Review of the Water Desalination Technologies, *Appl. Sci.* 11 (2021) 670.
- [6] M. Elimelech, W.A. Phillip, The Future of Seawater Desalination: Energy, Technology, and the Environment, *Science* 333 (2011) 712–717.
- [7] K.C. Ng, M. Burhan, Q. Chen, D. Ybyraimkul, F.H. Akhtar, M. Kumja, R.W. Field, M.W. Shahzad, A thermodynamic platform for evaluating the energy efficiency of combined power generation and desalination plants, *NPJ Clean Water* 4 (2021) 25.
- [8] H. Strathmann, Electrodialysis, a mature technology with a multitude of new applications, *Desalination* 264 (2010) 268–288.
- [9] S. Al-Amshawee, M.Y.B.M. Yunus, A.A.M. Azoddein, D.G. Hassell, I.H. Dakhil, H. A. Hasan, Electrodialysis desalination for water and wastewater: A review, *Chem. Eng. J.* 380 (2020), 122231.
- [10] M.E. Suss, S. Porada, X. Sun, P.M. Biesheuvel, J. Yoon, V. Presser, Water desalination via capacitive deionization: what is it and what can we expect from it? *Energy Environ. Sci.* 8 (2015) 2296–2319.
- [11] P. Srimuk, X. Su, J. Yoon, D. Aurbach, V. Presser, Charge-transfer materials for electrochemical water desalination, ion separation and the recovery of elements, *Nat. Rev. Mater.* 5 (7) (2020) 517–538.
- [12] M.E. Suss, V. Presser, Water Desalination with Energy Storage Electrode Materials, *Joule* 2 (1) (2018) 10–15.
- [13] M. Metzger, M.M. Besli, S. Kuppan, S. Hellstrom, S. Kim, E. Sebti, C.V. Subban, J. Christensen, Techno-economic analysis of capacitive and intercalative water deionization, *Energy Environ. Sci.* 13 (6) (2020) 1544–1560.
- [14] I. Atlas, S. Abu Khalla, M.E. Suss, Thermodynamic Energy Efficiency of Electrochemical Systems Performing Simultaneous Water Desalination and Electricity Generation, *J. Electrochem. Soc.* 167 (13) (2020) 134517, <https://doi.org/10.1149/1945-7111/abb709>.
- [15] B.T. Meshesha, N. Barrabés, J. Llorca, A. Dafinov, F. Medina, K. Föttinger, PdCu alloy nanoparticles on alumina as selective catalysts for trichloroethylene hydrodechlorination to ethylene, *Appl. Catal. A* 453 (2013) 130–141.
- [16] E. Díaz, A.F. Mohedano, L. Calvo, M.A. Gilarranz, J.A. Casas, J.J. Rodríguez, Hydrogenation of phenol in aqueous phase with palladium on activated carbon catalysts, *Chem. Eng. J.* 131 (2007) 65–71.
- [17] F. Ruiz-Beviá, M.J. Fernández-Torres, Effective catalytic removal of nitrates from drinking water: An unresolved problem? *J. Clean. Prod.* 217 (2019) 398–408.
- [18] P. Xu, S. Agarwal, L. Lefferts, Mechanism of nitrite hydrogenation over Pd/ γ -Al₂O₃ according a rigorous kinetic study, *J. Catal.* 383 (2020) 124–134.
- [19] K.D. Hurley, J.R. Shapley, Efficient Heterogeneous Catalytic Reduction of Perchlorate in Water, *Environ. Sci. Technol.* 41 (2007) 2044–2049.
- [20] H. Chen, Z. Xu, H. Wan, J. Zheng, D. Yin, S. Zheng, Aqueous bromate reduction by catalytic hydrogenation over Pd/Al₂O₃ catalysts, *Appl. Catal. B* 96 (2010) 307–313.
- [21] S. Al-Hallaj, F. Alasfour, S. Parekh, S. Amiruddin, J.R. Selman, H. Ghezel-Ayagh, Conceptual design of a novel hybrid fuel cell/desalination system, *Desalination* 164 (2004) 19–31.
- [22] Y. Zhang, L. Wang, V. Presser, Electrocatalytic fuel cell desalination for continuous energy and freshwater generation, *Cell Rep. Phys. Sci.* 2 (2021), 100416.
- [23] S. Abdalla, S.A. Khalla, M.E. Suss, Voltage loss breakdown in desalination fuel cells, *Electrochem. Commun.* 132 (2021), 107136.
- [24] S. Abu Khalla, M.E. Suss, Desalination via chemical energy: An electrodialysis cell driven by spontaneous electrode reactions, *Desalination* 467 (2019) 257–262.
- [25] G. Amikam, N. Manor-Korin, P. Nativ, Y. Gendel, Separation of ions from water and wastewater using micro-scale capacitive-faradaic fuel cells (CFFCs), powered by H₂(g) and air, *Sep. Purif. Technol.* 253 (2020), 117494.
- [26] G. Amikam, Y. Gendel, Capacitive-faradaic fuel cells (CFFCs) for ion separation: Macro-scale configurations and polarization mechanism, *Electrochem. Commun.* 124 (2021), 106945.
- [27] Y. Darom, G. Amikam, E.B. Ruck, Y. Gendel, Capacitive-faradaic fuel cells (CFFCs) for selective separation of copper(II) ions from water and wastewater, *Chem. Eng. J.* 421 (2021), 129950.
- [28] G. Amikam, Y. Gendel, Separation and hydrogenation of nitrate ions by micro-scale capacitive-faradaic fuel cells (CFFCs), *Electrochem. Commun.* 120 (2020), 106831.
- [29] E.B. Ruck, G. Amikam, Y. Darom, N. Manor-Korin, Y. Gendel, Catalytic selective recovery of silver from dilute aqueous solutions and e-waste leachates, *Sep. Purif. Technol.* (2021) 120303, <https://doi.org/10.1016/j.seppur.2021.120303>.
- [30] M. Tedesco, H.V.M. Hamelers, P.M. Biesheuvel, Nernst-Planck transport theory for (reverse) electrodialysis: I. Effect of co-ion transport through the membranes, *J. Membrane Sci.* 510 (2016) 370–381.
- [31] S. Schlumpberger, N.B. Lu, M.E. Suss, M.Z. Bazant, Scalable and Continuous Water Deionization by Shock Electrodialysis, *Environ. Sci. Technol. Lett.* 2 (12) (2015) 367–372.
- [32] H. Lu, L.i. Wang, R. Wycisk, P.N. Pintauro, S. Lin, Quantifying the kinetics-energetics performance tradeoff in bipolar membrane electrodialysis, *J. Membrane Sci.* 612 (2020) 118279, <https://doi.org/10.1016/j.memsci.2020.118279>.
- [33] G.J. Doornbusch, M. Bel, M. Tedesco, J.W. Post, Z. Borneman, K. Nijmeijer, Effect of membrane area and membrane properties in multistage electrodialysis on seawater desalination performance, *J. Membrane Sci.* 611 (2020) 118303, <https://doi.org/10.1016/j.memsci.2020.118303>.
- [34] I. Atlas, M.E. Suss, Theory of simultaneous desalination and electricity generation via an electrodialysis cell driven by spontaneous redox reactions, *Electrochim. Acta* 319 (2019) 813–821.
- [35] S.M. Shariatiannahi, M.S. Hatamipour, S. Rashid-Nadimi, M.K. Amini, Simultaneous saltwater desalination and power generation using an aluminum-powered cell, *J. Environ. Chem. Eng.* 9 (2) (2021) 104802, <https://doi.org/10.1016/j.jece.2020.104802>.
- [36] Y. Kim, B.E. Logan, Microbial desalination cells for energy production and desalination, *Desalination* 308 (2013) 122–130.
- [37] J. Dai, N.L. Win Pyae, F. Chen, M. Liang, S. Wang, K. Ramalingam, S. Zhai, C.-Y. Su, Y. Shi, S.C. Tan, L. Zhang, Y. Chen, Zinc-Air Battery-Based Desalination Device, *ACS Appl. Mater. Interfaces* 12 (23) (2020) 25728–25735.
- [38] P. Srimuk, L. Wang, Ö. Budak, V. Presser, High-performance ion removal via zinc-air desalination, *Electrochem. Commun.* 115 (2020) 106713, <https://doi.org/10.1016/j.elecom.2020.106713>.
- [39] Z.M. Bhat, D. Pandit, S. Ardo, R. Thimmappa, A.R. Kottaichamy, N. Christudas Dargily, M.C. Devendrachari, M. Ottakam Thotiyil, An Electrochemical Neutralization Cell for Spontaneous Water Desalination, *Joule* 4 (8) (2020) 1730–1742.
- [40] S. Porada, R. Zhao, A. van der Wal, V. Presser, P.M. Biesheuvel, Review on the science and technology of water desalination by capacitive deionization, *Prog. Mater. Sci.* 58 (8) (2013) 1388–1442.
- [41] Y.M. Volkovich, Capacitive Deionization of Water (A Review), *Russ. J. Electrochem.* 56 (2020) 18–51.
- [42] J. Chang, F. Duan, H. Cao, K. Tang, C. Su, Y. Li, Superiority of a novel flow-electrode capacitive deionization (FCDI) based on a battery material at high applied voltage, *Desalination* 468 (2019), 114080.
- [43] Y. Xu, F. Duan, Y. Li, H. Cao, J. Chang, H. Pang, J. Chen, Enhanced desalination performance in asymmetric flow electrode capacitive deionization with nickel hexacyanoferrate and activated carbon electrodes, *Desalination* 514 (2021), 115172.
- [44] S. Abu Khalla, I. Atlas, S. Litster, M.E. Suss, Desalination Fuel Cells with High Thermodynamic Energy Efficiency, *Environ. Sci. Technol.* (2022), <https://doi.org/10.1021/acs.est.1c07288>.
- [45] J. Martínez, A. Ortiz, I. Ortiz, State-of-the-art and perspectives of the catalytic and electrocatalytic reduction of aqueous nitrates, *Appl. Catal. B* 207 (2017) 42–59.
- [46] W. Vielstich, *Handbook of Fuel Cells*, 2010.
- [47] Green hydrogen: A guide to policy making, International Renewable Energy Agency, 2020.

4. Conclusions and Outlook

Electrochemical methods are attractive contenders for the design of energy-efficient water remediation technologies. Due to their high specific surface areas and high pore volumes, activated carbon materials are often applied in CDI to obtain a higher desalination capacity during each ion uptake cycle. Due to the co-ion and counter-ion exchange effect, CDI (without membranes) was considered suitable only for brackish water desalination. When the salt concentration increases to more than 100 mM, the charge efficiency of the desalination process will decrease dramatically. The application of battery materials is also advantageous for electrochemical desalination in high salt concentrations. However, the degradation mechanisms of the materials are poorly explored, and the high cost of materials and ion exchange membranes is a challenging issue for industrial applications.

In this doctoral thesis, the ion electrosorption of ultramicroporous carbon materials was studied in aqueous media using ultramicroporous carbon within the context of enabling seawater desalination. Ultramicroporous carbon materials with subnanometer average pore size distributions have higher charge efficiency and can suppress co-ion rejection during the cell cycling process. Due to this interesting property, ultramicroporous carbon has removed the paradigm that CDI is unsuitable for desalination at high salinity levels. By combining molecular dynamics (MD) simulations with experimental data on the pore structure, a predictable desalination performance in seawater-level ionic strength was obtained. It shows the desalination performance of carbon material with an average pore size of around 0.6 nm has a high desalination capacity (12 mg/g) due to its ionophobicity at PZC that leads to its intrinsic ion permselectivity during the cycling processes.

Ultramicroporous carbon materials not only enhance the desalination capabilities in feedwater with higher salt concentrations but can also enable ion separation. The combination of pore size, hydrated ion size, ion desolvation energy, and the charge number play an essential role in ion selectivity for multi-ion-contained electrolytes. The ions will be blocked at the entrance of the pores. They cannot be adsorbed inside of the pores if the pore size is smaller than the hydrated ion size and if the applied potential cannot overcome the dehydration energy barrier of the ions. This phenomenon is known as ion sieving. By applying ultramicroporous carbon material with an average pore size of 0.6 nm for CDI application in the multi-ion system, a selective monovalent cation removal is achieved due to the large hydrated ion size and high desolvation energies of the divalent cations. This ion

separation approach is suitable for size-dependent ion separation. However, applying size-dependent ion separation is challenging for such an ion in a very complicated aqueous environment. Therefore, a combination of multiple ion removable steps is required in industrial applications, potentially increasing the total costs for ion separation.

In the second part, this work explored other methods to enhance the desalination performance of the CDI system, namely the effects of feedwater concentration on MCDI performances. When applying free-standing IEMs and IEM coatings, there are more counter-ions inside of the IEMs due to the different degrees of membrane permselectivity and the volume of the water channel between the IEM and electrodes. The coated IEM, which exhibits a higher degree of swelling and lower permselectivity shows higher desalination performance in feedwater with lower salt concentrations. For MCDI cells with free-standing IEMs, more co-ions exist between the electrodes and IEMs due to better permselectivity and the water channel between the electrodes and the IEMs. Under these conditions, the best desalination performance at a seawater-level ionic strength is obtained (25 mg/g). This work shows the potential for MCDI serving in seawater desalination applications and obtaining a higher desalination performance by enhancing the ion permselectivity and cell design. Yet, this is accomplished at the cost of adding an ion-exchange membrane, whereby additional costs and processing steps incur. The aging and fouling of the IEMs will also lead to desalination failure over time in seawater. Another method to enhance desalination performance is to apply materials with high intrinsic permselectivity. For example, a desalination capacity of 8-12 mg/g with a charge efficiency of 85% is achieved by applying $Ti_3C_2T_x$ -MXene paired with activated carbon and proper mass balancing. However, the added price of the MXene material should also be considered for industrial applications.

The particle size distribution of the carbon materials is also essential to understand an electrode's desalination performance. Smaller particles will hinder the interparticle ions transportation, and larger particles will lead to longer diffusion lengths inside the particles. Thus, both interparticle and intraparticle ion diffusion will be influenced by the particle size distributions. A higher desalination performance can also be achieved by applying a mixture of both large and small particles and through better control of electrode density.

The electrochemical stability windows of carbon materials in H_2O and D_2O solvents are also studied. The hydrogen and deuterium electrosorption is seen to occur in microporous carbons. Between the H_2O and D_2O systems, lower ion mobilities and reactivities are

observed in the D₂O solvent. The ion diffusion kinetics also strongly depends on the pore size distributions of the microporous carbon materials. Carbon materials with ultramicroporous pore structures show a higher overpotential for water/heavy water splitting (-1.3 V to -1.4 V), which is important information for applying such material in aqueous electrolytes for higher energy storage capacities. This work shows ultramicroporous carbons have higher electrochemical stability windows in aqueous media, while carbon materials with higher overpotential for water splitting enable more ion uptake from the feedwater. This will benefit the application of CDI.

For materials that have ion storage properties, there is always a capacity limitation. After the charging process, the ions must be released from the materials be prepared for the next cycle of ion uptake. Since the ion uptake process of these materials requires electrical energy, we devise a system of utilizing the chemical energy of H₂ and O₂ via electrocatalytic reactions. Feedwater with seawater-level molarity can be continuously desalinated while also producing electrical energy, acid solution, and base solution. As a third-generation electrochemical desalination technology, fuel cell desalination (FCD) has the advantage of continuous concurrence of desalination and generation of electricity. Because the reaction mechanism is slightly different from a commercial fuel cell, however, the aging mechanism of the catalyst remains undiscovered. However, due to the possible side reactions and limited permselectivity of the IEMs, a better cell/material design is required, and the total energy efficiency of this technology must be improved.

All in all, efforts must be made to develop materials with better ion-uptake ability while being stable in the aqueous environment and not introducing too much extra cost. There are no clear statements of which generation of electrochemical water treatment technologies is more suitable or more efficient in brackish water or seawater. Advanced desalination cell design can greatly improve desalination performance and enables flexible electrochemical water treatment. Thus, both material and cell structural design are essential in electrochemical water desalination studies in future research.

5. References

- [1] A. Alkaisi, R. Mossad, A. Sharifian-Barforoush, A Review of the Water Desalination Systems Integrated with Renewable Energy, *Energy Procedia*, 110 (2017) 268-274.
- [2] M.A. Shannon, P.W. Bohn, M. Elimelech, J.G. Georgiadis, B.J. Mariñas, A.M. Mayes, Science and technology for water purification in the coming decades, *Nature*, 452 (2008) 301-310.
- [3] C. He, Z. Liu, J. Wu, X. Pan, Z. Fang, J. Li, B.A. Bryan, Future global urban water scarcity and potential solutions, *Nature Communications*, 12 (2021) 4667.
- [4] T.P. Barnett, J.C. Adam, D.P. Lettenmaier, Potential impacts of a warming climate on water availability in snow-dominated regions, *Nature*, 438 (2005) 303-309.
- [5] FAO, U. Water, Progress on level of water stress: Global status and acceleration needs for SDG indicator 6.4.2, Rome, (2021).
- [6] E. Vera, J. Ruales, M. Dornier, J. Sandeaux, R. Sandeaux, G. Pourcelly, Deacidification of clarified passion fruit juice using different configurations of electrodialysis, *Journal of Chemical Technology & Biotechnology*, 78 (2003) 918-925.
- [7] M. Fidaleo, M. Moresi, Electrodialysis Applications in The Food Industry, in: *Advances in Food and Nutrition Research*, Academic Press, 2006, pp. 265-360.
- [8] F. Gonçalves, C. Fernandes, P. Cameira dos Santos, M.N. de Pinho, Wine tartaric stabilization by electrodialysis and its assessment by the saturation temperature, *Journal of Food Engineering*, 59 (2003) 229-235.
- [9] S. Al-Amshawee, M.Y.B.M. Yunus, A.A.M. Azoddein, D.G. Hassell, I.H. Dakhil, H.A. Hasan, Electrodialysis desalination for water and wastewater: A review, *Chemical Engineering Journal*, 380 (2020),122231.
- [10] T.M. Missimer, R.G. Maliva, Environmental issues in seawater reverse osmosis desalination: Intakes and outfalls, *Desalination*, 434 (2018) 198-215.
- [11] D. Curto, V. Franzitta, A. Guercio, A Review of the Water Desalination Technologies, *Applied Science*, Basel, 11 (2021) 670.
- [12] A.F. Rusydi, Correlation between conductivity and total dissolved solid in various type of water: A review, *IOP Conference Series: Earth and Environmental Science*, 118 (2018) 012019.
- [13] D.K. Todd, L.W. Mays, *Groundwater hydrology*, Wiley, (1980).
- [14] L.N. Nthunya, S. Maifadi, B.B. Mamba, A.R. Verliefde, S.D. Mhlanga, Spectroscopic Determination of Water Salinity in Brackish Surface Water in Nandoni Dam, at Vhembe District, Limpopo Province, South Africa, *Water*, 10 (2018) 990.
- [15] L.F. Greenlee, D.F. Lawler, B.D. Freeman, B. Marrot, P. Moulin, Reverse osmosis desalination: water sources, technology, and today's challenges, *Water Research*, 43 (2009) 2317-2348.
- [16] D. Curto, V. Franzitta, A. Guercio, A Review of the Water Desalination Technologies, *Applied Sciences*, 11 (2021) 670.
- [17] L. Gurreri, A. Tamburini, A. Cipollina, G. Micale, Electrodialysis Applications in Wastewater Treatment for Environmental Protection and Resources Recovery: A Systematic Review on Progress and Perspectives, *Membranes*, 10 (2020) 146.
- [18] M. Shatat, S.B. Riffat, Water desalination technologies utilizing conventional and renewable energy sources, *International Journal of Low-Carbon Technologies*, 9 (2012) 1-19.
- [19] A.D. Khawaji, I.K. Kutubkhana, J.-M. Wie, Advances in seawater desalination technologies, *Desalination*, 221 (2008) 47-69.
- [20] A. Al-Karaghouli, L.L. Kazmerski, Energy consumption and water production cost of conventional and renewable-energy-powered desalination processes, *Renewable and Sustainable Energy Reviews*, 24 (2013) 343-356.
- [21] M. Al-Sahali, H. Ettonuey, Developments in thermal desalination processes: Design, energy, and costing aspects, *Desalination*, 214 (2007) 227-240.
- [22] F. Helfer, C. Lemckert, Y.G. Anissimov, Osmotic power with Pressure Retarded Osmosis: Theory, performance and trends – A review, *Journal of Membrane Science*, 453 (2014) 337-358.

- [23] K.C. Ng, M. Burhan, Q. Chen, D. Ybyraiymkul, F.H. Akhtar, M. Kumja, R.W. Field, M.W. Shahzad, A thermodynamic platform for evaluating the energy efficiency of combined power generation and desalination plants, *npj Clean Water*, 4 (2021) 25.
- [24] R.L. Stover, Seawater reverse osmosis with isobaric energy recovery devices, *Desalination*, 203 (2007) 168-175.
- [25] X. Liu, S. Shanbhag, T.V. Bartholomew, J.F. Whitacre, M.S. Mauter, Cost Comparison of Capacitive Deionization and Reverse Osmosis for Brackish Water Desalination, *ACS ES&T Engineering*, (2020) 261-273.
- [26] M.E. Suss, S. Porada, X. Sun, P.M. Biesheuvel, J. Yoon, V. Presser, Water desalination via capacitive deionization: what is it and what can we expect from it?, *Energy & Environmental Science*, 8 (2015) 2296-2319.
- [27] G. Amy, N. Ghaffour, Z. Li, L. Francis, R.V. Linares, T. Missimer, S. Lattemann, Membrane-based seawater desalination: Present and future prospects, *Desalination*, 401 (2017) 16-21.
- [28] A.M. Pernía, J.G. Norniella, J.A. Martín-Ramos, J. Díaz, J.A. Martínez, Up-Down Converter for Energy Recovery in a CDI Desalination System, *IEEE Transactions on Power Electronics*, 27 (2012) 3257-3265.
- [29] T. Kim, J.E. Dykstra, S. Porada, A. van der Wal, J. Yoon, P.M. Biesheuvel, Enhanced charge efficiency and reduced energy use in capacitive deionization by increasing the discharge voltage, *Journal of Colloid and Interface Science*, 446 (2015) 317-326.
- [30] S. Porada, L. Borchardt, M. Oschatz, M. Bryjak, J.S. Atchison, K.J. Keesman, S. Kaskel, P.M. Biesheuvel, V. Presser, Direct prediction of the desalination performance of porous carbon electrodes for capacitive deionization, *Energy & Environmental Science*, 6 (2013) 3700-3712.
- [31] C. Kim, P. Srimuk, J. Lee, S. Fleischmann, M. Aslan, V. Presser, Influence of pore structure and cell voltage of activated carbon cloth as a versatile electrode material for capacitive deionization, *Carbon*, 122 (2017) 329-335.
- [32] S. Porada, R. Zhao, A. van der Wal, V. Presser, P.M. Biesheuvel, Review on the science and technology of water desalination by capacitive deionization, *Progress in Materials Science*, 58 (2013) 1388-1442.
- [33] P. Bairi, S. Maji, J.P. Hill, J.H. Kim, K. Ariga, L.K. Shrestha, Mesoporous carbon cubes derived from fullerene crystals as a high rate performance electrode material for supercapacitors, *Journal of Materials Chemistry A*, 7 (2019) 12654-12660.
- [34] F. Xu, R. Cai, Q. Zeng, C. Zou, D. Wu, F. Li, X. Lu, Y. Liang, R. Fu, Fast ion transport and high capacitance of polystyrene-based hierarchical porous carbon electrode material for supercapacitors, *Journal of Materials Chemistry*, 21 (2011) 1970-1976.
- [35] A. Eatemadi, H. Daraee, H. Karimkhanloo, M. Kouhi, N. Zarghami, A. Akbarzadeh, M. Abasi, Y. Hanifehpour, S.W. Joo, Carbon nanotubes: properties, synthesis, purification, and medical applications, *Nanoscale Research Letters*, 9 (2014) 393.
- [36] L. Chico, V.H. Crespi, L.X. Benedict, S.G. Louie, M.L. Cohen, Pure carbon nanoscale devices: Nanotube heterojunctions, *Physical Review Letters*, 76 (1996) 971-974.
- [37] Y. Wan, Y. Shi, D. Zhao, Supramolecular Aggregates as Templates: Ordered Mesoporous Polymers and Carbons, *Chemistry of Materials*, 20 (2008) 932-945.
- [38] C. Liang, K. Hong, G.A. Guiochon, J.W. Mays, S. Dai, Synthesis of a Large-Scale Highly Ordered Porous Carbon Film by Self-Assembly of Block Copolymers, *Angewandte Chemie International Edition*, 43 (2004) 5785-5789.
- [39] Y. Meng, D. Gu, F. Zhang, Y. Shi, H. Yang, Z. Li, C. Yu, B. Tu, D. Zhao, Ordered mesoporous polymers and homologous carbon frameworks: amphiphilic surfactant templating and direct transformation, *Angewandte Chemie International Edition*, 44 (2005) 7053-7059.
- [40] Y. Huang, H. Cai, D. Feng, D. Gu, Y. Deng, B. Tu, H. Wang, P.A. Webley, D. Zhao, One-step hydrothermal synthesis of ordered mesostructured carbonaceous monoliths with hierarchical porosities, *Chemical Communications*, (2008) 2641-2643.
- [41] A. Eftekhari, Z. Fan, Ordered mesoporous carbon and its applications for electrochemical energy storage and conversion, *Materials Chemistry Frontiers*, 1 (2017) 1001-1027.

- [42] B. Krüner, J. Lee, N. Jackel, A. Tolosa, V. Presser, Sub-micrometer Novolac-Derived Carbon Beads for High Performance Supercapacitors and Redox Electrolyte Energy Storage, *ACS Applied Materials & Interfaces*, 8 (2016) 9104-9115.
- [43] F. Ji, Y. Shi, M. Li, S. Jiang, G. Chen, F. Liu, Z. Chen, Scalable Synthesis of Uniform Nanosized Microporous Carbon Particles from Rigid Polymers for Rapid Ion and Molecule Adsorption, *ACS Applied Materials & Interfaces*, 10 (2018) 25429-25437.
- [44] B.H. Hameed, A.T. Din, A.L. Ahmad, Adsorption of methylene blue onto bamboo-based activated carbon: kinetics and equilibrium studies, *J Hazard Mater*, 141 (2007) 819-825.
- [45] I.J. Kim, M.J. Jeon, S.H. Yang, S.I. Moon, H.S. Kim, Electrochemical Performance of Activated Carbon Electrode Added with LiCoO₂ for Hybrid Capacitor, *Solid State Phenomena*, 124-126 (2007) 947-950.
- [46] L.L. Zhang, X.S. Zhao, Carbon-based materials as supercapacitor electrodes, *Chemical Society Reviews*, 38 (2009) 2520-2531.
- [47] S. Porada, L. Weinstein, R. Dash, A. van der Wal, M. Bryjak, Y. Gogotsi, P.M. Biesheuvel, Water desalination using capacitive deionization with microporous carbon electrodes, *ACS Applied Materials & Interfaces*, 4 (2012) 1194-1199.
- [48] B. Krüner, T.S. Dörr, H. Shim, J. Sann, J. Janek, V. Presser, Gyroidal Porous Carbon Activated with NH₃ or CO₂ as Lithium-Sulfur Battery Cathodes, *Batteries & Supercaps*, 1 (2018) 83-94.
- [49] B. Krüner, P. Srimuk, S. Fleischmann, M. Zeiger, A. Schreiber, M. Aslan, A. Quade, V. Presser, Hydrogen-treated, sub-micrometer carbon beads for fast capacitive deionization with high performance stability, *Carbon*, 117 (2017) 46-54.
- [50] E. Raymundo-Piñero, K. Kierzek, J. Machnikowski, F. Béguin, Relationship between the nanoporous texture of activated carbons and their capacitance properties in different electrolytes, *Carbon*, 44 (2006) 2498-2507.
- [51] J. Chmiola, G. Yushin, Y. Gogotsi, C. Portet, P. Simon, P.L. Taberna, Anomalous increase in carbon capacitance at pore sizes less than 1 nanometer, *Science*, 313 (2006) 1760-1763.
- [52] S. Bi, Y. Zhang, L. Cervini, T. Mo, J.M. Griffin, V. Presser, G. Feng, Permselective ion electrosorption of subnanometer pores at high molar strength enables capacitive deionization of saline water, *Sustainable Energy & Fuels*, 4 (2020) 1285-1295.
- [53] J.G. Gamaethiralalage, K. Singh, S. Sahin, J. Yoon, M. Elimelech, M.E. Suss, P. Liang, P.M. Biesheuvel, R.L. Zornetta, L.C.P.M. de Smet, Recent advances in ion selectivity with capacitive deionization, *Energy & Environmental Science*, 14 (2021) 1095-1120.
- [54] K. Tang, Y.-h. Kim, J. Chang, R.T. Mayes, J. Gabitto, S. Yiacoumi, C. Tsouris, Seawater desalination by over-potential membrane capacitive deionization: Opportunities and hurdles, *Chemical Engineering Journal*, 357 (2019) 103-111.
- [55] Y. Zhang, P. Srimuk, M. Aslan, M. Gallei, V. Presser, Polymer ion-exchange membranes for capacitive deionization of aqueous media with low and high salt concentration, *Desalination*, 479 (2020) 114331.
- [56] P.M. Biesheuvel, A. van der Wal, Membrane capacitive deionization, *Journal of Membrane Science*, 346 (2010) 256-262.
- [57] J. Zhou, P. Zuo, Y. Liu, Z. Yang, T. Xu, Ion exchange membranes from poly(2,6-dimethyl-1,4-phenylene oxide) and related applications, *Science China Chemistry*, 61 (2018) 1062-1087.
- [58] J. Ran, L. Wu, Y. He, Z. Yang, Y. Wang, C. Jiang, L. Ge, E. Bakangura, T. Xu, Ion exchange membranes: New developments and applications, *Journal of Membrane Science*, 522 (2017) 267-291.
- [59] J. Kamcev, D.R. Paul, B.D. Freeman, Effect of fixed charge group concentration on equilibrium ion sorption in ion exchange membranes, *Journal of Materials Chemistry A*, 5 (2017) 4638-4650.
- [60] J. Kamcev, B.D. Freeman, Charged Polymer Membranes for Environmental/Energy Applications, *Annual Review of Chemical and Biomolecular Engineering*, 7 (2016) 111-133.
- [61] G.M. Geise, D.R. Paul, B.D. Freeman, Fundamental water and salt transport properties of polymeric materials, *Progress in Polymer Science*, 39 (2014) 1-42.
- [62] W. Reiman, III, Ion exchange (Helfferich, Friedrich), *Journal of Chemical Education*, 40 (1963) 231.

- [63] W.D. Richards, T. Tsujimura, L.J. Miara, Y. Wang, J.C. Kim, S.P. Ong, I. Uechi, N. Suzuki, G. Ceder, Design and synthesis of the superionic conductor Na₁₀SnP₂S₁₂, *Nature Communications*, 7 (2016) 11009.
- [64] J. Janek, W.G. Zeier, A solid future for battery development, *Nature Energy*, 1 (2016) 16141.
- [65] X. He, Y. Zhu, Y. Mo, Origin of fast ion diffusion in super-ionic conductors, *Nature Communications*, 8 (2017) 15893.
- [66] M. Torkamanzadeh, L. Wang, Y. Zhang, O. Budak, P. Srimuk, V. Presser, MXene/Activated-Carbon Hybrid Capacitive Deionization for Permselective Ion Removal at Low and High Salinity, *ACS Applied Materials & Interfaces*, 12 (2020) 26013-26025.
- [67] E. Toledo-Carrillo, X. Zhang, K. Laxman, J. Dutta, Asymmetric electrode capacitive deionization for energy efficient desalination, *Electrochimica Acta*, 358 (2020) 136939.
- [68] X. Gao, A. Omosebi, J. Landon, K. Liu, Enhanced Salt Removal in an Inverted Capacitive Deionization Cell Using Amine Modified Microporous Carbon Cathodes, *Environmental Science & Technology*, 49 (2015) 10920-10926.
- [69] P. Srimuk, M. Zeiger, N. Jäckel, A. Tolosa, B. Krüner, S. Fleischmann, I. Grobelsek, M. Aslan, B. Shvartsev, M.E. Suss, V. Presser, Enhanced performance stability of carbon/titania hybrid electrodes during capacitive deionization of oxygen saturated saline water, *Electrochimica Acta*, 224 (2017) 314-328.
- [70] Y.-H. Tu, C.-F. Liu, J.-A. Wang, C.-C. Hu, Construction of an inverted-capacitive deionization system utilizing pseudocapacitive materials, *Electrochemistry Communications*, 104 (2019) 106486.
- [71] X. Gao, A. Omosebi, J. Landon, K. Liu, Enhanced Salt Removal in an Inverted Capacitive Deionization Cell Using Amine Modified Microporous Carbon Cathodes, *Environmental Science & Technology*, 49 (2015) 10920-10926.
- [72] X. Gao, A. Omosebi, J. Landon, K. Liu, Surface charge enhanced carbon electrodes for stable and efficient capacitive deionization using inverted adsorption–desorption behavior, *Energy & Environmental Science*, 8 (2015) 897-909.
- [73] P.H. Tewari, A.B. Campbell, Temperature dependence of point of zero charge of cobalt and nickel oxides and hydroxides, *Journal of Colloid and Interface Science*, 55 (1976) 531-539.
- [74] E. McCafferty, Relationship between the isoelectric point (pHpzc) and the potential of zero charge (Epzc) for passive metals, *Electrochimica Acta*, 55 (2010) 1630-1637.
- [75] M.A. Anderson, A.L. Cudero, J. Palma, Capacitive deionization as an electrochemical means of saving energy and delivering clean water. Comparison to present desalination practices: Will it compete?, *Electrochimica Acta*, 55 (2010) 3845-3856.
- [76] B. Kastening, T. Boinowitz, M. Heins, Design of a slurry electrode reactor system, *Journal of Applied Electrochemistry*, 27 (1997) 147-152.
- [77] S.-i. Jeon, H.-r. Park, J.-g. Yeo, S. Yang, C.H. Cho, M.H. Han, D.K. Kim, Desalination via a new membrane capacitive deionization process utilizing flow-electrodes, *Energy & Environmental Science*, 6 (2013) 1471-1475.
- [78] Y. Gendel, A.K.E. Rommerskirchen, O. David, M. Wessling, Batch mode and continuous desalination of water using flowing carbon deionization (FCDI) technology, *Electrochemistry Communications*, 46 (2014) 152-156.
- [79] S. Porada, D. Weingarth, H.V.M. Hamelers, M. Bryjak, V. Presser, P.M. Biesheuvel, Carbon flow electrodes for continuous operation of capacitive deionization and capacitive mixing energy generation, *Journal of Materials Chemistry A*, 2 (2014) 9313-9321.
- [80] A. Rommerskirchen, Y. Gendel, M. Wessling, Single module flow-electrode capacitive deionization for continuous water desalination, *Electrochemistry Communications*, 60 (2015) 34-37.
- [81] B. Akuzum, L. Agartan, J. Locco, E.C. Kumbur, Effects of particle dispersion and slurry preparation protocol on electrochemical performance of capacitive flowable electrodes, *Journal of Applied Electrochemistry*, 47 (2017) 369-380.
- [82] K. Tang, S. Yiakoumi, Y. Li, J. Gabitto, C. Tsouris, Optimal conditions for efficient flow-electrode capacitive deionization, *Separation and Purification Technology*, 240 (2020) 116626.

- [83] J. Song, J. Ma, C. Zhang, C. He, T.D. Waite, Implication of Non-electrostatic Contribution to Deionization in Flow-Electrode CDI: Case Study of Nitrate Removal From Contaminated Source Waters, *Frontiers in Chemistry*, 7 (2019) 146.
- [84] Q. Dong, G. Wang, T. Wu, S. Peng, J. Qiu, Enhancing capacitive deionization performance of electrospun activated carbon nanofibers by coupling with carbon nanotubes, *Journal of Colloid and Interface Science*, 446 (2015) 373-378.
- [85] Y. Zhang, C. Prehal, H. Jiang, Y. Liu, G. Feng, V. Presser, Ionophobicity of carbon sub-nanometer pores enables efficient desalination at high salinity, *Cell Reports Physical Science*, (2021) 100689.
- [86] M. Metzger, M.M. Besli, S. Kuppan, S. Hellstrom, S. Kim, E. Sebti, C.V. Subban, J. Christensen, Techno-economic analysis of capacitive and intercalative water deionization, *Energy & Environmental Science*, 13 (2020) 1544-1560.
- [87] T. Luo, S. Abdu, M. Wessling, Selectivity of ion exchange membranes: A review, *Journal of Membrane Science*, 555 (2018) 429-454.
- [88] L. Wang, S. Lin, Mechanism of Selective Ion Removal in Membrane Capacitive Deionization for Water Softening, *Environmental Science & Technology*, 53 (2019) 5797-5804.
- [89] T. Luo, F. Roghman, M. Wessling, Ion mobility and partition determine the counter-ion selectivity of ion exchange membranes, *Journal of Membrane Science*, 597 (2020) 117645.
- [90] C. Prehal, C. Koczwara, H. Amenitsch, V. Presser, O. Paris, Salt concentration and charging velocity determine ion charge storage mechanism in nanoporous supercapacitors, *Nature Communications*, 9 (2018) 4145.
- [91] L. Wang, Y. Zhang, K. Moh, V. Presser, From capacitive deionization to desalination batteries and desalination fuel cells, *Current Opinion in Electrochemistry*, 29 (2021) 100758.
- [92] P. Srimuk, X. Su, J. Yoon, D. Aurbach, V. Presser, Charge-transfer materials for electrochemical water desalination, ion separation and the recovery of elements, *Nature Reviews Materials*, 5 (2020) 517-538.
- [93] M.R. Lukatskaya, B. Dunn, Y. Gogotsi, Multidimensional materials and device architectures for future hybrid energy storage, *Nature Communications*, 7 (2016) 12647.
- [94] O. Ghodbane, J.L. Pascal, F. Favier, Microstructural effects on charge-storage properties in MnO₂-based electrochemical supercapacitors, *ACS Applied Materials & Interfaces*, 1 (2009) 1130-1139.
- [95] J.P. Zheng, P.J. Cygan, T.R. Jow, Hydrous Ruthenium Oxide as an Electrode Material for Electrochemical Capacitors, *Journal of The Electrochemical Society*, 142 (1995) 2699-2703.
- [96] X. Su, H.J. Kulik, T.F. Jamison, T.A. Hatton, Anion-Selective Redox Electrodes: Electrochemically Mediated Separation with Heterogeneous Organometallic Interfaces, *Advanced Functional Materials*, 26 (2016) 3394-3404.
- [97] J. Lee, P. Srimuk, S. Fleischmann, X. Su, T.A. Hatton, V. Presser, Redox-electrolytes for non-flow electrochemical energy storage: A critical review and best practice, *Progress in Materials Science*, 101 (2019) 46-89.
- [98] J. Lee, P. Srimuk, S. Fleischmann, A. Ridder, M. Zeiger, V. Presser, Nanoconfinement of redox reactions enables rapid zinc iodide energy storage with high efficiency, *Journal of Materials Chemistry A*, 5 (2017) 12520-12527.
- [99] J. Lee, S. Choudhury, D. Weingarth, D. Kim, V. Presser, High Performance Hybrid Energy Storage with Potassium Ferricyanide Redox Electrolyte, *ACS Applied Materials & Interfaces*, 8 (2016) 23676-23687.
- [100] J. Lee, B. Krüner, A. Tolosa, S. Sathyamoorthi, D. Kim, S. Choudhury, K.-H. Seo, V. Presser, Tin/vanadium redox electrolyte for battery-like energy storage capacity combined with supercapacitor-like power handling, *Energy & Environmental Science*, 9 (2016) 3392-3398.
- [101] M. Naguib, O. Mashtalir, J. Carle, V. Presser, J. Lu, L. Hultman, Y. Gogotsi, M.W. Barsoum, Two-Dimensional Transition Metal Carbides, *ACS Nano*, 6 (2012) 1322-1331.
- [102] P. Srimuk, J. Lee, A. Tolosa, C. Kim, M. Aslan, V. Presser, Titanium Disulfide: A Promising Low-Dimensional Electrode Material for Sodium Ion Intercalation for Seawater Desalination, *Chemistry of Materials*, 29 (2017) 9964-9973.

- [103] P. Srimuk, J. Lee, S. Fleischmann, S. Choudhury, N. Jäckel, M. Zeiger, C. Kim, M. Aslan, V. Presser, Faradaic deionization of brackish and sea water via pseudocapacitive cation and anion intercalation into few-layered molybdenum disulfide, *Journal of Materials Chemistry A*, 5 (2017) 15640-15649.
- [104] L. Peng, Y. Zhu, D. Chen, R.S. Ruoff, G. Yu, Two-Dimensional Materials for Beyond-Lithium-Ion Batteries, *Advanced Energy Materials*, 6 (2016) 1600025.
- [105] J. Lee, S. Kim, J. Yoon, Rocking Chair Desalination Battery Based on Prussian Blue Electrodes, *ACS Omega*, 2 (2017) 1653-1659.
- [106] C. Masquelier, L. Croguennec, Polyanionic (phosphates, silicates, sulfates) frameworks as electrode materials for rechargeable Li (or Na) batteries, *Chemical Reviews*, 113 (2013) 6552-6591.
- [107] S.-H. Yu, X. Feng, N. Zhang, J. Seok, H.D. Abruña, Understanding Conversion-Type Electrodes for Lithium Rechargeable Batteries, *Accounts of Chemical Research*, 51 (2018) 273-281.
- [108] S. Arnold, L. Wang, Ö. Budak, M. Aslan, P. Srimuk, V. Presser, Antimony alloying electrode for high-performance sodium removal: how to use a battery material not stable in aqueous media for saline water remediation, *Journal of Materials Chemistry A*, 9 (2021) 585-596.
- [109] P. Srimuk, S. Husmann, V. Presser, Low voltage operation of a silver/silver chloride battery with high desalination capacity in seawater, *RSC Advances*, 9 (2019) 14849-14858.
- [110] J. Chang, F. Duan, C. Su, Y. Li, H. Cao, Removal of chloride ions using a bismuth electrode in capacitive deionization (CDI), *Environmental Science: Water Research & Technology*, 6 (2020) 373-382.
- [111] Y. Liu, X. Gao, Z. Wang, K. Wang, X. Dou, H. Zhu, X. Yuan, L. Pan, Controlled synthesis of bismuth oxychloride-carbon nanofiber hybrid materials as highly efficient electrodes for rocking-chair capacitive deionization, *Chemical Engineering Journal*, 403 (2021) 126326.
- [112] P.K. Dutta, Y. Myung, R. Kulangaramadom Venkiteswaran, L. Mehdi, N. Browning, P. Banerjee, S. Mitra, Mechanism of Na-Ion Storage in BiOCl Anode and the Sodium-Ion Battery Formation, *The Journal of Physical Chemistry C*, 123 (2019) 11500-11507.
- [113] P. Gao, M.A. Reddy, X. Mu, T. Diemant, L. Zhang, Z. Zhao-Karger, V.S. Chakravadhanula, O. Clemens, R.J. Behm, M. Fichtner, VOCl as a Cathode for Rechargeable Chloride Ion Batteries, *Angewandte Chemie International Edition*, 55 (2016) 4285-4290.
- [114] M. Pasta, C.D. Wessells, Y. Cui, F. La Mantia, A Desalination Battery, *Nano Letters*, 12 (2012) 839-843.
- [115] M.E. Suss, V. Presser, Water Desalination with Energy Storage Electrode Materials, *Joule*, 2 (2018) 10-15.
- [116] D. Xu, W. Wang, M. Zhu, C. Li, Recent Advances in Desalination Battery: An Initial Review, *ACS Applied Materials & Interfaces*, 12 (2020) 57671-57685.
- [117] E. Grygolowicz-Pawlak, M. Sohail, M. Pawlak, B. Neel, A. Shvarev, R. de Marco, E. Bakker, Coulometric Sodium Chloride Removal System with Nafion Membrane for Seawater Sample Treatment, *Analytical Chemistry*, 84 (2012) 6158-6165.
- [118] K.C. Smith, R. Dmello, Na-Ion Desalination (NID) Enabled by Na-Blocking Membranes and Symmetric Na-Intercalation: Porous-Electrode Modeling, *Journal of The Electrochemical Society*, 163 (2016) A530-A539.
- [119] T. Kim, C.A. Gorski, B.E. Logan, Low Energy Desalination Using Battery Electrode Deionization, *Environmental Science & Technology Letters*, 4 (2017) 444-449.
- [120] J.W. Blair, G.W. Murphy, Electrochemical Demineralization of Water with Porous Electrodes of Large Surface Area, in: SALINE WATER CONVERSION, American Chemical Society, 1960, pp. 206-223.
- [121] Z. Liu, X. Shang, H. Li, Y. Liu, A Brief Review on High-Performance Capacitive Deionization Enabled by Intercalation Electrodes, *Global Challenges*, 5 (2021) 2000054.
- [122] J. Lee, S. Kim, C. Kim, J. Yoon, Hybrid capacitive deionization to enhance the desalination performance of capacitive techniques, *Energy & Environmental Science*, 7 (2014) 3683-3689.
- [123] S. Vafakhah, L. Guo, D. Sriramulu, S. Huang, M. Saeedikhani, H.Y. Yang, Efficient Sodium-Ion Intercalation into the Freestanding Prussian Blue/Graphene Aerogel Anode in a Hybrid Capacitive Deionization System, *ACS Applied Materials & Interfaces*, 11 (2019) 5989-5998.
- [124] Z. Liu, W. Ma, H. Li, Elucidating the capacitive desalination behavior of Na_xCoO_2 : the significance of electrochemical pre-activation, *Nanoscale*, 12 (2020) 7586-7594.

- [125] F. Zhou, T. Gao, M. Luo, H. Li, Preferential electrosorption of anions by C/Na0.7MnO₂ asymmetrical electrodes, *Separation and Purification Technology*, 191 (2018) 322-327.
- [126] K. Wang, Y. Liu, Z. Ding, Z. Chen, G. Zhu, X. Xu, T. Lu, L. Pan, Controlled synthesis of NaTi₂(PO₄)₃/Carbon composite derived from Metal-organic-frameworks as highly-efficient electrodes for hybrid capacitive deionization, *Separation and Purification Technology*, 278 (2022) 119565.
- [127] J. Cao, Y. Wang, L. Wang, F. Yu, J. Ma, Na(3)V(2)(PO(4))(3)@C as Faradaic Electrodes in Capacitive Deionization for High-Performance Desalination, *Nano Letters*, 19 (2019) 823-828.
- [128] X. Gao, A. Omosebi, J. Landon, K. Liu, Voltage-Based Stabilization of Microporous Carbon Electrodes for Inverted Capacitive Deionization, *The Journal of Physical Chemistry C*, 122 (2018) 1158-1168.
- [129] S. Porada, G. Feng, M.E. Suss, V. Presser, Capacitive deionization in organic solutions: case study using propylene carbonate, *RSC Advances*, 6 (2016) 5865-5870.
- [130] C. Kim, P. Srimuk, J. Lee, V. Presser, Enhanced desalination via cell voltage extension of membrane capacitive deionization using an aqueous/organic bi-electrolyte, *Desalination*, 443 (2018) 56-61.
- [131] J. Lee, P. Srimuk, S. Carpier, J. Choi, R.L. Zornitta, C. Kim, M. Aslan, V. Presser, Confined Redox Reactions of Iodide in Carbon Nanopores for Fast and Energy-Efficient Desalination of Brackish Water and Seawater, *ChemSusChem*, 11 (2018) 3460-3472.
- [132] R. Narayanan, P.R. Bandaru, High Rate Capacity through Redox Electrolytes Confined in Macroporous Electrodes, *Journal of The Electrochemical Society*, 162 (2014) A86-A91.
- [133] P.R. Bandaru, H. Yamada, R. Narayanan, M. Hoefer, Charge transfer and storage in nanostructures, *Materials Science and Engineering: R: Reports*, 96 (2015) 1-69.
- [134] B. Akinwolemiwa, C. Peng, G.Z. Chen, Redox Electrolytes in Supercapacitors, *Journal of The Electrochemical Society*, 162 (2015) A5054-A5059.
- [135] E. Frackowiak, M. Meller, J. Menzel, D. Gastol, K. Fic, Redox-active electrolyte for supercapacitor application, *Faraday Discuss*, 172 (2014) 179-198.
- [136] L.-Q. Mai, A. Minhas-Khan, X. Tian, K.M. Hercule, Y.-L. Zhao, X. Lin, X. Xu, Synergistic interaction between redox-active electrolyte and binder-free functionalized carbon for ultrahigh supercapacitor performance, *Nature Communications*, 4 (2013) 2923.
- [137] F. Pan, Q. Wang, Redox Species of Redox Flow Batteries: A Review, *Molecules*, 20 (2015) 20499-20517.
- [138] J. Lee, P. Srimuk, R.L. Zornitta, M. Aslan, B.L. Mehdi, V. Presser, High Electrochemical Seawater Desalination Performance Enabled by an Iodide Redox Electrolyte Paired with a Sodium Superionic Conductor, *ACS Sustainable Chemistry & Engineering*, 7 (2019) 10132-10142.
- [139] X. Cao, X. Huang, P. Liang, K. Xiao, Y. Zhou, X. Zhang, B.E. Logan, A New Method for Water Desalination Using Microbial Desalination Cells, *Environmental Science & Technology*, 43 (2009) 7148-7152.
- [140] Y. Kim, B.E. Logan, Microbial desalination cells for energy production and desalination, *Desalination*, 308 (2013) 122-130.
- [141] Z. Borjas, A. Esteve-Núñez, J.M. Ortiz, Strategies for merging microbial fuel cell technologies in water desalination processes: Start-up protocol and desalination efficiency assessment, *Journal of Power Sources*, 356 (2017) 519-528.
- [142] Q. Ping, B. Cohen, C. Dosoretz, Z. He, Long-term investigation of fouling of cation and anion exchange membranes in microbial desalination cells, *Desalination*, 325 (2013) 48-55.
- [143] K.S. Jacobson, D.M. Drew, Z. He, Efficient salt removal in a continuously operated upflow microbial desalination cell with an air cathode, *Bioresource Technology*, 102 (2011) 376-380.
- [144] M. Mehanna, T. Saito, J. Yan, M. Hickner, X. Cao, X. Huang, B.E. Logan, Using microbial desalination cells to reduce water salinity prior to reverse osmosis, *Energy & Environmental Science*, 3 (2010) 1114-1120.
- [145] X. Chen, X. Xia, P. Liang, X. Cao, H. Sun, X. Huang, Stacked microbial desalination cells to enhance water desalination efficiency, *Environmental Science & Technology*, 45 (2011) 2465-2470.

- [146] Y. Kim, B.E. Logan, Series assembly of microbial desalination cells containing stacked electrodialysis cells for partial or complete seawater desalination, *Environmental Science & Technology*, 45 (2011) 5840-5845.
- [147] Z. Ge, C.G. Dosoretz, Z. He, Effects of number of cell pairs on the performance of microbial desalination cells, *Desalination*, 341 (2014) 101-106.
- [148] K. Zuo, J. Cai, S. Liang, S. Wu, C. Zhang, P. Liang, X. Huang, A ten liter stacked microbial desalination cell packed with mixed ion-exchange resins for secondary effluent desalination, *Environmental Science & Technology*, 48 (2014) 9917-9924.
- [149] F. Zhang, Z. He, Scaling up microbial desalination cell system with a post-aerobic process for simultaneous wastewater treatment and seawater desalination, *Desalination*, 360 (2015) 28-34.
- [150] Y. Liang, H. Feng, D. Shen, N. Li, Y. Long, Y. Zhou, Y. Gu, X. Ying, Q. Dai, A high-performance photo-microbial desalination cell, *Electrochimica Acta*, 202 (2016) 197-202.
- [151] S. Kim, G. Piao, D.S. Han, H.K. Shon, H. Park, Solar desalination coupled with water remediation and molecular hydrogen production: a novel solar water-energy nexus, *Energy & Environmental Science*, 11 (2018) 344-353.
- [152] F. Chen, R. Karthick, Q. Zhang, J. Wang, M. Liang, J. Dai, X. Jiang, Y. Jiang, Exploration of a photo-redox desalination generator, *Journal of Materials Chemistry A*, 7 (2019) 20169-20175.
- [153] S. Abu Khalla, M.E. Suss, Desalination via chemical energy: An electrodialysis cell driven by spontaneous electrode reactions, *Desalination*, 467 (2019) 257-262.
- [154] D. Desai, E.S. Beh, S. Sahu, V. Vedharathinam, Q. van Overmeere, C.F. de Lannoy, A.P. Jose, A.R. Völkel, J.B. Rivest, Electrochemical Desalination of Seawater and Hypersaline Brines with Coupled Electricity Storage, *ACS Energy Letters*, 3 (2018) 375-379.
- [155] P. Srimuk, L. Wang, Ö. Budak, V. Presser, High-performance ion removal via zinc-air desalination, *Electrochemistry Communications*, 115 (2020) 106713.
- [156] Y. Zhang, L. Wang, V. Presser, Electrocatalytic fuel cell desalination for continuous energy and freshwater generation, *Cell Reports Physical Science*, 2 (2021) 100416.
- [157] Z.M. Bhat, D. Pandit, S. Ardo, R. Thimmappa, A.R. Kottaichamy, N. Christudas Dargily, M.C. Devendrachari, M. Ottakam Thotiyil, An Electrochemical Neutralization Cell for Spontaneous Water Desalination, *Joule*, 4 (2020) 1730-1742.
- [158] I. Atlas, S. Abu Khalla, M.E. Suss, Thermodynamic Energy Efficiency of Electrochemical Systems Performing Simultaneous Water Desalination and Electricity Generation, *Journal of The Electrochemical Society*, 167 (2020) 134517.
- [159] M.E. Suss, Y. Zhang, I. Atlas, Y. Gendel, E.B. Ruck, V. Presser, Emerging, hydrogen-driven electrochemical water purification, *Electrochemistry Communications*, (2022) 107211.
- [160] I. Atlas, S. Abu Khalla, M.E. Suss, Thermodynamic Energy Efficiency of Electrochemical Systems Performing Simultaneous Water Desalination and Electricity Generation, *Journal of The Electrochemical Society*, 167 (2020) 134517.
- [161] W. Schmickler, *Electrochemical Theory: Double Layer*, in: Reference Module in Chemistry, Molecular Sciences and Chemical Engineering, Elsevier, 2014.
- [162] L. Ma, L. Huang, Y. Xu, C. Liu, F. Wang, H. Xing, S. Ma, Dynamics and Model Research on the Electrosorption by Activated Carbon Fiber Electrodes, *Water*, 13 (2021) 62.
- [163] T.B. Kinraide, Use of a Gouy-Chapman-Stern Model for Membrane-Surface Electrical Potential to Interpret Some Features of Mineral Rhizotoxicity, *Plant Physiology*, 106 (1994) 1583-1592.
- [164] P.M. Biesheuvel, Y. Fu, M.Z. Bazant, Diffuse charge and Faradaic reactions in porous electrodes, *Physical Review E: Statistical, Nonlinear, and Soft Matter Physics*, 83 (2011) 061507.
- [165] T. Teorell, Transport Processes and Electrical Phenomena in Ionic Membranes, *Progress in Biophysics and Biophysical Chemistry*, 3 (1953) 305-369.
- [166] P.M. Biesheuvel, R. Zhao, S. Porada, A. van der Wal, Theory of membrane capacitive deionization including the effect of the electrode pore space, *Journal of Colloid and Interface Science*, 360 (2011) 239-248.
- [167] A. Levy, J.P. de Souza, M.Z. Bazant, Breakdown of electroneutrality in nanopores, *Journal of Colloid and Interface Science*, 579 (2020) 162-176.

- [168] E. Partheniades, Forces between Clay Particles and the Process of Flocculation, in: E. Partheniades (Ed.) Cohesive Sediments in Open Channels, Butterworth-Heinemann, Boston, 2009, pp. 47-88.
- [169] C. Prehal, C. Koczwara, N. Jäckel, A. Schreiber, M. Burian, H. Amenitsch, M.A. Hartmann, V. Presser, O. Paris, Quantification of ion confinement and desolvation in nanoporous carbon supercapacitors with modelling and in situ X-ray scattering, *Nature Energy*, 2 (2017) 16215.
- [170] C. Prehal, D. Weingarth, E. Perre, R.T. Lechner, H. Amenitsch, O. Paris, V. Presser, Tracking the structural arrangement of ions in carbon supercapacitor nanopores using in situ small-angle X-ray scattering, *Energy & Environmental Science*, 8 (2015) 1725-1735.
- [171] C. Merlet, C. Pean, B. Rotenberg, P.A. Madden, B. Daffos, P.L. Taberna, P. Simon, M. Salanne, Highly confined ions store charge more efficiently in supercapacitors, *Nature Communications*, 4 (2013) 2701.
- [172] S. Kondrat, A. Kornyshev, Corrigendum: Superionic state in double-layer capacitors with nanoporous electrodes, *Journal of Physics: Condensed Matter*, 25 (2013) 119501.
- [173] R. Zhao, M. van Soestbergen, H.H.M. Rijnaarts, A. van der Wal, M.Z. Bazant, P.M. Biesheuvel, Time-dependent ion selectivity in capacitive charging of porous electrodes, *Journal of Colloid and Interface Science*, 384 (2012) 38-44.
- [174] J.E. Dykstra, J. Dijkstra, A. van der Wal, H.V.M. Hamelers, S. Porada, On-line method to study dynamics of ion adsorption from mixtures of salts in capacitive deionization, *Desalination*, 390 (2016) 47-52.
- [175] M.E. Suss, Size-based ion selectivity of micropore electric double layers in capacitive deionization electrodes, *Journal of the Electrochemical Society*, 164 (2017) E270-E275.
- [176] C.H. Hou, P. Taboada-Serrano, S. Yiacoumi, C. Tsouris, Electrosorption selectivity of ions from mixtures of electrolytes inside nanopores, *Journal of Chemical Physics*, 129 (2008) 224703.
- [177] C. Zhan, F. Aydin, E. Schwegler, A. Noy, T.A. Pham, Understanding Cation Selectivity in Carbon Nanopores with Hybrid First-Principles/Continuum Simulations: Implications for Water Desalination and Separation Technologies, *ACS Applied Nano Materials*, 3 (2020) 9740-9748.
- [178] B. Corry, Mechanisms of selective ion transport and salt rejection in carbon nanostructures, *MRS Bulletin*, 42 (2017) 306-310.
- [179] L. Eliad, G. Salitra, A. Soffer, D. Aurbach, Ion sieving effects in the electrical double layer of porous carbon electrodes: Estimating effective ion size in electrolytic solutions, *The Journal of Physical Chemistry B*, 105 (2001) 6880-6887.
- [180] J. Segalini, E. Iwama, P.-L. Taberna, Y. Gogotsi, P. Simon, Steric effects in adsorption of ions from mixed electrolytes into microporous carbon, *Electrochemistry Communications*, 15 (2012) 63-65.
- [181] S.A. Hawks, M.R. Ceron, D.I. Oyarzun, T.A. Pham, C. Zhan, C.K. Loeb, D. Mew, A. Deinhart, B.C. Wood, J.G. Santiago, M. Stadermann, P.G. Campbell, Using ultramicroporous carbon for the selective removal of nitrate with capacitive deionization, *Environmental Science & Technology*, 53 (2019) 10863-10870.
- [182] X. Zhang, K. Zuo, X. Zhang, C. Zhang, P. Liang, Selective ion separation by capacitive deionization (CDI) based technologies: a state-of-the-art review, *Environmental Science: Water Research & Technology*, 6 (2020) 243-257.
- [183] J.M. Dickhout, J. Moreno, P.M. Biesheuvel, L. Boels, W.M. de Vos, R.G.H. Lammertink, Produced water treatment by membranes: A review from a colloidal perspective, *Journal of Colloid and Interface Science*, 487 (2017) 523-534.
- [184] K. Zuo, J. Kim, A. Jain, T. Wang, R. Verduzco, M. Long, Q. Li, Novel composite electrodes for selective removal of sulfate by the capacitive deionization process, *Environmental Science & Technology*, 52 (2018) 9486-9494.
- [185] J. Kim, A. Jain, K. Zuo, R. Verduzco, S. Walker, M. Elimelech, Z. Zhang, X. Zhang, Q. Li, Removal of calcium ions from water by selective electrosorption using target-ion specific nanocomposite electrode, *Water Research*, 160 (2019) 445-453.
- [186] E.N. Guyes, T. Malka, M.E. Suss, Enhancing the ion-size-based selectivity of capacitive deionization electrodes, *Environmental Science & Technology*, 53 (2019) 8447-8454.

- [187] Z.Y. Leong, H.Y. Yang, Capacitive deionization of divalent cations for water softening using functionalized carbon electrodes, *ACS Omega*, 5 (2020) 2097-2106.
- [188] D.I. Oyarzun, A. Hemmatifar, J.W. Palko, M. Stadermann, J.G. Santiago, Ion selectivity in capacitive deionization with functionalized electrode: Theory and experimental validation, *Water Research X*, 1 (2018) 100008.
- [189] P. Liu, T. Yan, J. Zhang, L. Shi, D. Zhang, Separation and recovery of heavy metal ions and salt ions from wastewater by 3D graphene-based asymmetric electrodes via capacitive deionization, *Journal of Materials Chemistry A*, 5 (2017) 14748-14757.
- [190] Y. Zhang, J. Peng, G. Feng, V. Presser, Hydration shell energy barrier differences of sub-nanometer carbon pores enable ion sieving and selective ion removal, *Chemical Engineering Journal*, 419 (2021) 129438.
- [191] R.K. Kalluri, M.M. Biener, M.E. Suss, M.D. Merrill, M. Stadermann, J.G. Santiago, T.F. Baumann, J. Biener, A. Striolo, Unraveling the potential and pore-size dependent capacitance of slit-shaped graphitic carbon pores in aqueous electrolytes, *Physical Chemistry Chemical Physics*, 15 (2013) 2309-2320.
- [192] D.R. Lide, *CRC handbook of chemistry and physics*, CRC press, 2004.
- [193] Y. Zhang, P. Srimuk, S. Husmann, M. Chen, G. Feng, V. Presser, Effect of pore size on the ion electrosorption and hydrogen/deuterium electrosorption using sodium chloride in H₂O and D₂O, *Journal of The Electrochemical Society*, 166 (2019) A4158-A4167.
- [194] Y. Zhang, P. Ren, Y. Liu, V. Presser, Particle size distribution influence on capacitive deionization: Insights for electrode preparation, *Desalination*, 525 (2022) 115503.
- [195] J. Piwek, A. Platek-Mielczarek, E. Frackowiak, K. Fic, Enhancing capacitor lifetime by alternate constant polarization, *Journal of Power Sources*, 506 (2021) 230131.
- [196] M.D. Merrill, E. Montalvo, P.G. Campbell, Y.M. Wang, M. Stadermann, T.F. Baumann, J. Biener, M.A. Worsley, Optimizing supercapacitor electrode density: achieving the energy of organic electrolytes with the power of aqueous electrolytes, *RSC Advances*, 4 (2014) 42942-42946.
- [197] X. Shen, Y. Xiong, R. Hai, F. Yu, J. Ma, All-MXene-Based Integrated Membrane Electrode Constructed using Ti₃C₂Tx as an Intercalating Agent for High-Performance Desalination, *Environmental Science & Technology*, 54 (2020) 4554-4563.
- [198] I. Staffell, D. Scamman, A. Velazquez Abad, P. Balcombe, P.E. Dodds, P. Ekins, N. Shah, K.R. Ward, The role of hydrogen and fuel cells in the global energy system, *Energy & Environmental Science*, 12 (2019) 463-491.
- [199] N.P. Brandon, Z. Kurban, Clean energy and the hydrogen economy, *Philosophical Transactions of the Royal Society A Mathematical, Physical and Engineering Sciences*, 375 (2017) 20160400 .
- [200] U. Groos, D. Gerteisen, Micro Fuel Cells, in: *Fuel Cell Science and Engineering*, pp. 131-145.
- [201] X. Feng, N. Dementev, W. Feng, R. Vidic, E. Borguet, Detection of low concentration oxygen containing functional groups on activated carbon fiber surfaces through fluorescent labeling, *Carbon*, 44 (2006) 1203-1209.
- [202] B. Karamanova, A. Stoyanova, M. Shipochka, C. Girginov, R. Stoyanova, On the cycling stability of biomass-derived carbons as electrodes in supercapacitors, *Journal of Alloys and Compounds*, 803 (2019) 882-890.

Curriculum Vitae

Personal Information

Name	Yuan Zhang
Address	Kaiserstraße 25, 66111, Saarbrücken, Germany
Phone	+49 176 27696377
E-Mail	zhangyuand517@gmail.com
Date of birth / -Place	11,09,1990, China



Research and relevant activities

June. 2019 – 2020

MXene-CDI (PR-1173/11) DFG project

- Aqueous electrochemistry of MXenes
- Electrochemical desalination with MXene
- Data analysis and mechanism studies

June. 2021 – now

Lithium-recovery from mine water project (RAG-Stiftung)

- Cation-specific electrosorption studies
- Ion-selectivity quantification via online ICP-OES
- Material synthesis and characterization
- Data analysis and mechanism studies

Teaching activities

Winter term. 2019/2020

Lab Praktikum ENTV, Universität des Saarlandes

Cyclic voltammetry, galvanostatic cycling with the potential limitation

Summer term.
2020

Lab Protocol NBM-P, Universität des Saarlandes

Electrochemical energy storage

Apr. 2020 – Dec. 2020

Mentoring Master Student

Study ion-exchange membrane coating technique for membrane capacitive deionization applications

Jan. 2021 – Jul. 2021

Master student thesis

- *Title: Influence of materials and operation parameters on the performance of capacitive deionization with nanoporous carbon*

Poster Presentation

Nov. 2019

Ph.D. Student Day of Saarland University, Saarbrücken (Germany)

- *Electrochemical stability of sodium chloride in H₂O and D₂O in nanoporous carbon electrodes*

Oral Presentations

Sep. 2019

7th German-Japanese Symposium on the Development and Technology of Carbon Materials, Würzburg.

- *Title: Electrochemical stability of sodium chloride in H₂O and D₂O in nanoporous carbon electrodes. Nanoporous carbon electrodes.*

Apr. 2021

29th Topical ISE Meeting, online (due to COVID-19)

- *Title: Sub-nanometer carbon confinement: pore size effect on ion permselectivity and selectivity*

Education

Jun. 2018 - now

Ph.D. student

Leibniz Institute für neue Materialien
Universität des Saarlandes, Germany

- *Explore new materials for electrochemical water desalination*
- *Study materials for selective ion removal*
- *Research and development of the electrocatalytic water desalination techniques*

Aug. 2017 – Apr. 2018

Hiwi student

Helmholz Institute Ulm, Germany

- *Electrochemical study of Mg deposition applying in-situ EQCM characterization*
- *Nanoporous V₂O₅ synthesis for Li-ion battery application*

Oct. 2014 – Apr. 2017

Master of Science

Universität Ulm, Germany
Energy Science and Technology program

- *Electrochemical study of Li deposition applying in-situ EQCM characterization*

Sep. 2010 – Jun. 2014

Bachelor of Engineering

Central South University, School of thermal energy and engineering, Changsha, China

- *Development of configuration software and automation of the energy system for electrolytic aluminum production*

Scientific qualifications and expertise

Characterization skills

Gas sorption analysis, online ICP-OES, thermogravimetric analysis, in-situ dilatometry, in-situ EQCM, scanning electron microscopy, X-ray diffraction, Raman spectroscopy, and electrochemical characterization techniques

Language skills

English

Fluent (C1)

German

Intermediate (B1)

Mandarin

Mother language (C2)